

AD612766

FUEL CELL

RESEARCH & DEVELOPMENT

DDC AVAILABILITY NOTICE

Qualified requestors may obtain copies of this report from DDC. This report may be released to OTR.

HYDROCARBON - AIR FUEL CELLS

Semi-Annual
Technical Summary Report No. 6
1 July 1964 - 31 December 1964

COPY <u>2</u> OF <u>3</u> <i>final</i>	
HARD COPY	\$. 7.00
MICROFICHE	\$. 1.75

354p

ARPA ORDER: Number 247

CONTRACTS: Number DA44-009-ENG-4909

Number DA44-009-AMC-479(T)

ARCHIVE COPY

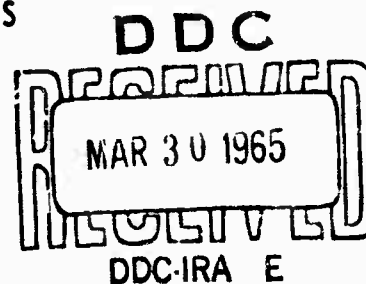
THE VIEWS CONTAINED HEREIN REPRESENT
ONLY THE VIEW OF THE PREPARING AGENCY
AND HAVE NOT BEEN APPROVED BY THE
DEPARTMENT OF THE ARMY.

U.S. ARMY
ENGINEER RESEARCH AND DEVELOPMENT LABORATORIES
FT. BELVOIR, VIRGINIA

DIRECT ENERGY CONVERSION OPERATION

GENERAL  ELECTRIC

950 WESTERN AVE., LYNN, MASS.



DISCLAIMER NOTICE

THIS DOCUMENT IS THE BEST
QUALITY AVAILABLE.

COPY FURNISHED CONTAINED
A SIGNIFICANT NUMBER OF
PAGES WHICH DO NOT
REPRODUCE LEGIBLY.

No DDC limit.

FUEL CELL

RESEARCH & DEVELOPMENT

HYDROCARBON - AIR FUEL CELLS

Semi-Annual
Technical Summary Report No.6
1 July 1964 - 31 December 1964

ARPA ORDER: Number 247
CONTRACTS: Number DA44-009-ENG-4909
Number DA44-009-AMC-479(T)

U.S. ARMY
ENGINEER RESEARCH AND DEVELOPMENT LABORATORIES
FT. BELVIER, VIRGINIA

DIRECT ENERGY CONVERSION OPERATION

GENERAL  ELECTRIC

950 WESTERN AVE., LYNN, MASS.

1.0 FOREWORD

This is Technical Summary Report Number 6 of a research program conducted by the General Electric Company under contract with the U.S. Army Engineer Research and Development Laboratories. The purpose of this program is to investigate Hydrocarbon-Air Fuel cells for military applications. This program continues the research effort on the direct oxidation of hydrocarbon fuels first undertaken by General Electric in November, 1960 under contract DA 44-009-ENG-3771. Investigation has continued under contracts DA 44-009-ENG-4853, DA 44-009-ENG-4909 and DA 44-009-AMC-479(T). This work is conducted at the Company's Research Laboratory in Schenectady, New York and at the Direct Energy Conversion Operation's Fuel Cell Laboratory in Lynn, Massachusetts. Program Management is the responsibility of the Direct Energy Conversion Operation.

These technical summary reports are issued on a semi-annual basis. The technical content is reviewed by ERDL prior to publication. The Contracting Officer's Technical Representative is Dr. Galen Frysinger.

This work is made possible by the support of the Advanced Research Projects Agency (Order No. 247) under Project Lorraine through the U.S. Army Engineer Research and Development Laboratories, Fort Belvoir, Virginia.

2.0 TABLE OF CONTENTS

<u>Section</u>		<u>Page No.</u>
1.0	FOREWORD	i
2.0	TABLE OF CONTENTS	iii
3.0	GENERAL SUMMARY	3-1
3.1	Program Summary	3-1
3.2	Research Status Summary	3-1
3.3	Program Conclusions	3-6
3.4	Personnel	3-9
3.5	Reports and Publications	3-10
4.0	DETAILS OF INVESTIGATION	4-1
4.1	Electrochemical Oxidation of Hydrocarbons	4-1
4.2	Electrocatalyst Research	4-123
4.3	Electrolyte Research	4-168
4.4	Electrode Structure Research	4-191
4.5	Electrochemical Cell Life Testing	4-216
4.6	Studies of Self-Sustaining Operation	4-239
5.0	APPENDIX	5-1
5.1	Electrochemical Oxidation of Hydrocarbons	5-1
5.2	Electrocatalyst Research	5-4
5.3	Electrode Structure Research	5-10
5.4	Summary of Electrochemical Cell Life Testing Data	5-29
5.5	Studies of Self-Sustaining Operation	5-33

BLANK PAGE

3.0 GENERAL SUMMARY

<u>Section</u>		<u>Page No.</u>
3.0	GENERAL SUMMARY	
3.1	Program Summary	3-1
3.2	Research Status Summary	3-1
	3.2.1 Electrochemical Oxidation of Hydrocarbons	3-1
	3.2.2 Electrocatalys. Research	3-4
	3.2.3 Electrolyte Research	3-4
	3.2.4 Electrode Structure Research	3-5
	3.2.5 Electrochemical Cell Life Testing	3-5
	3.2.6 Studies of Self-Sustaining Operation	3-5
3.3	Program Conclusions	3-6
3.4	Personnel	3-9
3.5	Reports and Publications	3-10

3.0 GENERAL SUMMARY

3.1 PROGRAM SUMMARY

The research investigations and results discussed in this report are the continuation of an integrated program directed toward the development of the direct hydrocarbon oxidation-air fuel cell technology. The ultimate objective is to develop a technology which will facilitate the design and fabrication of practical military fuel cell power sources for operation with ambient air and conventional hydrocarbon fuels. Consistent with this objective, practical limitations of fundamental and applied research being considered, maximum emphasis is placed on:

- high performance (e.g. power density and efficiency)
- low cost electrode materials and manufacturing reproducibility
- life and reliability

The discoveries evolving from the various areas of research, in addition to representing significant progress towards understanding fundamental mechanisms of the direct oxidation processes, bring with them the realization that practical hardware considerations cannot be overlooked. Thus, the development and evaluation of electrode structures which incorporate these discoveries is becoming increasingly important.

Of particular significance in this reporting period is the continued progress with the new family of fluoride electrolytes, the demonstration of hydrocarbon oxidation with small quantities of platinum on the boron carbide substrate, the promise of higher performance with platinum alloy electrocatalyst on Teflon-bonded electrode structures, the introduction of a new Teflon structure reinforcing agent to enhance reliability, and an extension of operating life to over 3000 hours with some of the best electrodes.

The principal elements of research together with specific objectives for each are illustrated in Table I for each major category of program research. Subsequent paragraphs contain a summary of the current research effort in each of the major program areas and a compilation of program conclusions. The details of the investigations and supporting appendices are provided in sections 4.0 and 5.0 of this report.

3.2 RESEARCH STATUS SUMMARY

3.2.1 Electrochemical Oxidation of Hydrocarbons

Multipulse potentiodynamic studies of ethane adsorption were conducted on platinum electrodes at elevated temperatures in phosphoric acid. Variations in surface area of the electrode, resulting in poor reproducibility of experimental data, were investigated. For the surface area variations, a "roughness factor" relationship to the reduction of "oxygen" film was identified. Subsequently, studies on ethane were made in perchloric acid at 60°C to determine rates of

TABLE I**Program Work Scope**

Research Activity	Objective
A. ELECTROCHEMICAL OXIDATION OF HYDROCARBONS	
1. Voltametric studies with semi-micro fuel cell electrodes.	To investigate the behavior of fuels on Teflon-bonded platinum black.
2. Chemical analysis combined with voltametry of fuel cell macro-electrodes.	To determine intermediates and side products of the hydrocarbon oxidation reactions.
3. Study of fuel activity in cesium fluoride-hydrofluoric acid (CsF-HF) mixtures.	To evaluate CsF-HF as an electrolyte for hydrocarbons.
4. Oxidation processes at thin electrolyte films.	To determine the influence of mass transport through electrolyte films.
5. Mechanism of ethane oxidation.	To determine the reaction mechanism for ethane in phosphoric acid at 150°C.
B. ELECTROCATALYST RESEARCH	
1. Platinum activated boron carbide and tantalum.	To develop an inexpensive platinum activated substrate electrocatalyst.
2. Catalyst compatibility with CsF-HF.	To determine the range of catalysts suitable for CsF-HF mixtures.
3. Evaluation of alloy catalyst.	To increase activity of platinum black electrocatalyst in phosphoric acid.
C. ELECTROLYTE RESEARCH	
1. Solubility of hydrocarbons, oxygen and air in electrolytes.	To obtain physical property data required to interpret electrolyte behavior.
2. Vapor pressure of fluoride type electrolytes.	Same as above.
D. ELECTRODE STRUCTURE RESEARCH	
1. Development of low cost screens compatible with phosphoric acid.	To greatly reduce cost of screen type electrodes.
2. Developmental electrode structures.	To develop practical electrodes which can be economically fabricated.
3. Failure mechanisms, characterization, and improvement of known electrodes.	To improve structural stability of electrodes to allow longer operating life.

TABLE I (Cont.)

E. STUDIES OF SELF-SUSTAINING OPERATION

- | | |
|---|--|
| 1. Study of $C_3 - C_{10}$ hydrocarbon fuel mixtures. | To determine relative reactivities and fuel utilizations for mixed hydrocarbons in $C_3 - C_{10}$ range. Objective is an electrode with a high fuel utilization of complex mixtures. |
| 2. Automatic self-induced anodic voltage cycling. | To characterize and understand voltage cycling phenomena for various fuels and conditions. |
-

F. ELECTROCHEMICAL CELL LIFE TESTING

- | | |
|---|--|
| 1. Operation of the ten life test stands. | To evaluate long term electrode performance and reliability. |
|---|--|
-

adsorption and of hydrogenation-desorption. Adsorption rates as a function of current density were obtained. The relationship of adsorption and hydrogenation-desorption to fundamental kinetic laws was investigated. Additionally, chemical fractions of the adlayer were studied to give insight on structural details.

Multipulse potentiodynamic techniques are being applied to the study of the behavior of hydrocarbons with semi-micro Teflon-bonded fuel cell electrodes. Particular attention is being given to rates of adsorption and the nature of the species that form on the surface of the electrode. Major attention has so far been focused upon the behavior of ethane with a perchloric acid electrolyte. Some work has also been done with several other hydrocarbon fuels and with hydrofluoric acid as an electrolyte.

Studies have continued on macro-electrodes possessing 10^3 to 10^6 times the hydrogen surface area of the micro and semi-micro electrodes. Periodic gas chromatographic analyses, galvanostatic CO_2 - time profiles and CO_2 - voltage profiles have been determined for propane at $65^\circ C$. Galvanostatic product-time profiles were also obtained during hydrogenation of the partially oxidized surface "propane".

The electrochemical oxidation of propane has been investigated in thin films of concentrated phosphoric solutions at elevated temperatures on electrodeposited platinum type catalyst electrodes. Experiments with hydrophobic electrode surfaces were performed. Resistance measurements in the meniscus and film region have been determined as a function of current distribution and correlated with previous analytical derivations.

The electrochemical oxidation of saturated hydrocarbons in fluoride electrolytes was investigated to determine the effect of electrolyte composition and temperature on propane performance. Multipulse potentiostatic and multipulse potentiodynamic investigations of propane on

platinum in the hydrofluoric azeotrope were initiated. The extents of surface coverage by propane and hydrogen have been measured as a function of propane adsorption time and temperature.

3.2.2 Electrocatalyst Research

Patterns of activity of binary alloys of the noble metals were studied by the methane-deuterium exchange technique. An alloy of ruthenium-iridium, more active than platinum in dehydrogenation at 100°C, is discussed. The adsorption and catalytic decomposition of normal and iso-butane on sintered platinum black was investigated as a function of temperature between 0 and 180°C. A flash desorption apparatus was constructed providing a useful tool to investigate the nature of these carbonaceous materials and the kinetics of their removal under various conditions. Additionally, the degree of dispersion and catalytic activity of platinum supported on boron carbide was investigated by gas phase techniques.

Investigations of platinum activated boron carbide were continued. Fabrication techniques of electrodes utilizing the boron carbide support were improved and delamination problems that existed at elevated temperatures have been overcome. High surface areas of platinum black obtained with the boron carbide support are discussed. Significant hydrocarbon oxidation has been obtained with better than an order of magnitude reduction in the platinum content used in the standard Alford-Niedrach electrode.

Studies of platinum activated tantalum were also continued. High surface area platinum is discussed as a function of tantalum particle size. New milling techniques were developed to facilitate a reduction of tantalum powder particle size. Anode and cathode electrode performance has been determined for alternate platinum loadings.

Electrochemical stability tests of potential electrocatalysts suitable for fluoride electrolytes were started.

3.2.3 Electrolyte Research

Static and dynamic systems were developed for measuring hydrocarbon and oxygen solubilities in hot, concentrated electrolytes. Data was obtained at elevated temperatures for solubilities of oxygen, propane, and octane in phosphoric acid. An all-Teflon equilibration apparatus was constructed for measurement of vapor pressures over corrosive electrolytes at elevated temperatures.

Some of the more important physico-chemical properties of the $\text{CsF-HF-H}_2\text{O}$ and $\text{HF-H}_2\text{O}$ systems were measured. The regions of investigation were usually confined to the composition and temperature ranges of interest for fuel cell and electrochemical work.

3.2.4 Electrode Structure Research

Commercially available metals and alloys were investigated as potential low cost screen materials for Teflon bonded electrodes. The studies were conducted in phosphoric acid at 150°C. The preliminary test results for selecting cathode and anode screen materials suitable for further investigation are presented.

The incorporation of fibrous reinforcing agents in the electrode structure was considered in terms of improving the electrode cracking and leakage problems. Asbestos fibers were chosen for initial studies because of their high strength and acid resistance. The tests were conducted using suitably modified Niedrach-Alford type electrodes.

Developmental electrode effort concentrated on improving the crack resistance and mechanical stability of the Niedrach-Alford electrode. Wetproofing films, pressed films, the addition of asbestos fibers, double layer electrodes, and variations in platinum loading and screen thickness were investigated. Electrode performance was evaluated on hydrogen, propane, oxygen and air.

Porosity, gas permeability and surface area measurements of Niedrach-Alford electrodes were started.

Failure analysis of Niedrach-Alford electrodes was continued. Samples of platinum black were subjected to treatment in 85 percent phosphoric acid at 150°C in the presence of various gases. The resulting reduction in surface area would account for the cracking and shrinkage experienced on electrode samples treated under the same conditions.

3.2.5 Electrochemical Cell Life Testing

Long duration life, water balance control, pulsed performance techniques, and barrier film water vapor suppression tests were performed. The results for over 3280 hours operating life with propane and air, and over 3850 hours life with n-octane and air as reactants, all utilizing phosphoric electrolytes, are discussed. Constant boiling hydrofluoric acid as a fuel cell electrolyte was evaluated on propane, hexane and octane (liquid) at 223°F.

3.2.6 Studies of Self-Sustaining Operation

A semi-empirical relationship has been derived to describe anodic over-voltage as a function of cell current and limiting current for pure and binary fuels. A computer program was used to obtain coefficients for this relationship, and to study their variance with fuel composition. Similarly, the limiting current can be predicted from the fuel composition.

Pure octane has been found to completely oxidize electrochemically in the phosphoric acid cell. Binary mixtures of hexane and octane show a general correlation between the current supplied by the hexane and the concentration of hexane in the cell, but no correlation for the octane.

A test system has been built to determine the behavior of non-vaporizing fuels over a broad range of flow parameters in a variable geometry, transparent anode chamber.

3.3 PROGRAM CONCLUSIONS

3.3.1 Multipulse potentiodynamic data on smooth platinum anodes suggests that "adsorbed ethane" consists of partially oxygenated and partially dehydrogenated species with adsorbed ethyl radicals as a common intermediary. Similar data on Teflon-bonded electrodes suggest that the adsorption processes on the fuel cell anode are at least qualitatively similar to those on smooth platinum.

3.3.2 The oxidation of propane on partially immersed platinum black electrodes occurs mainly in the upper meniscus and thin film region of the electrode surface. Furthermore, a simulated "wetproof" Teflon platinum-ruthenium-black structure exhibits much higher current than electrodes prepared in a similar manner without the addition of a wetproofing agent.

3.3.3 Fuel cell systems with hydrogen fluoride and cesium fluoride electrolyte compositions continue to show promise for high performance hydrocarbon oxidation. Performance equal to 75 watts/ft² (IR free) have been demonstrated on propane and oxygen at 150°C with the most optimum CsF-HF composition to date, compared with 55 watts/ft² (IR free) in phosphoric acid with the same fuels and operating temperature.

3.3.4 The higher performance demonstrated on a Teflon-bonded electrode with platinum-ruthenium alloy catalyst compared with an identical electrode with pure platinum catalyst is consistent with catalytic activity of just the electrocatalyst as measured by the methane-deuterium exchange techniques.

3.3.5 Metallic dispersions up to 149 square meters per gram can be obtained for platinum (Pt particle sizes as small as 16 angstroms) supported on boron carbide. The effectiveness of platinum per unit weight being increased by an order of magnitude, potential fuel cell material cost reductions are significant.

3.3.6 Tantalum is less attractive as a diluent or support for platinum than is boron carbide.

3.3.7 Potentiostatic corrosion tests in the $\text{HF-H}_2\text{O}$ azeotrope at temperatures up to 110°C have shown that platinum-gold, and 80% gold-20% palladium alloy have the stability, over the potential range of 0.0 to 0.2 volts vs. reversible hydrogen, necessary to be a potential electrocatalyst in hydrogen fluoride electrolyte compositions.

3.3.8 Newly developed, dynamic test equipment utilizing a rotating disc is effective for making oxidant and hydrocarbon fuel solubility determinations in phosphoric acid at room and elevated temperatures. The solubilities of propane and oxygen in concentrated phosphoric acid at 25°C have been shown to be $1/8$ and $1/5$ respectively of their values in water, and from 25°C to 170°C remain relatively insensitive to temperature.

3.3.9 Asbestos as a structural reinforcement agent for Teflon in bonded electrodes indicates resistance to electrode cracking can be improved. In initial testing, after more than 100 hours in identical fuel cell environments, electrodes reinforced with asbestos showed no physical or performance degradation while standard Teflon-bonded electrodes displayed the usual crack growth pattern.

3.3.10 Investigations of potentially low-cost screen materials, established that corrosion rates at anode potentials were less than one mil per year for commercial tungsten screen and 93% tungsten-7% nickel alloy in 88% phosphoric acid at 150°C . At cathode potentials, no materials have been found with the corrosion resistance of tantalum.

3.3.11 In cell life testing, performance in excess of 10 watts per square foot has been achieved on fuel cells with propane and air after 3000 hours life. Performance between 8 and 10 watts per square foot has been achieved on fuel cells with better than 1000 hours life for iso-octane-air and decane-air fuels.

3.3.12 Cycling (periodic fluctuation of electrical output) has been observed on all hydrocarbon/air fuel cells using phosphoric acid as the electrolyte. Typically, anode polarizations have been observed to cycle in a matter of seconds from a nominal 0.55 volts up to 0.75 volts and down to 0.35 volts, subsequently returning to the nominal polarization voltage. The time interval between cycles is dependent upon operating conditions and fuel composition. Again, typically varying from hundreds of hours between cycles to a few minutes between cycles for propane and hexane respectively. The same phenomena has not been exhibited for cells that were operated with azeotropic aqueous hydrofluoric acid electrolyte and with propane, n-hexane, and n-octane as fuels.

3.3.13 Binary mixtures of hexane and octane show that the current supplied by the hexane is proportional to the concentration of hexane and to the square root of the total cell current. No such correlation is evident for the current supplied by the octane.

PERSONNEL

Program Manager - E. R. White (Direct Energy Conversion Operation, Lynn, Mass.)
Research Laboratory, Schenectady, N.Y.

Supervision - Dr. H.A. Liebhafsky

Dr. W.T. Grubb*
Dr. L.W. Niedrach*
Mr. M.E. Lazarus
Mr. I.B. Weinstock
Mr. M. Tochner
Dr. E.J. Cairns*
Dr. J. Paynter*
Mr. A.M. Breitenstein
Mr. L.D. Sangermano
Dr. S. Gilman*
Dr. D.W. McKee*
Mr. H.I. Zelig
Mr. R.M. Hadsell
Mr. J.G. Lucas
Mr. E.J. McNerny

Fuel Cell Laboratory, Lynn, Mass.

Supervision - Dr. E. A. Oster

Mr. J. M. Amore
Mr. P. J. Chludzinski*
Dr. M. W. Gloor*
Mr. J. H. Huss
Mr. R. E. Kegan*
Mr. A. Kuchar
Mr. J. Lennon*
Mr. D. I. MacDonald*
Dr. H. J. R. Maget*
Dr. P. V. Popat*
Mr. R. J. Roethlein*
Dr. E. Y. Weissman*
Mr. H. J. Young

* Principal Investigators

3.5 REPORTS AND PUBLICATIONS

3.5.1 Previous Reports

Semi-Annual Technical Summary Report No. 5

1 January 1964 - 30 June 1964

Contracts DA 44-009-ENG-4909

DA 44-009-AMC-479 (T)

3.5.2 Publications

3.5.2.1 Papers

a) Studies of Anion Adsorption on Platinum by the Multipulse Potentiodynamic (MPP) Method. I. Kinetics of Chloride and Phosphate Adsorption and Associated Charge at Constant Potential, S. Gilman, J. Phys. Chem. 68, 2098 (1964).

b) Studies of Anion Adsorption on Platinum by the Multipulse Potentiodynamic (MPP) Method. II. Chloride and Phosphate Desorption and Equilibrium Surface Concentrations at Constant Potential, S. Gilman, J. Phys. Chem. 68, 2112 (1964)

c) Measurement of Hydrogen Adsorption by the Multipulse Potentiodynamic (MPP) Method, S. Gilman, J. Electroanalytical Chem., 7, 382-391 (1964).

d) Electrochemical Surface Oxidation of Platinum, S. Gilman, Electrochim. Acta 9, 1025 (1964).

e) Nature, S. Gilman, Sept. 12, 1964, p. 1130

f) A Methanol Fuel Cell with an Invariant Alkaline Electrolyte, E.J. Cairns and D.C. Bartosik, J. Electrochem. Soc., 111, 1205 (1964).

g) CHO Gas Phase Compositions in Equilibrium with Carbon and Carbon Deposition Boundaries at One Atmosphere, E.J. Cairns and A.D. Tevebaugh, J. Chem. Eng. Data, 9, 453 (1964).

h) An Electrolysis Cell for the Laboratory Scale Preparation of Aqueous Cesium Hydroxide Solutions, E. L. Simons, E. J. Cairns and L. D. Sangermano, *Electrochem. Tech.*, 2 (Nov. - Dec., 1964).

i) Galvanostatic and Volumetric Studies of Hydrocarbons Adsorbed on Fuel Cell Anodes, L. W. Niedrach, *J. Electrochem. Soc.*, 111, 1309 (1964).

j) A New High Performance Fuel Cell Employing Conducting Porous Teflon Electrodes and Liquid Electrolytes, L. W. Niedrach and H. R. Alford, *J. Electrochem. Soc.*, In press.

k) A High Performance Propane Fuel Cell Operating in the Temperature Range of 150-200°C, W. T. Grubb and C. J. Michalske, *J. Electrochem. Soc.*, 111, 1015 (1964).

l) On the Reactions of Propane at the Surface of a Working Fuel Cell Anode, W. T. Grubb, *J. Electrochem. Soc.* 111, 1086 (1964).

m) Hydrocarbon-Phosphoric Acid Fuel Cells, the Effect of Fuel Structure on Performance, W. T. Grubb and C. J. Michalske, *Proc. 18th Annual Power Sources Conference*, Atlantic City, N. J., May, 1964, p. 17.

n) Catalytic Activity of Platinum Black III. Adsorption and Decomposition of Butanes, D. W. McKee, Submitted to *J. A. C. S.*

o) Methane-Deuterium Exchange on Platinum-Rhodium Alloys, D. W. McKee and F. J. Norton, *J. Catalysis*, 4, 000 (1964), In press.

3.5.2.2 Talks

a) E. J. Cairns and G. J. Holm, Hydrocarbon Fuel Cells with Aqueous Cesium Salt Electrolytes, *Electrochemical Society Meeting*, Washington, D. C., October 11-15, 1964.

b) E. J. Cairns, Interrupter Techniques for Fuel Cell Investigation, *Interagency Power Group Meeting*, Ft. Belvoir, Va., October 16, 1964.

c) L. W. Niedrach and H. R. Alford, A New High Performance Fuel Cell Employing Conducting Porous Teflon Electrodes and Liquid Electrolytes, presented at the *Washington Meeting of the Electrochemical Society*, October, 1964.

d) W.T. Grubb and L.W. Niedrach, Hydrocarbon Fuel Electrodes - A Review of the Literature presented at the Washington Meeting of the Electrochemical Society, October, 1964.

e) Studies of Hydrocarbon Electrode Processes by the Multipulse Potentiodynamic (MPP) Method. I. Adsorption of Ethane on Platinum, S. Gilman, Meeting of the Electrochemical Society, Washington, D.C., October, 1964.

f) S. Gilman, Anion Adsorption by the MPP Method, Spring Meeting of the Electrochemical Society, Toronto, 1964.

4.0 DETAILS OF INVESTIGATION

<u>Section</u>		<u>Page No.</u>
4.0	DETAILS OF INVESTIGATION	4-1
4.1	Electrochemical Oxidation of Hydrocarbons	4-1
4.1.1	Anode Studies	4-1
4.1.2	Semi-Micro Fuel Cells	4-53
4.1.3	Studies of Hydrocarbon Macro Anodes	4-71
4.1.4	Thin Film Mass Transport Processes	4-80
4.1.5	Hydrofluoric Acid Electrolytes	4-90
4.1.6	Research Support for Development	4-121
4.2	Electrocatalyst Research	4-123
4.2.1	Exchange and Adsorption Studies	4-123
4.2.2	Platinum Activated Boron Carbide	4-143
4.2.3	Platinum Activated Tantalum	4-158
4.2.4	Stability of Electrocatalysts in Fluoride Electrolytes	4-162
4.2.5	Evaluation of Alloy Electrocatalysis	4-166
4.3	Electrolyte Research	4-168
4.3.1	Solubility Measurements	4-168
4.3.2	Physicochemical Properties of the CsF-HF-H ₂ O Electrolyte Systems	4-178
4.4	Electrode Structure Research	4-191
4.4.1	Low Cost Screen Materials	4-191
4.4.2	Asbestos as a Reinforcing Agent	4-195
4.4.3	Developmental Structures	4-201
4.4.4	Electrode Characterization	4-208
4.4.5	Failure Analysis	4-213
4.5	Electrochemical Cell Life Testing	4-216
4.5.1	Phosphoric Acid	4-216
4.5.2	Hydrofluoric Acid	4-234
4.6	Studies of Self-Sustaining Operation	4-239
4.6.1	Reactivities and Fuel Utilization	4-239
4.6.2	Transport Rates	4-251

LIST OF FIGURES

<u>Figure</u>	<u>List</u>	<u>Page No.</u>
1	Multipulse Potentiodynamic Equipment	4-3
2	Potential Sequences Used in This Work	4-4
3	"Oxygen Adsorption" Traces Recorded Initially (Trace 1) and After "Roughening" the Surface by Pulsing (Traces 2 and 3)	4-5
4	Potential Sequences Applied to the Test Electrode. (Time axis not to scale.)	4-13
5	Current-time (potential) Traces Obtained in Ethane-saturated Solution (Sequence I, Table III, with $U = 0.4$ v).	4-15
6	Dependence of "Ethane Adsorption Charge" upon Speed of the Linear Anodic Sweep.	4-16
7	Current-time (potential) Traces Obtained for Varying Adsorption Times at Constant Potential (Sequence I, Table III, $v = 10$ v./sec).	4-18
8	Semilogarithmic Representation of Ethane Adsorption Data. The Symbol "I" gives the Average Value and Average Deviation of that Value in Regions where Data Points Overlap Extensively	4-19
9	"Ethane Adsorption Charge" after 100 sec. at Fixed Potential for a Saturated Solution of Ethane	4-20
10	Charge Corresponding to Ethane Adsorption for Solutions Saturated with Ethane-Argon Mixtures of Various Compositions (small adsorption times)	4-20
11	Charge Corresponding to Ethane Adsorption for Solutions Saturated with Ethane-Argon Mixtures of Various Compositions (large adsorption times)	4-21
12	Hydrogen Co-deposition Traces Obtained in Ethane-Saturated Solution (Sequence II, Table III, with $U = 0.4$ v., $v = 50$ v./sec.)	4-22
13	Effect of Ethane Adsorption on Hydrogen Adsorption. ΔQ_{S_H} is the Reduction in Charge Corresponding to "Saturation Coverage" with Hydrogen. ΔQ_H is the Reduction in Hydrogen Charge Occurring at Fixed Potential	4-24
14	Charge Corresponding to Equilibrium Surface Coverage with Hydrogen	4-24
15	Variation of the Open-Circuit Potential with Adsorption Time	4-27
16	Variation in Fractional Free Surface with Adsorption Time. Solution Saturated with Designated Mixtures of Ethane and Argon	4-35
17	Potential Sequences Applied to the Test Electrode (Time axis not to Scale)	4-40
18	Current-time (potential) Traces Obtained during Desorption of Adsorbed Ethane (Sequence I, Table IV with $U = 0.06$ v.)	4-43
19	Hydrogen Adsorption During Desorption of Adsorbed Ethane (Sequence I, Table IV)	4-44
20	Charge Corresponding to the Desorption of Ethane at Various Potentials (Ethane Pre-adsorbed for 100 sec.)	4-46

<u>Figure</u>		<u>Page</u>
21	Charge Corresponding to Desorption of Ethane at 0.06 v. (Ethane Pre-adsorbed for Time, T_E .)	4-46
22	Rate of Desorption of Ethane in the Absence of Pre-adsorbed Ethane	4-47
23	Potential Sequences Applied to the Test Electrode	4-55
24	Current-time (potential) Traces for Varying Adsorption Times at 0.3V	4-58
25	Current-potential (time) Traces for Ethane Adsorbed at Several Potentials	4-59
26	Current-potential (time) Traces for Ethane Adsorbed at Several Temperatures	4-60
27	Surface Charge Associated with Adsorbed Ethane	4-62
28	Surface Charge Associated with Ethane Adsorbed at Different Potentials	4-62
29	Effect of Potential on Total Surface Charge and Prewave Charge from Adsorbed Ethane.	4-63
30	Effect of Temperature on Total Surface Charge and Prewave Charge for Adsorbed Ethane	4-63
31	Current-potential Curves for Several Carbonaceous Materials on Pt	4-65
32	Polarization Curve for Ethane with a Perchloric Acid Electrolyte	4-66
33	Current-potential Curves for Several Hydrocarbon Fuels After Equilibration at Different Potentials	4-68
34	Current-potential Curves for Ethane with HF and HClO_4 Electrolytes	4-70
35	Polarization Curve for Ethane with a Hydrofluoric Acid Electrolyte	4-70
36	Galvanostatic Oxidation of Propane at a Macro Anode-Anode/Reference Voltage vs. Time	4-74
37	Galvanostatic Oxidation of Propane at a Macro Anode CO_2 Production Rate vs. Time	4-74
38	Galvanostatic Oxidation of Propane at a Macro Anode CO_2 Production Rate vs. Anode/Reference Voltage	4-75
39	Carbon Dioxide vs. Time Profile for 10 ma Galvanostatic Oxidation of "Propane" Residue After Oxidation to 0.4 Volts and Exhaustive Removal of Hydrocarbons by Cathodic Hydrogenation	4-75
40	Anode/Reference Voltage vs. Time for 10 ma Galvanostatic Oxidation of "Propane" Residue After Potentiostatic Oxidation at 0.2 Volts and Exhaustive Removal of Hydrocarbons by Cathodic Hydrogenation	4-77
41	Carbon Dioxide vs. Time Profile for 10 ma Galvanostatic Oxidation of "Propane" Residue After Potentiostatic Oxidation at 0.2 Volts and Exhaustive Removal of Hydrocarbons by Cathodic Hydrogenation	4-77
42	Galvanostatic Oxidation of Carbon Monoxide at a Macro Anode CO_2 Production Rate vs. Time	4-78
43	Glass Test Cell	4-81
44	Current vs. Potential Behavior as a Function of Electrode Position	4-83

<u>Figure</u>		<u>Page</u>
45	Current vs. Height Behavior	4-83
46	Resistance Measurements in the Meniscus and Thin Film Regions	4-84
47	Dependence of Limiting Current and Reduced Limiting Current on Temperature for 90-wt. Percent Phosphoric Acid	4-87
48	Current vs. Potential Behavior on a Partially Immersed Wetproofed Pt-Ru Electrode	4-88
49	Current vs. Height Behavior of a Wetproofed Pt-Ru Electrode	4-88
50	Tafel Plots for Propane Cell with CsF-HF Electrolyte (HF/CsF = 2.1, H ₂ O = 29 Mole %) at 150°C	4-92
51	Current Density for Propane at an Anode vs. H ₂ Reference Potential of 0.5 V, as a Function of Fluoride: Cesium Ratio (by Equivalents)	4-92
52	Current Density for Propane at an Anode vs. H ₂ Reference Potential of 0.5 V as a Function of HF: (CsF + HF) Ratio. Solid Line is for Results Near HF:CsF = 2, Normalized at 12.5 Mole % H ₂ O. Dashed Line is not Normalized with Respect to Water Content.	4-94
53	Current Density for Propane at Constant Anode Potentials, as a Function of Electrolyte Water Content, Normalized to HF:CsF = 2.	4-95
54	Summary Plot Showing Current Density for Propane at an Anode vs. H ₂ Reference Potential of 0.5 V as a Function of HF:(CsF + HF) Ratio. Solid Lines are Normalized to Water Contents Indicated. Dashed Lines are not Normalized, and Show Approximate Behavior for Optimum Water Content Electrolytes.	
55	Summary Plot Showing Current Density for Propane at E _{a-r} = 0.5 V as a Function of Water Content, Normalized to Indicated HF:CsF Ratios for Several Temperatures	4-97
56	Enthalpy of Activation for Overall Anodic Oxidation of Propane as a Function of HF:(CsF + HF) Ratio, in the Temperature Range 80-170°C. ΔH^* is Insensitive to Water Content and Temperature	4-99
57	Tafel Plots for Propane Cell with HF-H ₂ O Electrolyte at 105°C	4-100
58	Effect of HF-H ₂ O Electrolyte Composition on Propane Performance at Different Temperatures. Solid Lines Indicate Electrolyte Compositions Which do not Boil at Temperature Shown	4-101
59	Comparison of Power Densities for Propane Cells Using CsF-HF-H ₂ O Electrolyte at 150°C and HF-H ₂ O Electrolyte at 105°C.	
60	Effect of Teflon Film Thickness on Propane Limiting Current Densities	4-103
61	Voltage Sequence Applied to Smooth Pt Test Electrode for Propane Investigations Using HF Electrolyte	4-105
62	Saturation Coverage of Hydrogen on Smooth Pt in HF, Expressed as Microcoulombs of Hydrogen Deposited per cm ² During Cathodic Voltage Sweeps	4-105
63	Potentiodynamic Current-Voltage for Propane on Smooth Pt in HF Electrolyte	4-107

<u>Figure</u>		<u>Page</u>
64	Surface Coverages of Propane and Hydrogen on Smooth Pt in HF, as a Function of Adsorption Time in Quiescent Electrolyte	4-113
65	Surface Coverages of Propane Oxidized Below 1.76 Volts vs. Rev H_2 , and Above 1.76 Volts on Platinum in HF as a Function of Adsorption Time	4-113
66	Potentiodynamic Current-Voltage Curve for Propane on Smooth Pt in HF Electrolyte	4-115
67	Surface Coverages of Propane and Hydrogen on Smooth Pt in HF, as a Function of Adsorption Time in Quiescent Electrolyte	4-115
68	Surface Coverages of Propane Oxidized Below 1.62 Volts and Above 1.62 Volts on Platinum in HF as a Function of Adsorption Time, for Two Sweep Speeds	4-116
69	Potentiodynamic Current-Voltage Curve for Propane on Smooth Platinum in HF Electrolyte	4-116
70	Surface Coverages of Propane and Hydrogen on Smooth Pt in HF, as a Function of Adsorption Time in Quiescent Electrolyte	4-117
71	Current-Potential Curves for the Oxidation of Propane on Smooth Pt for Various Temperatures	4-119
72	$CH_4 - D_2$ Exchange on 17% Ru-Ir Alloy, 100°C	4-125
73	$CH_4 - D_2$ Exchange on 17% Ru-Ir Alloy, 132°C	4-126
74	Adsorption Isotherms of n-butane on Platinum Black. Surface area = 8 m ² /g	4-129
75	Adsorption Isotherms of Iso-butane on Platinum Black. Surface area = 8 m ² /g	4-129
76	Adsorption and Decomposition of n-butane on Platinum (0.8-0.9g., 8 m ² /g) n-butane admitted = 3×10^{19} molecules	4-130
77	Adsorption and Decomposition of Iso-butane on Platinum (0.8-0.9g., 8 m ² /g) iso-butane admitted = 3×10^{19} molecules	4-131
78	Adsorption and Decomposition of n-butane. Pressure vs. Time n-butane admitted = 3×10^{19} molecules	4-131
79	Poisoning of Platinum by Carbonaceous Residues. Successive Cracking Runs with n-butane at 150°C	4-134
80	Flash Desorption Apparatus	4-140
81	Flash Desorption Chromatograms: (A) Ethylene on Platinum Black, (B) Ethylene on Alumina	4-140
82	Range of E_{AR} vs. C. D. for Pt Activated B_4C Electrodes at Pt Loading 0.16 mg/cm ² 6N H_2SO_4 , Room Temp.	4-145
83	Range of E_{AR} vs. C. D. for Pt Activated B_4C Electrodes at Pt Loading 0.16 mg/cm ² 5N KOH, Room Temp.	4-146
84	Range of E_{CR} vs. C. D. for Pt Activated B_4C Electrodes at Pt Loading 0.16 mg/cm ² 6N H_2SO_4 , Room Temp.	4-147

<u>Figure</u>		<u>Page</u>
85	Range of E_{CR} vs. C. D. for Pt Activated B_4C Electrodes at Pt Loading 0.16 mg/cm^2 5N KOH, Room Temp.	4-148
86	E_{AR} vs. C. D. for Pt Activated B_4C Electrodes H_2 , 6N H_2SO_4 , Room Temp.	4-150
87	E_{AR} vs. C. D. for Pt Activated B_4C Electrodes H_2 , 5N KOH, Room Temp.	4-150
88	E_{CR} vs. C. D. for Pt Activated B_4C Electrodes O_2 , 6N H_2SO_4 , Room Temp.	4-151
89	E_{CR} vs. C. D. for Pt Activated B_4C Electrodes O_2 , 5N KOH, Room Temp.	4-151
90	E_{CA} vs. C. D. for $C_3H_8 - O_2$ Cells with Pt Activated B_4C Anodes at 150°C in 85% H_3PO_4	4-152
91	C. D. at $E_{CA} = 0.5$ Volts vs. Pt Loading on B_4C Anodes for $C_3H_8 - O_2$ Cells, 85% H_3PO_4 , 150°C	4-152
92	Electron Micrograph of Boron Carbide Powder, Magnification 7500X (before reduction for printing)	4-154
93	Electron Micrograph of Single Particle Not Platinum Activated, Magnification 50,000 X (before reduction for printing)	4-155
94	Electron Micrograph of Single Particle from Sample Activated with 5% Pt by wt. Magnification 100,000 X (before reduction for printing)	4-156
95	Effect of Teflon Content on Performance of Platinized Tantalum Electrodes as H_2 Anodes	4-160
96	Performance of Platinized Tantalum Electrodes as H_2 Anodes	4-160
97	Performance of Platinized Tantalum Electrodes as O_2 Cathodes	4-161
98	Block Diagram of Potentiostatic Corrosion Apparatus	4-163
99	Details of Electrochemical Cell for Potentiostatic Corrosion Studies	4-164
100	Current-Potential Curves for Anodic Corrosion of Various Materials at 110°C in HF under Argon	4-165
101	Current-Potential Curves for Anodic Corrosion of Tungsten at 80°C and Molybdenum at 90°C in HF under Argon	4-165
102	Current-Potential Curves for Anodic Corrosion of Tungsten and Nickel at 25°C in HF under Argon	4-166
103	Performance Curves at 165° and 195°C . Anode — 50.9% Rh-Ru, Commercial Propane. Cathode — Pt, O_2 , 85% H_3PO_4	4-167
104	Schematic Diagram of Gas Solubility Apparatus for Room Temperature Studies	4-169
105	Schematic Diagram of Gas Solubility Apparatus for Measurements at Elevated Temperatures	4-170
106	Photograph of Contactors and Associated Equipment Arranged in Oven	4-170
107	Photograph of Disassembled Contactor	4-171

<u>Figure</u>		<u>Page</u>
108	Typical Stripping and Calibrations Curves for Oxygen in Water at 25°C	4-173
109	Calibration of Gas Solubility Apparatus for Oxygen	4-173
110	Solubility of Propane in Concentrated Phosphoric Acid	4-176
111	Gas Saturating Apparatus	4-176
112	Gas Stripping System	4-179
113	Apparatus for Measurement of Boiling Points, Freezing Points, and Densities of Electrolytes	4-180
114	Teflon Conductivity Cell	4-181
115	Boiling Point as a Function of Composition for the HF-H ₂ O System. ○, as Reported by Vieweg (3); □, This Work	4-182
116	Boiling Point Isotherms for the CsF-HF-H ₂ O System	4-183
117	Isochores for a Portion of the CsF-HF-H ₂ O System at 100°C	4-183
118	Density as a Function of Temperature for the HF-H ₂ O Azeotrope	4-185
119	Density as a Function of Composition for the HF-H ₂ O System at 15°C, According to Domange (4)	4-185
120	Phase Diagram for the HF-H ₂ O System, According to Cady and Hildebrand (5)	4-186
121	Partial Phase Diagram for the CsF-H ₂ O System. According to Cohen-Adad and Ferlin (6)	4-186
122	Partial Phase Diagram for the CsF-HF System, According to Windsor and Cady (7)	4-187
123	Estimate of a Portion of CsF-HF-H ₂ O Phase Diagram at 7.5 mole % H ₂ O	4-187
124	Conductivity of HF-H ₂ O Electrolytes as a Function of Composition at Several Temperatures	4-189
125	Conductivity of Some CsF-HF-H ₂ O Solutions as a Function of CsF Content for a Constant $\left(\frac{F}{H_2O}\right)$ Ratio of 37/63, at Three Temperatures	4-189
126	Effect of Asbestos Content on Performance as a H ₂ Anode with 5N H ₂ SO ₄ Electrolyte	4-198
127	Effect of Asbestos Content on Performance as an O ₂ Cathode with 5N H ₂ SO ₄ Electrolyte	4-198
128	Effect of Asbestos Content on Performance as a H ₂ Anode with 85% H ₃ PO ₄ Electrolyte	4-199
129	Effect of Asbestos Content on Performance as a C ₃ H ₈ Anode with 85% H ₃ PO ₄ Electrolyte	4-199
130	Appearances of Electrodes (Electrolyte Side) After a Week Under 85% H ₃ PO ₄ at 150°C in the Presence of Hydrogen (20X)	4-200

<u>Figure</u>		<u>Page</u>
131	Developmental Electrodes with Heavier Wetproofing Films-Performance on Propane and Oxygen vs. Film Weight	4-202
132	Heavy and Fluffy Wetproofing Films (after test). Appearance of Surface with "Poplar Tree" Formations	4-202
133	Comparison of Asbestos-Filled Electrode and Standard Electrode Surfaces	4-204
134	Double-layer Electrodes with Layers of Different Teflon Concentrations After Test. Appearance of Surface	4-205
135	Pore Size Distribution	4-210
136	Surface of Niedrach-Alford Electrode Sample. Porosity Measurement with Mercury Penetration	4-211
137	Cell Life Test Stand	4-217
138	Cell LT-7	4-218
139	Cell LT-7	4-218
140	Cell LT-7	4-219
141	Cell LT-7	4-219
142	Cell LT-8	4-221
143	Cell LT-8	4-221
144	Cell LT-8	4-222
145	Cell LT-9	4-223
146	Cell LT-9	4-223
147	Cell LT-9	4-224
148	Cell LT-9	4-225
149	Decane (Liquid)/H ₃ PO ₄ /Air	4-226
150	Decane (Liquid)/H ₃ PO ₄ /Air	4-227
151	Decane (Liquid)/H ₃ PO ₄ /Air	4-229
152	Decane (Liquid)/H ₃ PO ₄ /Air	4-229
153	Decane (Liquid)/H ₃ PO ₄ /Air	4-230
154	Pulsed Discharge Circuitry Schematic	4-231
155	Cell LT-16 C ₃ H ₈ /35% HF/Air	4-235
156	Propane and Air Comparison of H ₃ PO ₄ and HF Performance	4-236
157	Cells LT-20 and LT-33, Comparison of η Octane (Liquid)/HF/Air and η Octane/H ₃ PO ₄ /Air	4-237
158	Binary Fuel Recycle System	4-240
159	Fuel Feed and Exhaust for Chromatograph System — Binary Fuels	4-242
160	Anode Mass Balance	4-245
161	Dependence of Hexane Current in Hexane/Octane Fuel Mixtures	4-246

<u>Figure</u>		<u>Page</u>
162	"See-Through" Anode Chamber	4-248
163	Liquid Hydrocarbon Fuel Anode Test Apparatus	4-248
164	(a) Non-Vaporizing Fuel System	4-249
	(b) Pressurized Electrolyte System	4-249
165	Correlation of Regression Coefficients and Exponents of Equation (65) With a Number of Carbon Atoms in the Fuel	4-255

BLANK PAGE

LIST OF TABLES

Table No.	List	Page No.
I	Pulse Sequences Applied to Working Electrode	4-3
II	Variation of Q_0' with Electrode Pulse-Treatment	4-7
III	Procedures Followed During Potential Sequence of Fig. 4	4-10
IV	Procedures Followed During Potential Sequences of Fig. 17	4-41
V	Effect of Sweep Rate on Charge for Hydrogen Deposition	4-56
VI	Effect of Sweep Rate on Charge to Oxidize Adsorbed Ethane, 4.3N HClO_4 , $T = 60^\circ\text{C}$.	4-57
VII	Effect of Time and Potential on $Q_{E_1} : Q_{E_{\text{tot}}}$	4-61
VIII	Hydrocarbons Produced by Hydrogenation after Oxidation to 0.2 Volt	4-76
IX	Hydrocarbons Produced by Hydrogenation after Oxidation to 0.4 Volt	4-76
X	Influence of Propane Partial Pressure on Electrode Current	4-85
XI	Properties of the Electrochemical System	4-106
XII	Primary Data (C_3H_8 (Pt)/39.1 wt % HF - Temperature = 30°C)	4-109
XIII	Results (C_3H_8 (Pt)/39.1 wt % HF - Temperature = 30°C)	4-110
XIV	Primary Data (C_3H_8 (Pt)/39.1 wt % HF - Temperature = 60°C)	4-117
XV	Results (C_3H_8 (Pt)/39.1 wt % HF - Temperature = 60°C)	4-118
XVI	Primary Data (C_3H_8 (Pt)/39.1 wt % HF - Temperature = 90°C)	4-119
XVII	Results (C_3H_8 (Pt)/39.1 wt % HF - Temperature = 90°C)	4-120
XVIII	Rate of Methane-Deuterium Exchange on Ru-Ir Alloys	4-124
XIX	Cracking of Butanes on Platinum Black	4-132
XX	Activation Energies for Methane Formation Rate	4-133
XXI	Properties of Physically Adsorbed Butane Monolayers	4-134
XXII	Properties of Pt- B_4C Catalysts	4-142
XXIII	Correlation of the Measurements on Various Catalyst Powders With the Results Obtained in Fuel Cell Electrodes	4-158
XXIV	Electrode Compositions	4-159
XXV	Solubility of Oxygen in Phosphoric Acid at Approximately 25°C	4-172
XXVI	Solubility of Propane and Oxygen in Concentrated Phosphoric Acid	4-175
XXVII	Solubility of Octane in Phosphoric Acid	4-178
XXVIII	Properties of CsF -HF- H_2O Solutions	4-182
XXIX	Conductivities of Fluoride Electrolytes ($\text{ohm}^{-1}\text{cm}^{-1}$)	4-190
XXX	Composition of Dummy Electrodes	4-196
XXXI	Composition of Test Electrodes	4-196

LIST OF TABLES

<u>Table No.</u>	<u>Title</u>	<u>Page No.</u>
XXXII	Permeability Rates of Air on Standard Niedrach-Alford Electrodes	4-209
XXXIII	Surface Area of 3 x 3 in. Niedrach-Alford Electrodes	4-213
XXXIV	Surface Areas of Heat-Treated Platinum Black (20 Minutes at Temperature)	4-213
XXXV	Change in Surface Area of Platinum Black Treated with Hot Phosphoric Acid and Various Gases	4-214
XXXVI	Cell LT-7 Water Transport Rates	4-220
XXXVII	Water Transport with Ioplex Membrane	4-232
XXXVIII	Typical Cell Performance	4-234
XXXIX	Typical Cell Performance	4-238
XL	Propane Consumption and CO ₂ Production — Recycle System — Pure Propane/Air/H ₂ PO ₄	4-244
XLI	Coefficient and Exponents of Equation (65) and the Correlation Coefficient of the Regression Analysis	4-254

4.0 DETAILS OF INVESTIGATIONS

4.1 ELECTROCHEMICAL OXIDATIONS OF HYDROCARBONS

Research to develop a better understanding of electrochemical oxidation of hydrocarbons has continued. The scope of research activities and the specific objective for each are illustrated in part A of Table I (Section 3.1). Fundamental studies on adsorption and desorption at hydrocarbon anodes, thin films, and related semi-micro and macro fuel cell electrodes are presented. In addition, activity in mixtures of hydrofluoric acid electrolytes are discussed.

4.1.1 Anode Studies (Dr. S. Gilman)

Multipulse potentiodynamic (MPP) techniques were further developed and applied to the study of saturated hydrocarbons. Initial studies were performed in 85% phosphoric acid at temperatures of 120° and 150°C. It was observed that adsorption-time data was not sufficiently reproducible under these experimental conditions. This lack of reproducibility was caused by small, but highly significant, variations in the effective surface area of the electrode. These variations, in turn, could be traced to two sources:

- 1) Presence of adsorbable impurities in the electrolyte.
- 2) Changes in the surface area of the electrode at elevated temperatures, under the conditions of the measurement.

The first difficulty may, in principle, be avoided through removal of the trace impurities from the electrolyte. Changes in the surface area were studied in detail and are reported in section 4.1.1.1.

Largely because of the experimental difficulties encountered at the higher temperatures, detailed studies of ethane (the simplest saturated hydrocarbon possessing a carbon-carbon linkage) adsorption were subsequently performed in 1 N perchloric acid solution at 60°C.

The results of studies of ethane adsorption and hydrogenation-desorption studies are reported in sections 4.1.1.2 and 4.1.1.3, respectively.

4.1.1.1 Modification of the Surface Area of Platinum Electrodes by the Application of Single Pulses

Multipulse potentiodynamic sequences have been used in the study of a variety of adsorbates on platinum (1-4). It has been observed that the use of the appropriate pre-treatment sequence results in a highly reproducible surface in 1 N perchloric acid solution at temperatures of 30 or 60°C (1,2). This reproducibility is evidenced by reproducibility of the hydrogen-deposition

-
- (1) S. Gilman, J. Phys. Chem. 67, 78 (1963).
 - (2) S. Gilman, Electrochim. Acta 9, 1025 (1964).
 - (3) S. Gilman, J. Electroanalyt. Chem. 7, 382 (1964).
 - (4) S. Gilman, J. Phys. Chem. 68, 2098 (1964).

charge Q^S_H (1,1), the "oxygen-adsorption" charge, Q_0 (1,2) and of the electrode capacitance (2). The values of these quantities after a fraction of a second following pre-treatment can be reproduced to be within a few percent for over a year of use of the electrode, and upwards of one thousand operating cycles, when experiments are performed only at the lower temperatures. Variations in these quantities following a pre-treatment sequence occurs in a manner indicative of electrode contamination (1).

Recently, MPP measurement were attempted at temperatures of 90°C or higher in solutions of both perchloric and phosphoric acids. Gradual "roughening" of the surface was observed, as evidenced by increases in both Q^S_H and in Q_0 . The effect was slight, but observable at 90°C in both acids, and quite pronounced in phosphoric acid at 120°C. The investigation described below was undertaken to determine the origin of the electrochemical roughening of the surface observed at elevated temperatures.

A. Experimental

The specially developed multipulse potentiodynamic equipments were utilized in all experimental investigations.

Glassware and electronic equipment have been described previously (1). For the convenience of the reader, a block diagram of the circuit appears in Fig. 1. The signal generator consisted of several individual units whose output was added. Ramps were generated by means of an Exact Model 250 signal generator. Steps were generated with Tektronix type 161 delay units for steps of short duration, and with relays and batteries, for steps of several second's duration. The potentiostat used was a Wenking "fast rise" potentiostat. The current-time signals were recorded using a Tektronix 536 oscilloscope with type D and T plug-in units.

The working electrode was a length of C.P. platinum wire 0.020" in diameter and of 0.064 cm² geometric area. The electrolyte was an 85% solution of A.R. grade phosphoric acid. The test vessel was thermostated at 120°C in an air bath.

Charges corresponding to hydrogen-deposition and to "oxygen-adsorption" were measured by means of sequence 1 and 2 of Table I. Pulse sequences employed in the measurement of these charges are diagrammed in Fig. 2a and 2b. Fig. 2c - 2g are the repetitive signals tested for their effect on surface roughness.

B. Results

1. Initial Values of Q^S_H , Q_0 and R. F.

Sequence II of Table I was employed for measurement of the charge corresponding to hydrogen-deposition, Q^S_H . The application of step E of the sequence results in a hydrogen-deposition trace similar to that obtained at lower temperatures in perchloric acid (1). From this trace, Q^S_H was obtained, as previously, by integrating the area under the trace, making

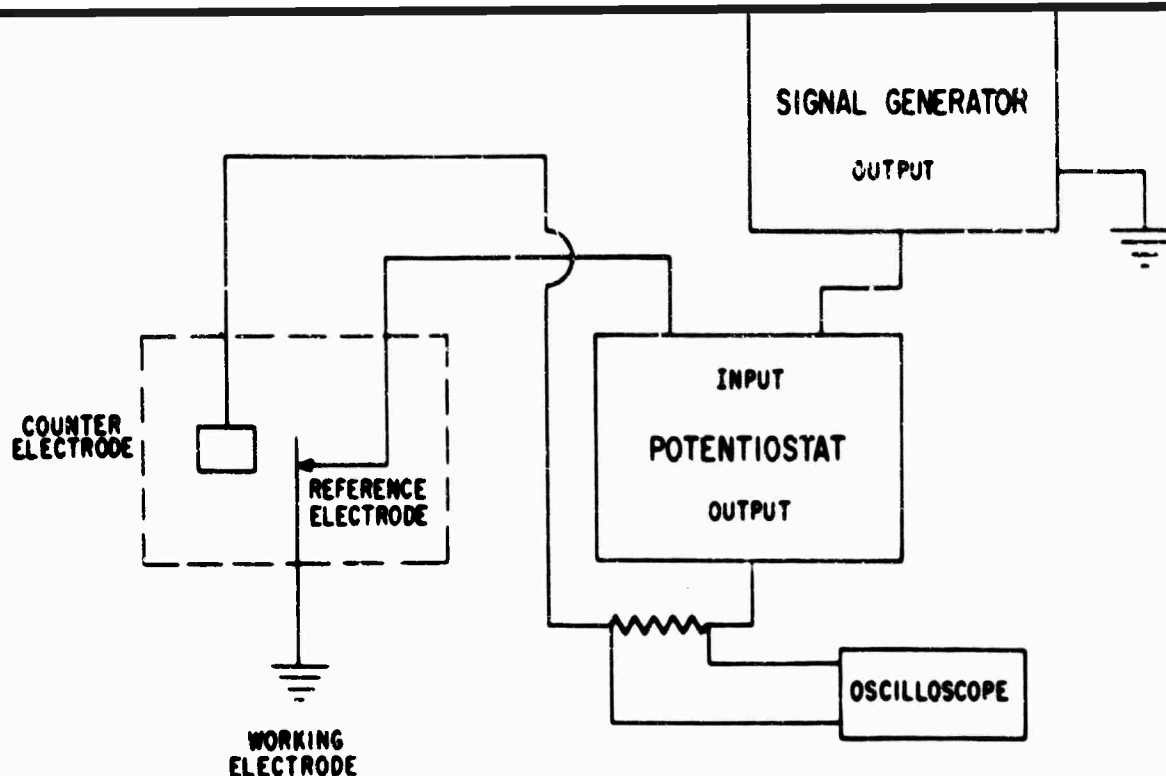


Fig. 1. Multipulse Potentiodynamic Equipment.

TABLE I

Pulse Sequences Applied to Working Electrode

<u>Sequence</u>	<u>Fig.</u>	<u>Step (Refers to Fig. 2)</u>	<u>Procedure</u>	<u>Purpose</u>
I	2a	A	1. Potential held at 0.0 v. for 10 sec., with argon flowing and paddle-stirring	1. To desorb foreign anions
		B	2. Stirring and argon flow continued while potential held at 1.8 v. for 15 sec.	2. To remove impurities which oxidize and/or are repelled at high potentials.
		C	3. Stirring and argon flow continued for 1/2 minute and solution allowed to become quiescent for 1-1/2 additional minutes. Potential held at 1.55 v. throughout this step.	3. To sweep molecular oxygen produced during step B into the bulk and to restore concentrations of dissolved species near surface to bulk values.
		D	4. Potential of 0.4 v. applied for time T_D	4. Surface is largely reduced within first few milliseconds exposing a reproducible surface to the electrolyte.
		E	5. Apply linear anodic sweep E of speed $v = 1000$ v./sec. and measure current-time trace.	5. Q_0' may be determined from the trace
II	2b	A - C D	1-4) Same as sequence I, 1-4. 5) Apply linear cathodic sweep E of speed $v = 50$ v./sec., and measure current-time trace.	1-4) Same as sequence I, 1-4. 5) Q^S_H may be determined from the trace.

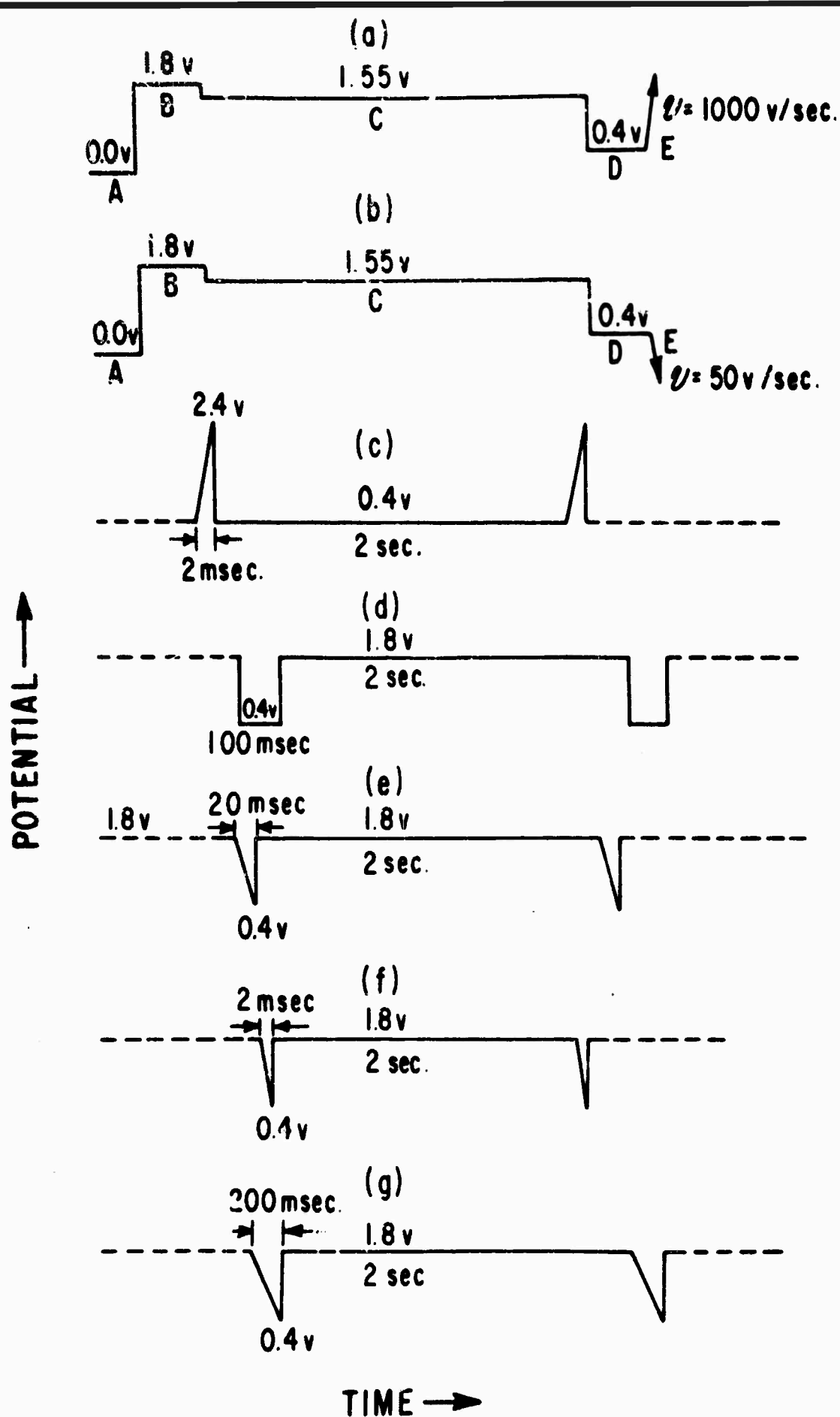


Fig. 2. Potential Sequences Used in This Work.

approximate graphical correction for double-layer charging. The value of Q^S_H obtained before alteration of the electrode surface was 0.31 mcoul./cm^2 . Assuming that 0.21 mcoul./cm^2 corresponds to a monolayer of hydrogen and a roughness factor, $R.F. = 1$, an original value of $R.F. = 1.47$ was calculated for the electrode.

Sequence I of Table I was employed in the measurement of the charge corresponding to "oxygen-adsorption". Trace 1 of Fig. 3 is the trace obtained initially by application of step E of sequence II. A charge, Q_0' was obtained from this trace by graphical integration of the area "abcda." This charge includes a charge Q_0 , corresponding to oxidation of the surface and also a charge corresponding to double-layer charging (2). The choice of the location of point c of Figure 3 must be somewhat arbitrary. To ensure standard conditions for the location of point c, and thereby, for the comparison of different values of Q_0' , point c was determined in the following way:

- 1) The maximum current of the trace was determined. Point e was chosen as that point on the trace corresponding (arbitrarily) to 120% of the maximum current.
- 2) A tangent to the trace was constructed at point e.
- 3) A tangent was constructed to the trace at a point corresponding to a time half-way between that of the maximum current and that corresponding to point e.

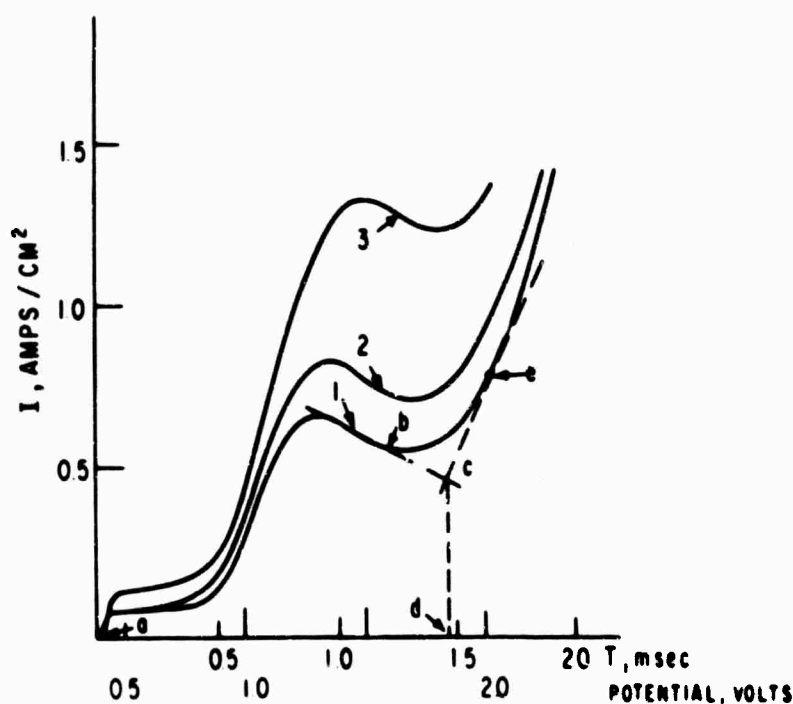


Fig. 3. "Oxygen Adsorption" Traces Recorded Initially (Trace 1) and After "Roughening" the Surface by Pulsing (Traces 2 and 3).

4) The intersection of the two tangents determines point c. The original value of Q_0' was found to be 0.553 mcoul./cm². After making approximate correction for double-layer charging on the assumption that the capacitance has a constant value of 70 microfd./cm², $Q_0 = 0.43$ mcoul./cm² and $Q_0/2Q^S H = 0.69$ which is lower than the corresponding value at 30° in 1 N perchloric acid (0.9 acc. to ref. 2). At least part of this decrease may be ascribed to the adsorption of phosphate on which partially blocks surface oxidation (4). Values of R.F. reported in Table II are calculated from Q_0' taking the original value of $Q_0' = 0.553$ to correspond to the R.F. of 1.47 and assuming that subsequent values of R.F. are directly equal to Q_0' .

2. Electrode Treatments Leading to No Change in Q_0'

After a pre-treatment sequence similar to that of procedure 1, Table I, the electrode was held at potentials of 0.1, 1.2, 1.55 and 1.8 v for 10 minutes. The particular potentials were chosen because they correspond to a variety of surface coverages with "oxygen" (2). Q_0' was found not to have varied at all at any of these constant potentials.

3. Electrode Treatments Leading to Change in Q_0'

Application of periodic pulses c, d and f of Fig. 2 lead to increase in Q_0' and hence in the calculated R.F. The reverse is true for pulses e and g. The results are summarized in Table II. The change in Q_0' is compared with the preceding value of Q_0' by the expression:

$$\text{Percentage change in } Q_0' = 100 \Delta Q_0' / Q_0', \text{ where}$$

$$Q_0' = (\text{final value of } Q_0') - (\text{initial value of } Q_0')$$

The value of Q_0' is the denominator of the above equation is taken as the initial value. The change in Q_0' is also given on a "per cycle" basis by dividing expression 1 by the total number of cycles.

C. Discussion

The results indicate that no change in R.F. occurs at any constant potential. According to Table II, increase in R.F. is associated with signals c, d and f on Fig. 2, where the surface is oxidized and rapidly reduced during each cycle. A decrease in R.F. is noted when the surface is first oxidized and then slowly reduced as in signals e and g of Fig. 2. Hence roughening of the surface is correlated most directly with speed of reduction.

The rate at which the R.F. of the surface is increased by rapid reduction depends on the extent of previous exposure of the surface to oxidizing conditions. Hence Q_0' changes by only 0.02% per cycle when the surface is partially oxidized using a fast linear anodic sweep (Fig. 2c) whereas the change is as large as 0.2% per cycle when the surface is first oxidized at 1.8 v for 2 sec. and then rapidly reduced either by a step or a fast linear sweep (Fig. 2d and 2f, respectively.)

TABLE II

Variation of Q_0 with Electrode Pulse-Treatment

Exp. No.	Signal (Fig. No.)	Q_0 Initial	mcoul./cm ²		Roughness Factor		Total Pulse Time, minutes	Number of Cycles	Percentage Change in Q_0	
			Final	Initial	Final	Initial			Total	Per Cycle
1	2c	0.553	0.580	1.47	1.55	1.55	10	300	5.1	0.017
2	2d	0.580	0.960	1.55	2.55	2.55	10	300	64.7	.216
3	2d	.960	1.14	2.55	3.04	3.04	5	150	19.1	.127
4	2e	1.43	0.98	3.83	2.62	2.62	5	150	-31.4	-.210
5	2e	.98	.71	2.62	1.90	1.90	10	300	-27.6	-.092
6	2f	.71	1.07	1.90	2.85	2.85	10	300	50.0	.166
7	2g	1.07	.98	2.85	2.61	2.61	10	300	-8.45	-.028
8	2e	.98	.74	2.61	1.96	1.96	10	300	-24.6	-.082
9	2e	.74	.69	1.96	1.83	1.83	25	750	-7.2	-.0096

For the surface largely oxidized at 1.8 v. the rate of decrease of R.F. depends also on the speed of reduction. Hence in experiment 4, Table II, signal 2e gave a rate of decrease of 0.2% per cycle during the first 5 minutes of pulsing whereas signal 2g gave an initial rate of change of only 0.03% per cycle. There is also evidence that a steady state R.F. exists corresponding to signal 2e. In experiments 4, 5, 8 and 9, it is seen that the rate of change of Q_0' drops with decreasing R.F. The last value of R.F. measured in 2 cases (experiments 5 and 9) are approximately the same. It is possible that a steady state value of R.F. may correspond to a variety of oxidation-reduction cycles. These effects may be of interest in preparing electrodes of desired R.F. in a reproducible manner.

Recently Hoare (5) examined "blackening" of platinum electrodes occurring at 25°C upon application of 60 cps AC voltage signals. The extent of surface roughening encountered in the present work only lead to a slight dulling of the surface. Conditions are less severe than in Hoare's work in that relatively few (equivalent to only a few seconds of 60 cps A.C.) cycles were studied here. On the other hand, conditions are more severe in that the temperature chosen was higher (120°C as compared with 25°C). Hoare believes that roughening of the surfaces comes about through the action of deposited hydrogen. In this work, reductions always were made at potentials no lower than 0.4v, under which condition there is no detectable hydrogen on the surface. Two general types of explanation of the observed phenomenon may be conceived:

1) The rapid reduction of a relatively extensive "oxygen" or "oxide" film does not allow time for the surface to "anneal" during reduction and this leads to progressive roughening of the surface.

2) Some very slight rate of solution of the "oxide" occurs during some portion of each cycle. This, or subsequent reduction of dissolved platinum, leads to roughening. The author considers the mechanism of the roughening process still an entirely open question.

4.1.1.2 Kinetics and Mechanism of Ethane Adsorption on Platinum

In the kinetics and mechanism of ethane adsorption on platinum studies, the multipulse potentiodynamic (MPP) method was applied to the determination of the mechanism and kinetics of adsorption of ethane on platinum in perchloric acid solution. Similar MPP methods have been applied previously to the study of surface processes involving organic molecules (1, 6-8) as well as neutral (2, 3) and ionic (4, 9) inorganic species.

A. Experimental

1. Equipment and Chemicals

The electrolyte was 1 N perchloric acid prepared from A.R. grade acid and triply distilled water. Ethane was Phillips Research Grade of 99.98% purity. The test electrode was a length of C.P. grade platinum wire sealed in a soft glass tube with 0.079 cm² of geometric area projecting. The exposed end of the wire electrode was sealed in a small bead of soft glass. The

(5) J. P. Hoare, *Electrochim. Acta* 9, 599 (1964).

(6) S. Gilman, *J. Phys. Chem.*, 66, 2657 (1962).

(7) S. Gilman, *J. Phys. Chem.*, 67, 1898 (1963).

(8) S. Gilman, *J. Phys. Chem.*, 68, 70 (1963).

(9) S. Gilman, *J. Phys. Chem.*, 68, 2112 (1964).

previous measured value of "saturation hydrogen coverage", S_{H}^{Q*} was 0.32 mCoul./cm²(1), suggesting a roughness factor of 1.5 if 0.21 mCoul./cm² is taken to correspond to R.F. = 1. All measurements were made in an air bath thermostated at 60 ± 0.1°C.

2. Procedure

The potential functions employed are diagrammed in Fig. 4 (times axes not to scale). The procedures followed during each step of each sequence of Fig. 4 is summarized in Table III along with the significance of each procedure. All potentials were measured against a reversible hydrogen electrode in 1 N perchloric acid.

B. Results

1. Establishment of Initial Boundary Conditions

For the quantitative study of adsorption, it is essential to establish well-defined initial conditions both on the electrode surface and in the adjacent solution. When using the MPP method, this goal is accomplished through the use of a sequence of potential pulses. While the exact potentials and durations of each pulse may be varied to suit the particular system under consideration (1-4, 7-9), the pulse sequence must accomplish the following specific tasks:

- 1) The surface must be cleansed of adsorbed materials (other than concentrated electrolyte species) including the adsorbate under study and impurities.
- 2) Provision must be made for converted and/or desorbed surface species (from 1) to be swept into the bulk of the solution and diluted, while protecting the electrode against re-adsorption.
- 3) The "protection" of step 2 must be removed rapidly when the adsorption process under investigation is to commence.

Step 2 can be accomplished, depending on the particular adsorbate, by either of two modes. The surface may be passivated at high potentials (1-3, 7-8), or a low (~ 0 v.) potential step (4, 9) may be applied, which serves to block adsorption either by dint of the presence of the hydrogen ad-layer, or some other potential-dependent effect. The use of the passivation principle is adequate where a small amount of "oxygen" retained (2) during part of step 3 is not significant (1). However, it might well be avoided where possible in the study of saturated hydrocarbons where the adsorptions are slow, and will possibly be affected by traces of oxygen.

Steps A-D of the sequences of Fig. 4 and Table III accomplish the surface pre-treatment with a minimum of exposure of the electrode to oxidizing conditions. The success of steps A-D in producing a clean surface is measured by comparison of the current-time traces obtained using sequences I and II of Table III ($U = 0.4v$) with those obtained using previous pre-treatments (1, 4) in the argon-saturated solution. The values of "oxygen adsorption" and hydrogen "adsorption" charges obtained by means of sequences I and II, respectively were found to remain

* The alternative symbol used previously was QSH.

TABLE III

Procedures Followed During Potential Sequence of Fig. 4

Sequence	Fig.	Step (Refers to Fig. 2)	Procedure	Purpose
I	4a	A	1. Bubble gas* through solution with paddle-stirring for $T_A = 15 \text{ sec.}^\dagger$	1. To keep solution saturated with gas while thoroughly reducing electrode surface. Also serves to remove anion impurities, if present, from surface.
		B	2. Continue gas-bubbling and stirring for $T_B = 2 \text{ sec.}$	2. To remove surface species which are oxidized and/or repelled at high potentials.
		C	3. Continue gas bubbling and stirring for 1/2 min. Stop bubbling and stirring and allow solution to become quiescent for 1-1/2 min. Total value of $T_C = 2 \text{ min.}$	3. The passive film of step B is retained while desorbed materials and oxygen released during step B are swept into the bulk of the solution and diluted. The solution is allowed to become quiescent to restrict mass transport to ordinary diffusion in subsequent steps.
		D	4. Solution quiescent. $T_D = 10 \text{ sec.}$	4. The passive film retained during step C is largely reduced within the first few milliseconds. The low potential serves to block adsorption of ethane, if present in solution. The electrode is in equilibrium with 10^{-4} atmos. of hydrogen.
		E	5. The potential is raised to U, for time, T_E .	5. To allow adsorption of ethane at potential U for time, T_E .
		F	6. Apply linear anodic sweep (l.a.s.) of speed v. Trigger oscilloscope at the beginning of the sweep, and measure current-time trace.	6. The charge corresponding to the oxidation of adsorbed ethane may be obtained through analysis of the current-time trace.
II	4b	A-F	1-5 Same as for Sequence I.	1-5 Same as for Sequence I.
		F	6. Apply linear cathodic sweep (l.c.s.) of speed v. Trigger oscilloscope at beginning of sweep and measure current-time trace.	6. The area under the current-time trace serves as a measure of hydrogen co-deposition.

* The gas is either ethane, argon, or a designated mixture of both.

† "T" with appropriate subscript is the duration of that step of the sequence.

TABLE III (Cont'd)

Sequence	Fig.	Step (Refers to Fig. 2)	Procedure	Purpose
III	4c	A-F	1-6 Same as for Sequence I with $U = 0.40$.	1-6 Same as for Sequence I.
		G	7. $T_G = 100$ msec.	7. To reduce the surface which was oxidized during step F. $T_G = 100$ msec. does not allow sufficient time for appreciable re-adsorption of ethane from solution.
		H	8. Apply l.a.s. of speed $v = 100$ v./sec. and measure resulting current-time trace.	8. Area under trace provides information on whether ethane adsorbed during step E is retained during steps F and G.
IV	4d	A-F	1-6 Same as for Sequence II.	1-6 Same as for Sequence II.
		G	7. $T_G = 100$ msec.	7. To eliminate adsorbed hydrogen and reduce the concentration of dissolved hydrogen adjacent to the electrode surface, so that anodic hydrogen current will be insignificant during step H. $T_G = 100$ msec. does not allow sufficient time for appreciable re-adsorption of ethane during step G.
		H	8. Apply l.a.s. of speed 100 v./sec. and measure current-time trace.	8. Area under trace indicates whether ethane was desorbed during step F.
V	4e	A-E	1-5 Same as for Sequence I.	1-5 Same as for Sequence I.
		F	6. Apply 0.4 v. step and measure resulting current-time trace.	6. All adsorbed hydrogen is oxidized at this potential. Integration of the current-time trace results in the corresponding charge.
VI	4f	A-F	1-4 Same as for Sequence I.	1-4 Same as for Sequence I.
		E	5. $T_E = 10$ msec.	5. To remove adsorbed hydrogen, and reduce the concentration of dissolved hydrogen adjacent to the surface.

TABLE III (Cont'd)

<u>Sequence</u>	<u>Fig.</u>	<u>Step (Refers to Fig. 2)</u>	<u>Procedure</u>	<u>Purpose</u>
	4f	F	6. Open circuit for time, T_F .	6. The open-circuit potential may be measured as a function of time. Alternatively, any value of the adsorption time, T_F , may be chosen and the amount of atomic hydrogen and of ethane adsorbed during T_F may be determined by subsequent steps.
		G	7. $T_G = 1$ msec.	7. This is sufficient time to remove hydrogen deposited on the surface as a result of dissociative chemisorption of ethane. This is preparative to measurement of Q_E by means of step H. Alternatively, the current-time trace resulting upon application of step G is recorded and the charge corresponding to the adsorbed hydrogen is estimated through integration of the trace.
		H	8. Apply l.a.s. of speed v , and measure resulting current-time trace.	8. Q_E may be determined through analysis of the trace.

constant for values of T_E from 10 msec. to 100 sec., and to agree to within a few percent with the results obtained using previous pre-treatments (1, 4). These values remained constant to within approximately 5% for values of T_E up to 1000 sec. when the solution was pre-electrolyzed by pulsing (1). This variation is due to adsorption of residual solution impurities, and served to limit adsorption times to 1000 sec. in this work.

2. Charge Corresponding to Oxidation of Adsorbed Ethane — Frequency Dependence

Sequence I of Table III was employed in this study. U was chosen at 0.4 v, and v was varied. The traces marked "1" in Fig. 5 were obtained upon application of the linear anodic

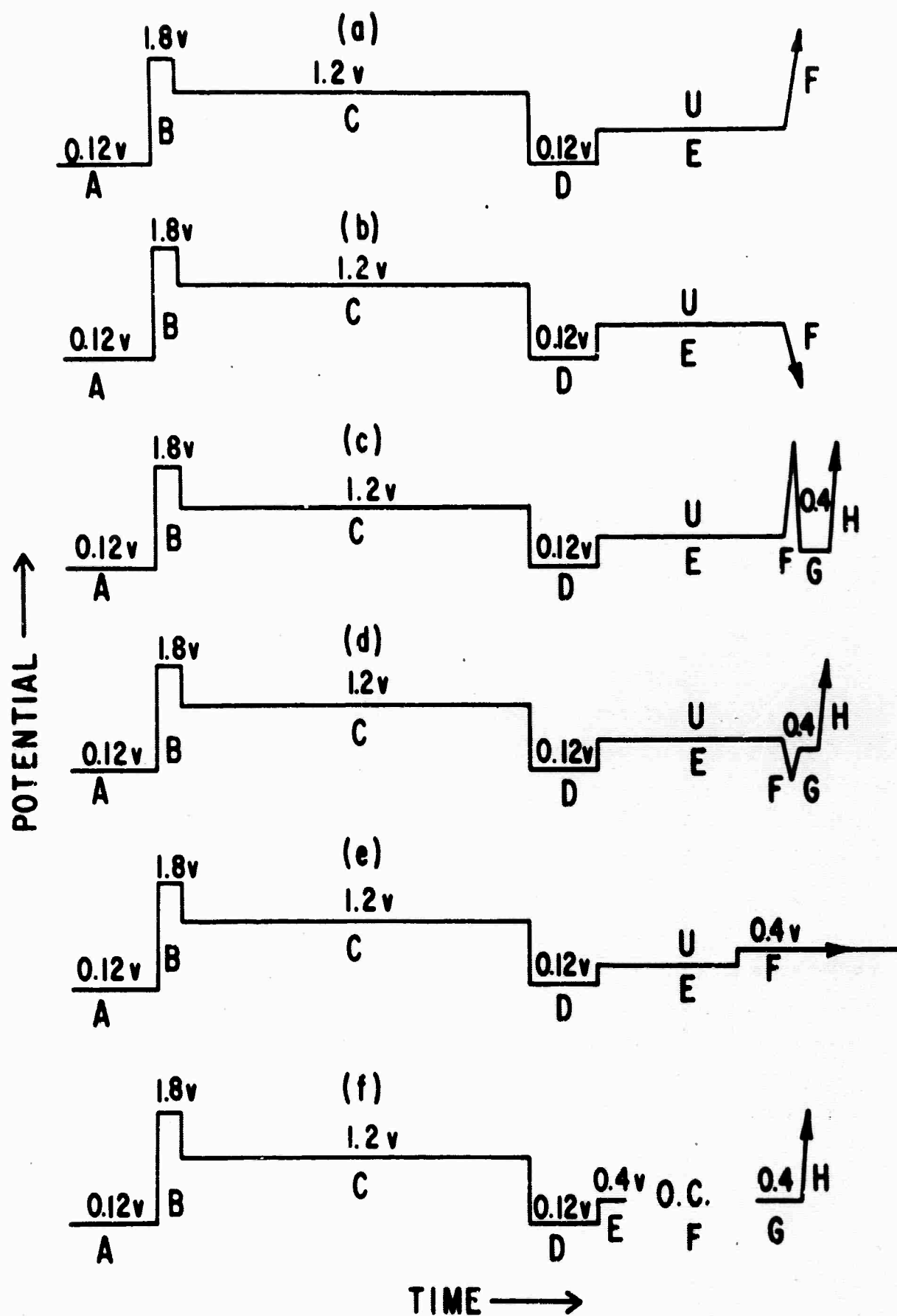


Fig. 4. Potential Sequences Applied To The Test Electrode.
(Time axis not to scale.)

sweep (l.a.s.) F for $T_E = 10$ msec. in ethane-saturated solution. They are identical (except for Fig. 4A which is very slightly different) with the traces obtained in argon-saturated solution for values of T_E of from 10 msec. to over 100 sec. This must indicate that the combined durations of steps E and F are too small (less than one sec., except for Fig. 5A) to permit appreciable adsorption of ethane. Hence traces 1 of Fig. 5 serve as "solvent" traces. The traces marked "2" correspond to $T_E = 100$ sec. in ethane-saturated solution. The shaded area included between the "solvent" and "ethane" traces of Fig. 5 and the dashed line (which helps eliminate purely capacitive charges lying to the left) will be referred to as Q_E' . This charge may include several terms:

$$Q_E' = Q_E + Q_E'' + \Delta Q_{cap.} + \Delta Q_0 \quad (1)$$

where

Q_E = charge corresponding to oxidation of ethane adsorbed on the surface during step E.

Q_E'' = charge corresponding to ethane not adsorbed during step E but which oxidizes during step F with or without a preceding adsorption step.

$\Delta Q_{cap.}$ = Difference in capacitive charges included under the "solvent" and "ethane" traces due to differences in initial surface states.

ΔQ_0 = Difference in charges due to surface oxidation, included under the "solvent" and "ethane" traces.

By comparison with Q_E , $\Delta Q_{cap.}$ will be small and will be taken as equal to zero. In the previous study (1) of CO adsorption, ΔQ_0 was assumed equal to zero, since the "solvent" and "CO" traces finally merged at high potentials, suggesting similar final surface states. For CO this assumption could be verified, since the adsorption proved to be diffusion-limited and the mathematically predicted charge-time relationship was obtained. The adsorption of ethane under these conditions is, on the other hand, very slow, and hence a similar proof may not be obtained. Also, Q_E'' corresponding to this situation may not be calculated as it may for any diffusion-controlled adsorption. The only test available here for the significance of Q_E' is the exploration of the frequency-dependence of Q_E' for fixed values of the adsorption time, T_E . Measurements of Q_E' corresponding to $T_E = 30, 100$ and 1000 sec. were made over a wide range of sweep speeds, v , and the results plotted in Fig. 6. The constancy of Q_E' over the lower range of sweep speeds is most simply explained as being due to:

$$Q_E'' = 0 = \Delta Q_0 \quad (2)$$

$$\text{and } Q_E' = Q_E = \text{constant, for constant } T_E. \quad (3)$$

} lower range of v .

It is also apparent from Fig. 6 that expression 3 must apply to increasingly larger values of v as the surface coverage with ethane decreases. In the higher range of sweep speeds, where Q_E' is not constant, the variation may have one or more of the following origins:

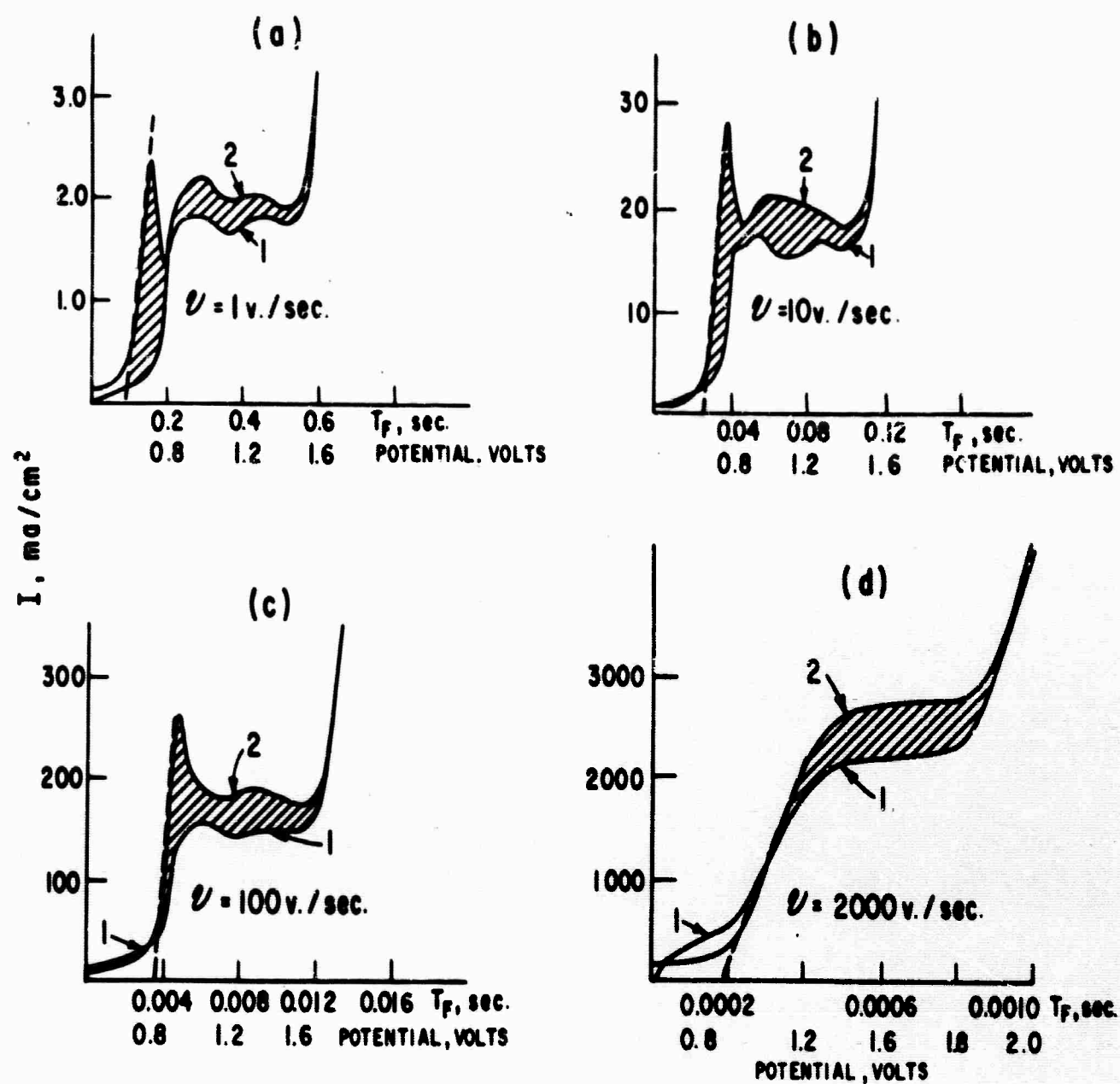


Fig. 5. Current-Time (Potential) Traces Obtained in Ethane-Saturated Solution (Sequence I, Table III, with $U = 0.4 \text{ v.}$)

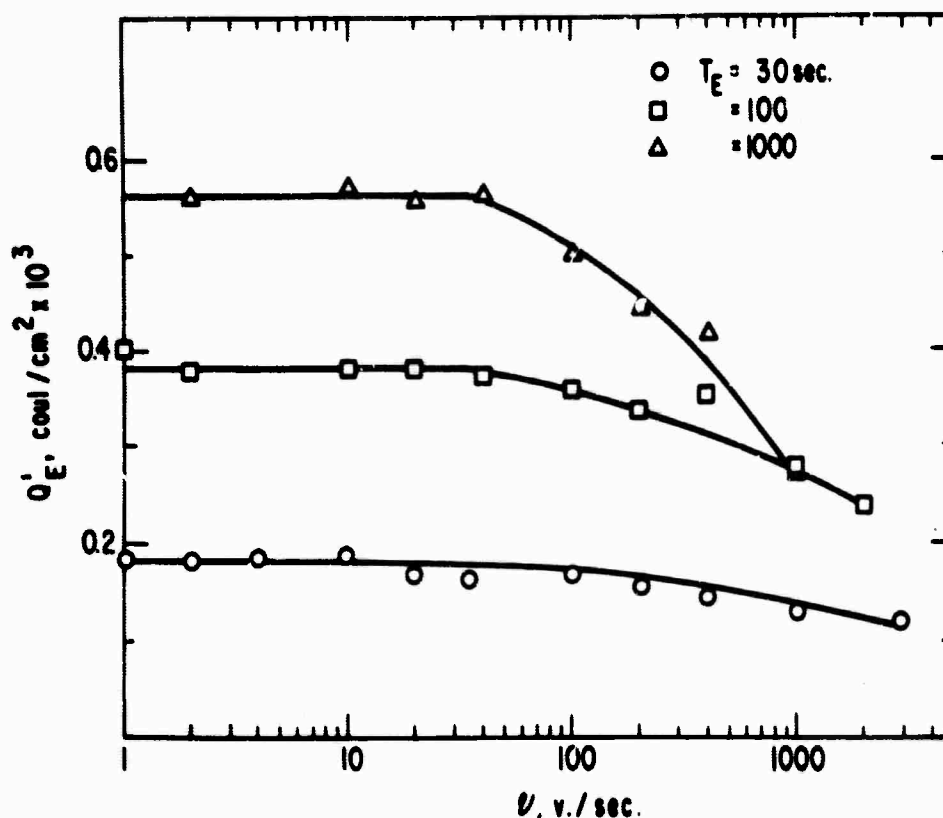


Fig. 6. Dependence of "Ethane Adsorption Charge" Upon Speed of The Linear Anodic Sweep.

1) All of the adsorbed ethane may not be oxidized by the time (and potential) the "solvent" and "ethane" traces merge at high potentials.

2) The average number of electrons involved in oxidizing the adsorbed ethane by means of the linear anodic sweep may decrease with increasing sweep speed.

3) ΔQ_0 may not be equal to zero for large values of v .

If either possibilities 1 and/or 3 were correct, the surface states for the "solvent" and ethane traces would not be the same at the high potential end of the linear anodic sweep, and the traces might be expected to cross, rather than to merge. This is already apparent in Fig. 5 D. More direct evidence was obtained by means of the experiment described in the next paragraph.

Sequence III of Table III was employed. Ethane was allowed to adsorb for $T_E = 1000$ sec., corresponding to the most obvious deviations of Q'_E from constancy in Fig. 6. During step F a l.a.s. of variable speed, v , was applied to the electrode with the amplitude of the sweep adjusted to the value at which the "solvent" and "ethane" traces were found to merge or intersect for the particular value of v , in a previous experiment. During step G, the surface was reduced for 100 msec. (insufficient time for appreciable re-adsorption of ethane from solution) and during step H a second l.a.s. of speed at 100 v./sec. was applied to the electrode. In the argon-saturated solution, the trace obtained during steps F and H were "solvent traces" and identical

(if F and H were of identical sweep speed). In the ethane-saturated solution, the trace obtained from step H would be the "solvent" trace only if all of the adsorbed ethane were removed during step F. It was found that for values of v greater than 20 v./sec., the trace obtained during step H was greater in area than the "solvent" trace, proving that ethane was indeed retained past step F for large values of the sweep speed. This incomplete oxidation of ethane at large values of v is at least one reason for decrease in Q_E' with increasing v . It is not unlikely that the other two possibilities listed in the paragraph above also contribute to the frequency-dependence at larger values of v .

As in other applications 1-4, 7-9) of the MPP method, l.a.s. traces corresponding to any fixed set of conditions were found to superimpose exactly if recorded on the same film.

3. Adsorption of Ethane as a Function of Potential

In the last section it was concluded that the $Q_E' = \sim Q_E = \text{constant}$ for any fixed value of the adsorption time, and at sufficiently low values of sweep speed. This implies that Q_E' may be used as a measure of surface coverage with ethane under the proper conditions. One important condition is that v not be chosen too small. The value of v is not too small if the adsorption has not yet gone to completion and the duration of the l.a.s. is negligible (less than 1%) compared with the adsorption time. This means that for any particular surface coverage with ethane there is a definite range of sweep speeds which may be employed for accurate estimation of the relative surface coverage. A value of v of 100 v./sec. and 10 v./sec. for adsorption times of less than, and greater than 10 sec., respectively can be shown always to fit into the safe range of sweep speeds. Using these sweep speeds and sequence I of Table III, "solvent" and "ethane" traces were obtained for a range of values of U , as a function of the adsorption time, T_E . Representative traces appear in Fig. 7. Values of Q_E obtained from such traces are plotted against the log of T_E in Fig. 8. From Fig. 7, it is apparent that for values of U less than approximately 0.35 v, noticeable charge is included under the current-time trace for values of T_E corresponding to potentials less than 0.4 v. This applies to both the "solvent" and "ethane" traces and corresponds to the presence of atomic hydrogen on the surface. The topic of hydrogen-adsorption will be deferred to a later portion of this section. Only Q_E which is a measure of adsorbed ethane species, other than atomic hydrogen will be treated in the next paragraphs.

In Fig. 8, for values of $T_E < \sim 14$ sec. the values of Q_E coincide for values of U between approximately 0.28 and 0.40 v, and provide a linear plot on rectangular coordinates (see Fig. 11). For $T_E > \sim 14$ sec., much of the data falls roughly on a straight line. Where these points overlap greatly, only the average value and the average deviation is supplied for those particular values of T_E . In the range 20 sec. $< T_E < 1000$ sec. data points which do not fall on the linear semilogarithmic plot fall into two categories:

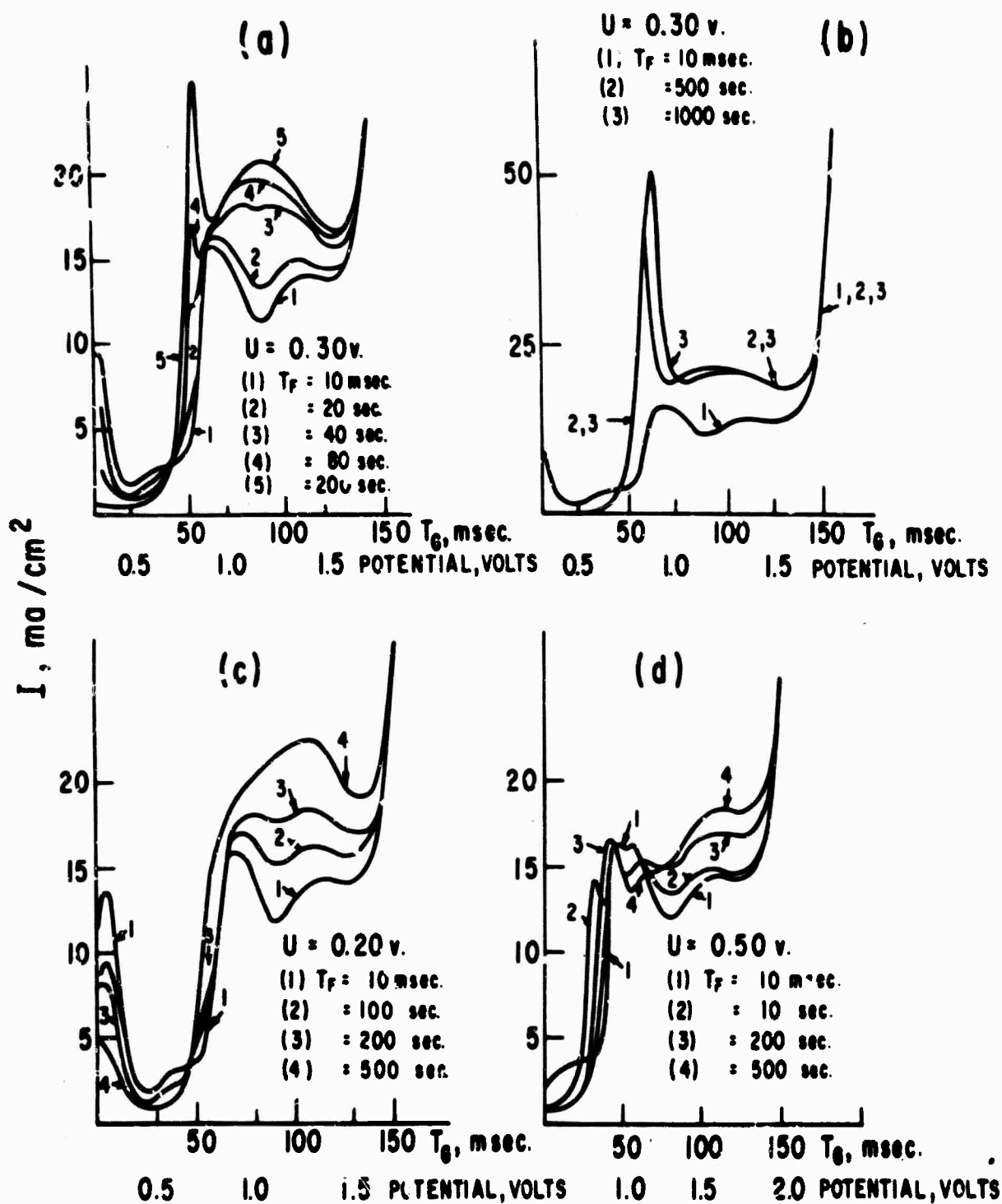


Fig. 7. Current-Time (Potential) Traces Obtained For Varying Adsorption Times At Constant Potential (Sequence I, Table III, $v = 10 \text{ v./sec.}$)

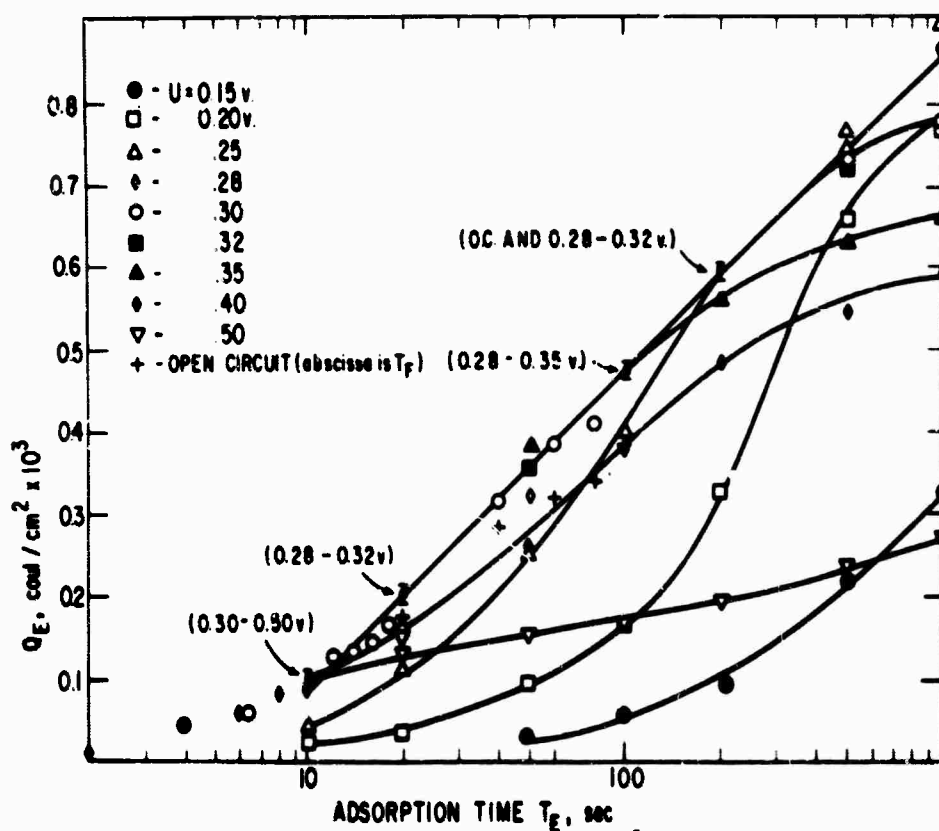


Fig. 8. Semilogarithmic Representation of Ethane Adsorption Data
The Symbol "I" Gives The Average Value and Average Deviation of That Value
in Regions Where Data Points Overlap Extensively.

1) Low potential (0.15, 0.20 and 0.25 v) points initially fall below the linear plot, but tend to merge with it as T_E increases. The points for 0.25 v actually do merge with the linear plot whereas the lower potential points do not.

2) High ($U > 0.30$ v) potential points tend to follow the linear plot for low values of T_E , but tend to break away from it at higher values of T_E . The larger the value of U , the sooner the departure from linearity. Values of Q_E measured at $T_E = 100$ sec., are plotted against U in Fig. 9. It is apparent from Fig. 9, that at high and low potentials, $\log Q_E$ changes rapidly with potential (for $T_E = 100$ sec.) but that a plateau value exists for $\sim 0.28 < U < \sim 0.36$ v. This is consistent with the idea that Q_E is related to an apparent rate of adsorption. At low potentials, the potential-independent "true" rate of adsorption is opposed by a potential-dependent rate of desorption. At high potentials, the "true" rate of adsorption is opposed by the potential-dependent rate of oxidation of adsorbed ethane. By this argument, the plateau potentials of Fig. 9 are those at which the rates of desorption and oxidation of ethane are insignificant compared with the true rate of adsorption. Since 0.3 v lies within this plateau region of potentials, it was this potential which was chosen for the experiments in the following section.

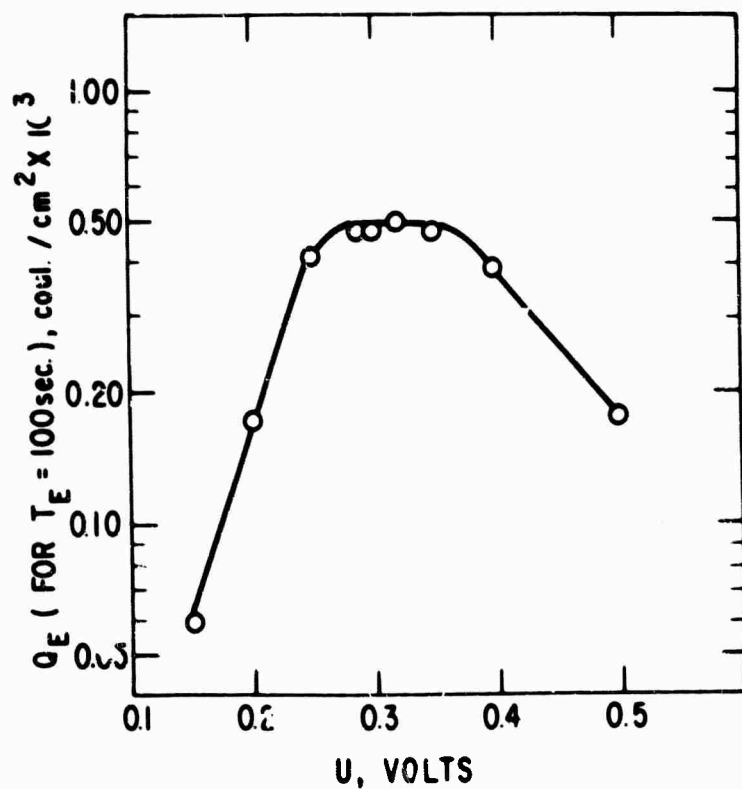


Fig. 9. "Ethane Adsorption Charge" After 100 Sec. At Fixed Potential For A Saturated Solution Of Ethane.

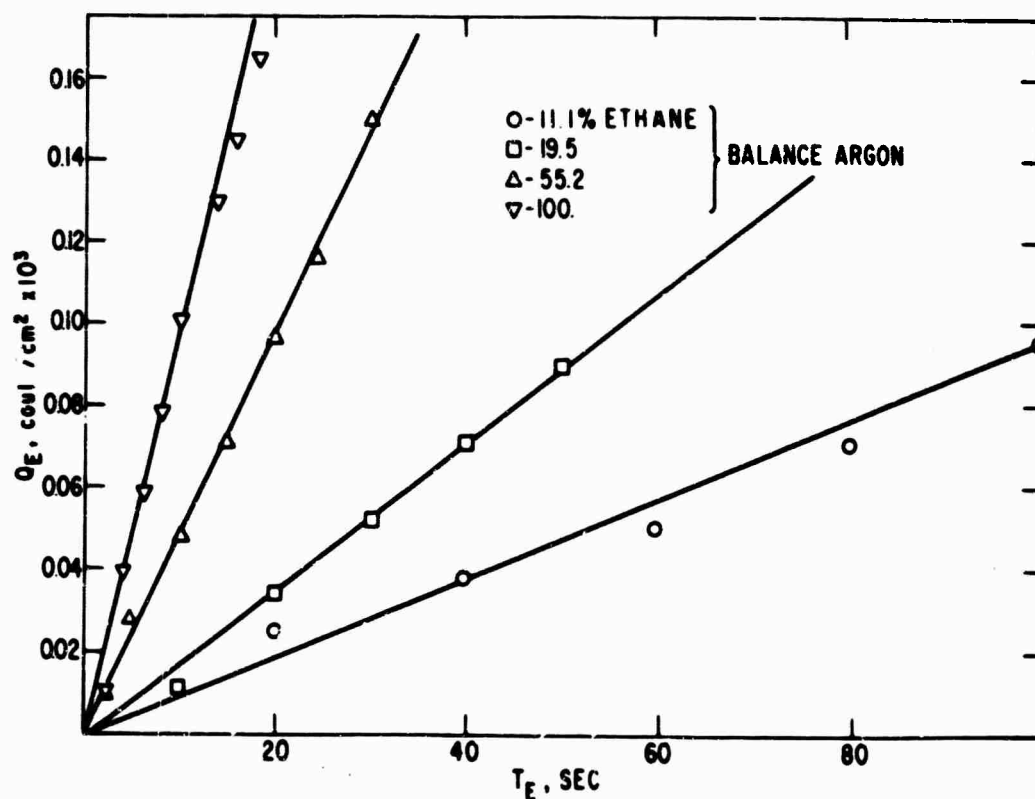


Fig. 10. Charge Corresponding To Ethane Adsorption For Solutions Saturated With Ethane-Argon Mixtures of Various Compositions (Small Adsorption Times).

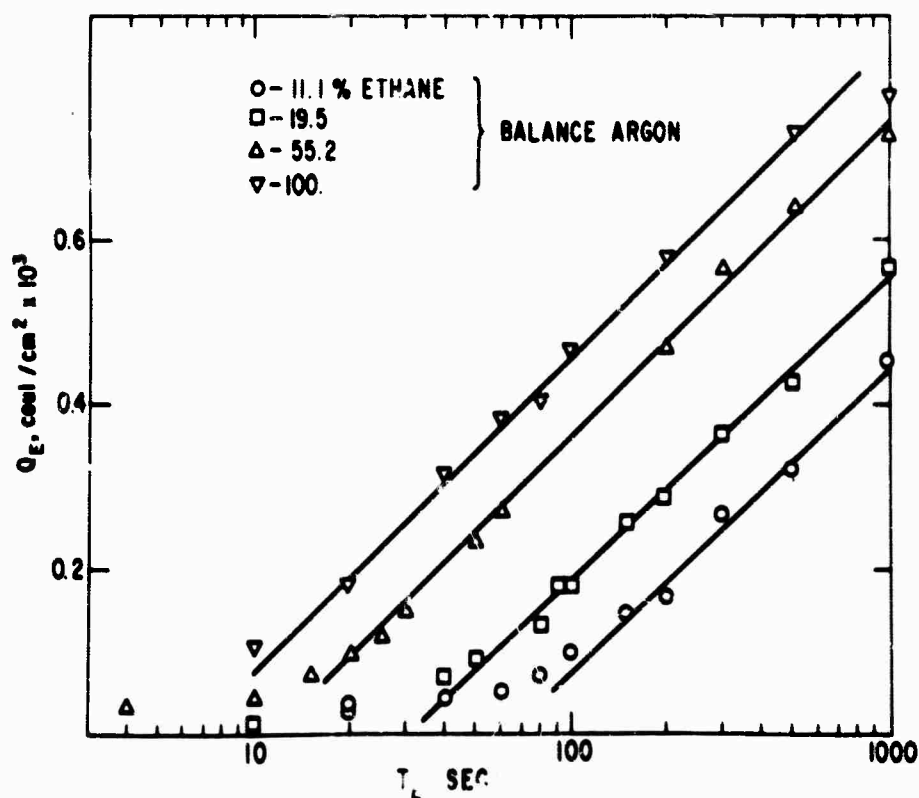


Fig. 11. Charge Corresponding To Ethane Adsorption For Solutions Saturated With Ethane-Argon Mixtures of Various Compositions (Large Adsorption Times).

4. The Effect of Ethane Concentration on Ethane Adsorption

The results of the previous paragraph suggest that at 0.3 v, the amount of ethane adsorbed is governed by a (relatively) potential-independent "true" rate of adsorption. In this section, the effect of ethane concentration on the rate of adsorption of ethane at 0.3 v will be explored. Sequence I of Table III, with $U = 0.3$ v, was employed in making the measurements. The solution was saturated with bottled and previously analyzed (mass spectrograph) gas mixtures of ethane and argon. Q_E was measured as a function of adsorption time for each gas mixture, as described in previous sections. The results for small values of T_E are plotted on rectangular coordinates in Fig. 10 and the results for larger values of T_E are plotted on semi-logarithmic coordinates in Fig. 11. Figure 10 reveals a fairly linear dependence of the initial rate of adsorption upon ethane concentration.

5. Hydrogen Co-deposition

The co-deposition of hydrogen on a surface partially covered with another adsorbate may provide information on the structure of the ad-layer (1). Sequence II of Table II was employed in the measurements on a solution saturated with ethane. The value 0.4 v. was chosen for U simply because at this potential there is ordinarily no hydrogen present on the

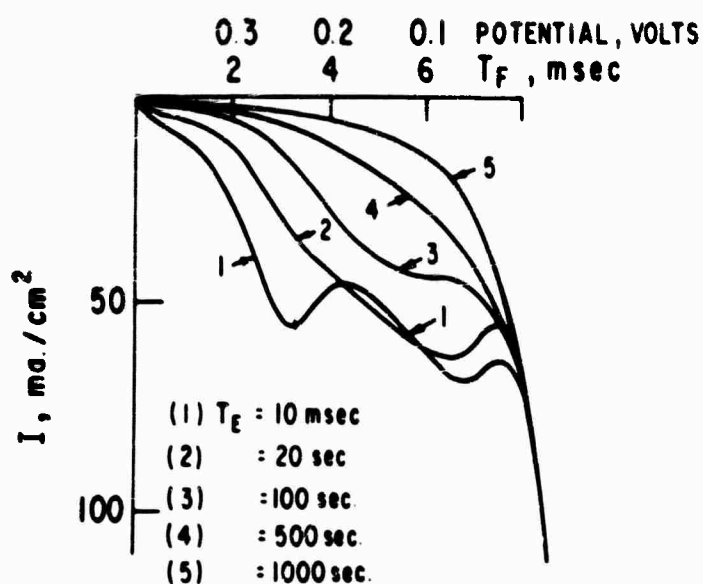


Fig. 12. Hydrogen Co-deposition Traces Obtained in Ethane-Saturated Solution (Sequence II, Table III, With $U = 0.4$ v., $v = 50$ v./sec.).

surface (10). Representative current-time (potential) traces obtained upon application of linear cathodic sweep (l.c.s.) F ($v = 50$ v/sec.), appear in Fig. 12. Trace 1 of the figure, obtained after 10 msec. adsorption time in the ethane-saturated solution, is identical with the trace obtained in an argon-saturated solution over a wide range of T_E , and represents hydrogen-adsorption on a surface free of ethane. The traces corresponding to the surface partially-covered with ethane merge with trace 1 in the low-potential region (of hydrogen gas evolution). The area enclosed between trace 1 of Fig. 12 and the trace corresponding to any value of T_E is equivalent to a charge which will be referred to as $\Delta_S Q_H$. This charge may serve as a measure of surface sites covered with ethane subject to making several assumptions which will be discussed later. One obvious condition which must be met is that the deposition of hydrogen does not cause desorption of adsorbed ethane. It is possible to check this point directly in this case as it was for carbon monoxide adsorption (1). Sequence IV of Table III was employed with $U = 0.4$ v. and for an adsorption time, T_E , of 100 sec. During step F , hydrogen was co-deposited, and the amplitude of the l.c.s. of step F was adjusted to the potential at which traces 3 and 1 merge in Fig. 12. Step G was introduced to eliminate adsorbed hydrogen and minimize the concentration of dissolved hydrogen, so

(10) A. N. Frumkin, Chap. V. in "Advances in Electrochemistry and Electrochemical Engineering", P. Interscience Pub., N.Y., 1963.

that current-contributions from these species would not interfere with the measurement of the current-time trace corresponding to step H. When step F was eliminated, an "ethane" trace identical with that of Fig. 5 was obtained. When step F was included, a trace almost identical with that of Fig. 5 was again obtained. This is proof that ethane is not appreciably desorbed under these conditions of hydrogen-codeposition, for if desorption did occur during step F, step G does not allow appreciable time for the re-adsorption of ethane, and the resulting "ethane" trace would display decreased currents. Although there is no evidence of appreciable desorption of ethane under these specific conditions, the rate of desorption of ethane at potentials in the vicinity of 0 v is found to be appreciable (section 4.1.2.4). The reason this causes no problem, in this situation, is that the low potentials are maintained only very briefly during step F of the sequence.

The second assumption made in interpretation of $\Delta S Q_H$ is similar to the commonly-made assumption that a monolayer of hydrogen is achieved at hydrogen pressures approaching one atmosphere in the gas-phase system. Even if this assumption is not rigorously correct, $\Delta S Q_H$ may be expected to serve as a measure of ethane surface coverage if the kinetics of hydrogen-evolution are not drastically (more than linearly) influenced by the ethane. The fact that the traces of Fig. 12 do tend to merge suggests that this is the case.

A plot of $\Delta S Q_H$ vs. Q_E appears in Fig. 13. There is no obvious change in slope with increase in Q_E . Hence there is no evidence for a discrete change in the average number of bonds per ethane ad-molecule with increase in surface-coverage. The slope of the plot is 0.37.

6. Hydrogen-Adsorption at Fixed Potential

a) Measurement of Hydrogen Adsorption by Means of a Linear Anodic Sweep

1) Argon-Saturated Solution

The kinetics of hydrogen deposition and removal are rapid on a clean platinum surface, and there is a readily established equilibrium surface coverage corresponding to any constant potential, U (10). The charge, Q_H , corresponding to hydrogen deposited at potential U may be measured with high reproducibility employing the MPP method and integrating the appropriate portion of the trace obtained upon applying a l.a.s. to the electrode (3). Q_H is related to the measured charge, Q_a , by (3):

$$Q_a = Q_H + Q_D + Q_{dl} \quad (4)$$

where Q_D and Q_{dl} are diffusional and capacitive contributions to the charge, respectively. For $U \geq 0.06$, Q_D may be shown to be negligible compared with Q_H for l.a.s. speeds of over 10 v/sec. (3). Q_{dl} may be expected to be quite small compared with Q_H and an approximate correction may be made. For these experiments, sequence I of Table II was employed with $v = 100$ v/sec. The traces obtained upon application of step F of the sequence are similar to the "solvent" traces

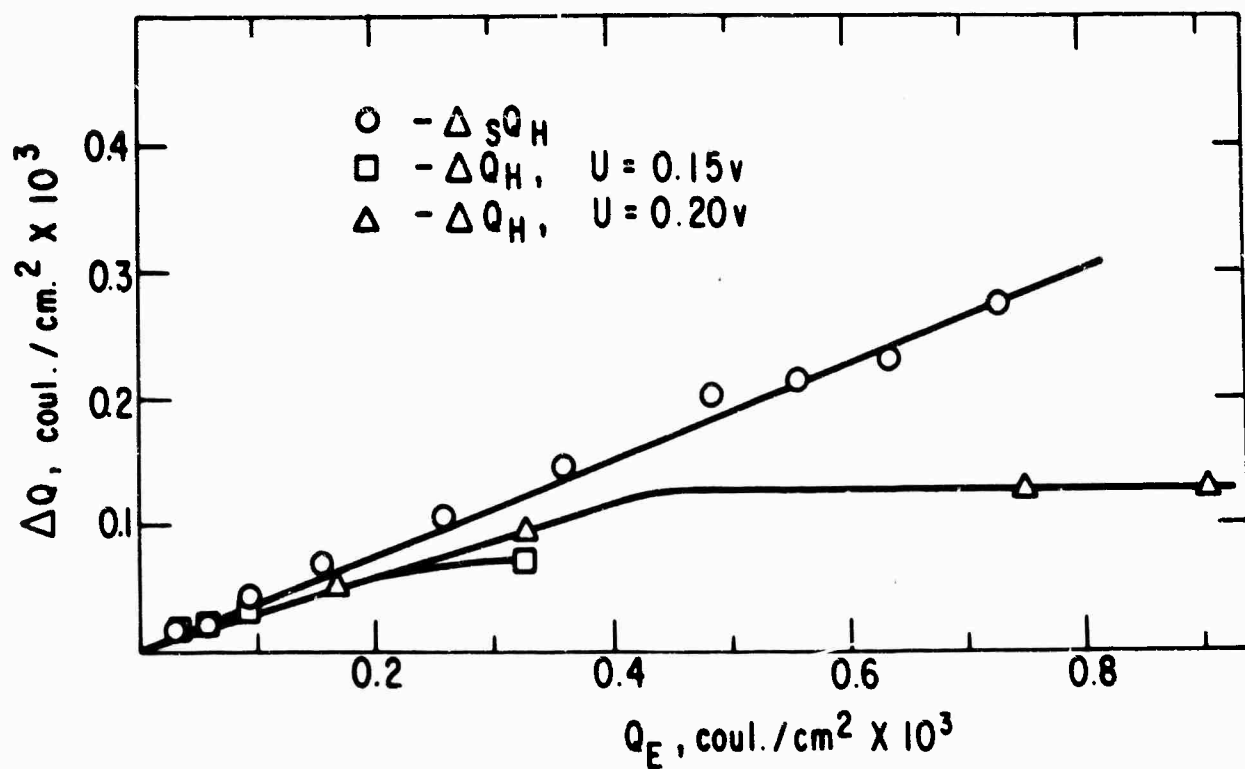


Fig. 13. Effect of Ethane Adsorption On Hydrogen Adsorption. $\Delta S Q_H$ is The Reduction In Charge Corresponding To "Saturation Coverage" With Hydrogen. ΔQ_H is The Reduction in Hydrogen Charge Occurring At Fixed Potential.

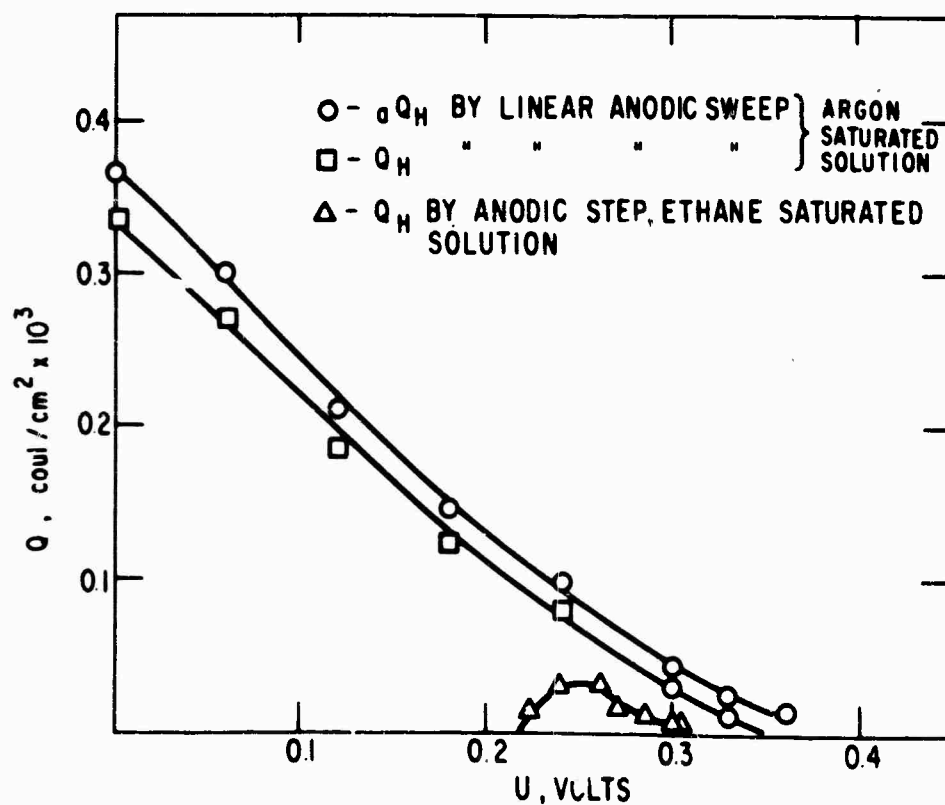


Fig. 14. Charge Corresponding To Equilibrium Surface Coverage With Hydrogen.

of Fig. 7. Since only the "hydrogen region" was of interest in this experiment, the highest possible sensitivities were used for both the current and time axes, eliminating that portion of the trace lying above approximately 0.5 v. To obtain ${}_aQ_H$, the current-time trace was integrated to the time corresponding to a potential of 0.5 v. Integration to higher potentials (to include overlap of hydrogen into the "double layer" region) was not necessary for the moderate sweep speed used. Values of ${}_aQ_H$ were identical (to within a few percent) for values of T_E from 10 msec to over 100 sec., in accordance with the expected rapid attainment of equilibrium hydrogen surface-coverage. The 10 sec. values of ${}_aQ_H$ are plotted against U in Fig. 14. The point corresponding to 0 v was obtained by comparison with previous (3) data. An approximate correction for Q_{dl} may be made by using the expression:

$$Q_{dl} = C (0.5 - U) \quad (5)$$

where the capacitance C is assumed to have the constant value $70 \mu\text{fd}/\text{cm}^2$. Values of Q_H obtained through use of equations 4 and 5 are also plotted in Fig. 14.

2) Ethane-Saturated Solution

In the paragraphs immediately above, it was demonstrated that in argon-saturated solution, the equilibrium surface concentration of hydrogen is established within the first few milliseconds and persists indefinitely. In the presence of dissolved ethane, the initial surface concentration of hydrogen is the equilibrium value for the clean surface but decreases as ethane is adsorbed. Q_H was measured as a function of adsorption time, T_E , for $U = 0.15$ and 0.20 as in section 6.a.1). above. The decrease ΔQ_H , in Q_H from the value for $T_E = 10$ msec., is plotted against values of Q_E in Fig. 13. The decrease is approximately linear at 0.20 v. The plateau corresponds to the absence of any hydrogen on the surface after the surface concentration of ethane exceeds a critical value.

b) Measurement of Hydrogen Adsorption by Means of an Anodic Step

An alternative method for the measurement of Q_H is to apply an anodic step from potential U to 0.4 v, at which potential any hydrogen present on the surface is rapidly stripped off. The quantity analogous to ${}_aQ_H$ is obtained by integration of the resulting current-time trace to the point at which the current apparently drops to zero. The quantity Q_H is then obtained, as for the l.a.s. experiment by making approximate correction for the capacitive charge. The use of a potential step has an advantage over a l.a.s. when making measurement of Q_H starting from an open-circuited condition. In the latter case it would be necessary to make very careful adjustment of the l.a.s. D.C. voltage level, which is instrumentally difficult. Values of Q_H for the argon-saturated solution were measured by means of sequence V, Table III for $U = 0.12, 0.24$ and 0.36 v to check against the values already obtained by means of the l.a.s. (Fig. 14). The values were found to agree to within a few percent.

7. Open-Circuit Potentials and the Measurement of Hydrogen Surface-Coverages

The measurements of hydrogen-adsorption reported above were all made after a specified time at a fixed potential, U . Under these conditions, it is the potential and the instantaneous surface state (which depends on elapsed time) which determine the surface coverage with hydrogen. If on the other hand, the circuit is opened after the pre-treatment sequence, the open-circuit potential (o.c.p.) and the surface coverages with hydrogen and ethane are all inter-dependent and have a complex dependence on time.

The potential sequences of Fig. 4 and Table III were chosen so that by the end of step D of any sequence there would be a minimum of dissolved oxygen gas in solution and only 10^{-4} atmospheres of hydrogen in equilibrium with the electrode. Step E of sequence VI was introduced to remove adsorbed hydrogen from the electrode surface and to deplete further, the concentration of dissolved hydrogen at the electrode-solution interface. If no dissolved hydrogen, oxygen or other adsorbable and/or electrochemically active material were present in solution, the o.c.p. of the electrode would remain indefinitely at 0.4 v during step F of sequence VI. Oxidizable and reducible species would tend to drive the o.c.p. downward and upward, respectively. The mere adsorption of a non-electrochemically active material would change the o.c.p. simply by changing the capacitance of the double layer. Under the present actual conditions, in an argon-saturated solution, the o.c.p. varies in the manner indicated in Fig. 15. Within the first 100 msec, the potential drops from 0.4 v to 0.33 v, which corresponds to equilibrium with 10^{-11} atmospheres of hydrogen. The potential does not rise above 0.4 v for 5 sec. The subsequent rise in potential from 0.4 v to 0.8 v ("double layer" region) involves only sufficient depolarizing action to change the charge stored in the ionic double layer, whereas a rise in potential above 0.8 v would require sufficient charge to initiate oxidation of the platinum surface (10). The slow drift in potential between 1 and 100 sec. could correspond to approximately 10^{-3} atmospheres of oxygen or its equivalent.

In the 0 - 100 sec. range, in the presence of a solution saturated with ethane, the o.c.p. first tends to a plateau at 0.22 v and then rises again (Fig. 15). These low potentials, compared with the argon-saturated solution must correspond to the presence of hydrogen on the surface resulting from the dissociative adsorption of ethane. By application of step G of sequence VI, Table III, a current-time trace corresponding to the amount of hydrogen accumulated after a specified time, T_F at open-circuit was obtained. Q_H was determined from the current-time trace as outlined in section 6. b. and the results plotted against the o.c.p. in Fig. 14. The values of Q_H at any potential are lower than the corresponding equilibrium values for the ethane-free surface. This is similar to the observation already made at constant potential. The points for the lowest potentials correspond to the largest adsorption times (within the first 100 sec.). Therefore it is apparent from Fig. 14 that the largest amounts of hydrogen are obtained at higher values of the potential and shorter adsorption times. This seems like an anomaly, but is not, since at

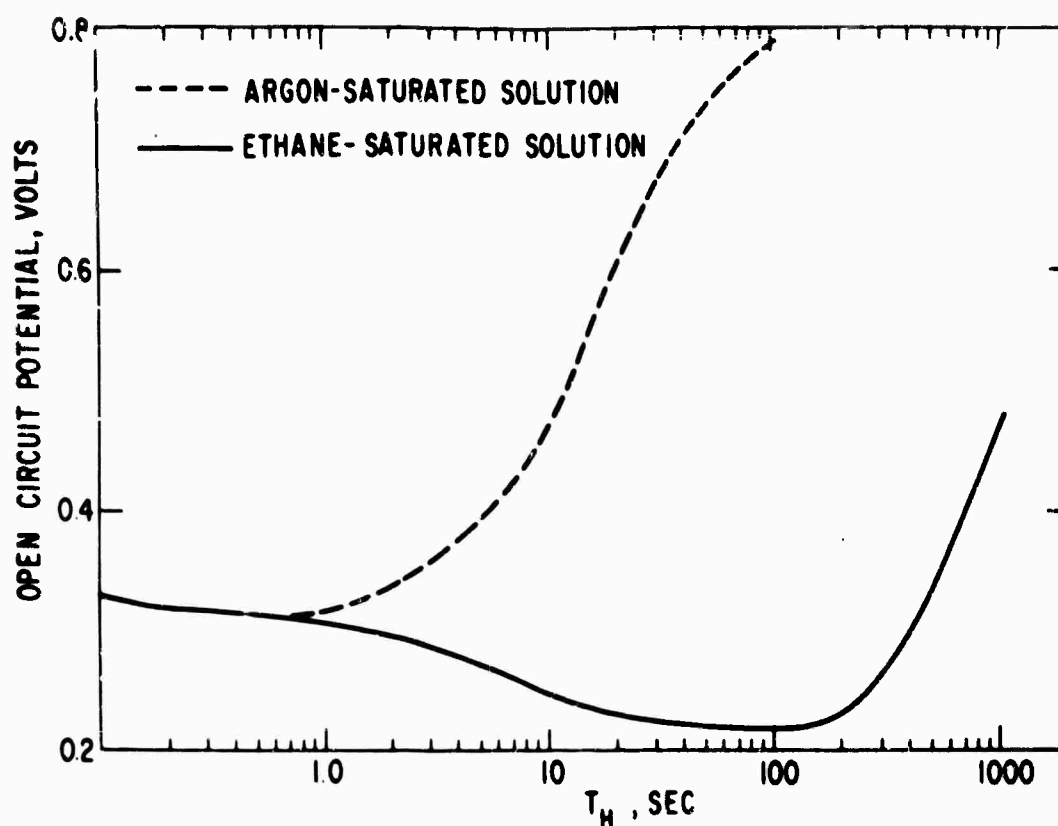


Fig. 15. Variation Of The Open-Circuit Potential With Adsorption Time.

larger values of T_F the amount of ethane on the surface is comparatively large and the amount of hydrogen which may remain co-adsorbed is relatively small, in spite of the low potentials. Only if all of the hydrogen which resulted upon adsorption of ethane were retained on the surface, would the ratio Q_H/Q_E be an indication of the extent of dehydrogenation of adsorbed ethane.

8. Ethane Adsorption at Open-Circuit

The adsorption of ethane at open-circuit may be regarded as a special case of adsorption at constant potential. The situation is complicated, since the instantaneous rate of adsorption depends both on the instantaneous surface coverage with ethane and on the instantaneous potential. It would therefore be reasonable to expect the results to depend considerably on the initial state of the surface. The pre-treatment sequence results in an initial potential at open-circuit, which lies in the "double layer" region and which remains in this region of potentials for considerable time. The initial conditions are quite close to a "neutral" situation and hence of general interest. Sequence VI of Table III was employed to obtain values of Q_E as a function of adsorption time T_F at open-circuit. After removal of adsorbed hydrogen during step G of the sequence, Q_E was obtained by the previously described integration of the current-time traces obtained upon application of l.a.s. at H. The values of Q_E obtained are plotted on Fig. 8. For small values of T_F , the points fall below the linear semi-log plot obtained for constant potentials

of about 0.2 - 0.3 v corresponding to the initial low o.c.p.'s achieved. At larger values of T_F , the adsorption follows the linear semilog plot corresponding to the medium o.c.p.'s achieved. At the largest values of T_F , when the o.c.p. rises, the apparent rate of adsorption decreases in more than an exponential manner with increase in Q_E , corresponding to similar observations made at constant high potentials.

C. Discussion

1. The Significance of Q_E

Application of a linear anodic sweep (l.a.s.) to an electrode (partially) covered with ethane, results in the measurement of a charge Q_E' after correction for electrode capacitance and for the oxidation of the platinum surface. Q_E' has the constant (for any constant surface-coverage with ethane) value Q_E if the sweep speed falls into the proper range. Under these conditions Q_E correspond to removal of ethane adsorbed before the application of l.a.s. In this range, the maximum value of sweep speed v for any particular amount of ethane adsorbed is given by a plot such as those of Fig. 6. The required minimum sweep speed must have a duration which is negligible ($< \sim 1\%$) compared with the adsorption time, provided that the adsorption is not yet complete. Decreases in Q_E' observed at high values of v correspond in part, at least, to corresponding decrease in Q_E due to the fact that all of the adsorbed ethane is not removed during the sweep.

To relate Q_E to a quantity of adsorbed ethane, it is necessary to have some knowledge of the composition of the ad-layer and of the products of application of the l.a.s. First we must note that Q_E includes charge corresponding to ethane species other than atomic hydrogen. Let us assume that there are "i" different adsorbed ethane species, each requiring the removal of n_i electrons per molecule before the species is removed from the surface. Then:

$$Q_E = \sum_i n_i F \Gamma_{E,i} \quad (6)$$

where F is the Faraday constant, and $\Gamma_{E,i}$ is the concentration of species "i" in moles/cm². Since Q_E remains constant for low values of v , it seems reasonable to conclude that the same products of oxidation of the ethane occur during the slow l.a.s., as do at steady-state. The steady-state products are carbon dioxide and water (14, 15). It is generally assumed that saturated hydrocarbons adsorb by dissociation of one or more carbon-hydrogen bonds. For hydrocarbon species ranging from stoichiometry C_2 to C_2H_6 , the value of n_i would range from 8 to 13. This serves to indicate the maximum error possible in evaluating Γ_E from Q_E . Hydrogen co-deposition data discussed below actually suggest the average stoichiometry C_2H_2 for which $n = 10$.

(14) W.T. Grubb and L.W. Niedrach, Proc. 17th Annual Power Sources Conf., Atlantic City, N.J., p. 69 (1963).

(15) M.J. Schlatter, "Fuel Cells", G.J. Young, editor, Reinhold Pub. Co., N.Y., p. 190 (1963).

BLANK PAGE

Further, the largest value of Q_E measured in this work was 8.6×10^{-4} coul./cm² (for $U = 0.28$ v, Fig. 8), and (from paragraph 1 below) this may correspond to a mono-layer. The value of Γ_E corresponding to this maximum surface coverage is, from equation 6, $\Gamma_E = 8.6 \times 10^{-10}$ moles/cm² or 5.2×10^{14} molecules/cm². Correction for a roughness factor of 1.5 results in 5.7×10^{-10} moles/cm² or 3.5×10^{14} molecules/cm².

2. Structure of the Ethane Ad-Layer

It was shown that Q_E provides an overall measure of the amount of adsorbed ethane on the surface but does not, in itself, provide information of the number of species, their structure, or stoichiometry. Two other experiments provide a clue to the solution of these problems. These are described below.

a. Hydrogen Co-deposition.

On the clean surface, $S Q_H$ is the charge corresponding to hydrogen-deposition preceding large-scale hydrogen evolution. This charge is diminished when ethane adsorbs on the surface. The decrease $\Delta S Q_H$ is related to Q_E as indicated in Fig. 13. A simple physical interpretation of the data may be made if the following assumptions are made:

1) $\Delta S Q_H$ increases because a definite bond appears between the ethane and the surface and the formation of one ethane-surface bond precludes the deposition of one hydrogen atom.

2) No steric effects block the co-deposition of hydrogen atoms.

3) Only a small number of carbon-carbon bonds are dissociated.

4) $\Delta S Q_H$ does not vary for reasons involving the kinetics of hydrogen evolution.

Some evidence that assumption 4) is approximately valid is offered by the fact that the traces of Fig. 12 do merge in the neighborhood of 0 v, where a (approximate) monolayer of hydrogen is believed to exist on the clean surface (10). The additional requirement that the deposition of hydrogen not cause desorption of ethane under the conditions of this experiment, has been verified experimentally as has already been described. Some evidence that assumption 3) is correct comes from the experiments of Niedrach who desorbed and analyzed the products obtained by the hydrogenation of adsorbed ethane. On platinum at room temperature, Niedrach found only a small percentage of methane (balance, ethane) even after several hours of adsorption, suggesting a small percentage of carbon-carbon cleavages.

Assume the formation of a single adsorbed species, C_2H_6-p , resulting from the dissociation of p carbon-hydrogen bonds and the formation of p bonds with the surface. Subject to the assumptions discussed above, the following expression may be written for $\Delta S Q_H$:

$$\Delta S Q_H = n_H \Gamma_H F = p \Gamma_E F \quad (7)$$

where n_H = number of electrons required to deposit one hydrogen atom = 1

Γ_H = surface concentration of hydrogen sites blocked by the formation of surface-ethane bonds.

Dividing equation 7 by equation 6

$$\frac{\Delta_{S}Q_H}{Q_E} = \frac{p}{n} = \frac{p}{14-p} \quad (8)$$

The theoretical values of $\Delta_{S}Q_H/Q_E$ calculated for values of "p" of 3, 4 and 5, are 0.27, 0.40 and 0.56, respectively. The value of $\Delta_{S}Q_H/Q_E$ obtained as the slope of the appropriate plot of Fig. 13, is 0.375, which best corresponds to the value $p = 4$, and the stoichiometry C_2H_2 , based on the simple interpretation of hydrogen co-deposition discussed above.

The existence of a stoichiometry of C_2H_2 for the ethane ad-layer may have the following different significances:

1) This may be a predominant stoichiometry, with small amounts of species of different molecular weight.

2) This may be an average stoichiometry, with considerable amounts of species with higher and lower hydrogen content. The absence of a discernable change in slope for the $\Delta_{S}Q_H$ plot of Fig. 13, seems to rule out the possibility that there is discrete and step-wise adsorption of species of more than one stoichiometry. Possibility 2 cannot be ruled out. It is possible that, contrary to the assumptions made in deriving equation 8, the dissociation of one carbon-hydrogen bond does not lead to the formation of a one carbon-surface bond.

b. Ethane Adsorption at Open-Circuit

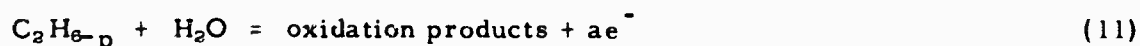
When ethane adsorbs dissociatively at fixed potentials higher than approximately 0.3 v, the surface concentration of hydrogen soon drops to a negligible value. Any atomic hydrogen released during the adsorption escapes via an electrochemical route. At open-circuit, the hydrogen produced during adsorption may be largely retained, and may serve as an indication of the stoichiometry of the process. Again assume that p carbon-hydrogen bonds are broken per molecule of ethane adsorbed. If these hydrogen atoms remained on the surface, then, analogous to equation 8,

$$Q_H/Q_E = p/(14-p) \quad (9)$$

The major difference between the significance of equations 8 and 9 is that $\Delta_{S}Q_H$ is a measure of hydrogen co-deposited on a previously hydrogen-free surface, whereas Q_H is a measure of hydrogen resulting from the adsorption of ethane. The ratio Q_H/Q_E was found to have the values 0.6, 0.4 and 0.5 after 2, 5 and 10 sec., respectively, and then dropped off to zero, presumably due to recombination of hydrogen atoms by the over-all reaction:



A second complication is that hydrogen need not appear by the simple dissociation of ethane, but could also result from electrochemical oxidation of ethane at low surface coverages:



Because of these possible complications and the fact that the ratios of Q_H/Q_E are greater than zero only for small values of both Q_H and Q_E (where the possible error in taking the ratio is high), we may conclude only that the results are not inconsistent with an adsorption involving the rupture of several carbon-hydrogen bonds per molecule.

3. The Kinetics of Ethane Adsorption

The rates of ethane adsorption measured in this work are so small (less than one-hundredth) the comparable estimated diffusion rates, that no correction for concentration changes will be made, and the concentration of dissolved ethane adjacent to the solution will be assumed equal to the bulk concentration.

Values of Q_E are plotted against the log of adsorption time, T_E , in Fig. 8 for a solution of 1 N perchloric acid saturated with ethane. For a critical examination of the plots, first observe that the slope of the semilog. plot is related to a rate of adsorption by:

$$\text{Slope} = \frac{d Q_E}{d \ln T_E} = T_E \frac{d Q_E}{d T_E} \quad (13)$$

$$\text{Rate of Adsorption} \sim \frac{d Q_E}{d T_E} = \text{Slope}/T_E \quad (14)$$

The linear semilog. plot which (approximately) joins much of the data for $T_E > \sim 14$ sec. has the property (according to equation 14) that although the slope remains constant, the rate of adsorption drops off in inverse proportion to T_E . It is also a consequence of this type of representation of the data, that although the slope of some of the non-linear plots is more steep (than the linear plot) for larger values of T_E , the rate of adsorption never exceeds the linear semilog. law for any fixed value of Q_E .

As previously noted, the maximum (linear semilog.) law is the one:

- 1) Followed at medium values of the potential, starting from $T_E = 0$ to $T_E > 100$ sec.
- 2) Approached at low potentials for large values of T_E .
- 3) Followed at high potentials for small values of T_E .

These observations and the plateau of Fig. 9 suggest that the apparent rate of adsorption, R , may be represented by:

$$\frac{d Q_E}{d T_E} \sim R = R_{ad} - R_d - R_{ox} \quad (15)$$

where R_{ad} = potential-independent rate of adsorption of ethane

R_d = potential-dependent rate of desorption of adsorbed ethane

R_{ox} = potential-dependent rate of oxidation of adsorbed ethane

The linear semilog. plot, and maximum adsorption rate of Fig. 8 corresponds to R_{ad} . According to this argument, for the higher values of potential, $R_d = 0$. If the potential is not too high, R_{ox} is

at first negligible compared with R_{ad} , but stays approximately constant with time, whereas R_{ad} drops off rapidly. For some value of T_E , R_{ox} finally becomes significant compared with R_{ad} and we have a deviation from the maximum adsorption law. At low potentials, $R_{ox} = 0$, but R_d is initially significant compared with R_{ad} and the apparent rate of adsorption is smaller than R_{ad} . Although R_{ad} falls off with time, R_d must fall off even more rapidly, and eventually R_d becomes negligible (for potentials which are not too low) compared with R_{ad} , and the points tend to approach the linear semilog. plot.

Corresponding to the linear semilog. plot of Fig. 8 for values of $T_E < \sim 14$ sec., a linear plot is obtained on rectangular coordinates for $T_E = 0$ to ~ 14 sec. for potentials of 0.3 and 0.4 v. These points correspond to the maximum rate of adsorption for small values of T_E and presumably correspond to R_{ad} . In Fig. 10, appear the linear (on rectangular coordinates) portions of the Q_E vs T_E data for electrolyte saturated with ethane-argon mixtures of several compositions. The data of Fig. 10 may be represented empirically by:

$$Q_E = k_1 C T_E \quad (16)$$

where C = concentration of dissolved ethane in moles/cm³

k_1 = appropriate constant in $\frac{\text{coul. -cm}}{\text{mole-sec.}}$

Assume that for a solution saturated with 100% ethane, C has the value for the solubility of ethane in water at 60°C or (by estimation) 1.8×10^{-6} moles/cm³ (12). Then assuming the applicability of Henry's Law, k_1 is obtained from the slopes of Fig. 10,

$$k_1 = 5.0 \frac{\text{coul. -cm}}{\text{mole-sec.}} \quad (17)$$

with an average deviation of 0.2 units.

In Fig. 11 appear semilog. plots corresponding to the gas mixtures of Fig. 10, but for larger values of T_E . These plots may be described empirically by:

$$Q_E = k_2 \log \frac{T_E}{T_0} \text{ for } Q_E > 0.1 \text{ mcoul./cm}^2. \quad (18)$$

where T_0 is the x - intercept obtained by extrapolation of the approximately linear portion of each plot backward to $Q_E = 0$. Since the linear plots are parallel k_2 is constant and has the value,

$$k_2 = 3.9 \times 10^{-4} \text{ coul./cm}^2 \quad (19)$$

The intercept T_0 may be related to the concentration of ethane by:

$$T_0 = k_3 / C \quad (20)$$

from the experimental plots of Fig. 11, k_3 is found to have the value,

$$k_3 = 3.3 \times 10^6 \frac{\text{sec. -cm}^3}{\text{mole}} \quad (21)$$

with an average deviation of 0.1×10^6 units.

(12) O.C. Culbertson, A.B. Horn and J.J. McKetta, Trans. Am. Inst. Mining Met. Engrs., Petrol. Div., 189, 1 (1950).

Thus far, no physical significance has been assigned to the empirical relationships 16 and 18. This may now be attempted. Assuming simple Langmuir kinetics for the adsorption,

$$\frac{d \theta_E}{d T_E} \propto \frac{d Q_E}{d T_E} = k_1 C (1 - \theta_E)^m \quad (22)$$

where θ_E is the fractional surface coverage with ethane, and m is the order of the adsorption reaction. For small values of θ_E and of m ,

$$\frac{d Q_E}{d T_E} = k_1 C \quad (23)$$

which upon integration gives equation 16. Therefore equation 16 is the initial constant rate of adsorption for a system following simple Langmuir kinetics of unknown order.

An initial comprehension of the significance of the experimental relationship 18 follows from the observation that when Q_E becomes too large, equation 16 will no longer apply even if equation 22 still applies or if some more complicated law predominates. The time at which the critical value of Q_E is achieved is dependent on the concentration through equation 16. This simple dependence of a critical value of Q_E upon T_E and C is reflected in the value of the empirical x - intercept of the semilog. plot as given by equation 20.

Whereas the existence of constant initial rates of adsorption helps to explain the translation of the $Q_E - \ln T_E$ plots of Fig. 11 along the $\ln T_E$ axis, it does not offer an explanation for the (approximate) semilog. relationship. This will now be attempted. The derivative of empirical relationship 18 is:

$$d Q_E = k_2 d \ln \frac{T_E}{T_0} = k_2 \frac{d T_E}{T_E} \quad (24)$$

$$\text{or} \quad \frac{d Q_E}{d T_E} = \frac{k_2}{T_E} \quad (25)$$

Substituting for T_E using equation 18,

$$\frac{d Q_E}{d T_E} = \frac{k_2}{T_0} \exp. (-Q_E/k_2) \quad (26)$$

which is a form of the Elovich Equation (13). Many systems which display slow adsorption kinetics (gas phase) can be represented by an expression similar to equation 26 over a region of surface coverages (13). Some physical models which can lead to such an empirical relationship include:

- 1) Increase in activation energy for adsorption with increase in surface coverage (13).
- 2) Steric effects (16).

These two possibilities will again be considered after attempting to obtain the order of the initial rate of adsorption.

(13) D.O. Hayward and B.M.W. Trapnell, "Chemisorption", Second Ed., Butterworth's, Inc., 1964.

(16) R. Coekelbergs, A. Brennet, G. Lienard, and P. Reisbois, J. Chem. Phys., 39, 585 (1963).

Referring to equation 22, it is seen that the order of the initial rate of adsorption may be determined if the fractional surface coverage with ethane is known. It is customary in gas phase studies to define the fractional surface coverage as the ratio of the volume of gas adsorbed at equilibrium:

$$\theta = q/q_{\infty} \quad (27)$$

Analogous to equation 27, we may write:

$$\theta_E = Q_E/Q_{E,\infty} \quad (28)$$

A determination of $Q_{E,\infty}$ is not practical however, due to the following complications:

1) R_{ad} (equation 15) becomes extremely small as a monolayer is approached, and it is difficult to tell whether R_d or R_{ox} are contributing to bringing about an apparent rate of adsorption of zero, as opposed to the achievement of such a steady state upon adsorbing a monolayer of ethane.

2) $Q_{E,\infty}$ may have no simple significance in terms of surface sites, since at the large values of adsorption time, the structure of the ad-layer may become quite complex due to slow surface conversions.

A better choice for the definition of fractional surface coverage under these circumstances may be:

$$\theta_E = \frac{\Delta S Q_H}{S Q_H} \quad (29)$$

Equation 29 defines ethane surface-coverage in terms of hydrogen sites, and therefore involves assumptions similar to those already made in the interpretation of hydrogen-codeposition (section 2A). From analysis of Fig 13, $\Delta S Q_H = 0.375 Q_E$, and the measured value of $S Q_H$ was 3.2×10^{-4} coul./cm². Therefore,

$$\theta_E = 1170 Q_E \quad (30)$$

Use of equation 30 suggests incidentally, that $\theta_E = 1$ after 1000 sec. at 0.28 v. From equation 22:

$$\ln \frac{d \theta_E}{d T_E} = \ln k_4 + m \ln \theta_F \quad (31)$$

where $\theta_F = 1 - \theta_E$ = fractional free surface.

To obtain a preliminary estimate of "m", values of θ_E for $U = 0.3$ v, were plotted against T_E , on

rectangular coordinates, and values of $\frac{d \theta_E}{d T_E}$ were obtained graphically. These slopes were then

plotted against θ_F on log. -log. coordinates. A good linear plot was obtained for values of θ_F from 1 to 0.6, where sharp departure from linearity was observed. The value of m obtained was 1.6 suggesting (predominantly) second-order kinetics. Integrating equation 31 with m=2:

$$1/\theta_F = KCT_E \quad (32)$$

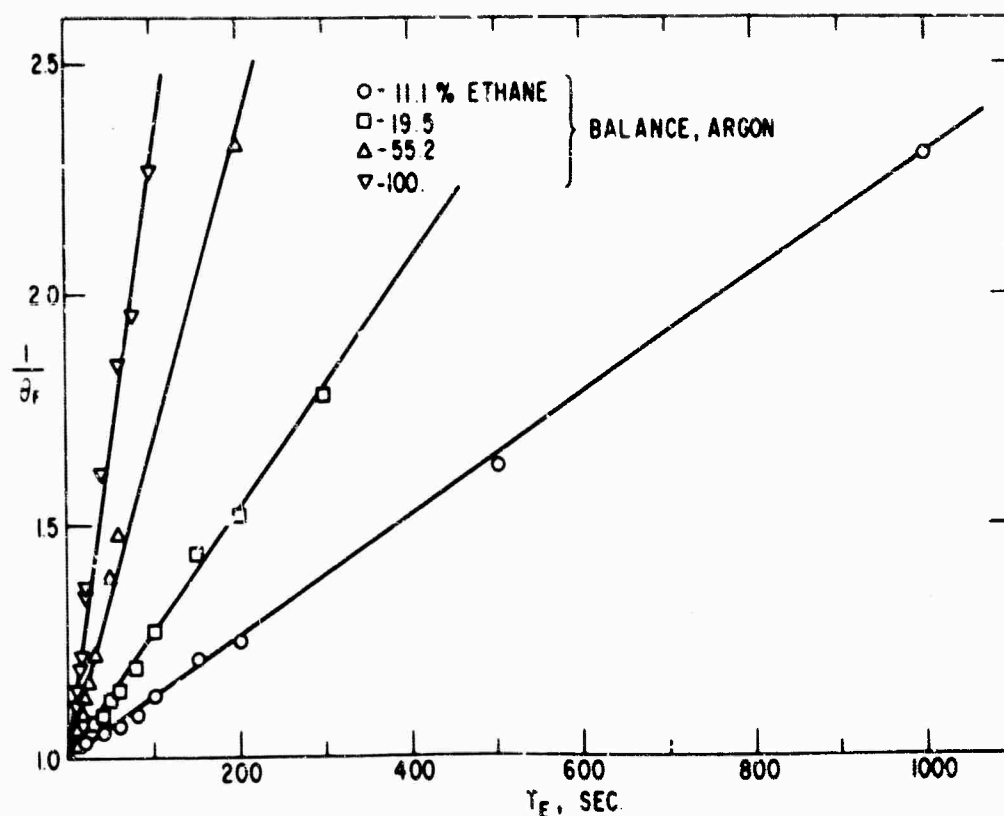


Fig. 16. Variation in Fractional Free Surface With Adsorption Time. Solution Saturated With Designated Mixtures of Ethane And Argon.

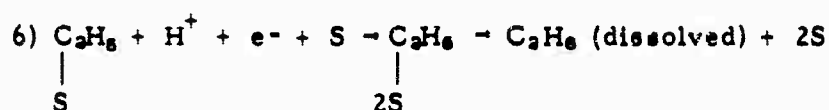
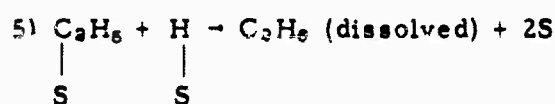
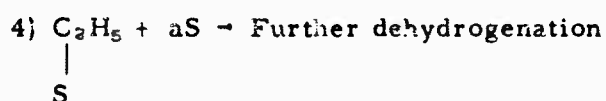
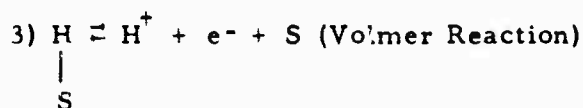
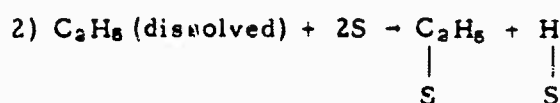
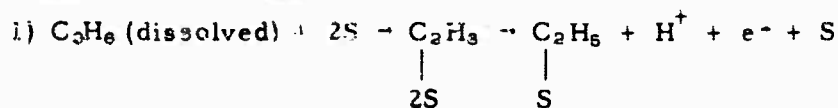
Plots of $1/\theta_F$ vs. T_E for $U = 0.3$ v and for various concentrations of ethane appear in Fig. 16. Good linearity was obtained for values of θ_F up to 0.3 for the solution saturated with pure ethane (not shown on plot). K has the average value of 1.31×10^4 $\text{cm}^3/\text{mole-sec.}$ with an average deviation of 0.15×10^4 units.

The results of this analysis suggest that simple adsorption kinetics, (first order in dissolved ethane and second-order in available surface sites), may satisfactorily account for the data obtained up to quite high ($\theta_E = 0.7$) surface coverages. It seems more reasonable to assign the departure from simple kinetics which occurs at high surface coverages to steric effects (16) than to variation in energy of adsorption (13). The latter effect is usually assumed to apply when the fractional surface coverage is only a few tenths.

4. Mechanism of the Adsorption of Ethane

The previous work presented evidence for the existence of a simple, relatively potential-independent rate of adsorption of ethane. This rate can be measured when the opposing and potential-dependent rates of adsorption and oxidation are made negligible by proper choice of the potential. The kinetic evidence further suggests that the elementary adsorption process is second-order in surface adsorption sites. Hydrogen co-deposition data suggests that four (hydrogen)

surface sites are obscured for each ethane molecule adsorbed. None of these sites correspond to hydrogen atoms released through dissociative adsorption of the ethane, since these are quickly discharged under the conditions of the experiment. Employing this evidence, we will attempt to choose from the adsorption processes listed below:



S = surface adsorption site

In reactions 1 and 2 an adsorbed ethyl radical was chosen as the simplest structural possibility corresponding to second order adsorption kinetics. Either Reaction 1 or 2 may represent the rate-determining step in the adsorption process. Reaction 1 suggests that the rate of adsorption will depend on the rate of an electron-transfer. This appears to be true only in a limited sense, i. e. the rate is retarded at low potentials, when there is atomic hydrogen on the surface, but reaches a plateau after the potential is sufficiently high so that the concentration of adsorbed hydrogen is zero. This causes us to prefer reaction 2, with the added condition that the surface concentration of hydrogen is maintained at zero level. This latter condition was easily fulfilled under our experimental conditions, by the operation of the very rapid forward Volmer reaction (reaction 3). Having chosen reaction 2 as the primary and rate-controlling adsorption step, we must next concern ourselves with the structure of the stable surface species produced when ethane is adsorbed. Hydrogen co-deposition experiments suggest 4 surface sites per surface species and hence argue for further dehydrogenation of the original adsorbed ethyl radical (equation 4) which would be a relatively rapid reaction relative to rate-determining step 2. The simplest interpretation of hydrogen-codeposition results would be that "a" of step 4 has the value "3", and that the predominant process of step 4 is the breaking of three carbon-hydrogen bonds to give a surface species of formula C_2H_3 . The observation has been made that the ad-layer oxidizes over a wide range of potentials upon application of a linear anodic sweep (Fig. 5 and 7), and that only a fraction of the

ad-layer is removable by hydrogenation. These observations suggest that there may be a variety of structures in the ad-layer and that the apparent number of sites per adsorbed ethane species may only be an average value. Under such conditions the adsorption rate data are non-complex simply because the kinetics depends only on the concentration of vacant surface sites.

Reactions 5 and 6 are possibilities for the low-potential desorption of adsorbed ethane, which opposes the elementary adsorption process at these potentials. Reactions 5 and 6 differ in that 5 depends on atomic hydrogen supplied by reverse reaction 3, whereas 6 depends on a direct electron-transfer reaction. The concentration of adsorbed hydrogen is appreciable, since the desorption becomes appreciable only at low potentials. Reaction 6 must clearly be potential dependent, but so must 5, since the concentration of atomic hydrogen depends on the potential. Hence 5 and 6 are kinetically indistinguishable under these conditions. The desorption process is given further consideration in section 4.1.2.4 of this report.

5. Ethane Adsorption and Hydrogen Desorption

In the hydrogen co-deposition experiments discussed previously in section 2.a., ethane was first adsorbed at potentials at which dissociated hydrogen produced during the adsorption would be consumed via the Volmer reaction. Atomic hydrogen was then deposited on the surface by gradually lowering the potential (by means of a linear sweep) to the point where large-scale evolution of hydrogen occurred. Interpretation of the reduction in hydrogen-deposition charge, ΔQ_H , attendant upon ethane adsorption was based partially on the assumption that surface sites not actually occupied by ethane would be covered by hydrogen by the time the low potentials and large-scale evolution of hydrogen were encountered. In addition to decreasing the total amount of hydrogen which may reside on the surface, the adsorption of ethane also decreases the amount of hydrogen which (thermodynamically) may exist on the surface of any potential greater than 0 volts, while the total surface coverage with both ethane and hydrogen is still much smaller than a monolayer. This is apparent from the plots of Fig. 13, and the spontaneous desorption of hydrogen at open-circuit. The effect is also manifested in the shift of the hydrogen-deposition traces of Fig. 12 to lower potentials as opposed to a drop in current only in the near vicinity of zero volts. One may simply conclude that adsorption of a second species tends to lower the heat of adsorption of hydrogen (10). This observation has been made in the adsorption on platinum of alcohols (17), CO (1), formic acid (18), and anions (4, 19).

(17) M. W. Breiter, J. Electrochem. Soc., 109, 42 (1962).

(18) M. W. Breiter, Electrochim. Acta, 8, 457 (1963).

(19) M. W. Breiter, Electrochim. Acta, 8, 925 (1963).

6. Some Remarks on the Electrochemical Oxidation of Adsorbed Ethane

A discussion of the detailed analysis of the kinetics and mechanism of oxidation of adsorbed ethane is planned in future work. It is possible at present, however, to make some observations of a general and qualitative nature on the material at hand.

a. Maximum Steady-State Rate of Oxidation of Ethane

The kinetics of oxidation of ethane already adsorbed on the surface, might be expected to be completely independent of the rate of adsorption of ethane under transient conditions. Under steady-state conditions the amount of ethane originally on the surface is trivial compared with that re-supplied from the solution. Under the latter conditions, the maximum possible current might be expected to approach equivalence with the maximum rate of adsorption of ethane. Equation 16 gives the maximum accumulation of ethane on the surface, expressed as the charge required to completely oxidize the ethane. The maximum current is equal to the derivative of Q_E , or

$$I_{\max} = \frac{d Q_E}{d T_E} = k_1 C = 5 C \quad (33)$$

assuming a saturated solution of ethane, and $C = 1.8 \times 10^{-8}$ mole/cm³

$$I_{\max} = 9 \times 10^{-8} \text{ Amp./cm}^2 \quad (34)$$

Equation 34 gives an estimate of the maximum steady-state oxidation current only if it is assumed that adsorption must precede oxidation.

b. Reactivity of Adsorbed Ethane

Fig. 7a and 7b contain current-voltage traces corresponding to the oxidation of partial monolayers of ethane adsorbed at 0.3 v. This particular potential is chosen for discussion since the evidence has suggested that the processes of desorption and oxidation are relatively unimportant here. The traces of Fig. 7a and 7b reveal two fairly distinct regions of oxidation of adsorbed hydrocarbon. The low potential region exhibits a sharp maximum below 0.8 v. The high potential region is fairly flat and extends from approximately 0.8 v up to potentials of appreciable oxygen-evolution (~ 1.6 v). Separation between these two regions becomes increasingly more obvious as the sweep speed is decreased (see Fig. 5). At the lowest sweep speeds employed, the low potential region is observed to begin at potentials of 0.5 v or less. The measurements of apparent rate of adsorption already discussed, suggest appreciable rate (compared with adsorption) of oxidation of ethane at potentials approaching 0.3 v.

Examination of the traces of Fig. 7a and 7b reveal that both the low and high-potential species increase gradually with increase in surface coverage. It has been observed that the low-potential species is not readily desorbed at low potentials as is the high-potential species. It is possible that these "species" are a manifestation of surface heterogeneity, or of gross differences in structure, or both.

Comparison of the current-voltage traces obtained for ethane (Fig. 5 and 7) with those obtained for CO (1, 6-8) offer an interesting contrast. Whereas the rate of adsorption of CO is quite high (1), and that of ethane quite low, the entire CO adsorption layer is electrochemically quite inactive compared with at least a part of the ethane ad-layer.

7. Comparison with Gas-Phase Studies of Ethane Adsorption

A platinum surface submerged in an electrolyte differs from that in the gas phase by the presence at the surface of water (weakly bonded) and of an ionic double-layer. The former may compete only slightly with adsorbates, such as hydrocarbons, having a high heat of adsorption. The latter opens the possibility of additional reaction routes, and of their control, through the control of the electric field at the surface. Perhaps the most significant difference between adsorption of hydrocarbons from the gas phase and from solution in an electrolyte, is that in the latter case there is the existence of the Volmer reaction, which allows hydrogen to desorb from the surface as well as to migrate freely from one surface site to another, in the protonic form. On the other hand, desorption of hydrogen (from the dissociative adsorption of a hydrocarbon) in the gas phase system, requires the mobility of atomic hydrogen on the surface and the making and breaking of chemical bonds. It has been shown that the adsorption of ethane is opposed by the hydrogenation-desorption process, which can be avoided electrochemically by rapid electrochemical removal of hydrogen. Under conditions of open circuit, hydrogen must recombine to form hydrogen molecules in order to desorb, but the Volmer reaction still may operate to provide rapid mobility on the surface for recombining hydrogen atoms. Thus a possible contribution to the slow rates (11, 13) of adsorption observed for hydrocarbon adsorptions on various surfaces from the gas phase may arise from sluggish hydrogen-desorption kinetics and a resulting appreciable rate of hydrocarbon hydrogenation-desorption.

While no comparable gas-phase data is available for the ethane-platinum system, brief consideration of the results obtained for ethane on nickel is of interest. Wright et al. (20) found that at 0°C., 4×10^{13} molec./cm² (true area basis) were adsorbed within the first minute as compared with approximately four times that amount adsorbed at 60°C in this work. Further adsorption was observed to occur with the log of time (as in this work) for two to three more hours. Final adsorption after 3 hours resulted in 1.2×10^{14} molecules/cm² as compared with an estimate of approximately three times that quantity at full coverage in this work. Wright et al. did not find any great change in the slope of the adsorption curve with increase in temperature.

(11) G.C. Bond, "Catalysis by Metals", Academic Press, N. Y., 1962.

(20) P.G. Wright, P.G. Ashmore and C. Kemball, Trans. Far. Soc., 54, (1958).

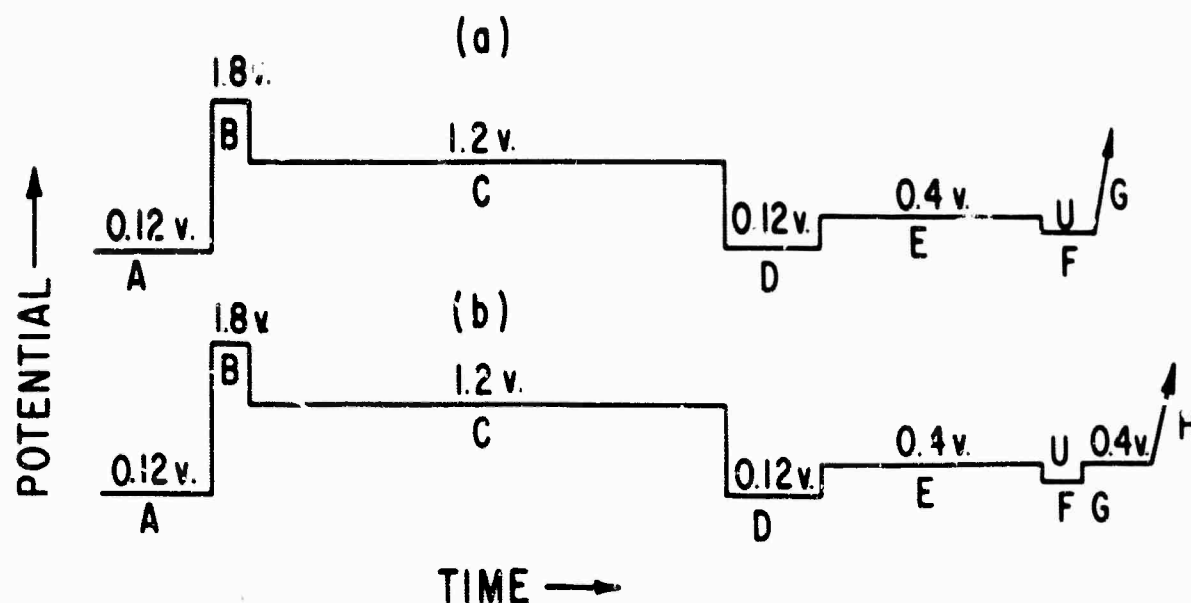


Fig. 17. Potential Sequences Applied To The Test Electrode
(Time Axis Not To Scale).

4.1.1.3 Kinetics and Mechanism of Desorption of Ethane From Platinum

In Section 4.1.1.2, a MPP method was established for the quantitative study of the ethane ad-layer on a platinum electrode. The method was applied toward elucidation of the kinetics and mechanism of the adsorption process which occurs at potentials several tenths of a volt positive to a reversible hydrogen electrode in the perchloric acid electrolyte. This section will be devoted to the desorption of adsorbed ethane, a process which occurs at relatively lower potentials on the hydrogen scale.

The desorption of adsorbed ethane species from platinum fuel cell electrodes was previously noted by Niedrach (21) who determined that the major desorption product was ethane (small percentage of methane). No kinetic information resulted from that study.

A. Experimental

Equipment, chemicals, etc., have been described in Section 4.1.1.2. Measurements were made at 60°C. in 1 N perchloric acid solution. The test electrode used was the same as that previously described, having $S_{QH} = 0.32 \text{ mcoul./cm}^2$ and an estimated roughness factor of 1.5.

(21) L. W. Niedrach, J. Electrochem. Soc., 111, 1309 (1964).

TABLE IV

Procedures Followed During Potential Sequences of Fig. 17

Sequence	Fig.	Step (Refers to Fig. 17)	Procedure	Purpose
I	17a	A	1) Bubble gas* through solution with paddle-stirring for $T_A = 15 \text{ sec.}^\dagger$	1) To keep solution saturated with gas while thoroughly reducing electrode surface. Also serves to remove anion impurities, if present, from surface.
		B	2) Continue gas-bubbling and stirring for $T_B = 2 \text{ sec.}$	2) To remove surface species which are oxidized and/or repelled at high potentials.
		C	3) Continue gas bubbling and stirring for 1/2 min. Stop bubbling and stirring, and allow solution to become quiescent for 1-1/2 min. Total value of $T_C = 2 \text{ min.}$	3) The passive film of step B is retained while desorbed materials and oxygen released during step B are swept into the bulk of the solution and diluted. The solution is allowed to become quiescent to restrict mass transport to ordinary diffusion in subsequent steps.
		D	4) Solution quiescent. $T_D = 10 \text{ sec.}$	4) The passive film retained during step C is largely reduced within the first few milliseconds. The low potential serves to block adsorption of ethane, if present in solution. The electrode is in equilibrium with 10^{-4} atmos. of hydrogen.
		E	5) The potential is raised to 0.4 v for time, T_E .	5) To allow adsorption of ethane at 0.4 v for time, T_E .
		F	6) The potential is lowered to U for time, T_F .	6) To allow desorption of adsorbed ethane for time, T_F .
		G	7) Apply linear anodic sweep (l.a.s.) of speed $v = 10 \text{ v/sec.}$	7) Trigger oscilloscope at beginning of step G and record current-time trace.
		A-F	1-6) Same as for Sequence I.	1-6) Same as for Sequence I.
		G	7) The potential is raised to 0.4 v for 10 msec.	7) To remove adsorbed hydrogen at a potential at which desorption of ethane does not occur.
		H	8) Apply l.a.s. of speed $v = 10 \text{ v/sec.}$	8) Trigger oscilloscope at beginning of step H and record current-time trace.
II	17b	A-F	1-6) Same as for Sequence I.	1-6) Same as for Sequence I.
		G	7) The potential is raised to 0.4 v for 10 msec.	7) To remove adsorbed hydrogen at a potential at which desorption of ethane does not occur.
		H	8) Apply l.a.s. of speed $v = 10 \text{ v/sec.}$	8) Trigger oscilloscope at beginning of step H and record current-time trace.

* The gas is either ethane, argon, or a designated mixture of both.

 † "T" with appropriate subscript is the duration of that step of the sequence.

Potential sequences employed in this work are diagrammed in Fig. 17. The procedures employed during each step of the potential sequences are summarized in Table IV.

B. Results

1. Desorption of Pre-Adsorbed Ethane

a. Hydrogen Surface-Coverage During Desorption of Pre-Adsorbed Ethane

Sequence I of Table IV was used in making these measurements. During steps A — D of the sequence, the surface is prepared and during step E ethane is allowed to adsorb at a constant potential of 0.4 v. This potential was chosen simply because no atomic hydrogen may exist on the surface at this high a potential, thereby eliminating one possible ethane ad-species. If step F of the sequence is omitted, the charge Q_E , corresponding to adsorption of ethane at 0.4 v may be determined by application of linear anodic sweep (l.a.s.) G, as previously described in Section 4.1.1.2. When step F of the sequence is included with $U < \sim 0.2$ v, two processes occur:

- 1) Hydrogen is instantaneously deposited on the surface in amounts determined by both U and the initial coverage of the surface with ethane species.
- 2) The continued application of potential U results in a decrease in Q_E , and a simultaneous increase in Q_H , corresponding to desorption of ethane and adsorption of hydrogen, respectively.

Fig. 18a and 18b are the traces corresponding to application of l.a.s. G of sequence I, Table IV, with $U = 0.06$ v. Ethane was pre-adsorbed for 100 sec. and for 10 sec. for the traces (other than "1") of Fig. 18a and 18b, respectively. The traces marked "1" correspond to an adsorption time T_E , of only 10 msec. which is insufficient time for the adsorption of any appreciable amount of ethane. The choices of $T_F = 10$ msec. for traces "1" is however, sufficient time for the deposition of the equilibrium hydrogen surface-coverage on the clean surface (3). Further, traces "1" are identical with those obtained in the absence of ethane for a wide range of values of T_E and T_F and hence serve as the "solvent" traces. Traces "2" of Fig. 18 were obtained after the adsorbed ethane was subjected to desorption conditions for only 10 msec. = T_F . For $U = 0.06$ v and $T_F = 10$ msec., there is little desorption of ethane, and the value of Q_E obtained by integration of the area lying between traces 1 and 2 and 0.8 v on the T_G axis, is approximately the same as obtained when step F is omitted. With increase in T_F , decrease in Q_E is evident. Corresponding to decreases in Q_E , there is an increase in the charge Q_H' which may be obtained by integrating the traces to the value of T_G corresponding to 0.7 v. Q_H , corresponding to hydrogen-adsorption may be obtained from Q_H' by making an estimated correction for charging of the ionic double layer. As T_F increases, Q_H approaches, but never equals the value obtained from traces "1", since an "ethane" residue persists on the surface.

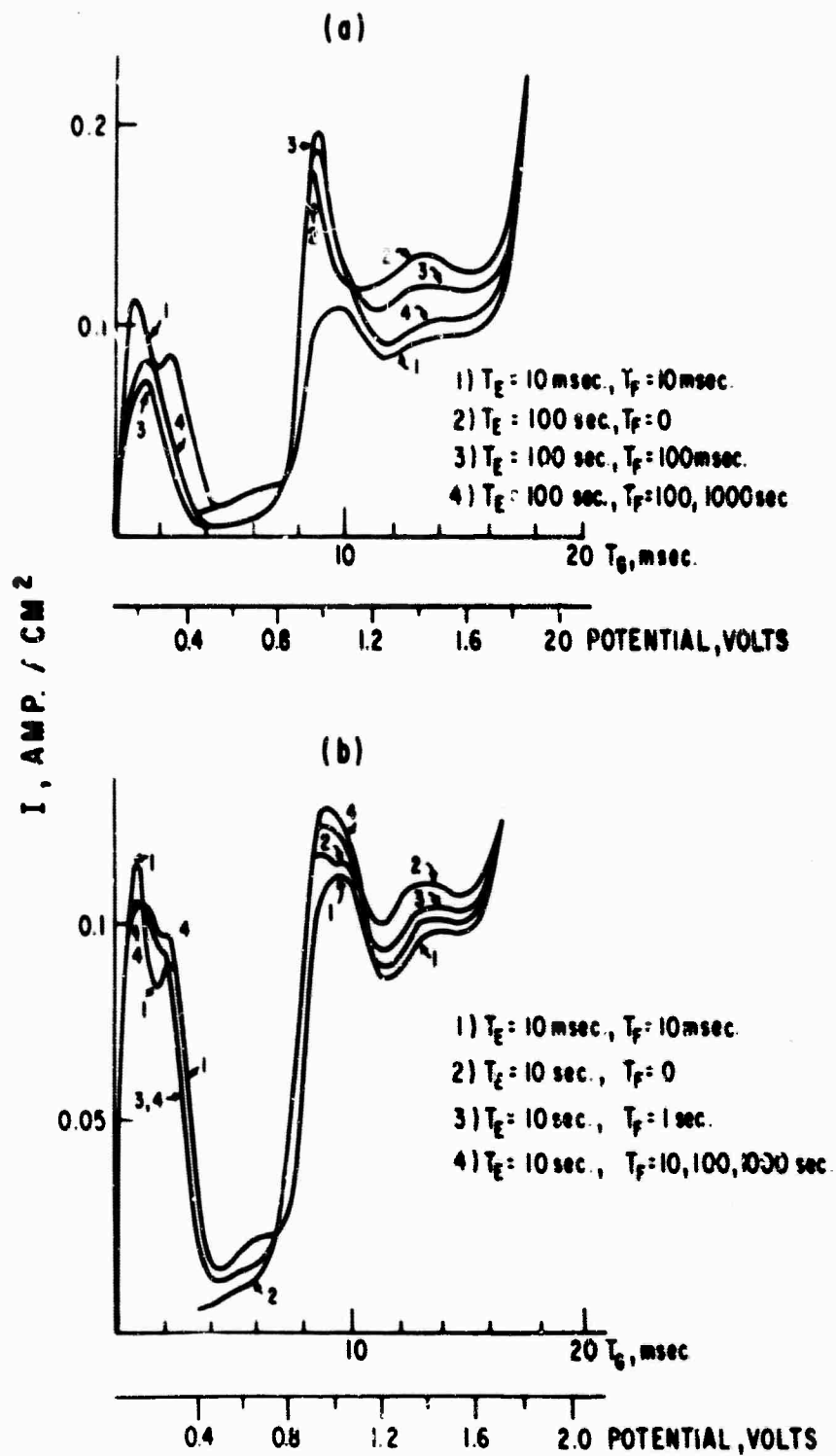


Fig. 18. Current-Time (Potential) Traces Obtained During Desorption of Adsorbed Ethane (Sequence I, Table IV With $U = 0.06 \text{ v.}$)

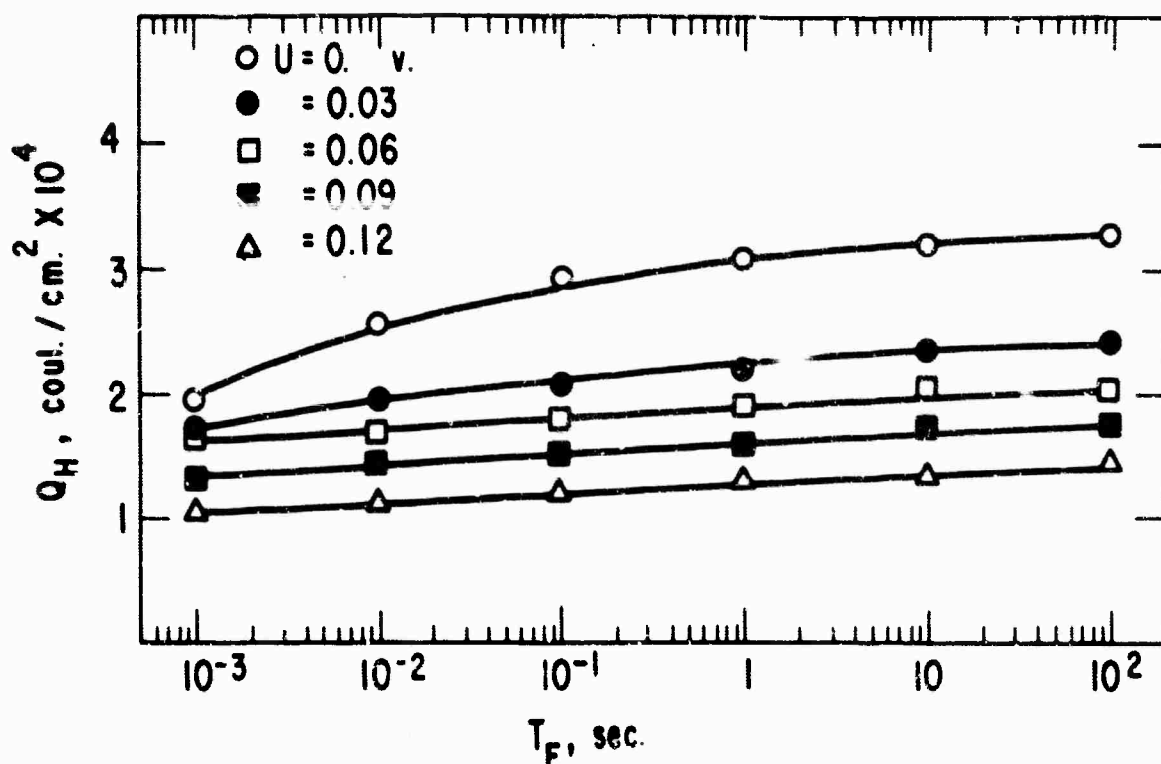


Fig. 19. Hydrogen Adsorption During Desorption of Adsorbed Ethane (Sequence I, Table IV).

It may be noted that a closed area is defined in the "hydrogen" region (at low values of potential by the intersection of traces "1" with any subsequent trace of Fig. 18a and 18b. This area is approximately ΔQ_H (neglecting a small capacitance term) for the two surface states. To obtain maximum resolution of the hydrogen charge for different values of U and of T_F , ΔQ_H was measured instead of Q_H . This was accomplished with maximum sensitivity by recording the "solvent" and "ethane" traces so that ΔQ_H occupied most of the photograph to the exclusion of other portions of the trace. Q_H was then calculated from ΔQ_H by subtraction from the known value of Q_H for the clean surface. Values of Q_H are plotted against T_F for several different values of U in Fig. 19. Ethane was pre-adsorbed for 100 sec. for each experiment, i. e., $T_E = 100$ sec.

b. Measurement of ΔQ_E

It was shown above that Q_E decreases when the potential is reduced to less than ~ 0.2 v after having adsorbed ethane at 0.4 v. The use of sequence I of Table IV for the measurement of the decrease in ethane charge, ΔQ_E , has the disadvantage that after the application of step F, the electrode is subjected to low potentials during the l.a.s. G while the hydrogen is being removed from the surface. This tends to make the desorption time uncertain when T_F is in the millisecond range. This problem is eliminated in sequence II of Table IV. Step G of

that sequence brings the potential to 0.4 v for 10 milliseconds. This allows hydrogen to be removed rapidly from the surface before the application of the l.a.s. and at a potential at which desorption of ethane does not occur. Also, 10 milliseconds is too small a period of time for the adsorption of any appreciable additional ethane, as shown in Section 4.1.1.2. The traces obtained during the step H of the sequence were qualitatively similar to those of Fig. 18a except that the sweep began at 0.4 v, eliminating the "hydrogen" region. For greatest resolution, the experiments were made in the following manner for obtaining a single data point:

- 1) A trace was recorded for $T_E = 100$ sec. and $T_F = 0$ (no desorption).
- 2) On the same photograph, a trace was recorded for $T_E = 100$ sec., and $T_F > 0$.
- 3) The area bounded by the two traces was determined graphically and is ΔQ_E .
- 4) Current and voltage sensitivities were chosen so that ΔQ_E occupied the maximum value on the photograph, even though the remainders of the traces were not recorded.

Values of ΔQ_E obtained for $T_E = 100$ sec., and different values of the desorption potential, U , are recorded in Fig. 20. Results for $U = 0.06$ v and several different values of T_E are recorded in Fig. 21. The values of Q_E corresponding to 15, 50 and 100 sec., as previously determined in Section 4.1.1.2, are 1.35 , 2.77 and 3.80×10^{-4} coul./cm², respectively. The maximum values of ΔQ_E achieved at 0.06 v. for these adsorption times is only a fraction of the original value of Q_E , which means that a considerable portion of the adsorbed ethane can not be removed by hydrogenation-desorption. For $T_E = 100$ sec., an adsorption experiment was conducted at a value of U as low as -0.2 v for $T_F = 100$ sec. The value of ΔQ_E so obtained was not greater than the maximum value obtained at $U = 0$ to 0.06 v, demonstrating that the residue is extremely resistant to removal. Inspection of Fig. 18a, reveals that this residue corresponds mainly to that part of the ethane ad-layer which oxidizes below approximately 1.0 v.

2. Measurement of Ethane Desorption Rate In the Absence of Pre-Adsorbed Ethane

In paragraph 1. above, ethane was first adsorbed on the surface at 0.4 v and then desorbed at potentials of 0.15 v or less. Starting with a surface concentration of zero, there is a net rate of adsorption of ethane at potentials between approximately 0.15 and 0.30 v which was previously represented (Section 4.1.1.2) by the equation:

$$R = R_{ad} - R_d \quad (35)$$

where R_{ad} is the potential-independent rate of adsorption and R_d is the potential-dependent rate of desorption. Values of R and R_{ad} were obtained graphically from the plots of Q_E versus adsorption time appearing in Section 4.1.1.2. From these values R_d was calculated employing equation 35, and the results are plotted against Q_E in Fig. 22.

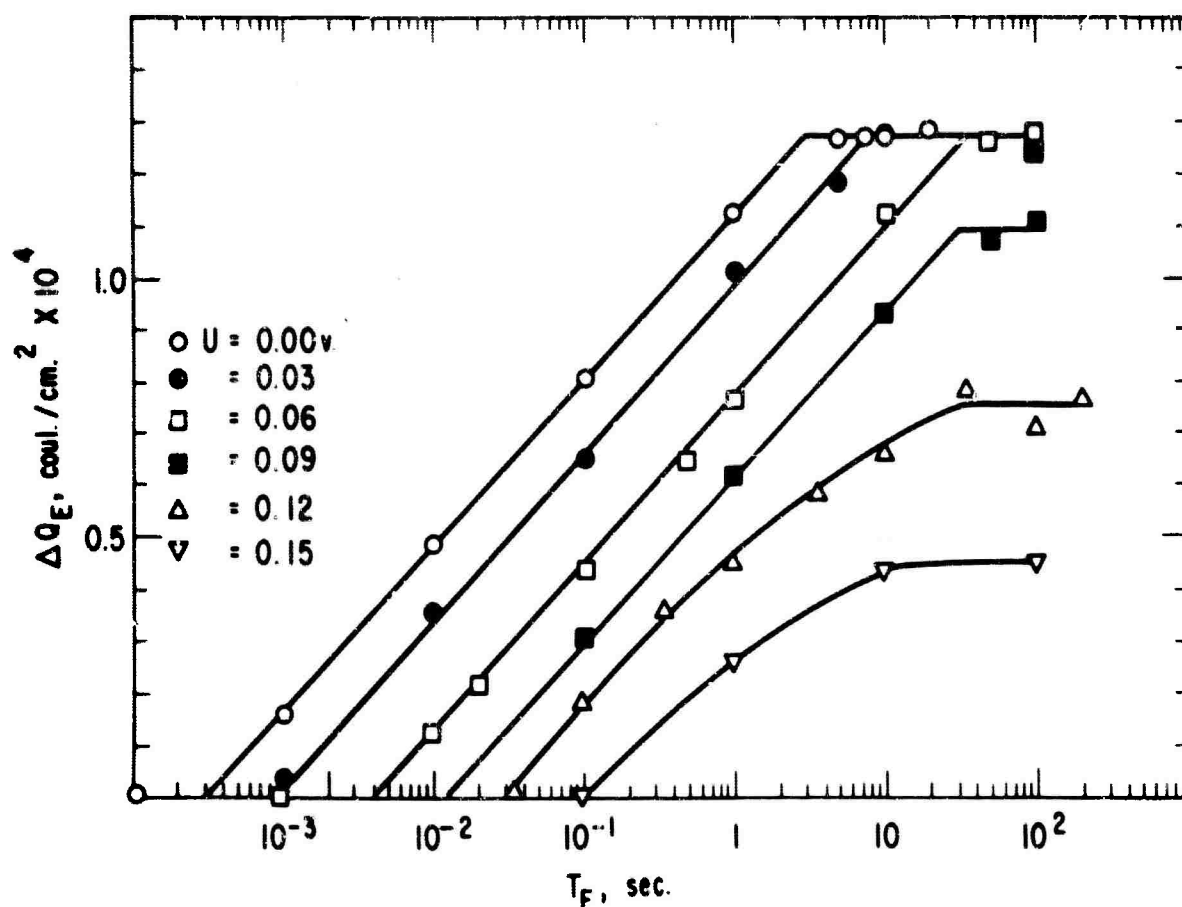


Fig. 20. Charge Corresponding To The Desorption Of Ethane At Various Potentia (Ethane Pre-adsorbed For 100 Sec.).

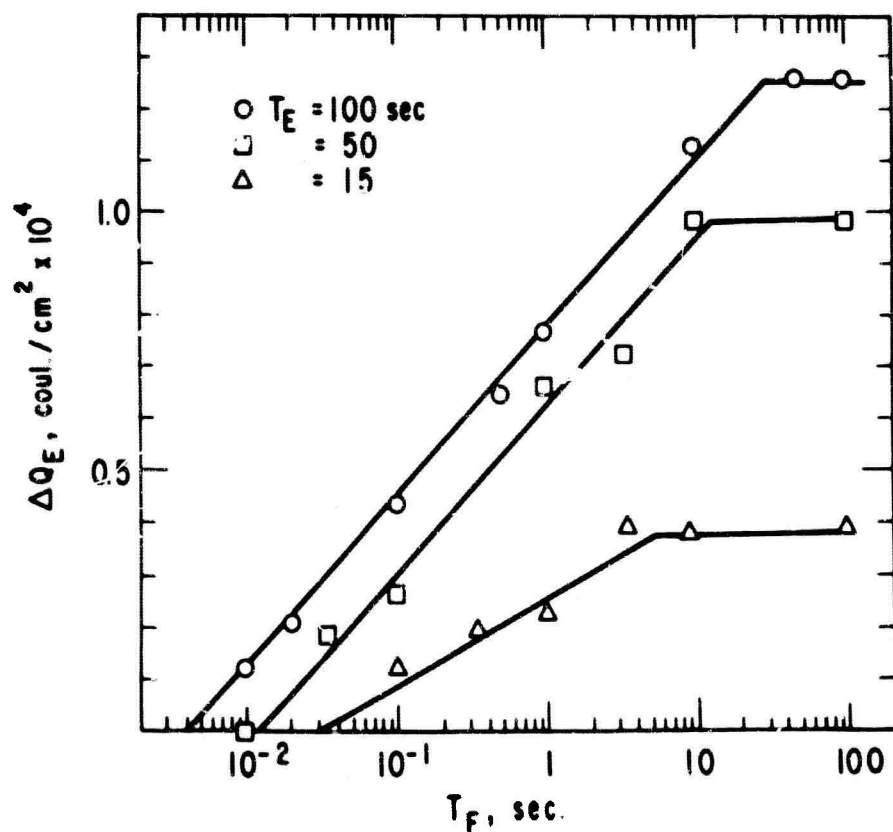


Fig. 21. Charge Corresponding To Desorption Of Ethane At 0.06 v. (Ethane Pre-adsorbed For Time, T_E .)

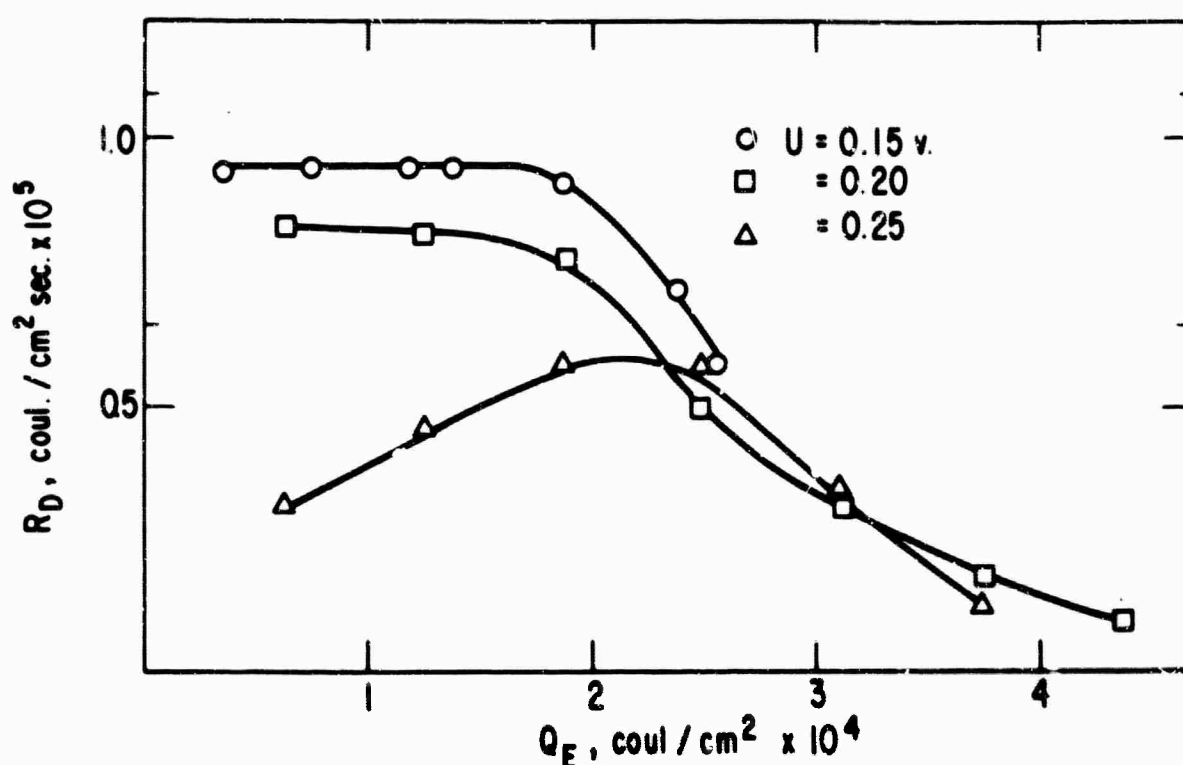


Fig. 22. Rate Of Desorption Of Ethane In The Absence Of Pre-Adsorbed Ethane.

C. Discussion

1. Kinetics of Desorption of Pre-Adsorbed Ethane

a. Fixed Initial Surface Concentration of Ethane, Various Potentials

To obtain the data of Fig. 20, ethane was first adsorbed at 0.4 v for 100 sec. and then desorbed at the specified constant potentials. Hence, all of the data corresponds to one initial surface coverage with ethane species. Most of the data of Fig. 20 falls on a family of parallel lines having the empirical formula:

$$Q_E = h_1 \ln \frac{T_F}{T_0} \quad (36)$$

where $h_1 = 1.39 \times 10^{-5}$ coul./cm²

$T_0 = x$ - intercept

A plot of $\ln T_0$ vs U reveals fair linearity and the empirical relationship:

$$U = h_2 \ln \frac{T_0}{h_3} \quad (37)$$

where $h_2 = 2.58 \times 10^{-2}$ v

$h_3 = 3 \times 10^{-4}$ sec.

Hence T_0 includes the potential-dependence of Q_0 in equation 36. The charge Q_E is related to the fractional surface coverage by a constant:

$$\theta_E = c_1 Q_E \quad (38)$$

where c_1 was found to have the value $1,170 \text{ cm}^2/\text{coul.}$ for this electrode. ΔQ_E is related to θ_E by:

$$c_1 \Delta Q_E = \theta_{E,0} - \theta_E \quad (39)$$

where $\theta_{E,0}$ is the initial surface concentration (after 100 sec. of adsorption), as opposed to the instantaneous value, θ_E . After substituting for ΔQ_E of equation 35, the value given by equation 39, and after taking the derivative of equation 35:

$$-\frac{d\theta_E}{dT_F} = \frac{h_1}{c_1 T_F} \quad (40)$$

Substituting for T_F the expression derived from Equations 36 and 39:

$$-\frac{d\theta_E}{dT_F} = H \exp(c_1 \theta_E/h_1) \quad (41)$$

where:

$$H = \frac{h_1}{c_1 T_0} \exp(-c_1 \theta_{E,0}/h_1) = \text{constant for constant } \theta_{E,0} \text{ and constant } U. \quad (42)$$

Equation 41 is a desorption rate equation similar to the Elovitch equation for adsorption, but with the sign of the exponent reversed. Such a relationship has already (13) been derived assuming that the energy of desorption effectively decreased linearly with increase in surface coverage. As for the Elovitch equation, it may be predicted that a number of physical models (13) including the effect of steric hindrance (16) could lead to such a relationship. An exponential rate law such as equation 41 is usually expected not to apply to the very low and high ranges of surface coverages, whereas the law seems to apply to the entire range of low-potential data points of Fig. 20. This is not contrary to expectations since the surface is initially covered to the extent $\theta_E = 0.45$ and drops to a minimum value of $\theta_E = 0.30$ (corresponding to the maximum value of ΔQ_E) and hence stays in a medium range of surface coverages throughout the experiment.

The potential-dependence of the rate of desorption may be properly examined by comparing rates of desorption at different values of U for constant values of θ_E . The same dependence will result for any value of θ_E so long as we stay within the region of straight parallel lines. Assuming that the rate of desorption involves a slow electron transfer, or alternatively, that the rate of desorption is determined by a field-dependent step followed immediately by a very rapid electron transfer, we may expect the rate of desorption to follow a Tafel relationship:

$$-\frac{d\theta_E}{dT_F} = h_0 \exp(\alpha n F U / RT) \quad (43)$$

where h_0 = a constant for constant value of θ_E

α = transfer coefficient

n = number of electrons in the rate-determining step and all other symbols have their usual significance. From equation 43 it is seen that a plot of the natural log of the

rate of desorption against the potential (at constant θ_E) would have a slope of $0.029 = \frac{RT}{\alpha n F}$ for $\alpha n = 1$. The rate of adsorption for the semi-logarithmic representations of Fig. 20 is related to T_F by:

$$-\frac{d\theta_E}{dT_F} \propto S/T_F = \text{constant}/T_F \quad (44)$$

where, S is the slope and is constant in the region where the data falls on straight parallel lines. Hence a plot of $\ln T_F$ (corresponding to constant value of θ_E) against the potential should also serve as a test of equation 43. For the special value $T_F = T_0$, equation 37 has shown that the experimental slope is 0.0258. Assuming that $\alpha = 0.5$, this serves as evidence that the rate-determining step involves the gain of $n = 2$ electrons by the adsorbed ethane. Further, the dependence of the rate of desorption both on surface coverage and potential can be emphasized by re-writing equation 41 as:

$$-\frac{d\theta_E}{dT_F} = H' \exp(\alpha n U F/RT)(m\theta_E) \quad (45)$$

where H' and m are the appropriate constants, and the potential term was removed from the previous term H of equation 41.

b. Fixed Potential, Varying Initial Ethane Surface Concentration

The results presented above correspond to a fixed initial adsorption time and a fixed initial surface concentration of $\theta_E = 0.45$. In Fig. 21, results have been plotted for $U = 0.06$ v, and for adsorption times of 15, 50, and 100 sec. which correspond to initial values of Q_E of 1.35, 2.77, and 3.80×10^{-4} coul./cm², respectively, and to values of θ_E of 0.16, 0.32 and 0.45, respectively. If equation 45 held precisely, the three plots of Fig. 21 should be parallel and yield equal rates of desorption at equal values of Q_E . The departure of the $E = 15$ sec. points from a parallel plot may be ascribed to the system's entering a range of θ_E too low for an experimental relationship to hold. When the rates for the 50 sec. and 100 sec. points are compared at equal values of Q_E or of θ_E , a 3000-fold greater rate is calculated for the 50 sec. points. If alternatively, results are compared at equal values of $(\Delta Q_{E, \max} - \Delta Q_E)$, where $\Delta Q_{E, \max}$ is the value of ΔQ_E reached at completion, there is only a three-fold greater rate for the 50 sec. points. This implies that the rate of desorption is more nearly dependent on the amount of desorbable ethane species, than on total ethane species. Hence for general applicability of equation 45,

$$m = a f \quad (46)$$

where f is that fraction of the surface coverage which is active toward desorption, and will be a function of $\theta_{E,0}$.

c. The Non-desorbable Residue

The experiments of Fig. 20 were begun with an initial value of θ_E of 0.45. The minimum value of θ_E (corresponding to maximum value of ΔQ_E) was achieved at $U = 0.09$ v and had the value $\theta_E = 0.30$. Choosing U as low as -0.20 v did not cause any appreciable further reduction in θ_E even after 100 sec. of desorption. Thus, there is a "fraction" of adsorbed ethane species which cannot be removed by hydrogenation-desorption under these conditions. Inspection of Fig. 18a reveals that this fraction of the ad-layer is that most readily oxidized at low potentials. It is possible that this specie or species has a higher heat of adsorption than hydrogen (i. e., that the desorption is thermo-dynamically not possible) or that the kinetics of desorption are highly hindered. Niedrach (21) has suggested the non-desorbed species might be "CO-like". It is also possible in addition, that subtle structural differences distinguish desorbable from non-desorbable "ethane". It may be noted that the minimum values of θ_E (maximum value of ΔQ_E) are not achieved at the higher potentials of Fig. 20. It seems likely that the plateau values achieved represent a quasi-equilibrium value due to a balance between the rate of adsorption and desorption at these potentials.

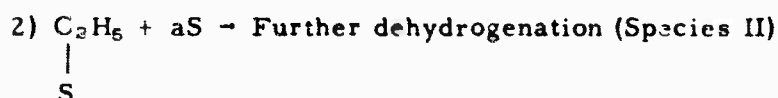
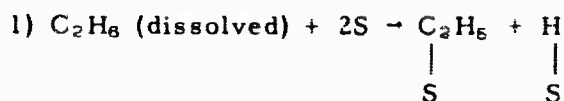
Fig. 21 reveals that plateau values for θ_E are also achieved when the initial surface coverages are less than 0.45. Corresponding to the initial adsorption times of 15, 50 and 100 sec., and initial surface coverages of 0.15, 0.32 and 0.45, final surface coverages of 0.11, 0.21 and 0.30, respectively are obtained or a desorption of approximately 30% in all three cases. This seems to suggest some constancy in the relative structure of the ad-layer with increase in both adsorption time and total surface coverage.

2. Measurement of Ethane Desorption Rate in the Absence of Pre-Adsorbed Ethane

The experiments discussed above involved the adsorption of a fixed amount of ethane at 0.4 v and a desorption of the ad-layer at potentials of 0.15 v or less. Under these conditions, there is a net desorption which reaches a final value at the lower potentials. If on the other hand, the experiment is begun with zero initial surface coverage, and at a potential between approximately 0.15 and 0.30 v, there is an over-all rate of adsorption which appears to include a desorption term (see section 4. i. 1.2). The rate of desorption, R_D , was calculated from previous data as already described, and the results plotted on Fig. 22. Whereas the rate of adsorption of pre-adsorbed ethane was found to increase exponentially with surface coverage (equation 45), R_D is found to decrease with increasing coverage. No simple law describes the dependence of R_D on Q_E or on U . The implication of this desorption rate is that it may correspond to the desorption of a transient species not present in the pre-adsorbed ethane ad-layer. This possibility will be given further attention below.

3. Mechanism of the Desorption of Ethane

The following mechanism has already been proposed for the adsorption of ethane (section 4.1.1.2):

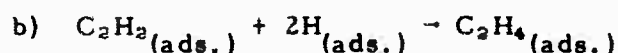
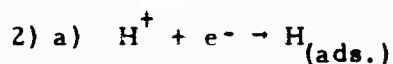
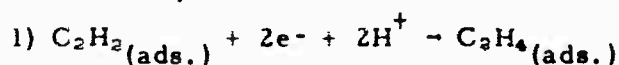


Reaction 2 was postulated because the rate of adsorption (production of adsorbed ethyl radicals) required two surface sites (second order) whereas the stable ad-molecule (species II) appeared to occupy four surface sites. The kinetic data discussed above appears to offer additional evidence for the existence of an adsorbed ethyl radical intermediate for the following reasons:

1) When ethane is adsorbed at 0.4 v it is only the stable species II which would appear on the surface and which may be desorbed at potentials $< \sim 0.15$ v. The desorption of species II follows an exponential law (Equation 45).

2) When there is initially no ethane on the surface, an apparent rate of adsorption may be measured for potentials greater than approximately 0.15 v. This apparent rate includes a desorption term (for potentials up to approximately 0.28 v). The desorption occurs in a range of potentials in which pre-adsorbed ethane (species II) does not noticeably desorb. Further, the rate of desorption does not increase exponentially with increase in surface coverage, as is the case for the pre-adsorbed ethane, but decreases with increasing surface coverage. This suggests that only the precursor of species II, i.e., adsorbed ethyl radicals, must be desorbed under these conditions.

The kinetic information discussed previously suggests that the reduction of species II involves two electrons. Assume for example that species II includes only one structure of stoichiometry C_2H_2 . Then the rate-determining step in the desorption of species II may be written in either of two ways:



Both paths 1 and 2 involve the proper number of electrons. The rate of path 1 would have the observed dependence on potential (equation 45). The anticipated kinetic expression for path 2 would be:

$$-\frac{d\theta_E}{dT_F} = h' f(\theta_H) \exp(m\theta_E) \quad (47)$$

where $f(\theta_H)$ = a function representing the activity of adsorbed hydrogen in terms of its surface

concentration. From Fig. 19, the instantaneous value of θ_H is only (approximately) linearly dependent on the potential. Hence for path 2 to have the proper potential-dependence it would be required that:

$$f(\theta_H) = H'/H'' \exp(\alpha n U F/RT) \quad (48)$$

or, in other words, that the activity of adsorbed hydrogen be proportional to the partial pressure of gaseous hydrogen in equilibrium with the surface, rather than simply proportional to the surface concentration. This possibility cannot be dismissed as unlikely. Hence either path one or two is possible. A similar set of mechanisms could be written for the reduction of a surface species of any stoichiometry from C_2 to C_2H_4 . The subsequent fast steps would involve further and relatively rapid reduction to C_2H_6 of the product of the first (slow) step.

Approximately two-thirds of the pre-adsorbed ethane of our experiments could not be desorbed. This residue could be formed directly from adsorbed ethyl radicals or could form from species II by further surface reaction. Since the major product of hydrogenation-desorption is ethane (21) it is reasonable to assume that species II contains only two carbons and hydrogen. It is possible that the non-desorbable residue may contain some oxygen (21).

4.1.1.4 Further Studies on the Mechanism of Ethane Surface Processes

As a result of the studies reported in sections 4.1.1.2 and 4.1.1.3 there is now some knowledge of the mechanism of adsorption and desorption of ethane under fuel cell conditions, and some preliminary information on the structure of the ethane ad-layer. Additional information on the structure of the ad-layer and its reactivity require a study of possible "intermediates" under the same conditions of study as used for ethane. Experiments are currently being conducted on ethylene.

The information obtained for ethane at 60°C now makes it possible to make some meaningful measurements in phosphoric acid at elevated temperatures. Equipment is being modified for that purpose.

4.1.1.5 Conclusions

The application of a pulse sequence to a platinum electrode at elevated temperatures leads to variation in the estimated surface roughness, as calculated from hydrogen-deposition or "oxygen-adsorption" measurements. These variations are brought about during the reduction of surface "oxygen". Relatively rapid reduction causes an increase in roughness, whereas relatively slow reduction leads to a decrease in roughness. By use of the proper signal, it is possible to adjust the roughness factor of the surface to any value somewhat above 1.0 and below the values corresponding to platinum "blacks".

Ethane may be adsorbed at a potential of 0.4 v, and the amount adsorbed may be measured by oxidation of the ad-layer and determination of the corresponding charge, Q_E . If the ad-layer is subjected to potentials lower than approximately 0.2 v, a decrease in Q_E can be measured, corresponding to desorption of species in the ad-layer. Q_E can be made to undergo a maximum decrease of approximately 30%. By following the time and potential-dependence of the desorption, it has been concluded that the rate of desorption is exponentially dependent on the electrode potential and on the extent of surface-coverage. The kinetic data allows speculation on the mechanism of desorption of ethane surface species.

When the desorption processes are minimized, the rate of adsorption of ethane is initially constant and then follows an empirical Elovich relationship. The data may be interpreted as indicative of an adsorption rate-determining step which is second-order in free surface sites, and first order in dissolved ethane concentration. This applies from zero to high fractional surface coverages. Departure from this law at highest surface coverages may be due to steric hindrance effects. Some qualitative observations on oxidizability of the ethane ad-layer may be made on the basis of the measured current-potential curves.

4.1.2 Semi-Micro Fuel Cell Electrodes (Dr. L.W. Niedrach, Dr. S. Gilman, I. Weinstock)

Multipulse potentiodynamic techniques are being applied to the study of the behavior of hydrocarbons with semi-micro Teflon-bonded fuel cell electrodes. At intermediate potentials ethane initially adsorbs at a linear rate and subsequently follows the Elovich relationship. When ethane adsorbed on the electrode is oxidized with a linear potential sweep, the behavior indicates that several species are present on the electrode surface; one appears to be partially oxidized and related to CO and/or formic acid. These results parallel similar results obtained with wire electrodes. The behaviors of methane and propane resemble that of ethane in the qualitative sense, but quantitative differences are seen. Unsaturated ethylene adsorbs more rapidly than the unsaturated hydrocarbons and the pre-wave is not obtained. Experiments with ethane with perchloric acid and hydrofluoric acids indicate no gross qualitative differences in its adsorption and surface behavior with the two electrolytes. Subtle quantitative differences, therefore, appear to account for the differences in behavior of hydrocarbons in fuel cells with perchloric and hydrofluoric acid electrolytes.

It is the purpose of this work to investigate, in more detail than can be done with complete fuel cells, the behavior of hydrocarbon fuels on Teflon-bonded, platinum black electrodes. Because the multipulse potentiodynamic techniques being employed are similar to those being used with wire micro-electrodes, it is anticipated that the present studies will also serve as an effective bridge in relating the latter work to the observed behavior of hydrocarbons in complete fuel cells. Particular attention is being given to the rates of adsorption and the nature of the

species that form on the surface of the electrode. Both of these aspects are, in turn, being related to the over-all polarization curve for the fuel electrode.

Major attention has so far been focused upon the behavior of ethane with a perchloric acid electrolyte in order to obtain maximum correlation with the work reported in Section 4.1.1. However, some work has also been done with several other hydrocarbon fuels and with hydrofluoric acid as an electrolyte.

4.1.2.1 Experimental

The three-compartment, electrochemical cell was made of Teflon and was similar to that illustrated in an earlier report (1). The anode, a miniature version of a fuel cell electrode, consisted of a 0.20 cm diameter Teflon-bonded platinum black electrode (2). This electrode, which was mounted in the center of a thin (approx. 0.005 inch) platinum washer, was horizontally fixed in the cell, with connections for admitting fuel and venting products made through the bottom. The electrolyte side of the support washer was electrically insulated from the electrolyte by bonding to it a thin, non-porous Teflon film. The electrical connection for the electrode to the external circuitry was also made through the bottom of the cell.

The reversible hydrogen reference electrode communicated with the anode through a Luggin capillary. A porous Teflon plug in this leg minimized diffusion of hydrogen to the anode chamber. The counter electrode was also separated from the anode chamber via a porous Teflon plug. Both electrodes were platinized platinum flags. The cell was operated in an air thermostat, enabling control of temperature to $\pm 0.1^\circ\text{C}$.

The 4.3 N perchloric acid electrolyte solution used for most of the work was prepared from reagent grade perchloric acid and quartz distilled water. A 36 wt % hydrofluoric acid electrolyte was prepared by diluting reagent grade acid with the quartz distilled water.

Electrolyte grade hydrogen was used in the reference electrode chamber, and Phillips research grade hydrocarbons were used as the fuels. Tank argon, de-oxygenated by passage over heated copper turnings, was used as the "fuel" for obtaining solvent blanks. Tank argon was also used for de-gassing the solution.

The signal generator was a Hewlett-Packard Model 202A, modified to generate single triangular sweeps. Potential steps were obtained using batteries and switches. The potentiostat was a Wenking "Fast Rise" Potentiostat, Model 61R. The current-time (potential) signals were measured with a Tektronix Type 536 oscilloscope using type D and type T plug-ins.

-
- (1) Technical Summary Report No. 4, Part 1, p. 5-82; Contract No. DA-44-009-ENG-4909, ARPA Order No. 247, Project No. 8A72-13-001-506, December 31, 1963.
 - (2) L. W. Niedrach and H. R. Alford, Saturated Hydrocarbon Fuel Cell Program; A New High Performance Fuel Cell Employing Conducting - Porous - Teflon Electrodes and Liquid Electrolytes. Contract DA 44-009-AMC-479 (T), ARPA Order No. 247, Project No. P4980.

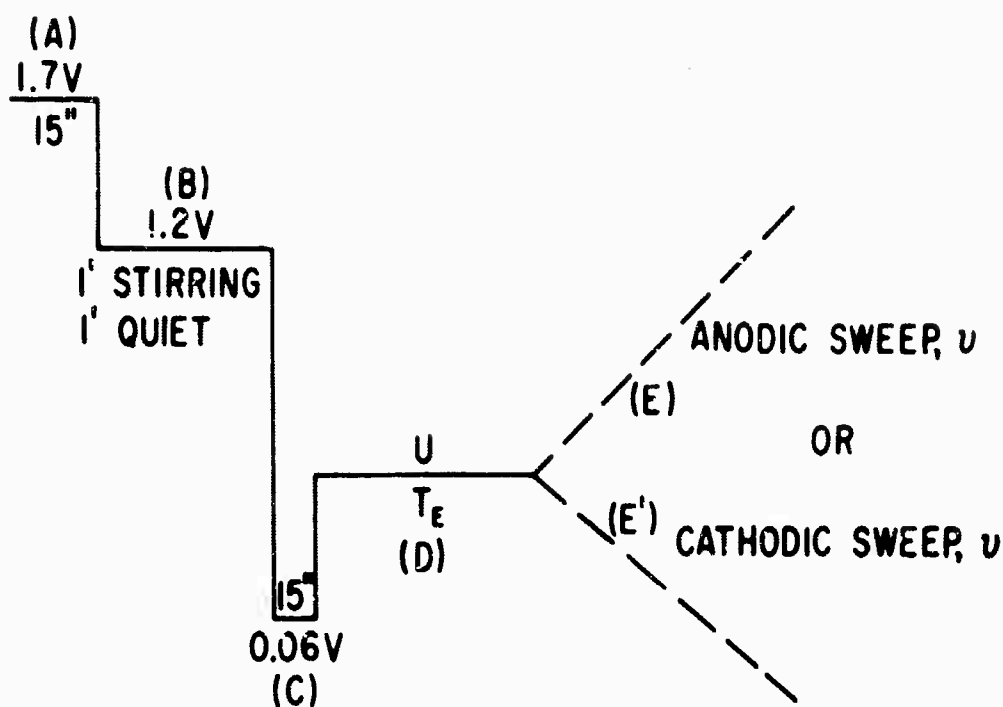


Fig. 23 Potential Sequences Applied To The Test Electrode.

The potential-time sequence applied to the anode for adsorption studies at constant potential is shown in Fig. 23. The significance of the steps is covered below.

- 1) Pre-treatment step (15 sec) to remove oxidizable impurities and to produce a layer of adsorbed oxygen which serves to block adsorption. The solution is vigorously stirred and purged with argon to remove molecular oxygen and oxidation products formed.
- 2) Potential step, during which the oxygen layer formed in 1) is maintained, and the solution is purged for an additional 1 minute. The solution is then allowed to become quiet for 1 minute.
- 3) Reduction step, during which the adsorbed oxygen layer is reduced within a few seconds. At this low potential the adsorption of the hydrocarbons is blocked. Omission of this step had no detectable effect on the equilibrations.
- 4) Adsorption step, during which the hydrogen from 3) is rapidly oxidized, exposing a reproducibly clean surface for adsorption. The duration of this step is the adsorption time, T_E .
- 5) Anodic sweep at rate $V = 0.1\text{v/sec}$. The adsorbed fuel is oxidized and the surface covered with a layer of adsorbed oxygen. Subtraction of the charge due to surface

oxidation from the total charge yields the charge required to oxidize the species derived from the adsorbed fuel. Or,

- 5a) Cathodic sweep at 0.025 v/sec which is used for determination of surface area by measurement of charge required for hydrogen deposition. In this case, argon is substituted for the hydrocarbon fuel.

Polarization curves were obtained in two ways. The first method involved sequential steps from one operating point to another. In the other method, the electrode was activated before each point and the current recorded after a 10-minute equilibration with the fuel at the desired voltage point. The two methods gave essentially identical results.

4.1.2.2 Results and Discussion

A. Frequency Dependence

In preliminary studies it had been found that slower sweep speeds must be used with the porous Teflon bonded electrodes than are premissible with wire electrodes (3). In large part, this reflects the diffuse structure of the electrode and internal IR drops inherent to it. Additional measurements have been made to more clearly establish the useful range of sweep rates.

As had been previously noted, the hydrogen deposition wave used for area measurements is more sensitive to sweep speed than the wave associated with the oxidation of the electrode surface. Oxidation of adsorbed ethane responds much as the surface oxidation.

The useful sweep rate range for the determination of the electrode area extends from 0.010 to 0.10 v/sec. As indicated by the data in Table V, the reproducibility within this range is about 5%. A sweep rate of 0.025 v/sec was routinely used for this purpose:

TABLE V
Effect of Sweep Rate on Charge for Hydrogen Deposition

<u>Sweep Rate</u> <u>(V/sec)</u>	<u>Millicoulombs</u>
0.010	12.3
0.015	10.8
0.025	11.9
0.040	11.0
0.060	12.1
0.080	12.4
0.10	10.9
(0.25)	(9.2)
Avg. 11.7 (0.25 v/sec value excluded)	

(3) Semi-annual Report No. 5 on "Hydrocarbon - Air Fuel Cells", 1 January 1964 - 30 June 1964, Contract Nos. DA 44-009-ENG-4909 and DA 44-009-ENG-479 (T), p. 4.3.

The effect of sweep frequency on the hydrocarbon oxidation wave was examined with ethane at 60°C. Preliminary qualitative examination of representative traces narrowed the potentially useful range down to 0.1 – 1.0 v/sec. At lower sweep rates, background currents associated with re-adsorbing fuel become excessive. At higher sweep rates the waves lose structure.

As indicated by the data in Table VI, sweep rates in the range 0.1 – 0.4 v/sec gave consistent values for the surface coverage as measured by the area bracketed by sweeps obtained in the presence and absence of fuel.

TABLE VI
Effect of Sweep Rate on Charge to Oxidize Adsorbed Ethane,
4.3 N HClO₄. T = 60°C.

<u>Sweep Rate</u> <u>(v/sec)</u>	<u>Millicoulombs</u>
0.092	21.7
0.18	21.8
0.40	19.8
0.92	15.2

Because of the more sharply defined structures of the traces obtained at 0.1 v/sec, this sweep rate was adopted for the work that follows.

B. Ethane with a Perchloric Acid Electrolyte

The general form of the current-voltage trace obtained during the oxidation of adsorbed ethane with a linear potential sweep is shown for a range of equilibration times, potentials, and temperatures in Figs. 24–26. Fig. 24 presents a series of traces showing the behavior of adsorbed ethane at 60°C for various equilibration times at a potential of 0.30 volt. A comparison showing the effect of the equilibration potential on the structure of the oxidation wave at 60°C appears in Fig. 25. These data were all obtained after 10-minute equilibrations, because it had become evident at this temperature that limiting or steady-state conditions were essentially attained after this interval. In each case two curves are shown. The lower trace, obtained with argon serving as the "fuel", provides a reference curve for the coverage of a clean electrode with oxygen. The upper trace is that obtained for the adsorbed fuel. Similar data showing the effect of temperature on the form of the oxidation wave for adsorbed ethane appear in Fig. 26. Here again, 10-minute equilibrations were employed; however, at the lower temperature, steady-state conditions were not reached within the 10-minute period.

At equilibration potentials below 0.7 volt, the curves for ethane can be seen to be composed of at least two distinct regions. The more active of these regions occurs at potentials

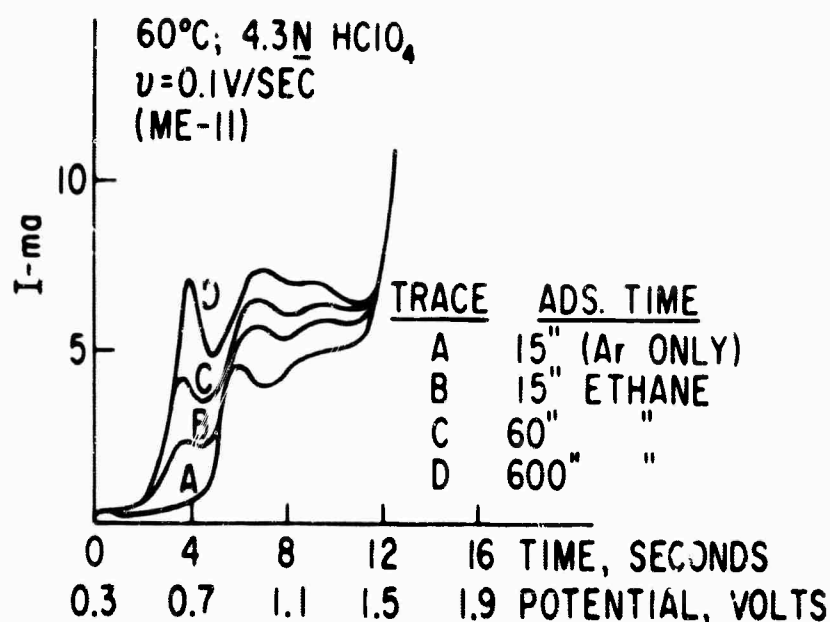


Fig. 24. Current-Time (Potential) Traces For Varying Adsorption Times At 0.3V.

below which oxidation of the platinum surface normally takes place. It is immediately evident that the magnitude of this "pre-wave" represents one of the more important variations relating to the experimental conditions. Therefore, in obtaining quantitative data relating to the effects of time, temperature, and potential, attention was focused upon the charge associated with the pre-wave as well as the over-all wave for the adsorbed ethane.

The magnitude of the charge associated with the oxidation of the material adsorbed after any time, Q_E , was obtained by integrating the area enclosed by the solvent curve and the region of the ethane adsorption curve of interest. The heavily shaded areas in Figs. 25 and 26 represent Q_{E_1} , the charge associated with the pre-wave. The entire shaded area represents $Q_{E \text{ tot}}$, the charge associated with all of the measurable carbonaceous species* on the surface. It is to be noted that any hydrogen formed by dissociation is not included in these measurements. Because a number of electrodes are being used in this work, all adsorption data have been

*In Section 4.1.1, evidence is presented for the accumulation of an extremely refractory species on the surface of an electrode. This species is but slowly removed, even in the oxygen evolution region. Indirect evidence has been seen for such a species in the present work, in that less material appears to be adsorbed at 0.3 volt after an intervening equilibration at 0.9 volt than when a direct step is taken to 0.3 volt after the activation treatment.

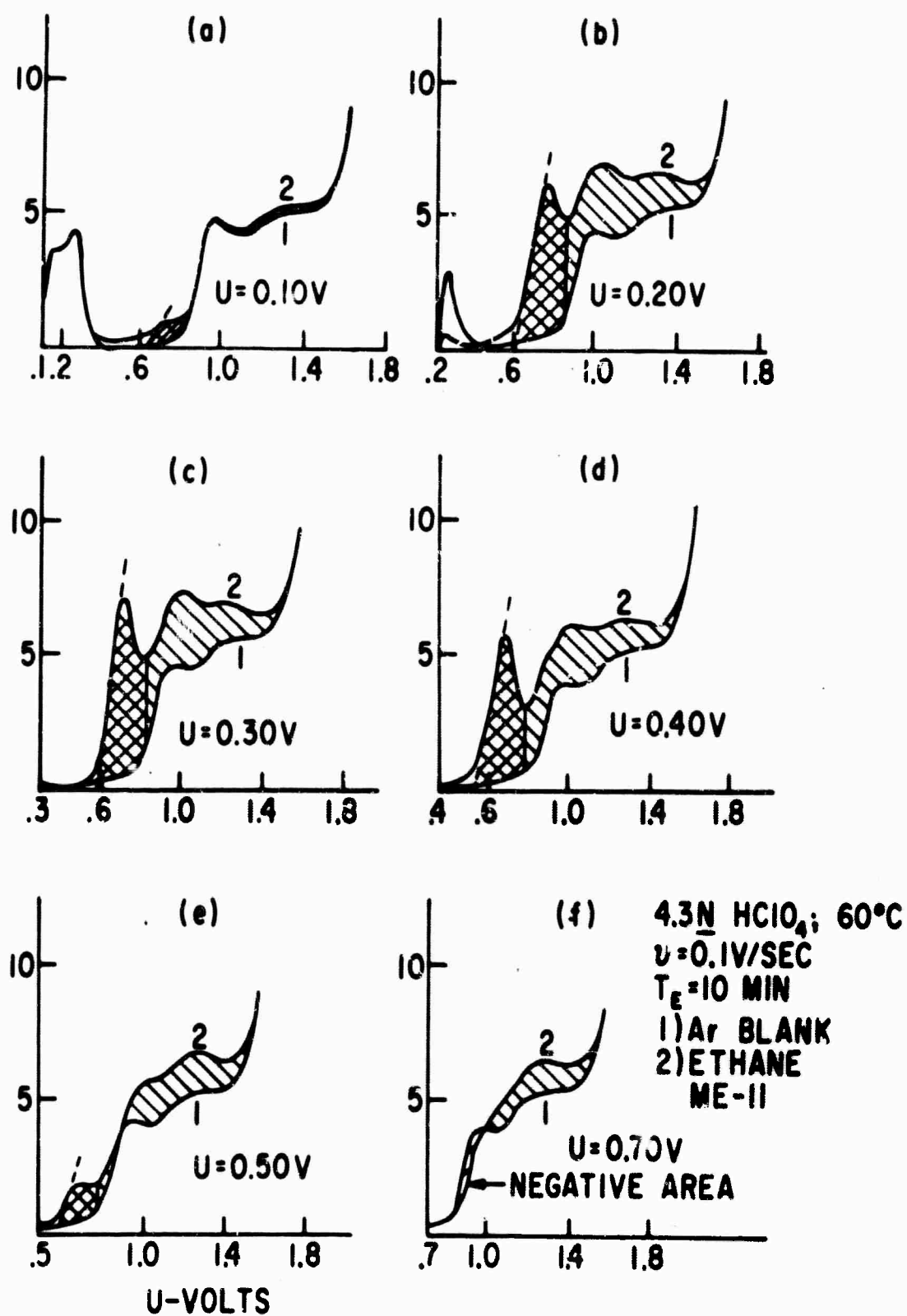


Fig. 25. Current-Potential (Time) Traces For Ethane Adsorbed At Several Potentials.

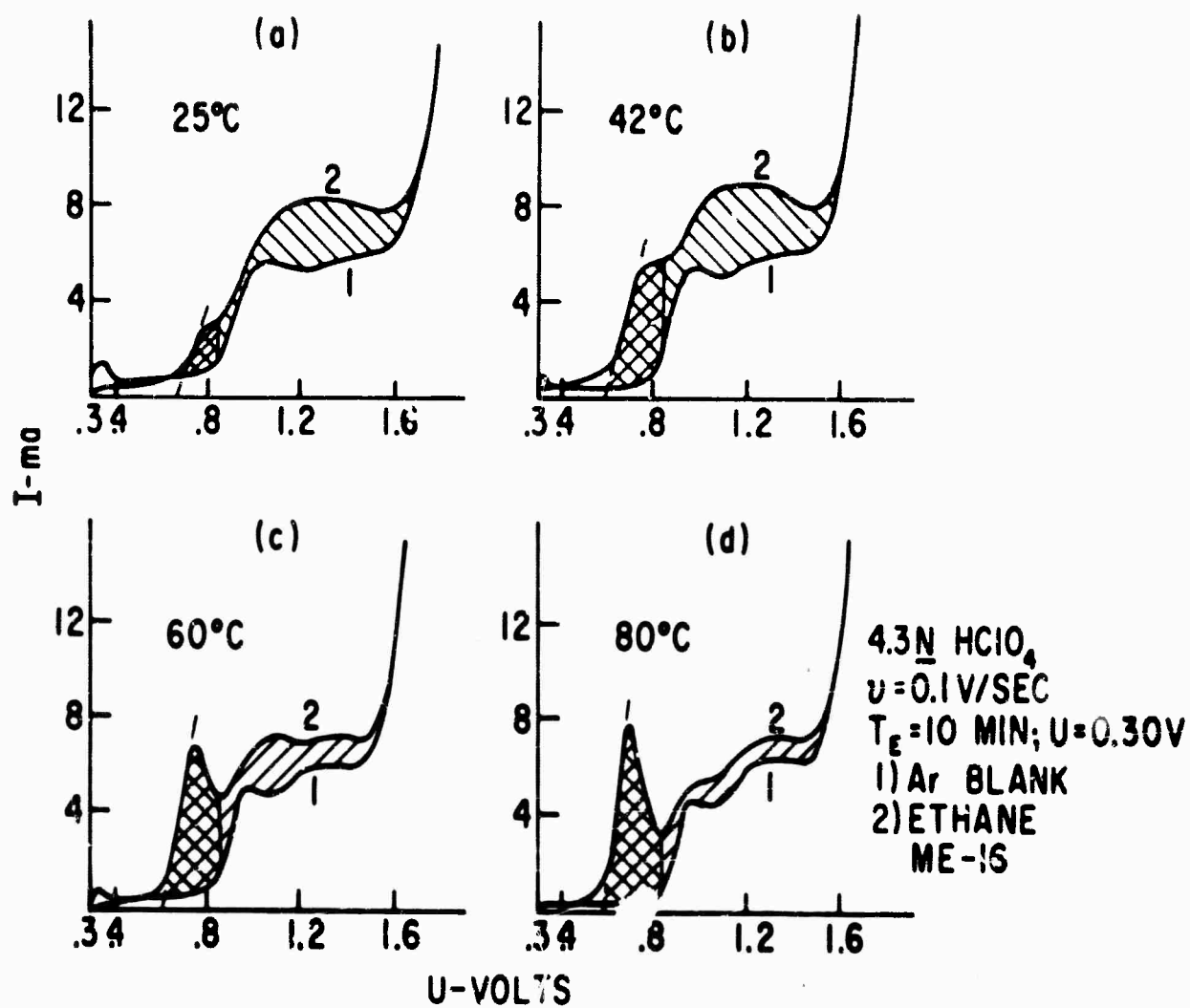


Fig. 26. Current-Potential (Time) Traces For Ethane Adsorbed At Several Temperatures.

normalized to charge per unit of "real" surface area as determined by cathodic deposition of hydrogen on the electrode. A conversion factor of 0.21 m coul / cm² was used in calculating the "real" area. This method of normalization also makes the data directly comparable with that in Section 4.1.1.

Variations in $Q_{E_{tot}}$ with time at different temperatures and potentials are shown in Figs. 27 and 28, respectively. The effect of time on the ratio of $Q_{E_1} : Q_{E_{tot}}$ is summarized in Table VII. It is significant that the ratio of $Q_{E_1} : Q_{E_{tot}}$ remains essentially constant with time at each potential. This justifies the use of a constant equilibration time in comparing the behavior at different equilibration potentials as is done in Fig. 29 for 60°C. Similar data showing the effect of temperature are summarized in Fig. 30. These last data are probably least meaningful, because as is evident from Fig. 27, surface saturation or steady state is not reached within 10 minutes at 25°C nor is it achieved at 42°C. Nevertheless, the pronounced trends associated with the magnitude of the pre-wave and its ratio to the total wave are probably significant.

In considering these data relating to the behavior of ethane in more detail, it will be most straightforward to examine the 60°C results first and to relate them to the corresponding work with wire micro-electrodes. In both cases the adsorbed hydrocarbon is oxidized in stages as the potential is swept from the equilibration value to higher values, and a clearly delineated "pre-wave" occurs at potentials below that at which an oxide film forms on the platinum.

TABLE VII
Effect of Time and Potential on $Q_{E_1} : Q_{E_{tot}}$
T = 60°C

Potential (volts)	Time (sec)	$Q_{act}^+ : Q_{tot}^+$
0.3	15	0.36
	30	0.42
	60	0.42
	120	0.41
	300	0.45
	600	0.48
0.35	15	0.50
	60	0.49
	120	0.48
	200	0.47
	600	0.50
0.50	15	0.43
	60	0.38
	120	0.35
	300	0.36
	600	0.33

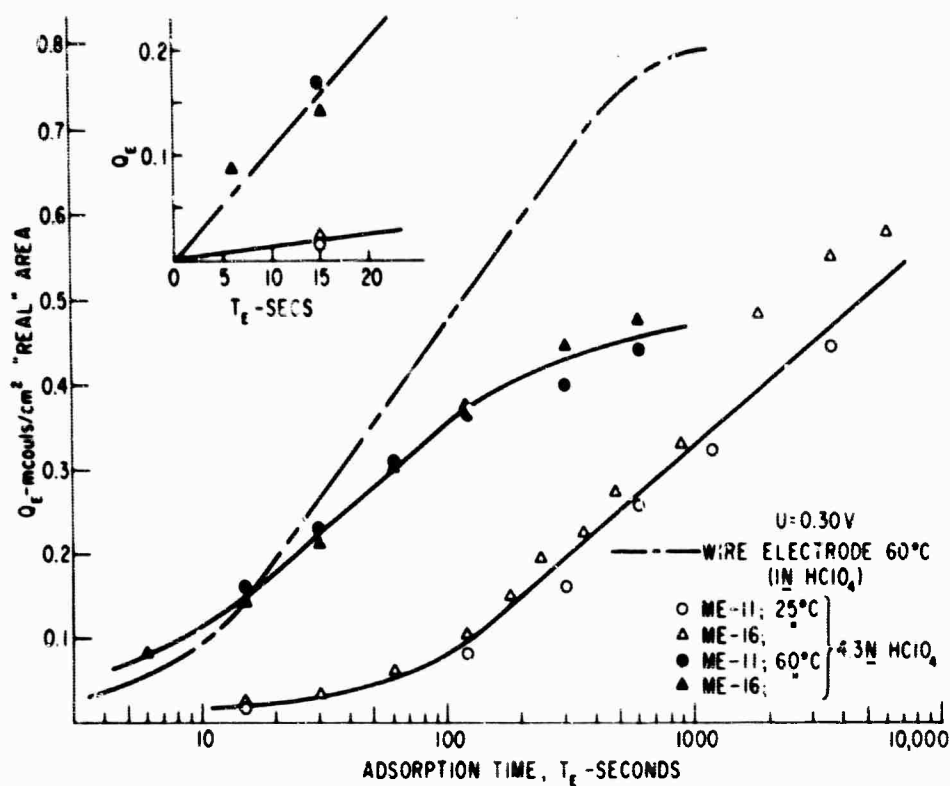


Fig. 27. Surface Charge Associated With Adsorbed Ethane.

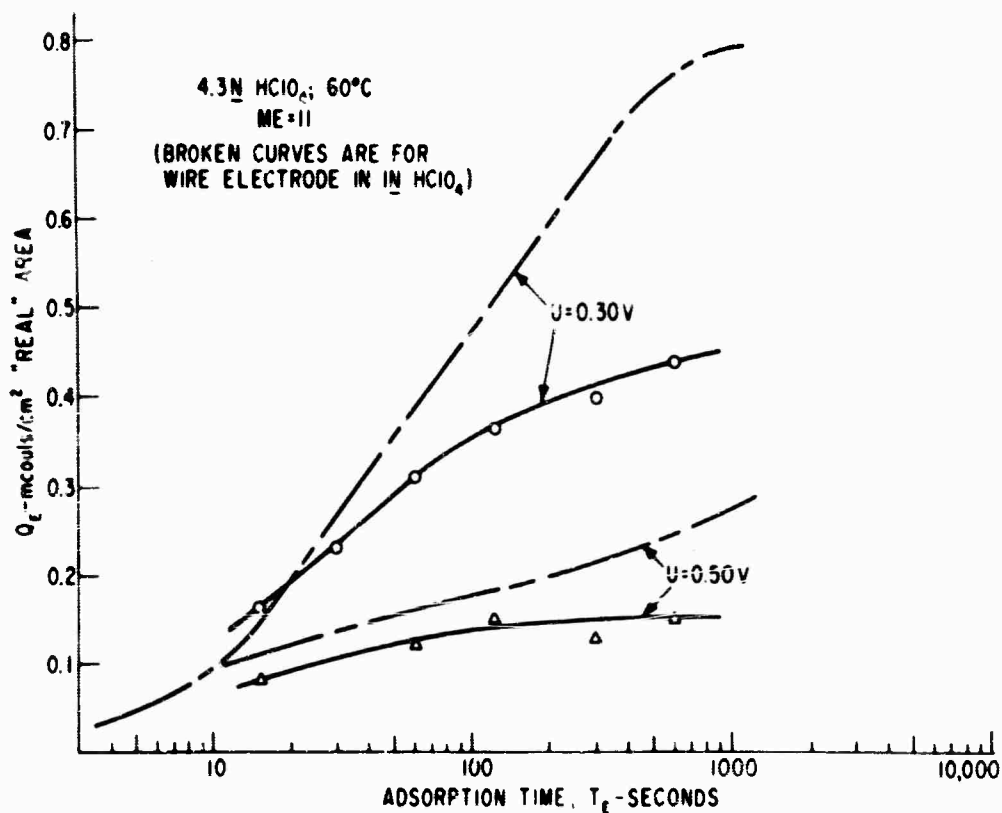


Fig. 28. Surface Charge Associated With Ethane Adsorbed At Different Potentials.

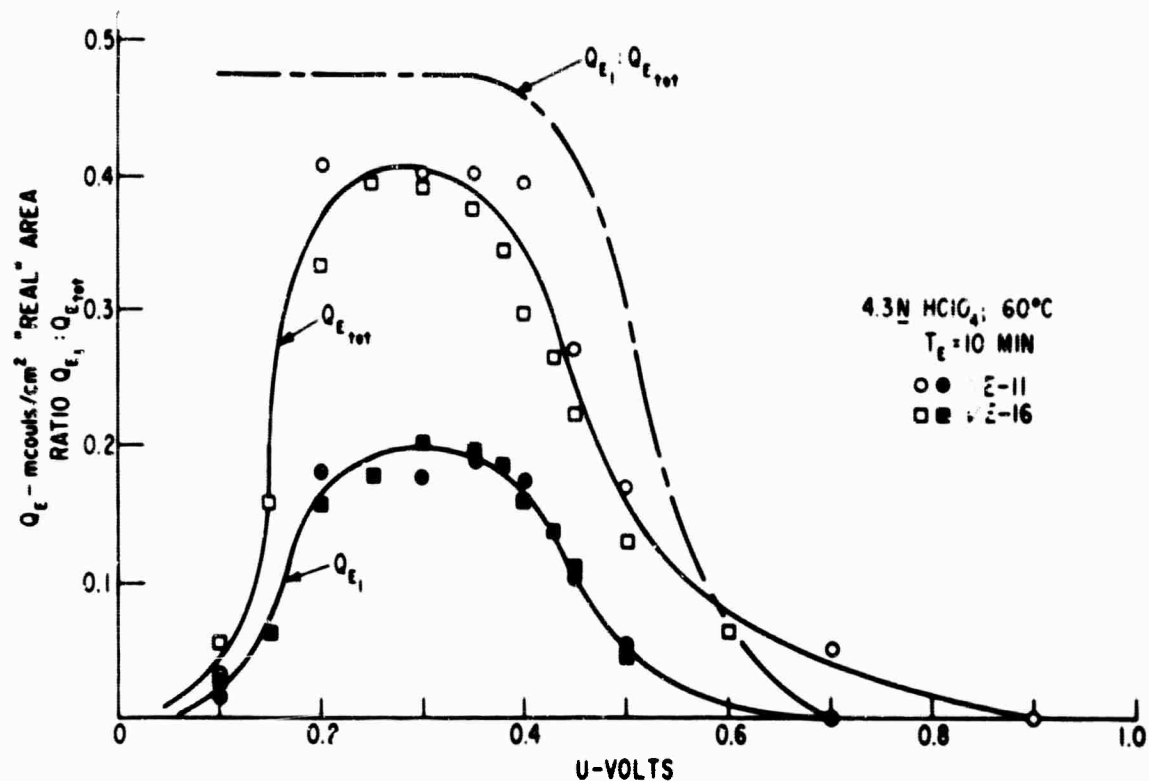


Fig. 29. Effect Of Potential On Total Surface Charge And Prewave Charge From Adsorbed Ethane.

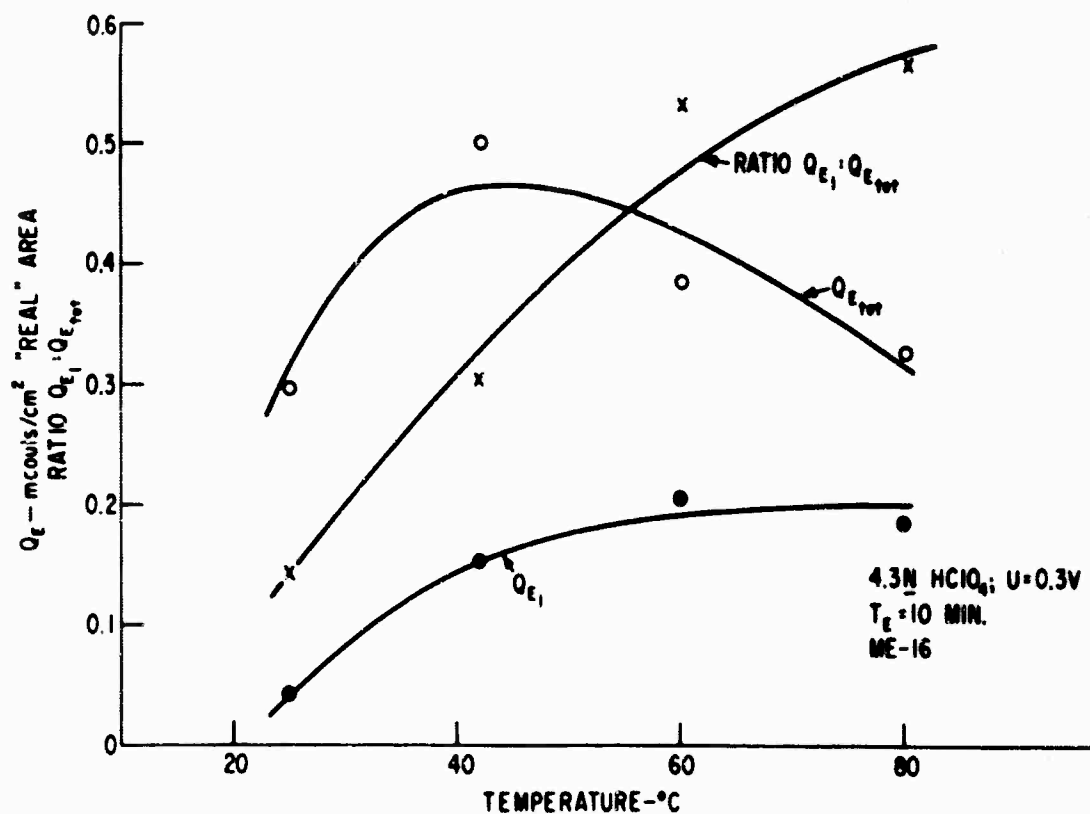


Fig. 30. Effect Of Temperature On Total Surface Charge And Prewave Charge For Adsorbed Ethane.

The data obtained at 60°C by the two approaches are also in reasonable quantitative agreement. It is thus seen that the maximum in the surface coverage, in terms of millicoulombs/cm², occurs in the region of 0.3 volt. At low potentials (< 0.1 volt) adsorption is severely hindered, undoubtedly because the required dissociation of the adsorbing hydrocarbon is repressed by the hydrogen on the electrode surface. At potentials above 0.3 volt, the coverage again declines as it adjusts to accommodate the adsorption rate to the rate of electro-oxidation.

The kinetic data, in terms of millicoulombs/cm² on the surface, in Figs. 27 and 28 obtained at 60°C are also in satisfactory agreement with the data of Section 4.1.1 (shown on Figs. 27 and 28 as broken lines). In both cases the rate of adsorption of ethane is initially constant (see Fig. 27) and then follows an empirical Elovich relationship over a moderate range. The maximum adsorption rate (corresponding to the initial linear region) is about 0.010 m coul/cm²/sec, or the equivalent current density of 10 microamps/cm² in both cases. With the Teflon bonded electrodes "saturation" coverages are lower than those observed with the wire electrodes; cf. the positions of the plateaus in Figs. 27 and 28.

With the information presently available, it is not possible to firmly identify the individual species involved on the surface. It is certain, however, that they do not correspond to undissociated ethane. More than likely, several species are involved, and from the data in Section 4.1.1 it appears that an average C:H ratio of 1 prevails. Additional inferences can be made from the observed temperature effects and other data.

Considering first the data of Figs. 26 and 30 showing the effect of temperature on the oxidation curves for adsorbed ethane, it is noted that the pre-wave becomes more prominent as the temperature is raised. An attractive explanation of this phenomenon based upon past observations is that the pre-wave is associated with a species derived from the reaction of a primary adsorption species with water. This might be via a direct chemical reaction or via an electrochemical route; the species might itself be either a necessary reaction intermediate along the major route involved in the over-all oxidation of ethane or it could be a byproduct that reaches a steady state on the surface.

This new species might thus be the "CO-like" surface species previously suggested by Niedrach (4) or the "reduced CO₂" of Giner (5), both of which undoubtedly refer to identical materials. To obtain additional information bearing on such an interpretation, experiments were performed at 60°C in which the electrode — after the standard activation procedure — was equilibrated with CO (at 0.3 volt), CO₂ (at 0.06 and 0.2 volt), and argon saturated with formic acid vapor at 25°C (at 0.06 and 0.2 volt) prior to a potential sweep. The results of these experiments are shown in Fig. 31.

(4) L. W. Niedrach, J. Electrochem Soc 111, 1309 (1964).

(5) J. Giner, Electrochimica Acta, 8, 857 (1963).

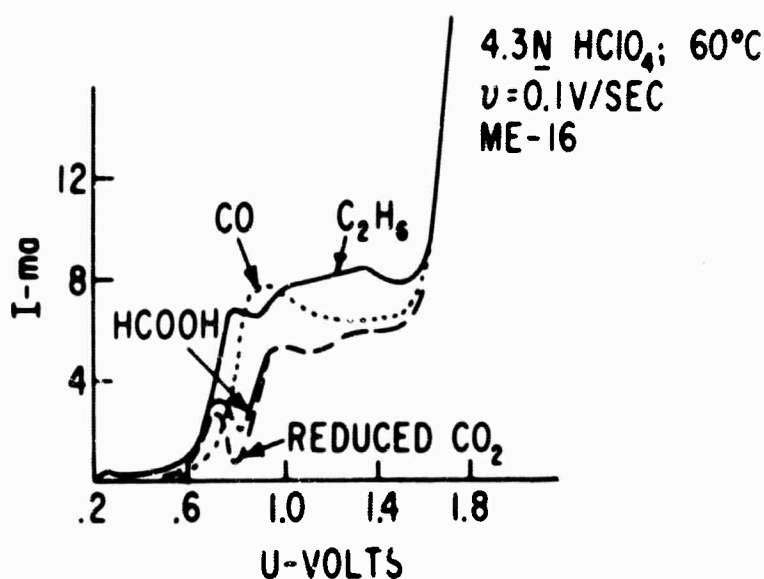


Fig. 31. Current-Potential Curves For Several Carbonaceous Materials On Pt

The positions of the oxidation waves for the three oxygenated materials relative to that of the pre-wave from ethane strongly suggest that a species closely related to them is involved in the oxidation of ethane. This idea is further supported by the observation that the pre-wave for ethane is not removed by cathodic hydrogenation of the electrode. As has been previously noted, carbon monoxide behaves in a similar fashion (4), and the waves for reduced CO_2 and formic acid were, of course, obtained after equilibrations at hydrogenating potentials; e.g. 0.06 volt. Additional evidence that the pre-wave is an oxygenated species derives from related observations on propane in section 4.1.4.

While the nature of the species associated with the pre-wave appears to be narrowed down to a partially oxidized species, related to CO and formic acid, additional work will be required to identify it more specifically and to define its role as an active intermediate or byproduct. Resolution of the latter point is of particular importance in view of the fact that the "CO-like" species already strongly manifests itself at potentials as low as 0.15 volt.

As far as the second wave for ethane is concerned, the present work sheds no light in this area. It would appear likely, however, that this wave involves a partially dehydrogenated ethylenic species. Because the state of the hydrogenation is uncertain, it is not possible to reach definitive conclusions concerning the over-all saturation of the surface sites on the electrode.

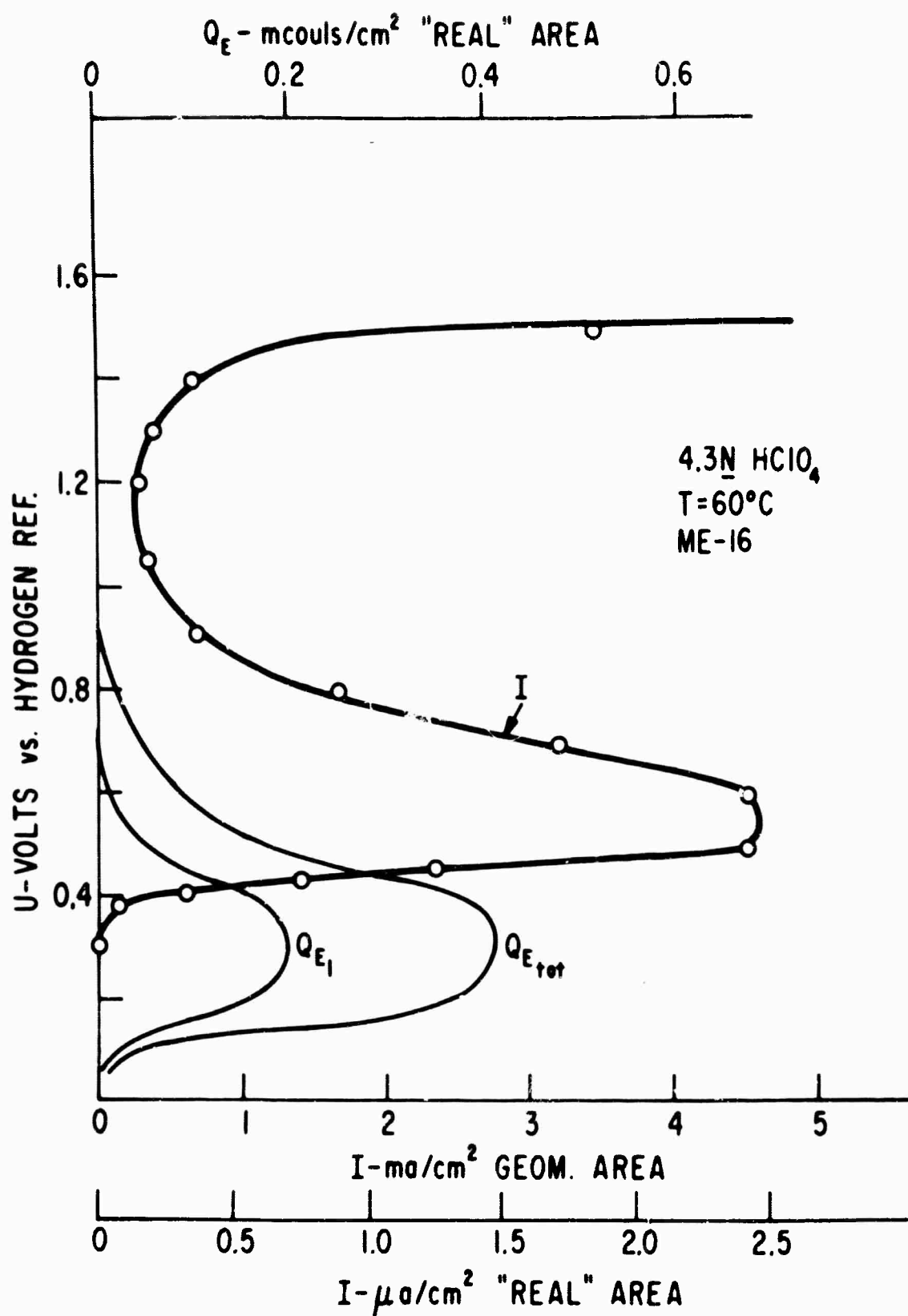


Fig. 32. Polarization Curve For Ethane With A Perchloric Acid Electrolyte

In the discussion so far, the effect of temperature in the rate of adsorption has not been considered. The data in Fig. 27 shows that the over-all adsorption at 25°C, when expressed in terms of millicoulombs/cm² of "real" electrode area, follows a pattern similar to that observed at 60°C. Similar results were also obtained at 42°C (not shown). Although the equilibrations at the lower temperatures were not continued to "saturation", it is significant that higher total surface charges were realized in both these cases than in the equilibration at 60°C. This undoubtedly reflects the influence of the partially oxidized "CO-like" species on the surface at the higher temperatures.

One additional point for consideration is the relationship between the adsorption data and the polarization curve for the electrode operating on ethane. Such a curve obtained at 60°C is shown in Fig. 32. The abscissa is expressed in terms of the current density per unit of "real" and geometrical area of the electrode. Therefore, the data may be related to the adsorption studies as well as performance curves for real fuel cells. Also shown in Fig. 32 are the measured surface coverage^s, Q_{E_1} and $Q_{E_{tot}}$, from Fig. 27. The form of the polarization curve is typical of those for a variety of fuels when the data are obtained potentiostatically. Even hydrogen shows the minimum in the region from 0.9 to 1.4 volt on smooth platinum. Over the potential range from 0.3 to 0.45 volt, the curve has a linear Tafel region with a slope of 0.066 v/decade of current. The magnitude of the "maximum" current is somewhat low on the basis of the adsorption rate for ethane on a clean surface — 0.0024 ma/cm² "real" area vs a calculated value of >0.010 ma/cm². This, as well as the fact that the "maximum" occurs when there is yet an appreciable concentration of adsorbed material on the electrode surface, indicates that the maximum current is established in this case neither by a limiting rate of mass transport nor by a limiting over-all rate of adsorption on a clean surface. It could, however, reflect a limiting adsorption rate on a surface partially covered with refractory hydrocarbon residues, oxygen (at 60°C the surface oxide starts to form between 0.6 and 0.7 volt), and adsorbed ions. Additional work will be required to establish this limiting step.

C. Other Fuels with a Perchloric Acid Electrolyte

A limited amount of data have been obtained for fuels other than ethane. These are shown in Fig. 33 in the form of voltage sweep traces after equilibrations at various potentials.

Qualitatively, all of the saturated hydrocarbons show similar behaviors. The pre-wave shows greatest prominence in the case of methane and ethane, but it also manifests itself for propane. The structure of the trace for propane at the higher potentials is more complex than for the lower hydrocarbons. This undoubtedly reflects a greater variety of surface species from this more complex molecule.

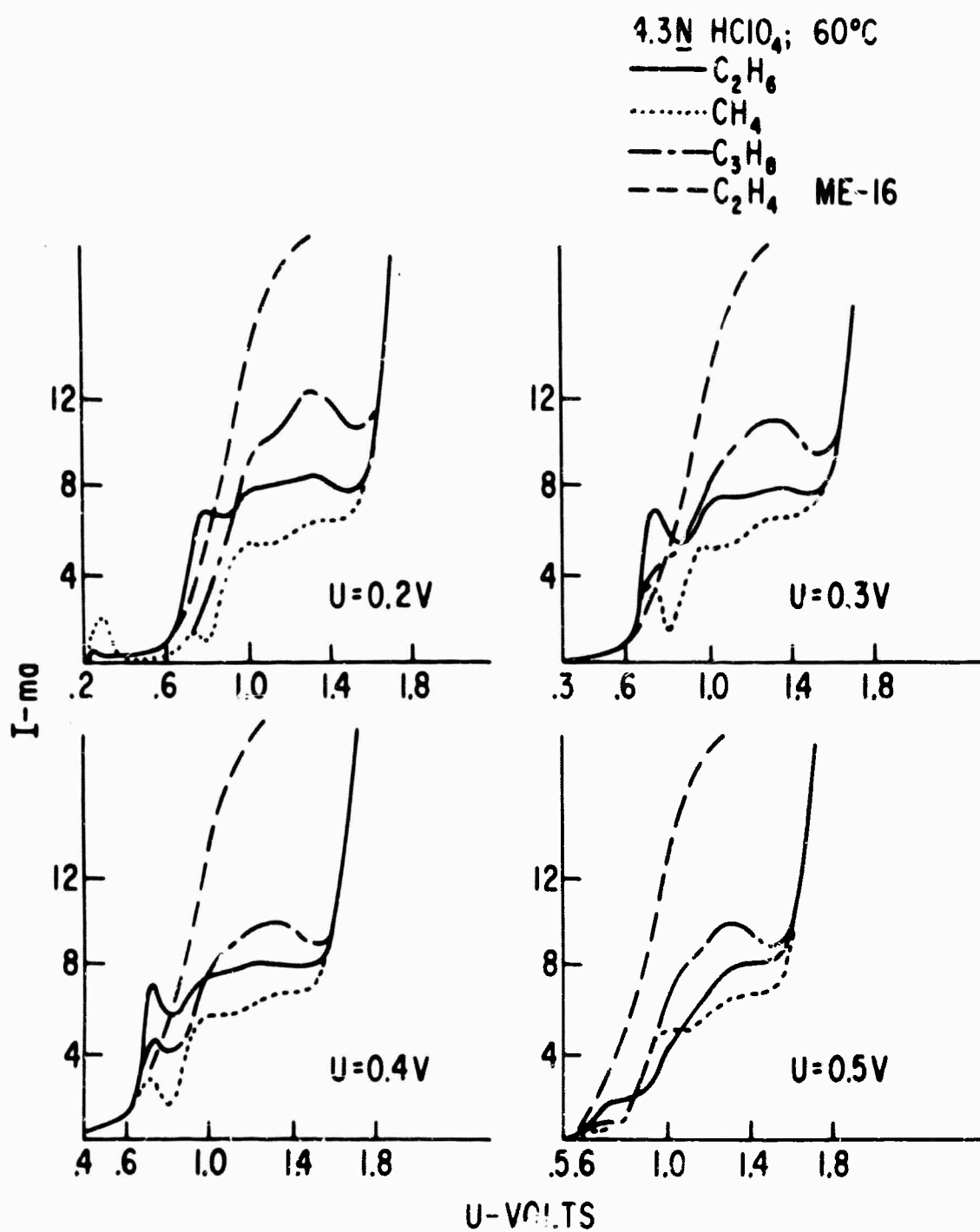


Fig. 33. Current-Potential Curves For Several Hydrocarbon Fuels After Equilibration At Different Potentials.

The behavior of ethylene on the semi-micro fuel cell electrode is quite different from that of the saturates. No evidence is seen for the pre-wave under any circumstances, and the adsorption rates are much higher than for the saturates. These observations are in accord with previous volumetric and galvanostatic studies of the same fuels at 25°C (4).

D. Ethane with a Hydrofluoric Acid Electrolyte

It is planned to use ethane in a rapid examination of the effect of various acid electrolytes on the behavior of hydrocarbons on fuel cell electrodes. Because of recent observations that higher hydrocarbons appear to show improved performance with hydrofluoric acid as the electrolyte (6), this material was chosen for initial work. Of particular interest was any difference in behavior that could account for the higher, steady current densities that can be supported in HF cells without the appearance of voltage decay and oscillations.

A 36% solution of HF was employed and all measurements were made at 60°C. As shown by the traces in Fig. 34, the behavior of adsorbed ethane is similar with HF and HClO₄ electrolytes. This similarity extends over the entire voltage scale that was examined — 0.3 to 0.9 volt. With both electrolytes the clearly defined pre-wave attributed to a "CO-like" species is evident. Quantitatively, it is seen that the amount of ethane adsorbed is higher in the case of the HF and rate of adsorption was also noticeably higher.

A polarization curve obtained with the HF electrolyte is shown in Fig. 35. The polarization curve obtained with HClO₄ is included for reference, as are curves showing the surface coverage with adsorbed species.

It is clear that the general form of the polarization curve is similar with both electrolytes, as is their relation to the surface coverage. The enhanced performance of hydrocarbons with the HF electrolytes therefore does not appear to relate to a gross qualitative difference in behavior, but rather to subtle quantitative differences. This may well be associated with differences in anion adsorption and the general structure of the double layer. These observations are in accord with those discussed in Section 4.1.5. Similar variations in maximum currents have been reported for other reacting species, e.g. hydrogen, when electrolytes have been varied. It is not felt that additional work on this electrolyte with the semi-micro fuel cell electrode will be helpful.

4.1.2.3 Conclusions

The adsorption and surface behavior of ethane, as a representative hydrocarbon fuel, on semi-micro Teflon-bonded fuel cell electrodes has been found to parallel that on wire electrodes in both the qualitative and quantitative senses. In both cases during adsorption at intermediate

(6) Reference 3, p. 4-41 ff; p. 4-78 ff.

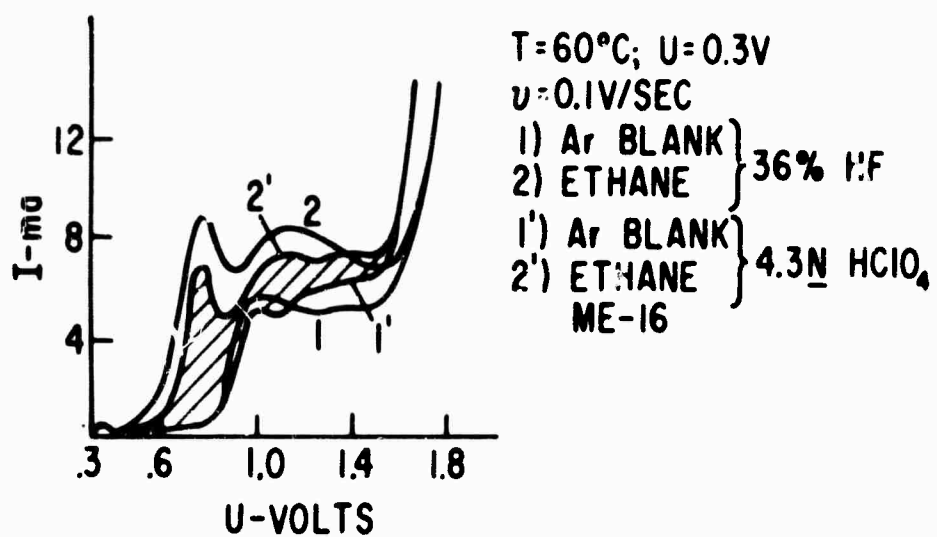


Fig. 34. Current-Potential Curves For Ethane With HF And HClO₄ Electrolytes

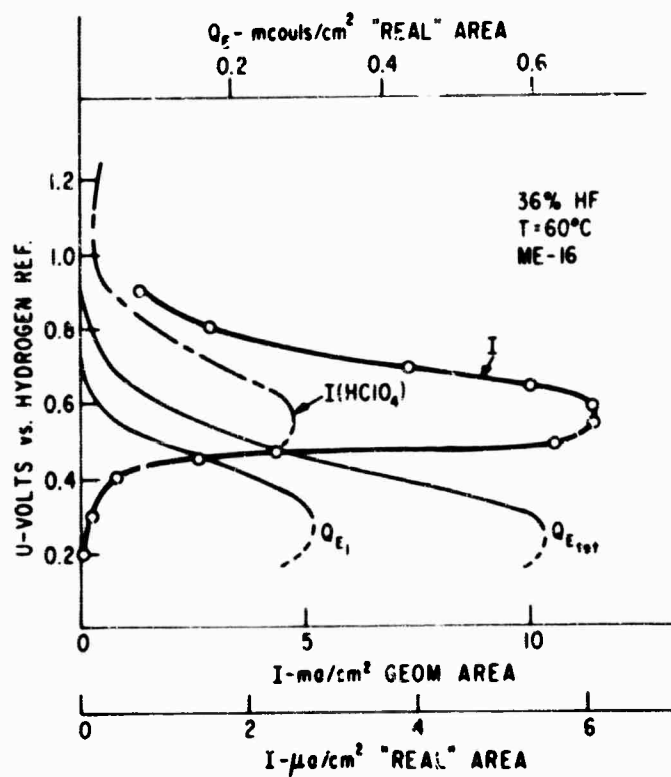


Fig. 35. Polarization Curve For Ethane With A Hydrofluoric Acid Electrolyte

potentials a linear law is followed at low coverages and the Elovich relationship at higher coverages. Numerous properties of a "pre-wave" seen during the oxidation of adsorbed ethane with a linear sweep suggest that one of the surface species is partially oxygenated and related to carbon monoxide and/or formic acid. The behaviors of methane and propane resemble that of ethane in the qualitative sense, but quantitative differences are seen. Unsaturated ethylene adsorbs more rapidly than the unsaturated hydrocarbons and the pre-wave is not obtained. Experiments with ethane with perchloric acid and hydrofluoric acids indicate no gross qualitative differences in its adsorption and surface behavior with the two electrolytes. Subtle quantitative differences therefore appear to account for the differences in behavior of hydrocarbons in fuel cells with perchloric and hydrofluoric acid electrolytes (6).

4.1.3 Studies of Hydrocarbon Macro Anodes (Dr. W. T. Grubb/M. E. Lazarus)

Micro electrode investigations (see Sections 4.1.1, 4.1.2, and 4.1.5) rely heavily upon electrical measurements to deduce the composition of surface species and the nature of surface reactions that occur. This becomes increasingly difficult as the reacting molecules become more complex, for example gas with hydrocarbons. For this reason, a study of large area fuel cell electrodes with which constant current, constant potential, and other experiments could be combined with the analysis of products and intermediates was initiated.

During the preceding report period, a cell with associated electronic system was constructed and tested. During the present report period, a means for rapid, periodic gas chromatographic analyses has been integrated into the system. The working electrode had a hydrogen surface area 10^3 to 10^6 times as great as the micro and semi-micro electrodes of Sections 4.1.1, 4.1.2, and 4.1.5. This apparatus is discussed in Appendix 5.1.

Using this apparatus, galvanostatic product-time profiles have been measured, and a test for the presence of surface CO bonds has emerged from this work. With propane as fuel at 65°C in a phosphoric acid electrolyte, it has been found that carbon dioxide evolution is negligible below about 0.3 volt * and rising to a peak value at 0.4 volt. However, partial surface carbon oxidation takes place as low as 0.2 volt. Since the open circuit voltage of the propane anode was 0.17 volt, there is probably no potential region in which only hydrogen electrochemically oxidizes without some oxidation of carbon occurring. There is a definite potential region, however, in which carbon partially oxidizes without evolution of CO_2 . This region between propane open circuit and 0.32 volts, therefore, favors the formation of intermediates which could possibly be desorbed and identified.

* All voltages in this section are against reversible hydrogen potential in the same electrolyte, and the sign convention is such that an oxygen electrode would be positive.

When CO is oxidized, the galvanostatic CO₂-time profile approaches the expected form of a square wave with edges smeared out by diffusion. The height of this wave indicates some loss of CO₂ into the electrolyte in the order of 10-15% at the point of maximum concentration. It should be possible to calibrate this loss as a function of concentration and residence time of the sample in the cell anode chamber. The CO₂ percentages so far obtained in the hydrocarbon experiments are not precise and are on the low side of true values by several percent.

4.1.3.2 Electrodes

This work has made use of high area, Teflon-bonded platinum black electrodes of the Niedrach-Alford structure (1). Teflon-bonded electrodes used with immobilized electrolyte have previously been investigated with hydrocarbon fuels at room temperature (2) using chromatographic techniques to determine cracking and association products at open circuit. However, it is known that cracking is suppressed under anodic load (3), and no investigations of the present type involving the essentially continuous monitoring of carbon dioxide have been reported.

Propane was selected as the fuel for the initial experiments because of the availability of a chromatograph and column system with extensive calibrations which gave good resolution between propane, the products of cracking, and carbon dioxide. An interference between ethane (cracking product) and carbon dioxide was resolved by the use of a carbon dioxide adsorbing train before a second chromatograph system.

In terms of total capacity in hydrogen coulombs, the micro and semi-micro electrodes of Sections 4.1.1, 4.1.2, and 4.1.5 compare with the present electrodes as follows:

Micro electrode (Gilman, Sec. 4.1.1)	0.02 millicoulombs
Micro electrode (Cairns, Sec. 4.1.5)	0.143 millicoulombs
Semi-micro electrode (Niedrach Sec. 4.1.2)	12 millicoulombs
Present electrodes	17,000 millicoulombs

(1) Saturated Hydrocarbon Fuel Cell Program, "A New High Performance Fuel Cell Employing Conducting-Porous-Teflon Electrodes (Niedrach-Alford) and Liquid Electrolytes", Contract Number DA 44-009-AMC-479 (T), ARPA Order Number 247, Project Number P4980.

(2) Niedrach, L.W. Electrochem. Soc. 111, 1309 (1964).

(3) Grubb, W.T., J. Electrochem. Soc. 111 1086 (1964).

Despite the high area, the analytical methods must have high sensitivity since 17 coulombs of hydrogen are still only about 90 micromoles. It is fortunate that larger coulombic equivalents are observed for propane. When adsorbed at 0.2 volts, 63 coulombs of propane (and its intermediates) were adsorbed as shown by subsequent complete oxidation. Thus, total oxidation of propane gave between 3 and 4 (3.7) electrons per hydrogen site. The coulombic equivalents of several hydrocarbons were similarly measured and the order of total coulombs was methane < ethane < propane = n butane = i butane. The measured values should be several percent on the low side of true values due to the CO₂ diffusion problem.

4.1.3.3 Oxidation of Propane

A propane experiment will be described in detail as illustrative of the procedure employed in the work. Pre-treatment of the electrode was as follows. Oxygen was evolved from the working electrode for about 15 hours at a constant current of 3-10 ma. The electrode was then reduced by evolving hydrogen for a few minutes. The potential was then set at 0.4 volts, and the current allowed to come to equilibrium. A small blank current was observed. Propane was then adsorbed on the open-circuited electrode by flowing excess propane through the cell. The cell was then set at 0.2 volt and potentiostatically maintained at that potential. Current was monitored as a function of time. The run was continued until blank current value was reached (about 1 hour). The anode was maintained in contact with excess of gas phase propane during this step. Integration of the charge showed that about 1/4 of the total charge (as determined by this and the subsequent galvanostatic oxidation step) was removed at 0.2 volt.

The system was then set to oxidize at constant current, usually 10 ma, with a slow known flow of helium sweep gas through the cell anode chamber and into the gas analysis system.

The voltage-time profile observed during a typical propane run is presented in Fig. 36. The arrows indicate the points at which gas analyses were made. Due to line volume and slow flow rate, there is a time lag in the gas analysis which can be rather closely estimated by dividing the measured line volume by the measured flow rate. The galvanostatic carbon dioxide-time profile is presented in Fig. 37. The ordinate is the volume percent of CO₂ in the sample injected with the gas sampling valve and is proportional to the rate of CO₂ production, since total flow is constant. The shape of the plot in Fig. 37 is characteristic of propane and the coincidence at point A with the theoretical rate of CO₂ production by a 4 electron reaction at 10 ma was repeated several times in separate experiments. Nevertheless, it does not indicate that carbon alone is being oxidized because it can be shown that part of the CO₂ is formed from the oxidation of material(s) on the surface that contain carbon-oxygen bonds already formed at lower potentials. A different way of presenting the results is to plot the galvanostatic CO₂-voltage profile taking into account the time lag in the gas analysis. This is presented in Fig. 38. An interesting feature of

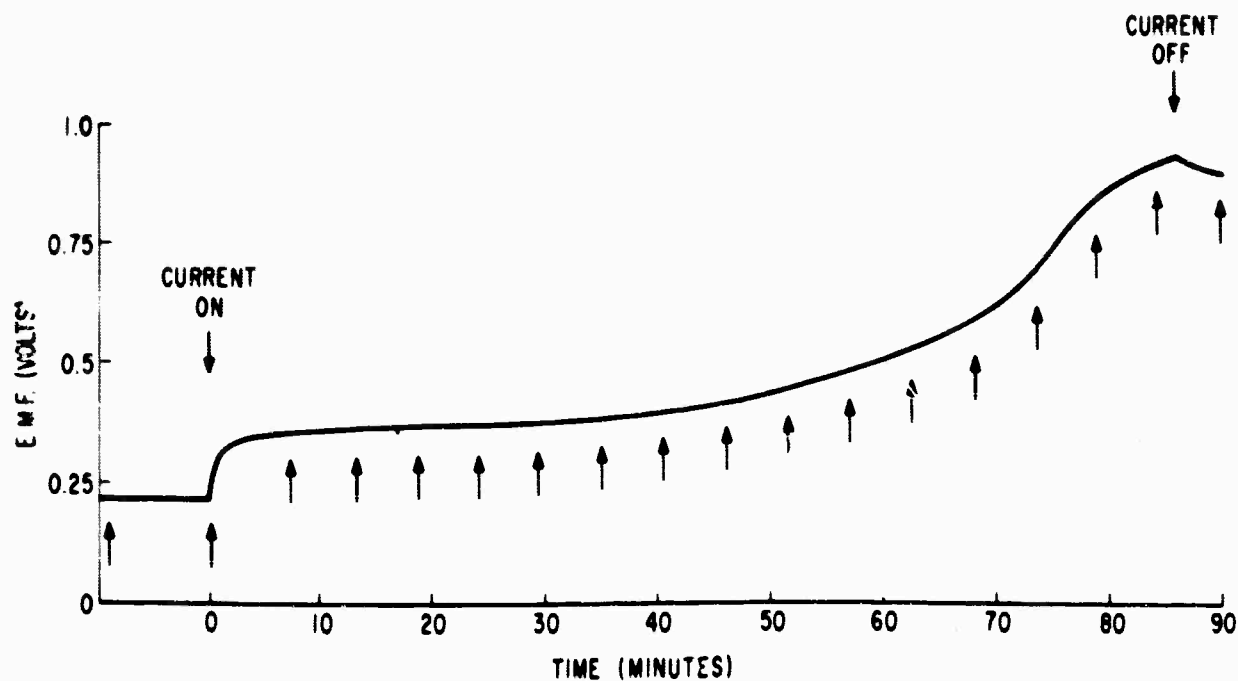


Fig. 36. Galvanostatic Oxidation of Propane At A Macro Anode
Anode/Reference Voltage vs. Time

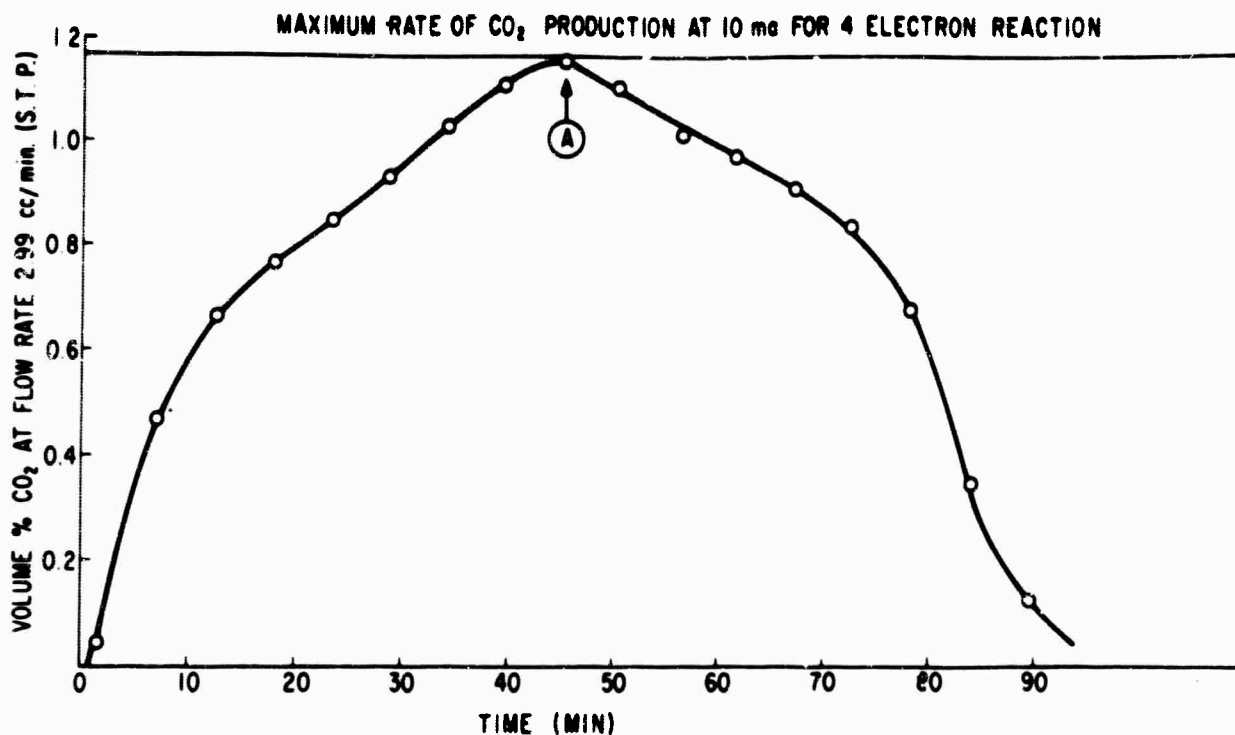


Fig. 37. Galvanostatic Oxidation of Propane At A Macro Anode
CO₂ Production Rate vs. Time

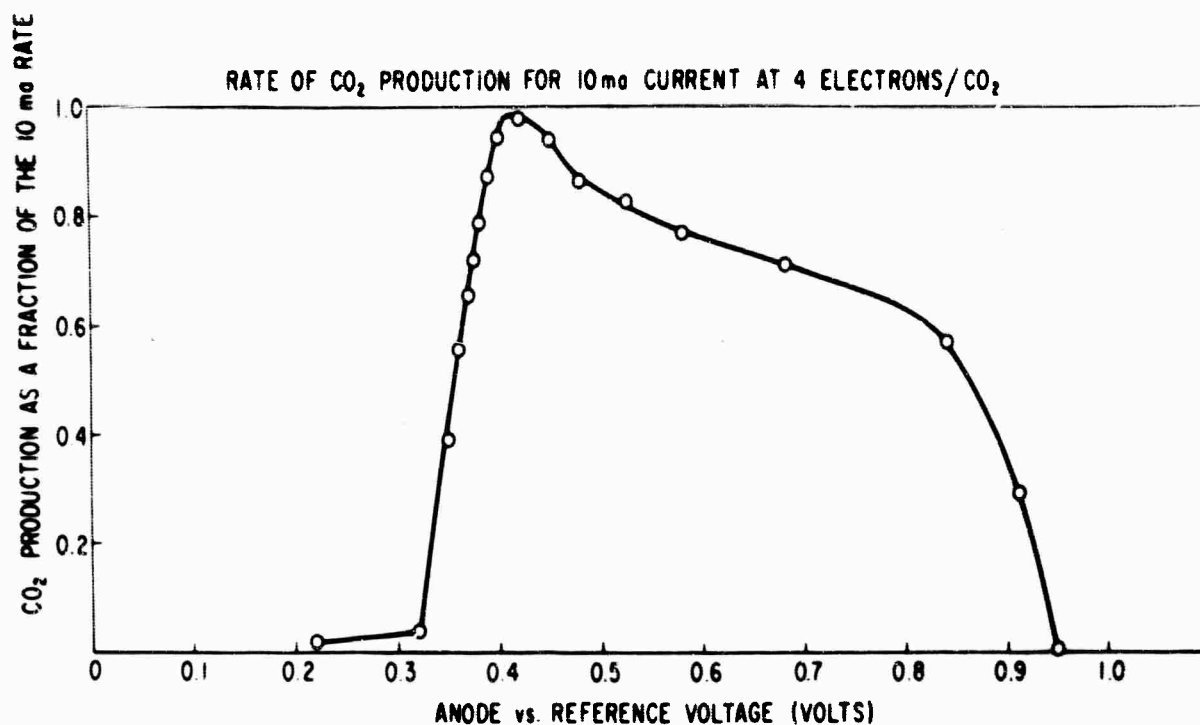


Fig. 38. Galvanostatic Oxidation Of Propane At A Macro Anode
CO₂ Production Rate vs. Anode/Reference Voltage

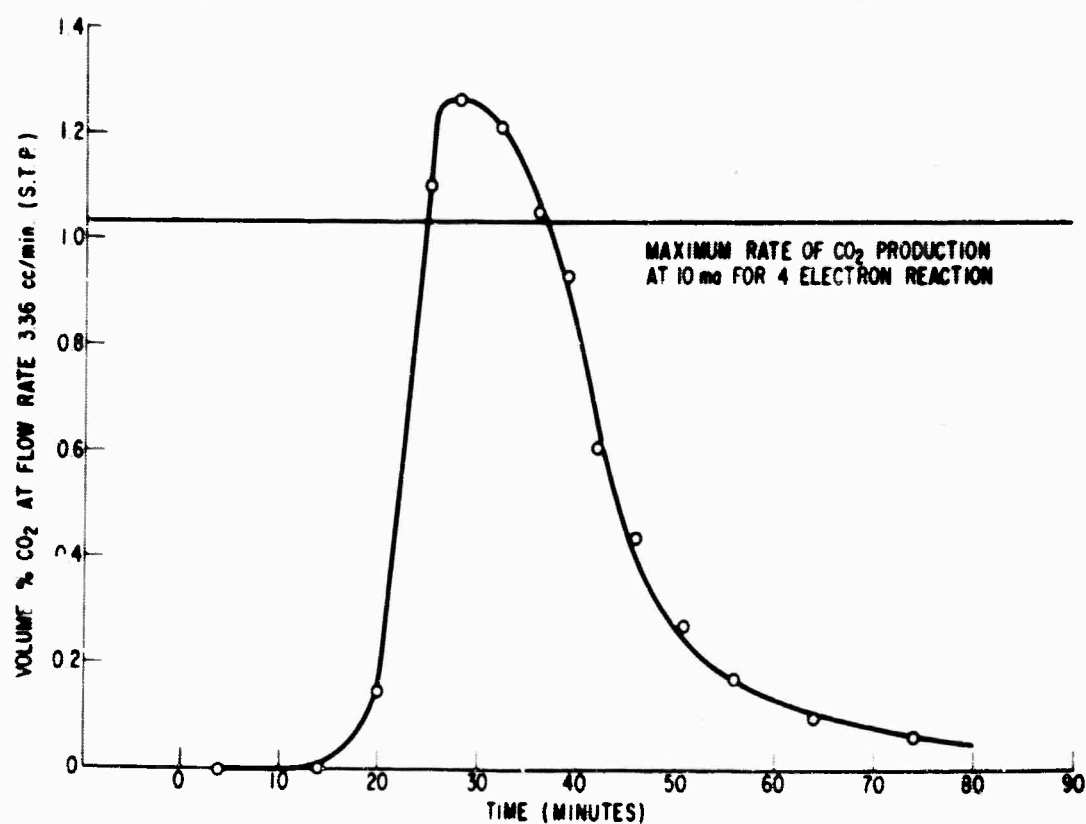


Fig. 39. Carbon Dioxide vs. Time Profile For 10 ma Galvanostatic Oxidation of "Propane" Residue After Oxidation to 0.4 Volts and Exhaustive Removal of Hydrocarbons by Cathodic Hydrogenation

this curve is the essential absence of CO_2 production below about 0.32 volts, followed by a sudden rise to a very high value.

It was shown that the coincidence at point A is caused by a combination of reactions and not by the single reaction $\text{C} + 2 \text{H}_2\text{O} = \text{CO}_2 + 4\text{e}^-$ in the following manner. An experiment was interrupted at point A and the anode was hydrogenated at constant current. Monitoring the gaseous products of the hydrogenation, propane, ethane, and methane were found in order of decreasing concentration. Hydrogenation was continued until no more products were produced. Following this step, the galvanostatic oxidation was started again. This time the CO_2 profile rose about 20% above the line for 10 ma CO_2 production by a 4 electron reaction, indicating the presence of oxidized carbon species not removed by the hydrogenation. This is shown in Fig. 39.

The same hydrogenation experiment was carried out after the 0.2 volt potentiostatic oxidation, the same hydrogenation products were observed, and subsequent oxidation again showed the C-O bonds were present on the surface. The results of the subsequent 10 ma oxidation for this case are presented in Figs. 40 and 41. Fig. 40 shows the plateau for the oxidation of carbonaceous species beginning at about 0.4 volt. Fig. 41 is the galvanostatic CO_2 -time profile which shows that more CO_2 is produced than can be produced by 10 ma by a 4 electron reaction, and this again proves the presence of surface C-O bonds. This C-O containing surface species (possibly a mixture of many species) may be identified with the material responsible for the "pre-wave" found in voltage sweep experiments with propane in Section 4.1.2 and with ethane in Sections 4.1.1 and 4.1.2.

Hydrocarbons formed during the hydrogenations were chromatographically determined for the two cases in which oxidation was carried out to 0.2 and 0.4 volt, respectively. See Tables VIII and IX.

TABLE VIII

Hydrocarbons Produced By Hydrogenation After Oxidation to 0.2 Volt

<u>Hydrocarbon</u>	<u>cc at S. T. P.</u>	<u>Fraction of Total</u>
C_3H_8	0.48	0.82
C_2H_6	0.16	0.17
CH_4	0.01	0.01

TABLE IX

Hydrocarbons Produced By Hydrogenation After Oxidation to 0.4 Volt

<u>Hydrocarbon</u>	<u>cc at S. T. P.</u>	<u>Fraction of Total</u>
C_3H_8	0.35	0.80
C_2H_6	0.08	0.18
CH_4	0.01	0.02

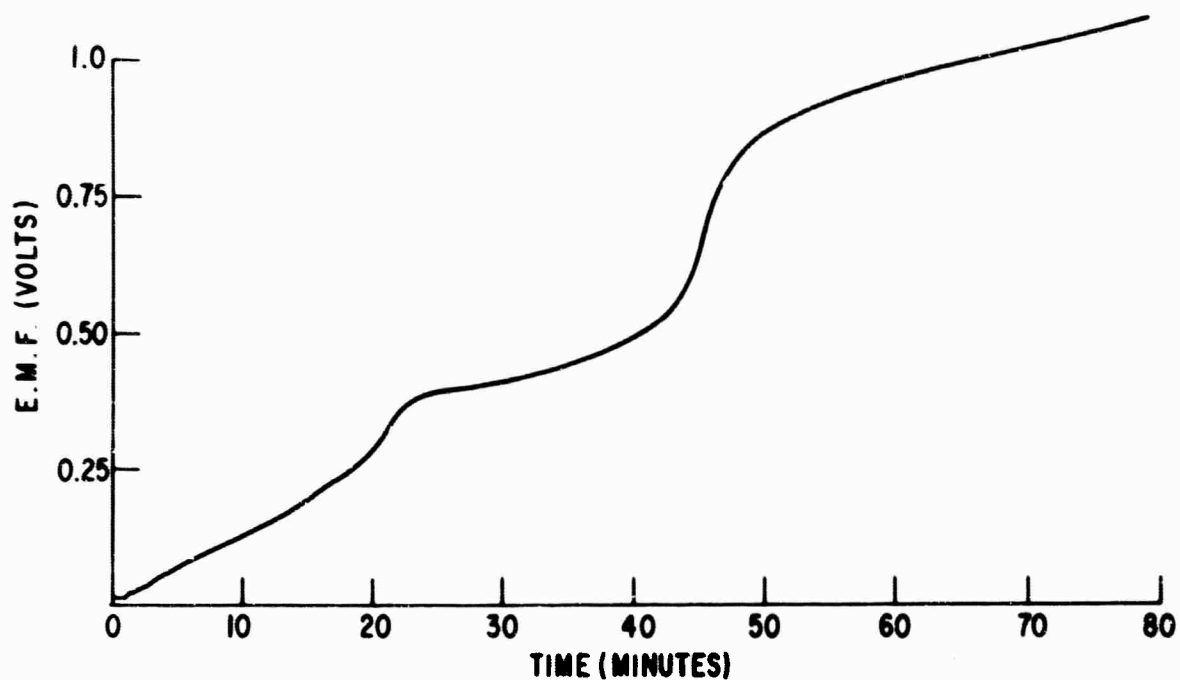


Fig. 40. Anode/Reference Voltage vs. Time For 10 ma Galvanostatic Oxidation of "Propane" Residue After Potentiostatic Oxidation At 0.2 Volts And Exhaustive Removal Of Hydrocarbons By Cathodic Hydrogenation

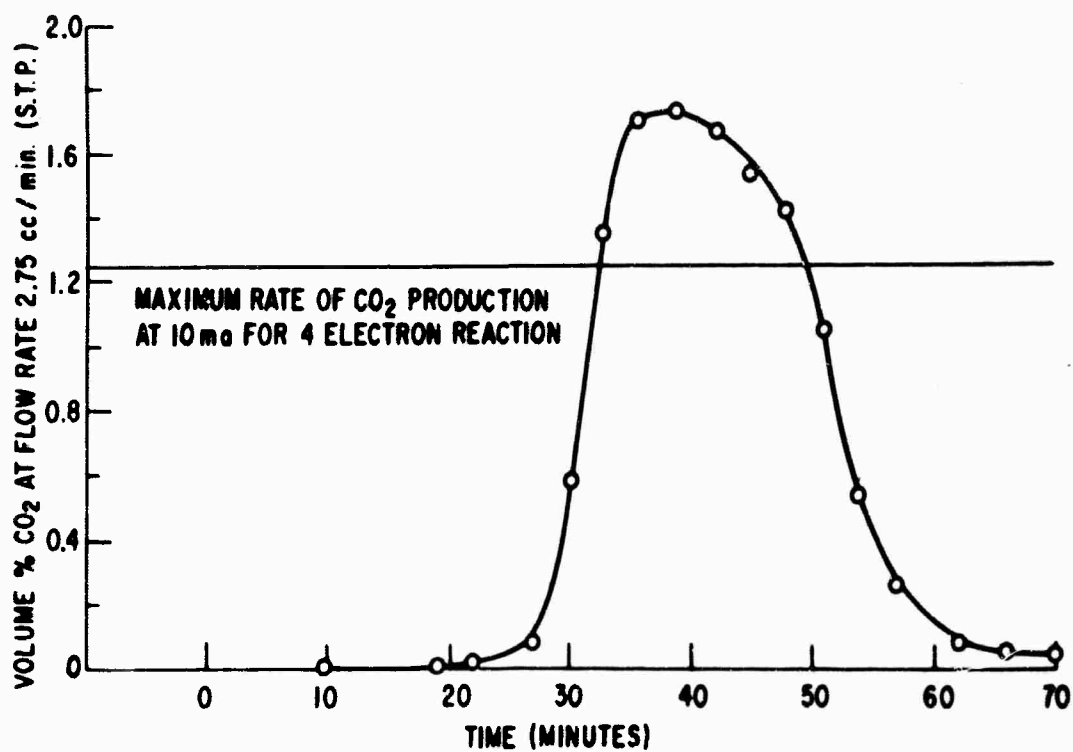


Fig. 41. Carbon Dioxide vs. Time Profile For 10 ma Galvanostatic Oxidation of "Propane" Residue After Potentiostatic Oxidation at 0.2 Volts And Exhaustive Removal of Hydrocarbons By Cathodic Hydrogenation

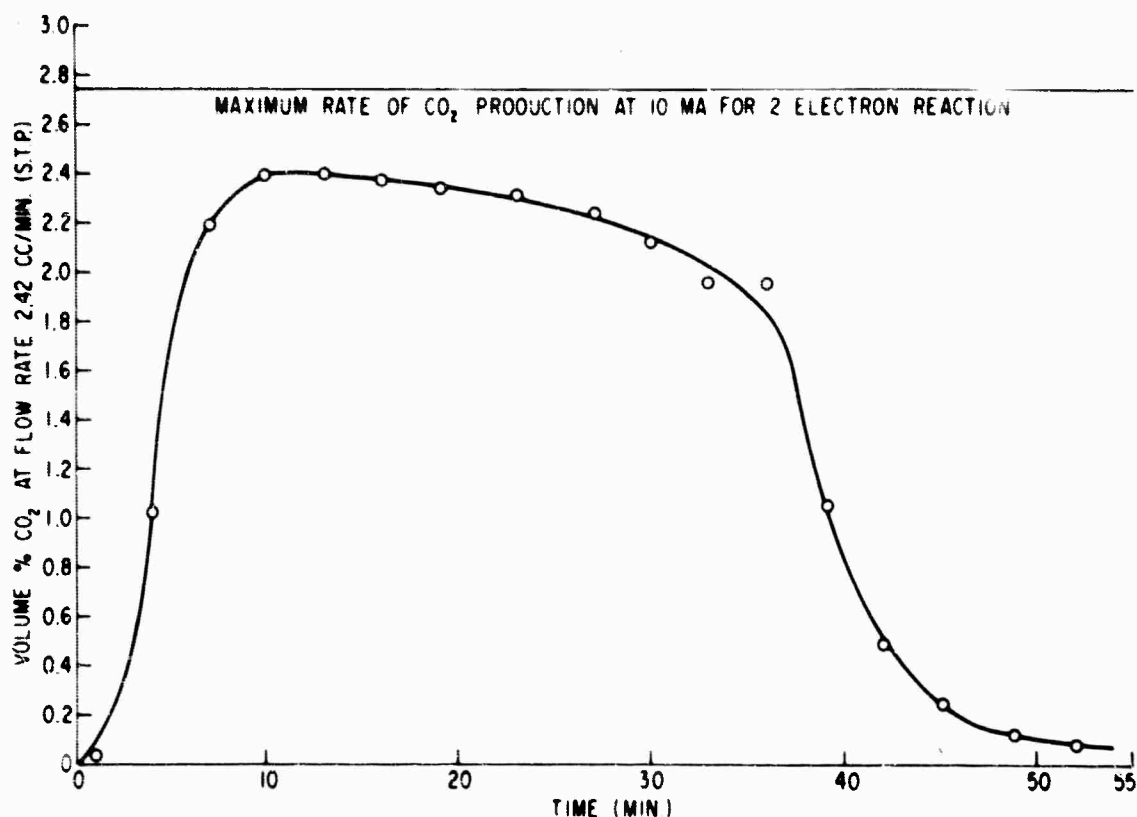


Fig. 42. Galvanostatic Oxidation Of Carbon Monoxide At A Macro Anode
CO₂ Production Rate vs. Time

It is observed that the ratio of propane to ethane does not change very much, that propane predominates, and methane is very small. Even after oxidation to 0.4 volt, representing about 65% of complete oxidation, there is considerable retention of the C₃ structure on the anode surface.

4.1.3.4 Oxidation of Carbon Monoxide

When CO is oxidized at constant current, the galvanostatic CO₂-time profile as shown in Fig. 42, approaches the expected form of a square wave with the edges smeared out by diffusion. The sloping top is caused by charging of the double layer capacity with an increasing part of galvanostatic current. At the maximum CO₂ rate, however, the voltage is not changing. Therefore, the CO₂ rate falls below that for a 2 electron CO₂ producing reaction at 10 ma, very probably because of diffusion into the electrolyte. CO oxidation at various He sweep gas flow rates and currents may offer a way of determining a correction for this effect which may be applied to the hydrocarbon oxidation experiments.

4.1.3.5 Conclusions

From oxidation of propane adsorbed on macro electrodes with periodic gas chromatographic analyses, galvanostatic CO₂-time profiles and CO₂-voltage profiles have been determined for propane at 65°C. No CO₂ is formed below 0.3 volt but surface C-O bonds are formed as low

as 0.2 volt. The latter are detected by exhaustive cathodic hydrogenation of the partially oxidized surface "propane", followed by further galvanostatic oxidation of the unhydrogenatable residue with accompanying CO_2 analyses. Since open circuit for propane was 0.17 volt under the conditions of the experiment, it appears that there is no potential region in which only hydrogen is oxidized. There is, however, a definite potential region in which surface carbon oxidation occurs without CO_2 evolution. Galvanostatic product-time profiles were also obtained during hydrogenation of the partially oxidized surface "propane". After both 25% and 65% of complete oxidation (oxidation to 0.2 and 0.4 volt, respectively), the hydrogenation product was 80% propane within the errors of measurement. This indicates considerable retention of C_3 structure on the surface. Galvanostatic (and potentiostatic) product-time profiles can be a very useful tool toward understanding the course of electrochemical oxidation of complex molecules.

4.1.4 Thin Film Mass Transport Processes (R. Roethlein/H. Maget)

The understanding of basic reaction mechanisms for hydrocarbon oxidation is of primary importance if eventual improvement of practical electrode structure is to be accomplished. Correct interpretation of the results obtained on simple electrode systems will, therefore, yield information regarding the behavior of complex practical structures.

The objective of this study is to determine if the reaction rates for propane oxidation are controlled by mass transport of the reactant species through thin electrolyte films; as compared to other rate-controlling processes, for a simple electrode configuration.

Previous work (1 and 2) has shown that for simple gases such as hydrogen and oxygen, the rate-limiting step for mass transport is controlled by the diffusion of the reacting gas through a thin film of electrolyte which forms on a partially immersed electrode structure. With the use of a simplified model of a large cylindrical pore, studies were made of the rates of propane oxidation at elevated temperatures in concentrated H_3PO_4 solutions on noble metal black surfaces. Rates of reaction were measured with and without the presence of a thin electrolyte film on the electrode surface to determine if there are potential regions where mass transport through the thin film is rate determining. A brief examination was also conducted into the effects produced on hydrophobic electrode surfaces.

4.1.4.1 Experimental Technique

A. Experimental Apparatus

The experiments were carried out in a Pyrex glass cell consisting of a large central compartment and two smaller sections separated from the main section by fine pore, fritted glass disks (Fig. 43). The middle compartment, which served as the test electrode section, also contained a thermometer well and a gas bubbler which was capable of keeping a steady gaseous flow over the electrolyte solution. One of the side compartments contained a platinum-black mesh electrode which served as the counter electrode. The other section served as a reference cell and had a Luggin capillary extending into the main compartment. The reference consisted of two platinum-black electrodes with a constant current of 1.0 ma flowing between them. The electrode which evolved hydrogen gas came to a steady overpotential value within a few minutes; this then served as the reference potential.

The test electrode consisted of a piece of platinum tubing, 99.99% pure, 1.0 cm long, 1.5 cm in diameter, and 0.2 cm in wall thickness. Electrical connection was made by spot welding Teflon-covered platinum wire to the inner wall of the platinum tubing. The cylindrical electrode was

-
1. F. Will, J. Electrochem. Soc., Vol. 110, 152, 1963.
 2. H. J. R. Maget and R. J. Roethlein, Vol. 9, Abst. 2, Battery Div. Fall Meeting of Electrochem. Soc., Oct. 11-15, 1964, Wash. D.C.

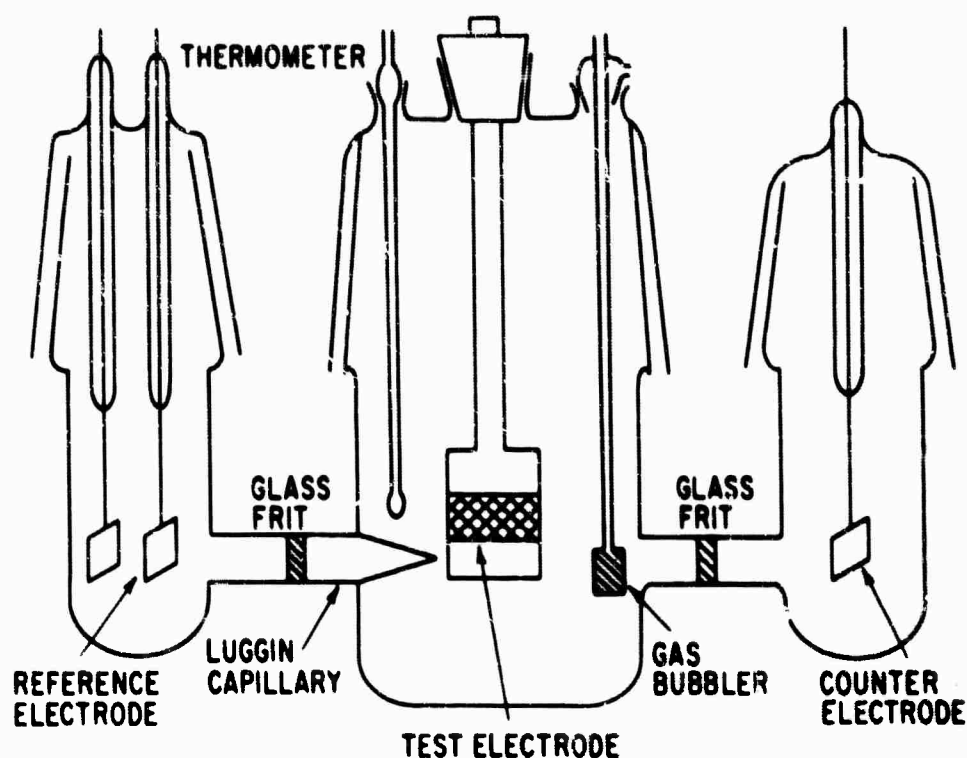


Fig. 43 Glass Test Cell

then mounted on a Teflon assembly and held rigid by a Teflon-coated tantalum rod, which was tightly threaded into a Teflon stopper. A modified 10/30 Teflon gland provided a closed system and still enabled the electrode structure to be raised or lowered into solution without allowing the system to be open to the atmosphere. Measurements of electrode height above the solution were made by means of a specially modified L.S. Starret vernier height gauge with an accuracy of $\pm 1.2 \times 10^{-3}$ cm.

Electrical resistance measurements were obtained by means of a semicircular platinum foil 1.0 cm in diameter and 1.27×10^{-2} cm thick, sealed between two cylindrical glass tubes and finely polished to form a continuous smooth surface. Electrical contact was made by spot-welding a platinum wire to the foil inside of the glass cylinder. This apparatus was also varied in height by the L.S. Starret vernier height gauge. Resistance measurements were obtained by means of an a-c resistance bridge operating at 1000 cps.

B. Electrode Preparation

The electrode surface was pre-treated by electrodeposition with spongy platinum from a 3 wt % chloroplatinic acid solution with traces of lead acetate at 10 ma/cm^2 for 60 seconds. A co-electro-deposit of platinum and ruthenium was also prepared in a similar manner from a 5 wt % solution of their chloride salts; the ratio of platinum to ruthenium being 95 to 5, based on the metal content of the solution.

A hydrophobic surface was prepared using these salts and procedure with the addition of 1/2 wt % of dispersed (T-30) Teflon mixture to the plating solution. The deposit was then sintered in an oven at 660°F for 2 minutes.

C. Experimental Procedure

Polarization measurements were made with a "fast rise" Wenking potentiostat (Model 61 TR) which has an operating potential source of ± 2 volts, current measurement accuracy of 1.5% full scale, and a zero point stability of 5 mv/day. All gases used in these experiments were of a high grade pre-purified quality. Since the temperature range of investigation was mainly greater than 100°C, a silicone oil constant-temperature bath was constructed which enabled temperatures to be held constant within $\pm 1.0^\circ\text{C}$ of the desired study temperature.

All reactant gases were preheated and humidified to the same temperature as that of the test electrolyte by passing through a gas bubbler which contained electrolyte of the same temperatures and concentration as that in the test cell.

The various phosphoric acid concentrations used in these experiments were prepared from C. P. reagent stock solution using doubly distilled water containing less than 0.4 ppm impurities.

4.1.4.2 Results and Discussion

A. Current-Potential Behavior

Current voltage curves taken on platinum-black electrodes for the oxidation of propane in H_3PO_4 show an increase in current when the electrode is raised from a submerged condition to one in which a full meniscus and film are present on the extended electrode surface. Fig. 44 shows that at an applied potential of 0.6 volt vs. hydrogen, there is a threefold increase in current when a thin electrolyte film is formed on the electrode surface. Below 0.4 volt vs. hydrogen, no increase in current is observed, which would be indicative of an activation-controlled process for this potential region.

Fig. 45 shows the variation of current with electrode position above the electrolyte level, at a constant applied potential of +0.55 volt vs. hydrogen. The initial currents below 0.25 cm are due to a bulk diffusion-controlled process and shown no variation until the electrode enters into a region which coincides with the formation of the upper meniscus edge and thin film above the intrinsic meniscus. Further withdrawal of the electrode from solution causes no increase in current once the full meniscus and film have been formed. The decrease in current near the end of the electrode is due to the loss of submerged surface area currents as the electrode is drawn out of solution.

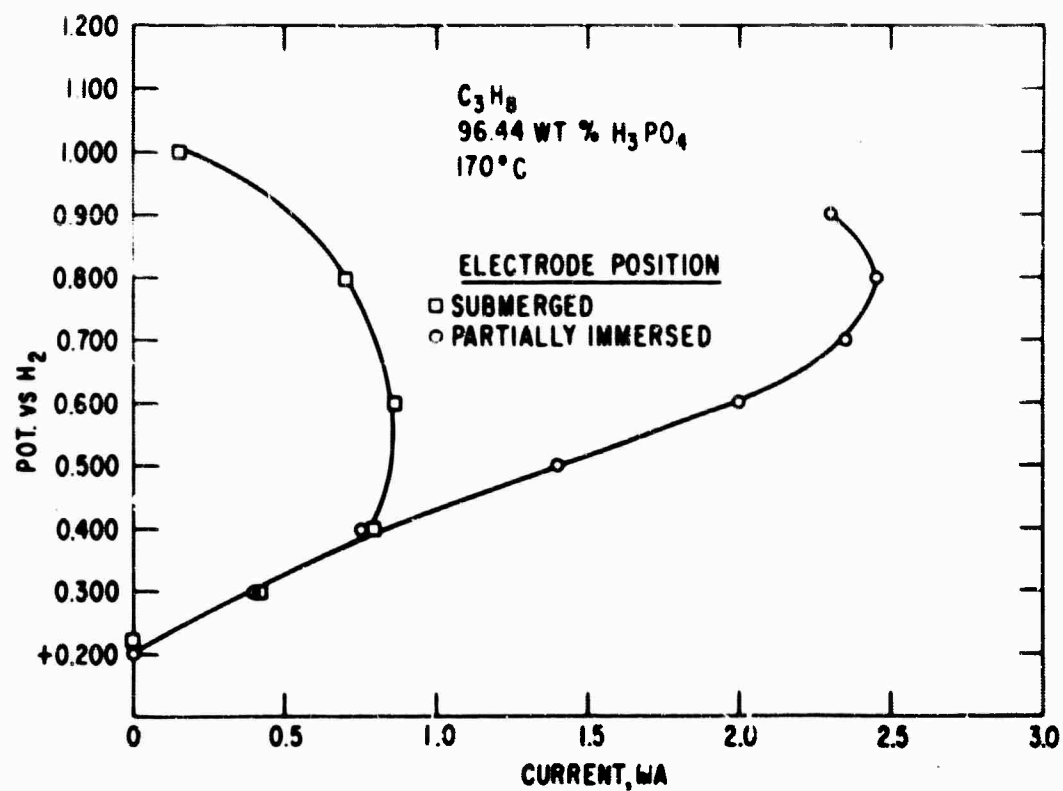


Fig. 44 Current vs. Potential Behavior as a Function of Electrode Position.

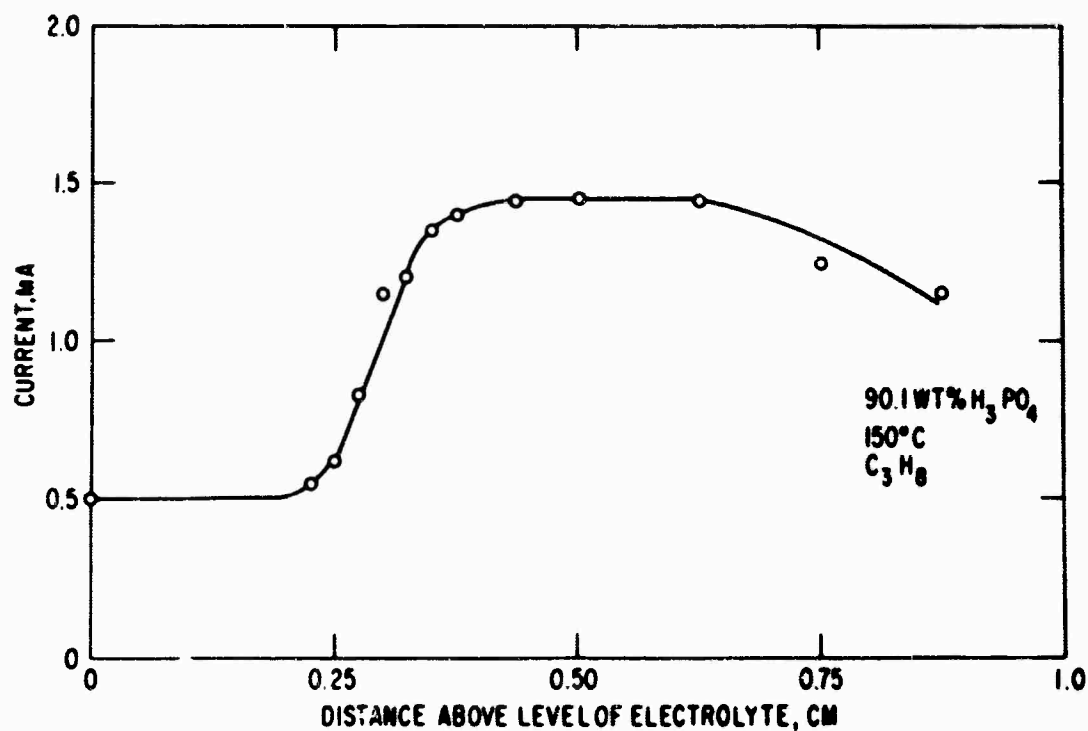


Fig. 45 Current vs. Height Behavior

Variation of propane partial pressure on a partially immersed platinum-black electrode exhibits a square root relationship with limiting current. This relationship shown in Table X was recorded at two temperatures and in H_3PO_4 acid concentrations ranging from 92 to 96 wt %.

This square root relationship is probably due to the applied potential drop induced by the longitudinal ohmic resistance in the thin film, as has already been shown in the case of the electrochemical reduction of oxygen (3).

Measurements of the resistance changes for various positions in the meniscus and thin film region were obtained on a specially constructed electrode. Fig. 46 shows a plot of ohmic resistance divided by electrolyte resistivity to account for variations in electrolyte conductivity versus x/h , which is the relative position in the meniscus. From the shape of the curve it is evident that there is only a gradual increase in resistance with height in the meniscus region. However, upon entering into the thin film region the resistance increases rapidly and in a linear fashion. The slope of this curve can be used to calculate the electrolyte film thickness.

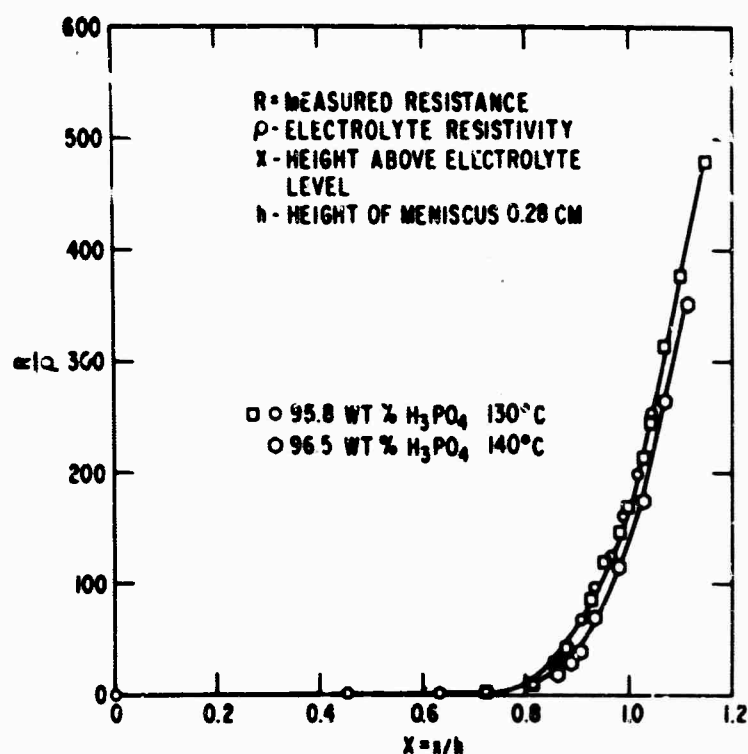


Fig. 46 Resistance Measurements in the Meniscus and Thin Film Regions

3. H. J. R. Maget and R. J. Roethlein, op. cit.

TABLE X

Influence of Propane Partial Pressure on Electrode Current

	Electrolyte Conc. wt % H_3PO_4	* Partial Pressure of Propane $P_{\text{C}_3\text{H}_8}$	Total Current i_L , ma	$i_L / P_{\text{C}_3\text{H}_8}^{1/2}$
Temp. 150°C	95.4	0.044	0.40	1.91
	93.6	0.076	0.62	2.24
	92.0	0.640	1.65	2.06
	93.3	0.190	0.88	2.00
	93.6	0.710	1.75	2.07
	92.5	0.430	1.25	1.91
Temp. 170°C	96.4	0.718	2.50	2.94
	95.5	0.319	1.75	3.08
	95.7	0.183	1.30	3.04
	96.0	0.073	0.78	2.89
	92.6	0.020	0.42	2.94
	92.5	0.004	0.20	3.16

*Corrected for vapor pressure of H_2O . Total Pressure: 1 atm.

The interfacial liquid-gas geometry of the intrinsic meniscus and film can be approximated by the expression:

$$\delta = \delta_h + A(1-X)^2, \text{ for } X \leq 1 \quad (49)$$

where: δ = meniscus thickness, cm; δ_h = film thickness, cm; $X = x/h$ represents the relative position in the meniscus; and A can be theoretically evaluated from properties of the electrolyte as presented by Landau and Lifshitz (4). However, since the surface tension in phosphoric acid at 130°C is not known, it is better to evaluate A from resistance measurements.

It can be shown that, near the meniscus-film interface, the ionic resistance is expressed by:

$$R(x) = \frac{\rho h}{2b\pi} \frac{1}{(A \delta_h)^{1/2}} \left\{ \frac{\pi}{2} - \tan^{-1} \left(\frac{A}{\delta_h} \right)^{1/2} (1-X) \right\} \quad (50)$$

where: ρ = electrolyte resistivity, ohm-cm; b = electrode radius, cm; h = height of the intrinsic meniscus, cm.

4. L. D. Landau and E. M. Lifshitz, "Fluid Mechanics", Pergamon Press, 1959, p. 235.

The film thickness, δ_h , can be determined from the linear section of the resistance plot, and A can be evaluated from the total meniscus resistance, R_m , for which:

$$R_m = \frac{\rho h}{4b(A\delta_h)^{\frac{1}{2}}}; \text{ and } \left(\frac{dR}{dX} \right)_F = \frac{\rho h}{2\pi b \delta_h} \quad (51)$$

For the case of the results presented in Fig. 46, the film thickness is calculated to be 0.5 micron, and the resistance can be represented by:

$$R = 253 \left\{ \frac{\pi}{2} - \tan^{-1} 16(1-X) \right\} \quad (52)$$

and the meniscus-film geometry by:

$$\delta = [0.5 + 130(1-X)^2] \times 10^{-4} \quad (53)$$

for values of $X \geq 0.9$, at a level in the meniscus and film where the largest contribution to the total current is observed.

A current temperature relationship was obtained on a co-electro-deposited Pt-Ru-black electrode in 90 wt % H_3PO_4 , between 100 and 153°C. Fig. 47 shows that an exponential relationship exists between $1/T$ and the limiting current and also the limiting current divided by the square root of propane partial pressure and electrolyte conductivity. Such a plot is based on the assumption that only the diffusion coefficient is an exponential function of $1/T$, the solubility varying only slightly for this temperature range. Thus, from the slopes of $i_L / \frac{1}{P_{C_3H_8}^{\frac{1}{2}}} K^{\frac{1}{2}}$ vs. $1/T$,

a tentative value can be obtained for the activation energy for diffusion. The energy value obtained, 9.7 k cal/mole, would be at the upper limit for processes which are diffusion-controlled. Further work is recommended to verify the above results.

The influence of electrolyte concentration on electrode limiting currents seems negligible up to approximately 97 wt % H_3PO_4 . Beyond this point there seems to be a significant decrease in performance as the electrolyte concentration increases. At two temperatures, 150 and 170°C, in a 101 wt % solution, the electrode current dropped to approximately half the value obtained between 90 and 97 wt % phosphoric acid. Appreciable quantities of pyro-phosphates also tend to build up in solution at these concentrations. (5)

For one of these highly concentrated solutions at an applied potential of 1 volt and an electrolyte temperature of 170°C, a periodic current oscillation was observed. These oscillations could be stopped by briefly anodizing the electrode at a higher anodic potential. No explanation can be offered at this time concerning this phenomenon.

An initial investigation was conducted into the effect of hydrophobic noble metal electrode structures. A platinum-ruthenium black electrode structure was prepared with the addition

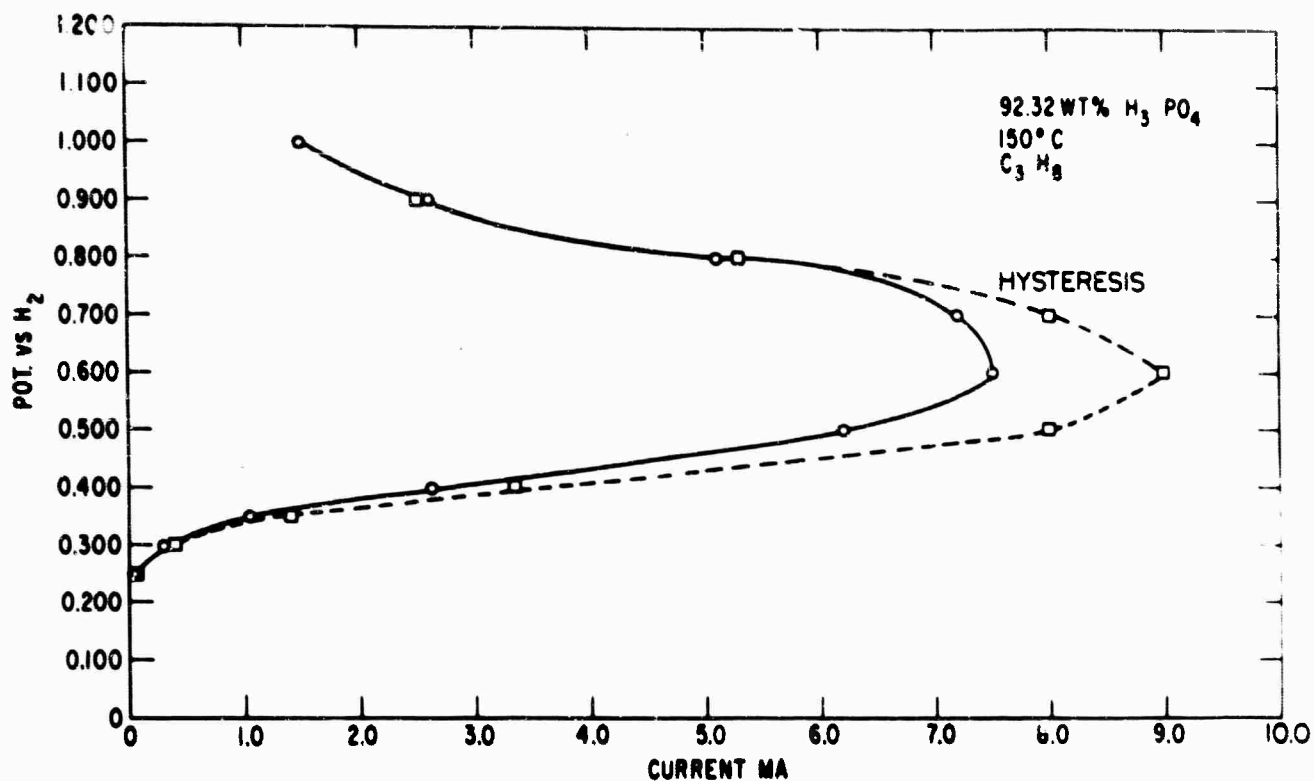


Fig. 48 Current vs. Potential Behavior of a Partially Immersed Wetproofed Pt-Ru Electrode

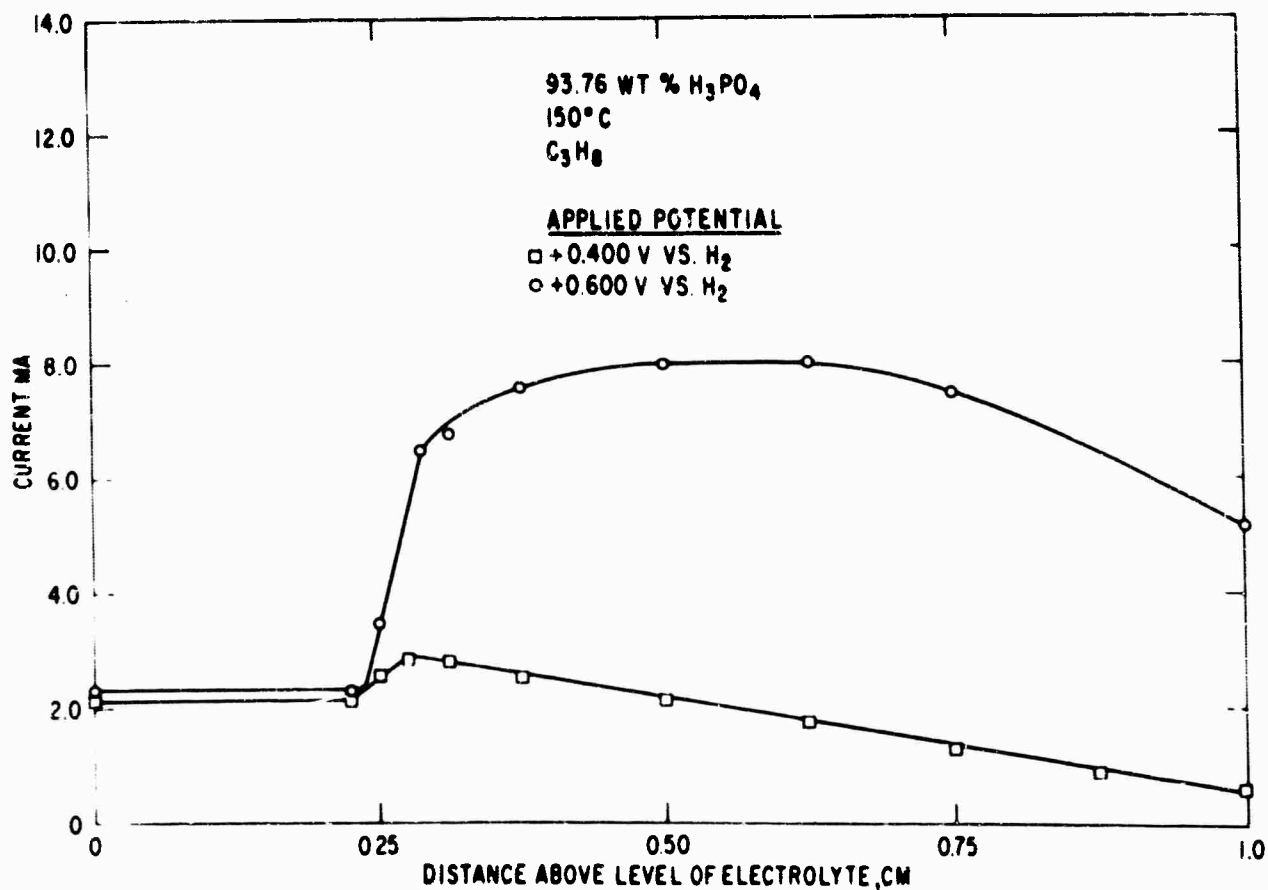


Fig. 49 Current vs. Height Behavior of a Wetproofed Pt-Ru Electrode

come rate-controlling. These currents, however, are not steady values and generally decay with time at a constant applied potential to some lower steady-state value. At present there are many theories concerning this phenomenon, none being conclusive. It is the general opinion of many investigators, however, that anodization removes partially oxidized species on the electrode surface by oxidizing them to CO_2 . Thus, on lowering the potential, a greater percentage of sites on the electrode surface would be free for hydrocarbon oxidation. Many of these sites with time would again become covered with partially oxidized products, causing a gradual reduction of current.

4.1.4.3 Conclusions

The oxidation of propane at potentials greater than 0.5 volt on partially immersed platinum black electrodes, in concentrated phosphoric acid solutions and at elevated temperatures, occurs mainly in the upper meniscus and thin film region of the electrode surface. This is clearly shown by the current increase associated with the gradual withdrawal of a potentiostatically polarized electrode from a completely submerged condition to one of partial immersion. Further indication of mass transport control through the thin film is shown by the square root relationship obtained between limiting current and the partial pressure of propane. Equations developed by Will (6) and Wagner have shown that this relationship exists when a process is mass transfer controlled through a thin electrolyte film.

The exponential relationship obtained between limiting current and temperature for propane oxidation on a partially immersed electrode has also provided a tentative value for the activation energy of diffusion.

Measurement of the resistance change in the meniscus and film region of a concentrated H_3PO_4 solution at elevated temperatures has provided an approximate value, 0.5 micron, for the thickness of the liquid film immediately above the intrinsic meniscus. This data has also verified previously derived equations describing the resistance and electrolyte thickness for levels in the meniscus and film where the largest contribution to the total current is observed.

For concentrations of H_3PO_4 greater than 97% a general decrease in electrode current is observed with increasing electrolyte concentrations. Below this concentration no significant variation in electrode current was observed.

The simulated "wetproof" Teflon Pt-Ru-black structure exhibits much higher current than electrodes prepared in a similar manner without the addition of a wetproofing agent. This substantial increase in current is attributed to interstitial wetting of the electrodeposited catalysis matrix by a thin film of electrolyte. This wetted layer provides greater area for C_3H_8 oxidation and a larger path for electron flow without causing an increased resistance to gas diffusion across the electrode interface.

6. F. Will, loc. cit.

4.1.5 Fluoride Electrolytes (E. J. Cairns)

Investigations of the electrochemical oxidation of saturated hydrocarbons in fluoride electrolytes have continued, with emphasis on the effect of electrolyte composition on performance. In the ternary system $\text{CsF-HF-H}_2\text{O}$, there are two independent composition variables.

The effects of the ratio $\left(\frac{\text{HF}}{\text{CsF} + \text{HF}}\right)$ and the water content on performance have been separated and studied. The effects of temperature on cell performance have also been studied, and the interrelationships among several of the important variables have been established.

Fundamental work on the rate and extent of propane adsorption on platinum in the $\text{HF-H}_2\text{O}$ azeotrope (37 mole% HF) has begun.

4.1.5.1 Fuel Cell Studies with Fluoride Electrolytes

A. Experimental

The shift in emphasis from $\text{Cs}_2\text{-CO}_3\text{-H}_2\text{O}$ electrolytes to $\text{CsF-HF-H}_2\text{O}$ and $\text{HF-H}_2\text{O}$ electrolytes made it desirable to modify some of the fuel cell apparatus. The continuing need for additional space in the air thermostat has been satisfied by the installation of a new, large volume, horizontal flow air thermostat with appropriate porting and sufficient power (4kva) for rapid startup. The electrolyte pump and all reservoirs are now located inside the thermostat, providing improved temperature control and uniformity. The electrolyte circulation system has been improved from the standpoint of water loss by more completely closing the system and by the addition of a more efficient reflux condenser. This improvement allows better control of the composition of electrolytes under high vapor pressure conditions.

Several modifications have been made in the apparatus which allow more rapid data collection. A number of thermocouples have been installed and connected to direct-reading temperature meters. An electrometer has been installed for use with the second bridge circuit on the Kordes-Marko interrupter, giving a continuous indication of the anode vs. reference potential. A central control panel has been added, collecting all electrical controls, providing for more convenient operation.

Data collection procedures are generally the same as those reported earlier (1-4).

The electrode performance results are reported on an IR-free basis unless otherwise noted.

- (1) E. J. Cairns, Technical Summary Report No. 5, Jan. 1 - June 30, 1964, ARPA Order No. 247, Contract Nos. DA44-009-ENG-4909 and DA44-009-AMC-479(T).
- (2) E. J. Cairns, Technical Summary Report No. 4, Part I, Task IV, July 1 - Dec. 31, 1963, ARPA Order No. 247, Contract No. DA44-009-ENG-4909, Project No. 8A72-13-001-506.
- (3) E. J. Cairns and A. D. Tevebaugh, Technical Summary Report No. 3, Part I, Task IV, Jan. 1 - June 30, 1963, ARPA Order No. 247, Contract No. DA44-009-ENG-4909, Project No. 8A72-13-001-506. See also E. J. Cairns and D. C. Bartosik, J. Electrochem. Soc. 111, 1205 (1964).
- (4) E. J. Cairns, Interrupter Techniques for Fuel Cell Investigation, Paper presented at the Interagency Power Group Meeting, Ft. Belvoir, Va., October 16, 1964.

Cell resistances are reported where measured, and resistance-included performance curves can be calculated using the relation

$$E = E_{a-c} - iAR$$

where

- E_{a-c} = potential between anode and cathode on an IR free basis
- i = the current density (amp/cm²),
- A = the geometric area of the electrode, 11.38 cm² in all cases,
- R = the cell resistance (ohms).

Several variables have been studied in connection with their effect on cell performance with emphasis on propane as the fuel:

- 1) Electrolyte composition.
- 2) Operating temperature.
- 3) Electrode structure (incidental to other studies).

The results to be reported were gathered from a total of over 50 runs on more than 20 cells, primarily using C₃H₈ as the fuel.

B. Results and Discussion

1. Effect of Electrolyte Composition on Cell Performance for the CsF-HF-H₂O

System

During the previous reporting interval, the discovery was made that the ratio of fluoride to cesium content in the electrolyte was an important variable in determining the performance of saturated hydrocarbons in fluoride electrolyte fuel cells. (See Fig. 34 of Reference 3). The cell performance was such a strong function of electrolyte composition ($\frac{F^-}{Cs^+}$ ratio) that it seemed important to verify and extend the performance-composition relationship. Experiments with this objective were performed by preparing electrolytes of specified compositions and checking the propane performance at 150°C against that expected on the basis of Fig. 34, Reference 3. The reported relationship was closely checked, and it can be stated with confidence that the performance on propane at 150°C is primarily determined by the ratio ($\frac{HF+CsF}{CsF}$) which is equivalent to the (fluoride/cesium) ratio.

The maximum observed cell performance was obtained using an electrolyte of 10 mole % H₂O, 61 mole % HF and 29 mole % CsF ($\frac{HF}{CsF} = 2.1$). The Tafel plots for this cell are shown in Fig. 50, where E_{c-r} , E_{a-c} and E_{a-r} are the potential between cathode and reference, anode and cathode, and anode and reference. The verified relationship between the current density at an anode vs H₂ reference potential of 0.5 volts (in the absence of mass transport overvoltage) and the (fluoride/cesium) ratio is shown in Fig. 51. The data points have been obtained from several cells. Each datum point represents an average value obtained

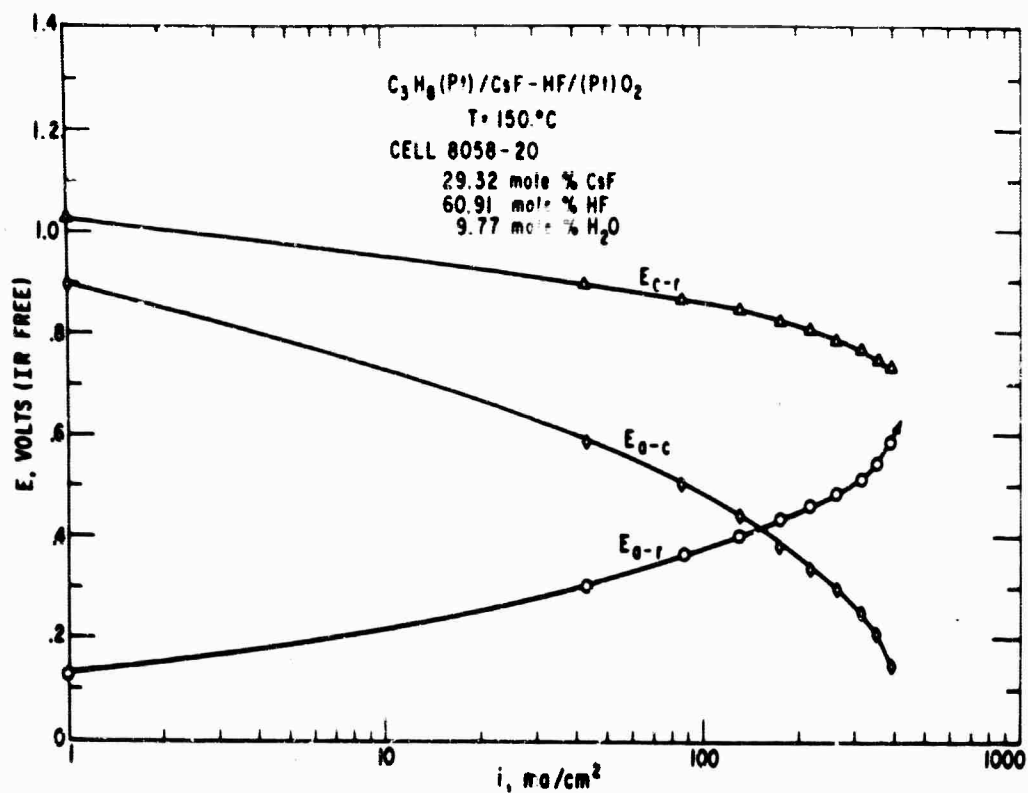


Fig. 50 Tafel Plots for Propane Cell with CsF-HF Electrolyte (HF/CsF = 2.1, H_2O = 29 Mole %) at $150^\circ C$.

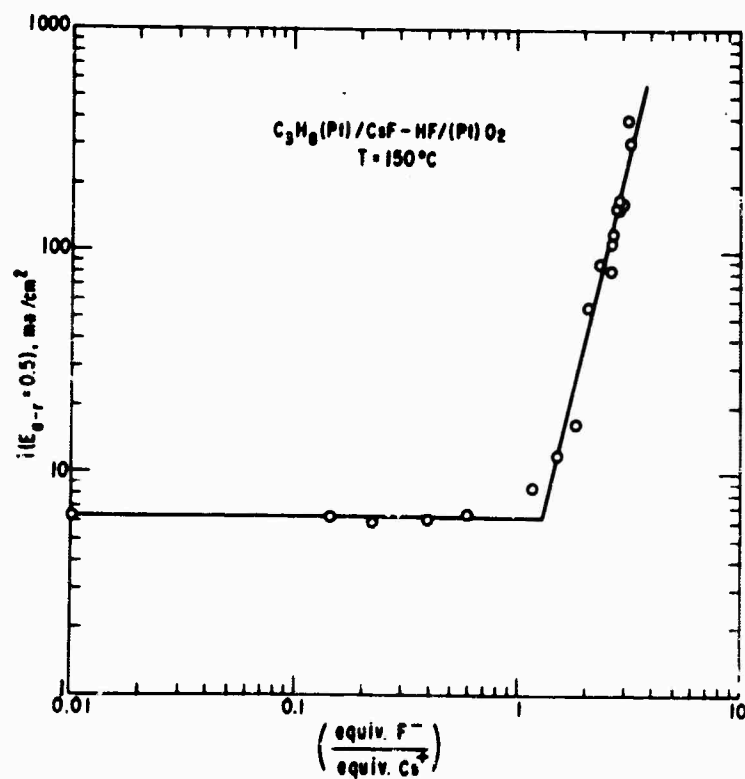


Fig. 51 Current Density for Propane at an Anode vs H_2 Reference Potential of 0.5 V, as a Function of Fluoride: Cesium Ratio (by Equivalents).

from all cells operated at that particular F/Cs ratio. The steep portion of the curve was the most closely checked, and here up to five cells were used to determine the value for a single datum point.

The water content of the electrolyte also influences cell performance, but to a lesser extent. The task of separating the effects of fluoride:cesium ratio, and water content is a difficult iterative procedure. It is necessary to hold the hydrogen fluoride:cesium fluoride ratio constant while investigating the effect of water content. The value of 2.0 was chosen for the hydrogen fluoride:cesium fluoride ratio, and the data for $i_{(E_{a-r}=0.5)}$ at $150^{\circ}C$ in the range $1.8 < HF/CsF < 2.1$ were normalized to the current density expected for $HF/CsF = 2.0$ using Fig. 51 to establish the normalization factors. Once the data were normalized, a plot of $i_{(E_{a-r}=0.5)}$ vs. H_2O content for $HF/CsF = 2.0$ was prepared. This plot then permitted normalization of the data with respect to water content (12.5 mole % H_2O) for use in the preparation of a new plot of current density vs. $(HF/CsF + HF)$. This iterative procedure was continued until the scatter of the data on each of the two plots was minimized. The results of this double correlation procedure are shown in Figs. 52 and 53. The optimum water content was found to be in the range of 12-13 mole % H_2O for an $HF:Csf$ ratio of 2.0. There is insufficient data to establish a correlation involving water content at significantly lower fluoride contents. Significantly higher F/Cs ratios were not accessible at $150^{\circ}C$ because of boiling-point limitations.

2. Effect of Temperature on Propane Performance

Using an activation energy of 15 kcal/mole (as determined from $\log i$ vs $1/T$ plots) for the range $150-130^{\circ}C$, and $1.8 < HF/CsF < 2.2$, the $150^{\circ}C$ data were translated to the corresponding values of current density for $130^{\circ}C$. These data, plus the data taken at $130^{\circ}C$, were used to establish the relationship of performance to electrolyte composition at $130^{\circ}C$ shown in Figs. 54 and 55. The closed points are data gathered at the temperature shown; the open points are those translated from $150^{\circ}C$. Similar procedures were followed in correlating the data for 110 and $90^{\circ}C$. A F/Cs ratio of 3.0 was chosen for these latter two correlations, since this composition is accessible at these lower temperatures.

Figs. 54 and 55 completely summarize the effects of electrolyte composition on the current density at an anode vs H_2 reference potential of 0.5 volt. The solid lines in Fig. 54 represent the portion of the line normalized to a certain HF/CsF ratio and water content. The dotted portions of the lines are less well established and are based on data for various water concentrations. The intercepts on the right-hand ordinate $[HF/(CsF+HF)=1.0]$ are determined by the results in the $HF-H_2O$ system, and are normalized to an optimum water content. It is clear that the F/Cs ratio should be maximized for a given temperature of operation, while the water content should be optimized in the range 10-15 mole percent for H^+, CsF

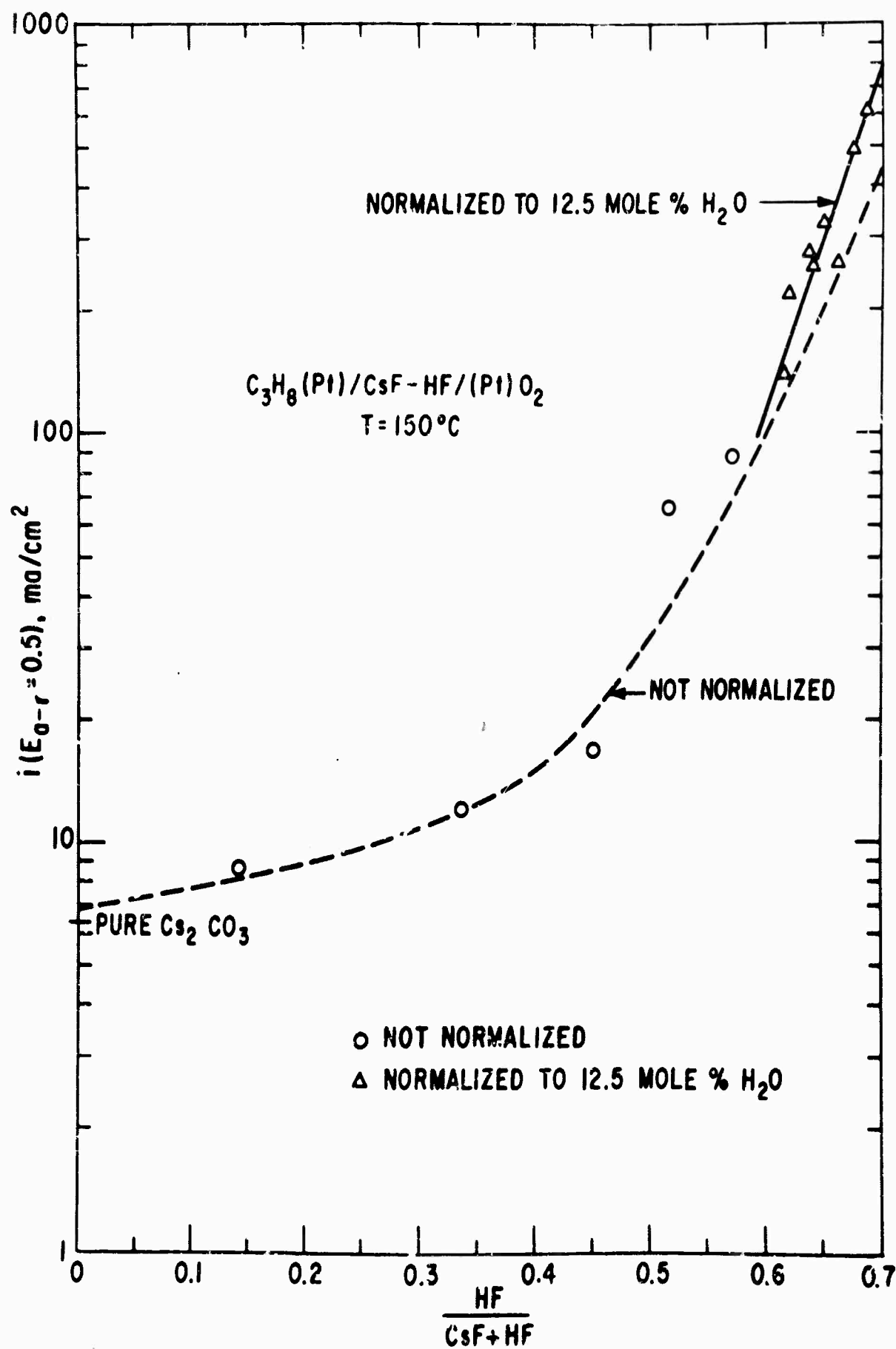


Fig. 52 Current Density for Propane at an Anode vs H_2 Reference Potential of 0.5 V as a Function of $\text{HF}:(\text{CsF} + \text{HF})$ Ratio. Solid Line Is for Results Near $\text{HF}:\text{CsF} = 2$, Normalized at 12.5 Mole % H_2O . Dashed Line Is Not Normalized with Respect to Water Content.

BLANK PAGE

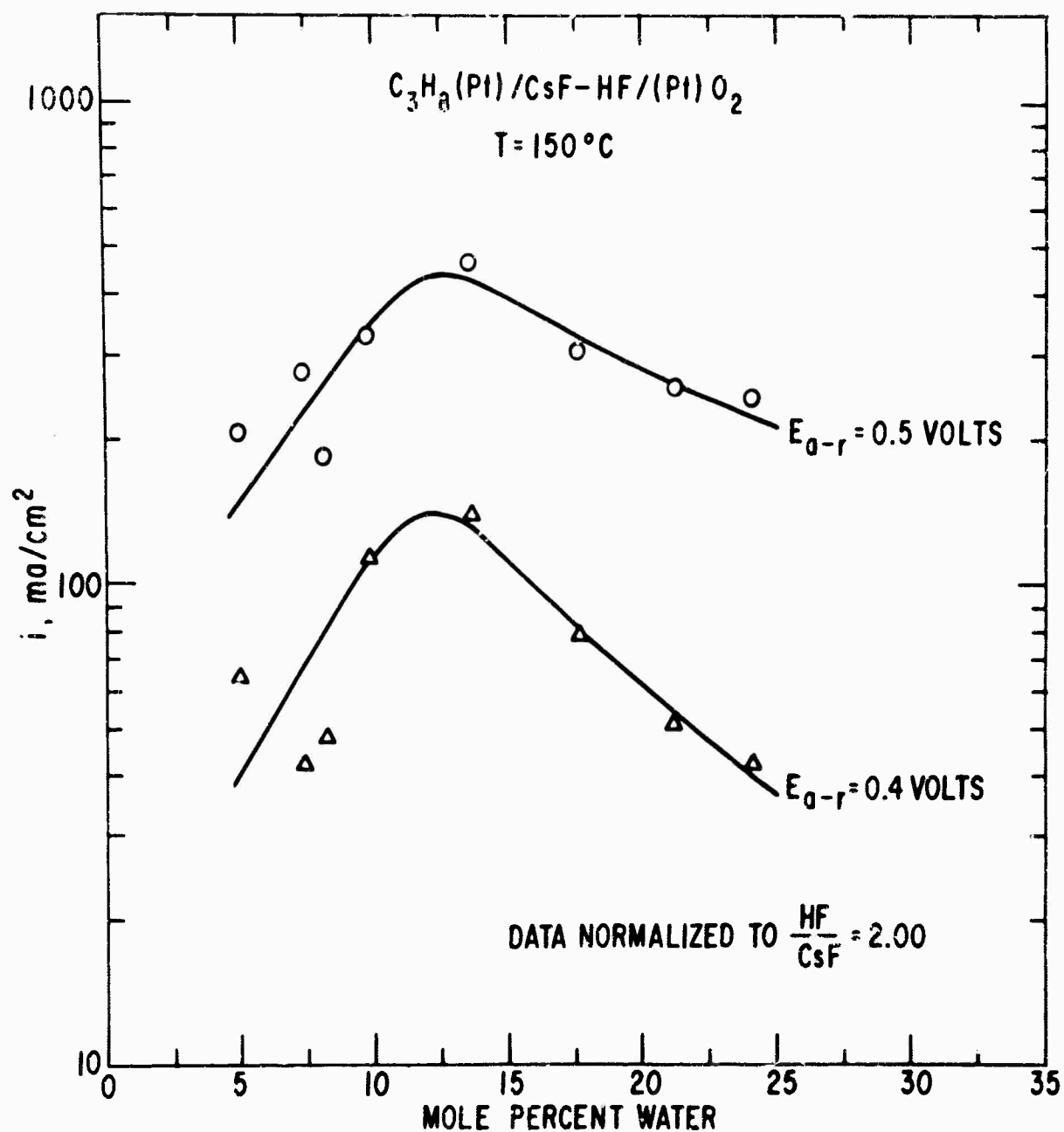


Fig. 53 Current Density for Propane at Constant Anode Potentials, as a Function of Electrolyte Water Content, Normalized to $HF:CsF = 2$.

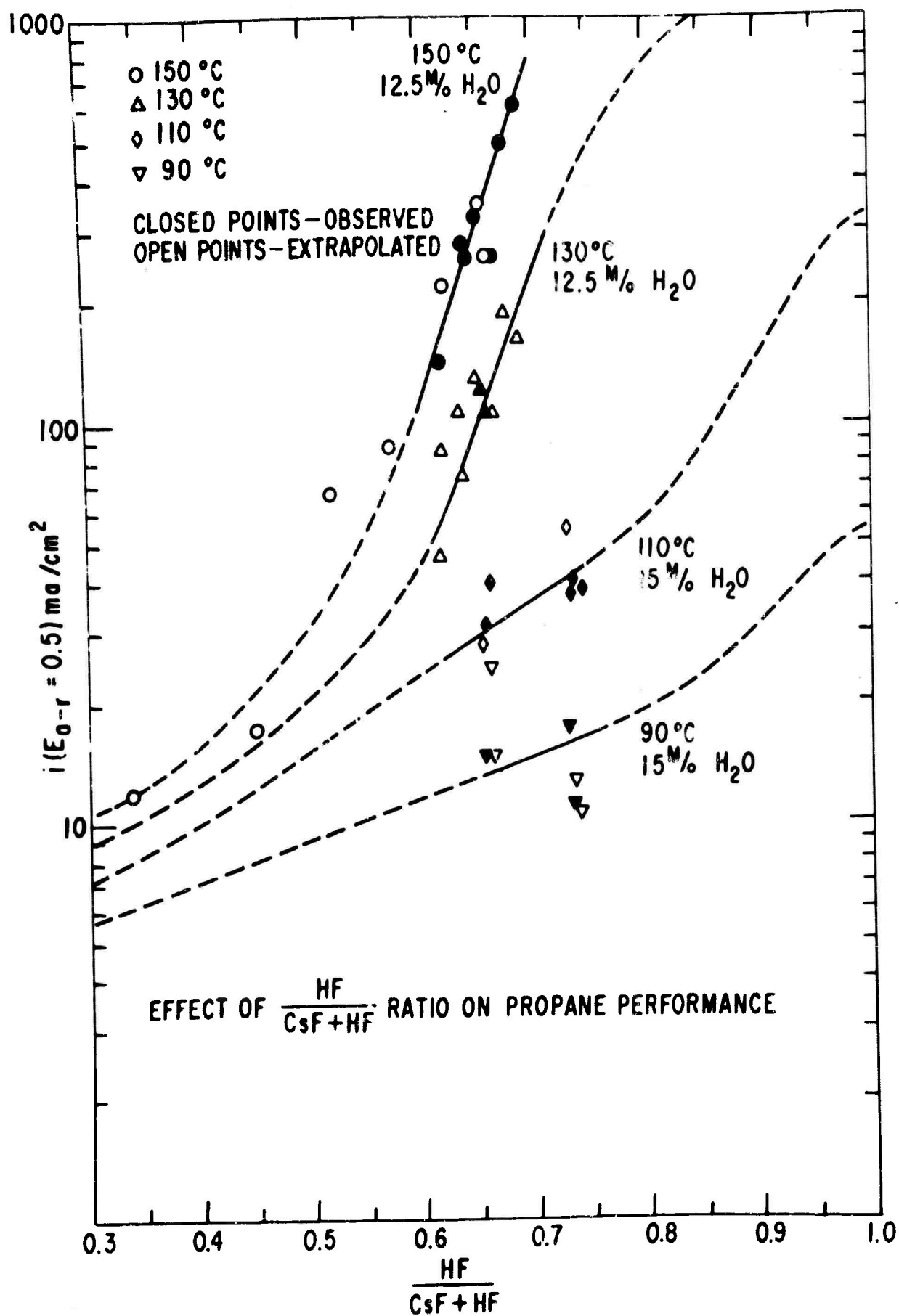


Fig. 54 Summary Plot Showing Current Density for Propane at an Anode vs H₂ Reference Potential of 0.5 V as a Function of HF:(CsF + HF) Ratio. Solid Lines Are Normalized to Water Contents Indicated. Dashed Lines Are Not Normalized, and Show Approximate Behavior for Optimum Water Content Electrolytes.

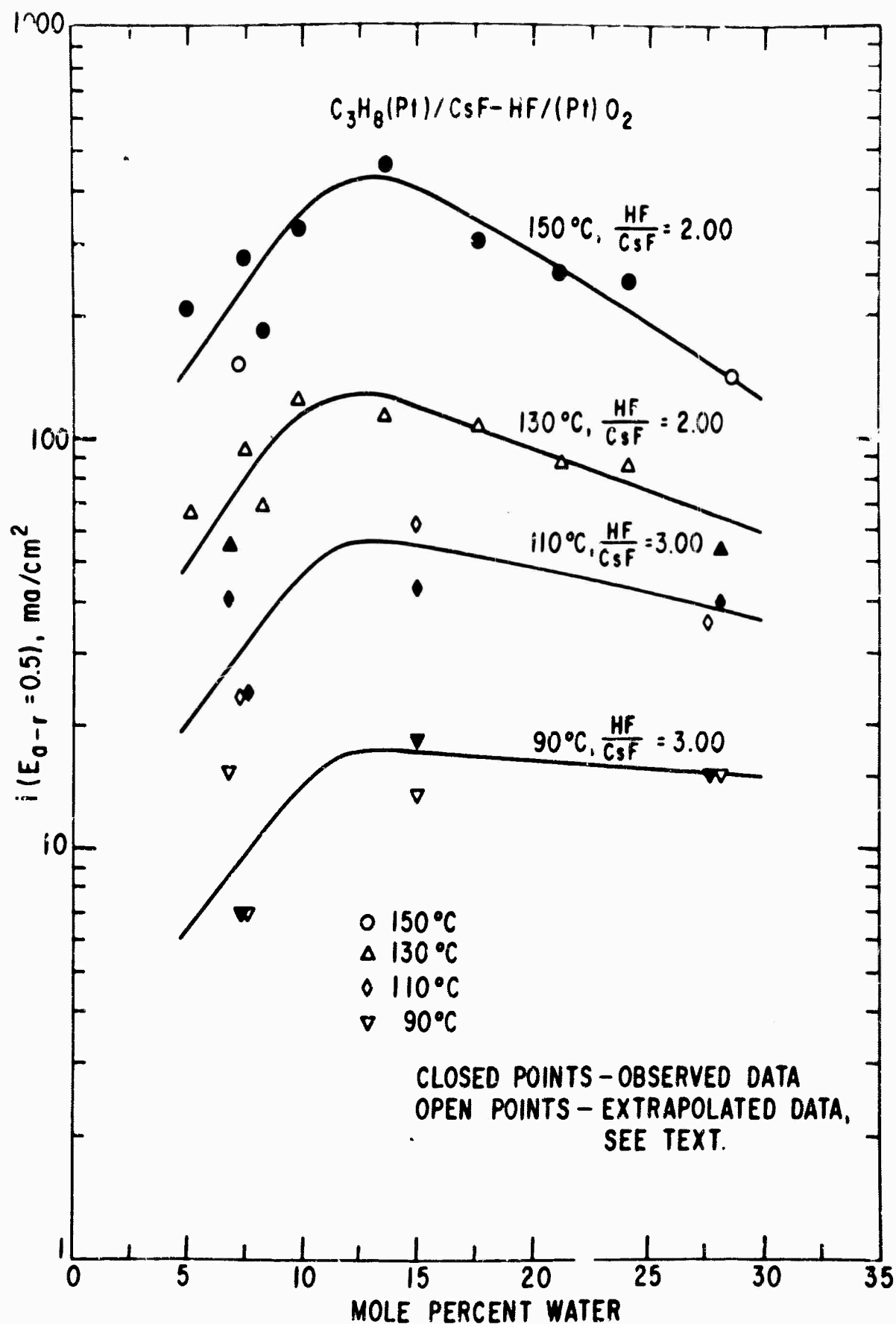


Fig. 55 Summary Plot Showing Current Density for Propane at $E_{a-r} = 0.5 \text{ V}$ as a Function of Water Content, Normalized to Indicated HF:CsF Ratios for Several Temperatures.

ratios in the range 2-3. The maximum HF/CsF ratio for a given operating temperature will be set by the boiling point - composition relationship discussed in Section 4.3.2.

Concomitant with the data correlation for the effect of composition on performance, the activation energy, ΔH^* , for the current density (measured at an anode vs H_2 reference voltage of 0.5 volt) was correlated with the HF/CsF ratio. It was found that ΔH^* varied with the F/Cs ratio, but not with temperature, and was quite insensitive to water content. The relationship between ΔH^* and composition is shown in Fig. 56. Caution should be exercised in applying Fig. 56 to results from any given cell for purposes of extrapolation to other temperatures, since it is necessary to establish that the αn value (or Tafel slope) does not change over the temperature interval of interest. This point will probably be investigated further during the next reporting period.

The lower activation energies shown in Fig. 56 are values characteristic of physical processes (e.g. diffusion has a $\Delta H^* = 3.6$ kcal/mole). The higher values, nearly 20 kcal/mole, are definitely characteristic of chemical or electrochemical processes. The transition region occurs near $HF/CsF + HF = 0.67$, which corresponds to $CsF \cdot 2HF$, a stable compound, and therefore represents a reduction of the HF activity. The HF in excess of $CsF \cdot 2HF$ has a relatively high activity and may be important in causing a change in ΔH^* (cf. the phase diagrams in Section 4.3.2).

3. Effect of Composition and Temperature on Propane Performance for the HF- H_2O System

In the binary system HF- H_2O , there is only one composition variable, allowing rather straightforward data reduction procedures to be applied. The best performance with propane at 105° in the HF- H_2O azeotrope is shown in Fig. 57. These results compare quite favorably with those in Fig. 50, when it is recognized that Fig. 57 corresponds to an operating temperature $45^\circ C$ lower than that of Fig. 50. Note that it is possible to obtain 70 ma/cm^2 at an anode vs cathode voltage (IR-free) of 0.4 volt. Since there was a gas-phase mass transport limitation in Fig. 57, it is likely that even higher performance could be obtained by using a thinner film on the gas sides of the electrodes, particularly the anode.

Fig. 58 shows the effect of composition and temperature on propane performance for the HF- H_2O system. The temperature coefficient of current density at a constant anode vs H_2 reference voltage corresponds to an activation energy of 18 kcal/mole. The solid lines in Fig. 58 show those composition regions accessible at the indicated temperature. The dotted portions of the lines correspond to compositions which have boiling points below the indicated operating temperature and are therefore not accessible at atmospheric pressure. The data points on the dotted lines were obtained by extrapolation on $\log i$ vs $1/T$ plots and are used for the purpose of establishing the shape of the curves. It is interesting to note that the optimum water content in this binary system is about 70 mole percent, in

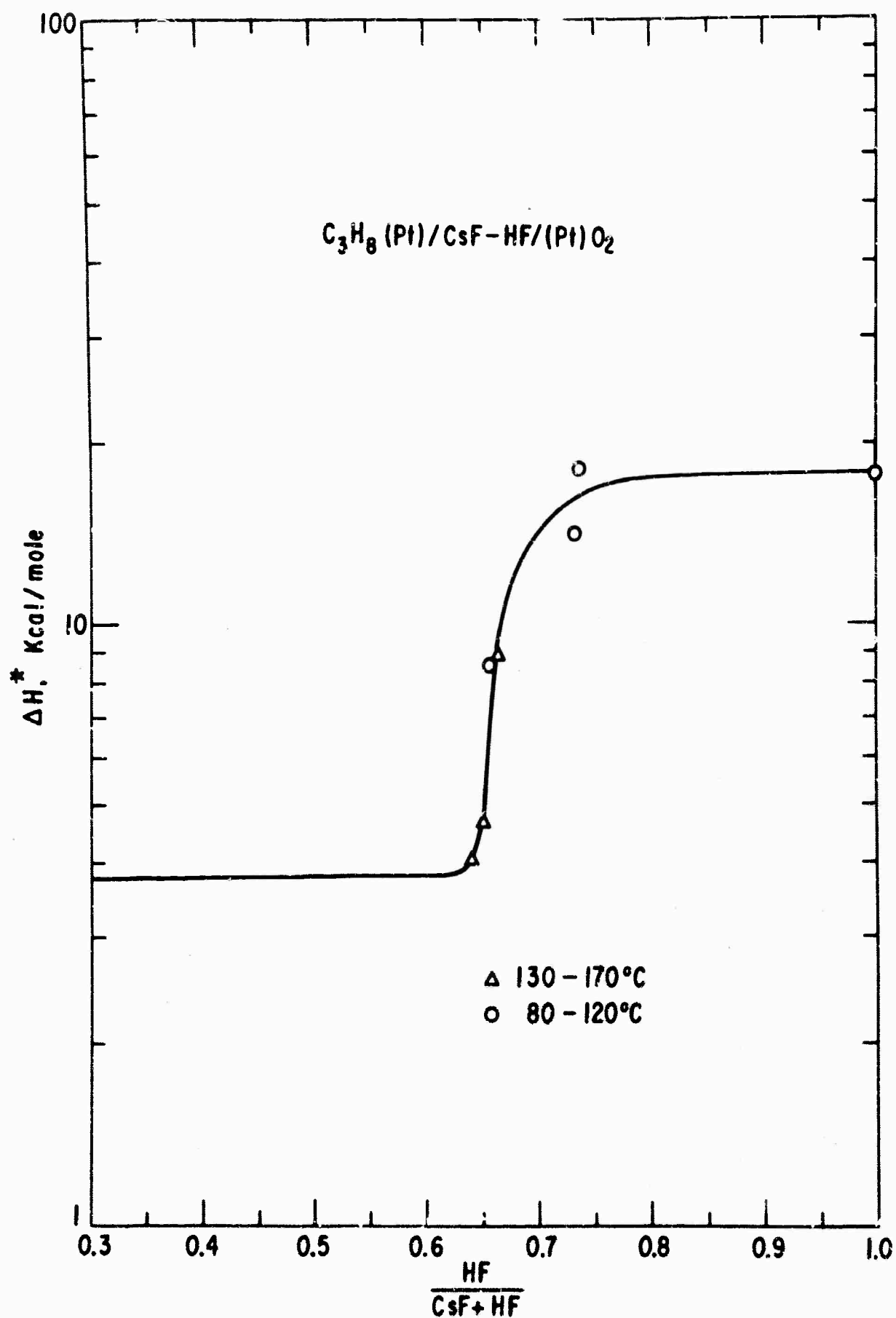


Fig. 56 Enthalpy of Activation for Overall Anodic Oxidation of Propane as a Function of HF:(CsF + HF) Ratio, in the Temperature Range 80-170°C. ΔH^* Is Insensitive to Water Content and Temperature.

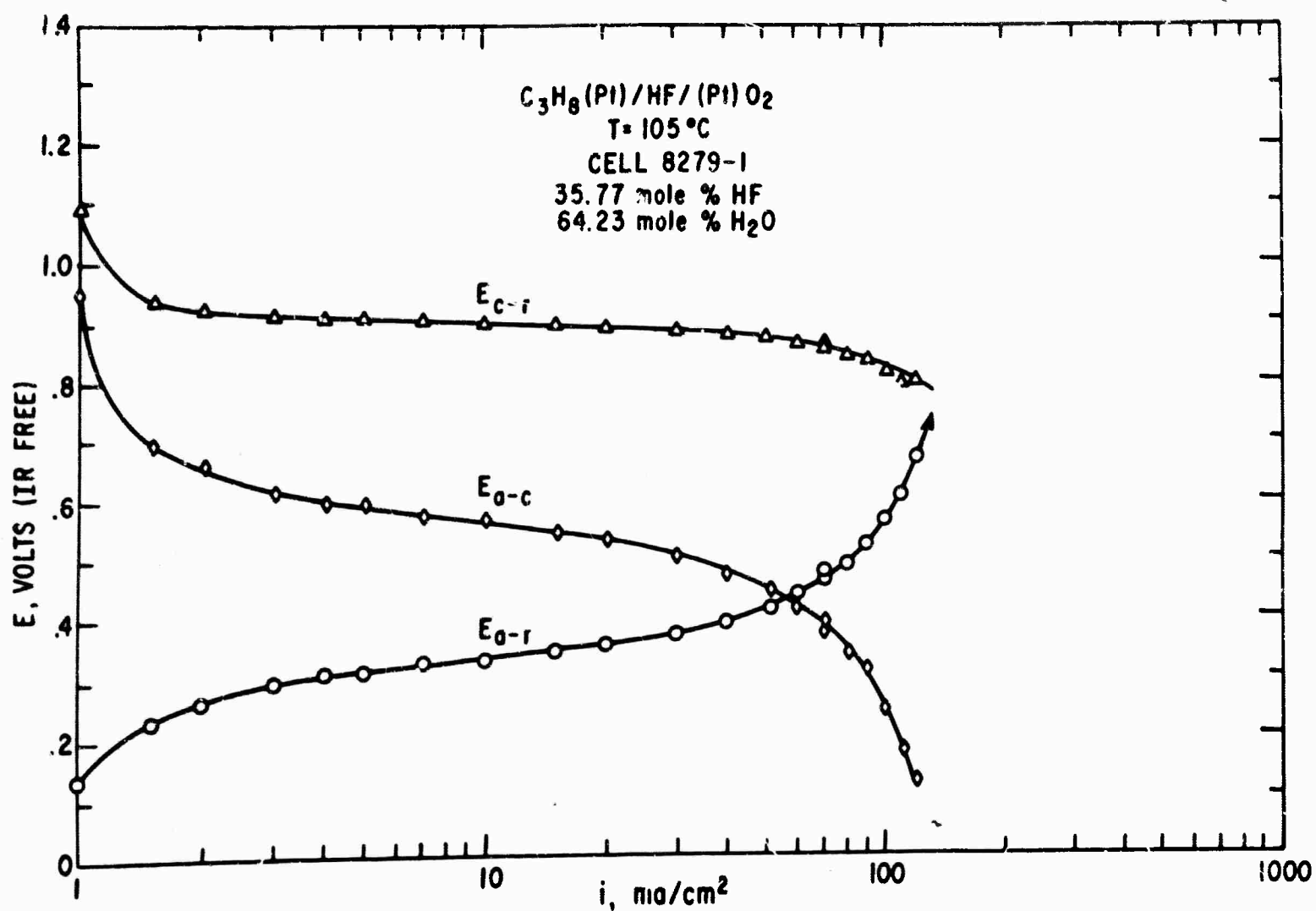


Fig. 57 Tafel Plots for Propane Cell with HF- H_2O Electrolyte at $105^\circ C$.

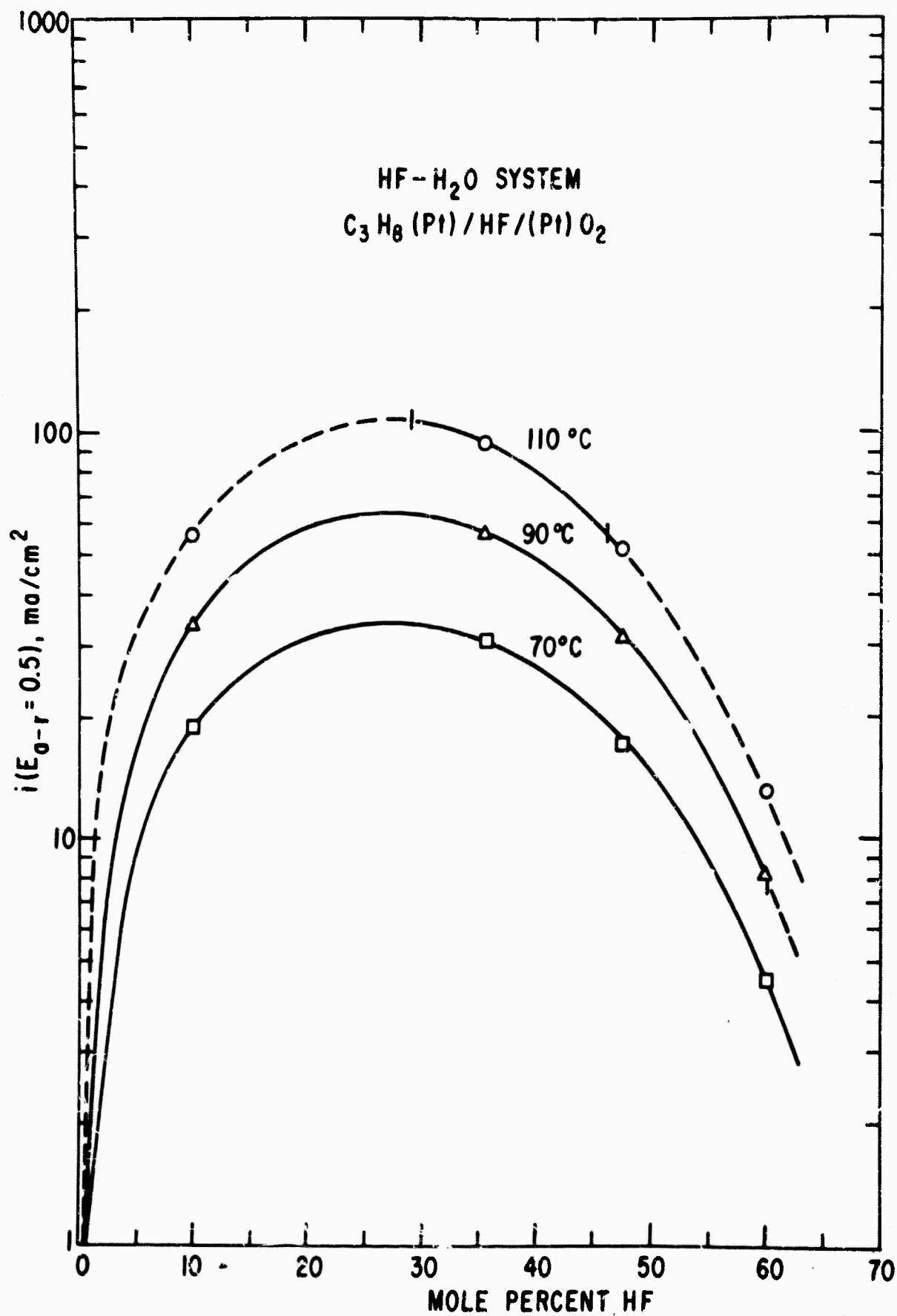


Fig. 58 Effect of HF-H₂O Electrolyte Composition on Propane Performance at Different Temperatures. Solid Lines Indicate Electrolyte Compositions Which Do Not Boil at Temperature Shown.

contrast to the 12 to 15 mole percent found in the ternary $\text{CsF-HF-H}_2\text{O}$ system at $\text{CsF} \cdot 2\text{HF}$ and $\text{CsF} \cdot 3\text{HF}$.

4. Performance Comparisons for Two Electrolytes

The best performances for propane in each of the two fluoride systems are compared in Fig. 59. The solid curves show the power densities as a function of the cell voltage, on an IR-free basis. The peak power in the $\text{HF-H}_2\text{O}$ system is about 30 mw/cm^2 at 105°C , while 80 mw/cm^2 is obtained in the $\text{CsF-HF-H}_2\text{O}$ system at 150°C . For a more practical comparison, the dashed curves were prepared using the actual electrolyte resistivity data reported in section 4.3.2. and a 1/16 in. electrode spacing. The comparison with IR losses included shows less of an advantage for the 150°C cell because IR losses are higher at the increased current densities.

5. Effect of TFE Film Thickness on Propane Limiting Currents

The effect of the TFE Film weight per unit area on the limiting current densities at propane anodes was investigated for a series of electrodes prepared under the same conditions except for film weight. These electrodes contained 52 mg of Pt/cm^2 and about 0.2 gm TFE binder/gm Pt. They were pressed at 350°C for two minutes at a total force of 8500-9000 lb. The propane limiting currents were relatively insensitive to temperature, except at temperatures below about 110°C , where mass transport was not responsible for the observed limiting currents.

Two limiting cases are important in determining the limiting current density of a porous gas diffusion electrode with a film of non-electroactive material on the gas side:

- 1) Diffusion through the porous film is limiting at large film thicknesses.
- 2) Diffusion into and within the porous structure of the anode is limiting for very thin (or zero) film thicknesses.

In case 1) the limiting current density should be proportional to the reciprocal of the film weight (or thickness). This would yield a straight line through the origin on a plot of i_L vs (1/film weight), the slope of which is determined by the gas partial pressures, their transport properties, and the properties of the film. In case 2) the limiting current density should be independent of the film weight.

Fig. 60 shows the two limiting cases. The positions of the lines are determined by the experimental results. In the "no film" case, an electrode with no film was made and tested, giving the i_L shown. For the conditions of electrode preparation indicated above, it is desirable to have a film of 0.4 mg/cm^2 or less in order to prevent a decrease in i_L due to diffusion through the film. The "no film" value of i_L can be increased by using less force when pressing the electrode and by optimizing the catalyst:binder ratio. These values will change with the catalyst material being used.

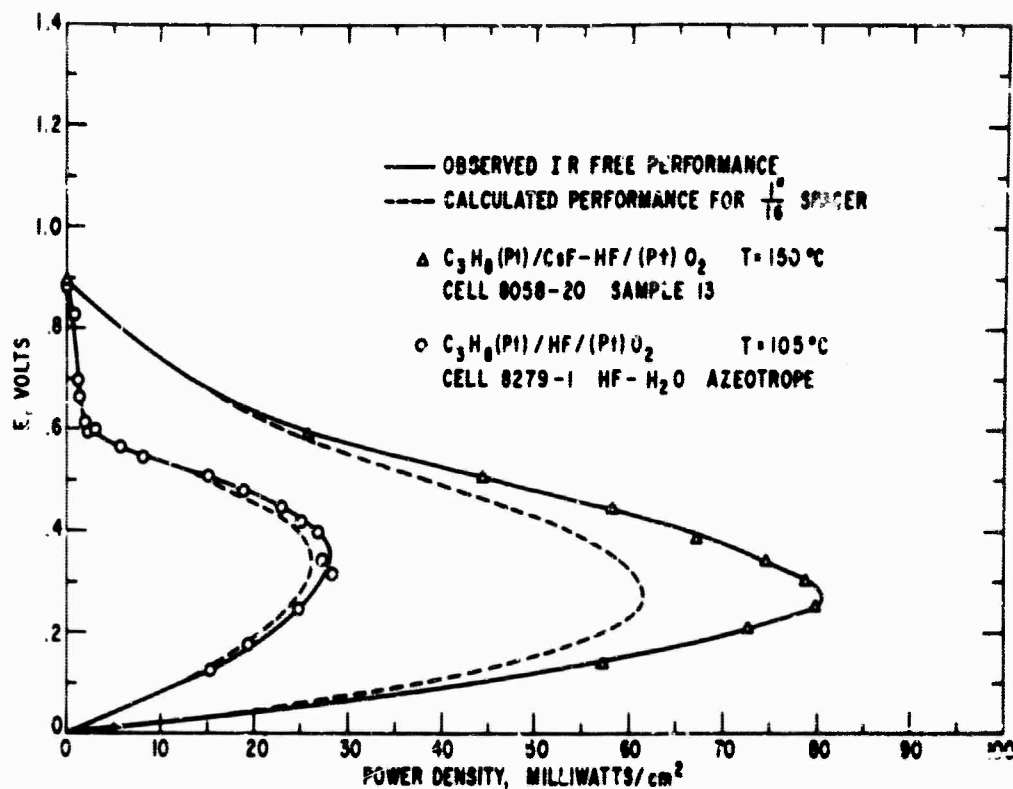


Fig. 59 Comparison of Power Densities for Propane Cells Using $CaF-HF-H_2O$ Electrolyte at $150^\circ C$ and $HF-H_2O$ Electrolyte at $105^\circ C$.

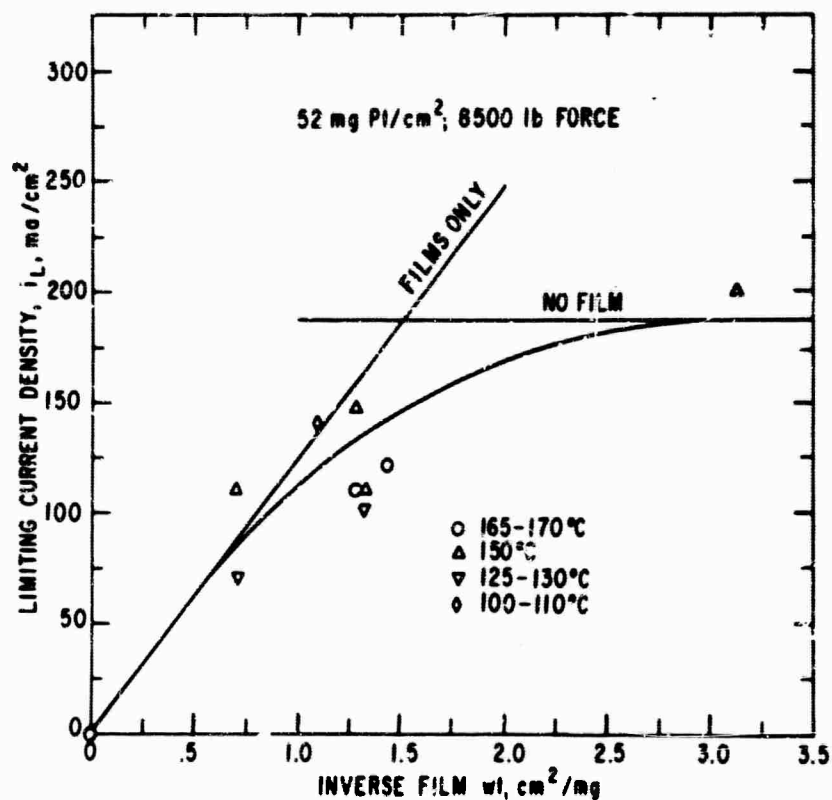


Fig. 60 Effect of Teflon Film Thickness on Propane Limiting Current Densities.

C. Conclusions

1) Relationships describing the effect of electrolyte composition and temperature (over the range 90-150°C) on propane performance have been established.

2) Maximum propane performance at a given temperature is obtained with the maximum HF/(CsF + HF) ratio, and at an optimum water content of 12-15 mole percent for the range HF/CsF = 2.0 to 3.0.

3) Good propane performance can be retained in the HF-H₂O system at operating temperatures down to 90°C.

4) Power densities (IR-free) of 80 milliwatts/cm² at 150°C and 30 milliwatts/cm² at 105°C are possible for propane in optimum composition fluoride electrolytes.

4.1.5.2 Electrochemistry in Fluoride Electrolytes

Techniques for preparation of reproducible electrode surfaces (1) have been worked out for platinum electrodes in HF electrolytes and investigations of the adsorption and electrochemical oxidation of hydrocarbons on platinum in 37 mole % HF have begun.

A. Experimental

Multipulse potentiostatic and multipulse potentiodynamic experiments have been performed using the apparatus described on pages 4-60 and 4-61 of Reference 1. The electrode cleanup procedure has been the application of alternate anodic and cathodic potentiostatic pulses (Fig. 61) of 15 seconds duration, and of equal anodic and cathodic current densities (see A in Fig. 61), followed by a rapid oxidation of the platinum surface at 1.6 volts (B) to form an oxide layer which prevents the adsorption of hydrocarbon species. After formation of the oxide layer is complete, the potential is then reduced to 1.2 volts (C) while the desired mass transport conditions are set up in the electrolyte. During period C, propane was bubbled and the electrolyte was stirred to obtain uniform saturation with C₃H₈. This was followed by a period of no stirring and no bubbling (also at 1.2 volts) to set up a quiescent mass transfer condition. After the appropriate waiting time (usually 1 to 3 minutes), the potential was reduced to the value U_a (D) for time τ_a , during which adsorption of the propane took place. The potential was then increased at a linear rate of $dE/dt = 0.2$ to 10 volts per second during which the adsorbed material was oxidized while a current-voltage and/or current-time trace was photographed on the oscilloscope.

The oxidation current measured is that due only to the adsorbed species, and not species in the bulk electrolyte because the sweep speed is chosen to be rapid enough that no appreciable adsorption can take place from the bulk liquid phase during the sweep (5). After a given

(5) S. Gilman, J. Electroanal. Chem., 7, 382 (1964).

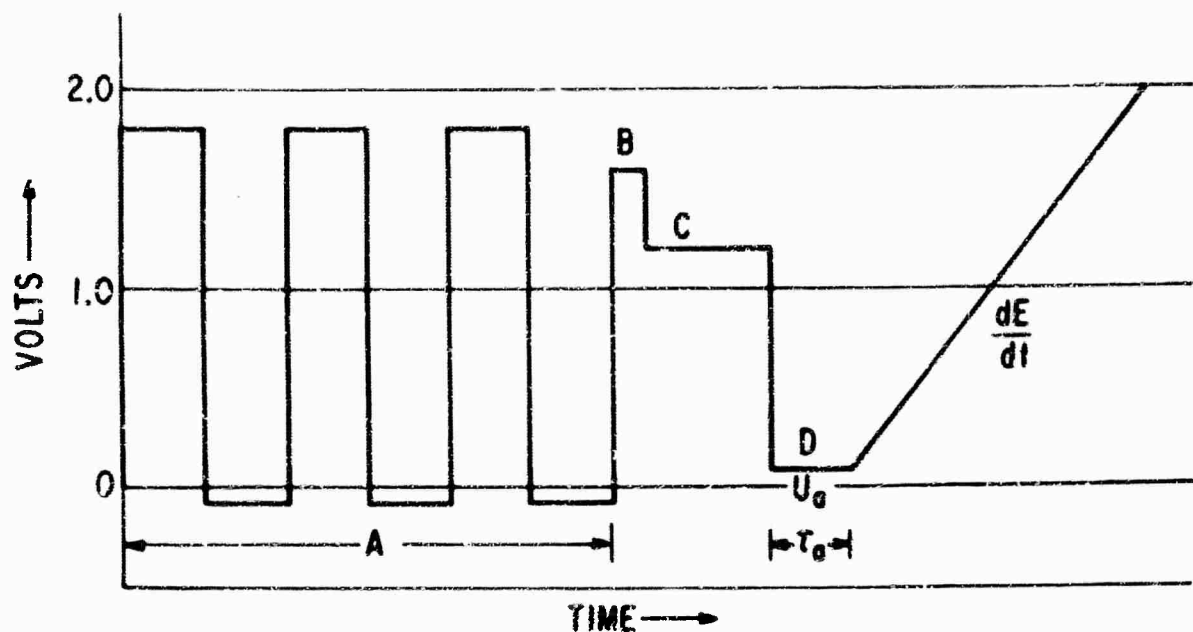


Fig. 61 Voltage Sequence Applied to Smooth Pt Test Electrode for Propane Investigations Using HF Electrolyte.

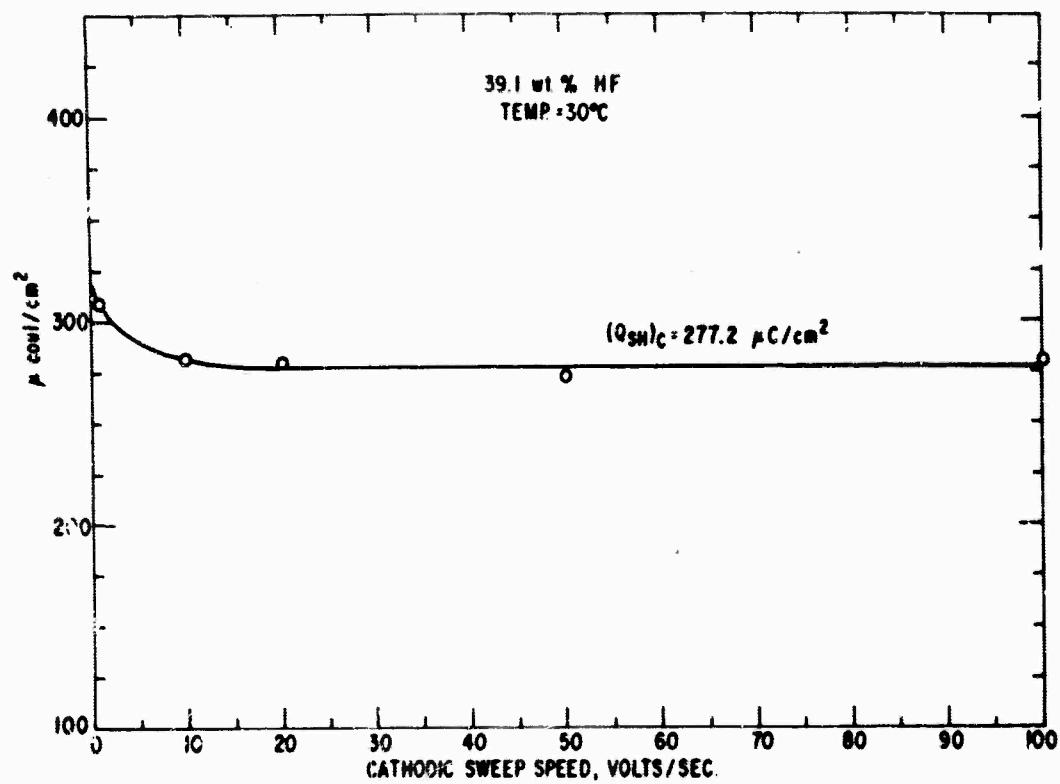


Fig. 62 Saturation Coverage of Hydrogen on Smooth Pt in HF, Expressed as Microcoulombs of Hydrogen Deposited per cm^2 During Cathodic Voltage Sweeps.

voltage sequence was completed, the cleanup procedure was repeated and the electrode was ready for another sequence.

Electrolyte solutions were prepared from quartz redistilled water and Mallinckrodt analytical reagent grade 48% hydrofluoric acid and stored under nitrogen in polypropylene or polyethylene bottles. The composition used was the maximum-boiling azeotrope of 37 mole percent HF. All gas streams were passed through Teflon and platinum saturators filled with the same electrolyte at the same temperature as the cell in order to prevent evaporation from the electrochemical cell.

Some of the pertinent data relating to the apparatus and chemicals are shown in Table XI.

TABLE XI

Properties of the Electrochemical System

Electrolyte: 39.1 wt % HF, Mallinckrodt, A. R.
Electrode: Smooth Platinum Wire, 0.060 in. dia. .
Electrode Geometric Area: 0.515 cm²
Saturation Hydrogen Coverage: 277.2 mcoul/cm²
Surface Roughness: 1.3
Propane: Matheson Instrument Grade, 99.5% min.
Argon: Matheson, 99.998% min., oxygen removed.

B. Results and Discussion

The number of coulombs of hydrogen corresponding to a monolayer on the smooth Pt electrode was estimated by using cathodic sweep dE/dt of 1, 10, 20, 50, and 100 volts/second at the end of the voltage sequence shown in Fig. 61. Step D of the voltage sequence was 0.4 volt, and τ_a was 10 seconds. The atmosphere was argon. The area under the cathodic current-time trace was integrated and corrected for double layer capacity. The results are shown in Fig. 62. The value used for a monolayer of hydrogen is 277.2 μ coul/cm². This yields a roughness factor of about 1.26 assuming 1.37×10^{16} platinum atoms/cm², which approximates a statistical mixture of the 100, 110, and 111 planes of platinum at the surface.

The experiments with propane at 30°C were carried out using the voltage sequence of Fig. 61 with $U_a = 0.1$ volt vs. reversible H₂, τ_a values of 1, 5, and 15 minutes, and dE/dt values of 1.0 and 10.0 volts per second. The anodic sweep for 1.0 volts per second and an adsorption time of 15 minutes in quiescent, propane-saturated (0.97 atm) electrolyte is shown in Fig. 63. The blank trace for an argon atmosphere is shown for comparison. The following three features are important:

- 1) The area under the hydrogen oxidation peaks is reduced by the presence of adsorbed propane.

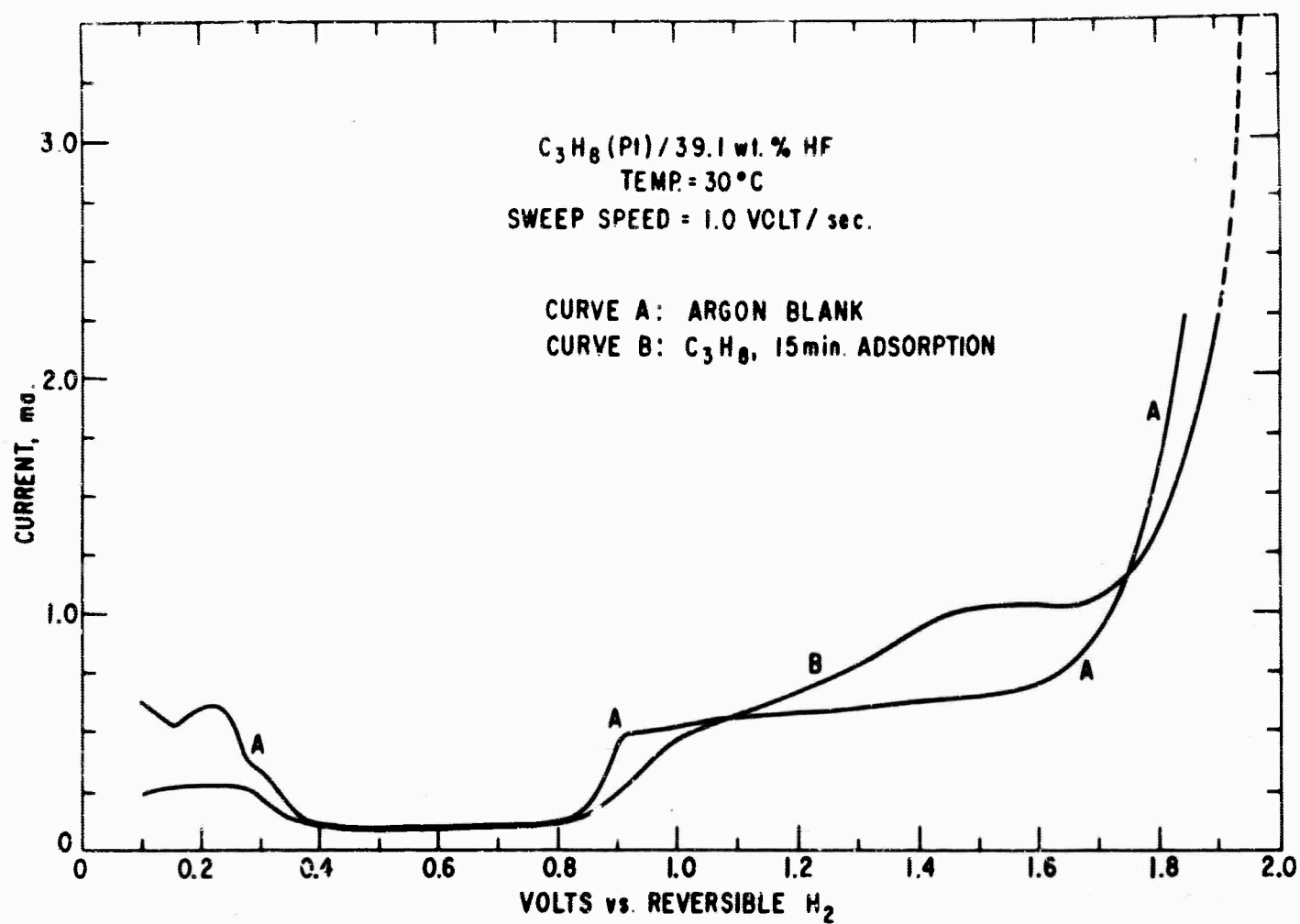


Fig. 63 Potentiodynamic Current-Voltage for Propane on Smooth Pt in HF Electrolyte.

2) The propane adsorbed on the electrode is being oxidized in the range above 0.8 volts.

3) The evolution of molecular oxygen in the vicinity of 2.0 volts is hindered by the presence of unoxidized propane residue.

The above three features of the curve in Fig. 63 form the basis for the calculation of surface coverages of hydrogen, propane oxidized below 1.76 volts (see cross-over point in Fig. 63), and propane remaining on the surface above 1.76 volts.

The total surface covered by the propane is considered to be proportional to the reduction in the number of coulombs of hydrogen on the surface upon substitution of propane for argon:

$$0.1\theta_{HC} = 1 - \frac{0.6 \left[Q_H \right]_{HC}}{0.6 \left[Q_H \right]_{Ar}} \quad (54)$$

$0.1\theta_{HC}$ is the fraction of the surface covered by propane at 0.1 volts. $\frac{0.6 \left[Q_H \right]_{HC}}{0.1}$ is the number of coulombs obtained by integrating the area under curve B of Fig. 61 between 0.1 and 0.6 volts, corrected for the charging of the double layer. It represents the number of coulombs of hydrogen on the surface at 0.1 volt, in the presence of dissolved propane at about 0.97 atmosphere partial pressure. $\frac{0.6 \left[Q_H \right]_{Ar}}{0.1}$ is the number of coulombs of hydrogen on the surface at 0.1 volt under an argon atmosphere, and is obtained by integration of curve A, Fig. 63 over the range 0.1 to 0.6 volt and correcting for the double-layer capacity.

The values of $\frac{0.6 \left[Q_H \right]_{HC}}{0.1}$ for various adsorption times at 30°C, and for sweep speeds of 1.0 and 10.0 volts/second are given in Table XII. The computed values of $0.1\theta_{HC}$, using equation 54 are summarized in Table XIII.

The number of coulombs of propane oxidized between 0.6 volts and 1.76 volts (the cross-over point in Fig. 63) is estimated by integrating the area under Curve B, Fig. 63 and subtracting the area under Curve A, Fig. 63, both in the range 0.6 to 1.76 volts. This subtraction gives an approximate correction for the coulombs required for surface oxidation of the platinum electrode. The values of $\int_{0.6}^{1.76} \left[Q_{HC} \right]$ for 30°C are given in Table XII. Comparison of these values with 277.2 $\mu\text{coul}/\text{cm}^2$ for saturation coverage with hydrogen gives a qualitative indication of the amount of propane oxidized in this voltage range.

The propane residue on the platinum surface which is not oxidized at 1.76 volts hinders the evolution of oxygen. This hindrance gives a measure of the fraction of the surface that is blocked by the presence of propane residue, since the oxygen evolution current at a

TABLE XII

Primary Data

 C_3H_8 (Pt)/39.1 wt % HF

Temperature = 30°C

Adsorption potential = 0.1 V vs rev H_2 .

a. Sweep speed = 1.0 volt/sec

Adsorption time (min.)	0	1	5	15
$\frac{0.6}{0.1} [Q_H]_{HC} \left(\frac{\mu\text{coul}}{\text{cm}^2} \right)$	189.54*	149.03	109.01	76.60
$\frac{1.76}{0.6} [Q_{HC}] \left(\frac{\mu\text{coul}}{\text{cm}^2} \right)$	0	(67.93)	228.2	346.2
$\frac{1}{1.86} [i_{O_2}] \text{ (ma)}$	2.37	2.03	1.815	1.755

b. Sweep speed = 10.0 volts/sec

Adsorption time (min.)	0	1	5	15
$\frac{0.6}{0.1} [Q_H]_{HC} \left(\frac{\mu\text{coul}}{\text{cm}^2} \right)$	203.36*	150.63	112.82	72.60
$\frac{1.76}{0.6} [Q_{HC}] \left(\frac{\mu\text{coul}}{\text{cm}^2} \right)$	0	60.44	193.55	237.20
$\frac{1}{1.86} [i_{O_2}] \text{ (ma)}$	10.30	8.70	7.60	7.12

*Measurement carried out under argon.

given potential is proportional to the surface area taking part in the reaction. Therefore:

$$\frac{\infty}{1.76} [\theta_{HC}] = 1 - \frac{[i_{O_2}]_{HC}}{[i_{O_2}]_{Ar}} \quad (55)$$

The symbol $\frac{\infty}{1.76} [\theta_{HC}]$ represents the surface coverage of propane residue which is oxidizable only at high potentials (above 1.76 volts, hence the interval 1.76 to ∞). $[i_{O_2}]_{HC}$ is the oxygen evolution current in the presence of adsorbed propane residue, and is obtained from a Tafel plot of the current-voltage relationship of Fig. 63. The Tafel plots are straight, parallel lines at the high voltages for all the sweep speeds used here (0.2 to 10 v/s), indicating negligible oxidation of the residue during the sweep. The currents at 1.86 volts as obtained from the Tafel plots are given

in Table XII for 30°C. Equation 55 was used for the computation of the $\frac{\infty}{1.76} [\theta_{HC}]$ values listed in Table XIII.

TABLE XIII

Results

C_3H_8 (Pt)/39.1 wt % HF

Temperature = 30°C

Adsorption potential = 0.1 V vs rev H_2

a. Sweep Speed = 1.0 volt/sec

<u>Adsorption time (min.)</u>	0	1	5	15	<u>Average</u>
θ_T	0.6838	0.7514	0.8181	0.8722	
$0.6 \frac{[\theta_H]}{0.1} HC$	0.6838*	0.5376	0.3933	0.2763	
$0.1 \theta_{HC}$	0	0.2138	0.4248	0.5959	
$1.76 \frac{[\theta_{HC}]}{0.6}$	0	0.0803	0.1885	0.3364	
$\frac{\infty}{1.76} [\theta_{HC}]$	0	0.1435	0.2363	0.2595	
$1.76 \frac{[q_{HC}]}{0.6}$	-	846.0	1210.6	1029.1	1028.6
$1.76 \frac{[\eta_{HC}]}{0.6}$					3.71

b. Sweep Speed = 10.0 volts/sec

<u>Adsorption time (min.)</u>	0	1	5	15	<u>Average</u>
θ_T	0.7336	.8027	.8622	0.9049*	
$0.6 \frac{[\theta_H]}{0.1} HC$	0.7336*	0.5434	0.4070	0.2619*	
$0.1 \theta_{HC}$	0	0.2593	0.4452	0.6430*	
$1.76 \frac{[\theta_{HC}]}{0.6}$	0	0.1040	0.1831	0.3343*	
$\frac{\infty}{1.76} [\theta_{HC}]$	0	0.1553	0.2621	0.3087*	
$1.76 \frac{[q_{HC}]}{0.6} \frac{\mu \text{ coul}}{\text{cm}^2}$	-	581.15	1057.1	709.5	782.6

TABLE XIII (Cont.)

b. Sweep Speed = 10.0 volts/sec (Cont.)

A Adsorption time (min.)	0	1	5	15	Average
$1.76 \begin{bmatrix} \eta_{HC} \end{bmatrix}$ $0.6 \begin{bmatrix} \eta_{HC} \end{bmatrix}$	—				2.82
$1.76 \begin{bmatrix} q_{HC} \end{bmatrix} \frac{\mu \text{ coul}}{\text{cm}^2}$	—	672.0	470.8	2215.4	1119.4
$1.76 \begin{bmatrix} \eta_{HC} \end{bmatrix}$					4.04

*These values are of lower accuracy than the others in this table, since a low-sensitivity oscilloscope trace was used.

The surface coverage of hydrogen at 0.1 volt is given by:

$$\frac{0.6 \begin{bmatrix} \theta_H \end{bmatrix}_{HC}}{0.1 \begin{bmatrix} \theta_H \end{bmatrix}_{HC}} = \frac{0.6 \begin{bmatrix} Q_H \end{bmatrix}_{HC}}{(Q_{SH})_C} \quad (56)$$

where $(Q_{SH})_C$ has the value $277.2 \mu \text{ coul/cm}^2$, and $0.6 \begin{bmatrix} \theta_H \end{bmatrix}_{HC}$ is given in Table XII. The values of $0.6 \begin{bmatrix} \theta_H \end{bmatrix}_{HC}$ shown in Table XIII were calculated from equation 56.

Since the total coverage of propane at 0.1 volt has been calculated, and that above 1.76 volts is known, the difference should be the coverage which has been oxidized off of the electrode below 1.76 volts, or:

$$\frac{1.76 \begin{bmatrix} \theta_{HC} \end{bmatrix}}{0.6 \begin{bmatrix} \theta_{HC} \end{bmatrix}} = 0.1 \theta_{HC} - \frac{1.76 \begin{bmatrix} \theta_{HC} \end{bmatrix}}{1.76} \quad (57)$$

There are now two kinds of results relating to the oxidation of propane in the range 0.6 to 1.76 volts: the surface coverage $\frac{1.76 \begin{bmatrix} \theta_{HC} \end{bmatrix}}{0.6 \begin{bmatrix} \theta_{HC} \end{bmatrix}}$ (see Table XIII and the amount of charge required for the oxidation, $\frac{1.76 \begin{bmatrix} Q_{HC} \end{bmatrix}}{0.6 \begin{bmatrix} Q_{HC} \end{bmatrix}}$). The amount of charge per monolayer is given by:

$$\frac{1.76 \begin{bmatrix} q_{HC} \end{bmatrix}}{0.6 \begin{bmatrix} q_{HC} \end{bmatrix}} = \frac{0.6 \begin{bmatrix} Q_{HC} \end{bmatrix}}{1.76 \begin{bmatrix} \theta_{HC} \end{bmatrix}} \quad (58)$$

The credibility of the assumptions and the validity of the computational procedures can be evaluated by the reasonableness of the values of $\frac{1.76 \begin{bmatrix} q_{HC} \end{bmatrix}}{0.6 \begin{bmatrix} q_{HC} \end{bmatrix}}$. The average value of

$\frac{1.76}{0.6} [q_{HC}]$ for 30°C is 1028.6 $\mu\text{coul}/\text{cm}^2$ which corresponds to 3.71 electrons per surface site:

$$\frac{1.76}{0.6} [\eta_{HC}] = \frac{\frac{1.76}{0.6} [q_{HC}]}{(Q_{SH})_c} = \frac{1028.6}{277.2} = 3.71 \quad (59)$$

This corresponds to about five surface sites per propane molecule, a reasonable value. At 30°C, it is fairly likely that no appreciable amount of hydrogen is produced on the surface from the dissociation of propane in periods of up to 15 minutes (6). Another check on the present results is obtained by considering the results for $\frac{1.76}{0.6} [Q_{HC}]$ and $\frac{\infty}{1.76} [\theta_{HC}]$ at different sweep speeds. At higher sweep speeds, $\frac{1.76}{0.6} [Q_{HC}]$ is expected to decrease while $\frac{\infty}{1.76} [\theta_{HC}]$ is expected to increase, due to the irreversibility of the propane oxidation. Furthermore, there should be a proportionality between $\frac{1.76}{0.6} [\Delta Q_{HC}]$ and $\frac{\infty}{1.76} [\Delta \theta_{HC}]$, and the proportionality constant should have a value near $\frac{1.76}{0.6} [q_{HC}]$. The calculation was made according to:

$$\frac{1.76}{0.6} [\bar{q}_{HC}] = \frac{\frac{1.76}{0.6} [\Delta Q_{HC}]}{\frac{\infty}{1.76} [\Delta \theta_{HC}]} \quad (60)$$

and the value obtained was 4.04, in good agreement with 3.71 found from equation 59.

With the reasonableness of the results established, it is worthwhile to consider the surface coverage values for the various species as a function of adsorption time. Fig. 64 shows the surface coverages for hydrogen, propane, and their sum, θ_T , as obtained with sweep speeds of 1.0 and 10.0 volts per second at 30°C, as a function of adsorption time at 0.1 volt vs. reversible H_2 in the same electrolyte. Good agreement was obtained between the results at the two speeds. The coverage of propane increases from 0.1 θ_{HC} of zero to about 0.62 in 15 minutes. This is quite a slow rate of adsorption, and is too slow for diffusion to be controlling. The hydrogen is displaced from the surface, starting with θ_H of 0.7, and decreasing to 0.26 after 15 minutes. The total surface covered increased from 70 to 90% during the same period.

Fig. 65 shows that initially, the amount of difficultly oxidized propane residue increases rapidly, but it levels off at about $\frac{\infty}{1.76} [\theta_{HC}] = 0.5$. The easily oxidized material builds up more slowly, but is present in approximately the same amount after about 10 minutes of

(6) L. W. Niedrach, J. Electrochem. Soc., 111 1309 (1964).

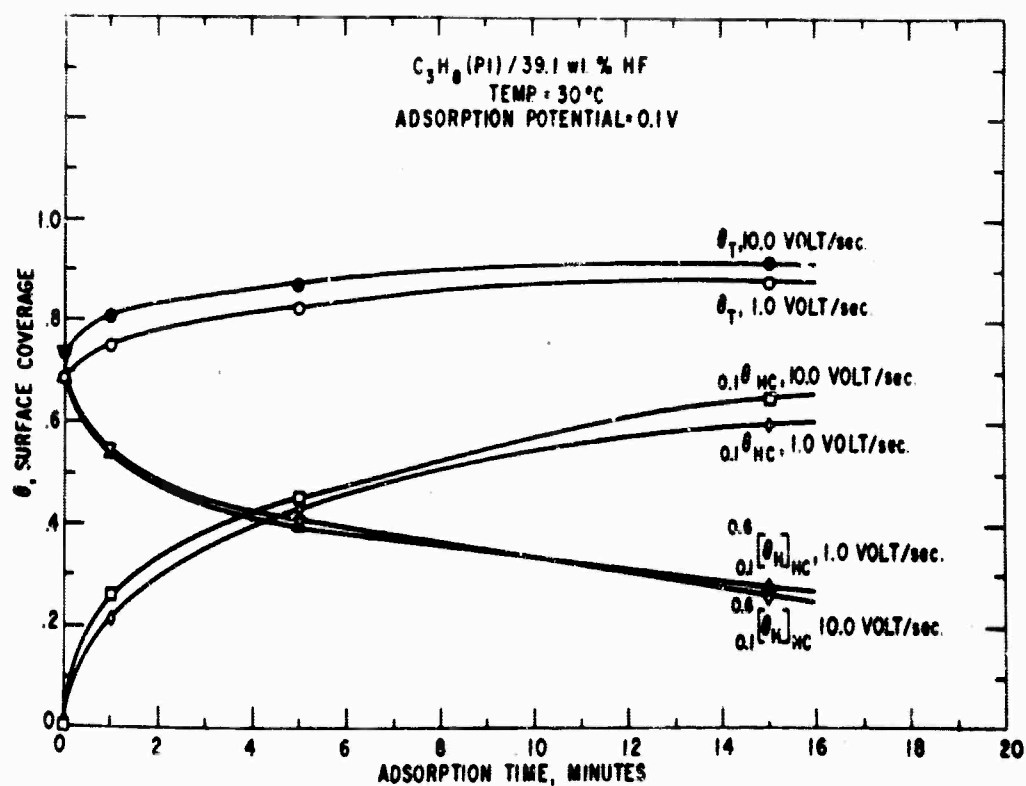


Fig. 64 Surface Coverages of Propane and Hydrogen on Smooth Pt in HF, as a Function of Adsorption Time in Quiescent Electrolyte.

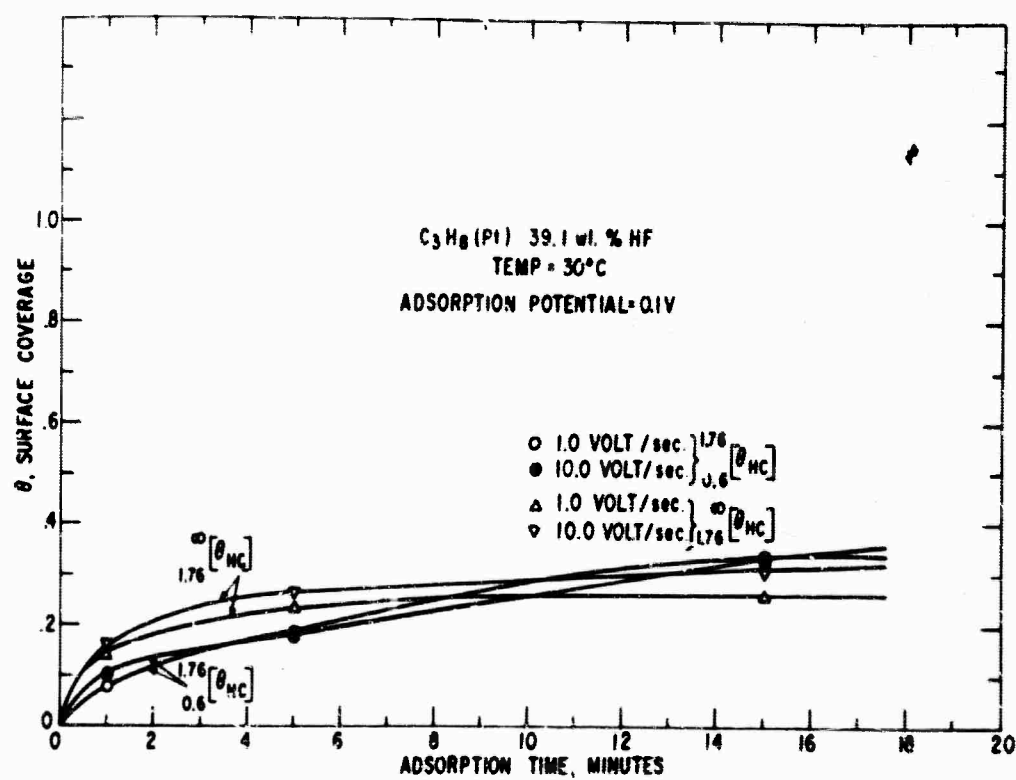


Fig. 65 Surface Coverages of Propane Oxidized Below 1.76 Volts vs Rev H_2 , and Above 1.76 Volts on Platinum in HF as a Function of Adsorption Time.

adsorption, and continues to increase slowly. This indicates that the majority of the initially adsorbed propane is rather tightly bound and difficult to oxidize.

Similar, though less complete, experiments have been performed for propane on platinum in 39.1 wt % HF at 60 and 90°C. The data reduction was very similar to that outlined above, but the adsorption potential was 0.3 volts and, therefore, very little hydrogen was present on the electrode surface. No measure was made of the possible formation of hydrogen from propane. This may be included in future work. Current-voltage curves for propane at 60°C for 15 minutes adsorption time at 0.3 volt are shown in Fig. 66, for a sweep speed of 1.0 v/sec. Note that propane oxidation supports higher currents at lower voltages at 60°C than at 30°C. The surface coverage results for 60°C are summarized in Tables XVI and XVII, and are speeds of 0.2 and 1.0 volt per second. Fig. 67 shows that the initial rate of propane adsorption is significantly greater than at 30°C, and the saturation coverage is about $0.3 \theta_{\text{HC}} = 0.9$. The slight discrepancy in initial rates could be due to small convection currents caused by vibrations in the apparatus. Essentially no hydrogen is on the surface in the presence of adsorbed propane, at 0.3 volt. Fig. 68 shows that a large fraction of the adsorbed propane is oxidized at potentials below 1.62 volts, and more is oxidized at low potentials when the sweep speed is decreased, leaving less than 0.1 - 0.2 monolayer to be oxidized at potentials above 1.7 volts. The initial rates of adsorption are nearing values where mass transport could be rate limiting in the very early stages of adsorption ($\theta < 0.1$). This point will be checked further.

Characteristic current-voltage traces for propane on Pt in 39.1 wt % HF at 90°C are shown in Fig. 69. The sweep speed was 1.0 v/sec, performed after an adsorption of 5 minutes at 0.3 volt vs reversible H_2 . Note that a new peak has appeared at 0.8 volts. The peak near 1.2 volts is still present, so the 0.8 volt peak is not merely a shift of the higher potential peak. There is some propane oxidation at potentials below 0.6 volt. The appearance of this peak is the first indication that propane can be oxidized on smooth platinum in HF in the potential range where no oxide layer is present. The previous peaks (Figs. 63 and 66) were superimposed on the surface oxidation waves, indicating simultaneous oxidation of propane and the platinum surface. Fig. 69 indicates that two propane oxidation processes of similar rates do occur. Of course, the peak at 0.8 volt is of primary interest to the fuel cell problem.

The results for the surface coverage of hydrogen and propane at 90°C are summarized in Tables XVI and XVII, and are plotted in Fig. 70. Note that adsorption is essentially complete after about 1 minute at 90°C, while 5 minutes are required at 60°C, and about 15 minutes are necessary to 30°C. The total surface coverage amounts to about a monolayer at 90°C, 75% of which can be oxidized at 1.0 v/sec in the potential range below 1.56 volts. About one quarter of the easily oxidized material is oxidized at potentials less than 0.9 volts vs. reversible H_2 at a sweep speed of 1.0 v/sec.

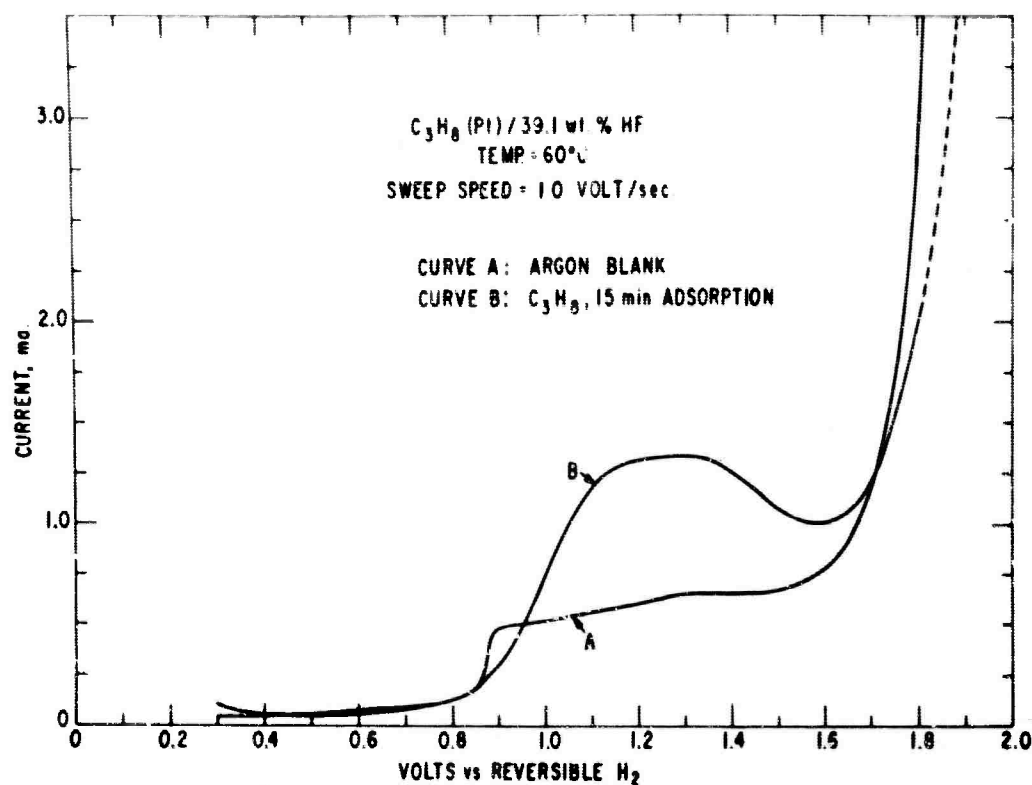


Fig. 66 Potentiodynamic Current-Voltage Curve for Propane on Smooth Pt in HF Electrolyte.

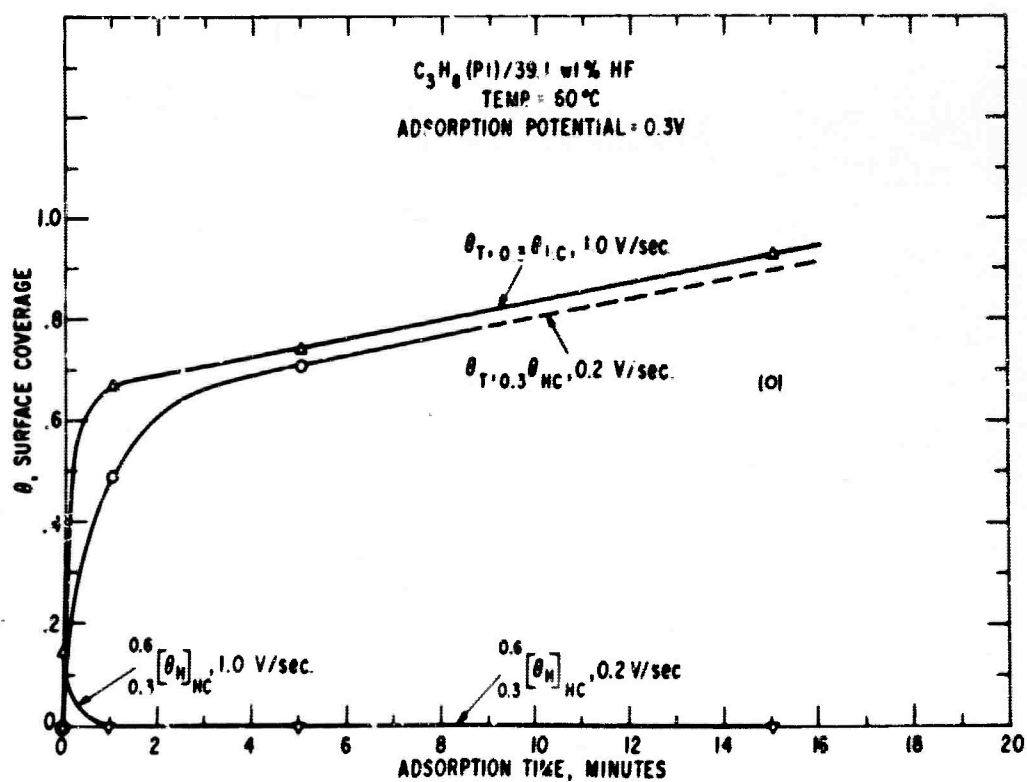


Fig. 67 Surface Coverages of Propane and Hydrogen on Smooth Pt in HF, as a Function of Adsorption Time in Quiescent Electrolyte.

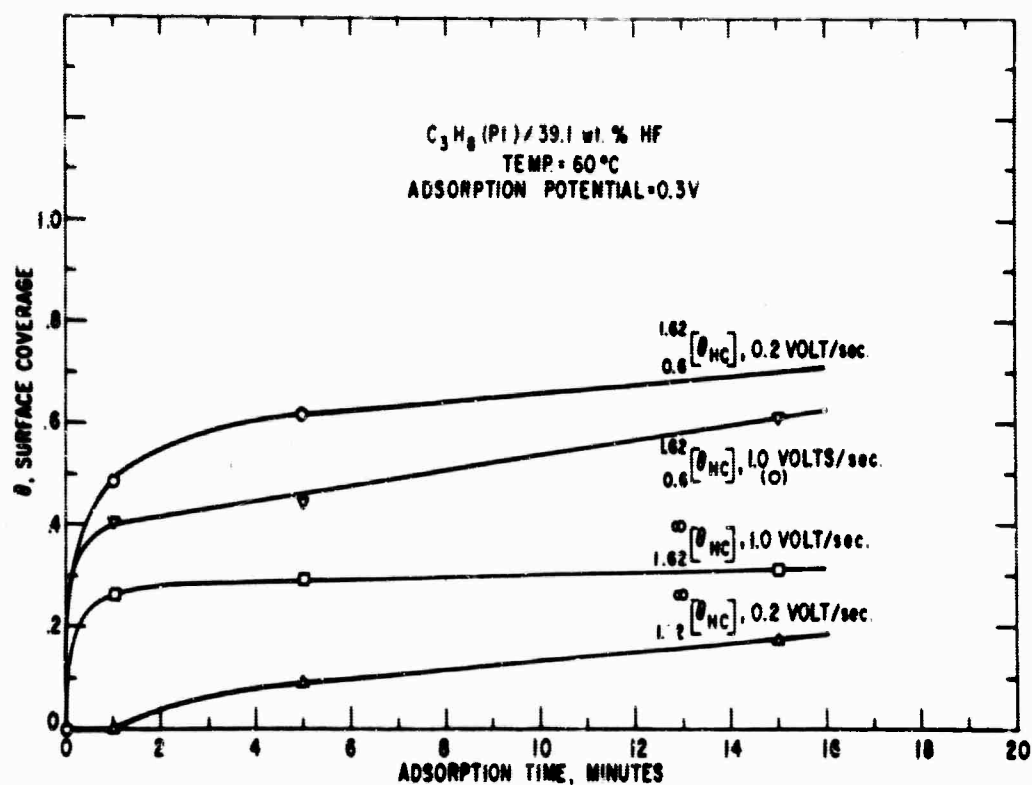


Fig. 68 Surface Coverages of Propane Oxidized Below 1.62 Volts and Above 1.62 Volts on Platinum in HF as a Function of Adsorption Time, for Two Sweep Speeds.

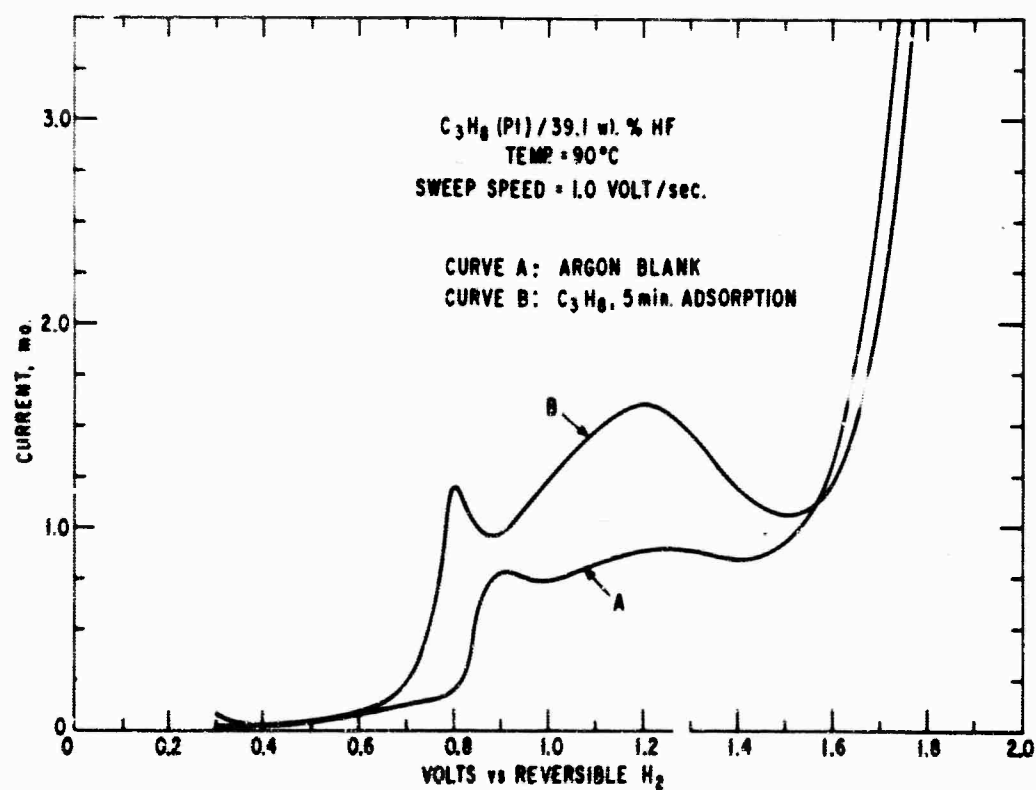


Fig. 69 Potentiodynamic Current-Voltage Curve for Propane on Smooth Platinum in HF Electrolyte.

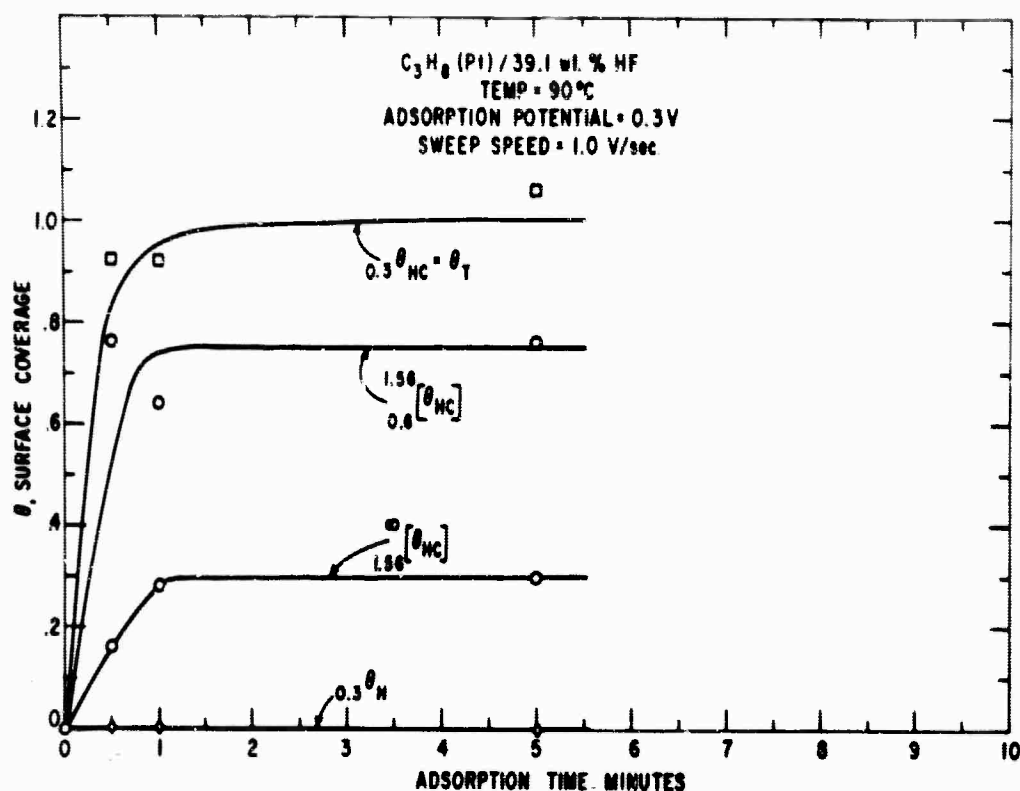


Fig. 70 Surface Coverages of Propane and Hydrogen on Smooth Pt in HF, as a Function of Adsorption Time in Quiescent Electrolyte.

TABLE XIV

Primary Data

C_3H_8 (Pt)/39.1 wt % HF

Temperature = 60°C

Adsorption potential = 0.3 V vs rev H_2

a. Sweep Speed = 0.2 volt/sec

Adsorption time (min.)	0	1	5	15
$\frac{1.7}{0.6} [Q_{HC}] \left(\frac{\mu \text{ coul}}{\text{cm}^2} \right)$	0	500.3	634.5	(150.2)†
$i_{1.76}$ (ma)	0.775	0.775	0.705	0.640
$\frac{0.6}{0.3} [Q_H] \left(\frac{\mu \text{ coul}}{\text{cm}^2} \right)$	40.62	0	0	0

b. Sweep Speed = 1.0 volt/sec

Adsorption time (min.)	0	1	5	15
$\frac{1.7}{0.6} [Q_{HC}] \left(\frac{\mu \text{ coul}}{\text{cm}^2} \right)$	0	418.4	456.9	629.8
$i_{1.7}$ (ma)	0.920	0.680	0.650	0.635

† Values in parentheses indicate uncertainty due to decreased current sensitivity.

TABLE XV

Results

 C_3H_8 (Pt) 39.1/wt % HF

Temperature = 60°C

Adsorption Potential = 0.3 V vs rev H_2

a. Sweep Speed = 0.2 volt/sec

Adsorption time (min.)	0	1	5	15	Average
θ_T	0	0.4864	0.7072	(0.6700)†	
$\frac{0.6}{0.3} [\theta_H]_{HC}$	0	0	0	0	
$0.3 \theta_{HC}$	0	0.4864	0.7072	(0.6700)	
$\frac{1.62}{0.6} [\theta_{HC}]^*$	0	0.4864	0.6169	(0.4960)	
$\frac{\infty}{1.62} [\theta_{HC}]$	0	0	0.0903	0.1740	

b. Sweep Speed = 1.0 volt/sec

Adsorption time (min.)	0	1	5	15	Average
θ_T	.146	0.6675	0.7355	0.9222	
$\frac{0.6}{0.3} [\theta_H]_{HC}$	0.146	0	0	0	
$0.3 \theta_{HC}$	0	0.6675	0.7355	0.9222	
$\frac{1.62}{0.6} [\theta_{HC}]^*$	0	0.4067	0.4420	0.6123	
$\frac{\infty}{1.62} [\theta_{HC}]$	0	0.2608	0.2935	0.3099	

* Assumed $\frac{1.76}{0.6} [q_{HC}] = 1028.6$ from 30°C results.

† Values in parentheses indicate uncertainty due to decreased current sensitivity.

TABLE XVI

Primary Data

 C_3H_8 (Pt)/39.1 wt % HF

Temperature = 90°C

Adsorption Potential = 0.3 V vs rev H_2

Sweep Speed = 1.0 Volt/sec

Adsorption time (min.)	0	0.5	1.0	5.0
$0.6 \left[Q_H \right] \left(\frac{\mu \text{ coul}}{\text{cm}^2} \right)$	2	0	0	0
$1.56 \left[Q_{HC} \right] \left(\frac{\mu \text{ coul}}{\text{cm}^2} \right)$	0	783.74	658.34	783.74
$i_{1.76} \text{ (ma)}$	4.78	4.00	3.43	3.35

It is interesting to compare the currents in excess of the blank current for the same sweep speed at the different temperatures. These results are shown in Fig. 71. The current-potential curves show peaks in the range 1.2 to 1.5 volts for all three temperatures. The 90°C curve shows an additional peak at 0.8 volt, indicating rapid oxidation rates starting at 0.6 volt. It is this peak which deserves special attention in connection with fuel cells. As a result of the occurrence of the low-voltage peak, further work will emphasize the higher temperatures.

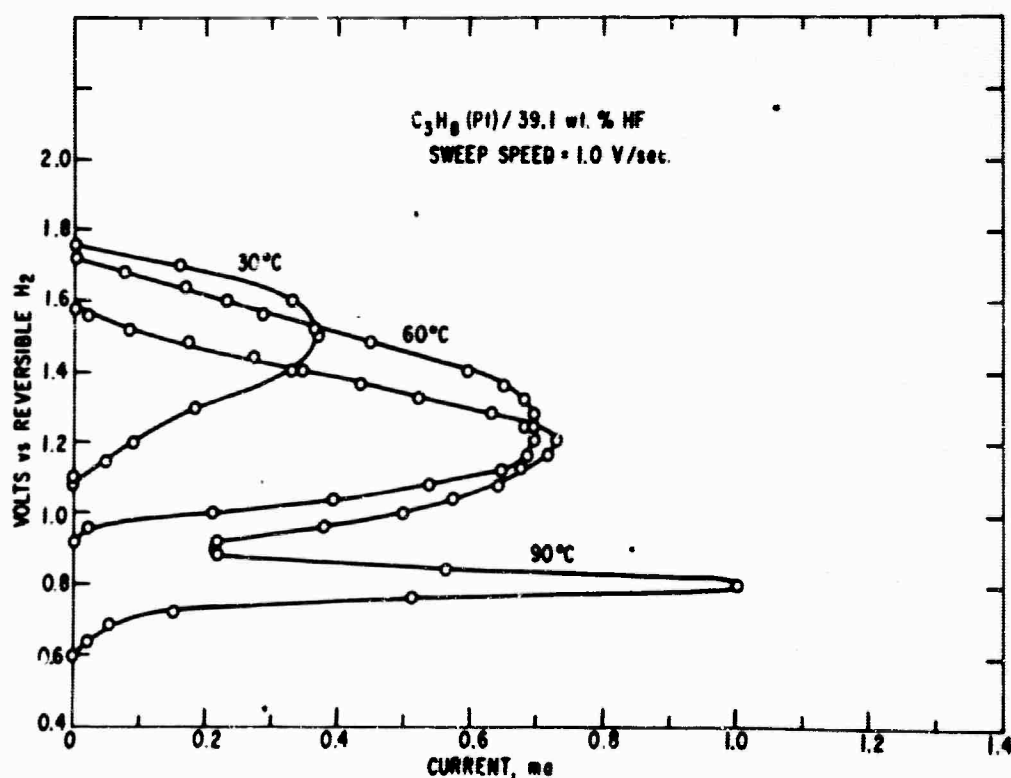


Fig. 71 Current-Potential Curves for the Oxidation of Propane on Smooth Pt for Various Temperatures.

TABLE XVII

Results C_3H_8 (Pt)/39.1 wt % HF

Temperature = 90°C

Adsorption Potential = 0.3 V vs rev H_2

Sweep Speed = 1.0 volt/sec

Adsorption time (min.)	0	0.5	1.0	5.0
θ_T	0.006	0.9251	0.9224	1.0611
$\frac{0.6}{0.3} [\theta_H]_{HC}$	0.006	0	0	0
$0.3 \theta_{HC}$	0	0.9251	0.9224	1.0611
$\frac{1.56}{0.6} [\theta_{HC}]^*$	0	0.7619	0.6400	0.7619
$\frac{\infty}{1.76} [\theta_{HC}]$	0	0.1632	0.2824	0.2992

* Assumed $\frac{1.76}{0.6} [q_{HC}] = 1028.6$ from 30°C results.

C. Conclusions

1. Propane in 39.1 wt % HF is adsorbed on smooth platinum at low rates at temperatures below about 60°C. At 90°C, adsorption is complete after one minute in a quiescent electrolyte.

2. The reduction in hydrogen coverage can be used as a quantitative measure of the amount of adsorbed propane on the platinum surface.

3. At temperatures up to 60°C in 39.1 wt % HF, propane is not oxidized at appreciable rates below 0.9 volt vs H_2 . Oxidation, therefore, occurs in the presence of a partially oxidized Pt surface.

4. At 90°C in HF, a rapid oxidation of propane takes place on the unoxidized surface of smooth Pt, at potentials in the range 0.6 to 0.9 volt. This peak corresponds to the oxidation current of practical interest for fuel cells.

4.1.6 Research Support for Development

The progress of the foregoing sections in developing a better understanding of hydrocarbon oxidation mechanisms is basic to continued performance improvements of the fuel cell, i.e., an understanding which includes the fundamental processes taking place on the electrode surface, as well as the knowledge of the rates at which these processes occur. In this relatively unexplored area of anodic H.C. oxidation at low temperatures, the available information regarding reaction mechanisms and rate-controlling processes is limited.

It is conceivable that specific catalysts are required, if dissociative adsorption results in the formation of relatively stable intermediate species, which may cause incomplete oxidation and possible voltage fluctuations. Also, if the activation energies for catalyzed H.C. oxidation are high, it may be required to lower the activation energy barrier by using specific catalysts, capable to induce electrochemical reactions compatible with complete H.C. oxidation. These mechanistic studies must be complemented by the determination of reaction rates and the rate-controlling processes as they will occur on practical electrodes. These rates will undoubtedly be dependent on the conditions at which the oxidation occurs as well as on the same geometric factor, as encountered in electrode structures, which may hinder increased rates, i.e., cell current densities.

The following examples, extracted from the studies conducted during this period of the contract, are reported to illustrate how results and implications will affect performance improvements of the direct oxidation of hydrocarbons.

- The anodic oxidation of ethane may yield two categories of surface species displaying different reactivities. Accumulation of one of these species may result in surface "poisoning." Development of specific catalyst or operation conditions (temp., electrolyte, etc.) may hinder or eliminate the formation of these relatively stable species and yield a somewhat "cleaner" reaction. These results and their interpretation will probably also be applicable to other hydrocarbons.
- Scale-up from wire electrodes to semi-micro fuel cell electrodes has substantiated the results observed on wires. This shows, indeed, applicability of techniques and results to practical porous electrodes and the significance of these fundamental investigations in terms of practical systems. In addition, similarity in behavior of methane and propane as compared to ethane has been shown.
- Further evidence of the formation of intermediate species has been demonstrated on macro-anodes representing a scale-up of 10^3 - 10^6 over wire electrodes. At low current densities these processes will affect anodic over-voltage and in practice, overall cell voltage.
- At high current densities, reaction rates on practical electrodes will be affected by mass transport processes as observed from results on thin electrolyte films.

These films will be present in porous metallic electrodes and become transport rate limiting, independently from the surface processes. These results combined with engineering data on fuel and water transport rates will allow one to define optimum pore geometries to yield high electrode currents and minimize water transport from the electrolyte. Results will affect the structural electrode configurations and become a guide to the design of hydrocarbon electrodes. Active catalytic deposition techniques on porous structure may become a by-product of these investigations.

- Reaction mechanisms and rates cannot only be affected by the electrocatalyst, but also by environmental conditions., e.g., type of electrolyte. Hydrofluoric acid represents a type of electrolyte, which allows for high transport rates and power densities, i.e., 80 milliwatts/cm² at 150°C (IR free). Once reaction mechanisms and fundamental properties resulting in this increased performance are understood, criteria for selection of electrolytes may be established and integrated with the engineering requirements for overall self-sustaining fuel cell systems.

Immediate benefits, however, are derived from the research by the continuous fall-out of design criteria for concurrent development work. The porous electrode development program, for example, is striving to achieve first, structures with the high porosity and "wetproofing" essential to permit rapid access of the gas phases at the electrolyte-fuel interfacial geometry in order to maximize dissociative adsorption (rate limiting process) of the fuel at the electrocatalysts surfaces; and secondly, structures with pore diameter and population that present an electrolyte film meniscus geometry to maximize transport rates. In both cases an electrolyte concentration for maximum fuel solubility is required.

4.2 ELECTROCATALYST RESEARCH

Electrocatalyst research is directed at the development of a low cost, highly active, stable catalyst system. The technical approach to reduce cost is utilization of a low cost diluent or substrate for extending platinum or a platinum alloy. Tantalum and boron carbide substrate studies are discussed in this section. Catalyst compatibility with the hydrogen fluoride electrolytes was also investigated. Evaluation of alloy catalysts has been introduced during this reporting period as a new and distinct area of investigation. The principal objective will be to enhance activity with an electrocatalyst system which may fully utilize lower cost substrate technology. The work elements of electrocatalyst research together with the respective objectives are summarized in Table I, Section 3.1.

4.2.1 Exchange and Adsorption Studies (D. W. McKee)

Investigation of binary alloy electrocatalysts for use in hydrocarbon fuel cells is continuing together with studies of dispersions of platinum on conducting substrates. Evaluation of new catalyst systems by means of gas phase adsorption and exchange techniques has been discontinued under this contract.

4.2.1.1 Exchange Studies

Further use of the methane-deuterium exchange technique has been made in the study of catalytic activity patterns in binary alloys of the platinum group. As previously noted (1), a definite correlation seems to exist between the ability of a metal or alloy system to catalyze this exchange reaction and its activity as an electrocatalyst in a hydrocarbon fuel cell. A logical basis for this correlation exists if the rate determining step at the fuel cell anode involves dissociative adsorption of the hydrocarbon molecule.

The results of previous exchange measurements (1, 2) have shown that the activities of noble metal alloys can approach or even exceed that on pure platinum in certain cases. In particular, ruthenium seems to possess the ability to increase the catalytic activity of platinum over certain ranges of alloy composition. As a sequel to this finding, the exchange activities of alloys of ruthenium are being investigated in the hope of discovering other combinations with enhanced activity for hydrocarbon dehydrogenation.

Preliminary results with a 38% Ru-Ir alloy were encouraging. As previously reported (2), this alloy showed an exchange rate considerably greater than either ruthenium or iridium alone but still somewhat less than that of pure platinum under the same conditions.

-
- (1) Technical Summary Report No. 4, December 31, 1963, Contract No. DA 44-009-ENG-4909, p. 5-7 through 5-18.
 - (2) Technical Summary Report No. 5, June 30, 1964, Contracts DA 44-009-AMC-479CT, DA 44-009-ENG-4909, p. 4-12, through 4-27.

Figs. 72 and 73 illustrate typical exchange results on a 17% Ru-Ir alloy at 100 and 132°C respectively. This alloy was prepared in the usual way by reduction of a mixed solution of ruthenium and iridium chlorides with 5% sodium borohydride solution. The range of complete solid solution in this system is quite limited, and X-ray diffraction patterns indicated that the alloys consisted of two phases, one hexagonal (Ru rich) and the other cubic (Ir rich). The surface areas of these samples have not yet been determined, but after reduction in hydrogen may be assumed to lie in the usual range 7-12 m²/g.

Both Ru-Ir samples investigated showed mainly multiple exchange, a result which is not unexpected as both pure elements promote this type of exchange mechanism in contrast to platinum and palladium, which give rise to step-wise exchange. Whereas the 38% Ru-Ir alloy showed somewhat lower activity than platinum black prepared under the same conditions, the 17% Ru-Ir alloy was more active than platinum, as shown below.

TABLE XVIII

Rate of Methane-Deuterium Exchange on Ru-Ir Alloys

<u>Sample No.</u>	<u>Composition</u>	<u>Rate at 100°C</u>
Y-1	38% Ru-Ir	8.0×10^{15} molecules/sec/g.
Y-2	17% Ru-Ir	8.6×10^{15} molecules/sec/g.
	100% Pt	1.8×10^{16} molecules/sec/g.

Alloys of the platinum group that possess exchange and dehydrogenation activities exceeding that of platinum itself thus include: Pt-Ru (around 15 wt. % Ru), Pt-Rh (15-80 wt. % Pt), Ru-Ir (around 17 wt. % Ru). Preliminary results also indicate that the Pd-Ru system shows similar properties. Similar patterns of catalytic activity have been found for Pt-Ru and Pt-Rh alloys in hydrocarbon fuel cell operation (3), but no fuel cell data has yet been published for the other alloys mentioned above. The "synergistic" action of ruthenium appears to be unique among the platinum group metals.

4.2.1.2 Adsorption Studies

A. Adsorption and Decomposition of Butanes on Platinum Black

The mechanism by which a hydrocarbon adsorbs and decomposes on a metal electrocatalyst is fundamental to the operation of the hydrocarbon fuel cell. Electrochemical measurements (Sections 4.1.1 and 4.1.2) indicated that the dissociative adsorption of the hydrocarbon may be the rate determining step in the electrochemical oxidation of hydrocarbons on platinum electrodes. Such investigations are, however, unable to give direct information on the nature of

(3) USAEL Report No. 3, Engelhard Industries, April 1963, Contract No. DA-36-039 SC-90691.

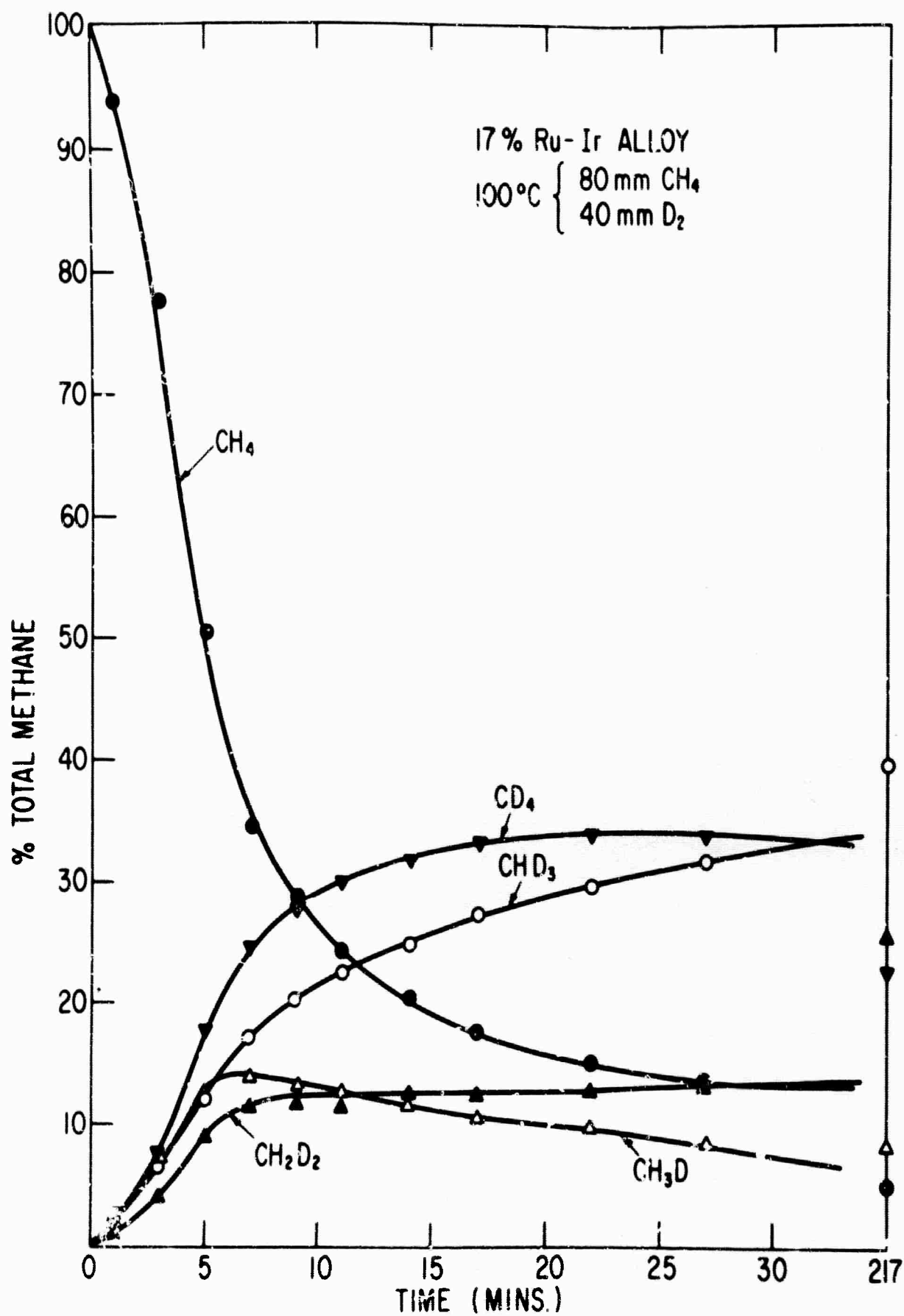


Fig. 72 CH₄-D₂ Exchange on 17% Ru-Ir Alloy, 100°C

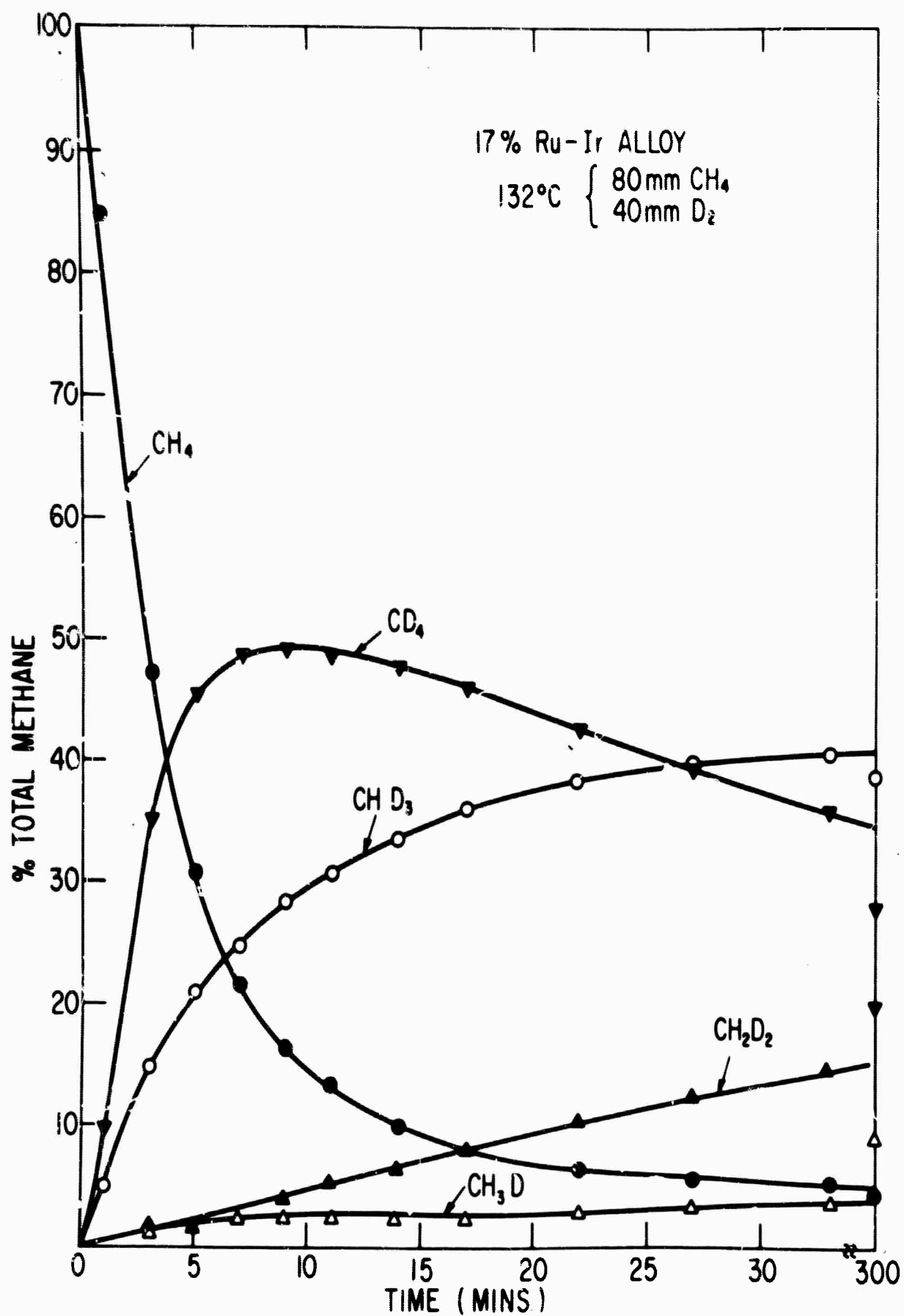


Fig 73 CH₄-D₂ Exchange on 17% Ru-Ir Alloy, 132°C

the decomposition products or on the energetics of the dissociation process over a wide range of temperature.

In an attempt to investigate the effect of molecular structure on the mechanism of hydrocarbon decomposition on a metal surface, the kinetics of cracking and the extent of adsorption of n- and iso-butaness on platinum black have been studied over the temperature range 0 to 180°C. As only preliminary results were included in the previous report, a more detailed account of this investigation is given below.

1. Experimental

a) Materials

The platinum black used in this work was obtained from Fisher Co., and was part of the same batch used in previous investigations (4). The unreduced black as received had a B.E.T. nitrogen surface area of 19.5 m²/g. but in order to eliminate sintering during the catalytic experiments, the metal was initially subjected to a standard reduction-evacuation procedure. After sealing 0.8–0.9 g. of the black into the vacuum system, evacuation was carried out at 150° overnight to a pressure below 1×10^{-6} mm. After cooling to room temperature, 10 cm. of dry nitrogen was admitted to the sample and pure hydrogen was allowed to flow slowly into the catalyst chamber through a palladium leak. The presence of nitrogen tended to moderate the initial sintering of the catalyst. After reduction in flowing hydrogen at room temperature for one hour, the temperature of the sample was slowly raised to 150° over a period of 30 mins., the flow of hydrogen continuing during this time. Finally the catalyst was evacuated at 150° for several hours to a pressure below 1×10^{-6} mm. This procedure was found to reduce the surface area of the black to 7–8 m²/g. and no further changes in surface area occurred during the subsequent catalytic runs.

The normal and iso-butaness were Phillips "Research Grade" materials and had purities of 99.90 and 99.98 mol % respectively, the major impurities being the isomeric butaness. These gases were condensed, degassed and distilled into the apparatus from a liquid nitrogen trap.

b) Apparatus and Procedure

The adsorption apparatus and experimental techniques were essentially those described previously (4). Following sintering and reduction of the catalyst, in the case of adsorption measurements at low temperatures, increments of butane were added to the thermostated sample and either pressure followed as a function of time, or constant pressure, measurements were made after equilibration at the isotherm temperature. Temperature control was generally made to within 0.5° and pressure measurements to ± 0.01 mm. At higher temperatures, where decomposition was appreciable, samples of the gas phase were condensed, after suitable time intervals, in cooled demountable traps attached to the apparatus and the contents analyzed in

(4) D. W. McKee, J. Phys. Chem. 67, 841 (1963); 67, 1336 (1963).

an F & M Temperature Programmed Gas Chromatograph Model 300, using an 8 ft. silica gel column. The residual noncondensable gas after cooling to -195° was always found to be methane, no gas phase hydrogen being detected in any of the cracking experiments. The initial dose of butane admitted to the samples in these runs was adjusted to $3.0 \pm 0.2 \times 10^{19}$ molecules and analysis of the gas phase was usually carried out after a 60 min. contact period. It was found, however, that at the higher temperatures where the initial pressure decrease due to adsorption was negligible, the rate of pressure rise was an accurate measure of the rate of formation of methane in the gas phase.

As in previous studies, it was found that cracking of hydrocarbons led to the deposition of carbonaceous material on the metal surface which could only be slowly and often incompletely removed by hydrogen reduction at elevated temperatures. In fact, as discussed below, poisoning of the catalyst by carbonaceous residues appeared to be more pronounced with butane than with lower molecular weight hydrocarbons. For this reason a new sample of platinum black was generally used after each high temperature cracking experiment. Following adsorption measurements at temperatures below 80° , adsorbed hydrocarbons could be completely removed by evacuation and reduction of the metal at 150° and hence the same sample could be used for a series of adsorption experiments.

2. Results

a) Adsorption of Butanes on Platinum Below 60°

Adsorption of n- and iso-butaness was found to occur readily on the sintered platinum black samples at temperatures in the range 0 to 60° . With each increment of adsorbate the gas pressure fell to an equilibrium value in 10 to 20 mins. and in this way the typical isotherms shown in Figs. 74 and 75 were measured. The isotherms were entirely reproducible after reduction with hydrogen for a few minutes at 100° followed by evacuation at this temperature, however, it was not generally found possible to desorb the hydrocarbon completely by evacuation at the isotherm temperature and this irreversibility became increasingly marked with increase in the adsorption temperature. The volumes of butane adsorbed at constant pressure decreased with increasing temperature as expected for physical adsorption. Average values for the isosteric heat of adsorption of n-butane dropped from around 9.5 kcals/mole at low coverages to values of about 6.5 kcals/mole around the B.E.T. monolayer capacity whereas the mean value for iso-butane was 11.2 kcals/mole. The heat of adsorption was thus significantly greater than the heat of liquefaction which is around 5 kcals/mole for both adsorbates. The isotherms showed no tendency to approach limiting values, suggesting that adsorption proceeded beyond the monolayer with both hydrocarbons. The values of the heats of adsorption and the general nature of the isotherms indicated that in this temperature range the adsorption was predominately physical in nature. However, the slow rate of desorption found at the higher temperatures suggested that some

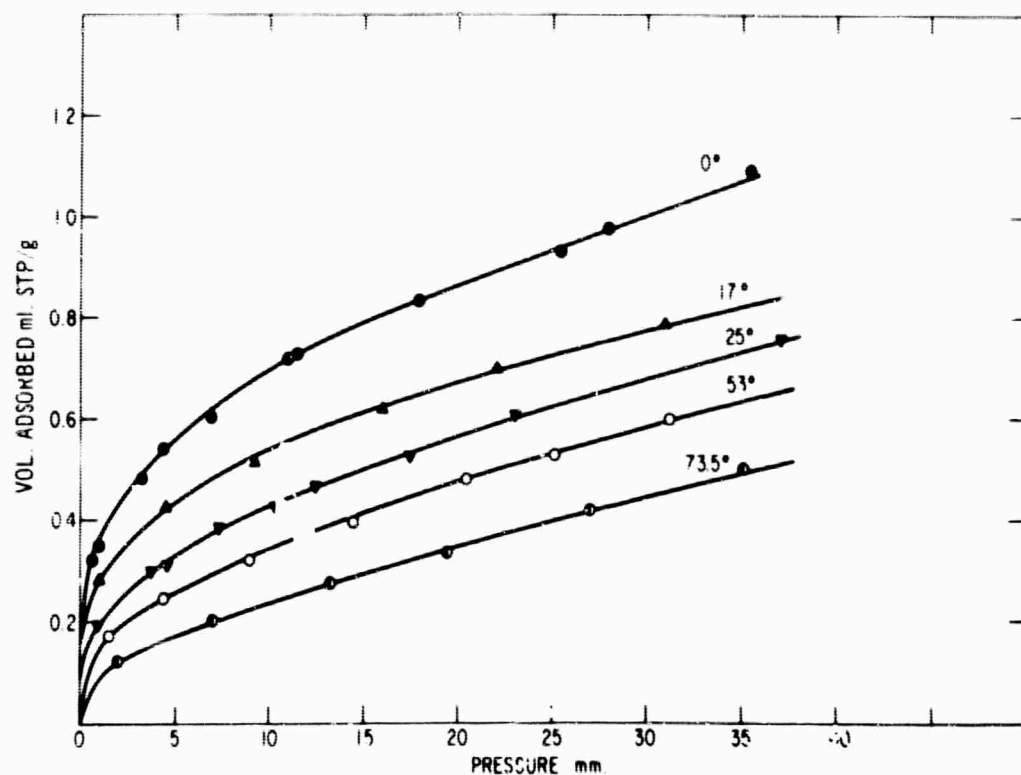


Fig. 74 Adsorption Isotherms of n-butane on Platinum Black. Surface area = $8 \text{ m}^2/\text{g}$

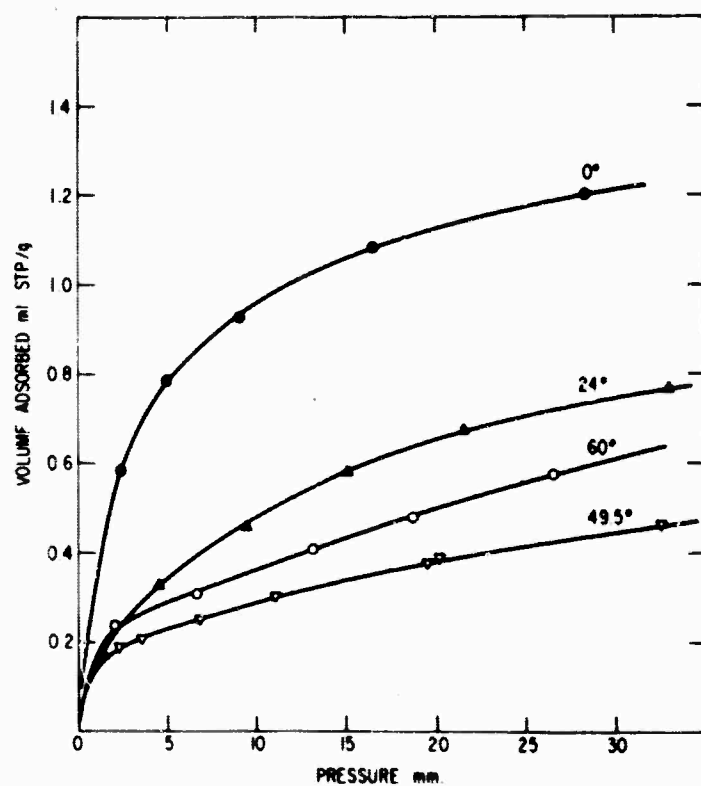


Fig. 75 Adsorption Isotherms of iso-butane on Platinum Black. Surface area = $8 \text{ m}^2/\text{g}$

chemisorption was taking place, the chemisorbed species being removed by hydrogen reduction but not by evacuation.

b) Adsorption and Decomposition of Butanes Above 80°

On admitting a sample of either butane to platinum black above 80°, the gas pressure over the metal at first decreased, reached a minimum value and then increased slowly with time. Subsequent analysis of the gas phase indicated the presence of decomposition products, mostly methane, with small quantities of ethane and propane. The rate of cracking of the hydrocarbon increased rapidly with increasing temperature. The onset of cracking is illustrated in Figs. 76 and 77, which also show the adsorption isobar for the two adsorbates at an equilibrium pressure of 10 mm. n-butane cracked more easily than iso-butane at temperatures above 120° but the distribution of products was similar in both cases. Below 120°, a greater proportion of propane and a smaller proportion of ethane was formed from iso-butane than n-butane.

Typical pressure vs. time curves for n-butane are shown in Fig. 78 at a series of temperatures. Below 80° the pressure fell monotonically with time as a result of adsorption of the hydrocarbon on the metal surface. Above this temperature the curves were composites of the pressure decrease due to adsorption and pressure increase due to the liberation of gaseous decomposition products. At temperatures above 130° where adsorption effects are negligible, the total

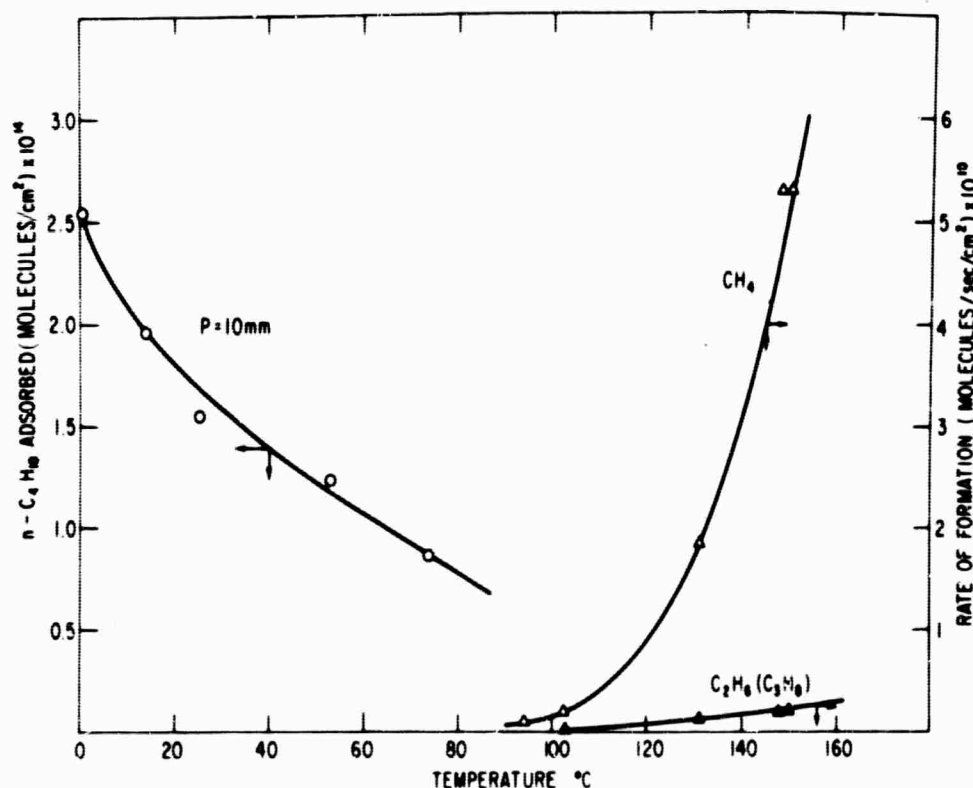


Fig. 76 Adsorption and Decomposition of n-butane on Platinum
(0.8-0.9g., 8 m²/g) n-butane admitted = 3×10^{19} molecules

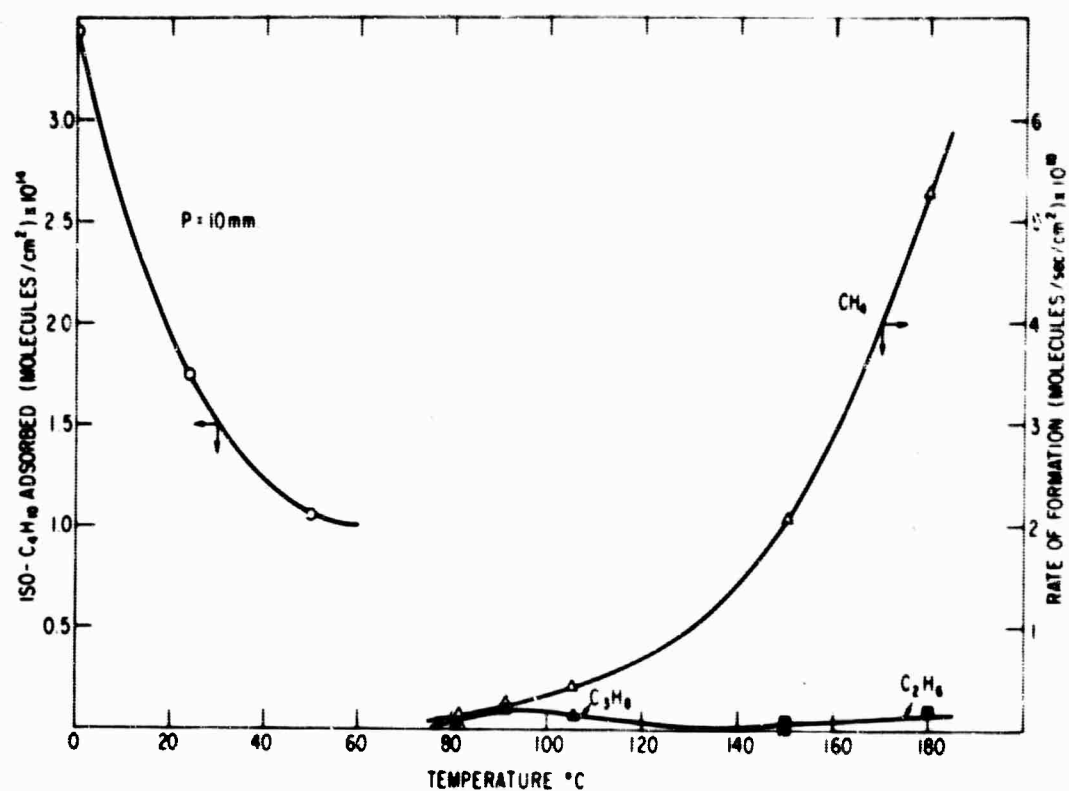


Fig. 77 Adsorption and Decomposition of Iso-butane on Platinum
(0.8-0.9g., 8 m²/g) iso-butane admitted = 3×10^{19} molecules

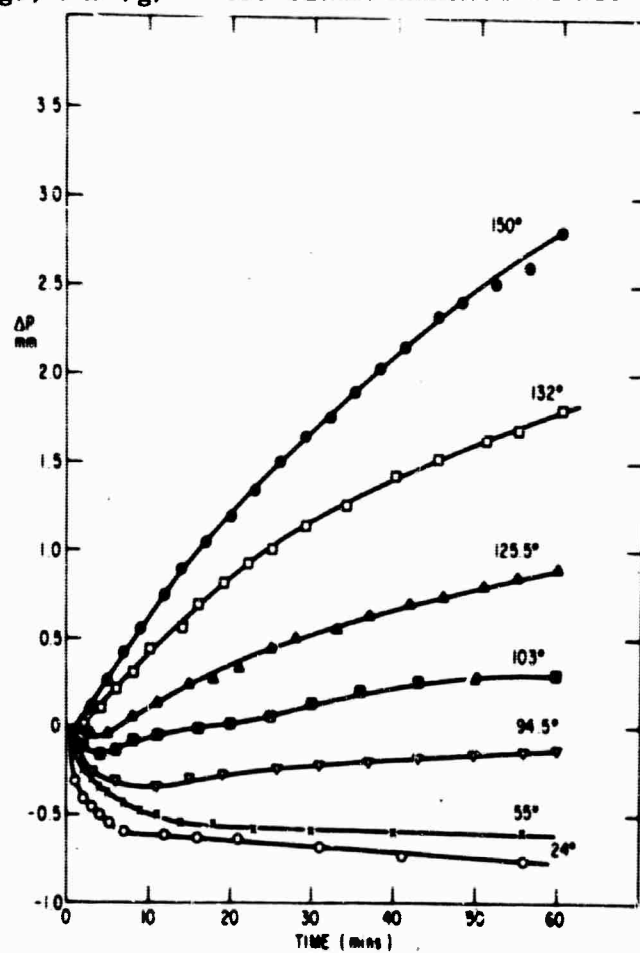


Fig. 78 Adsorption and Decomposition of n-butane. Pressure vs. time
n-butane admitted = 3×10^{19} molecules

increase in pressure over a 60 min. time interval agreed well with the pressure of methane found by analysis of the gas phase. The rate of pressure rise was not in general linear throughout this period due to the poisoning of the metal and retardation of the cracking reaction by carbonaceous residues which progressively built up on the catalyst surface.

A summary of results for several different samples of platinum black is shown in Table XIX. The second column gives the temperature of the run, the third and fourth columns the initial rate of pressure increase and the total pressure change after 60 mins. The remaining columns give the percentage composition of the gas phase at the end of this period.

TABLE XIX

Cracking of Butanes on Platinum Black

Catalyst Wt. = 0.8-0.9 g. Surface area = 7-8 m²/g.

Initial pressure of butane 12 ± 1 mm.

<u>Hydrocarbon</u>	<u>Temp.</u> °C	<u>(dΔP/dt)₀</u> mm/min	<u>ΔP</u> mm	<u>CH₄</u> %	<u>C₂H₆</u> %	<u>C₃H₈</u> %
n-butane	148	0.1	5.75	96.1	3.7	0.2
	131	0.049	1.82	88.7	6.4	4.9
	125.5	0.02	0.90	85.1	6.4	8.5
	110	0.02	0.71	73.7	15.8	10.5
	94.5	-	-	76.9	15.4	7.7
iso-butane	180	0.12	4.83	95.9	4.1	-
	150	0.056	2.45	88.9	6.0	4.9
	105	0.025	0.97	64.5	3.2	32.3
	91	0.020	0.77	55.1	4.1	40.8

At the lower temperatures, iso-butane gave a higher percentage of propane and a lower percentage of ethane than did n-butane.

Three different methods were used to estimate the activation energy of the cracking reaction. The rate of formation of methane was obtained from the initial rate of pressure rise over the metal $(\Delta P/dt)_0$, from the total increase in gas pressure after a 60 min. time interval, ΔP and from the total volume of methane formed during this period, V , as obtained by analysis. The first method was subject to errors at the lower temperatures due to initial adsorption of the hydrocarbon and the other two methods were rendered uncertain at high temperatures by the deposition of carbonaceous residues on the metal. A summary of the results obtained by the three methods is given in Table XX.

TABLE XX

Activation Energies for Methane Formation Rate

Reactant	$\log_{10}(\Delta P/dt)_0$	$\log_{10} \Delta P$	$\log_{10} V$
n-C ₄ H ₁₀	17.0	16.2	18.0
		Mean Value <u>17.1</u> kcal/mole	
iso-C ₄ H ₁₀	9.7	9.0	11.3
		Mean Value <u>10.0</u> kcal/mole	

n-butane showed a significantly higher activation energy than iso-butane. The corresponding mean frequency factors were 4.2×10^{19} and 3.2×10^{15} molecules/sec/cm² for the normal and iso-paraffin respectively.

c) Carbonaceous Residues

The chemisorption of the butanes and their decomposition above 80° was always accompanied by the build up of strongly adsorbed residues on the metal surface. This material had an overall C/H ratio between 0.8 and 1.2. After contact with butane at 100°, the metal could be completely reactivated by treatment with hydrogen for a few minutes at 100°, however more lengthy reduction was required after cracking runs at higher temperatures and, following butane decomposition at 150° and above, it became impossible to restore the metal to its original activity. The progressive poisoning of a platinum black sample on successive cracking runs with n-butane at 150° is illustrated in Fig. 79, the metal being reduced with hydrogen for several hours at 150° and then evacuated to 1×10^{-6} mm. after each run. The activity of the catalyst decreased rapidly in spite of this treatment and the proportion of ethane and propane in the products increased steadily.

3. Discussion

The behavior of butane at the surface of platinum black can be divided into three temperature regions.

1) Below about 50°, adsorption is mostly reversible, rapid, and probably physical in nature. The heats of adsorption are somewhat greater than expected for pure physical adsorption and as desorption becomes progressively slower on raising the temperature, it is likely that even at these temperatures there is some contribution from chemisorption. The monolayer capacities as calculated by application of the B. E. T. equation to the low temperature isotherms are shown in the third column of Table XXI below and the corresponding cross-sectional areas of the adsorbate molecules in the monolayer are given in the fourth column. These latter values are slightly smaller than the values calculated from the liquid density, assuming twelve nearest neighbors

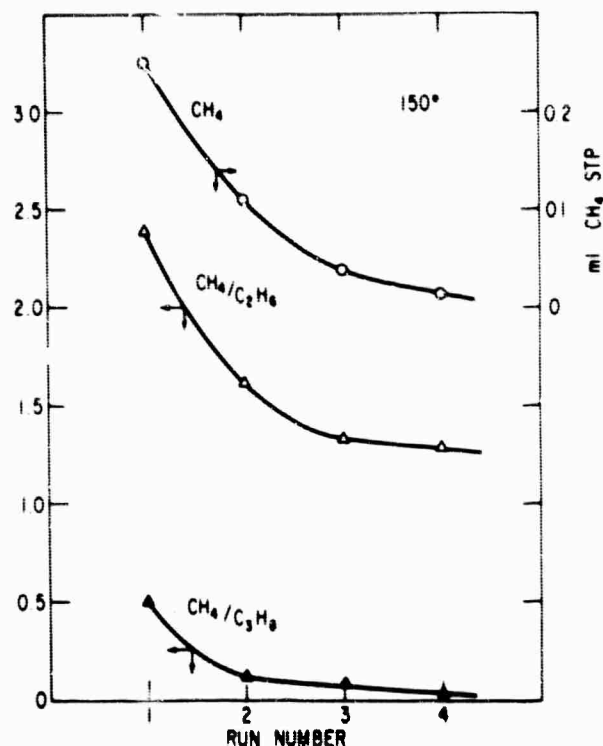


Fig. 79 Poisoning of Platinum by Carbonaceous Residues. Successive Cracking Runs with n-butane at 150°C.

(last column), suggesting that at 0° the adsorbate molecules are more tightly packed than in a condensed liquid.

TABLE XXI

Properties of Physically Adsorbed Butane Monolayers

<u>Adsorbate</u>	<u>Temp.</u>	V_m <u>ml. STP/g</u>	A_m <u>\AA^2</u>	A_L <u>\AA^2</u>
n-C ₄ H ₁₀	0°	1.0	27.7	32.1
	17°	0.87	31.9	
iso-C ₄ H ₁₀	0°	1.27	21.8	32.9

2) Between 50° and 80° the adsorption is still appreciable but irreversible. Although no gaseous decomposition products are detected in this range, chemisorption is certainly taking place, probably with some dissociation of C-H bonds in the surface layer. At these temperatures the metal is mostly covered with chemisorbed fragments. Thus an adsorption of 0.26 ml. STP/g on a surface of 7 m²/g amounts to 1.0×10^{14}

molecules/cm². Assuming that there are approximately 1.2×10^{15} Pt sites/cm², one adsorbed butane would occupy 12 metal sites.

3) Above 80° decomposition takes place with the formation of methane, small amounts of ethane and propane and the deposition of a carbonaceous residue on the metal surface. No hydrogen could be detected in the gas phase although the analytical method was rather insensitive to small amounts of hydrogen, chemisorbed hydrogen atoms were certainly present in the surface. No isomeric butanes were found in the products. The carbonaceous material on the catalyst could only be partially removed by hydrogenation and the fraction remaining irreversibly adsorbed increased with the temperature of decomposition.

The results indicate that the metal surface is substantially covered with a layer of chemisorbed material before decomposition of the hydrocarbon becomes appreciable. A similar conclusion was reached in the case of propane cracking on nickel (5). The extent of decomposition was greater for n-butane than iso-butane between 110 and 180° although the activation energy for methane formation was somewhat lower in the case of iso-butane. This difference may be related to the configuration of the hydrocarbon molecule, the branched chain conferring additional stability. Thus the free energy of formation of iso-butane is less than that of n-butane below about 170° (6). However, the thermodynamic stability of the molecules may not be related to the ease of dissociation of C-H bonds. Thus Galwey and Kemball (7) report that dissociative chemisorption takes place more readily with 2-methylbutane than with n-pentane over supported nickel and results of exchange experiments of iso-butane with deuterium have indicated that on some metals exchange of the tertiary hydrogen atom occurs much more rapidly than the primary hydrogens (8). It is possible that the higher isosteric heat of adsorption observed with iso-butane than with n-butane is traceable to the lower energy of dissociation of the tertiary hydrogen in the former case.

The reaction rates and product distributions in this work are quite different from those observed in the case of hydrocracking by Anderson and Baker (9) on platinum films in the presence of a large excess of hydrogen. The rates were generally considerably greater in the latter case and it is likely that the excess hydrogen tends to keep the metal surface free of carbonaceous residues. The rate determining step of the overall reaction is probably different for hydrocracking and the proportion of higher molecular weight products tends to be greater.

(5) D. W. McKee, J.A.C.S. 84, 4427 (1962).

(6) National Bureau of Standards Circular C461, 1947, p. 352.

(7) A. K. Galwey and C. Kemball, Trans. Faraday Soc. 55, 1959 (1959).

(8) C. Kemball, Proc. Roy. Soc. (London), A229, 377 (1954).

(9) J. R. Anderson and B. G. Baker, Proc. Roy. Soc. (London), A271, 402 (1963).

as a result of potential dependent removal of surface species, would tend to become more pronounced with higher molecular weight hydrocarbons. Further information on the nature of these species and the kinetics of their removal under a variety of conditions are needed before these complex processes can be completely understood.

B. Flash Desorption Apparatus

Important information on the nature of chemisorbed species on metals has recently been obtained by application of the flash-desorption technique (12). In this method the rate of desorption of gases from a metal filament is measured during the application of a temperature pulse to the filament. Quantitative information and the activation energy of desorption can be obtained if the filament temperature is increased linearly with time. A modification of this technique by Cvetanovic and Amenomiya (13) using a much slower rate of temperature increase has been used to obtain information on the nature of chemisorbed olefins on alumina. An apparatus based on this principle has been constructed for use with metal powders and preliminary results have been obtained for the adsorption of ethylene on platinum black.

The apparatus is shown in Figure 80. The right hand side is composed of a series of gas burettes and manometers for introducing measured doses of adsorbate to the catalyst contained in the central adsorption cell. Following admission of the hydrocarbon, the metal sample is evacuated at room temperature to remove excess adsorbate and then a stream of dry helium is allowed to pass over the metal at a constant rate. When the catalyst temperature is raised at a uniform rate by means of the temperature programmer, desorbed material is carried in the helium stream through a thermal conductivity cell, the response of which is plotted on a recorder chart. Since the flow rate of helium is constant, the deflection of the recorder due to the presence of desorbed hydrocarbon in the carrier gas should be proportional to the rate of desorption. The rate of desorption increases with temperature at first but eventually begins to decrease as a result of depletion of adsorbed material, so that a peak is recorded. The recorded peaks are referred to as the flash-desorption chromatogram. The temperature at which the peak maximum occurs is related to the activation energy of desorption, E_d by the equation

$$2 \log T_m - \log \beta = \frac{E_d}{2.303RT_m} + \log\left(\frac{E_d v_m}{R K}\right)$$

where T_m = the peak temperature,

β = the rate of temperature increase,

(12) G. Ehrlich, J. Chem. Phys. 34, 29, 39 (1961). P. A. Redhead Trans. Faraday Soc. 57, 641 (1961).

(13) Y. Amenomiya and R. J. Cvetanovic J. Phys. Chem. 67, 144 (1963).

v_m = the volume of hydrocarbon adsorbed at complete coverage,

K = a constant.

In the present apparatus, the rate of temperature increase can be varied from 0.5° to 30°C/min.

A typical flash desorption chromatogram for ethylene adsorbed on platinum black is shown in Fig. 81 (A) for one rate of temperature rise. Approximately 10 cm. of ethylene were allowed to stand over the freshly activated metal for 15 min. at room temperature, before evacuation at the same temperature for a further 30 min. Interpretation of the chromatogram is complicated by the fact that decomposition of the ethylene takes place at elevated temperature, the desorbed phase consisting of ethylene, methane, ethane and possibly hydrogen (14). Nevertheless, the chromatogram consists of a single peak, the maximum rate of desorption occurring at a temperature of about 180°C. This situation may be compared with the flash-desorption chromatogram of ethylene on alumina shown in Fig. 8 (B). In this case two distinct peaks are observed, representing different adsorption sites on the alumina surface, the largest peak probably corresponding to physical adsorption. The smaller peak, however, still persists after prolonged evacuation at 100°C after adsorption and represents strong chemisorption with a heat of adsorption of 36.4 kcal/mole. In the case of adsorption on platinum, the position of the peak suggests a somewhat lower heat of adsorption, however the adsorption is somewhat irreversible as the area under the peak decreases on successive runs. It is likely that carbonaceous material is accumulating on the metal surface. The kinetics of hydrogenation of these residual fragments can be measured by substituting hydrogen for helium as the carrier gas. Such information is of importance in understanding the mechanism of the dissociative adsorption of hydrocarbons on metals.

C. Adsorption and Catalytic Properties of Boron Carbide-Supported Platinum

Considerable interest has recently arisen in the use of finely powdered boron carbide as a catalyst substrate for low concentrations of platinum and other active metals. (15) Encouraging performance has been obtained with electrodes containing only small amounts of platinum supported on boron carbide in fuel cells running on hydrogen and propane (Section 4.2.2). It is therefore of considerable importance to study the nature of platinum on this substrate, the effective area of active metal as a function of platinum loading and the rate of sintering or growth of platinum crystallites as a function of temperature. Preliminary results have been obtained by application of gas adsorption techniques.

(14) D. W. McKee, J.A.C.S. 84, 1109 (1962).

(15) Technical Summary Report No. 5, June 30, 1964, Contract No. DA-44-009-ENG-4909, p. 4-27.

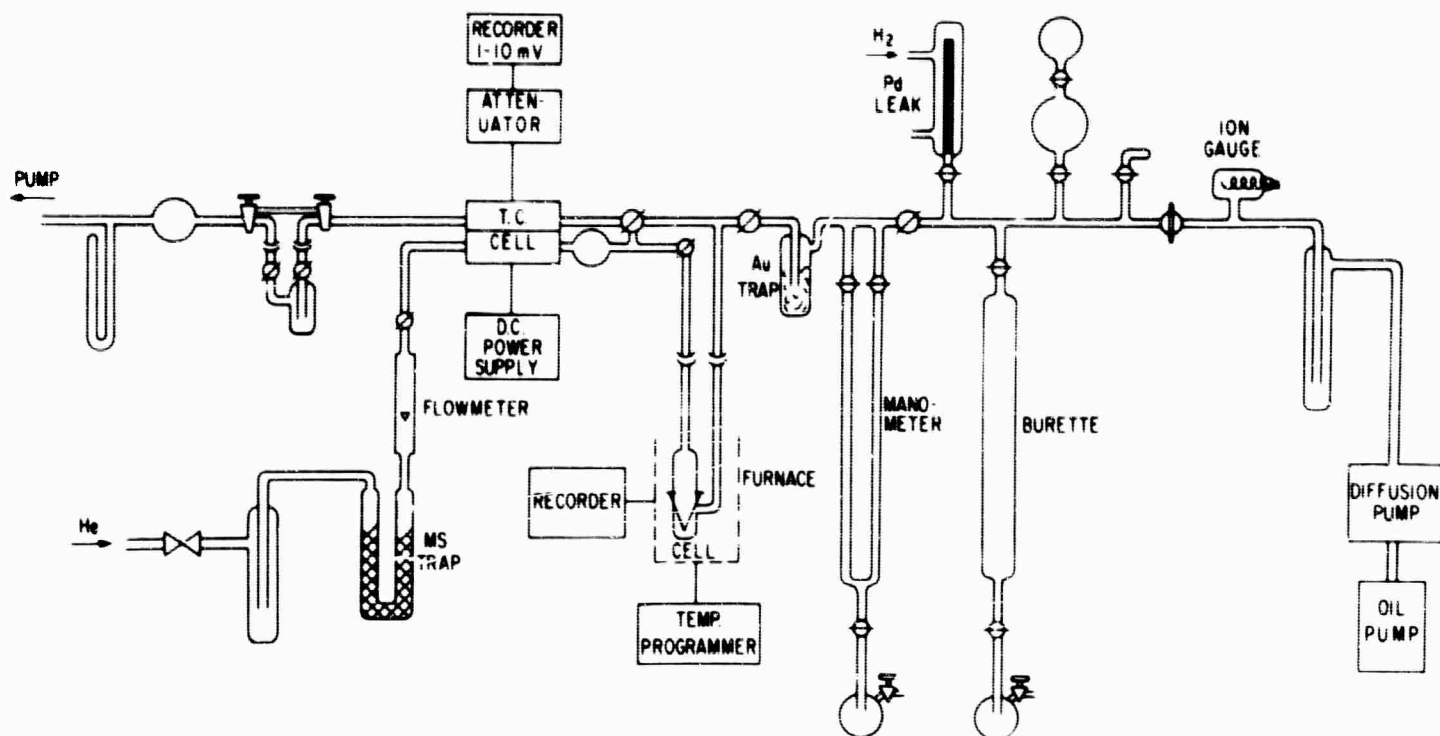


Fig. 80 Flash Desorption Apparatus

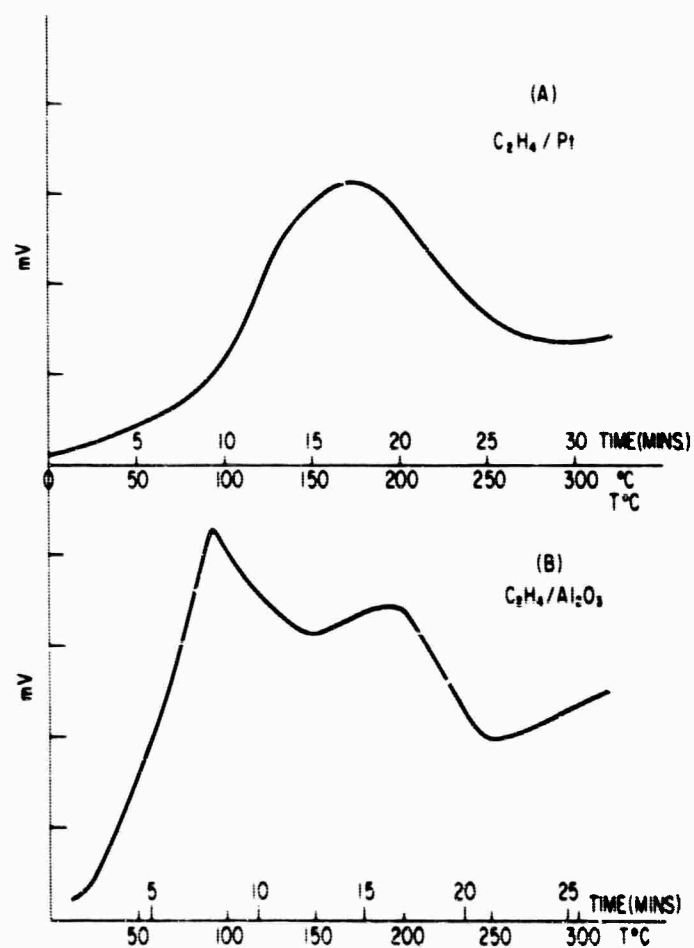


Fig. 81 Flash Desorption Chromatograms: (A) Ethylene on Platinum Black, (B) Ethylene on Alumina

1. Experimental

Five samples have been used to date, these contained 0, 0.5, 2.0, 4.8 and 9.1 wt. % platinum respectively deposited on the boron carbide by means of thermal decomposition of $\text{Pt}(\text{NH}_3)_2(\text{NO}_2)_2$ salt. Each sample was sealed into the adsorption apparatus and evacuated at 150°C overnight to a pressure less than 1×10^{-6} mm. The adsorption of nitrogen at -195°C was then measured on each sample and the total surface area evaluated by application of the B. E. T. adsorption equation (16). The samples were then heated and evacuated at 170° , and reduced at this temperature in a stream of pure hydrogen for one hour. Finally the samples were evacuated again at 170° for a further hour. The adsorption of hydrogen at 170° was then measured on each catalyst sample. The volume of hydrogen adsorbed gives a measure of the effective area of the platinum in each sample.

The samples were then heated and evacuated at 200°C and the rate of exchange of deuterium and methane was measured at this temperature using an initial mixture of 40 mm. D_2 and 80 mm. methane. The rate of this reaction, expressed in the specific units, molecules/sec/cm², gives a measure of the activity of each sample for the dehydrogenation of a simple hydrocarbon.

2. Results

The chemisorption of hydrogen has frequently been used in the past to determine the effective area of the metallic component of a supported catalyst, such as platinum dispersed on alumina (17). The method requires that hydrogen form a complete monolayer on the metal surface, each adsorbed hydrogen atom occupying one surface metal site. Assuming a reasonable value for the number of metal atoms per cm², the effective area of the metal can be calculated. The volume of nitrogen physically adsorbed at its boiling point gives the total surface area of the catalyst sample. The metallic phase is probably dispersed on the substrate in the form of small crystallites and the average size of these deposits can be obtained from the adsorption data by assuming that each crystallite is a cube of side d with five exposed faces, one being in contact with the support. The exposed surface is then $5d^2$ the weight being $d^3\rho$ where ρ is the density of the metal. Thus the average crystallite size is $5/S\rho$ where S is the surface area of the metal per gram. The results found for three Pt- B_4C samples are shown in Table XXII. The total surface area of the substrate was $11.9 \text{ m}^2/\text{g}$. The third column shows the volume of hydrogen adsorbed/g. of sample. The last four columns give the effective area of the platinum, the total Pt area per g. of sample, the average Pt crystallite size and the rate of $\text{CH}_4\text{-D}_2$ exchange at 200°C .

(16) S. Brunauer, P. H. Emmett and E. Teller J.A.C.S. 60, 309 (1938).

(17) L. Spenadel and M. Boudart, J. Phys. Chem. 64, 204 (1960).

TABLE XXII

Properties of Pt-B₄C CatalystsSurface area of substrate 11.9 m²/g.

Sample No.	Wt. % Pt	H ₂ Adsorbed ml. STP/g	Surface Area Pt m ² /g Pt	Total Pt Area m ² /g sample	Pt Cryst. Size Å	Rate of Exchg. 200°C moles/sec/cm ²
B ₄ C	-	0.041	-	-	-	-
14	0.5	0.197	149	0.75	16	1.7×10^9
21	2.0	0.310	65.3	1.31	36.5	7.5×10^9
19	4.8	0.679	63.5	3.05	38	12.0×10^9
20	9.1	1.007	50.7	4.61	47	15.2×10^9

The catalyst containing 0.5 wt. % Pt exhibits a very high degree of dispersion of the metal, however the Pt content of this sample is too low to give rise to appreciable rates of CH₄-D₂ exchange and would be expected to be quite inactive in the hydrocarbon fuel cell.

On increasing the loading of platinum the specific surface area decreases as the crystallites grow in size. It is interesting that the average crystallite size of sample 19, obtained from electron micrographs (Section 4.2.2) agrees well with the value obtained from adsorption measurements. In both sample 19 and 20, the surface area of the platinum is about twice as great as that of a commercial platinum black and as expected an electrode made of this material is more active, per unit weight of platinum, than a conventional Pt black electrode. The effective surface area of the Pt on these samples may be tending to a limit of about 40 m²/g at high loadings. The rate of CH₄-D₂ exchange is roughly proportional to the total Pt area of the samples and to the current density obtained from fuel cell electrodes made of the same material. (Section 4.2.2.) This finding confirms again that the rate of the exchange reaction is a useful criterion for predicting electrocatalytic activity. Additional work along these lines is planned for boron carbide impregnated with platinum alone and in combination with other active metals.

The use of hydrogen chemisorption in the determination of the effective area of the metallic component of a supported catalyst is subject to the assumption that activated diffusion of adsorbed hydrogen atoms away from the metal sites along the substrate surface does not occur. This assumption has recently been shown to be invalid for the case of platinum dispersed on carbon, where a slow uptake of hydrogen apparently arises from the migration of hydrogen atoms from the metal to the carbon surface (18). This effect does not seem to occur with alumina and in the present case the rate of hydrogen adsorption was always quite rapid. Also the volumes of hydrogen adsorbed and the sizes of the platinum crystallites are consistent enough with electron micrographs of the samples to suggest that surface migration of hydrogen is not an important factor with this substrate.

(18) A. J. Robell, E. V. Ballou and M. J. Boudart, J. Phys. Chem. 68, 9 (1964).

4.2.1.3 Conclusions

Ruthenium has the unique property among the platinum metals of promoting the catalytic activity of other metals of the group when combined in alloy form. Thus the dehydrogenation activities of the alloys Pt-Ru, Ir-Ru and Pd-Ru, as measured by the rate of methane-deuterium exchange, are greater than pure platinum over certain composition ranges. It is to be expected that the activity of these alloys in hydrocarbon fuel cells would show similar trends.

Results of a study of the adsorption and decomposition of butanes on platinum black show that n-butane generally cracked more easily than the branched chain isomer, but both were less stable than propane under the same conditions. The rates of decomposition were generally determined by the kinetics of removal of residual carbonaceous material, the strength of binding of which to the metal surface generally increased with the molecular weight of the hydrocarbon.

A high degree of metallic dispersion can be obtained for platinum supported on boron carbide. The effective area of the platinum approaches $150 \text{ m}^2/\text{g}$ with samples containing 0.5 wt. % Pt, but the metal area decreases with increasing platinum content as the metallic crystallites grow in size. The catalytic activity as measured both by methane-deuterium exchange and by fuel cell performance seems to be a function of total platinum effective area.

4.2.2 Platinum Activated Boron Carbides (Dr. Grubb/J.G. Lucas/R.M. Hadsell)

Data in the preceding report of this series indicated that platinum activated, boron carbide, Teflon-bonded electrodes are promising for acid or alkaline electrolyte hydrogen-oxygen cells at room temperature. Such electrodes prepared by the standard procedure (1) were found to be unsuitable for high temperature operation because they delaminated, i.e., the Teflon-bonded catalyst layers blistered and broke away from the supporting screen. When the blisters ruptured, massive leakage of electrolyte through the electrode occurred, and it became useless for further operation. Previous work was confined to activation at a very small platinum content only 1/2 percent of the boron carbide by weight. For unknown reasons, the delamination of the structure seemed to be aggravated by the incorporation of larger amounts of platinum. This problem was therefore a serious obstacle to be solved before boron carbide electrodes could be successfully evaluated on hydrocarbons.

A series of electrodes was investigated using the standard technique of preparation at the 0.5 wt. % platinum loading in order to optimize some of the variables of the catalyst preparation and some of the electrode composition variables. Following this series of runs, the delamination problem was solved, and the results obtained in hydrogen-oxygen cells on boron carbide electrodes of various platinum contents are reported.

-
- (1) Saturated Hydrocarbon Fuel Cell Program, "A New High Performance Fuel Cell Employing Conducting-Porous-Teflon Electrodes (Niedrach-Alford) and Liquid Electrolytes" Contract No. DA 44-009-AMC-479(T), ARPA Order Number 247, Project No. P4980.

Initial performance data for propane in H_3PO_4 cells at $150^\circ C$ are presented. They indicate that the platinum supported on boron carbide is up to 10 times as effective in promoting the electro-oxidation of propane as the commercial platinum black used in our standard electrodes. Since these are initial results, further improvement may be possible.

4.2.2.1 Survey of Variables With Standard Electrodes

A survey of variables was carried out using electrodes prepared by the standard procedure. The electrodes were prepared from boron carbide activated with 0.5 weight percent platinum and tested on hydrogen and oxygen at room temperature. The variables evaluated were:

- 1) the source and mesh size of boron carbide powder;
- 2) various pretreatments of the boron carbide;
- 3) the platinum salt used for activation;
- 4) hydrogen reduction variables;
- 5) electrode pressing variables such as time, temperature, and press force.

The range of performance of these electrodes on hydrogen or oxygen in 6N sulfuric acid or 5N potassium hydroxide electrolyte at room temperature are presented in Figs. 82 through 85. Electrode #57 exceeds the performance of the best electrode (#28) of the previous report (2), and the worst electrodes in the survey are much worse than #28. The same electrode, #57, is best under 4 different conditions and electrode #39 was worst for 3 out of 4 conditions. The two worst electrodes were both prepared using solutions of chloroplatinic acid, while #57 and #28 were from boron carbide activated with a solution of diammino dinitrito platinum. Several electrodes prepared in the manner of #57 performed almost equally well.

This survey was by no means exhaustive. Nevertheless, the very good performance of electrode #57 at the low platinum loading of 0.16 mg/cm^2 indicates that the program of running 30 electrodes under 4 different cell conditions led to a reasonable degree of optimization in this very complex system.

Residual chloride remained in the electrodes activated with chloroplatinic acid even after long reduction in hydrogen at $400^\circ C$ and higher. This appears to have a detrimental effect on electrocatalytic activity in this system.

The resistivities of boron carbide powders varied widely among different sources and the activation with platinum had some effect on this parameter. A device for measuring the powder resistivities and some resistivity data are presented in Appendix 5.2.

(2) Hydrocarbon-Air Fuel Cells, Semi-Annual Technical Summary Report No. 5, pp. 4-29 - 4-37. ARPA Order No. 247, Contracts No. DA 44-009-ENG-4909, DA 44-009-AMC-479(T).

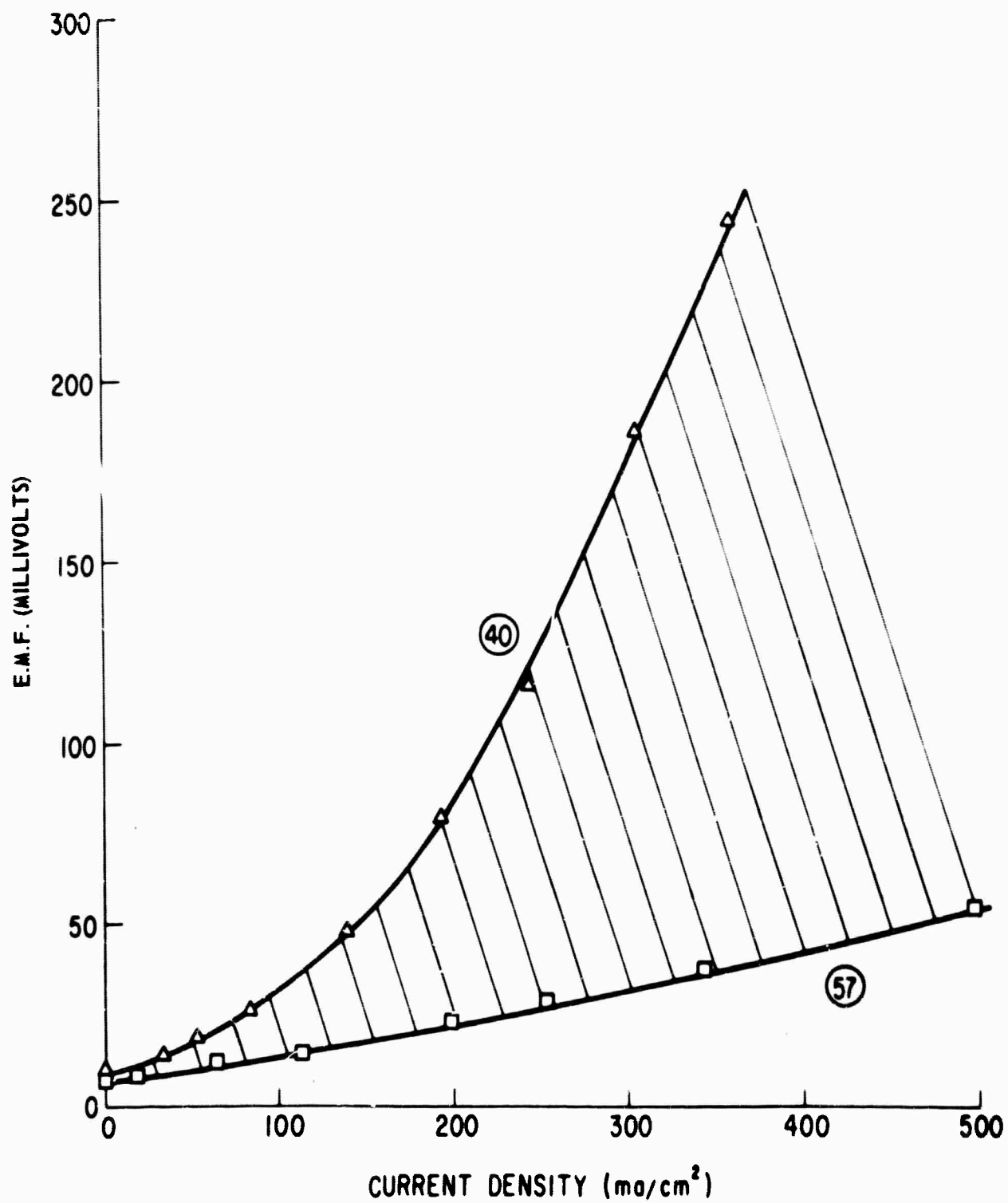


Fig. 82 Range of E_{AR} vs. C.D. for Pt Activated B_4C Electrodes at Pt Loading 0.16 mg/cm^2 $6N \text{ H}_2\text{SO}_4$, Room Temp.

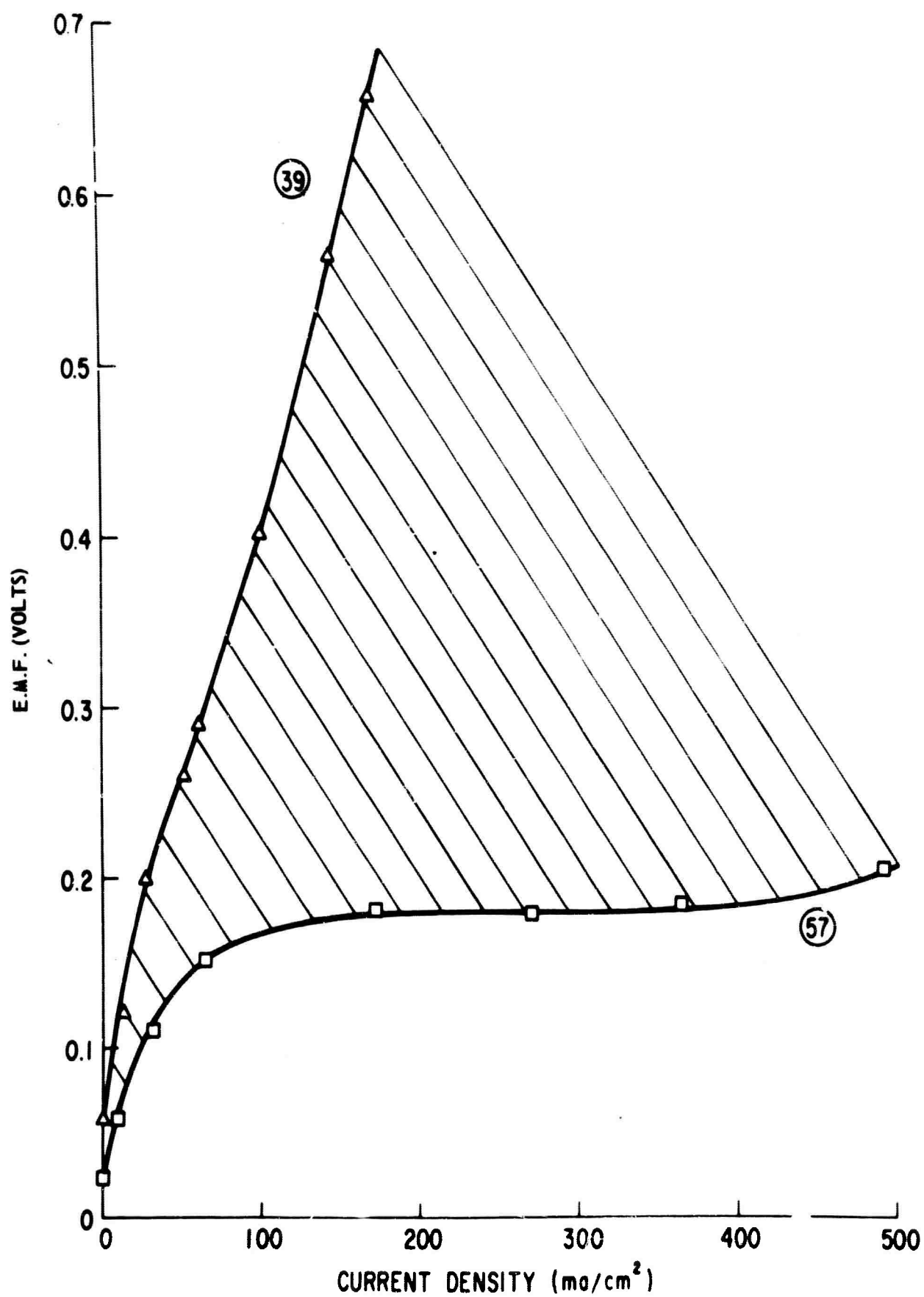


Fig. 83 Range of E_{AR} vs. C.D. for Pt Activated B_4C Electrodes at Pt Loading 0.16 mg/cm^2 5N KOH, Room Temp.

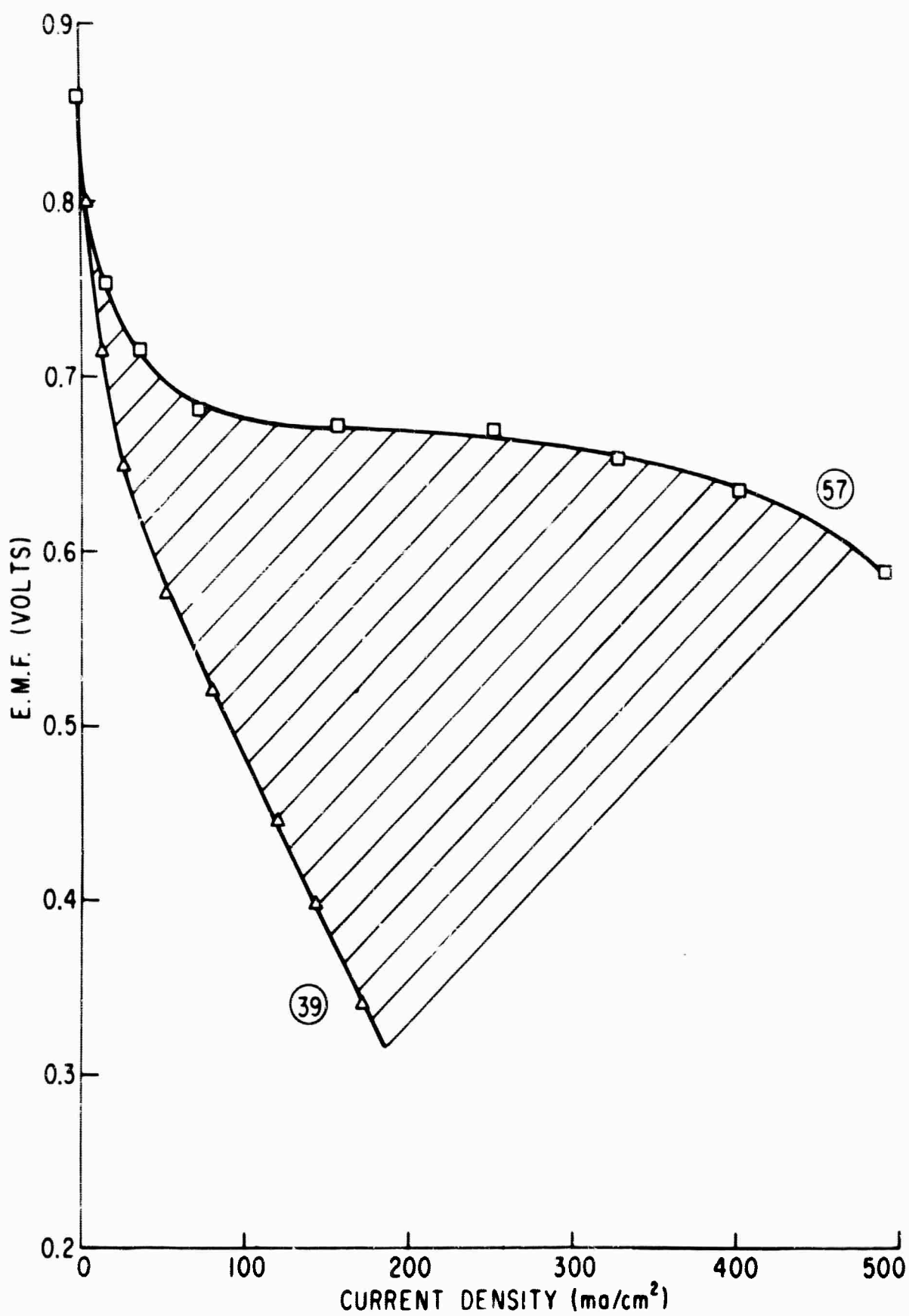


Fig. 84 Range of E_{CR} vs. C.D. for Pt Activated B_4C Electrodes at Pt Loading 0.16 mg/cm^2 $6N \text{ H}_2\text{SO}_4$, Room Temp.

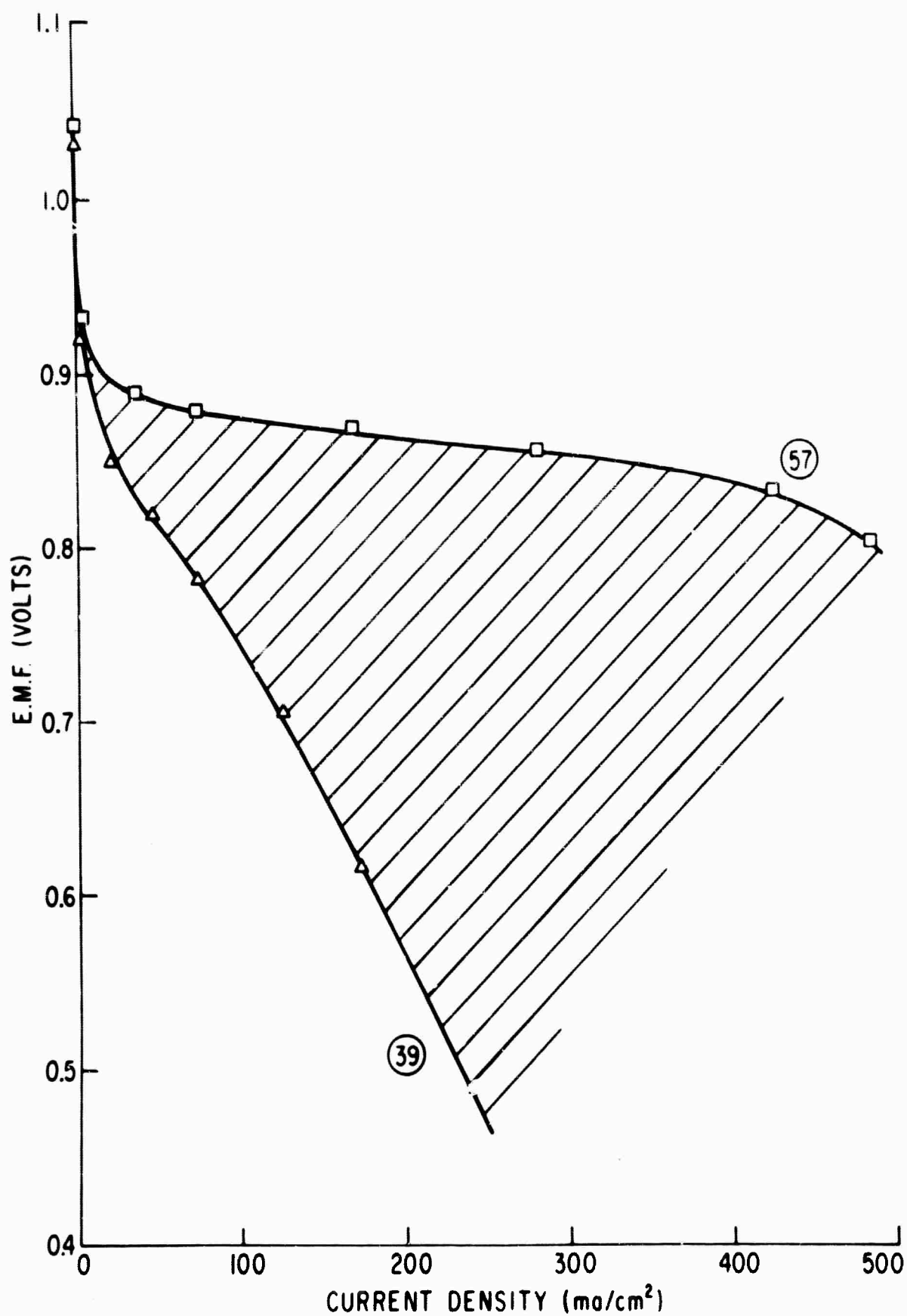


Fig. 85 Range of E_{CR} vs. C.D. for Pt Activated B_4C Electrodes at Pt Loading 0.16 mg/cm^2 5N KOH, Room Temp.

4.2.2.2 Results with Non-Delaminating Electrodes

A variation in the electrode preparation procedure (Appendix 5.2.1.4) produced non-delaminating electrodes that withstood operation at elevated temperatures. These were evaluated at several platinum loadings, on hydrogen and oxygen at room temperature. The results are presented in Figs. 86 through 89. Fig. 86 shows that the platinum activated boron carbide electrodes containing area platinum loadings 0.5 and 1.1 mg/cm² are equivalent to average or better than average standard platinum electrodes as hydrogen anodes in 6N sulfuric acid. Fig. 87 shows that the platinum activated boron carbide electrodes containing 1.1 and 2.2 mg/cm² are equivalent to average, or better than average, standard platinum electrodes as hydrogen anodes in 5N KOH. It further appears that 1.1 and 2.2 mg/cm² of platinum give essentially the same result. Such electrodes may be limited not by surface reaction rate but by other factors. These and higher platinum contents should be evaluated on fuels less reactive than hydrogen in order to determine the relative effectiveness of the surface activation.

Fig. 88 and 89 show the performance of electrodes of several platinum contents as oxygen cathodes in 6N sulfuric acid and 5N potassium hydroxide. In the acid electrolyte performance is rather markedly affected by the platinum loading. In alkali, the platinum loading hardly makes any difference in the range investigated. It will be recalled that the boron carbide itself is effective as an electrocatalyst for oxygen reduction in alkaline systems as observed in the preceding report.

The initial performance results with propane at 150°C in phosphoric acid are presented in Fig. 90. Performance is a strong function of platinum loading in this system, and the current density at anode vs cathode voltage of 0.5 volts is approximately linear with the platinum loading per unit area as shown in Fig. 91. It is of particular interest to note that the current density at 0.5 volts for a platinum loading of 2 mg/cm² is 10 ma/cm² and that for a standard platinum electrode it is about 20 ma/cm² for a platinum loading of 45 mg/cm². Thus, roughly 1/20 of the platinum loading gives 1/2 the current density and the platinum appears to be about ten times as effective in the B₄C electrode. However, the loads on the platinum activated boron carbide electrodes were not steady at values of cathode vs anode voltage below about 0.4 volts. This is unexpected and could be due to electrode structure effects. The load performance in the region indicated by the curves in Fig. 90 was however quite steady, and, for example, at point A anode number 89 was operated for 2 hours with essentially no change in performance, a promising indication. It is planned to continue the above studies to higher platinum contents.

Fig. 91 indicates a certain "efficiency" in the utilization of platinum which equals about 7 ma/mg for the electrode of 1.1 mg/cm² platinum loading for a propane-oxygen cell at 0.5 volts. A straight line drawn through the points in Fig. 91 indicates a slope of 5 ma/mg. Assumption of linearity up to high platinum loadings would suggest a very high performance at high platinum loadings. Five ma/mg of platinum for propane current at 150°C and at 0.5 volts cell potential is higher

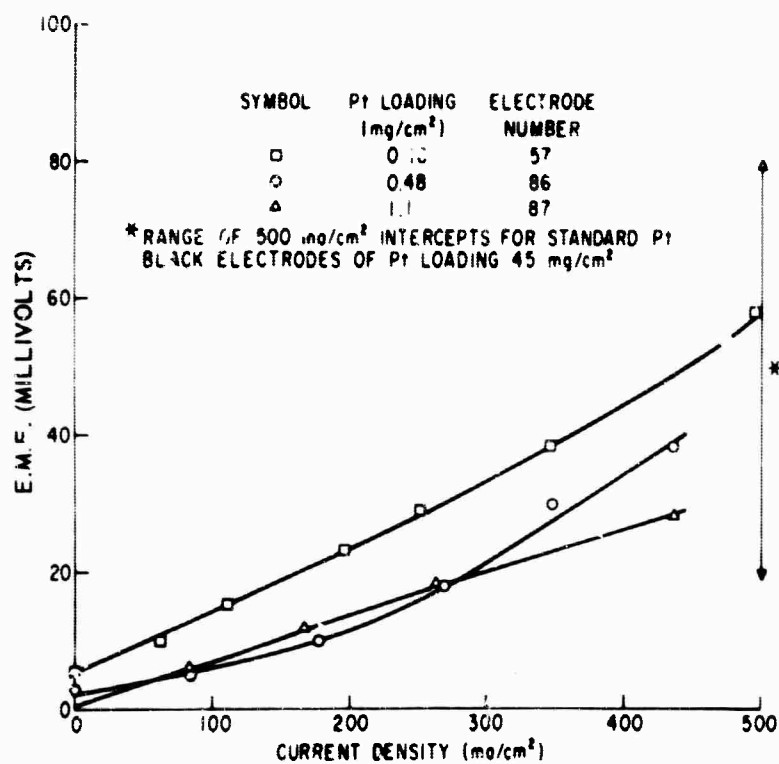


Fig. 86 E_{AR} vs. C.D. for Pt Activated B_4C Electrodes
 H_2 , 6N H_2SO_4 , Room Temp

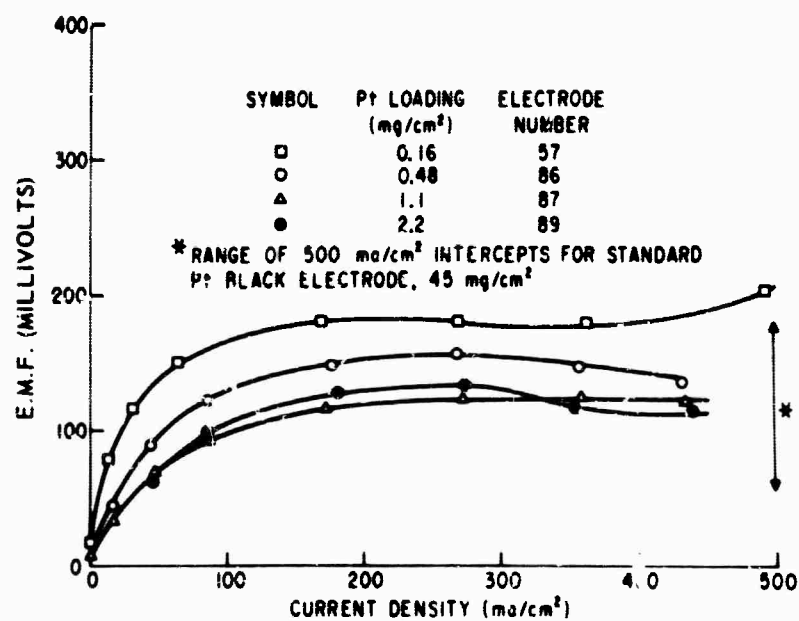


Fig. 87 E_{AR} vs. C.D. for Pt Activated B_4C Electrodes
 H_2 , 5N KOH, Room Temp.

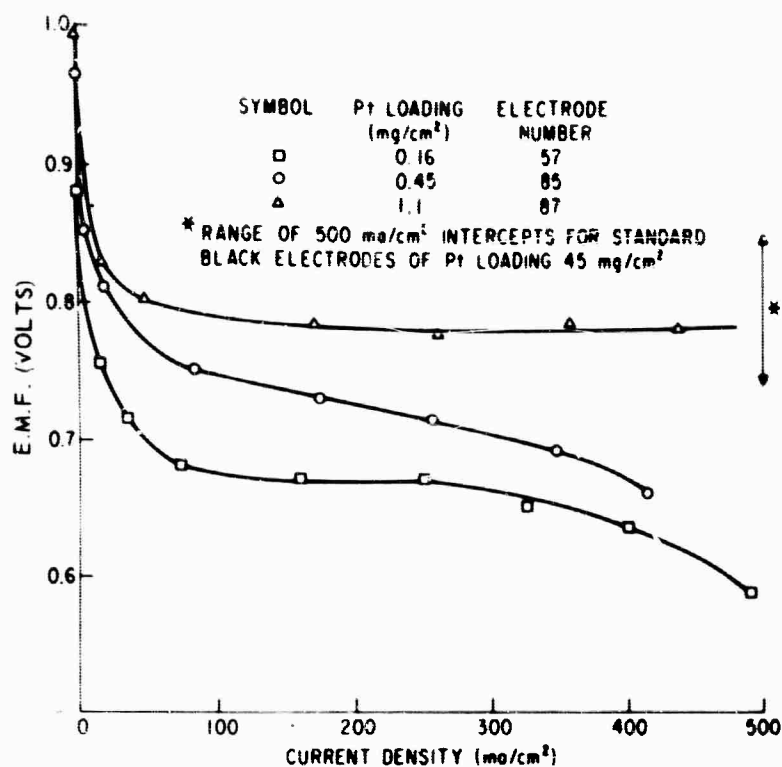


Fig. 88 E_{CR} Vs. C.D. for Pt Activated B_4C Electrodes
 O_2 , 6N H_2SO_4 , Room Temp.

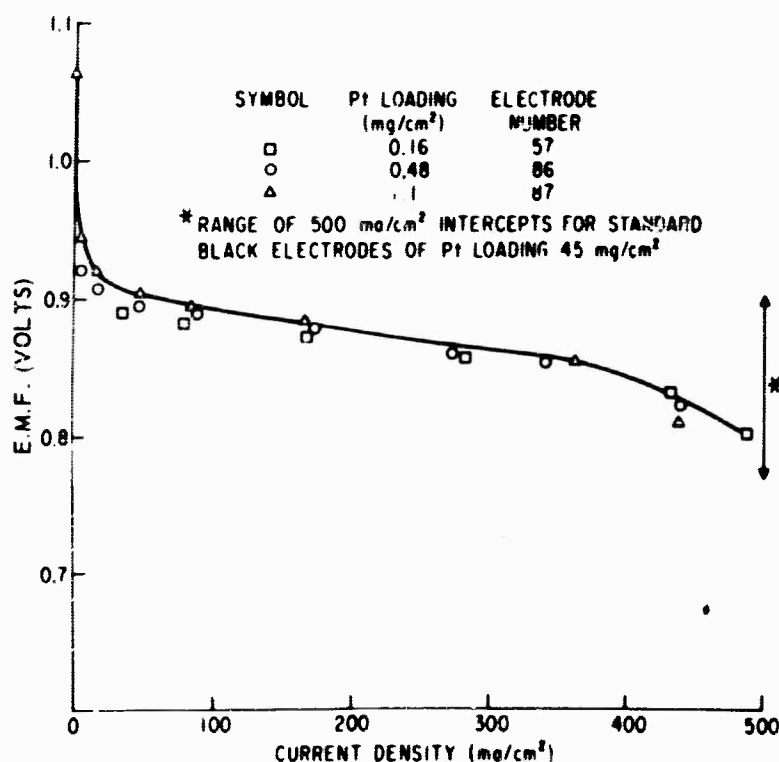


Fig. 89 E_{CR} vs. C.D. for Pt Activated B_4C Electrodes
 O_2 , 5N KOH, Room Temp.

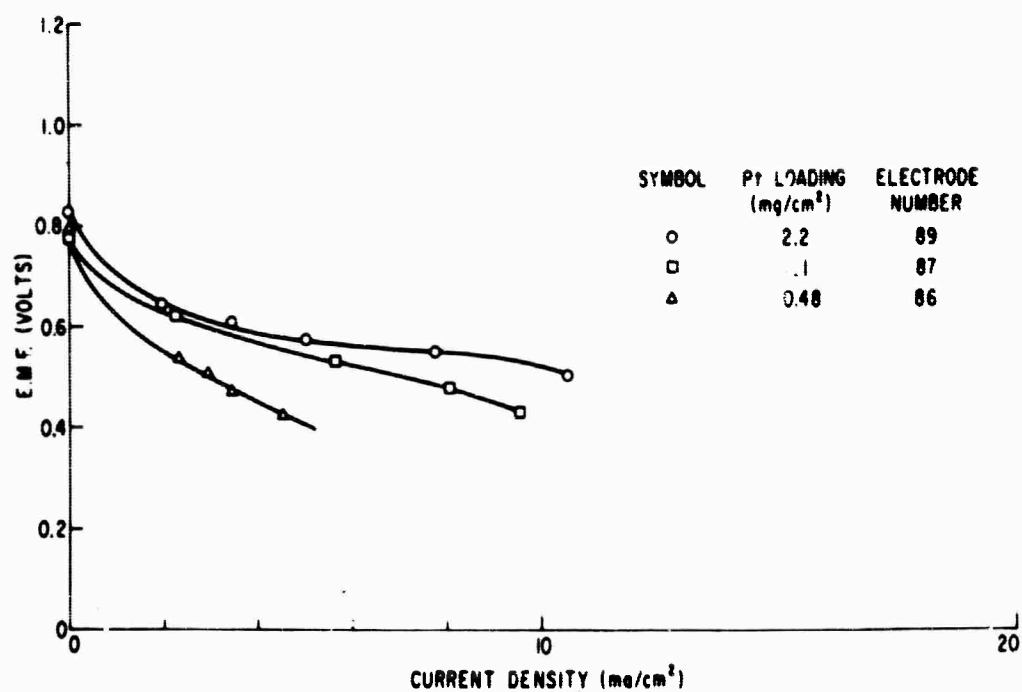


Fig. 90 E_{CA} vs. C.D. for $C_3H_8-O_2$ Cells with Pt Activated B_4C Anodes at $150^\circ C$ in 85% H_3PO_4

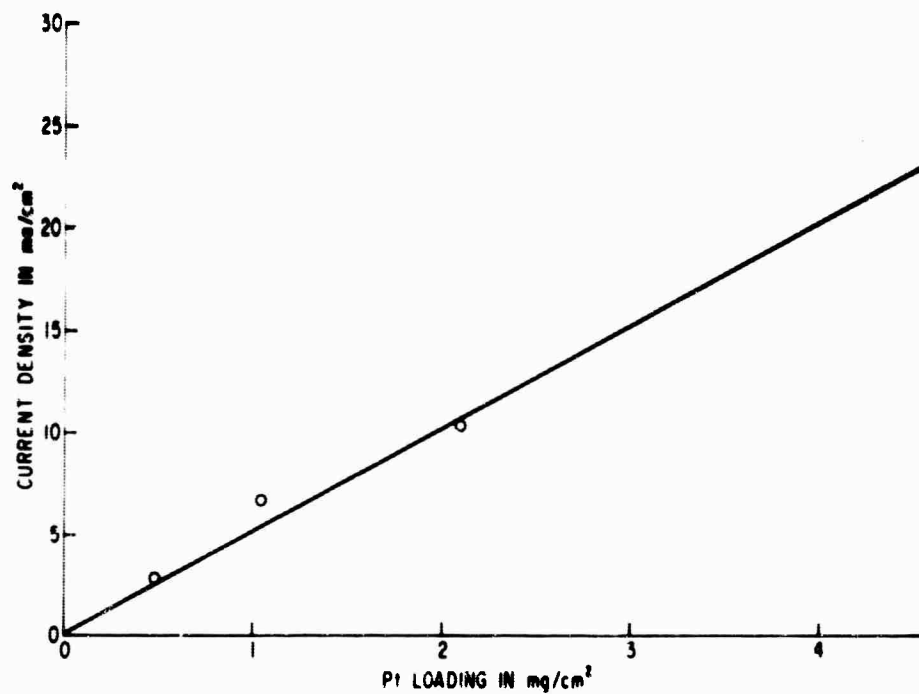


Fig. 91 C.D. at $E_{CA} = 0.5$ Volts vs. Pt Loading on B_4C Anodes for $C_3H_8-O_2$ Cells, 85% H_3PO_4 , $150^\circ C$

than that observed with electrodes containing mechanical mixture of platinum black with tantalum. Previously this system showed about 0.7 ma/mg of platinum for propane under these same conditions, and a mechanical mixture of platinum black with boron carbide gave similar results (3).

Whether we can expect constant high effectiveness of the platinum at higher surface coverages on the boron carbide brings up the question of the surface state of the platinum in these catalysts. Some information along this line has been provided by a measurement of the platinum surface area in a sample of boron carbide activated with 0.5 wt.% platinum (catalyst #14 used in electrode #57). By hydrogen adsorption (Section 4.2.1) a surface area for the platinum of 149 square meters per gram was determined. This is equivalent to an average spherical particle diameter for the platinum of about 16 angstrom units.

Further light is shed on the surface state of platinum on boron carbide by electron microscopy. Fig. 92 shows the starting boron carbide powder used in all of the electrodes of Figs. 86-89 and electrode #57 of Figs. 82-85. This material obviously possesses a wide range of particle sizes and some particles which are transparent to the electron beam. Since the X-ray diffraction diagrams of this material showed some carbon lines, the electron transparent particles may be wholly or partly graphite. It has been reported (4) that molten boron carbide on the carbon rich side of B_4C shows the separation of a lamellar graphite phase upon cooling.

Fig. 93 shows a higher magnification of a "transparent" particle from the boron carbide substrate. Fig. 94 is a higher magnification of a "transparent" particle from a boron carbide sample activated with 4.8 wt.% of platinum (catalyst #19). This is the catalyst used in the highly active electrode #87 of Figs. 86-89. The pattern of fine dots seen on all of the particles having some transparency in the electron micrographs of this material consists of small platinum crystallites. The magnification of Fig. 94 is 100,000. On this scale 1 mm = 1000 Angstrom units. The size of the small dots of platinum is consistent with the average particle diameter estimated from hydrogen adsorption.

The degree of activation of boron carbide by small weight percentages of platinum is quite phenomenal. As a hydrogen anode in $6NH_4SO_4$, unactivated boron carbide produced a current density of about 0.04 ma/cm² at 60 millivolts overvoltage. With only 0.16 mg/cm² of platinum the current density was 500 ma/cm² at 60 millivolts overvoltage. This 10,000 fold increase at such a small platinum loading is in part due to the high degree of dispersion of the platinum.

Initial platinum area measurements (Section 4.2.1) appear to show a decrease in the specific surface area of the platinum as its weight percentage in the boron carbide catalyst increases. Probably a more significant parameter would be the weight of platinum per unit boron

(3) Hydrocarbon-Air Fuel Cells, Semi-Annual Technical Summary Report No. 4, p. 5-59 (Fig. 27). ARPA Order No. 247, Contract No. DA 44-009-ENG-4909.

(4) Adlassnig, K. Plansee für Pulvermetallurgie 6 92-103 (1958).

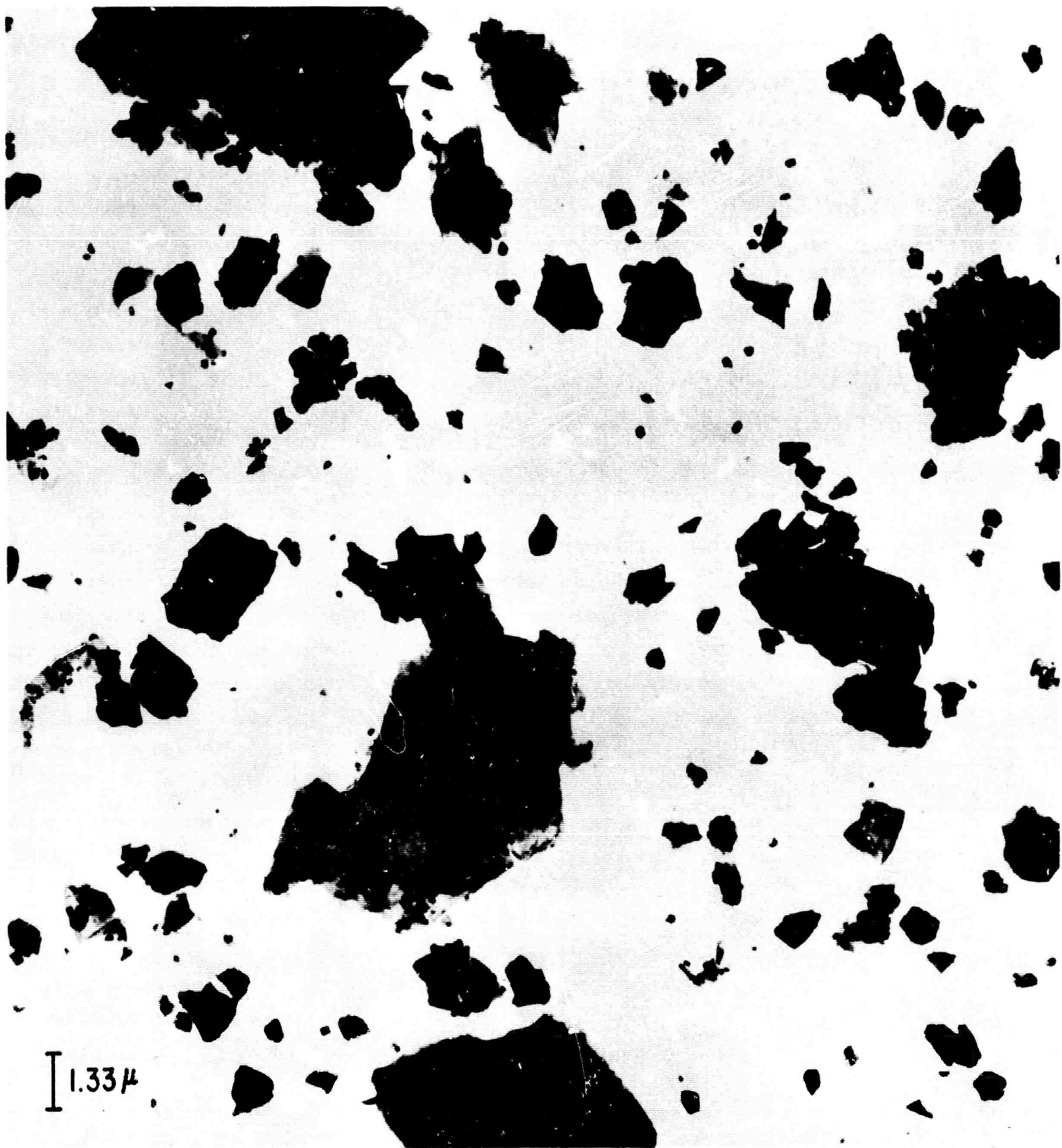


Fig. 92 Electron Micrograph of Boron Carbide Powder,
Magnification 7500 X (before reduction for printing)

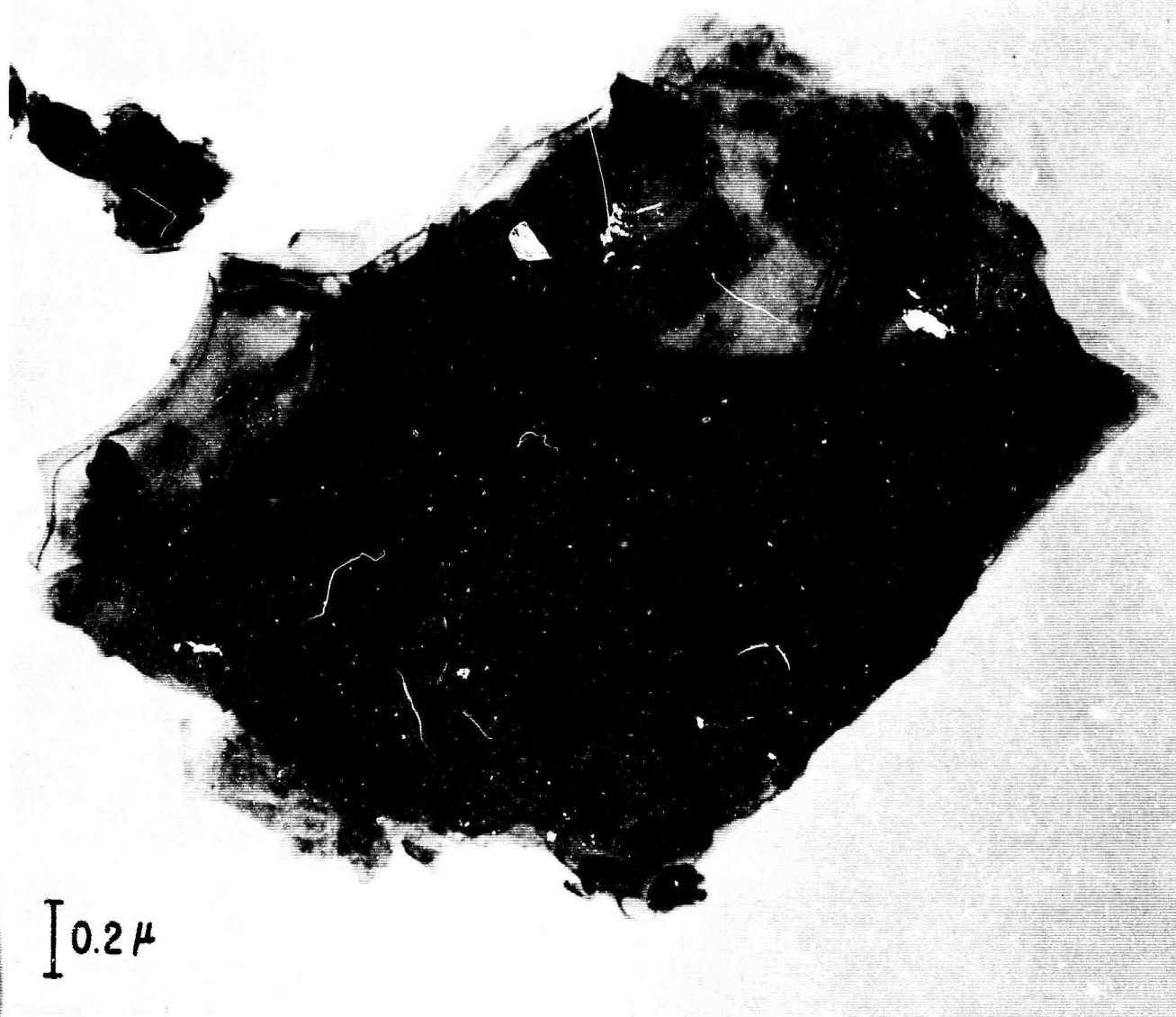


Fig. 93 Electron Micrograph of Single Particle Not Platinum Activated.
Magnification 50,000 X (before reduction for printing)

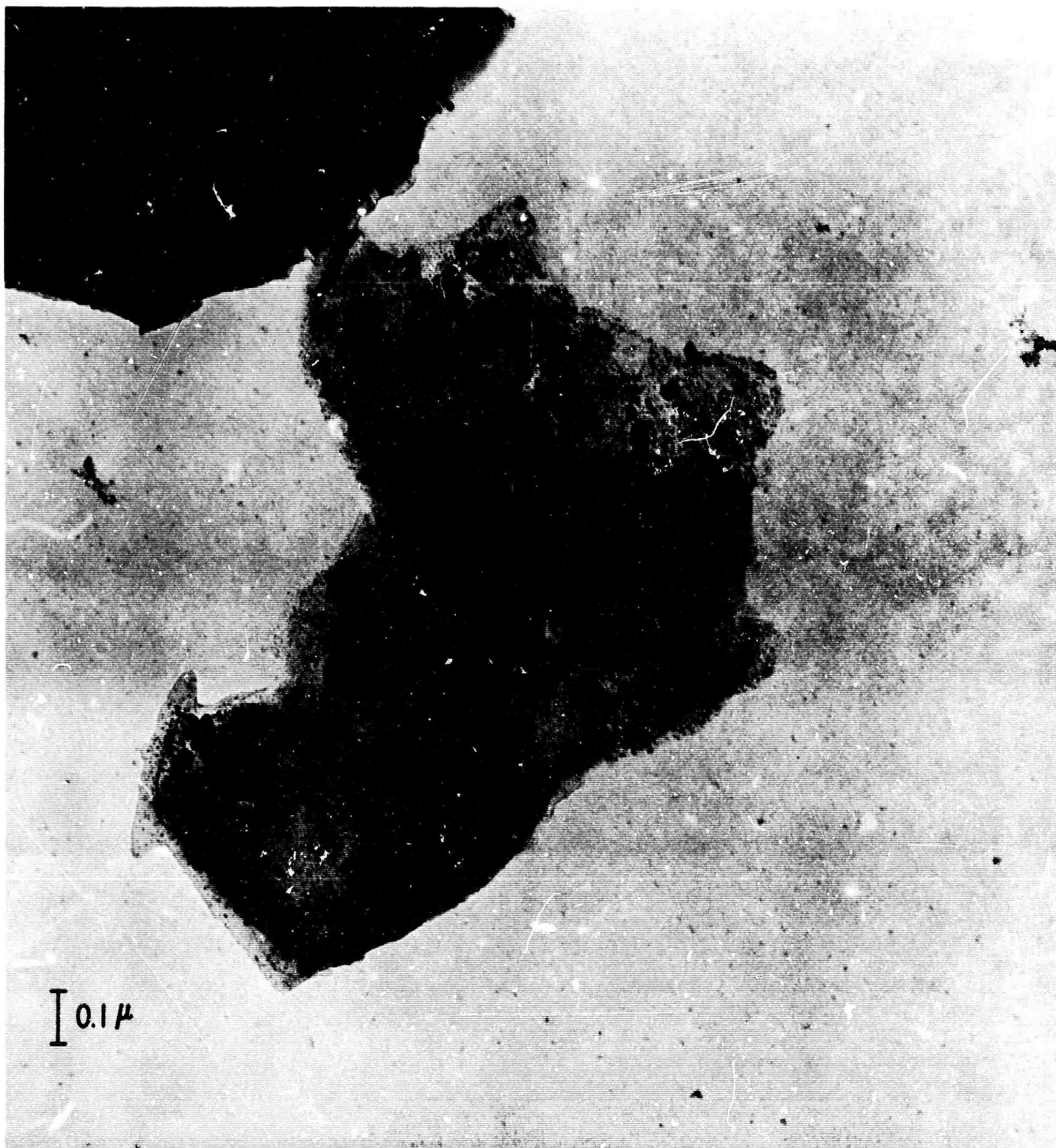


Fig. 94 Electron Micrograph of Single Particle from Sample Activated with 5% Pt by wt. Magnification 100,000 X (before reduction for printing)

carbide surface area or the extent of surface coverage θ . It is of interest to evaluate the range of θ covered in the work to date.

In terms of equivalent monolayers of platinum atoms, θ_{Pt-m} , it is given by

$$\theta_{Pt-m} = \frac{W_{Pt} \cdot N \cdot A_{Pt}}{10^3 \cdot M_{Pt} \cdot S_B \cdot 10^4}$$

where

M_{Pt} = atomic weight of platinum

W_{Pt} = weight percent of platinum in B₄C catalyst

N = Avogadro's number

A_{Pt} = area occupied by a surface platinum atom in cm²

S_B = surface area of boron carbide in square meters/gm

Using $A_{Pt} = 10^{-16}$ cm² and the measured value $S_B = 11.9$, $\theta_{Pt-m} = 0.26 W_{Pt}$

The catalysts evaluated to date have covered a range from 0.5 to 9.1 weight percent of platinum or from 0.13 to 2.4 equivalent monolayers on the boron carbide surface. It is probably desirable to keep θ as low as possible in order to maintain the highest effective platinum area. For a given loading of platinum per unit geometric electrode area, this can be accomplished by either increasing S_B , which may be difficult, or by increasing the electrode thickness. In a thicker electrode the amount of boron carbide is greater and for given weight of Pt per unit of electrode area θ or W_{Pt} is lower. The latter approach is experimentally easier, but both factors must be considered since the thickness of the electrode has been shown by other fuel cell investigators (5) to influence the effectiveness of the platinum. At higher values of W_{Pt} and θ the conditions of hydrogen reduction used in preparing the catalyst are expected to be more critical with respect to their influence on the effective area of the platinum. Further exploration of these factors may lead to improved performance.

For the purpose of correlating the measurements (Section 4.2.1) on various catalyst powders with the results obtained in fuel cell electrodes, Table XXIII shows the various electrode numbers for which data are reported, the catalyst preparation used, the weight percentage of platinum in the catalyst, and the area platinum loading in the electrode.

(5) Esso Research and Engineering Co. Hydrocarbon-Air Fuel Cell Report #5, p. 20. ARPA Order No. 247, Contract No. DA 36-039-AMC-03743(E).

TABLE XXIII

Correlation of the Measurements on Various Catalyst Powders With the Results

Electrode #	Obtained in Fuel Cell Electrodes		
	Catalyst Preparation #	Wt. % of Pt in Catalyst	Area Loading of Pt in Electrode (mg/cm ²)
28	2	0.5	0.16
39	3	0.5	0.16
40	4	0.5	0.16
57	14	0.5	0.16
35	21	2.0	0.45
86	21	2.0	0.48
87	19	4.8	1.1
89	20	9.1	2.2

4.2.2.3 Conclusions

Platinum activated boron carbide electrocatalysts continue to look promising for fuel cell electrodes. A previous difficulty in the electrode structure that caused failure at elevated temperatures and at increased platinum loadings has been solved. Electrodes were evaluated on hydrogen and oxygen at room temperature, and propane at 150°C, as a function of platinum content. At low percentages by weight, the platinum on boron carbide is up to 10 times as effective as a commercial platinum black in the anodic oxidation of propane based on current density at 0.5 volts cell potential. A hydrogen anode in sulfuric acid containing 0.16 mg of platinum catalyst per square centimeter produced 500 ma/cm² at an overvoltage of 60 millivolts. Both electron micrographs and hydrogen adsorption measurements show that the platinum is in a highly dispersed state on the boron carbide surface. Average spherical particle diameter is 16 Angstrom units for a 0.5 wt. % platinum catalyst based on hydrogen adsorption measurements. The apparent platinum particle size in electron microscope pictures is consistent with this number.

4.2.3 Platinum Activated Tantalum (L. W. Niedrach/M. Tochner)

Work has been continued on reducing the platinum content in the electrodes of Niedrach and Alford (1) with the aid of finely divided tantalum. Previously the platinum content was reduced by dilution with tantalum powder in the form of a physical mixture (2, 3). Because it has become evident that this approach results in general loss of performance as the platinum content is lowered, work during the present period has been concentrated on the use of the tantalum as a

-
- (1) L. W. Niedrach and H. R. Alford, Saturated Hydrocarbon Fuel Cell Program: A New High Performance Fuel Cell Employing Conducting Porous-Teflon Electrodes and Liquid Electrolytes, Contract DA-44-009-AMC-479(T).
 - (2) Technical Summary Report No. 4 "Saturated Hydrocarbon Fuel Cell Program", 1 July - 31 Dec. 1963, Contract No. DA44-009-ENG-4909, p. 5-47.
 - (3) Technical Summary Report No. 5 "Hydrocarbon-Air Fuel Cells", 1 January 1964 - 30 June 1964, Contract Nos. DA 44-009-ENG-4909 and DA 44-009-AMC-479(T), p. 4-113.

support for the platinum catalyst. In this way it was hoped that a higher specific activity would be realized for the platinum. In conjunction with this approach continuing effort was devoted to further reducing the particle size of the tantalum powder in order to improve the electrode structure.

Modifications of milling techniques (5.2.2 Appendix) have yielded a high surface area tantalum powder ($8.0 \text{ m}^2/\text{g}$) which is easily fabricated into electrodes by the standard techniques for the Niedrach-Alford Teflon-bonded electrode. It was found that 1.0 g of the material was sufficient to obtain a satisfactory structure. This is a considerable improvement over the 2.0 g necessary with some of the earlier, coarser materials.

The high area tantalum powder was activated with platinum by hydrogen reduction (9 to 12 hrs. at 400°C) of platinum salts as previously described for the activation of boron carbide (4). Two different salts were used $\text{Pt}(\text{NH}_3)_2(\text{NO}_2)_2$ and PtCl_4 . Table XXIV summarizes information concerning the platinizations and the compositions of the electrodes prepared from the materials. All of the electrodes contained a total of 1.0 g catalyst spread uniformly over an area of 17.7 cm^2 .

TABLE XXIV

Electrode Compositions

1.0 gm catalyst/ 17.7 cm^2 area; 1.6 mg Teflon/ cm^2 film on gas side

<u>Electrode #</u>	<u>Source of Pt</u>	<u>Pt content per gm Ta</u>	<u>Quantity of Pt/cm^2</u>	<u>T-30 Binder cc/g Catalyst</u>
646	$\text{Pt}(\text{NH}_3)_2(\text{NO}_2)_2$	22.4 mg	1.3 mg	.06
647	"	22.4	1.3 mg	.06
648	"	22.4	1.3 mg	.10
649	"	22.4	1.3 mg	.14
655	"	67.8	3.8 mg	.08
657	"	7.5	0.4 mg	.06
663	Pt Cl_4	67.8	3.8 mg	.08

4.2.3.1 Performance of Electrodes with Platinized Tantalum as Anodes

The effect of the ratio of T-30 binder to catalyst was first examined with electrodes 647-9 to attempt to optimize the structure. Fig. 95 shows polarization curves obtained with these electrodes serving as hydrogen anodes in $5\text{N H}_2\text{SO}_4$ cells at 25°C . Standard platinum black electrodes ($34 \text{ mg}/\text{cm}^2$) were utilized for the counter electrodes. The intermediate T-30 bonding appears to provide the best structure. This series of experiments was used as a guide for the production of subsequent electrodes.

Fig. 96 contains a series of polarization curves obtained with $5\text{N H}_2\text{SO}_4$ at 25°C for electrodes with different quantities of platinum on the high area tantalum powder. As hydrogen anodes, the electrodes with $3.8 \text{ mg Pt}/\text{cm}^2$ showed performances typical of a standard platinum

(4) *ibid.* p. 4-30

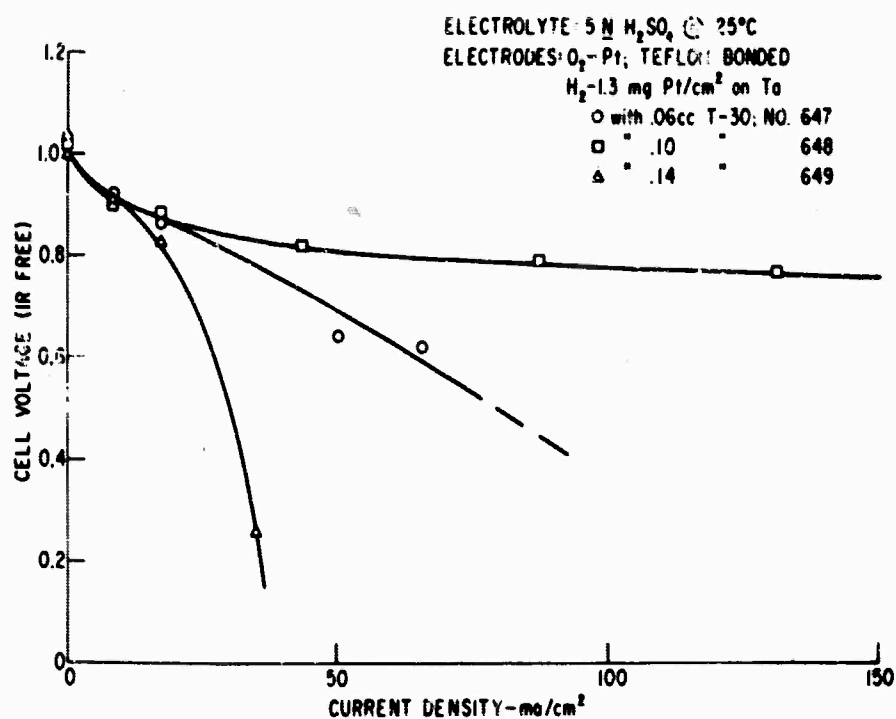


Fig. 95 Effect of Teflon Content on Performance of Platinized Tantalum Electrodes as H_2 Anodes.

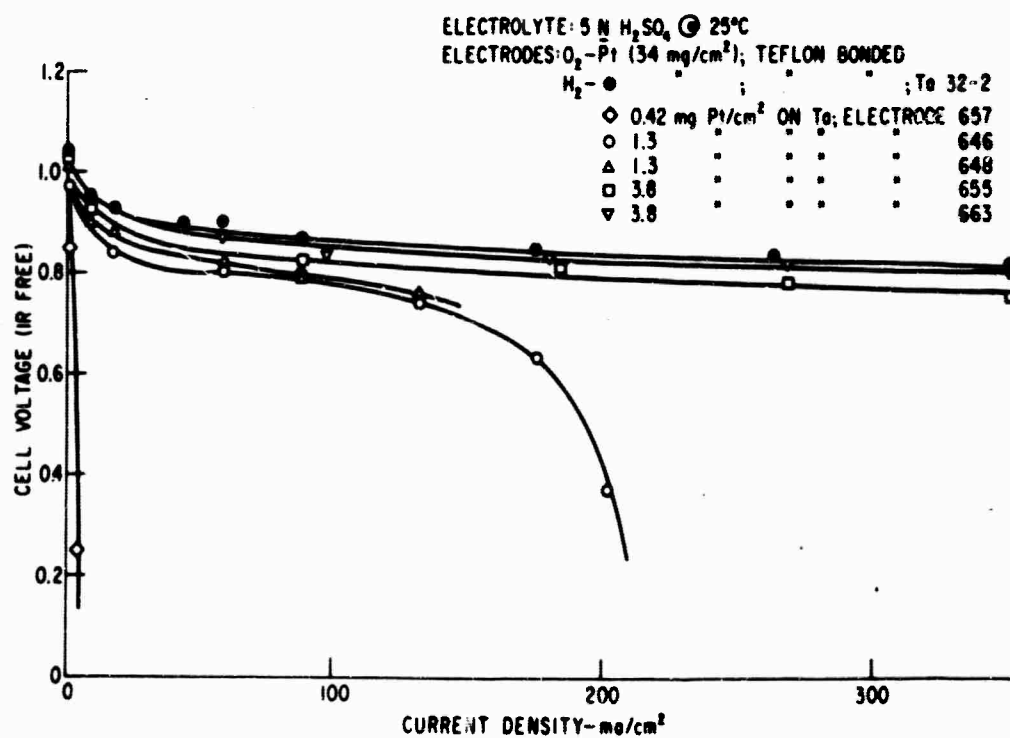


Fig. 96 Performance of Platinized Tantalum Electrodes as H_2 Anodes.

BLANK PAGE

(34 mg Pt/cm²) electrode. Little difference is observed between the two catalysts platinized with the different salts. The electrodes with lower quantities of platinum yielded substandard performance.

Electrode 663 with 3.8 mg Pt/cm² was run on hydrogen with 85% H₃PO₄ at 150°C with a standard platinum electrode as the oxygen cathode. Here again, the performance was comparable with that of a standard platinum anode. These data reflect the high exchange current of hydrogen on platinum and provide further indication that the platinum content of a standard electrode (34 mg/cm²) is in excess of that required for a hydrogen anode.

With propane on electrode 663 in 85 percent H₃PO₄ at 150°C the performance was poorer than that of a standard electrode, but comparable with that previously reported for similar mixtures of platinum with tantalum (2).

4.2.3.2 Performance of Electrodes with Platinized Ta as Cathodes

In the room temperature work with 5N H₂SO₄ at 25°C the electrodes with 1.3 mg Pt/cm² and less polarized markedly almost immediately. Even at 1 ma/cm² strong polarization was observed. Fig. 97 shows the polarization curves for electrodes 655 and 663, both with 3.8 mg Pt/cm², on oxygen vs. a standard platinum hydrogen anode. Electrode 663, the best of the series, was also run with oxygen at 150°C with an 85 percent H₃PO₄ electrolyte. The IR free

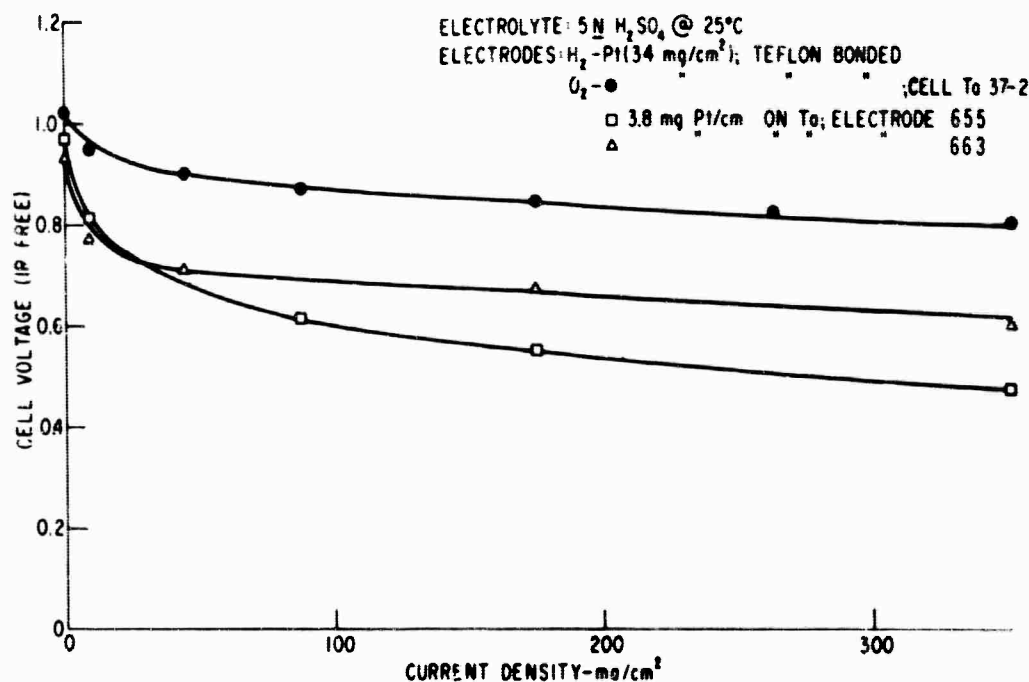


Fig. 97 Performance of Platinized Tantalum Electrodes as O₂ Cathodes.

(2) Technical Summary Report No. 4 "Saturated Hydrocarbon Fuel Cell Program", 1 July - 31 Dec. 1963, Contract No. DA 44-009-ENG-4909, p. 4-113.

voltage was 0.85 v at 2 ma/cm². All of the performances with oxygen were comparable with those previously reported for similar mixtures of platinum with tantalum (2); that is, the performance was approximately proportional to the platinum content of the electrode.

4.2.3.3 Conclusions

Although electrodes fabricated with the platinized tantalum performed successfully as hydrogen anodes, they have been substandard on propane and oxygen. The platinized material has not shown an improvement over that of the comparable mixtures of platinum black with tantalum. In view of these results, the extensive processing that must be undertaken to obtain a high area tantalum powder for such electrodes, and the fact that more encouraging results have been forthcoming with boron carbide, the work with tantalum will be discontinued.

4.2.4 Stability of Electrocatalysts in Fluoride Electrolytes (E. J. Cairns)

The electrocatalyst stability tests have continued, with emphasis on potentiostatic anodic corrosion tests in fluoride electrolytes.

4.2.4.1 Experimental

The general layout of the apparatus was shown in Fig. 41 of (1). Some changes in the circuitry have been made and the new circuit is shown in Fig. 98. It is now possible to have the potentiostat follow a desired voltage program from the function generator, and record the current-voltage trace on an X-Y plotter. This results in a more rapid comparison of results for various test electrodes.

Some modifications have been made in the electrochemical cell. The new version is shown in Figs. 99a and b. A Luggin capillary is now used, giving better anode vs. reference readings (minimizing the IR component) and protecting the reference electrode from dissolved metal cations. The cathode is now enclosed, preventing hydrogen access to the test electrode. Electrolyte volume has been minimized.

Steady-state (point-by-point) and voltage sweep experiments have been performed in order to obtain the current density-voltage relationships for the test materials under an argon atmosphere in 37 mole % HF at various temperatures.

(1) Semi-Annual Technical Summary Report No. 5, January 1 - June 30, 1964, ARPA Order No. 247, Contract Nos. DA 44-009-ENG-4909 and DA 44-009-AMC-479(T).

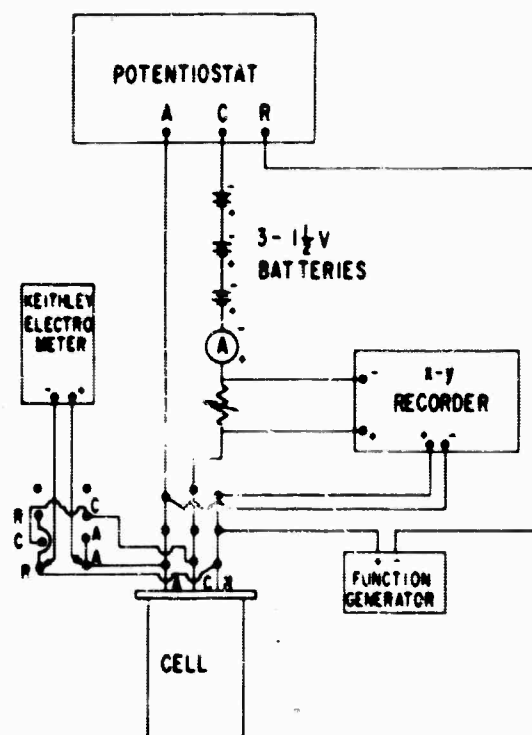


Fig. 98 Block Diagram of Potentiostatic Corrosion Apparatus

4.2.4.2 Results and Discussion

The results in Fig. 43 of (1) were reported incorrectly due to typographical errors on the abscissa. The corrected presentation is shown in Fig. 100. Platinum, gold, and gold-palladium alloys rich in gold are very stable in the HF azeotrope at 110°C. Very low current densities due to possible oxidation are found at all potentials up to oxygen evolution (above 1.5 volts vs. hydrogen reference). Silver is suitable up to about 0.4 volt.

Fig. 101 shows some results of anodic corrosion tests in 36 mole % HF with some of the less noble metals. Molybdenum is anodically attacked at appreciable rates at potentials (vs. hydrogen reference) above 0.15 volt at 90°C. Tungsten corrodes very slowly at potentials below 0.35 volt at 80°C. This result is reasonably encouraging with respect to the possibility of using tungsten or a tungsten alloy at low potentials (vs. hydrogen reference) in a fluoride electrolyte.

Room temperature anodic corrosion results are shown in Fig. 102. Nickel corrodes rapidly at potentials above 0.1 volt in 37 mole % HF. Again, the tungsten results are favorable at potentials below about 0.32 volt vs. hydrogen reference.

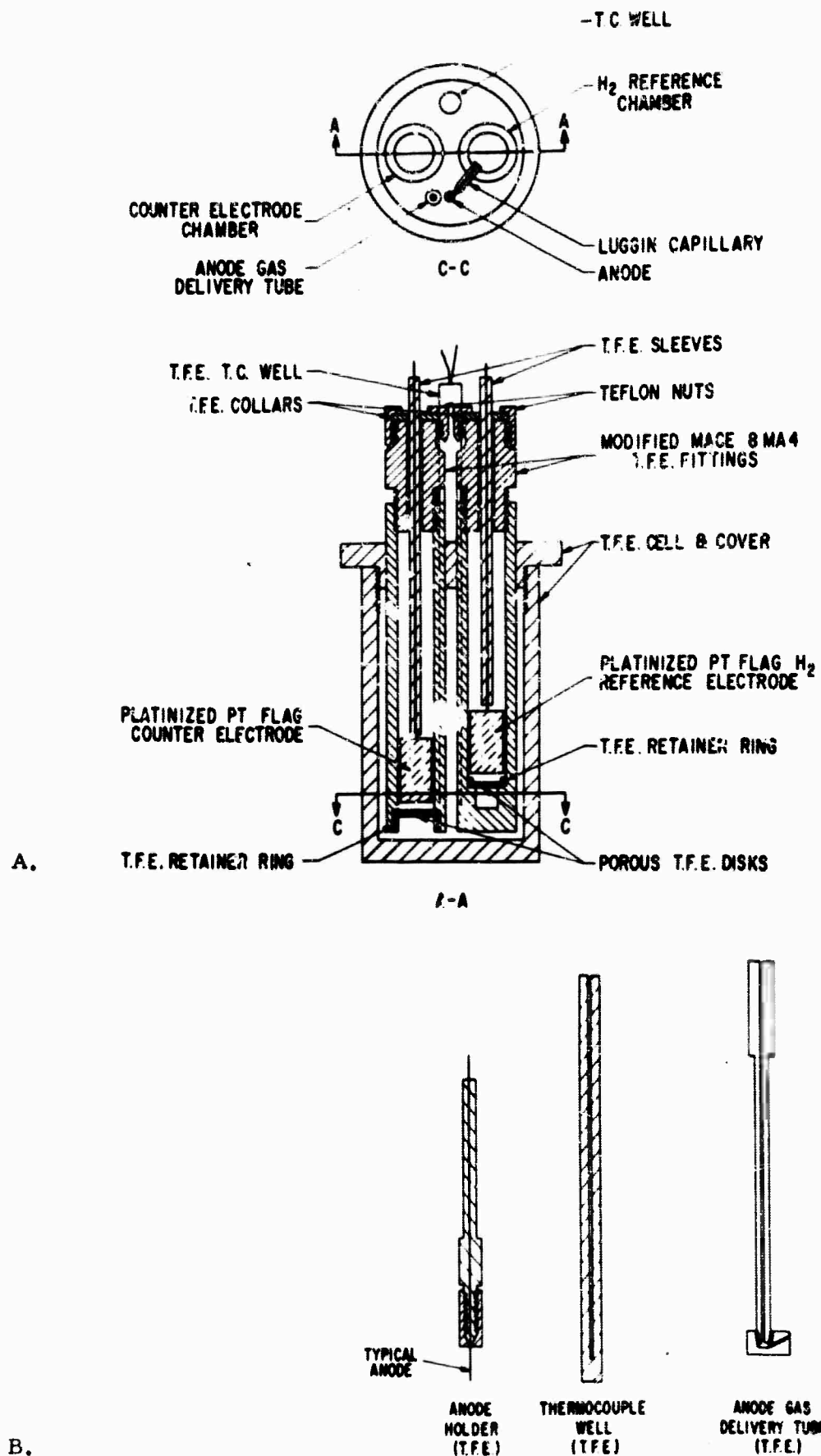


Fig. 99 Details of Electrochemical Cell for Potentiostatic Corrosion Studies

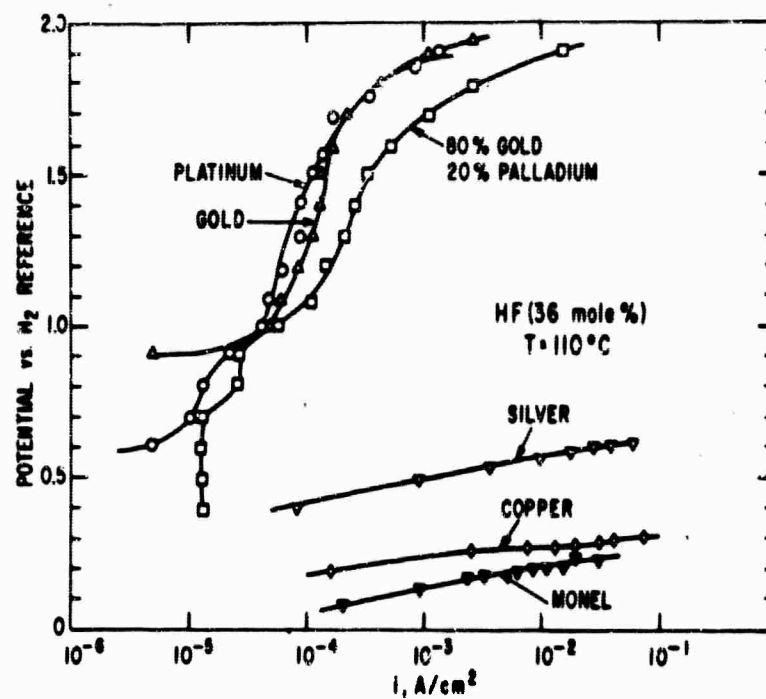


Fig. 100 Current-Potential Curves for Anodic Corrosion of Various Materials at 110°C in HF under Argon

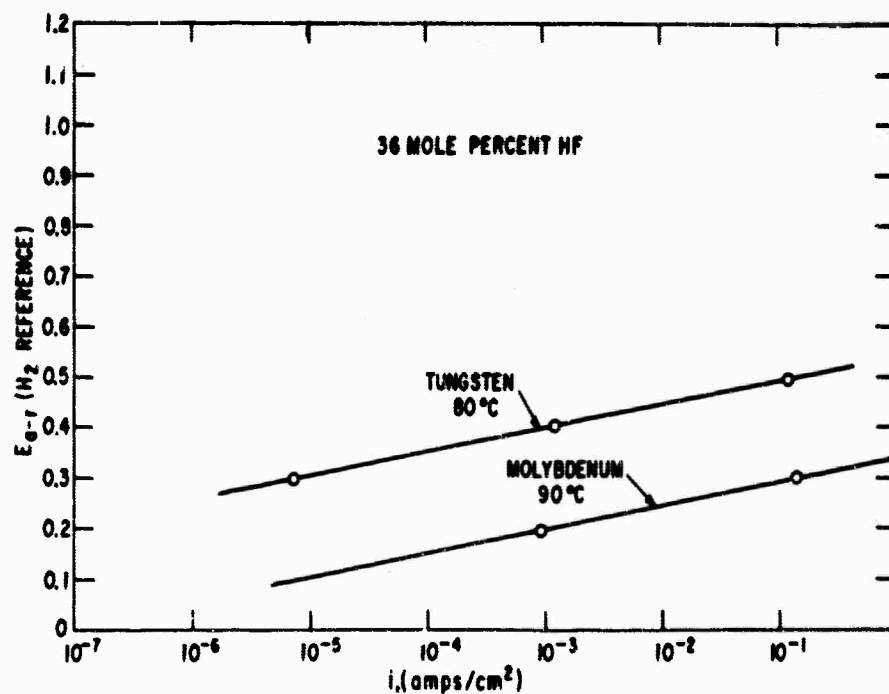


Fig. 101 Current-Potential Curves for Anodic Corrosion of Tungsten at 80°C and Molybdenum at 90°C in HF under Argon

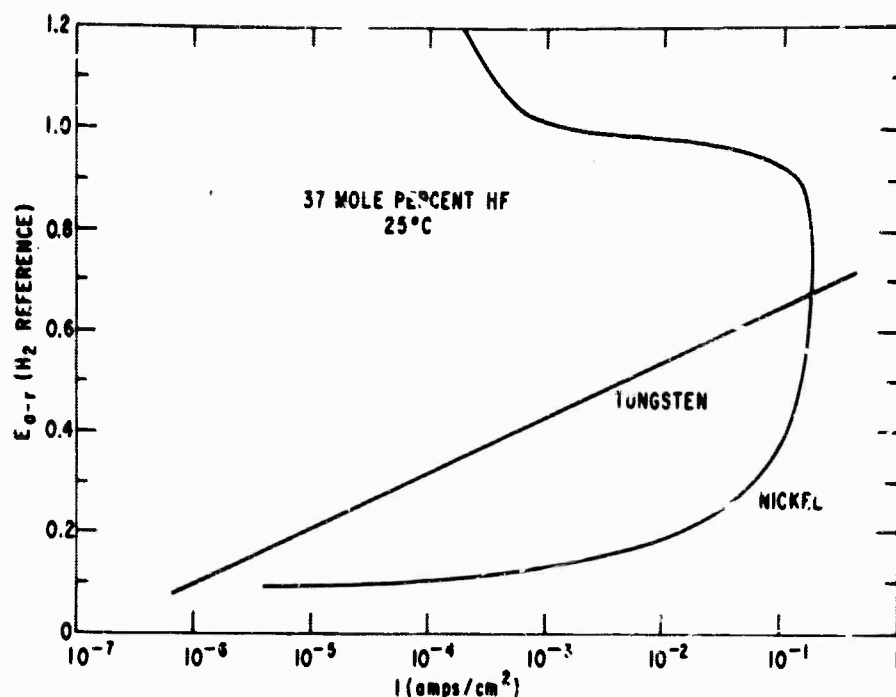


Fig. 102 Current-Potential Curves for Anodic Corrosion of Tungsten and Nickel at 25°C in HF under Argon

4.2.4.3 Conclusions

Potentiostatic corrosion tests in the HF-H₂O azeotrope at temperatures up to 110°C have shown that platinum, gold, and 80% gold-20% palladium alloy have excellent stability over the potential range 0.0 to 2.0 volts vs. reversible hydrogen. Silver and tungsten show reasonable stability in the range 0.0 to 0.35 volt vs. reversible hydrogen.

4.2.5 Evaluation of Alloy Electrocatalyst (D. W. McKee/L. Niedrach)

Previously reported data on hydrocarbon exchange reactions has indicated that several combinations of noble metals possess catalytic activity which rival that of pure platinum. As fuel cell data is non-existent for many of these potentially useful alloy systems, a program is under way to test these materials in a standard propane-85% H₃PO₄-oxygen cell. The catalyst samples prepared for study by means of gas phase techniques had generally been reduced in hydrogen at 300-350° for several hours. This treatment had sintered the samples to surface areas of 3-10 m²/g and the residues were often granular in texture. Considerable difficulties were experienced in preparing satisfactory electrodes with these materials and the proportion of teflon in the spreads often had to be increased over that required for a platinum black electrode. Fig. 103 shows typical polarization curves for commercial propane at two temperatures for an electrode

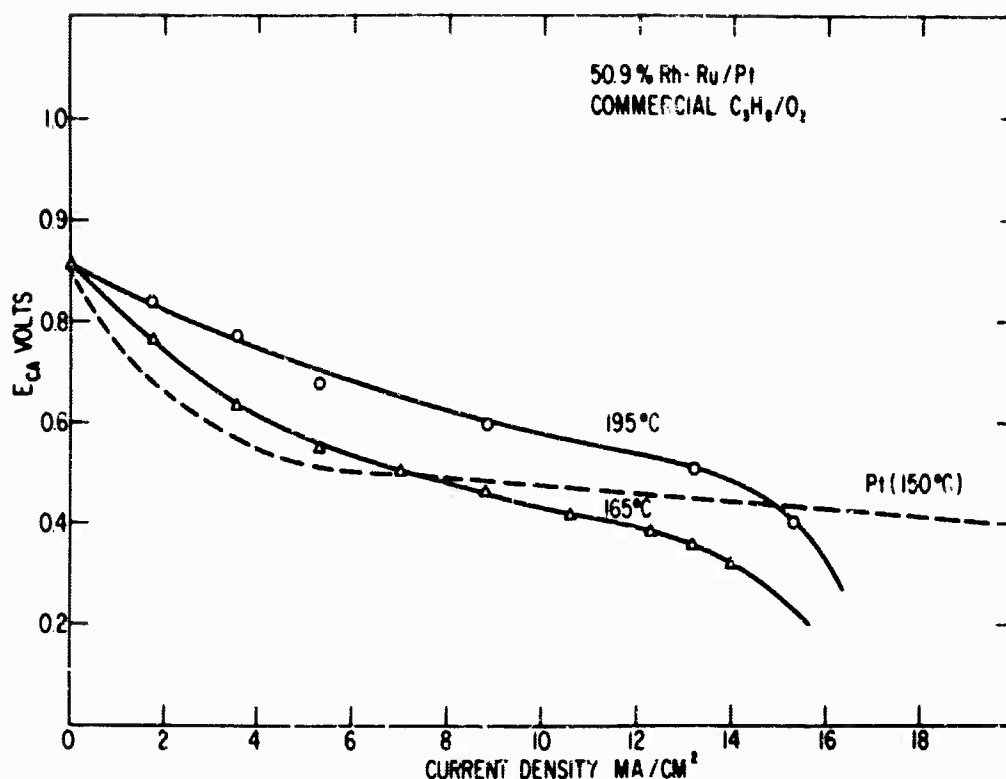


Fig. 103 Performance Curves at 165° and 195°C. Anode — 50.9% Rh-Ru, Commercial Propane. Cathode — Pt, O₂. 85% H₃PO₄.

containing 50.9% rhodium-ruthenium alloy. The cathode vs. anode voltage was obtained with a Kordes-Marko Bridge arrangement in the usual way. Also included in the figure is a polarization curve obtained with a platinum sample prepared by the same method and possessing about the same low surface area. Although the current densities obtained with this electrode were low, substantial improvement would be expected with increase in surface area of the alloy.

In attempting to either enhance the activity or find an effective substitute for platinum in the hydrocarbon fuel cell, increased attention will be given to methods of preparing high surface area alloy catalysts. Promising alloy combinations will be given a preliminary corrosion test in sulfuric acid to eliminate materials which are obviously too reactive. Electrochemical and gas phase reactivity tests will be used to evaluate the catalysts before fuel cell performance data is obtained. Attention will be paid to both noble metal alloys and to base metal combinations containing no platinoid elements.

4.3 ELECTROLYTE RESEARCH

The electrolyte research area is concerned with obtaining physical property data necessary to interpret electrolyte behavior in fuel cell systems. Research effort was concentrated in two areas: the development of techniques for measuring hydrocarbon and oxygen solubilities in electrolytes, and the measurement of the more important properties of electrolyte systems, as they relate to the hydrocarbon-air fuel cell environment.

4.3.1 Solubility Measurements (J. Paynter/D. MacDonald)

Hydrocarbon and oxygen solubilities in electrolytes are needed for the understanding of transport processes at hydrocarbon fuel cell electrodes and will influence the choice of fuel cell operating conditions. Although solubility data exist for hydrocarbons in dilute ($<5N$) H_2SO_4 and H_3PO_4 between $20^\circ C$ and $80^\circ C$ (1) and for oxygen in 0 - 90 wt % KOH, H_2SO_4 , and H_3PO_4 at $25^\circ C$ and $-30^\circ C$ (2), no measurements at the higher temperatures and concentrations of interest to fuel cell work (up to $200^\circ C$, 100% electrolyte) have been reported. A dynamic and a static technique for making these measurements are described in this section. The solubilities of propane, octane, and oxygen in concentrated H_3PO_4 have been measured during the present period.

4.3.1.1 Dynamic Method for Solubility Measurements

Development of a gas solubility technique based on a multi-rotating disk contactor continued during the current reporting period. Mass transfer characteristics of the stripper were studied in an effort to optimize gas-liquid contacting conditions. Accuracy and precision were tested at room temperature with oxygen in water and in phosphoric acid. The contactor and associated apparatus were modified for use at elevated temperatures. Data gathering for propane and oxygen in concentrated phosphoric acid between room temperature and $150^\circ C$ has begun.

A. Experimental

A block diagram of the apparatus used for room temperature studies is given in Fig. 104. Essential features of the Lucite gas-liquid contactor were described in the previous Technical Summary Report. (3). Gas detection is carried out with a Carle Model 100 thermal conductivity cell and bridge thermostated in a water bath at $36.0 \pm 0.1^\circ C$ and an L and N Inv. full scale recorder. Bubblers are used to presaturate gases with water vapor. The bubbles in

(1) California Research Corporation, Progress Reports Nos. 9, 10, and 12, HDL and ARPA Contract No. DA-49-186-ORD-929.

(2) K. E. Gubbins and R. D. Walker, Jr., "The Solubility and Diffusivity of Oxygen in Fuel Cell Electrolytes," Electrochemical Society Meeting, Washington, D.C., Oct., 1964.

(3) Technical Summary Report No. 5, Jan. 1-June 30, 1964, Contracts No. DA44-009-ENG-4909 and No. DA44-009-AMC-479 (T).

the carrier gas system contain glass frits specially selected to produce bubbles of small and uniform size to minimize flow noise. A needle valve between contactor and sample side of the detector serves to further reduce flow noise by introducing a small back pressure in the system. Drierite is used to remove water vapor from the gas stream prior to detection.

Following an initial sweeping of the system with He and with disks rotating, stopcocks "A", "B", and "C" are turned so that the gas under study flows through the contactor and is vented to the atmosphere, while He continues to flow through the detector. Disk rotation is then stopped and He is allowed to sweep out the system until the recorder trace remains unchanged with time at the sensitivity to be used to record the stripping curve. The disks are then set in motion and recording continued until the trace again becomes constant. The apparatus is calibrated by introducing known amounts of gas with a gas-tight syringe at the sample injection port between bubblers and contractor. Areas are measured with a planimeter.

Fig. 105 gives a schematic diagram of the apparatus modified for use at elevated temperatures. The arrangement of magnets, preheater coil, contactors and drying tubes in the oven is shown in Fig. 106. The apparatus differs from the previous one in the following respects: gas bubblers are replaced with a second multi-rotating disk contactor to reduce flow noise to an acceptable level for the low solubilities, and thus, high detector sensitivities anticipated; one presaturator is used for both carrier and solute gases to minimize the number of joints and

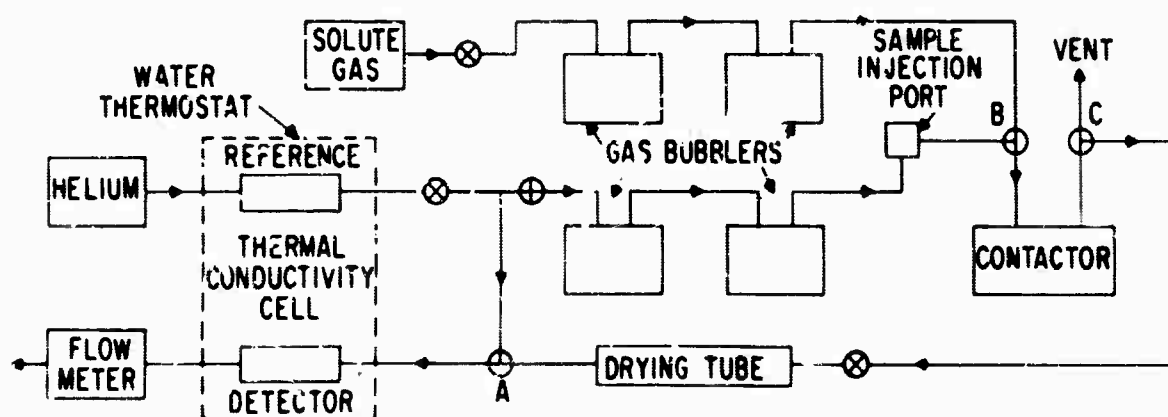


Fig. 104 Schematic Diagram of Gas Solubility Apparatus for Room Temperature Studies

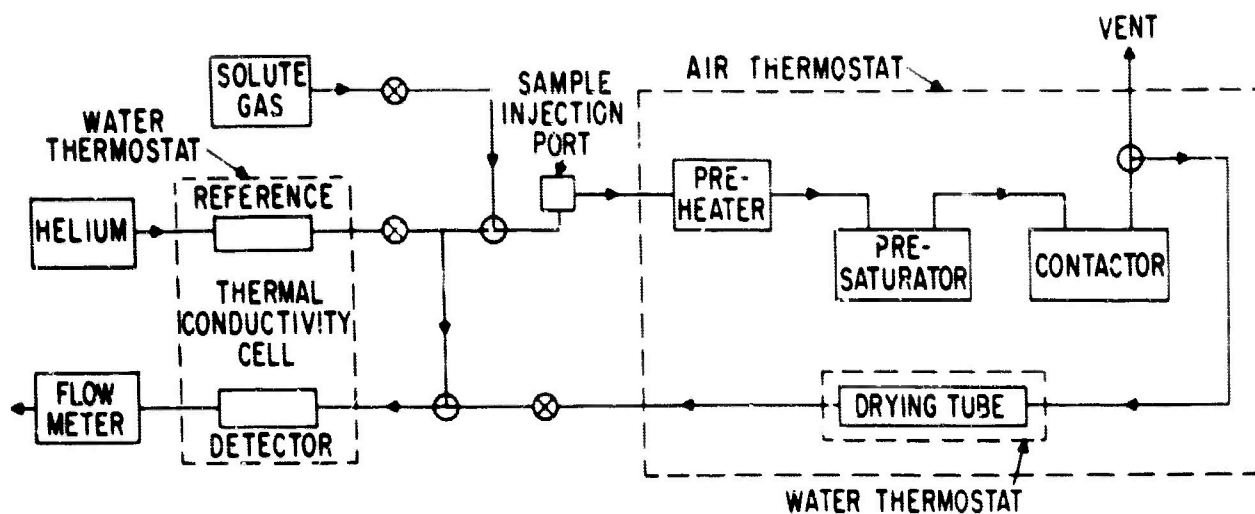


Fig. 105 Schematic Diagram of Gas Solubility Apparatus for Measurements at Elevated Temperatures

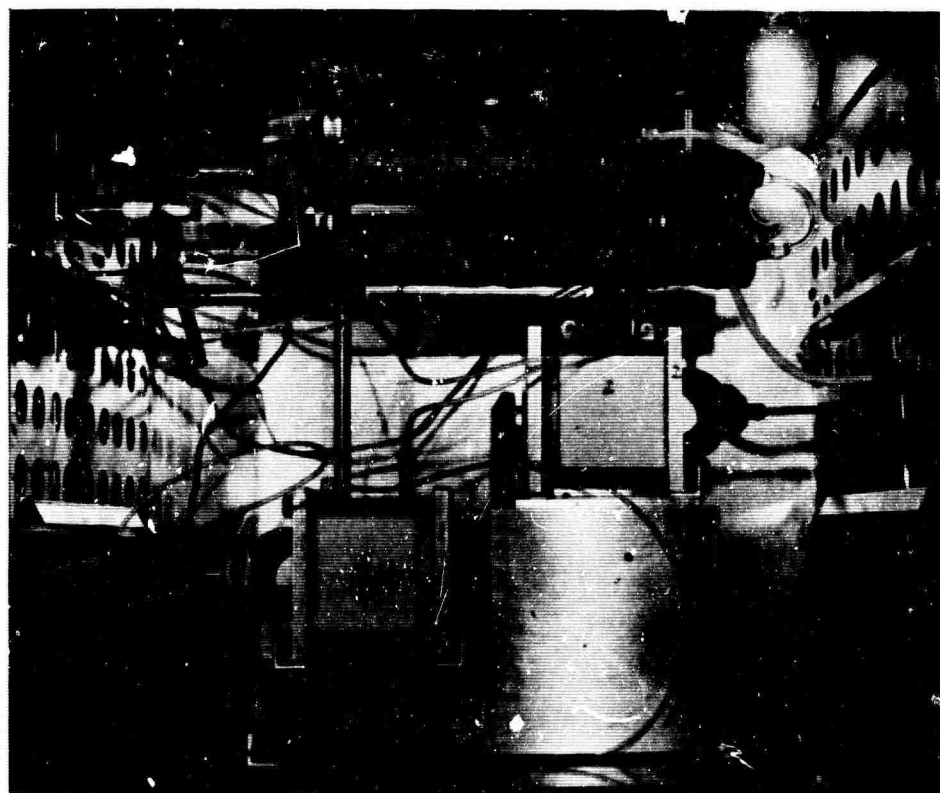


Fig. 106 Photograph of Contactors and Associated Equipment Arranged in Oven

manipulations inside the oven; the drying tube is jacketed and kept well below 100°C with flowing water; and both contactors are constructed entirely of Teflon. Fig. 107 shows a photograph of a disassembled contactor. The Teflon encased magnet is enclosed in a disk to eliminate liquid splashing by the magnet and to increase gas-liquid contacting area.

Experimental procedure is similar to that described previously for the room temperature method. Only differences are noted here. Contactors and electrolyte are heated separately and brought to oven temperature before securing metal end plates and Teflon taper joints. After an initial degassing with He, the gaseous phase in both contactors is flushed with the gas under study at 300-400 ml/min for approximately 10 minutes, with disks not rotating. Solute gas flow is then reduced to 10-20 ml/min to ensure presaturation with water vapor and the disks in both contactors rotated for an additional 10 minutes. The presaturator disks continue to rotate during gaseous phase flushing and liquid phase stripping with He.

B. Results and Discussion

In the interests of high accuracy and economy of time, it is desirable to minimize the extent of tailing of the stripping curves. In principle, carrier gas flow rate, number of disks, rotational speed and liquid volume can all affect the form of the curves. For the purpose of obtaining a reasonable balance between optimum and practical conditions, a study of the effects of

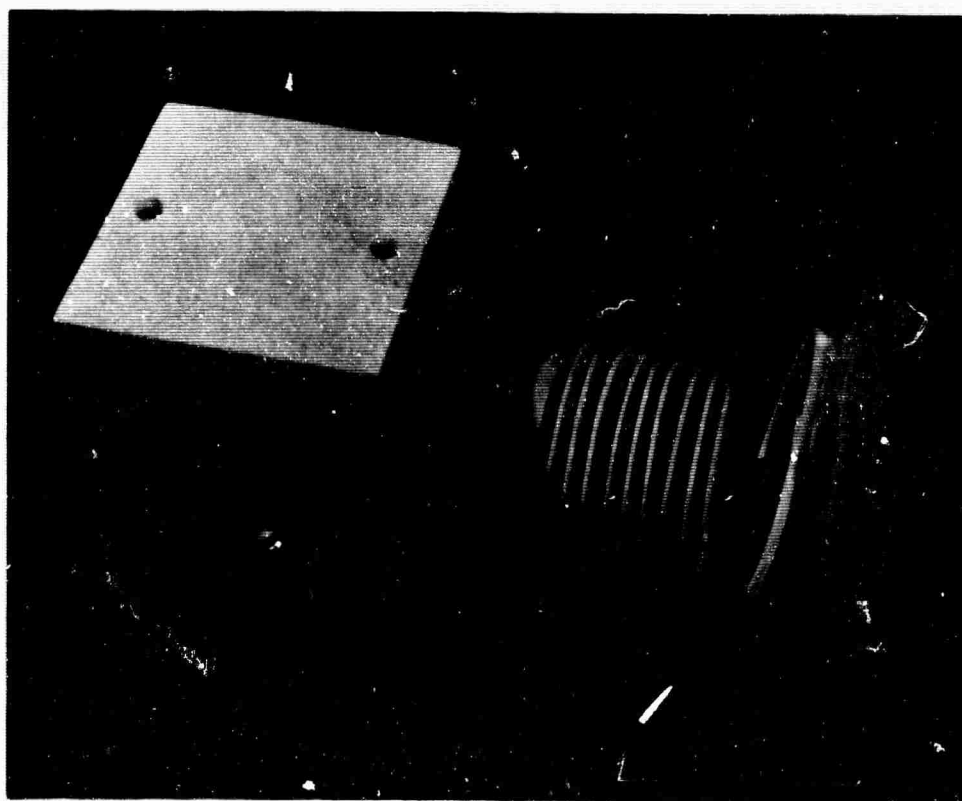


Fig. 107 Photograph of Disassembled Contactor

these parameters was undertaken. In practice, it was found that although the peak height and the slope of the ascending portion of the stripping curves vary considerably, only the carrier gas flow rate exerts a significant influence on the extent of tailing over a fairly wide range of these parameters.

The predominant effect of increasing liquid volume to 100 ml (contactor capacity ~ 160 ml), rotational speed above 200 rpm, and number of disks above six is to increase the peak height and the slope of the ascending portion of the curves. The total time needed to obtain a stripping curve decreases, but the tails can be superimposed by shifting the curves on the time axis. Thus under these conditions, the gas is removed from the liquid in a relatively short time and tailing is due primarily to poor gaseous phase contacting in the stripper.

An attempt was made to improve gaseous phase mixing by introducing multiple gas entrance and exit ports (12 of each) between the disks in the Lucite contactor. For He flow rates greater than 30 ml/min, no improvement was found. Thus at higher flow rates, mixing is optimized even with only one entrance and exit port, and tailing simply reflects the time needed to displace solute gas from the contactor.

An upper limit is set on the carrier gas flow rate for two reasons. First, sensitivity loss because of dilution at higher flow rates may be sufficient to prohibit the making of some measurements. Secondly, the sudden release of gas at the start of stripping brings about a pressure change in the system and the recorder trace may not return to the original baseline before solute gas reaches the detector. A flow rate of about 100 ml/min was found to yield sufficient sensitivity and sufficient time for baseline recovery without producing extensive tailing.

The results of a study of the technique's accuracy and precision with oxygen in 0, 54 and 85 wt % phosphoric acid, at room temperature, are given in Table XXV. A typical stripping curve and calibration curve are shown in Fig. 108 and 109. The apparatus shown schematically in Fig. 104 was used.

TABLE XXV
Solubility of Oxygen in Phosphoric Acid at Approximately 25°C

Wt. % H ₃ PO ₄	Measured Solubility (millimoles/liter - atms.)	Literature Value
0	1.245, 1.260, 1.240, } 1.249 ± .011 1.238, 1.260	1.285 (24°C)* 1.263 (25°C)* 1.242 (26°C)*
54	0.543, 0.542	0.55**
85	0.275, 0.280, 0.277	0.27**

*Obtained from Handbook of Chemistry and Physics, 43rd Ed., The Chemical Rubber Publishing Co., Cleveland, Ohio, 1962, p. 1706.

**Estimated from a graphical presentation in Reference (2).

manipulations inside the oven; the drying tube is jacketed and kept well below 100°C with flowing water; and both contactors are constructed entirely of Teflon. Fig. 107 shows a photograph of a disassembled contactor. The Teflon encased magnet is enclosed in a disk to eliminate liquid splashing by the magnet and to increase gas-liquid contacting area.

Experimental procedure is similar to that described previously for the room temperature method. Only differences are noted here. Contactors and electrolyte are heated separately and brought to oven temperature before securing metal end plates and Teflon taper joints. After an initial degassing with He, the gaseous phase in both contactors is flushed with the gas under study at 300-400 ml/min for approximately 10 minutes, with disks not rotating. Solute gas flow is then reduced to 10-20 ml/min to ensure presaturation with water vapor and the disks in both contactors rotated for an additional 10 minutes. The presaturator disks continue to rotate during gaseous phase flushing and liquid phase stripping with He.

B. Results and Discussion

In the interests of high accuracy and economy of time, it is desirable to minimize the extent of tailing of the stripping curves. In principle, carrier gas flow rate, number of disks, rotational speed and liquid volume can all affect the form of the curves. For the purpose of obtaining a reasonable balance between optimum and practical conditions, a study of the effects of

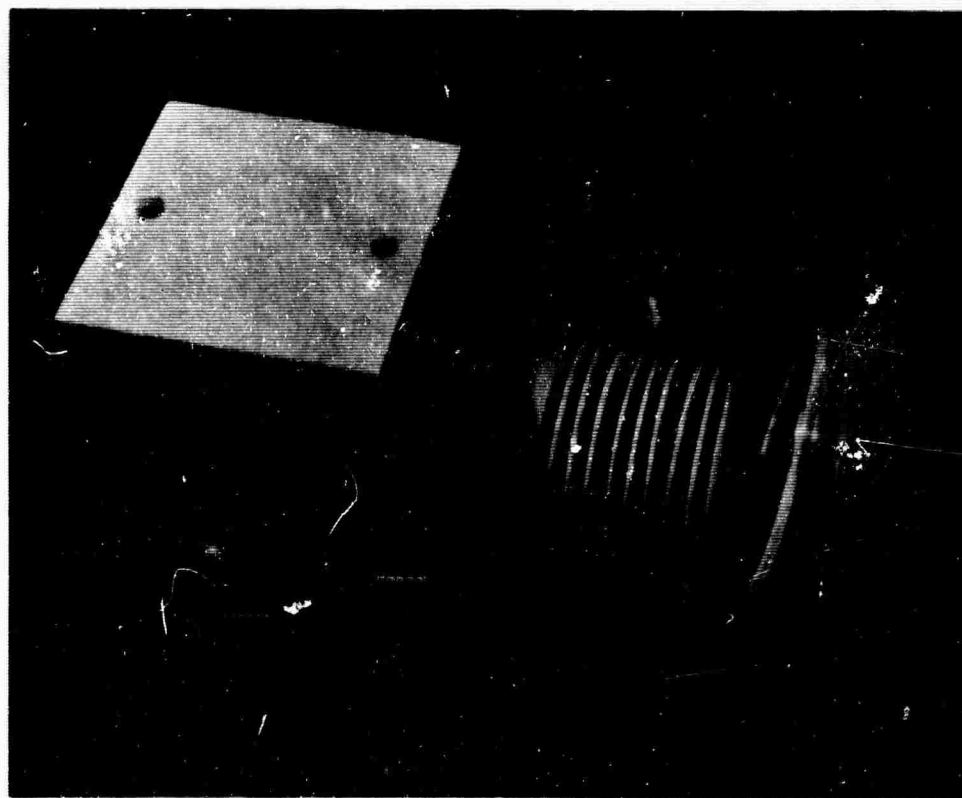


Fig. 107 Photograph of Disassembled Contactor

these parameters was undertaken. In practice, it was found that although the peak height and the slope of the ascending portion of the stripping curves vary considerably, only the carrier gas flow rate exerts a significant influence on the extent of tailing over a fairly wide range of these parameters.

The predominant effect of increasing liquid volume to 100 ml (contactor capacity ~ 160 ml), rotational speed above 200 rpm, and number of disks above six is to increase the peak height and the slope of the ascending portion of the curves. The total time needed to obtain a stripping curve decreases, but the tails can be superimposed by shifting the curves on the time axis. Thus under these conditions, the gas is removed from the liquid in a relatively short time and tailing is due primarily to poor gaseous phase contacting in the stripper.

An attempt was made to improve gaseous phase mixing by introducing multiple gas entrance and exit ports (12 of each) between the disks in the Lucite contactor. For He flow rates greater than 30 ml/min, no improvement was found. Thus at higher flow rates, mixing is optimized even with only one entrance and exit port, and tailing simply reflects the time needed to displace solute gas from the contactor.

An upper limit is set on the carrier gas flow rate for two reasons. First, sensitivity loss because of dilution at higher flow rates may be sufficient to prohibit the making of some measurements. Secondly, the sudden release of gas at the start of stripping brings about a pressure change in the system and the recorder trace may not return to the original baseline before solute gas reaches the detector. A flow rate of about 100 ml/min was found to yield sufficient sensitivity and sufficient time for baseline recovery without producing extensive tailing.

The results of a study of the technique's accuracy and precision with oxygen in 0, 54 and 85 wt % phosphoric acid, at room temperature, are given in Table XXV. A typical stripping curve and calibration curve are shown in Fig. 108 and 109. The apparatus shown schematically in Fig. 104 was used.

TABLE XXV
Solubility of Oxygen in Phosphoric Acid at Approximately 25°C

Wt. % H_3PO_4	Measured Solubility (millimoles/liter - atms.)	Literature Value
0	1.245, 1.260, 1.240, } 1.249 ± .011 1.238, 1.260	1.285 (24°C)* 1.263 (25°C)* 1.242 (26°C)*
54	0.543, 0.542	0.55**
85	0.275, 0.280, 0.277	0.27**

*Obtained from Handbook of Chemistry and Physics, 43rd Ed., The Chemical Rubber Publishing Co., Cleveland, Ohio, 1962, p. 1706.

**Estimated from a graphical presentation in Reference (2).

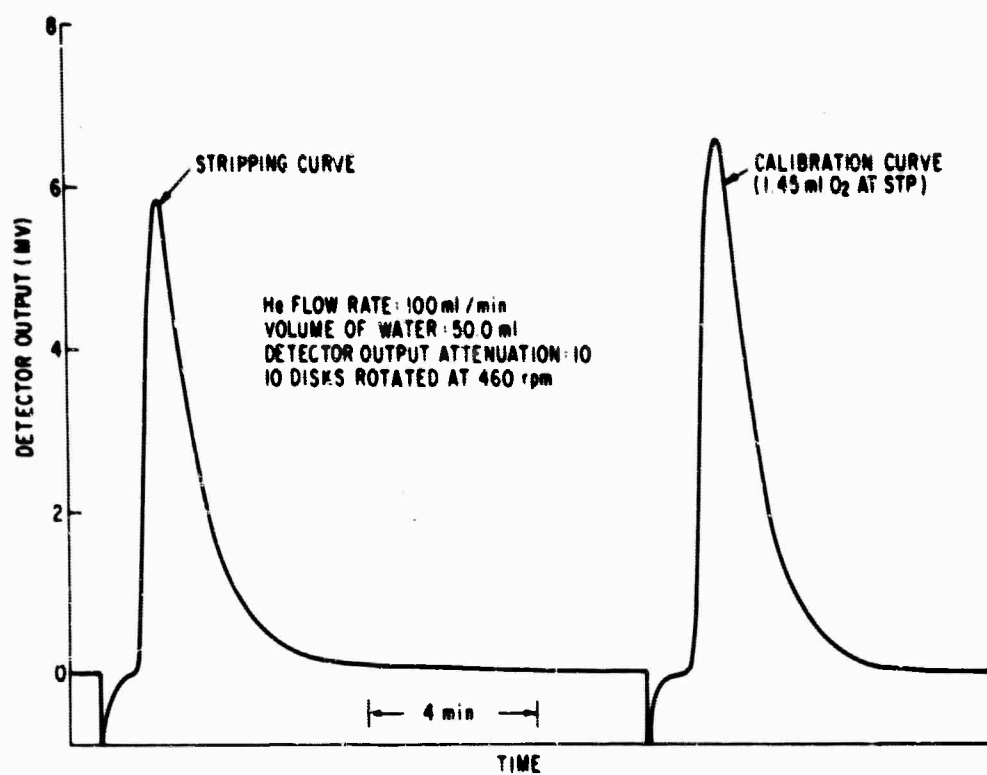


Fig. 108 Typical Stripping and Calibrations Curves for Oxygen in Water at 25°C

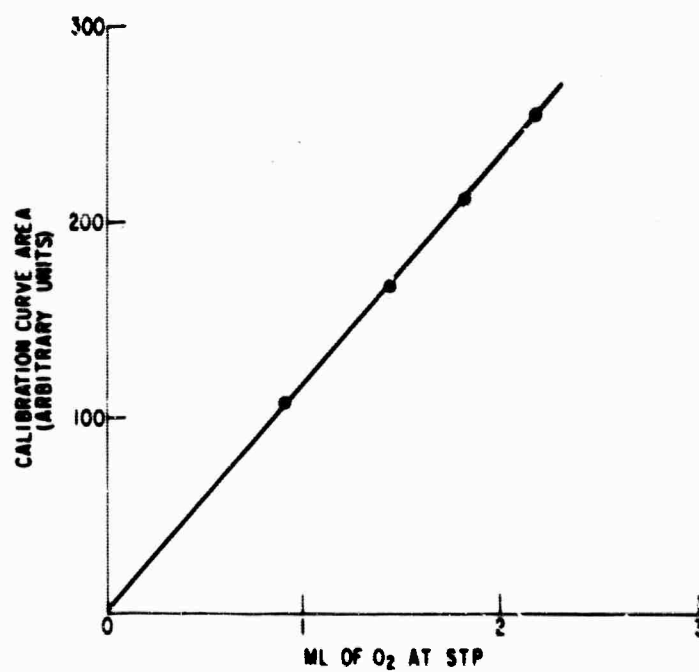


Fig. 109 Calibration of Gas Solubility Apparatus for Oxygen

Precision ($< 1\%$ maximum deviation from the mean for oxygen in water) and accuracy under the experimental conditions are good. Some uncertainty exists in the results because the liquid temperature during saturation was not known exactly. The largest uncertainty is due to the loss of solute gas while sweeping with He prior to rotating the disks. The magnitude of this uncertainty was estimated by varying the sweeping time in successive experiments. Data in Table XXV were obtained with a flushing time of 16 minutes at 100 ml He/min (50 ml of liquid present). The baseline was essentially flat after 14-15 minutes. It was found that increasing the flushing time to 20 minutes decreases the solubility value by 3.5 percent. The percentage decrease for a given increase in flushing time is reduced by more than one half when the liquid volume is doubled. Fortunately, the rate of loss of solute gas is considerably smaller during the initial stage of sweeping, since an appreciable partial pressure of solute gas is maintained above the liquid. Similar studies with other liquid levels and He flow rates indicate that overall accuracy is better than ± 5 percent if flushing is stopped when the baseline is flat. This accuracy is considered adequate for the uses intended. A gain in accuracy is achieved only at a cost of a considerable gain in complexity of the apparatus and technique.

Results obtained for propane and oxygen in concentrated phosphoric acid during the present reporting period are given in Table XXVI. These data were obtained with the apparatus shown in Figs. 105, 106, and 107. The necessary vapor pressures and densities were obtained from References (4) and (5).

The results for propane at 100°C are in good agreement with those obtained previously by a different technique (6) and as shown in Fig. 110. * It is noteworthy that appreciable propane and oxygen solubilities (relative to the room temperature values) are maintained even at $150 - 170^{\circ}\text{C}$. More data are needed to clearly distinguish between the effect of temperature and the effect of composition on the solubilities.

*Fig. 110 is a corrected version of Fig. 66 which appeared in the previous Technical Summary Report. The abscissa was incorrectly shown in Fig. 66.

(4) Technical Summary Report No. 4, Part 2, Task I, July 1 - Dec. 31, 1963, Contract No. DA44-009-ENG-4909, ARPA Order No. 247, Project No. 8A72-13-001-506.

(5) Monsanto Chemical Co., Technical Bulletin 1-239.

(6) Technical Summary Report No. 5 Jan. 1 - June 30, 1964, ARPA Order No. 247, Contracts No. DA44-009-ENG-4909 and No. DA44-009-AMC-479 (T).

TABLE XXVI

Solubility of Propane and Oxygen in Concentrated Phosphoric Acid

Temperature °C	Wt. % H_3PO_4	Solubility in Millimoles/Liter-Atms.	
		Propane	Oxygen
25	85.8	0.229 .225 .215	—
25	93.2	—	0.240 .249 .240
66	96.6	0.164 .165	—
100	89.1	0.192 .188 .188	—
100	93.2	0.179 .178	0.312 .328
100	96.2	0.173	0.319 .329
130	97.3	0.168 .159	—
130	97.6	0.154	0.293 .298
150	96.8	0.180 .183	—
150	97.7	0.189 .182 .184	0.339 .341
170	99.3	0.165 .157 .157	—

4.3.1.2 Static Method for Solubility Measurements

A. Experimental

A schematic diagram of the gas saturation apparatus is given in Fig. 111. The apparatus was designed primarily to equilibrate electrolytes with high boiling hydrocarbons such as octane at known partial vapor pressures of solute. It is constructed of pyrex glass with vacuum stopcocks.

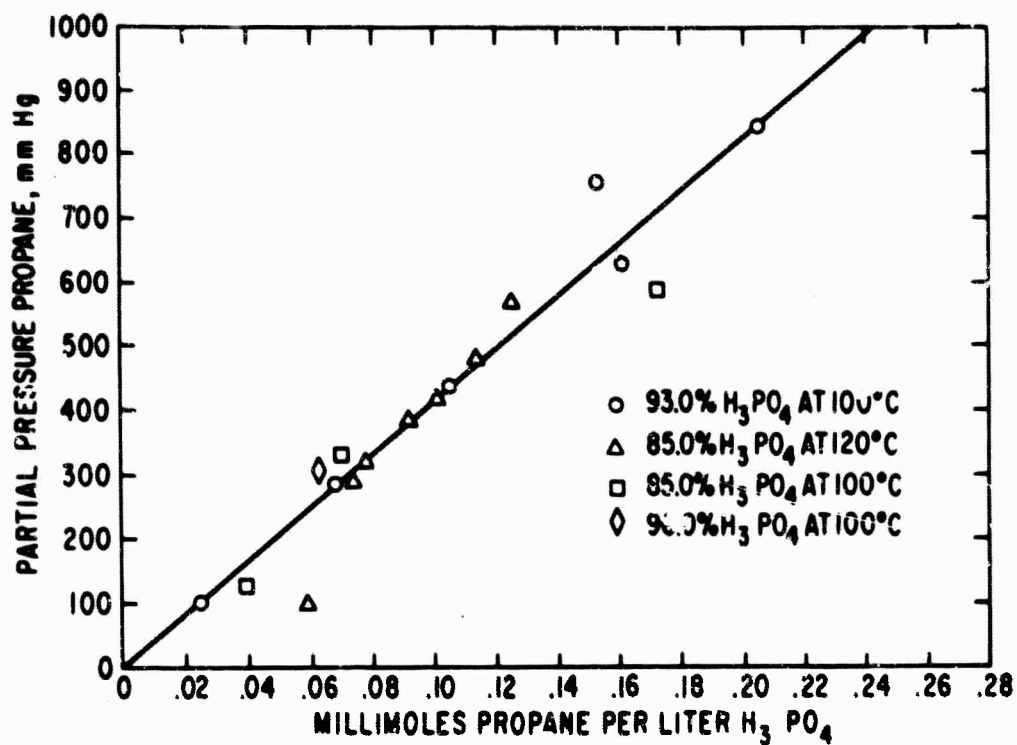


Fig. 110 Solubility of Propane in Concentrated Phosphoric Acid

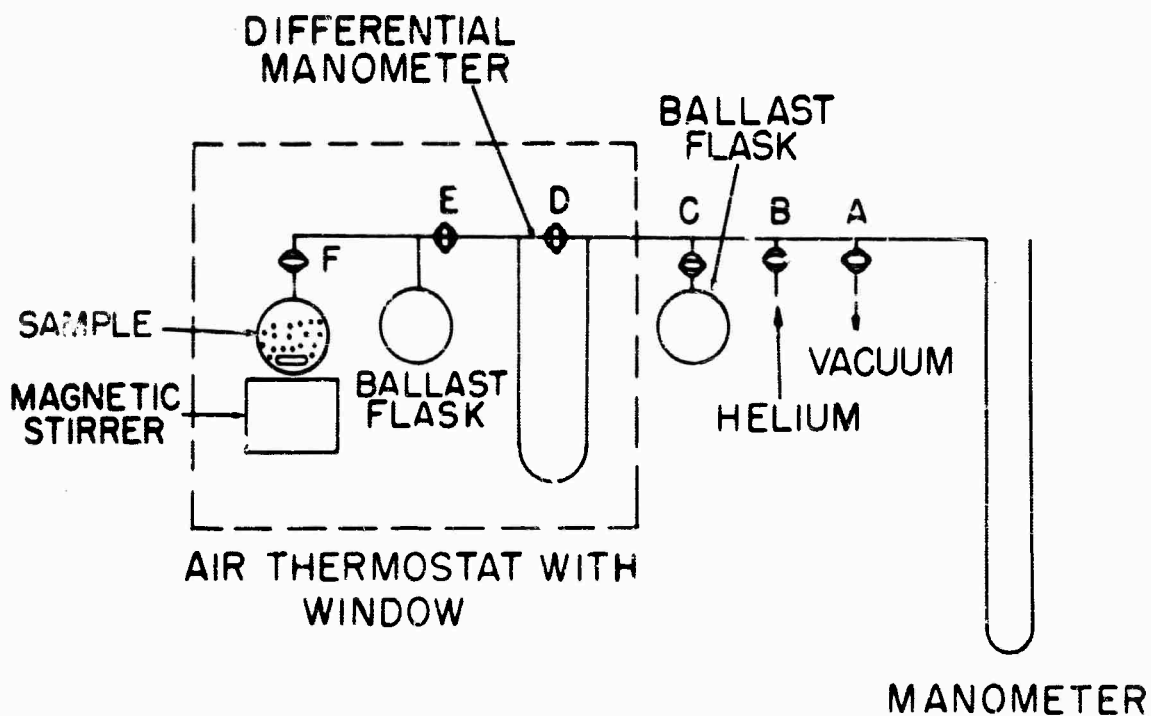


Fig. 111 Gas Saturating Apparatus

The volume of the system was measured, and used to calculate approximate volumes of liquid hydrocarbon required to attain desired pressures. This amount of solute was injected into the sample flask containing the acid (prepared by dehydration of 85% acid). Usually, about 20-30 cc H_3PO_4 was used, and less than 1 cc octane was introduced. The sample flask was then connected to the system, and all air was removed by alternate cooling and warming of the sample flask while under vacuum. After removal of air, stopcock "D" on the differential mercury manometer was closed and the oven turned on. The increase in pressure as the temperature increased was balanced by applying pressure to the external leg of the differential manometer. The stirrer was turned on, and the system allowed to come to equilibrium (usually 16 hours at temperature). After equilibration, the external manometer read the sum of the water vapor pressure and the octane vapor pressure. Since the water vapor pressures had previously been measured as functions of composition and temperature for phosphoric acid, the octane partial pressure was obtained by difference.* The sample flask was then disconnected while hot and a portion of the liquid taken by syringe for analysis of dissolved hydrocarbon.

The apparatus for stripping and analysis of solute is shown in Fig. 112. By suitable valving, the solute is stripped from the liquid by an inert gas and trapped by liquid nitrogen. It then goes to a chromatograph with hydrogen flame detector for analysis.

In practice, with valves "A" and "B" closed and "C", "D", and "E" open, pre-heated helium flows through the heated gas stripping cell to the coil immersed in liquid nitrogen and then out at "C". An acid sample (usually 1.00 cc) is injected through the rubber septum of the stripping cell and dissolved hydrocarbon is removed and trapped (stripping usually continued for 30 minutes). Valves "C" and "D" are then closed and the trap warmed up. Valves "A" and "B" are then opened, valve "E" closed, and the heated carrier gas flows through the trap to the chromatograph. A column (polyethylene glycol on Teflon T-6) is used to separate water, and the hydrocarbon is determined with a hydrogen flame detector. The system was calibrated with octane by injection of known microliter quantities. Peak areas were determined with a disk chart integrator.

Experimental results for octane solubility in phosphoric acid are listed in Table XXVII. Data is not extensive enough to permit correlation of temperature and concentration parameters. Either poor equilibration with vapor or analytical problems seem to cause scattered results in this static method for solubilities.

*An all-Teflon manifold (similar to the glass apparatus used for the determination of water vapor pressures over phosphoric acid) has been constructed. The Teflon system has the corrosion resistance required for work with new electrolytes.

TABLE XXVII
Solubility of Octane in Phosphoric Acid

Temperature °C	Wt. % H ₃ PO ₄	Partial Pressure Octane	H ₃ PO ₄ Solubility (millimoles/liter)
130	85.2	100	0.000557
130	85.2	200	0.000972
130	85.2	300	0.00175
130	85.2	400	0.00182
130	85.4	400	0.00674
130	85.4	400	0.00672
130	94.2	664	0.00703
130	96.0	100	0.000127
130	96.0	400	0.00275
130	96.0	400	0.00345
140	94.2	625	0.00651
150	93.1	435	0.0163
150	93.1	437	0.0131
150	93.1	437	0.0271
150	93.1	440	0.0118
150	93.4	250	0.00706
150	93.4	357	0.00755
150	94.2	564	0.00679
150	94.2	564	0.00511
150	95.4	251	0.00462
150	95.4	421	0.0175
150	95.4	426	0.0175
170	94.6	400	0.00308
170	94.6	426	0.000979
170	94.6	430	0.000761
170	94.6	430	0.000739

4.3.1.3 Conclusions

The solubilities of propane and oxygen in concentrated phosphoric acid at room temperature are approximately 1/8 and 1/5 respectively of their values in water. Over the range 25-170°C, the solubilities remain relatively insensitive to temperature. Appreciable solubilities of these gases in concentrated phosphoric acid (relative to their room temperature values) are maintained at temperatures as high as 170°C.

The solubility of octane in concentrated phosphoric acid at elevated temperature is an order of magnitude smaller than that of propane.

4.3.2 Physicochemical Properties of the C₂F₄-HF-H₂O Electrolyte System (E.J. Cairns)

As an adjunct to the fuel cell investigations, some of the more important physicochemi-

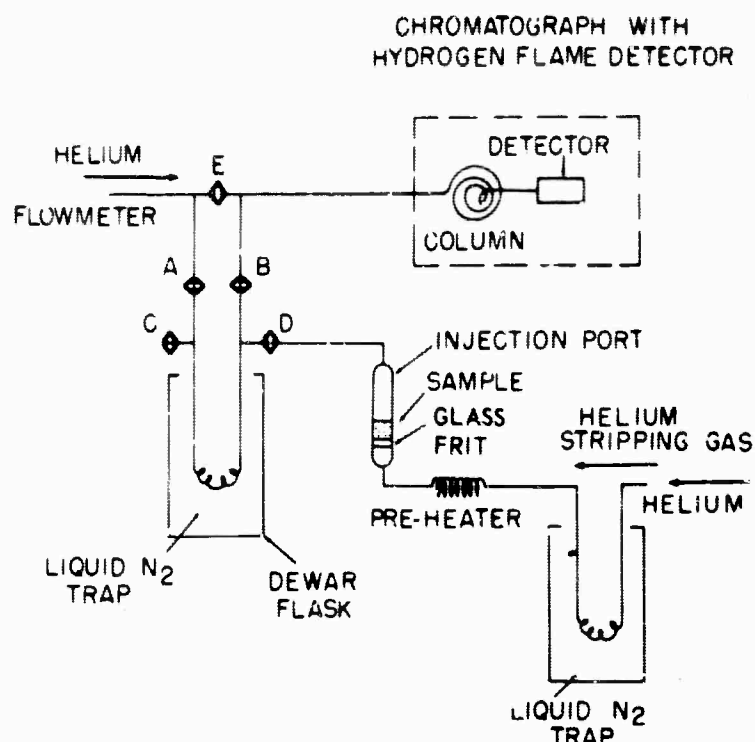


Fig. 112 Gas Stripping System

cal properties of the $\text{CsF-HF-H}_2\text{O}$ and $\text{HF-H}_2\text{O}$ systems have been measured. The regions of investigation were usually confined to the composition and temperature ranges of interest for fuel cell and electrochemical work.

4.3.2.1 Experimental

The measurements of electrolyte boiling points, freezing points, and densities were carried out in the single apparatus shown in Fig. 113. The density was determined by weighing a solid gold sphere in air and then in the electrolyte (at any temperature up to its boiling point). The volume of the gold sphere was determined from the relation:

$$\text{Vol of sphere} = \frac{\text{Wt in air} - \text{Wt in H}_2\text{O}}{\rho_{\text{H}_2\text{O}}}$$

and the density of the electrolyte was calculated from

$$\rho = \frac{\text{Wt in air} - \text{Wt in electrolyte}}{\text{Vol of sphere}}$$

The boiling point was measured by recording a temperature-time heating curve. Heat was supplied by a heating mantle with a temperature controller; temperatures were recorded using a thermocouple and a potentiometric recorder with zero suppression in order to maintain good sensitivity. Freezing points were determined from cooling curves. Solid CO_2 (in powder form) surrounding the sample beaker provided the cooling for the freezing point determination.

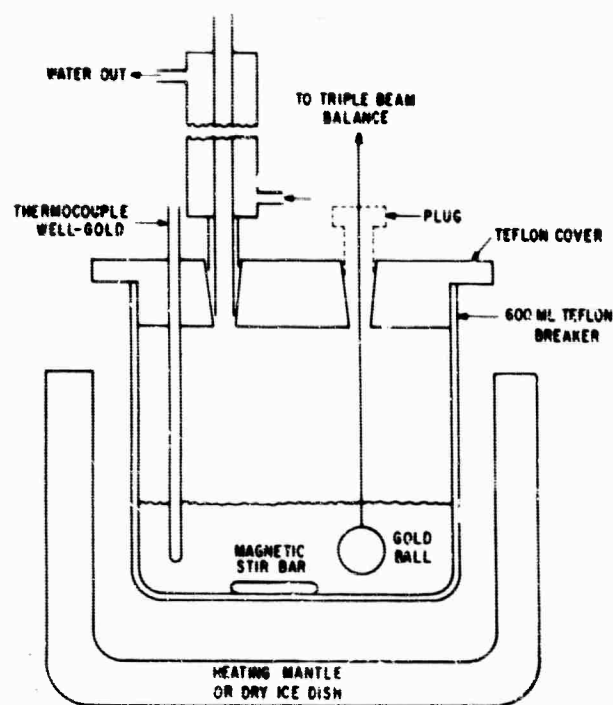


Fig. 113 Apparatus for Measurement of Boiling Points, Freezing Points, and Densities of Electrolytes.

Electrical conductivities were determined using the all-Teflon cell shown in Fig. 114 equipped with a reflux condenser (not shown). The temperature of the cell was maintained by use of the apparatus shown in Fig. 41, p. 4-54 of (1). The cell constant was 0.3184 cm^{-1} at 77°C , determined using 7.177 N KOH , having a specific conductance of $1.321 \text{ ohm}^{-1}\text{cm}^{-1}$ (2) at 77°C . It was desirable to determine the cell constant at an elevated temperature because the conductivities of the fluoride electrolytes were to be measured at temperatures up to 140°C . The effect of temperature on the cell constant was estimated using the coefficient of thermal expansion of Teflon, and was found to be less than 1% in the temperature range reported. All resistance measurements were carried out with a General Radio type 1650A impedance bridge, using a 1000 cps signal.

4.3.2.2 Results and Discussion

The boiling point, freezing point and density results for the $\text{CsF-HF-H}_2\text{O}$ system are summarized in Table XXVIII. The boiling point as a function of composition for the $\text{HF-H}_2\text{O}$ system, as reported by Vieweg(3), is shown in Fig. 115. The circular data points are those of Vieweg; the

-
- (1) Semi-Annual Technical Summary Report No. 5., Jan. 1 - June 30, 1964, ARPA Order No. 247, Contract Nos. DA44-009-ENG-4909 and DA44-009-AMC-479 (T).
 (2) P.M. Korotkov and N. K. Sokolov, J. Gen. Chem., USSR, 3, 670 (1933).
 (3) R. Vieweg, Chem. Tech., 15, 734 (1963).

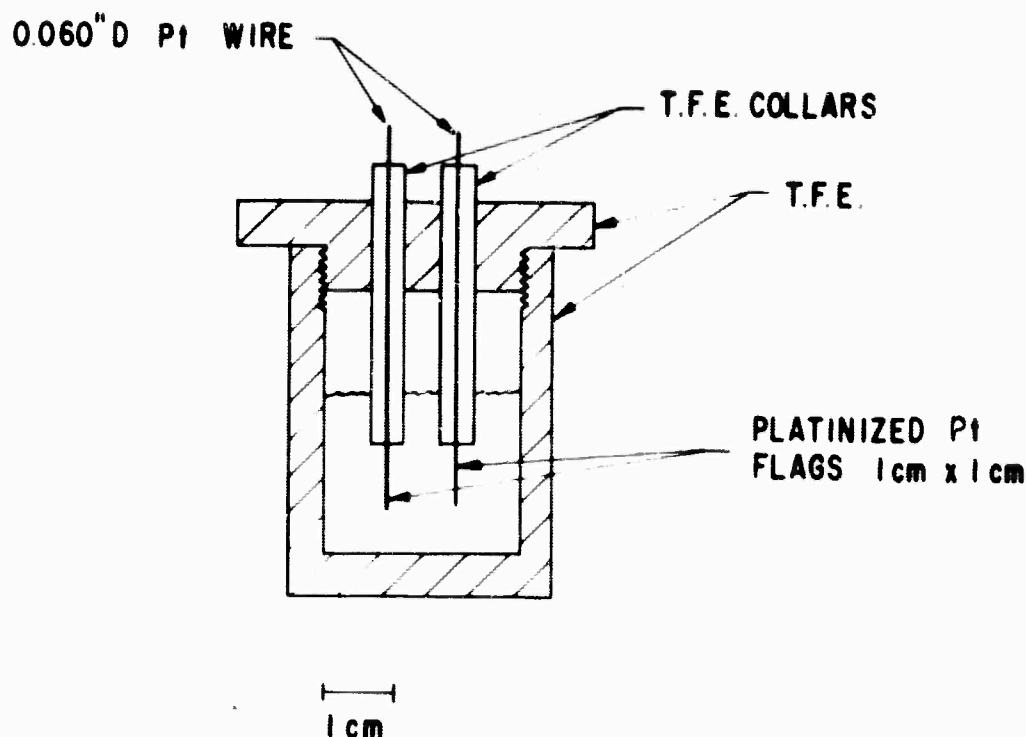


Fig. 114 Teflon Conductivity Cell

square ones are ours. The data of Table XXVII and Fig. 115 combined with boiling point data for aqueous cesium-salt solutions were used to construct the boiling point isotherms shown in Fig. 116. The precision of the isotherm location is highest near the H_2O -HF axis and in the region between 5 and 20 mole % water near $\frac{\text{HF}}{\text{CsF}} = 2$ to 3. Note that the single most important factor in determining the boiling point is the mole % CsF, which serves to raise the boiling point in a relatively uniform manner, regardless of the HF: H_2O ratio, above the boiling point of about 100°C . The two straight lines from the H_2O vertex correspond to $\text{CsF} \cdot 2\text{HF}$ and $\text{CsF} \cdot 3\text{HF}$. The regions of high HF content are only accessible at low water contents (for a boiling point of say, 150°C). The maximum cell performance at 150°C is obtained at $\text{HF}:\text{CsF} > 2.0$, $\text{H}_2\text{O} = 12.5$ mole %. The upper limit of the HF:CsF ratio, due to a boiling point requirement of 160°C , is 2.2. This means that regulation of the electrolyte composition will be an important factor in maintaining peak cell performance.

The density data of Table XXVIII were plotted against composition, and these plots were used for the construction of the triangular density-composition diagram shown in Fig. 117. The isochores or constant density lines shown (for 100°C) are consistent with density-composition data for other cesium salt-water systems, and with the density data available for the HF- H_2O system at 15°C (4). The

(4) L. Domange, Proc. Acad. Sci. Fr. ___, 459 (1934).

TABLE XXVIII
Properties of CsF-HF-H₂O Solutions

$\frac{\text{HF}}{\text{Cs F}}$	Mole % H ₂ O	Boiling Point (°C)	Freezing Point (°C)	Density (g/cc)
0.1644	69.26	160	—	—
0.5070	48.97	160	—	—
0.8211	35.37	160	—	—
1.080	27.61	160	—	—
1.344	37.52	160	—	—
1.619	13.52	160	—	—
1.647	4.89	160	—	—
1.85	5.87	175	—	2.85
1.88	87.6	102	—	—
1.91	27.1	153	22	2.72
1.93	30.5	133	-10	2.40
1.94	30.12	133	-10	—
1.95	7.19	196	38	—
1.998	9.71	168	27	2.72
2.05	75.2	106	—	—
2.077	9.77	160	—	—
2.22	17.61	160	—	—
2.86	7.91	142	20	2.418
3.00	14.90	138	2	—

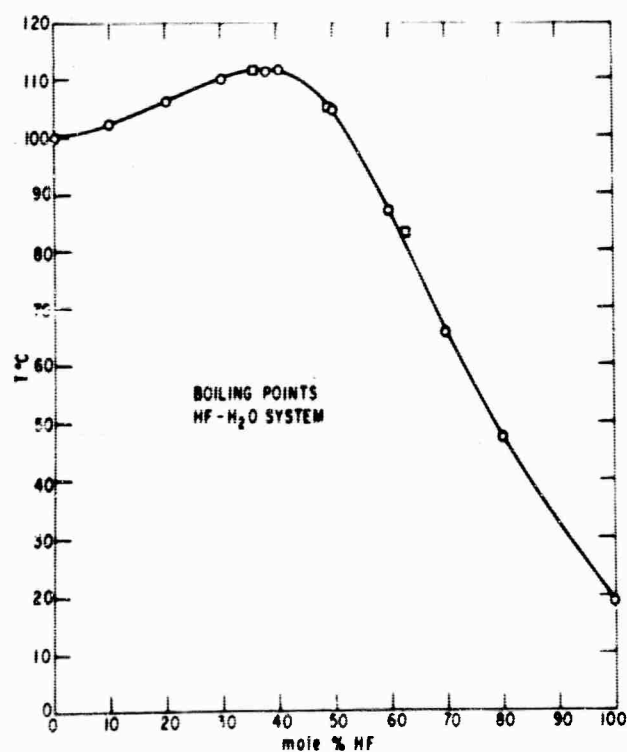


Fig. 115 Boiling Point As a Function of Composition for the HF-H₂O System. ○, As Reported by Vieweg (3); □, This Work.

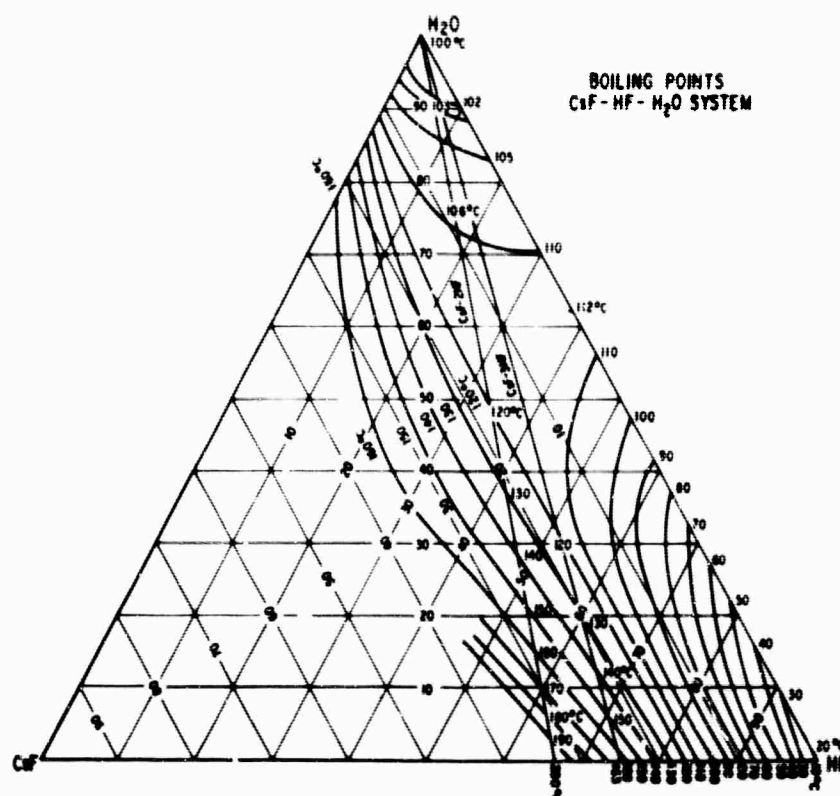


Fig. 116 Boiling Point Isotherms for the CsF-HF-H₂O System.

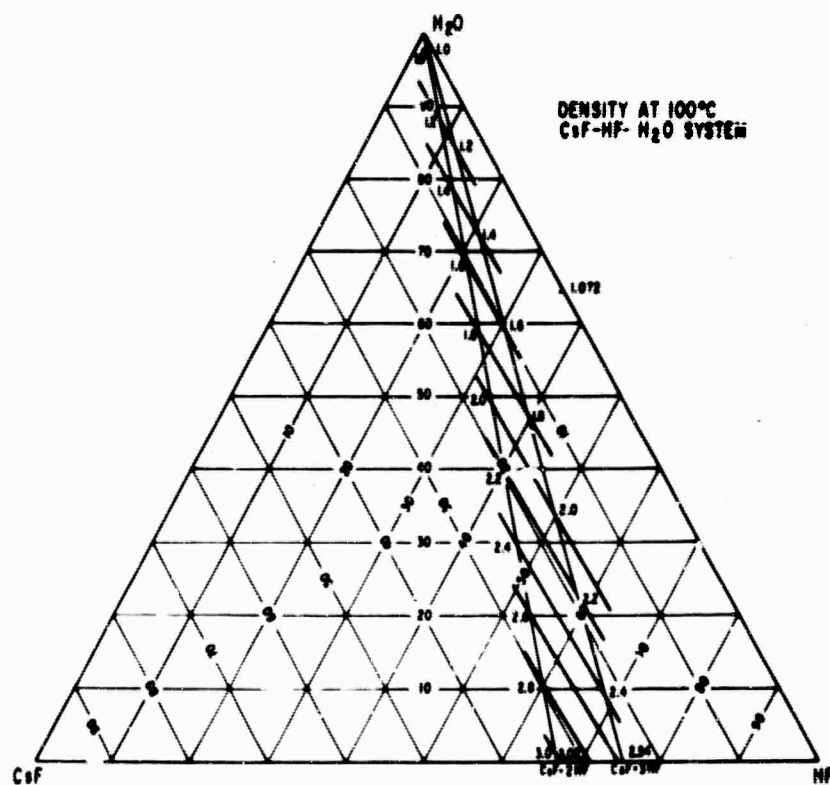


Fig. 117 Isochores for a Portion of the CsF-HF-H₂O System at 100°C.

HF-H₂O azeotrope has a rather strong temperature dependence of density, as shown by the results in Fig. 118. The circles are our data, the square point is interpolated from Fig. 119(4).

The freezing point data for the CsF-HF-H₂O should, in principle, allow the construction of the triangular composition - freezing point diagram, however, due to the large number of compounds formed by the three possible binary systems, it is difficult to construct the ternary phase diagram without a very large amount of data. Some of the features of the ternary system can be seen by considering the three binary diagrams shown in Figs. 120, 121 and 122. The HF-H₂O system(5) (Fig. 120) shows the formation of three compounds: H₂O · HF, H₂O · 2HF, and H₂O · 4HF. Note the very low freezing points. The HF-H₂O azeotrope freezes in the vicinity of -50°C. The portion of the CsF-H₂O system which is of most interest has recently been determined(6), and is shown in Fig. 121. Three compounds have already been identified in this system: CsF · H₂O, CsF · 1.5 H₂O, and CsF · 3 H₂O. The freezing points for compositions containing less than 60 mole % H₂O become rather high and, fortunately, these compositions (near the CsF-H₂O axis of the ternary diagram) are not particularly interesting for use in hydrocarbon fuel cells.

The HF-rich portion of the CsF-HF phase diagram (Fig. 122) (7) is important to the operation of hydrocarbon cells and to the preparation of CsF-HF-H₂O electrolyte. The compound CsF · HF has a melting point of 176°C, making this a convenient intermediate in electrolyte preparation. The compound CsF · HF is prepared by heating a mixture of CsF and HF (with a 10-20% excess of HF), evaporating the excess H₂O (if any) and HF, and periodically determining the freezing point. When a value of 176°C is obtained, compound formation is complete, and excess reactants have been evaporated. It is noteworthy that the freezing points of CsF · HF mixtures decrease sharply as the HF content increases, so that freezing points in the vicinity of room temperature and lower are obtained in the regions corresponding to F/Cs ratios exhibiting good fuel cell performance on hydrocarbons. There are at least four compounds formed in this binary system: CsF · HF, CsF · 2HF, CsF · 3HF, and CsF · 6HF.

The freezing point data from Table XXVIII were used together with the data from Fig. 122 for the construction of a pseudo-binary diagram, which is a section of the ternary taken parallel to the CsF-HF face, but at 7.5 mole % H₂O. Note that the whole diagram as shown in Fig. 123 is depressed by about 12°C below that in Fig. 122. This diagram is nearly the pseudo-binary which contains compositions exhibiting maximum performance at 150°C. The important freezing points are in the range 5-30°C.

(5) G. H. Cady and J. H. Hildebrand, J. Am. Chem. Soc., 52, 3843 (1930).

(6) R. Cohen - Adad and C. Ferlin, Compl. Rend. 258, 4057 (1964).

(7) R. V. Windsor and G. H. Cady, J. Am. Chem. Soc., 70, 1500 (1948).

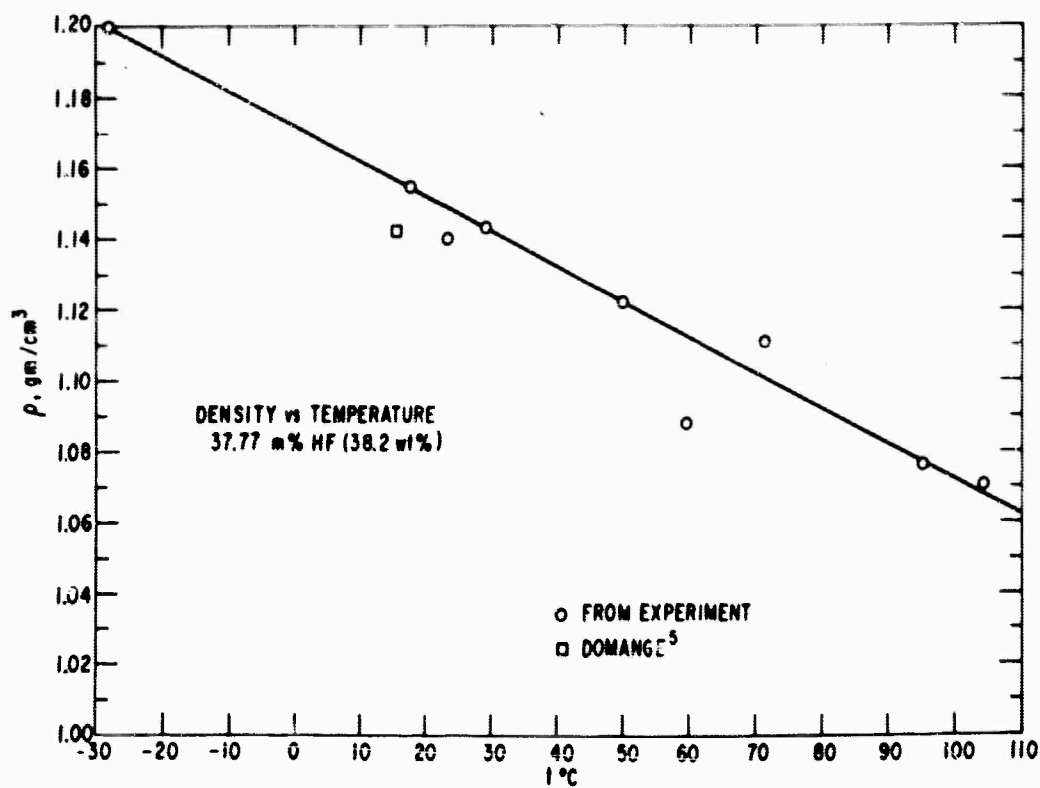


Fig. 118 Density as a Function of Temperature for the HF-H₂O Azeotrope.

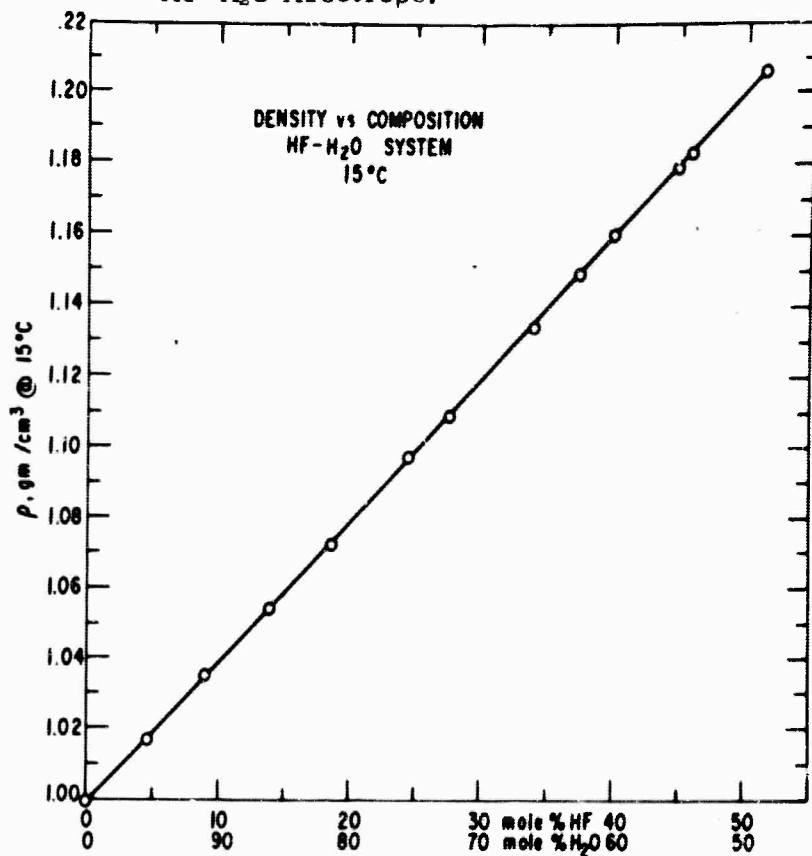


Fig. 119 Density as a Function of Composition for the HF-H₂O System at 15°C, According to Domange (4).

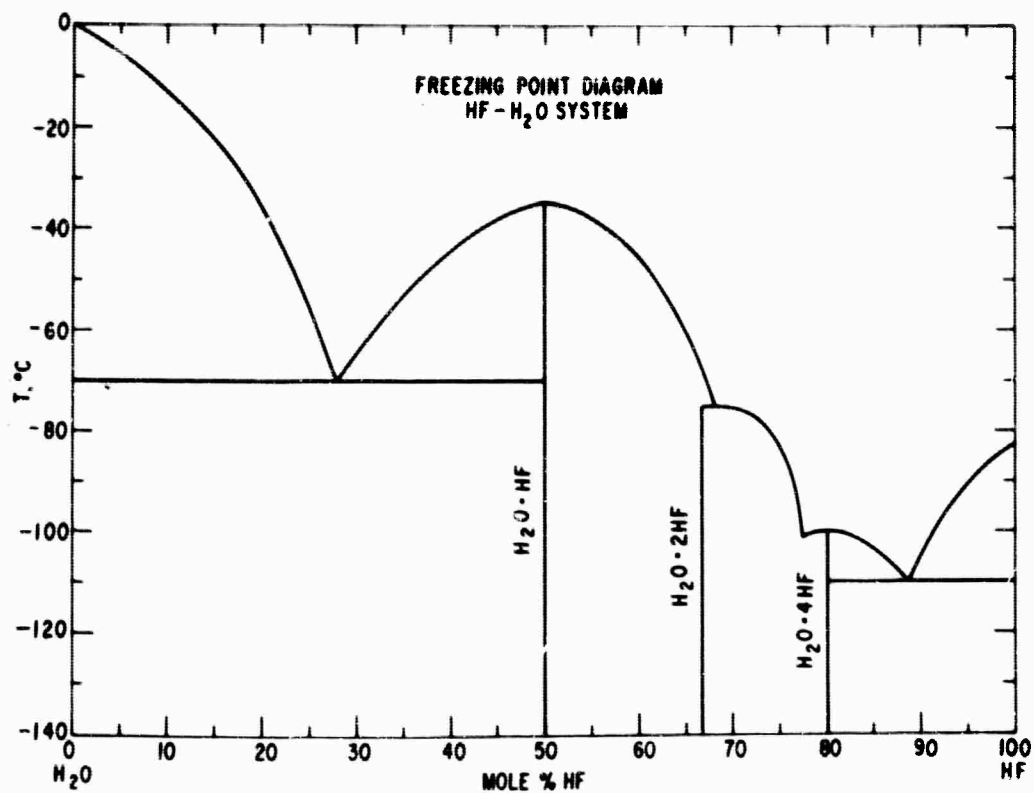


Fig. 120 Phase Diagram for the HF-H₂O System, According to Cady and Hildebrand (5).

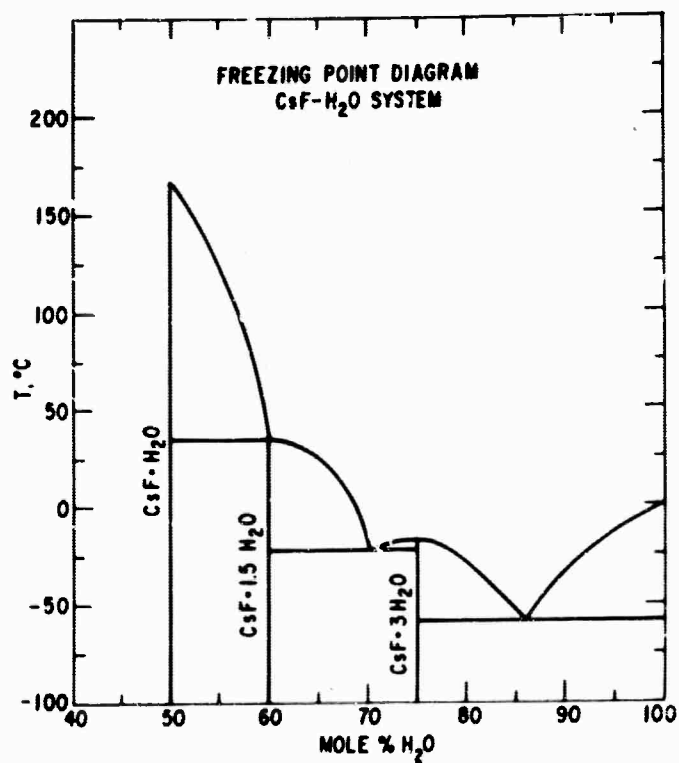


Fig. 121 Partial Phase Diagram for the CsF-H₂O System, According to Cohen-Adad and Ferlin (6).

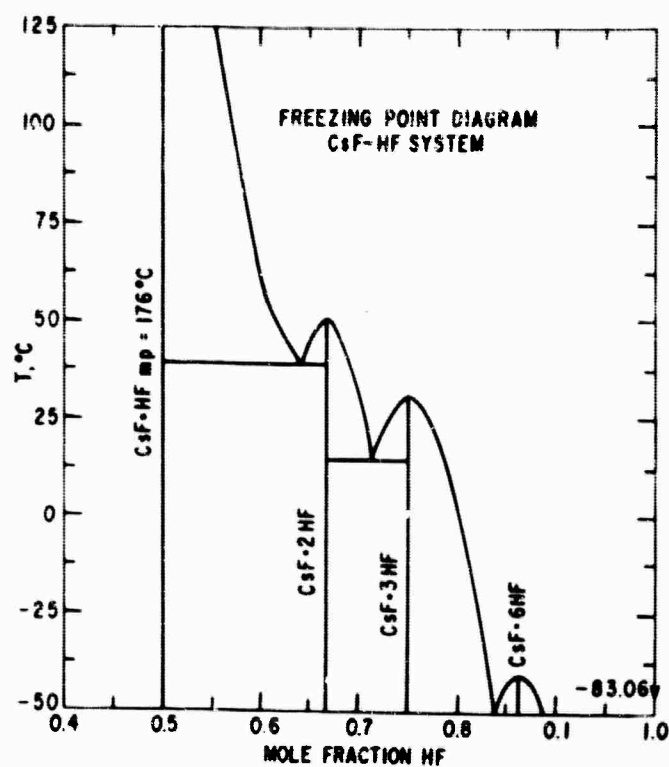


Fig. 122 Partial Phase Diagram for the CsF-HF System, According to Windsor and Cady (7).

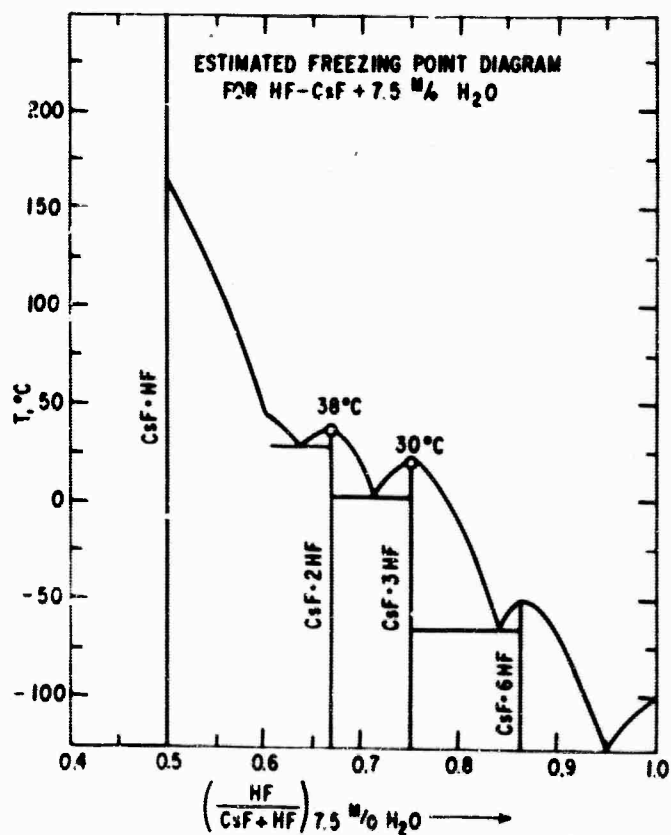


Fig. 123 Estimate of a Portion of CsF-HF-H₂O Phase Diagram at 7.5 mole % H₂O.

The specific conductances for the HF-H₂O and CsF-HF-H₂O systems as a function of temperature and composition are summarized in Table XXIX. The results for the HF-H₂O system are compared to those of other investigations (8, 9) in Fig. 124. The agreement is rather good. Fig. 125 shows how the conductivity of a CsF-HF-H₂O mixture varies with the amount of Cs present at constant fluoride: water ratio of 37:63. It is interesting that the solutions containing 10 mole % CsF or more have a higher conductivity at 100°C than the HF-H₂O system with the same fluoride content. This indicates that the replacement of some of the H with Cs actually increases the conductivity, even though the Cs⁺ ion has a lower mobility than the H⁺ ion. The HF is not totally ionized, and it may be that the total number of ions in the system is significantly greater for the Cs - containing system than for the HF-H₂O binary of the same fluoride concentration.

4.3.2.3 Conclusions

1) The boiling point - composition diagram for the ternary system CsF-HF-H₂O has been determined with an accuracy of about 3°C in the composition range of most interest.

2) The densities of the CsF-HF-H₂O system in the range $2 < \frac{\text{HF}}{\text{CsF}} < 3$ for all water contents have been determined at 100°C with an accuracy of about 1%. The density of the HF-H₂O azeotrope has been determined as a function of temperature in the range -28°C to 105°C.

3) The freezing point diagram for the CsF-HF-H₂O system at a constant water content of 7.5 mole % has been estimated; freezing points for other selected compositions have been reported.

4) The conductivities of the HF-H₂O system and selected compositions in the CsF-HF-H₂O system have been determined over the temperature range 25-125°C. Certain CsF-HF-H₂O solutions show higher conductivities than the corresponding HF-H₂O solution of equal fluoride concentration.

(8) E.G. Hill and A.P. Sirkar, Proc. Roy. Soc., 83, 130 (1910).

(9) S.J. Broderick, J. Chem. Eng. Data, 7, 55 (1962).

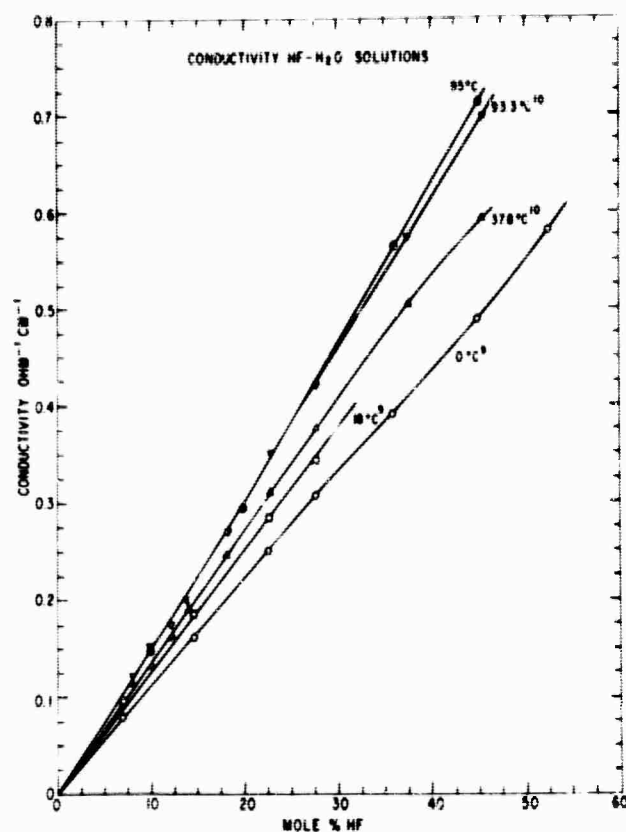


Fig. 124 Conductivity of HF-H₂O Electrolytes as a Function of Composition at Several Temperatures.

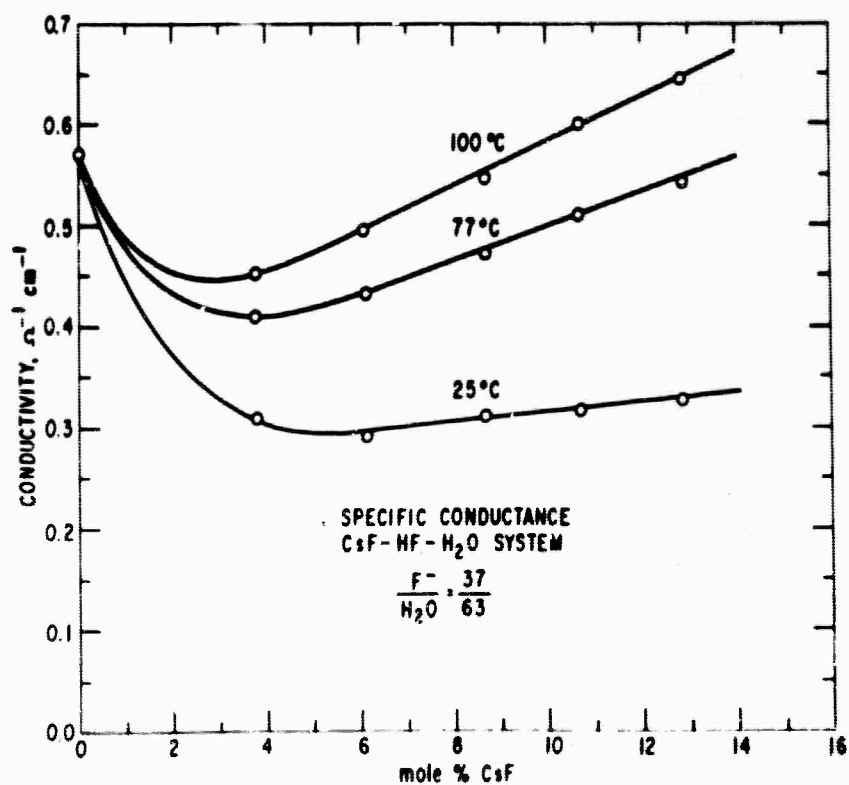


Fig. 125 Conductivity of Some CsF-HF-H₂O Solutions as a Function of CsF Content for a Constant $\left(\frac{F}{H_2O}\right)$ Ratio of 37/63, at Three Temperatures.

TABLE XXIX

Conductivities of Fluoride Electrolytes ($\text{ohm}^{-1} \text{cm}^{-1}$)

Mole %			Temp °C									
CsF	HF	H ₂ O	25	27.5	70	77	80	95	100	105	125	150
0	10	90		0.142				0.146				
0	20	80		0.281				0.294				
0	36	64		0.555		0.561*		0.564		0.565		
0	40	60				0.591						
0	45	55		0.715				0.712				
0	57	43		1.015	1.061							
3.78	52.55	63.66	0.308			0.409			0.451*			
6.10	30.84	63.07	0.291			0.433			0.497*			
8.64	28.98	62.38	0.311			0.472			0.546*			
10.64	27.28	62.08	0.318			0.510			0.600*			
12.85	25.81	61.34	0.328			0.541			0.645*			
23.81	46.19	30.00	0.173				0.358				0.516	0.635*
30.0	60.0	10.0	0.166				0.350				0.500*	0.580*

* These data were obtained from extrapolations of the $\log L$ vs $\frac{1}{T}$ plots.

4.4 ELECTRODE STRUCTURE RESEARCH

The electrode research effort puts into practice the understanding and discoveries that evolve from all other areas of the research program. Furthermore, the failure analysis, coupled with the life testing, provide the yardstick to evaluate progress and enhance improved developments.

Consistent with the objectives outlined in Table 1 Section 3.1, the studies on low cost electrode screen materials and the discovery of asbestos as an electrode structure reinforcing agent are reported in the subsequent paragraphs. The progress on new developmental designs, characterization, and failure analysis is also discussed.

4.4.1 Low Cost Screen Materials (P. V. Popat)

The investigations to select and evaluate low cost metallic materials for electrode screens are discussed in the subsequent paragraphs. These screens must be resistant to corrosion in the concentrated phosphoric acid at 150°C used as the CO₂-rejecting electrolyte for the hydrocarbon-air fuel cells.

The metallic screens are critical components in which very little corrosion or dimensional changes can be tolerated during extended periods of operation, open-circuit or stand-by conditions. For these screens to function satisfactorily over extended periods, it is believed that their corrosion rates under the fuel cell operating environments should generally be of the order of one mil per year. Apart from the effects of corrosion on the structural stability, porosity and critical dimensions, excessive corrosion is also undesirable because the corrosion products may poison the electrocatalysts or otherwise impair the electrode performance. A primary consideration was to select and evaluate low-cost, non-noble metallic materials. The data reported in an earlier progress report (1) show that tantalum is one of the best materials for screens from the point of view of corrosion resistance; however, its cost is rather high. It is desirable, therefore, to have a material with essentially the same degree of corrosion resistance as tantalum, but only a fraction of its cost.

The preliminary selection of low cost metals and alloys was arbitrarily based upon three considerations:

- 1) Available corrosion data for a variety of metals and alloys (1). These data were confirmed and/or extended for certain promising low cost materials.

(1) Interim Report No. 1, April 1, 1964, General Electric Company; U.S. Army Engineer Research and Development Laboratories, Contract No. DA-44-009-AMC-479(T) ARPA Order No. 247, Program Code No. 4980; Project No. P-4980.

2) Qualitative predictions based upon the theories of passivity assumed to be due to certain stable electronic configurations and related alloying principles (2-4). These principles are semi-empirical at present and apply primarily to low temperature corrosion. Passive layers break down at elevated temperatures.

3) Private communications with other investigators and with suppliers of special alloys. Most of the alloys tested are not available commercially and difficult to make. The alloys were, in general, custom made for experimental evaluation. Phase separation of the various constituents during testing was the single most serious problem encountered with most of the alloys.

Since some experimental work with concentrated hydrofluoric acid as the electrolyte also appeared promising, a preliminary screening of some of the selected materials for stability in 48% hydrofluoric acid at 23°C and 100°C was completed during the present reporting period. Further work on this phase of the task was postponed by mutual agreement between the representatives of ERDL and the General Electric Company. The preliminary data obtained is contained in Table I of Appendix 5.3.1. No further work with hydrofluoric acid is planned.

4.4.1.1 Experimental

The experimental set-up was the same as used earlier for chemical corrosion work(1). The test procedure was modified to simulate actual fuel cell environments as closely as possible. Each specimen, after appropriate cleaning procedure, was immersed in 88 weight percent phosphoric acid at 150°C (300°F) under the following environments:

- 1) Hydrogen gas bubbling This simulates strong reducing environments at the anode.
- 2) Hydrogen gas bubbling, the test sample in contact with platinum black electrodes. This simulates the actual environments, including galvanic cells between the substrate and the low overvoltage electrocatalyst used for fuel oxidation.
- 3) Propane gas (as the typical saturated hydrocarbon fuel) bubbling over the test specimen.
- 4) Same as 3) with the test specimen in galvanic contact with platinum black electrode.
- 5) Oxygen bubbling over the test specimen. This simulates the oxidizing conditions at the air cathode.
- 6) Same as 5) with the test specimen in galvanic contact with platinum black electrode. This simulates the actual environments in the air cathode in a hydrocarbon-air fuel cell.
- 7) Some tests were conducted in a non-aerated acid solution, exposed to the atmosphere at the condenser head.

-
- (2) Uhlig H.H., "Electron Configuration in Alloys and Passivity" Z. Elektrochem, 62, 700 (1958).
 - (3) Robins, D.A., "An Interpretation of Some of the Properties of the Transition Metals and Their Alloys" J. Less Common Metals, 11, 396 (1959).
 - (4) Landau and Oldach C.E., "Corrosion of Binary Alloys", Trans. Electrochem. Soc. 81, 521 (1942).

4.4.1.2 Results and Discussion

The corrosion data for each specimen in 88 wt % phosphoric acid at 150°C (300°F) under the reducing or oxidizing environments are given in Table II Appendix 5.3.1. It is clear from the table that, in general, the corrosion rates of metals and alloys in the oxidizing environments are several orders of magnitude higher than under the reducing environments. Neglecting the kinetic factors, for the moment, the higher corrosion rates under oxidizing conditions follow directly from the higher oxidation potentials (greater free energy changes) with oxygen environments, as compared to hydrogen or propane environments. Higher corrosion rates with propane environments as compared to the hydrogen environments can be explained with similar arguments. The experimentally observed potential established with propane as fuel is more oxidizing than the potential established with hydrogen, other conditions being equal.

In the case of an oxygen environment, the cathodic reduction process in the overall electrochemical corrosion of the metal can be either reduction to a peroxide, a complete reduction to water, or a combination of both processes. Relative contribution of each process will depend on the catalytic activity for hydrogen peroxide decomposition or for complete reduction of oxygen to water. In any case, the corrosion rates in the presence of oxygen appear to be cathodically controlled. This is particularly so in those cases where the corrosion rate in the oxygen atmosphere is accelerated by the presence of platinum black electrode in metallic contact with the test specimen. The cathodic reduction process, which is rate controlling, is speeded up in the presence of platinum black catalyst, and consequently so are the overall corrosion rates. In the case of reducing environments, the overall corrosion rate appears to be controlled both by the anodic dissolution of the metal, as well as the cathodic evolution of hydrogen (mixed control). In those cases where the rate remains essentially the same in the presence of platinum black electrode as in its absence, one can conclude that the overall corrosion rate is probably controlled by anodic process.

One very important parameter which has not been considered in the studies reported so far is the metallographic aspect of the several alloys. The basic assumption underlying the various electronic theories of the passivity (e.g., alloying to produce corrosion resistant stainless steel alloys) is that the alloy forms a solid solution or one homogeneous phase. In contrast to this, it was observed (by optical microscopy at high magnification) that many alloys, particularly iron and chromium alloys, exhibited distinct phase separation or segregation. Different areas of the same specimen showed distinctly different crystal structures and rates of corrosion, as judged from the different appearance of the various areas on the same specimen. Many of the alloys were melted and remelted in vacuum several times, and even then, phase segregation was evident at the end of the corrosion test. This metallurgical factor will be more closely controlled in the future work since it has a very large effect on the overall corrosion behavior of the alloy.

4.4.1.3 Conclusions

On the basis of the data reported in Table II, of Appendix 5.3.1 the following general conclusions can be made:

A. Anode (Fuel Electrode) Substrates

1) Commercially available tungsten screen as well as 93% tungsten-7% nickel alloy are sufficiently resistant to corrosion in 88 wt % phosphoric acid at 150°C in the reducing environments (hydrogen or propane) as exhibited by their corrosion rates of less than one mil per year. This corrosion resistance is unaffected by the presence of platinum black in contact with the test specimen.

2) The corrosion rate of the tungsten-nickel alloys increases generally as the percentage of nickel in the alloy increases.

3) Molybdenum nickel alloy (89% Mo, 11% Ni) is resistant to the phosphoric acid at 150°C in the presence of hydrogen but not in the presence of propane (2-6 mpy). Also the corrosion rates of the molybdenum-nickel alloys having 71% or less molybdenum tend to increase, in some cases, rather significantly, in the presence of a platinum black electrode. For instance, the corrosion rate of 71% Mo, 11% Ni in an H₂ environment in the absence of platinum was 1.8 mpy, whereas in the presence of platinum black, the rate increased to 550 mpy.

4) Iron-chromium and cobalt-chromium alloys are quite unsuitable for anode or cathode substrates. Nionel appears to be satisfactory (0.6 mpy) in the absence of platinum black. Further work, including obtaining corrosion data in the presence of platinum black, will be needed before final conclusions concerning the suitability of Nionel can be made.

B. Cathode (Air Electrode) Substrates

1) None of the metallic materials investigated during this report period have corrosion resistance to oxidizing environments equal to or better than that of tantalum or noble metals reported previously (1).

2) Of the materials investigated during this report period, titanium carbide (3.8 mpy in absence of platinum black electrode) and tungsten alloy #11 (composition not yet available) appear to be the most promising candidates for further evaluation.

Future work will be directed towards materials with homogeneous (single phase) alloy compositions containing a small percent of a noble metal. Emphasis will be on low cost tungsten alloys and carbides. Theories of electronic bonding as applied to surface properties of alloys for corrosion resistance will be examined in detail to arrive at the optimum composition for maximum stability in phosphoric acid at 150C under oxidizing conditions.

4.4.2 Asbestos as a Reinforcing Agent (L.W. Niedrach/M. Tochner/H.I. Zeliger)

The incorporation of fibrous reinforcing agents into the electrode structure was investigated since it offered potential improvement to the electrode cracking and leakage problem. Asbestos fibers were chosen for initial studies because of their known high strength as well as their acid resistance.

Electrodes for test were prepared with but minor modifications to the standard procedure for the Niedrach-Alford electrodes (1). Before use, the asbestos was digested with concentrated hydrochloric acid on a steam bath to remove acid soluble materials, water rinsed and dried. All electrodes were supported on 45 mesh platinum screens and had a film containing 1.6 mg Teflon/cm² on the gas side. In some electrodes the platinum and asbestos were distributed uniformly throughout, in others, a dual-layer structure was used with different amounts of platinum and/or asbestos on the electrolyte and gas sides of the electrode.

4.4.2.1 Evaluation Procedures

Two types of evaluation were performed. The first consisted of operation in a fuel cell against a standard platinum black counter-electrode. Tests were performed in 5N sulfuric acid cells at ambient temperature, and in 85% phosphoric acid cells at 150°C. In the former case, the electrodes were tested with hydrogen and oxygen, in the latter with hydrogen and propane. For the second evaluation, representative examples of the electrodes were digested for a week under 85% phosphoric acid at 150°C in a hydrogen atmosphere. Utilizing this test, electrodes without asbestos reinforcement have been shown to develop cracks in a few days. (2)

4.4.2.2 Results and Discussion

A number of dummy electrodes were prepared without supporting screens to obtain a general assessment of the effect of compositional variables prior to testing in fuel cells. The proportions of materials used are indicated in Table XXX.

-
- (1) L.W. Niedrach and H.R. Alford, Saturated Hydrocarbon Fuel Cell Program: A New High Performance Fuel Cell Employing Conducting Porous-Teflon Electrodes and Liquid Electrolytes, Contract DA-44-009-AMC-479 (T). J. Electrochem. Soc, in press.
 - (2) Technical Summary Report No. 5, Jan. 1-June 30, 1964, Contract Nos. DA 44-009-ENG-4909 and DA 44-009-AMC-479 (T), p. 4-93 ff.

TABLE XXX
Composition of Dummy Electrodes

Electrode No.	Pt. (gm)	Composition *	
		Asbestos (gm)	T-30 (cc)
1	0.6	-	0.06
2	0.6	0.06	0.06
3	0.6	0.12	0.06
4	0.6	0.18	0.06

* Amounts spread over 17.7 cm² area.

Over this range there was an increase in strength with increasing asbestos content. The all platinum spread was brittle and crumpled easily. Dummy electrode 4, on the other hand, was significantly stronger and could be bent and forth without cracking. Measurements showed that the electrical conductivity was not impaired by the asbestos additions.

A number of screen supported electrodes covering the range of composition were subsequently manufactured for tests in fuel cells. Included among them were electrodes having a dual-layer structure with different amounts of platinum and/or asbestos on the gas and electrolyte sides of the supporting screen. A summary of the electrode compositions appears in Table XXXI.

TABLE XXXI
Composition of Test Electrodes*

Electrode No.	Composition * *					
	Electrolyte Side			Gas Side		
	Pt (gm)	Asbestos (gm)	T-30 (cc)	Pt (gm)	Asbestos (gm)	T-30 (cc)
636, 637 (controls)	0.3	-	0.03	0.39	-	0.03
638, 639	0.3	0.03	0.03	0.3	0.03	0.03
644	0.3	0.09	0.03	0.3	0.09	0.03
642	0.3	0.09	0.03	0.3	-	0.03
643	-	0.3	0.03	0.3	-	0.03
660	0.3	0.09	0.06	0.3	0.09	0.06

* Supported on 45 mesh, 0.0078 in. wire Pt screens,
1.6 mg Teflon/cm² film on gas side

** Amounts spread over 17.7 cm² area.

Increasing the amounts of asbestos to 0.15 and 0.24 gm per 0.3 gm Pt resulted in electrodes lacking in strength. It is likely, however, that increased Teflon loadings could counteract this effect. The layer that was prepared without platinum also was lacking in strength, which again appears to reflect a deficiency in the amount of Teflon binder.

Performance data for the various electrodes are presented in Figs. 126 through 129. Anode vs. cathode polarizations are shown for cells with the test electrode on the indicated reactant and a standard electrode (or equivalent) serving as the counter electrode. The ohmic drops have been eliminated for normalization purposes because some data were obtained with 1/8 inch electrolyte gaps and others with 3/8 inch gaps. With the exception of electrode 643, none of the asbestos electrodes contributed a detectable increase in the cell resistance. Electrode 643, which had no platinum on the electrolyte side, produced a sizeable increase in cell resistance. This was partly associated with the wetting properties of the electrodes since vacuum impregnation of the electrode was required before satisfactory performance could be obtained.

Apart from this increase in cell resistance for electrode 643, all of the electrodes performed as well as the standard electrodes on hydrogen, oxygen and propane. This includes the performance of electrode 644 after a week's digestion in phosphoric acid at 150°C in a hydrogen atmosphere.

The effect of the asbestos addition on resistance to cracking is shown dramatically in Fig. 130. Electrodes 636 and 644, as well as 639 and 646, were immersed for a week under 85% phosphoric acid at 150°C in a hydrogen atmosphere. Reinforced electrode 644 shows marked resistance to cracking. In contrast, extensive cracking is evident in the control electrode. While both pictures were taken after a week's exposure, visual examination after two days indicated that many of the cracks in the control had already formed.

A few incipient cracks were visible in electrodes 639 and 642 containing intermediate amounts of asbestos after a week's digestion under the phosphoric acid. These cracks were concentrated in thinner areas, and, in contrast to those in the control, did not penetrate through the structure.

These results indicate that the incorporation of fibrous material into Conducting-Porous-Teflon electrodes can markedly improve their structural integrity. Further work in this area is desirable, particularly with regard to optimization on the basis of longer term tests.

4.4.2.3 Conclusions

Asbestos is effective in improving the structural integrity of Teflon-bonded electrodes. The use of these or similar fibers should be effective in overcoming cracking problems associated with the Teflon bonded electrodes.

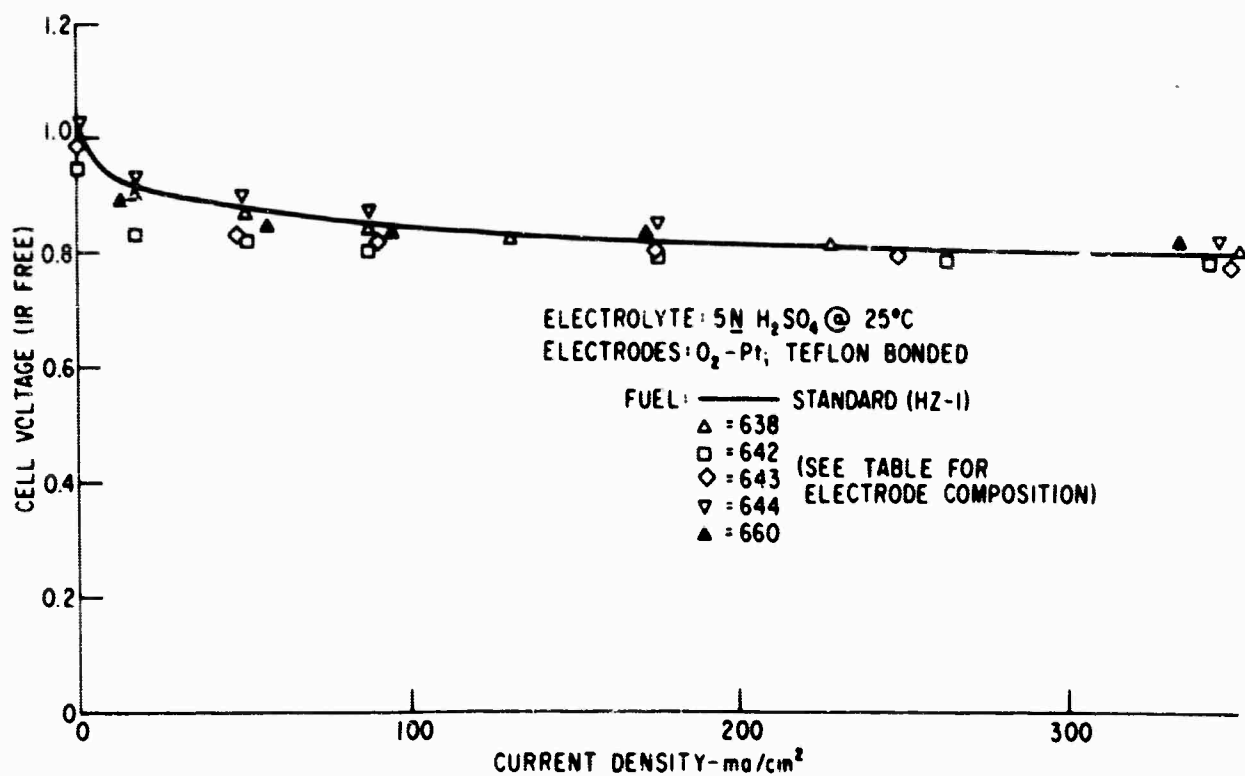


Fig. 126 Effect of Asbestos Content on Performance as a H_2 Anode With 5N H_2SO_4 Electrolyte

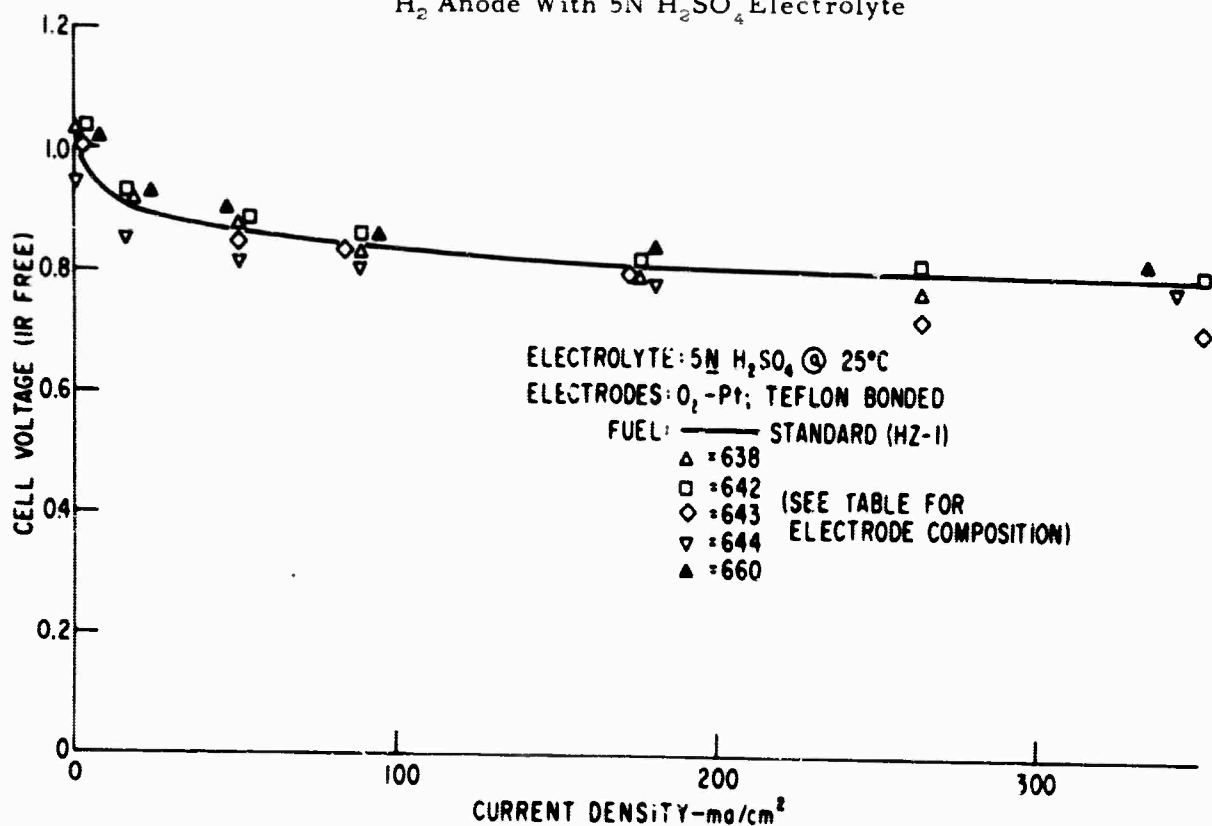


Fig. 127 Effect of Asbestos Content on Performance as an O_2 Cathode With 5N H_2SO_4 Electrolyte.

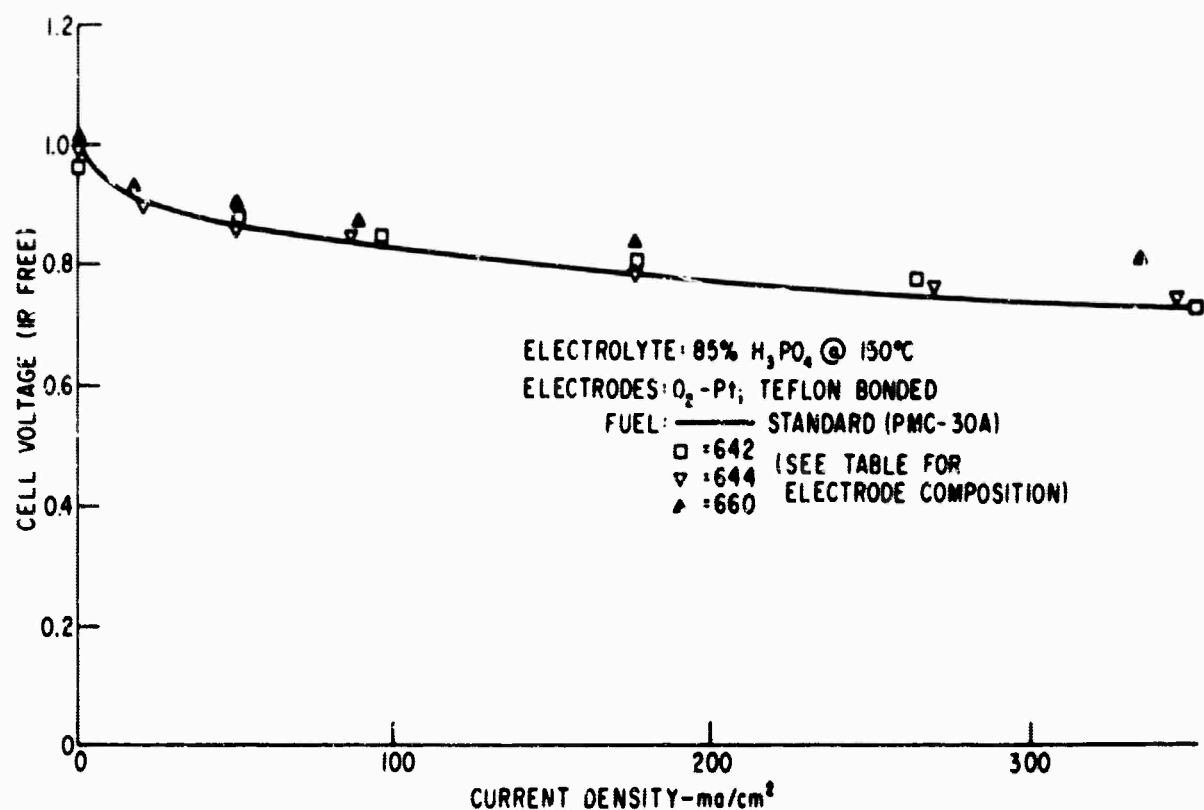


Fig. 128 Effect of Asbestos Content on Performance as a H_2 Anode With 85% H_3PO_4 Electrolyte.

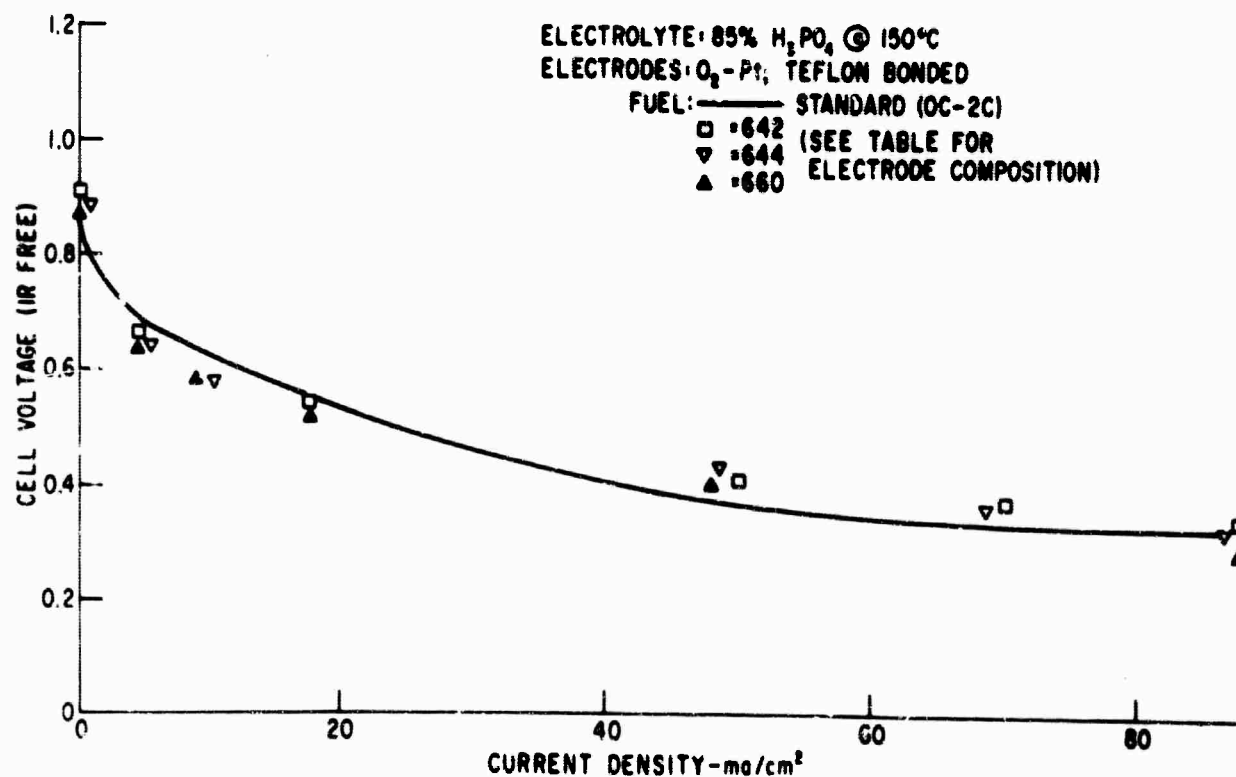


Fig. 129 Effect of Asbestos Content on Performance as a C_2H_2 Anode With 85% H_3PO_4 Electrolyte.



Fig. 130 Appearances of Electrodes (Electrolyte Side) After a Week Under 85% H_3PO_4 at 150°C in the Presence of Hydrogen (20X)

4.4.3 Developmental Electrodes (Dr. M. Gloor)

The effort in preparation and testing of developmental electrode structures was entirely concentrated on modification of the Niedrach-Alford electrode. The primary objective was to improve the performance and reliability (crack-resistance or mechanical stability) of the standard electrode.*

All test electrodes were of 3 x 3 in. size, with 58 sq cm total catalyst area and 42.8 sq cm active area (1/20 of a square foot). Each electrode was tested on hydrogen, propane, oxygen, and air. Relatively high air flow rates were used in order to obtain reproducible polarization curves. The cell resistance is approximately 0.015 ohm. The test data are given as electrode potentials (IR-free) vs. a hydrogen electrode in the same environment (85% H_3PO_4 , 50°C). Test equipment limits current density measurements to a maximum of 200 amps/square ft.

4.4.3.1 Wetproofing Film Evaluation

The use of heavy wetproofing films was considered as a possible method of decreasing the leak rates of cracked electrodes. The films usually applied on standard electrodes as Teflon suspension, were either sprayed on the electrodes or transferred from metal foils. These films have an average loading of about 6 mg fluorocarbon/sq in. An air gun was used to spray the heavier film onto the developmental electrodes. The electrodes were fixed in a mechanical traversing table, thus providing uniform spraying conditions. The film loading could be accurately controlled and was directly determined by weighing. The finished electrode was heat treated at 350°C for 50 minutes in order to consolidate the film. Two electrodes (including no. 5111) were heat treated for 100 minutes and performed poorly.

The performances of 10% T-30 electrodes with sprayed-on film are summarized in Table VIII, App. 5.3.2. The electrodes with films of 40 to 60 mg/sq in. (10 times usual loading) worked best and as good or slightly better than the best standards (1). Loadings of 110 mg/sq in. were still satisfactory, whereas 160 mg/sq in. blocked the gas access to the electrode. Electrode performance on propane and oxygen is plotted vs. film loading in Fig. 131. The increased performance of electrodes with heavier films on propane may be due to better penetration of the film into the electrode as a result of longer spraying times or better water retention necessary for good performance. The performance of electrodes on oxygen and air is better than on standards made during the first half of 1964 (2). It is obvious that the thicker films give no additional gas diffusion polarization up to quite high loadings. Microscopic inspection of the films revealed

* The standard electrode consists of 2.4 gr catalyst mix (10% by weight of teflon binder and 90% platinum black) processed onto a tantalum screen. The total area is 3 x 3 inches. No platinum screens were used for developmental electrodes.

(1) Technical Summary Report No. 5, Jan. 1 - June 30, 1964, ARPA Order No. 247, Contract No. DA44-009-ENG-4909 and No. DA44-009-AMC-479 (T), P. 4-100, 5-2.

(2) Ibid. P. 4-100, 5-2.

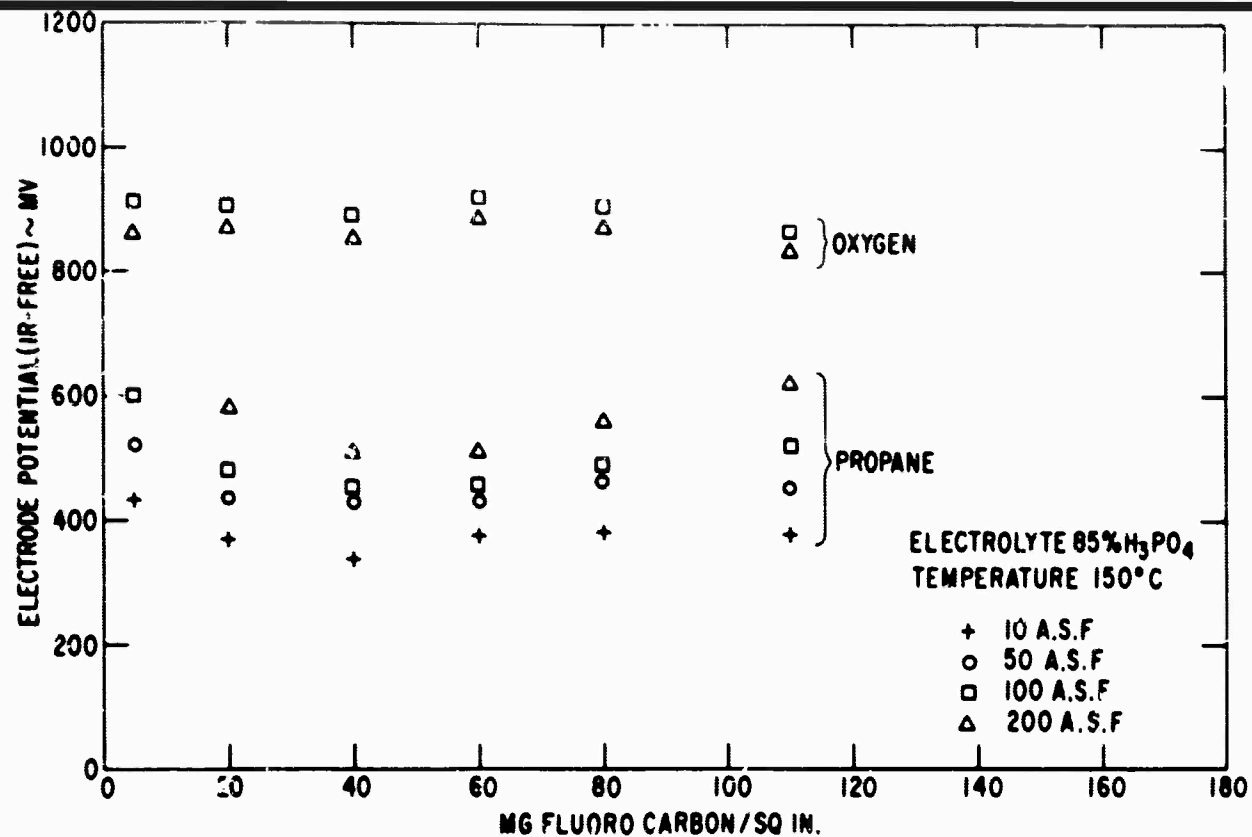
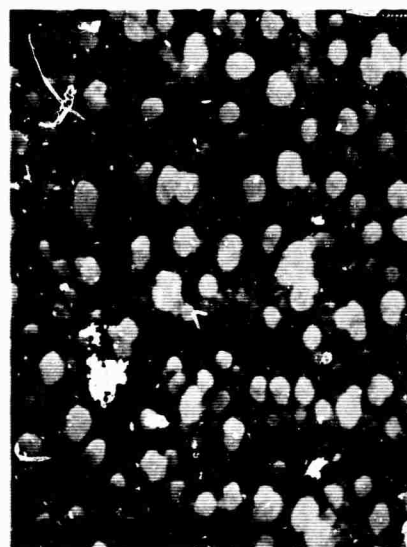
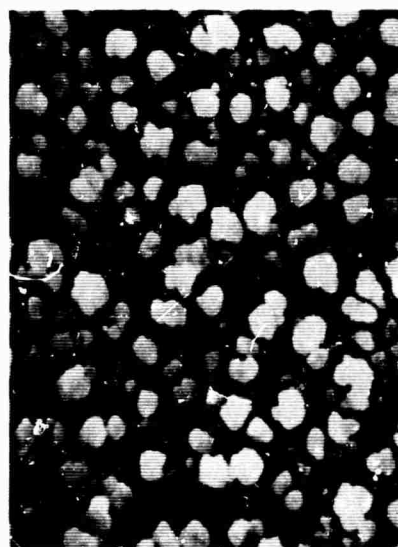


Fig. 131 Developmental Electrodes With Heavier Wetproofing Films-Performance on Propane and Oxygen vs. Film Weight.



Electrode 3188
Film cracked



Electrode 3189

Fig. 132 Heavy and Fluffy Wetproofing Films (after test). Appearance of Surface with "poplar tree" formations. 36X.

a uniform build-up of the layer to about 20 mg/sq in. As the layer thickness is increased by further spraying, formations having the appearance of poplar trees start growing out of the layer. See Fig. 132. The leakage of these electrodes seemed to be diminished but not entirely stopped. There is insufficient data available to statistically express the improvement.

The Teflon content of the catalyst layer has a marked influence on the final performance when these sprayed films are used. In previous work (3), it has been shown that the performance of standard electrodes is unaffected with up to 20% T-30 and 30% T-7 at current densities of 50 A.S.F. Table IV, App. 5.3.2, indicates the performance of electrodes with machine-sprayed films on 20% T-30, 20% T-7 and 30% T-7. As can be seen, rather low limiting current densities were experienced. After hot pressing these electrodes with 20 tons pressure, the performance and limiting current densities on propane generally increased. See Tables IV and V, App. 5.3.2. The oxygen and air performances are somewhat decreased but not to the extent expected by "closing the porous films" to the degree expected from the hot pressing.

4.4.3.2 Asbestos as Electrode Filler Material

Following up on the discovery that asbestos has been shown to exhibit good performance and improved mechanical stability, seven electrodes scaled up to 3 x 3 in. size were prepared. Some of these electrodes had varied Teflon and asbestos concentrations. The performance data were as good as the best standards. See Table VI, App. 5.3.2. After a few days of testing, the electrolyte sides of these electrodes were undamaged or only faintly cracked. See Fig. 133. The standard 10% Teflon electrodes, however, showed the usual crack pattern. Some of these asbestos-loaded electrodes are now on life test. It should be noted that the dilution of the catalyst did not reduce performance as was the case with tantalum (4).

The compositions and catalyst loadings of asbestos-filled electrodes are listed in Table VII, App. 5.3.2. Electrodes with 18% asbestos and 10% Teflon give reproducibly good performance. (During test of electrode no. 3240 a faulty reference electrode produced polarization curves with a constant deviation. Performance was good.) Decrease of the asbestos concentration to 7% had no influence on performance (electrode no. 3243). An increase in asbestos and Teflon levels to 25%, 20%, respectively, resulted in decreased performance of one out of two electrodes.

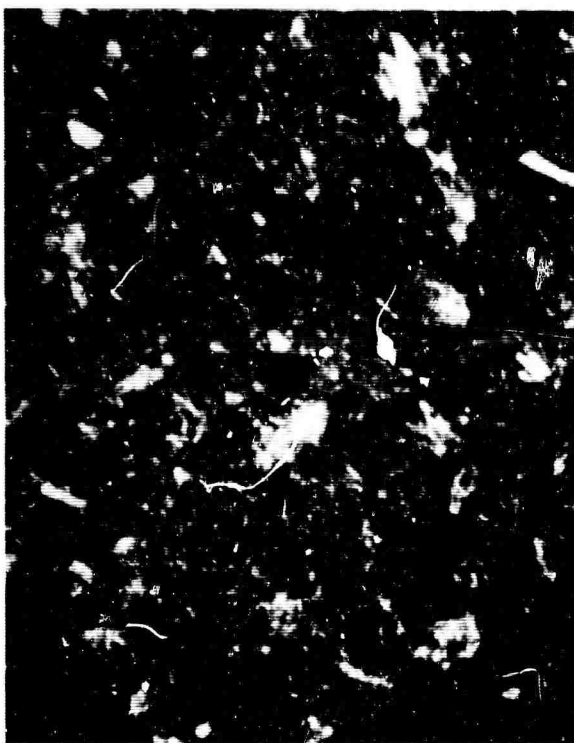
4.4.3.3 Double-Layer Electrodes

Two active catalyst layers are usually pressed onto a screen to form a Niedrach-Alford electrode. A more stable electrode could be produced by replacing one of these active layers with a more crack-resistant one containing additional Teflon or an inert material like tantalum. In that this electrode would have an active layer and an inactive layer, the interface between gas and

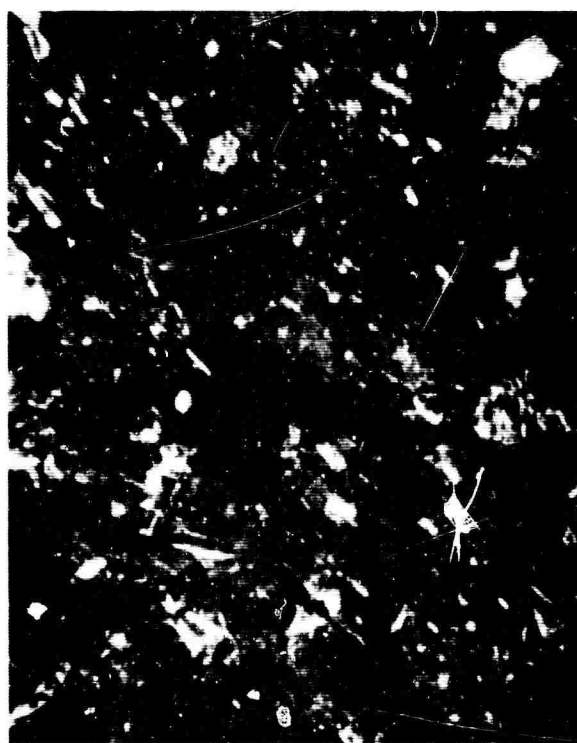
3. Ibid. P. 4-100

4. Ibid. P. 4-101 thru 4-105

Gas Side

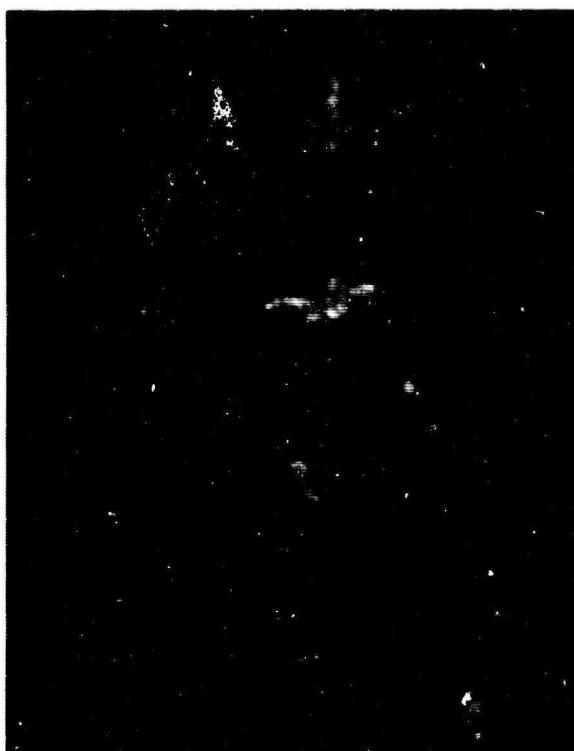


Electrolyte Side (Small Cracks)

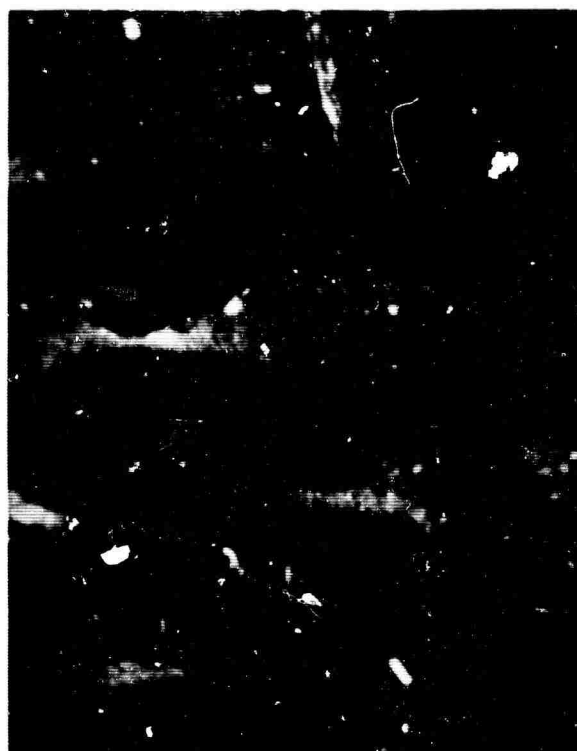


a. Asbestos-filled Electrode No. 3241. Surface After Test. 36X.

Electrolyte Side Before Test



Electrolyte Side After Test

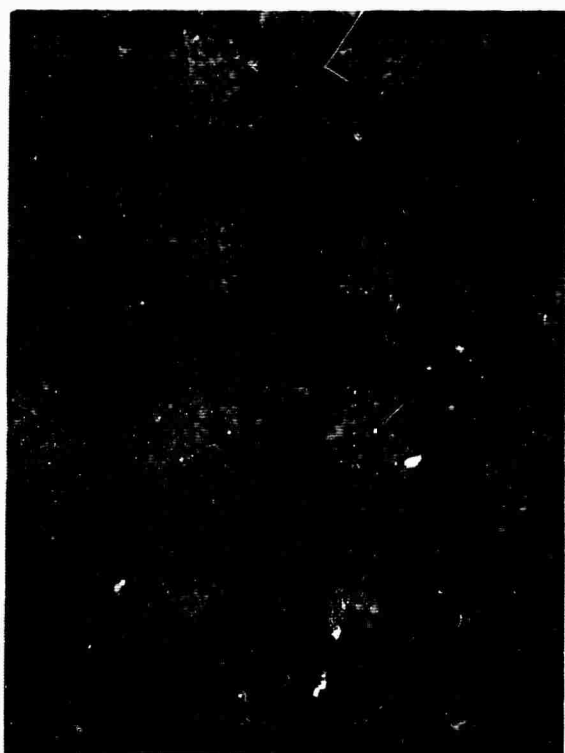


b. Standard Electrode. Tested with No. 3241. 36X.

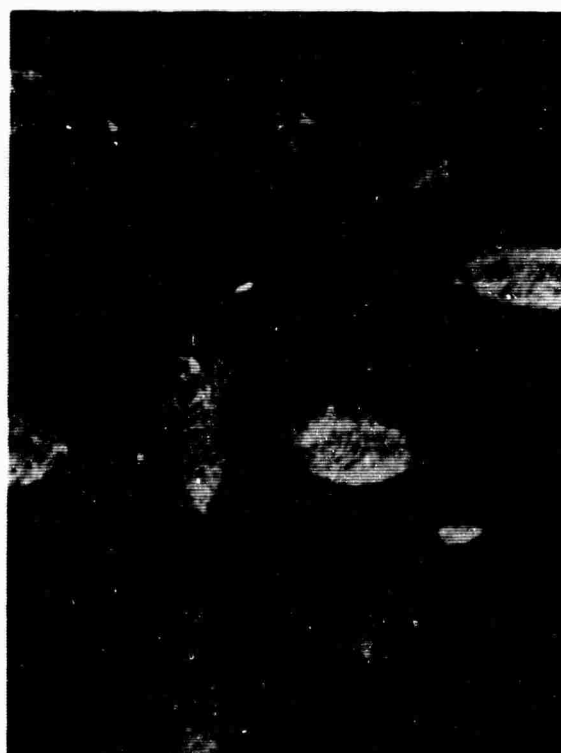
Fig. 133 Comparison of Asbestos-Filled Electrode and Standard Electrode Surfaces.

electrolyte must be established in the active layer. As the electrode may be operated with the active face either against the gas side or the electrolyte side, a wetproofing film is simply sprayed on the active layer or is sandwiched between the active and inert (or lower activity) layers. Moreover, the inert layer should be porous enough for adequate mass transport rates in either the gas phase or the electrolyte phase.

A series of electrodes were made on this principle with 10 and 30% Teflon layers and with the wetproofing film on the gas side. See Table VIII A, App. 5.3.2. The performances are largely determined by the Teflon content on the gas side and otherwise approach standard values up to 50 A.S.F. See Table IX, App. 5.3.2. Electrode no. 5174 with 30% T-30 in the gas side shows reduced limiting current density. Table IX indicates if the layer on the gas side contains 10% T-30, 10% T-7 or 30% T-7, the performance is good. Electrode no. 3163 was identical to no. 824 but did not demonstrate similar performance. The 30% T-7 region was found to be good performing but seems to be the upper limit for T-7 content. Variation in this limiting value would explain the contradiction between electrodes no. 824 and 3163 performance levels. Fig. 134 shows the two surfaces of the electrodes after about 15 to 20 hours of test. As seen in Fig. 134, 30% Teflon on the gas side does not crack, while 10% Teflon has a few very fine cracks. The electrolyte side always cracks, but there is a great difference between 10 and 30% Teflon.



Electrode 5174 Gas Side



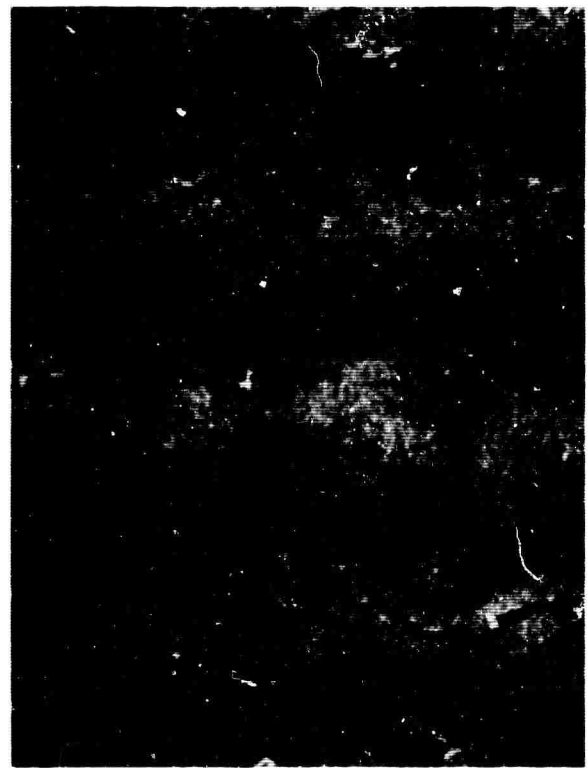
Electrode 5174 Electrolyte Side

Fig. 134 Double-layer Electrodes with Layers of Different Teflon Concentrations After Test. Appearance of Surface. 36 X.

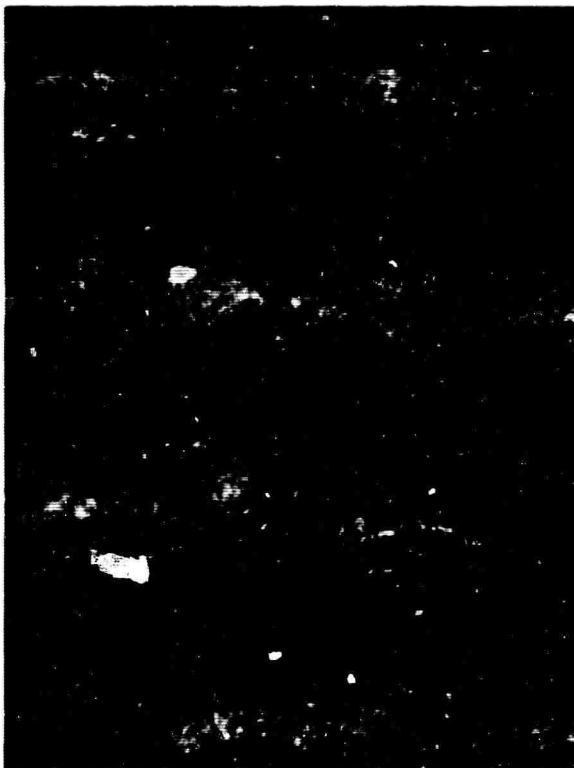
Electrode 5106 Gas Side



Electrode 5106 Electrolyte Side



Electrode 3163 Gas Side



Electrode 3163 Electrolyte Side



Fig. 134 (Cont.)

Two double-layer electrodes were made with a tantalum layer and a platinum-black layer. One of these electrodes had nickel powder as a spacing agent in the tantalum layer and which was dissolved out before testing. See Table VIII B, App. 5.3.2, for the composition of the layers. As shown in Table X, App. 5.3.2, the increased porosity of the stable tantalum layer resulted in poor performance of electrode no. 3198 and good performance at practical current densities with electrode 3209. The limiting current density increased from 45 to 110 A.S.F. on propane. This value is still lower than usual and may be caused by the tantalum layer or the high Teflon percentage. Both sides of the two electrodes were uncracked after the tests.

In a further series of double-layer electrodes, wetproofing films of various loadings were sandwiched between a tantalum and a platinum layer (for composition see Table VIII C, App. 5.3.2). At this time, the best results are obtained by spraying the film onto the pressed platinum layer and then adding the tantalum layer. Electrode 3226 with 1.6 mg/sq in. Teflon film (1/4 of a normal film density) was very leaky, as shown in its electrical performance (see Table XI, App. 5.3.2). Electrodes 3228 and 3229 with standard films performed well up to 30 A.S.F., with some leakage. On all these electrodes the platinum (electrolyte) side was cracked, whereas the tantalum (gas) side showed no cracks after tests. The moderate leakage experienced indicates that the wetproofing was not continuous and, therefore, part of the active layer was drowned by electrolyte. The better performance of electrode 3229 over 3228 may stem from the fact that 3229 was hot-pressed before depositing the film. This resulted in a smoother and more continuous film. The film was obviously too thick on electrode 3230. After the test, electrodes 3226 and 3228 were sprayed with a wetproofing film on the catalyst side and operated in a cell with the catalyst towards the gas side. Performance and limiting current density of electrode 3226 increased markedly, whereas electrode 3228 performance dropped slightly and the limiting current density increased.

4.4.3.4 Application of Wetproofing Films

The adherence of the wetproofing film or even the penetration into the catalyst layer may be an important factor in good electrode performance. Wetproofing films were applied to two standard electrodes under vacuum suction. A film of 40 mg/sq in. Teflon was sprayed on electrode 5135 by an air gun with 5 inches Hg vacuum applied across the electrode. The sprayed areas dried slowly but the pressure drop through the electrode seemed insufficient to pull the suspension into the electrode. The performance was normal and improved somewhat after the electrode was hot-pressed for the second test. See Table XII, App. 5.3.2. A different method of wetproofing electrode 5150 was used. This electrode was covered with Teflon suspension and a vacuum of 10 inches Hg applied. The suspension started filtering without visible deposition. Acetone was added to coagulate the Teflon which was then filtered to dryness onto the electrode and then

sintered at 360°C. The performance is good but not outstanding. The deposition of films with the described methods gave no improvement in performance.

4.4.3.5 Tantalum Substructures

A few so-called tantalum substructures were prepared by pressing a mixture of tantalum powder, Teflon, and a spacing agent such as nylon fibers, nickel powder or aluminum powder onto a screen. After leaching of the highly pressed electrode, a porous structure remained which was tough or soft depending on the concentrations used in the mix. These porous structures were difficult to activate. The best performance so far was achieved by filtration of a platinum black-Teflon-water slurry onto the electrode. See Table XIII, App. 5.3.2. The performance was relatively good, with sufficient limiting current density up to 80 A.S.F. Adhesion of the catalyst to the basic layer was poor.

4.4.3.6 Alloy Catalysts

A few electrodes have been prepared with alloy catalysts such as Ti-Ta-Pt alloy. Only those catalysts which were etched prior to preparation of the electrode showed significant performance levels and these were poor on propane and fair on oxygen.

4.4.3.7 Catalyst Loading

The influence of catalyst loading on straight platinum black, 10% Teflon electrodes was tested with 3.5, 1.5 and 1.2 gr total loading (platinum + Teflon) vs 2.4 gr standard weight. There was no appreciable difference in performance, although the 1.2 gr loading seemed to contribute to better performance at current densities up to 50 A.S.F. The heavy loading was only fair at high current densities, the 1.5 gr loading very good, and the 1.2 gr loading cut off at 80 A.S.F. See Table XIV, App. 5.3.2.

Furthermore, an electrode was pressed at 100 tons (40 tons nominal) and showed normal performance. See Table XV, App. 5.3.2. The use of several screens with 4 mil wire instead of 8 mil (both the same 45 mesh/inch) proved to give no difference in performance, but the more rigid 8 mil wire screen is preferable for better mechanical stability of the electrode.

4.4.4 Electrode Characterization (Dr. M. Gloor)

The knowledge of structural and other properties of electrodes, such as surface area of the catalyst and location of the wetproofing zone, may prove to be important tools in evaluation of manufacturing procedures and preparation of defined structures in order to correlate and optimize these properties with performance as well as to insure reproducibility. During this period, porosity and surface area measurements were developed with the use of standard equipment.

4.4.4.1 Electrode Porosity Measurements

Gas permeability will give qualitative information about average porosity of new electrodes. The electrodes were carefully checked for pinholes with a microscope and a bright light source below the electrode. Permeability rates were measured from 0 to 25 inches H₂O pressure and found to be linear in this region. Table XXXII below lists the permeability rates for air at 5 inches H₂O for six standard Niedrach-Alford electrodes with wetproofing films. The reason for the very low permeability exhibited by electrode 3201 is presently unknown. The average permeability is 105 ± 23 cc/min. of air (excluding electrode 3201) or 90 ± 40 cc/min. (including electrode 3201), the range being the mean square deviation.

TABLE XXXII
Permeability Rates of Air on Standard Niedrach-Alford Electrodes

<u>Electrode No.</u>	<u>Permeability (cc air/min.)</u>	
5117	148	
3167	93	
3201	14	Electrode area: 42.8 cm ²
3170	97	Pressure drop: 5 inches H ₂ O
5118	80	
5119	109	

By introducing the permeability values into the Kozeny equation for laminar flow of fluids through porous media, an internal area responsible for frictional pressure loss can be calculated. With the simplified assumption of cylindrical and straight pores and known porosity, a mean pore diameter may be obtained. Thus, 65% measured porosity (see later in this section) and 100 cc/min. permeability rate at 5 inches H₂O pressure drop result in pore size of about 0.1 μ , which is reasonable. This mean diameter naturally does not represent the actual structure but may be a useful parameter for quick evaluation of reproducibility of the porosity. Later on, with more data available, correlation to polarization data and limiting current densities may also be possible.

Bubblepoint pressure measurements on carefully wetted electrodes indicate that the largest pores are about 30 to 50 μ in diameter, as calculated with the aid of capillary pressure. These first blown-out channels may be single pores or "pore bundles".

Measurements of porosity and pore size distribution were attempted on two different samples with a mercury penetration porosimeter. The first sample was cut out of a catalyst-decal which had been pressed onto a porous tantalum sheet to yield an only fair performing

electrode (1). The decal had a porosity of 30%, as compared with 65% for the second sample which consisted of a good performing Niedrach-Alford electrode. This 65% value relates only to the catalyst layer and does not include the screen. These different porosities may account for the difference in performance, but other properties such as masking of the catalyst by the binder, etc., will have to be considered for a complete analysis. The pore size distributions of both samples are represented in Fig. 135. In curve a of Fig. 135 the largest pores measure 30μ in diameter and the main concentration of pores occurs between 0.1 to 1μ diameter. Because the Niedrach-Alford electrode was compressed and cracked during the test, the distribution under curve b of Fig. 135 is probably inaccurate.

Fig. 136 shows the Niedrach-Alford electrode sample before the test, after the test with the mercury leached out, and with the platinum black dissolved by aqua regia. Seven disks of the decal electrode were simultaneously measured. The thickness of the disks averaged 3.28 mils before (14 measurements) and 3.42 mils after the test. The diameters of $19/32$ in. were unchanged. Therefore, no irreversible volume change had occurred and probably no change at all since porous fluorocarbons are not elastically deformable. The porosities were calculated

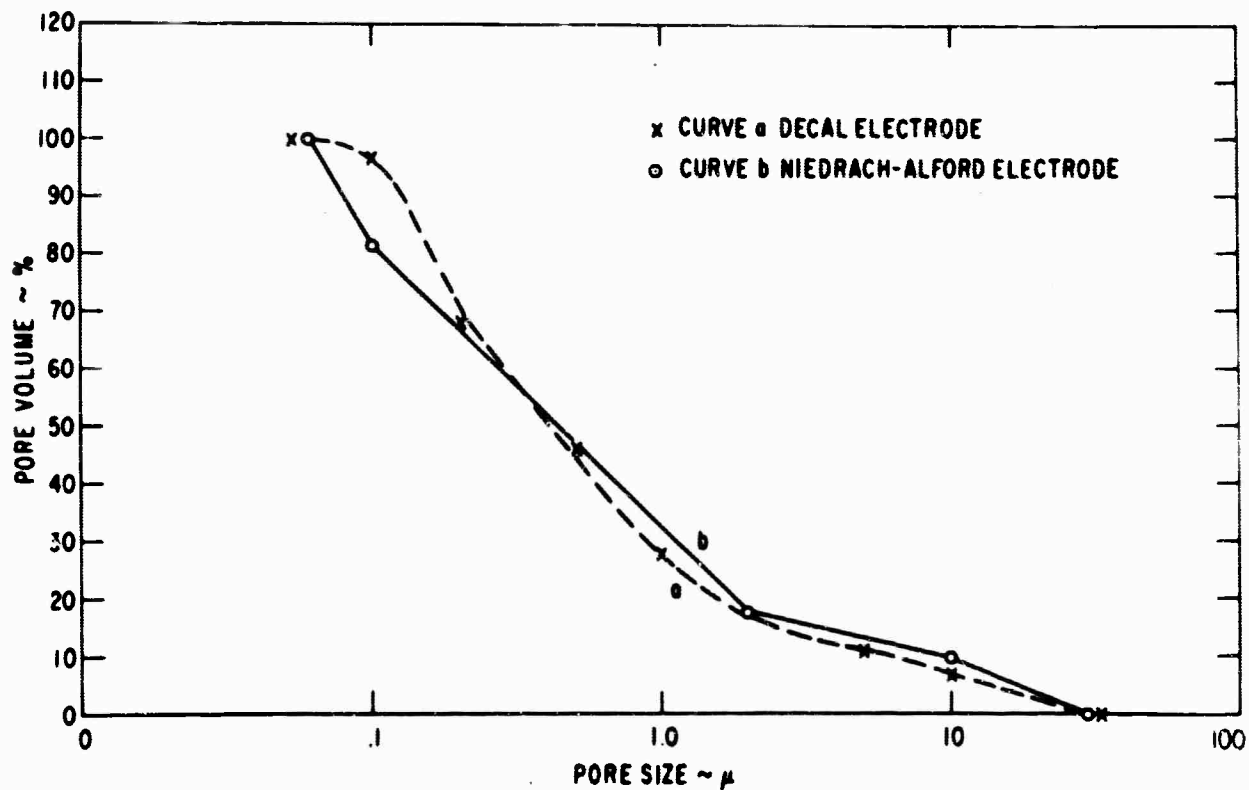
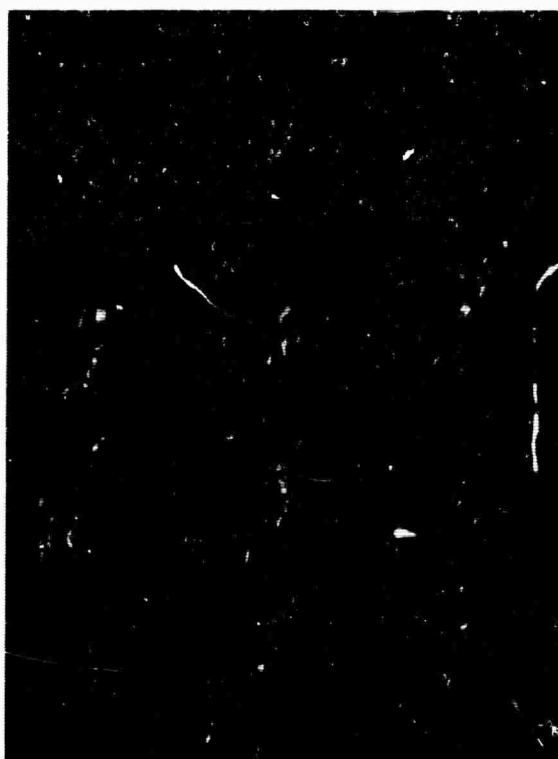


Fig. 135 Pore Size Distribution

(1) Technical Summary Report No. 5, Jan 1 - June 30, 1964, ARPA Order No. 247, Contract No. DA 44-009-ENG-4909 and No. DA 44-009-AMC-479 (T), p. 4-110 and 4-112.



Before Test



After Test, with Mercury Removed



After Test, with Platinum-Black Removed

Fig. 136 Surface of Niedrach-Alford Electrode Sample. Porosity Measurement with Mercury Penetration. 36 X.

from the total volume, V_t , and the integrated pore volume, V_p , down to 0.06μ . The volume of the solids, V_s , was measured separately and checked out as $V_t - V_p$ within 1% accuracy. The screen volumes of the Niedrach-Alford electrode were calculated and determined after removal of the catalyst layer.

Work has been started to determine the structure by metallographic means. The first samples looked encouraging but refinement of embedding techniques is necessary to decide whether larger voids are part of the original structure or were caused by the potting of the samples.

4.4.4.2 Electrode Surface Area Measurements

Surface area measurements of the catalyst on 3 x 3 in. electrodes with the BET-method (nitrogen adsorption) have been started. The electrodes were welded into flat stainless-steel containers with 1/32 in. clearance for measurements. These containers were leaktight at liquid nitrogen temperature (adsorption) and 250°C (de-gassing). The steel envelope is sawed open after the measurement is taken. The results were evaluated by a computer program which directly calculated the specific surface area. Table XXXIII gives the surface areas of four Niedrach-Alford electrodes. Electrodes 5118, 3168 and 3204 are standard electrodes with platinum black of $24 \text{ m}^2/\text{gr}$ original surface area and 10% Teflon binder. Considering the nominal platinum loading of the total electrode area the surface areas of the catalyst came out to be 4.2, 10.4 and $7.0 \text{ m}^2/\text{gr}$, which is quite a reduction of the original value.

Table XXXIV shows the surface areas of platinum black samples which have been heat-treated in air for 20 minutes. There is no sintering effect up to 600°F and a slight one at 660°F . Therefore, masking of the surface area by the binder or lowering of the sintering temperature by reducible matter may be responsible for the large losses during electrode manufacturing. After the measurement on electrode 3204, the catalyst was dissolved in aqua regia and the surface of the remaining screen and porous binder measured again. As can be seen from Table XXXIII, the contribution to the surface area is nil. Electrode 5167 was made with a high surface area platinum black ($33 \text{ m}^2/\text{gr}$) which may have a greater tendency for sintering and thus explain the low area.

The electrodes were scratched after test because the sample holder was too tight. A larger gap in the new holders will remedy the fault and will prevent damage to the specimen.

TABLE XXXIII

Surface Area of 3 x 3 in. Niedrach-Alford Electrodes

<u>Electrode No.</u>	<u>Total Area (m²)</u>	<u>Pt - loading (gr)</u>	<u>Specific area (m²/gr)</u>
5118*	9.2	2.16	4.2
3168*	22.4	3.24	10.4
3204*	22.7	2.16	7.0
3204 **	0	None	None
5167 *	4.9	2.16	2.3

* 5118 new; 3168, 3204 and 5167 measured after performance tests.

** Platinum-black removed.

TABLE XXXIV

Surface Areas of Heat-Treated Platinum Black (20 Minutes at Temperature)

<u>Temperature (°F)</u>	<u>Specific Surface Area (m²/gr)</u>
300	25.2
400	25.3
500	25.9
600	25.9
660	22.4
None	25.0

4.4.5 Failure Analysis (Dr. M. Gloor)

The results of previous work (1) indicated that the cracking of the catalyst layer of Niedrach-Alford electrodes is probably due to the instability of platinum black in hot phosphoric acid, especially under reducing conditions. These experiments were performed on electrode coupons (samples cut from standard size test electrodes). It was of interest to observe changes of surface area of platinum black powders which were subjected to the same testing conditions. Table XXXV summarizes the results obtained by treating platinum black samples in 85% phosphoric acid at 150°C with various gases bubbling through the samples.

(1) Technical Summary Report No. 5, Jan 1 - June 30, 1964, ARPA Order No. 247, Contract No. DA 44-009-ENG-4904 and DA 44-009-AMC-479 (T). P. 4-96.

The platinum black samples were immersed in 40 cc of 85% H_3PO_4 for 276 hours. Then the acid was diluted, the samples allowed to settle and the liquid decanted. The samples were washed free of acid with distilled water at least eight times and separated from the liquid by means of a centrifuge (settling proved to take too long). The untreated platinum black yielded $24.9 \text{ m}^2/\text{gr}$ area. A blank immersed for two days in cold phosphoric acid was given the same wash treatment. The unchanged area of $24.7 \text{ m}^2/\text{gr}$ proved that the rinsing was adequate. The platinum black samples that were in contact with hydrogen, propane, and nitrogen suffered losses in surface area of -58%, -37%, and -20%, respectively, which supports the evidence for catalyst instability found on electrode coupons. The samples tested with oxygen and no gas (air over the solution) showed increases in surface area of +25% and +8%, respectively. Platinum was found in the phosphoric acid (acid + first rinse) as indicated in Table XXXV. It is obvious that hydrogen and propane precipitate any dissolved platinum or suppress its dissolution.

TABLE XXXV

Change In Surface Area of Platinum Black Treated with Hot Phosphoric Acid and Various Gases

<u>Sample</u>	<u>Gas</u>	<u>Surface Area (m^2/gr)</u>	<u>Area Change After Treatment (%)</u>	<u>Pt in Solution (mg)</u>
Untreated	--	24.9	--	--
Blank	--	24.7	None	--
11	None	26.9	+ 8%	86
12	O_2	31.3	+25%	145
13	H_2	10.4	-58%	None
14	N_2	19.9	-20%	170
15	C_3H_8	15.7	-37%	None

Test Conditions:

Approximately 4 gr of platinum black + 40 cc of 85% H_3PO_4 , 150°C , 276 hours.

4.4.3.8 Conclusions

Inclusion of asbestos fibers in the catalyst binder mixture substantially increased the crack resistance of the electrodes. Performance is comparable to the standard electrodes without asbestos, i.e., no loss is encountered from the resulting catalyst dilation.

Experiments with various thicknesses of wetproofing films established that fluffy films approximately 10 times the standard loading result in good reproducible performance equal to that of the best standard electrodes. It is believed that the film decreases the leak rates. Wetproofing films applied under conditions which should produce better adherence and some penetration into the electrode did not show performance improvements.

Dual layer electrodes composed of layers of different Teflon content, or an inert tantalum and an active platinum layer, with sandwiched wetproofing fibers, show good crack resistance but only fair to good performance up to 30-50 ASF. Performance reproducibility is not satisfactory. Leachable spacing powders in the inert layer were found to be beneficial in that they facilitate gas diffusion.

Catalyst decals applied with low pressures to a tantalum substructure show fair to good performance; however, poor adhesion of the active decal results in short life.

Tantalum-platinum catalysts, used for decreased catalyst recrystallization, were deficient in performance.

Varied manufacturing pressures and a thinner type of screen, each tried separately - did not change the performance appreciably compared with a standard electrode.

With the variety of independent technology developments, a "new standard" electrode has been designated for the development program objective. The electrode is envisioned to incorporate 10 mg/cm² of platinum-ruthenium catalyst on a B₄C substrate, pressed on a tantalum screen with a Teflon binder which is reinforced with asbestos. The wetproofing film will be comparable to the present standard electrode. Development efforts are aimed at identifying material composition and fabrication processes which will result in performance comparable to the previous standard.

4.5 ELECTROCHEMICAL CELL LIFE TESTING (P. J. Chludzinski/J. Lennon)

The cell life testing effort is designed to evaluate the performance of a variety of electrode compositions, using phosphoric and hydrofluoric acid electrolytes and a variety of hydrocarbon fuel compositions. The life test program has proven to be an invaluable tool in providing the essential feedback for evaluating the progress and effectiveness of program research and developments.

A series of long-duration life tests was conducted during this reporting period, involving a total of 29 cells, employed in 44 different combinations. Additionally, tests of an evaluating nature such as water balance control, pulsed performance techniques, and barrier film water vapor suppression were performed. A summary of electrochemical cell life testing data is contained in Appendix 5. Results of these tests are presented and discussed in this section.

4.5.1 Phosphoric Acid Electrolyte

This section describes the tests performed using various combinations of anode/cathode compositions and reactants with phosphoric acid electrolyte.

Views of the test stand used in the cell life testing work are shown in Fig. 137. Additionally, work on pulsed performance and barrier films for water vapor pressure suppression is discussed.

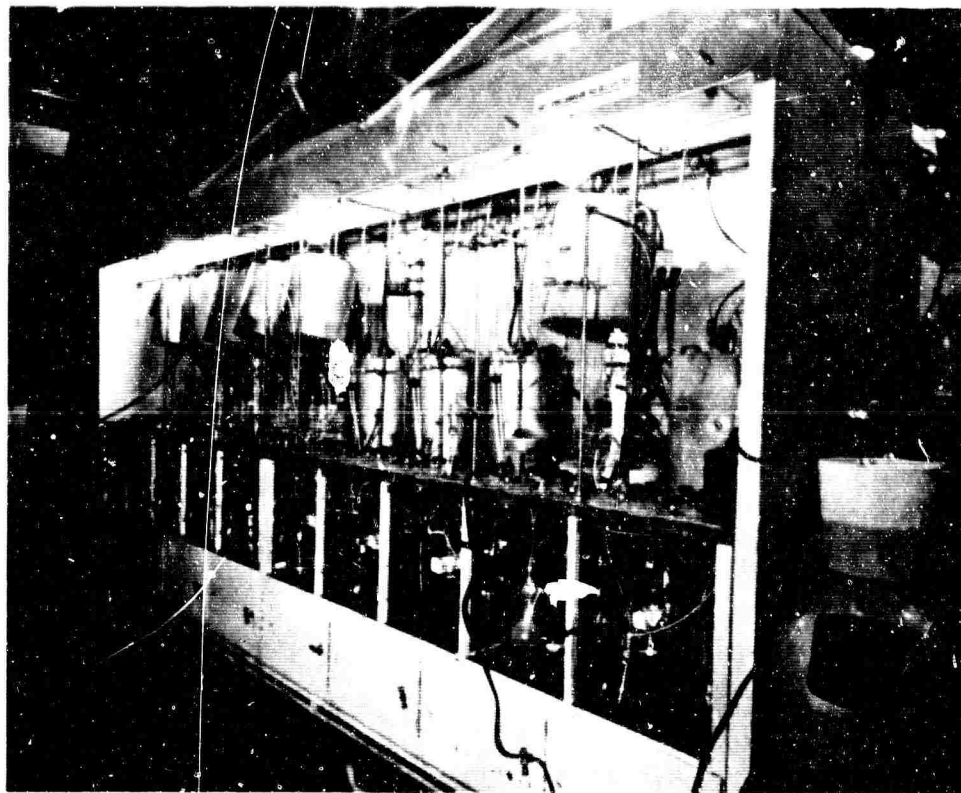
4.5.1.1 Cell LT-7 Iso-octane Phosphoric Acid/Air

Total operating time for the cell with these electrodes was 1990 hours. Average operating current density for the first 1100 hours was 5 amps/sq ft; the remaining part of the test was performed at an average current density of 10 amps/sq ft.

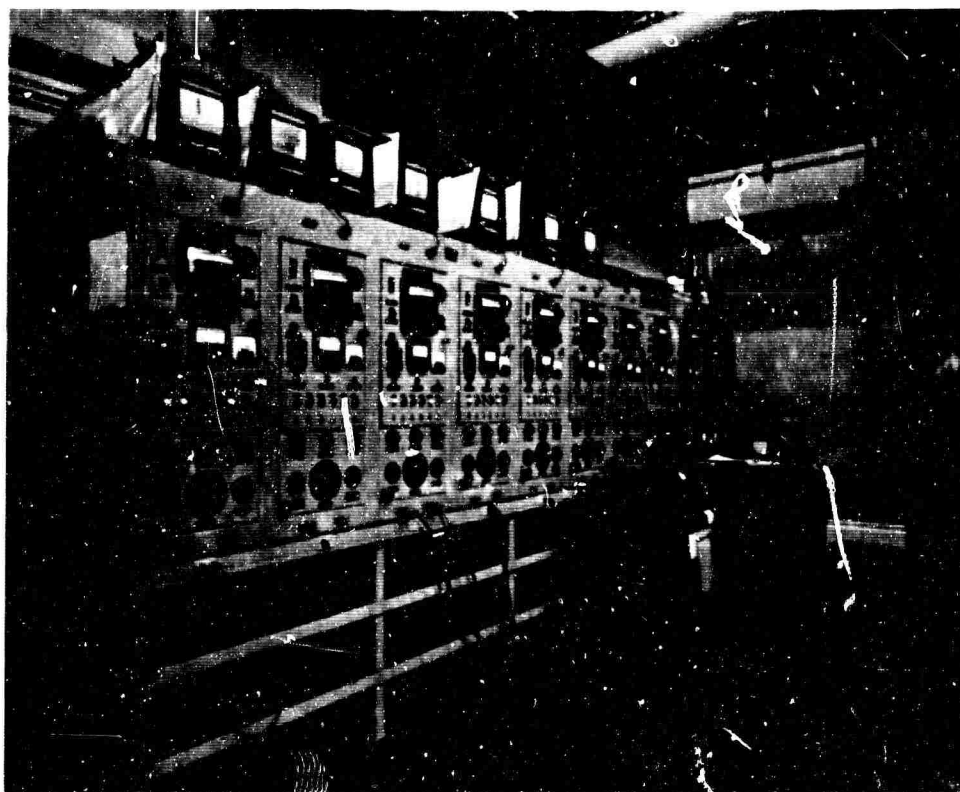
The first 336 hours of test was performed at 300°F (149°C), and the remainder at 350°F (177°C). Comparative performance for various points in the test is shown in Figs. 138 - 141. Comparison of performance at 0.45 VDC shows an initial output of 20 amps/sq ft degrading to 15 amps/sq ft after 330 hours of operation at 300°F (149°C). Fig. 139 is a comparison of performance at the same concentration for 300°F (149°C) and 350°F (177°C). High-temperature performance at 0.45 volt shows an initial output of 25 amps/sq ft, degrading to 15 and 10 amps/sq ft after 1030 and 1650 hours, respectively.

For 1650 hours of operation with cathode back pressure equal to 7.5 inches H₂O, there was no detectable leakage of electrolyte to the cathode (air) stream. In the anode (fuel) stream, electrolyte leakage was undetectable when the back pressure was increased to 10 inches H₂O.

After 1900 hours of operation, failure was induced by loss of electrolyte head and perforation of electrodes. The cell was shut down when electrolyte became markedly discolored with corrosion products and could not sustain a load.



Front View



Rear View

Fig. 137 Cell Life Test Stand

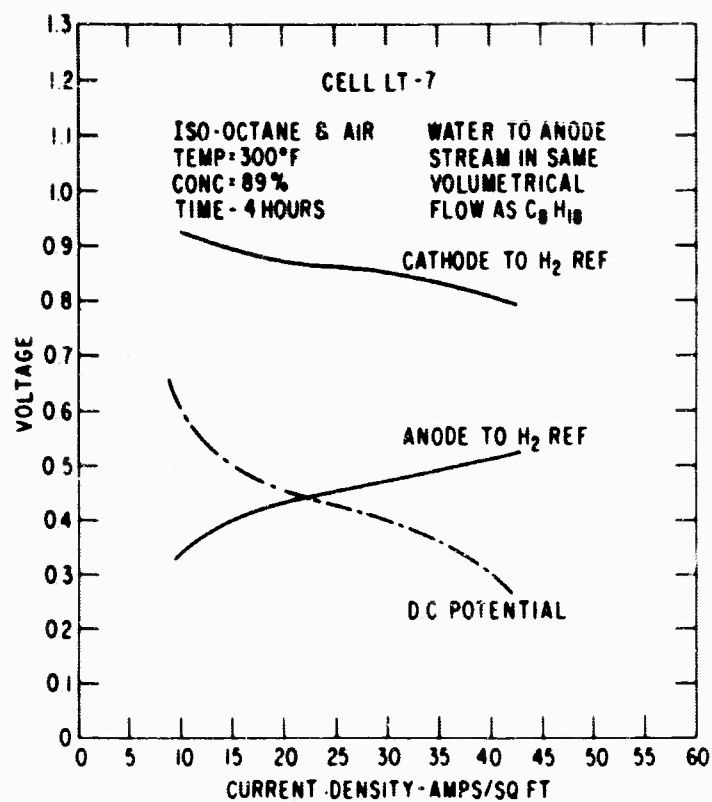


Fig. 138

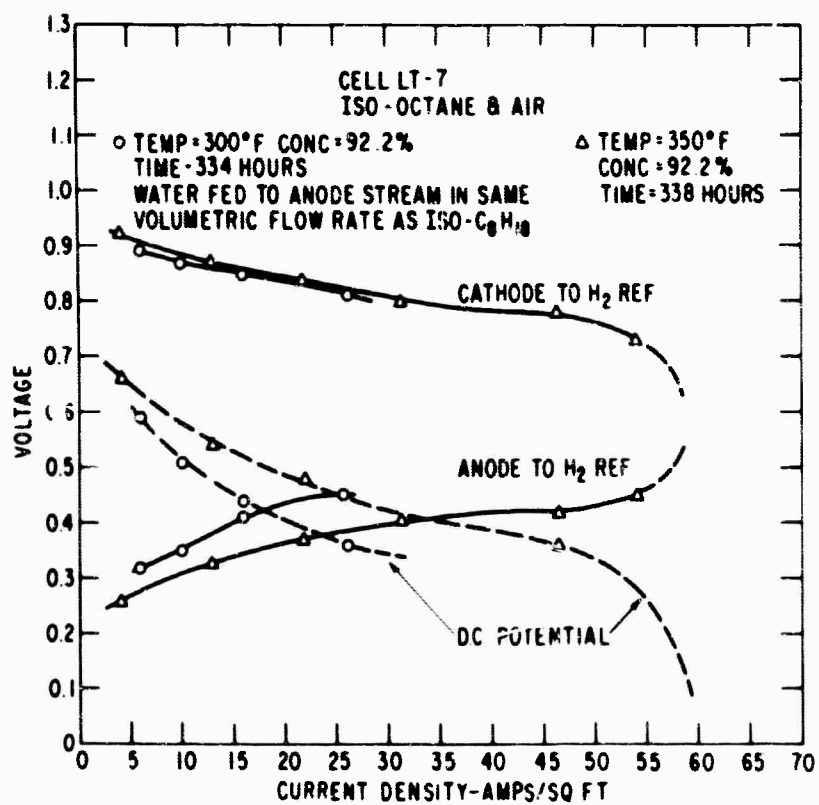


Fig. 139

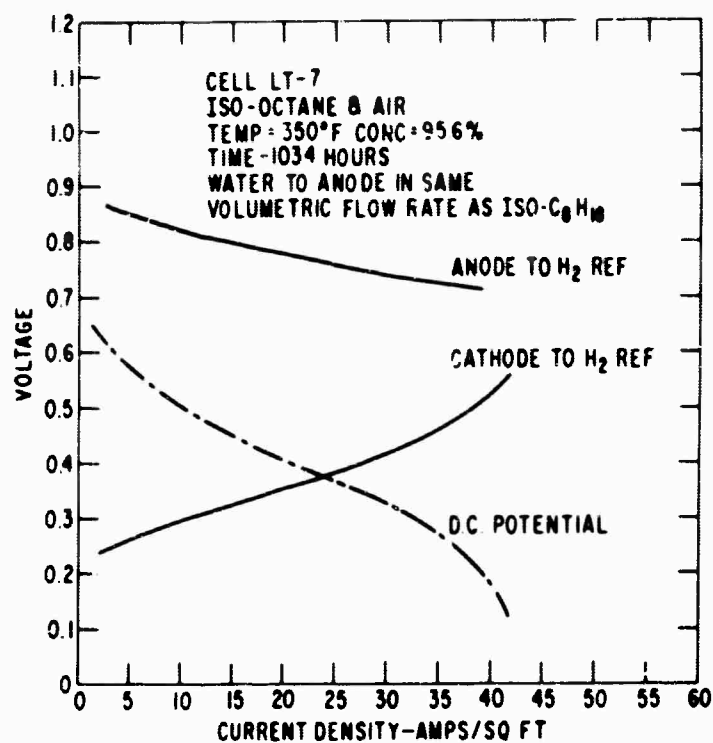


Fig. 140

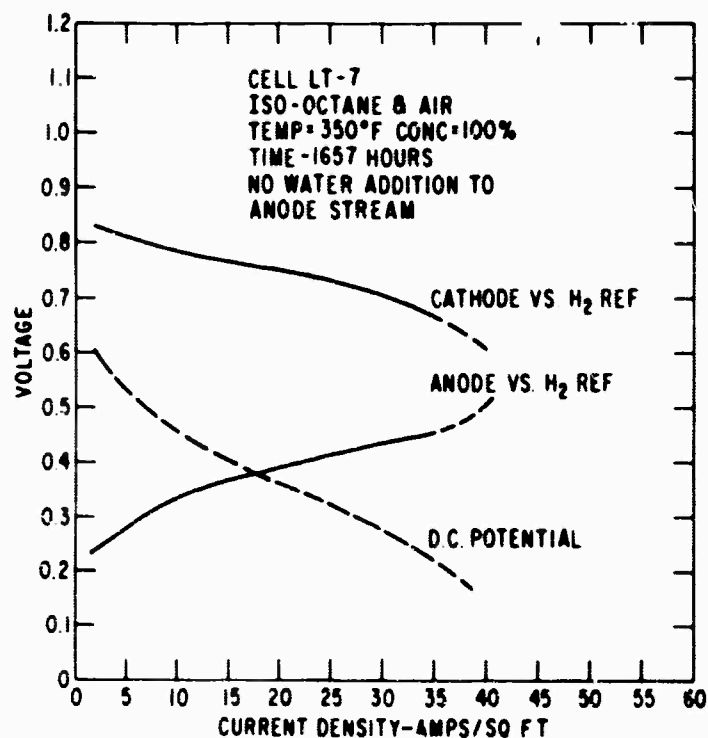


Fig. 141

Water transport was checked at the cathode at various times during the test at various electrolyte concentrations and temperatures. It was noted that the maximum deviation from the empirical formula of the previous report (1) is 20%. See Table XXXVI.

TABLE XXXVI
Cell LT-7 Water Transport Rates

<u>Operating Time (Hrs)</u>	<u>H₃PO₄ Conc. (% wt.)</u>	<u>Temp. (°F)</u>	<u>Calculated Rate* (ml/hr)</u>	<u>Actual Rate (ml/hr)</u>
120	92.0	300	1.72	1.44
300	92.4	300	1.64	1.40
600	97.0	300	0.75	0.72
900	95.5	350	0.935	0.84
1000	96.0	350	0.80	0.72

* From formula $R = Kps R_e^{2/3}$

where:

R = rate of water transported, in moles/sec

K = 1.4×10^{-7}

ps = vapor pressure of water above the electrolyte at the cell temperature

R_e = Reynolds Number for air flow for free H₂O transport through electrodes

4.5.1.2 Cell LT-8 n-Octane/Phosphoric Acid/Air

This cell is still operating after 3940 hours on tests. Performance curves are shown in Figs. 142-144. Initial performance of this cell was not of a high level. The cell is being operated to obtain long-life data for future comparison purposes and as a test vehicle for pulse technique investigation.

The degradation of output with time is apparent from a comparison of performance plots. Initial performance at 0.45 VDC does not decrease markedly after 1000 hours of operation, although the short circuit current capability has decreased by almost 50%. After 2300 hours on test, the useful output at 0.45 volt decreased to almost 25% of the original current density. During 3800 hours of testing on this cell, electrolyte leakage to cathode is undetectable. Cathode stream back pressure has been maintained at 3 inches H₂O. Maximum electrolyte leakage to anode stream after 3800 hours of operation is 1 ml/hr at a back pressure of 3.5 inches H₂O. For the initial 1500 hours of the test, electrolyte leakage was less than 0.125 ml/hr.

(1) Technical Summary Report No. 5, Hydrocarbon-Air Fuel Cells. Jan. 1-June 30, 1964, ARPA Order No. 247, Contract Nos. DA 44-009-ENG-4909 and DA 44-009-AMC-479 (T), p. 4-120.

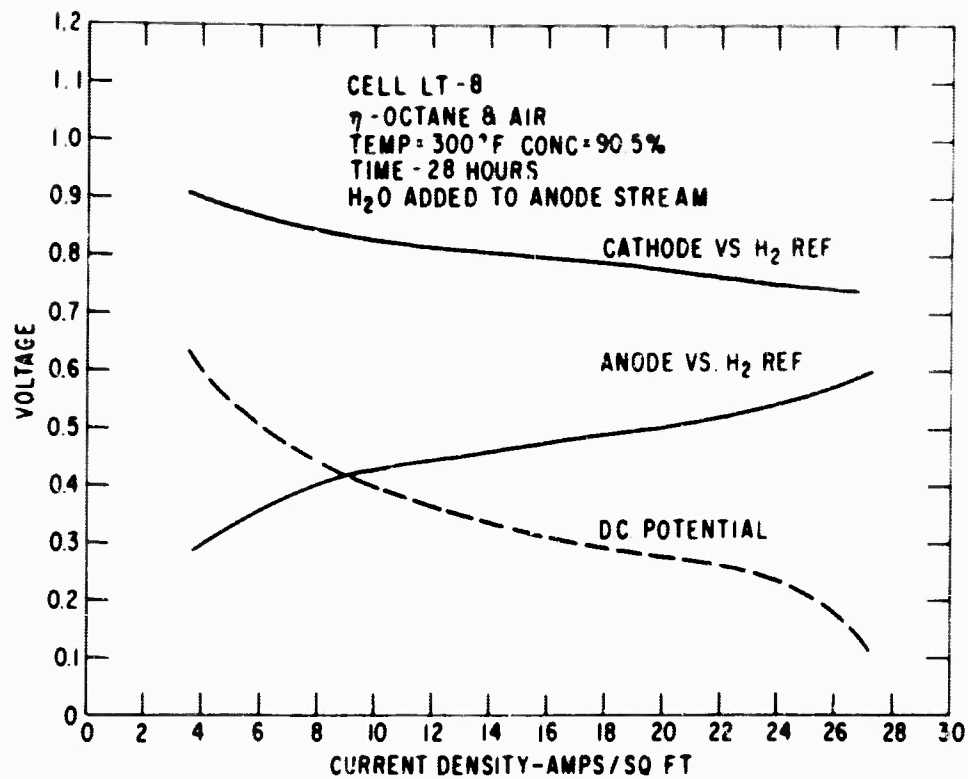


Fig. 142

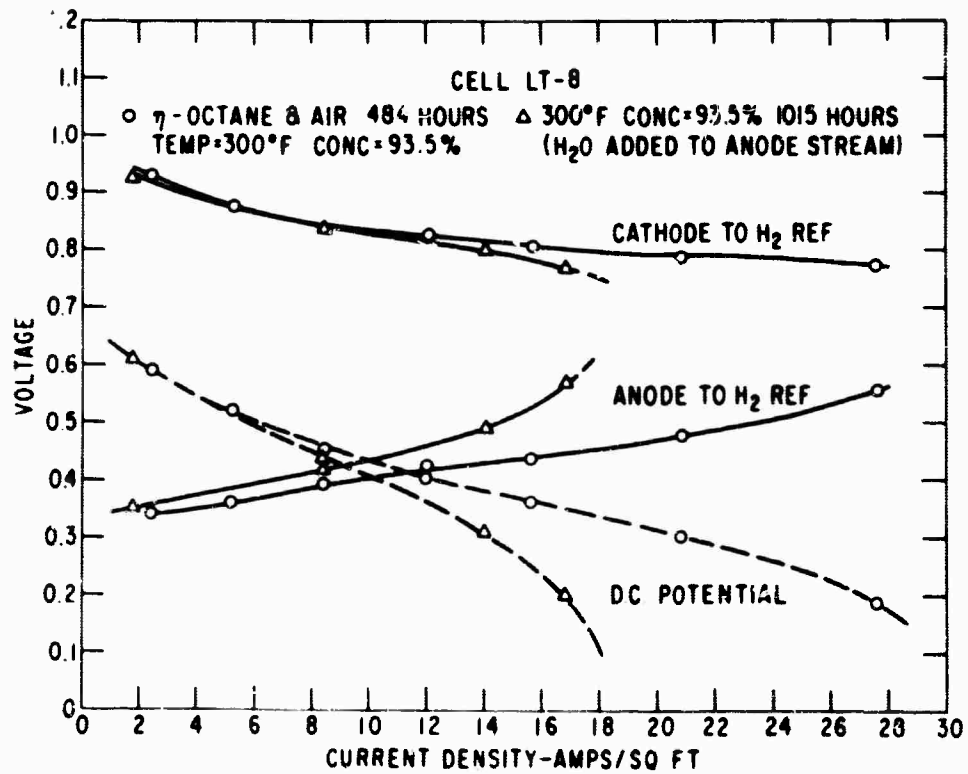


Fig. 143

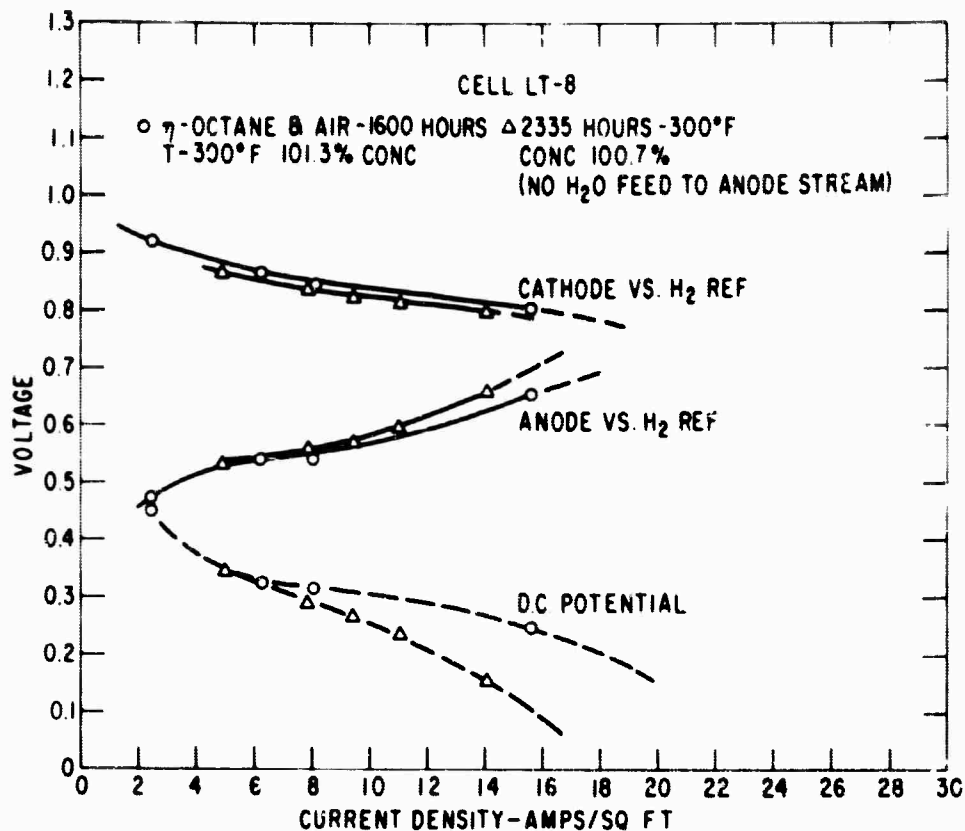


Fig. 144

For the first 1500 hours, the cell was operated at an average current density of 7 amps/sq ft. For the remainder of the test, cell output was reduced to an average of 5 amps/sq ft. Cycling occurred five times per hour at the 7 amps/sq ft level and approximately twice per hour at the 5 amps/sq ft level.

4.5.1.3 Cell LT-9 Propane/Phosphoric Acid/Air

To this report date, total operating time on this life test cell is 3286 hours. The test has been run continuously except for three interruptions. After 2060 hours, the propane supply tank became exhausted. After 2180 hours, the electrolyte pump failed. After 3115 hours, an open circuit in a control circuit cut off power to the test stand. In each case, the cause of failure was corrected and testing resumed within two hours.

Operation for the first four hours was with n-pentane and air. Performance curves for propane show cell performance vs. time. The curves of Fig. 145 show relative performance at different electrolyte concentrations at 300°F (149°C). At a cell potential of 0.45 volt, there is an increase in current of 220 ma (approximately 4.4 amps/sq ft) for the H₃PO₄ concentration of 88.6%, as compared to that at 96.2%.

Fig. 146 shows the influence of time with electrolyte maintained at approximately the same concentration (101%). After 1200 hours performance at this concentration, electrical output

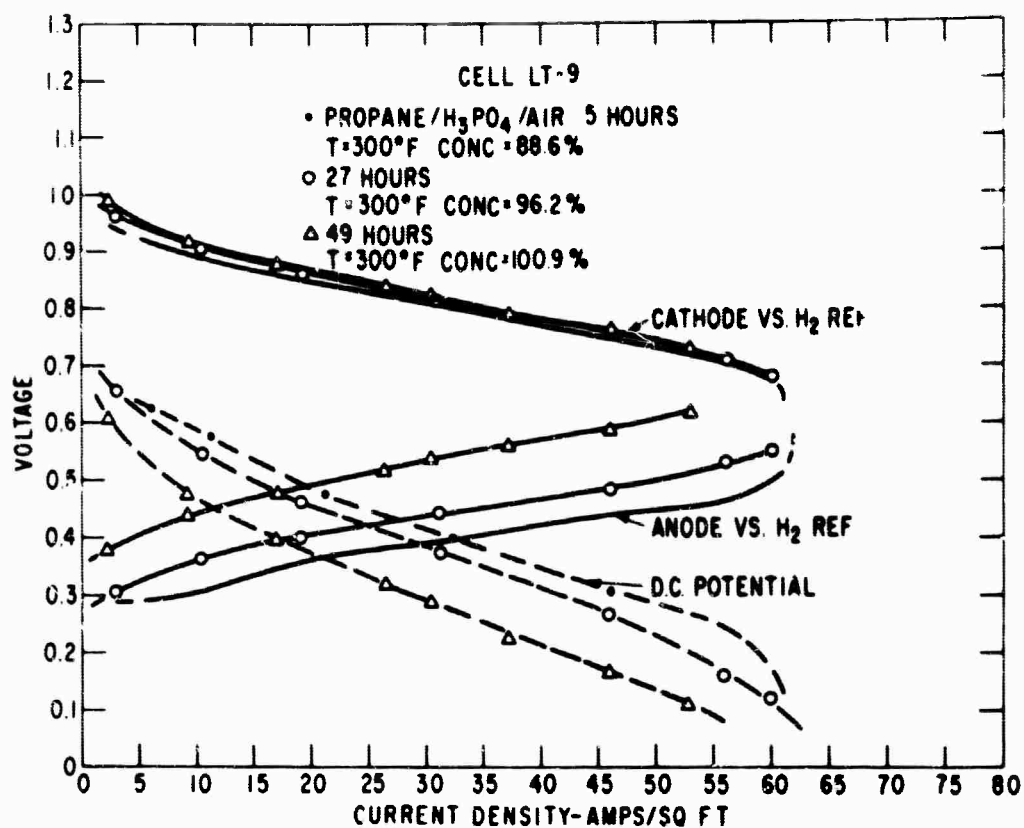


Fig. 145

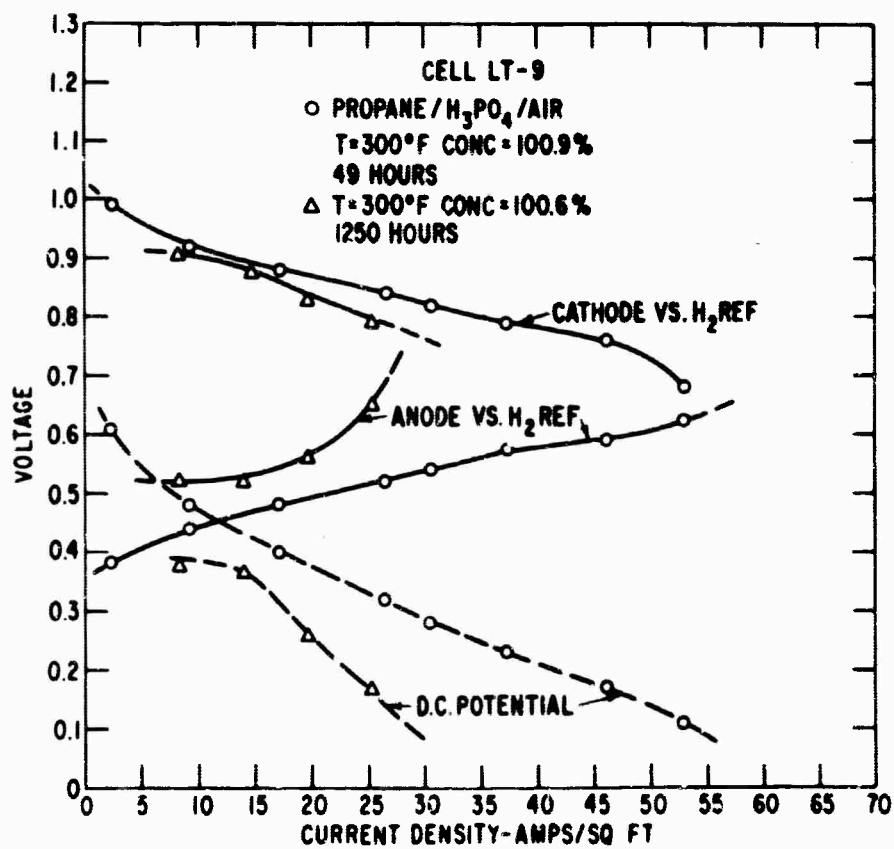


Fig. 146

has decayed from 360 mv at 20 amps/sq ft (after 50 hours of test) to 260 mv at the same current density. Short circuit current capability has been almost halved. Maximum current density attained after 1200 hours at 100% H_3PO_4 concentration is only 30 amps/sq ft.

After 1850 hours, as shown in Fig. 147, there is a marked increase in performance. Electrolyte concentration was still approximately 100% H_3PO_4 . Short circuit current capability had increased to almost 50 amps/sq ft. At 20 amps/sq ft, cell potential had decayed from the original value of 7.2 A.S.F. after 50 hours to only 6.7 A.S.F. It is noted that during the 250 hours prior to obtaining this polarization curve, the cell was activated daily by driving anode potential to a value greater than 850 mv. vs. hydrogen potential for a one-minute interval.

The cell was operated for a period in excess of 2600 hours, maintaining the electrolyte concentration at $100 \pm 1\%$ H_3PO_4 , to determine performance for self-sustaining operation at this concentration. The only make-up electrolyte added was 100% H_3PO_4 to satisfy leakage to cathode (air) stream. During this period, average output was 15-18 amps/sq ft. Air flow was maintained at three times stoichiometric requirement and propane flow at 12 times stoichiometric.

After 2665 hours of testing, water was introduced into the air stream to evaluate the effect of electrolyte concentration on performance. At a flow rate of 0.036 cc/min. liquid water,

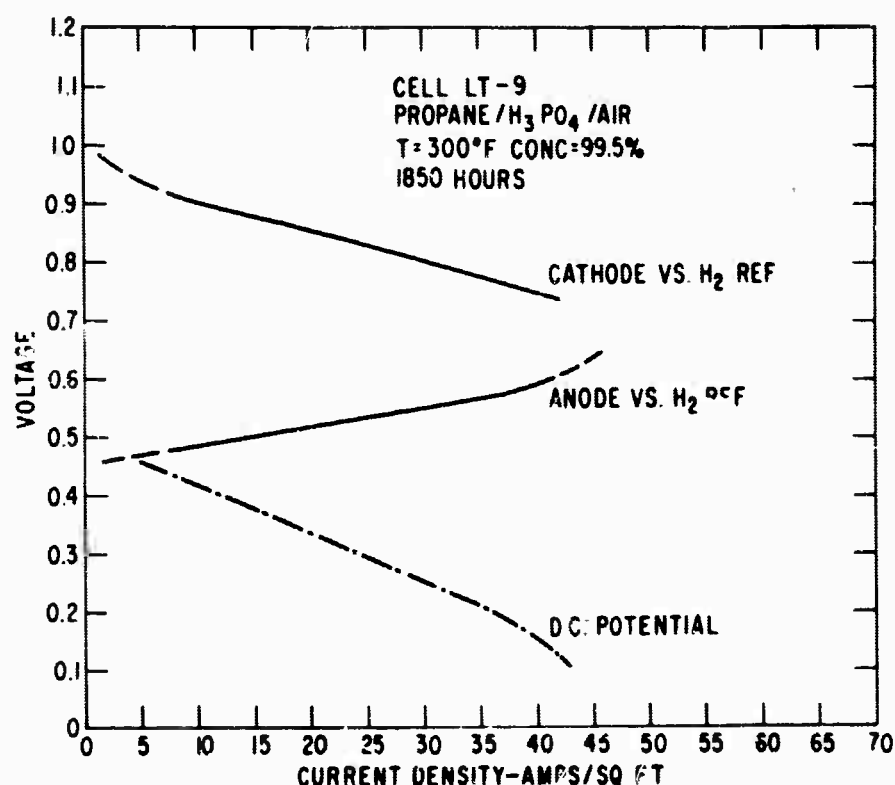


Fig. 147

BLANK PAGE

the acid concentration was maintained at $91 \pm 1\%$ H_3PO_4 . Figure 148 shows a performance curve of the cell at an electrolyte concentration of 92% at 300°F (149°C) after 2760 hours of operation. At 20 amps/sq ft, DC potential is 100 mv. At the start of test the corresponding voltage was approximately 465 mv. Short circuit current capability has been reduced from approximately 60 to 48 amps/sq ft.

After 3187 hours, performance was again checked after reducing water feed to fuel stream to 0.018 cc/min. and stabilizing electrolyte concentration at $95 \pm 1\%$ H_3PO_4 . Also plotted on Fig. 148, are cell characteristics at this time and acid concentration of 94.1%. There is no marked difference in performance except for an increase in short circuit current capability. Again, the only explanation for the increased performance was the fact that the cell was activated for a few days prior to the performance run when anode potential was maintained above 900 mv for one minute daily.

During the first 2280 hours of operation, no leakage was detected in the anode. After this period and up to 3000 hours, leak rate to anode was approximately 0.37 ml/hr. Anode back pressure was maintained above 7 inches H_2O .

Leakage in the cathode was apparent after 400 hours of operation when cathode back pressure was reduced from 9 to 3 inches H_2O to damp out a reference voltage fluctuation on the

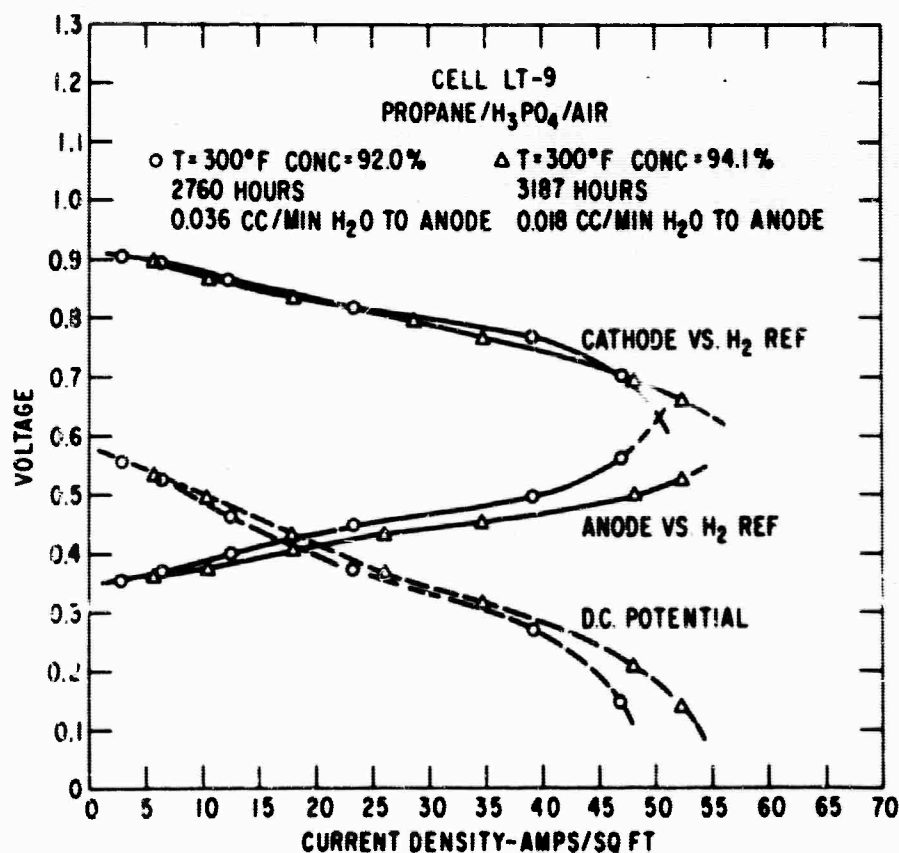


Fig. 148

recorder trace. After 2000 hours of operation, maximum leakage is 0.37 ml/hr at a cathode back pressure of 2.5 inches H_2O . After 3000 hours with back pressure at 4 inches H_2O , leakage was 0.31 ml/hr.

During the first 1500 hours of operation, the cell cycled once every 50-100 hours at current densities of 15-18 amps/sq ft. After this period cycling was not detectable, due to the periodic activation of the cell.

4.5.1.4 Decane (liquid)/Phosphoric Acid/Air

Because decane is liquid at cell operating temperature, the anode compartment of this cell test fixture was modified to accommodate a liquid fuel feed. Three fuel electrodes (LT-10, LT-11 and LT-12) were tested before a satisfactory compromise between fuel leakage through the electrode and performance was attained.

A. Cell LT-10

LT-10 (Standard Electrode) was operated for three hours before it was shut down because of decane leakage into the electrolyte. The approximate leakage rate was 4 ml/hr. The test set-up was modified to provide a constant head feed of fuel to the anode chamber. Performance is shown in Fig. 149.

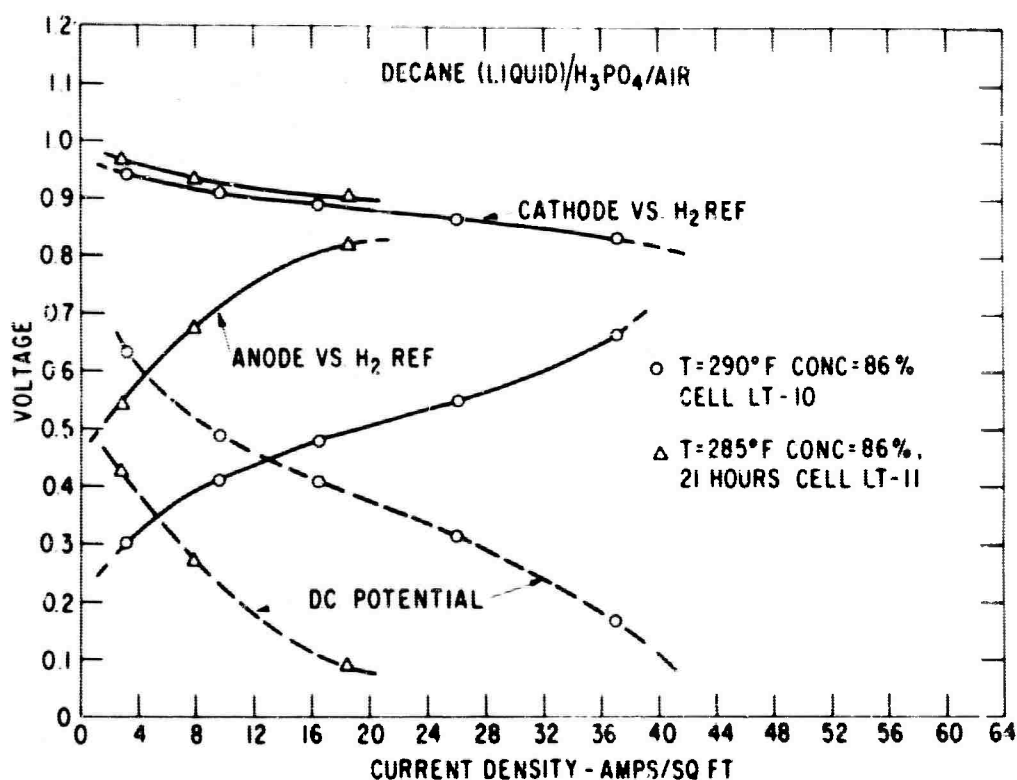


Fig. 149

B. Cell LT-11

LT-11 (50% Pt, 50% T-7 with a 5 mg/sq in T-30 film) was operated for 24 hours and shut down due to poor performance and decane leakage to electrolyte of approximately 1 ml/hr. Performance is shown in Fig. 149.

C. Cell LT-12

LT-12 (FEP Film Sprayed on Standard 20% T-30, 90% Pt Catalyst Mix) was started up at 255°F (124°C). There was no detectable leakage of decane to the electrolyte for the first 500 hours of operation, although decane transport to cathode exhaust was noted after 24 hours of operation. The rate of decane transport remained approximately constant at .035 ml/hr up to 980 hours of operation. Performance curves are shown in Fig. 150 for decane and air at 255°F (124°C) after 2 and 28 hours on test. After 170 hours, cell temperature was raised to 275°F (135°C). Performance curves of Fig. 151 indicate polarization after 170 and 450 hours at this temperature. After 500 hours, cell temperature was increased to 285°F (141°C). Fig. 152 shows performance at the increased temperature. After 980 hours, the cell was shut down to replace the cathode which was leaking electrolyte.

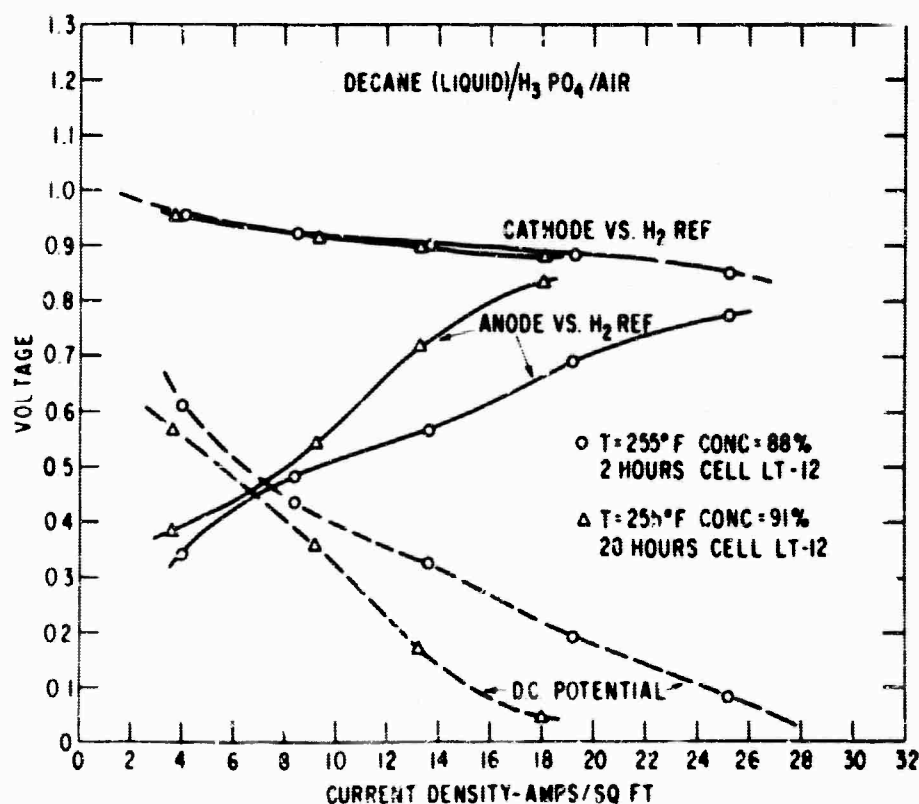


Fig. 150

D. Cell LT-19

This cell (same anode as LT-12) was maintained at 300°F (149°C). The new cathode was a standard electrode. After 120 hours of operation, (total FEP anode time = 1100 hours) the performance curve in Fig. 152 was taken. Performance is shown to be degrading from that at 795 hours and 285°F (141°C).

After 500 hours of operation (FEP anode time = 1480 hours) there was a noticeable reaction product buildup in the anode compartment which was settling out into the fuel reservoir attached to bottom of cell fuel inlet. This was causing serious performance degradation. Draining and flushing of the anode chamber reactivated the cell for approximately 8 hours, after which cycling stopped and output declined to as low as 2.0 A.S.F. at 40 mv cell potential.

With 816 hours (FEP anode time = 1796 hours) testing of cell LT-19, another polarization curve was taken at 300°F (149°C) after draining and flushing the anode chamber of reaction product buildup. This curve is included in Fig. 152. After 818 hours of operation of LT-19, (total FEP anode time = 1798 hours) the cell was shut down to replace the anode. Inspection of the anode revealed pinpoint holes and considerable brown deposit on the fuel side of the electrode.

E. Cell LT-30

This cell has been in operation for 250 hours. Performance after 24 hours of life testing is plotted in Fig. 153. The cell has been cycling at 9-10 cycles/hour. In order to obtain comparable performance, the standard practice of activating the cell to a cell potential of 850 to 1000 mv was used. Cell voltages and current were then recorded after a three minute wait for stabilization. As current level increases, cell output becomes more unstable.

The average output for this time period was 26.0 A.S.F. at 300 mv. Water is being added to the air stream to maintain electrolyte at a given concentration, i.e., 95 wt. % H_3PO_4 .

4.5.1.5 Pulsing Evaluation

• In conjunction with life testing, an attempt is being made to determine possible performance gains and to define significant parameters to improve fuel cell performance.

As a beginning, cell LT-8 operating on n-octane and air was manually pulsed to ascertain any obvious performance gain. The cell was allowed to operate at its normal output of 5.0 A.S.F. at 250 mv. By means of a Kordes-Marko bridge the cell was loaded to 25 A.S.F. (anode potential to 800 mv vs. hydrogen electrode). The pulse duration was 5 seconds and was induced every 5 minutes for a one-hour period. The average output increased from 5.0 A.S.F. at 250 mv (cell had been cycling at this load twice per hour) to 5.6 A.S.F. at 270 mv. When operating at this discharge pulse frequency and duration, cell output tended to degrade with time. Increasing

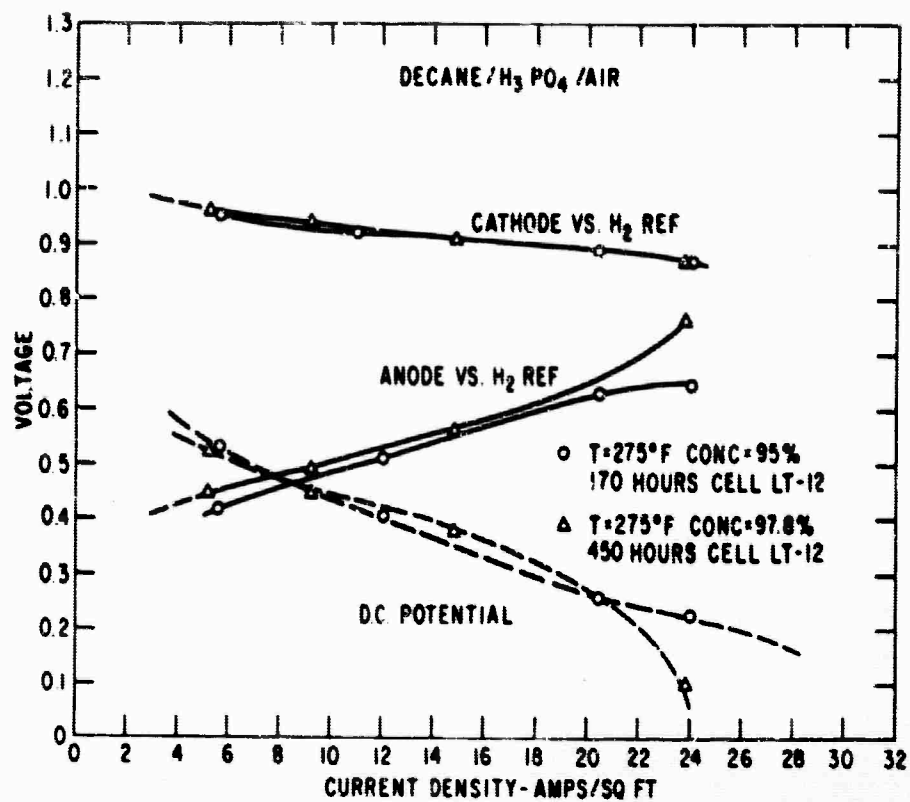


Fig. 151

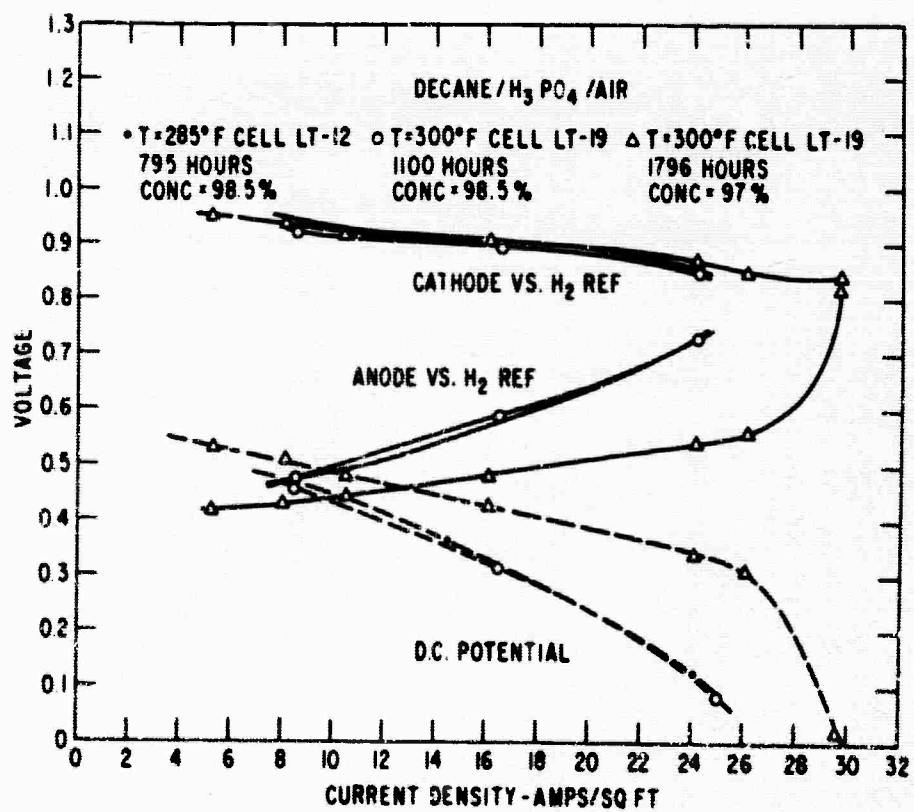


Fig. 152

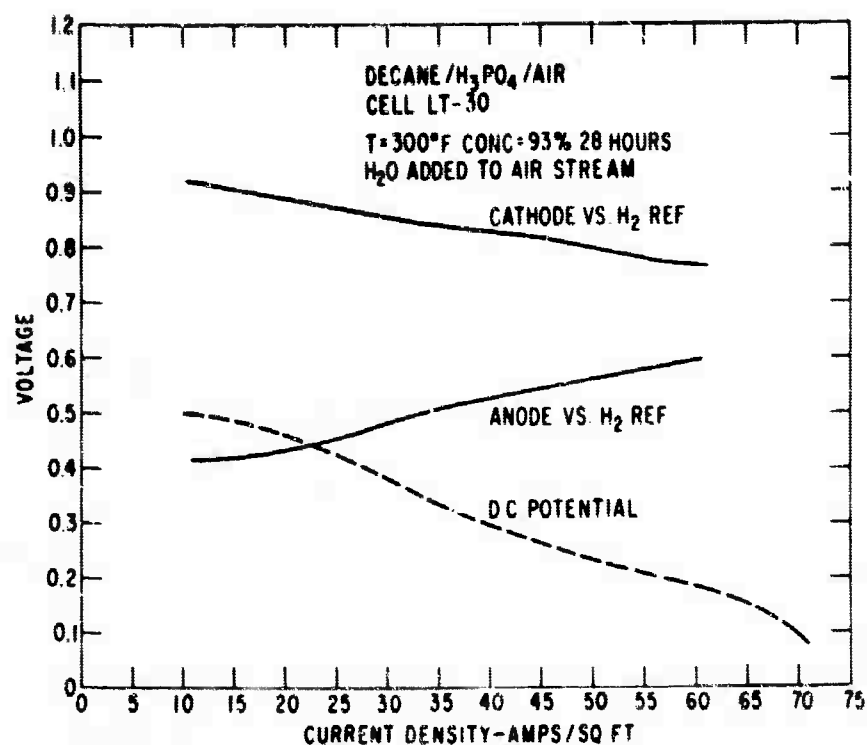


Fig. 153

pulse duration to 10 seconds showed no marked increase in output and no attenuation in slope of output degradation.

An estimate of the power gain associated with this pulsed discharge over a one-hour period yielded a net energy gain of approximately 19%.

It is noted that this testing was only performed for a two-hour period, manually controlled, and that initial performance of this test cell was very much degraded. Also since the pulsed output was obviously degrading with time, no definite conclusions can be drawn until an automatic testing sequence is set up on a normally performing cell for extended periods.

A. Automatic Pulsing Equipment

In order to further evaluate performance gains due to periodic cell activation (pulse discharge techniques) an automatic pulsing device consisting of the Kordesch-Marko type bridge circuit equipped with automatic electronic timers to control pulse intervals and pulse durations was built. A schematic of the equipment is shown in Fig. 154.

When the equipment is in the cell circuit, a variable resistance controls cell current at a fixed value for a given time interval controlled by a timer. At the completion of this interval, a second timer switches the cell output to a lower resistance (deep discharge pulse) for a

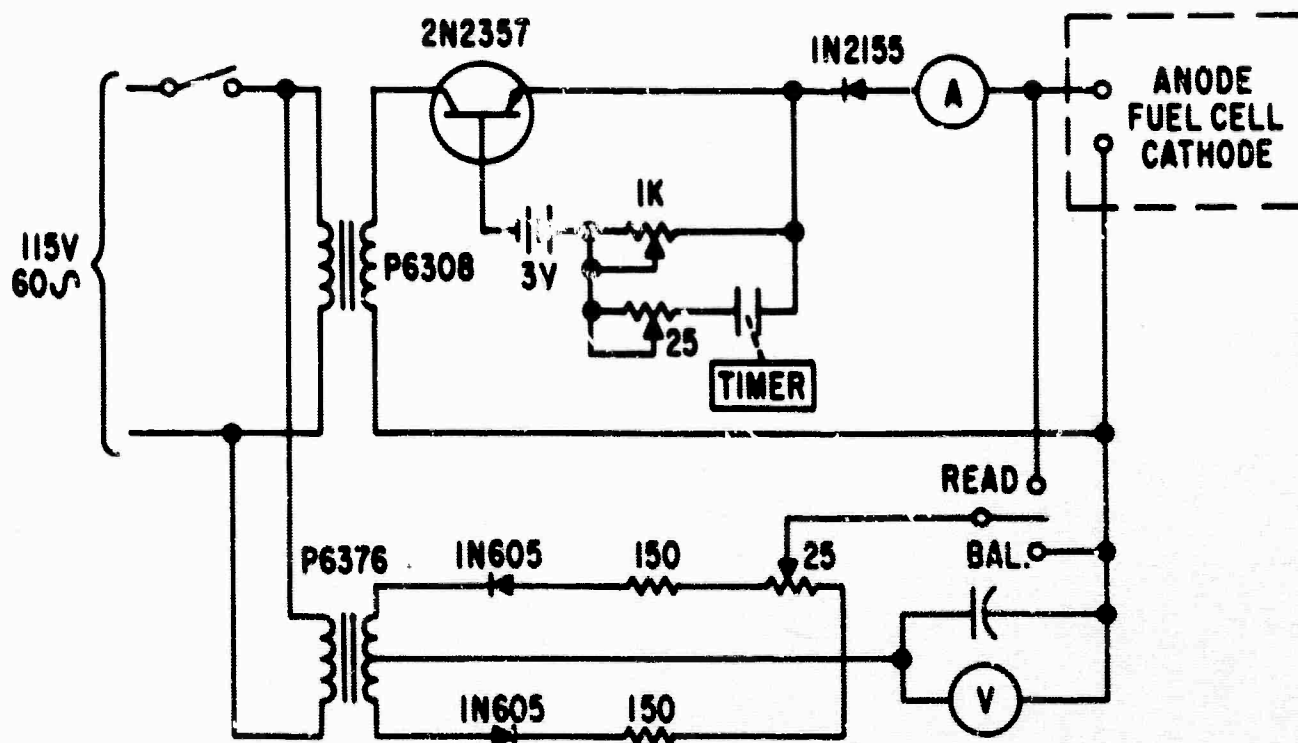


Fig. 154 Pulsed Discharge Circuitry Schematic

short period. The second timer then switches out and the cycle is continuously repeated in this fashion.

Cell LT-8, was again used as a test specimen for evaluation of the equipment. After approximately 3400 hours of operation, this n-octane/ H_3PO_4 /air fuel cell was pulsed for a duration of 3 seconds every 3 minutes. Current output was maintained at a constant value of 9.0 A.S.F. Average voltage output from the cell was 0.290 volt during the 3 minute pulse interval. The cell operated approximately 1 hour at this pulse duration before anode overvoltage caused cell deactivation. With the pulse interval adjusted to 2 minutes and current reduced to 8.0 A.S.F., the cell operated for 3 hours without deactivation, at an average output of 8.0 A.S.F. at 320 mv. Prior to pulsing, the cell had been operating at 5.6 A.S.F. and 210 mv. Thus far, cells have not been subjected to continuous pulsing for periods greater than 8 hours.

4.5.1.6 Evaluation of Barrier Films For Water Vapor Pressure Suppression

Test cells LT-13, 14, and 15 were used as specimens to evaluate an Ioplex membrane saturated with phosphoric acid (as obtained from Amicon Corp., Cambridge, Mass.). In all cases, the cells were operated on Iso-octane/ H_3PO_4 /air.

The three separate tests used for the film evaluation consisted of: 1) pressing the approximately 2 mil thick membrane to the electrolyte side of a standard cathode and collecting water in a silica gel drying column in the cathode exhaust; 2) pressing the membrane to electrolyte side of both electrodes and measuring water transport in both exhaust streams; and 3) measuring water transport across two standard electrodes with no film pressed to either electrode. Experimental results are presented in Table XXXVII. The experimental rates for water transport across the membrane/electrode matrix are somewhat lower than the calculated rates from the equation as stated in Table XXXVI.

TABLE XXXVII
Water Transport with Ioplex Membrane

Test	Weight H ₂ O (gm)	Time (hr)	H ₃ PO ₄ Conc. Start/End (wt. %)	Cell Temp. (° F)	P _s Avg (mm Hg)	R, Actual (cc/hr)	R, Calc. (cc/hr)
No 1	10.38	28	85-90	250	160	0.370	0.435
Membrane on cathode	11.50	68	90-95		75	0.169	0.205
No 2	12.53	76	93-97	285	85	0.167	0.230
Membrane on both electrodes	2.	40	97-98		45	0.067	0.122
No 3	16.19	71	85-93.8	250	95	0.228	0.259
Standard electrodes, no membrane	2.05	25	93.8-95.1		55	0.082	0.150

Although the tests were not critically controlled as to electrolyte concentration, the initial results did not warrant a more sophisticated test set-up and evaluation of the Ioplex membrane for water balance control was discontinued. Performance of the cells was not significantly altered by the presence of the Ioplex at the electrolyte interface. Also, these membranes displayed discoloration (possible degradation) and brittleness after exposure to the environmental conditions.

4.5.1.7 Conclusions

A. Phosphoric Acid Electrolyte

A cell (LT-9) operating with propane, aqueous phosphoric acid, and air demonstrated life in excess of 3280 hours. A *iso*-octane, phosphoric acid air cell (LT-7) operated

for 1990 hours before failure. A cell (LT-8) composed of n-octane, phosphoric acid, and air demonstrated life in excess of 3850 hours.

Electrode failures early in life test have, in general, been caused by delamination of catalyst mix, and excessive cracking and separation of the catalyst from the electrode screens.

Electrolyte invariance is obtained with H_3PO_4 wt. % of $100 \pm 1\%$. However, performance is decreased. This indicates a possibility of obtaining moisture balance of the complete cell.

Rate of water transport at cell temperature and phosphoric acid concentration can be estimated based on engineering studies, and, consequently, acid concentration can be stabilized by water feed control to fuel stream.

Decane which is liquid at cell operating temperature ($300^\circ\text{F}/140^\circ\text{C}$) was reacted with air and phosphoric acid electrolyte for 1798 hours. Initial problems of decane to electrolyte leakage (mixing of electrolyte and fuel phases) can be corrected by replacing the T-30 film of standard electrodes with an FEP film on the fuel side of the electrode.

Performance decay with time has been exhibited on all hydrocarbon/air fuel cells with phosphoric acid electrolyte. The reason for this decay is not known at this time. Reaction product build-up on the fuel side of the anode is considerable in all long-life cells examined thus far. Cells can be reactivated at similar performance levels as those obtained initially, by periodic deep discharge of the cell, as was shown for propane.

Cycling (periodic fluctuation of electrical output) has been observed on all hydrocarbon/air fuel cells using phosphoric acid as the electrolyte. From data taken thus far, cycling frequency increases with carbon atom chain length, and with current density.

B. Pulsing Evaluations

Initial testing indicates that performance gains can be made by periodic deep discharge (pulsing) of operating hydrocarbon-air fuel cells with phosphoric acid electrolyte.

C. Barrier Films

The use of a barrier type film on electrode surfaces was not successful in suppressing water vapor pressure over phosphoric acid on cells operating from 250 to 285°F (121 to 141°C).

D. Performance Summary

Performance on a variety of hydrocarbon fuels illustrative of typical phosphoric acid electrolyte fuel cell life are summarized below:

TABLE XXXVIII
Typical Cell Performance

Test Cell	Time (Hrs)	Temperature (°F)	Electrolyte Concentration (Wgt. %)	Power Density (Watts/Ft ²)
LT-7				
Iso-Octane/Air	4	300	89	12.6 @ 35 ASF
	334	300	92	10.2 @ 30 ASF
	338	300	92	16.6 @ 45 ASF
	1034	350	96	9.5 @ 35 ASF
	1657	350	100	8.25 @ 30 ASF
				7.7 @ 35 ASF
LT-8				
n-octane/Air	23	300	91	5.75 @ 23 ASF
	484	300	93	6.4 @ 22 ASF
	1015	300	93	4.3 @ 14 ASF
				0.0 @ 23 ASF
	1600	300	101	3.9 @ 16 ASF
	2335	300	101	2.6 @ 11 ASF
LT-9				
Propane/Air	5	300	89	14.4 @ 50 ASF
	27	300	96	12.5 @ 40 ASF
				11.5 @ 50 ASF
	49	300	100	9.0 @ 33 ASF
				6.75 @ 50 ASF
	1250	300	100	5.25 @ 15 ASF
				0.0 @ 50 ASF
	1850	300	100	7.5 @ 30 ASF
				0.0 @ 50 ASF
	2760	300	92	10.4 @ 40 ASF
	3187	300	94	11.2 @ 40 ASF
LT-19				
Decane/Air (Liquid)	2	255	89	4.5 @ 15 ASF
	795	285	93	5.2 @ 15 ASF
	1798	300	97	8.2 @ 24 ASF
LT-30				
Decane/Air (Liquid)	28	300	93	11.8 @ 50 ASF
LT-33				
n-octane/Air	28	380	96	14.5 @ 50 ASF

4.5.2 Hydrofluoric Acid Electrolyte

A number of cells were tested for extended periods using constant boiling hydrofluoric acid as the electrolyte, with the primary aim of substantiating initial test results.

The electrolyte was an aqueous solution of hydrofluoric acid (36% HF by weight). Operating temperature was 107°C (223°F). All material in the electrolyte circuit is Teflon where practicable. The pre-heater for HF is made of platinum tubing. Electrolyte sump and constant head tank are also made of Teflon.

The fuel (anode) system is also fabricated of Teflon where practicable. In the case of propane, fuel exhausts overboard through a bed of KOH to absorb any HF leakage through electrode. The air side is similar to the fuel system with trap provided to absorb any HF leakage.

4.5.2.1 Cell LT-16 Propane/HF/Air

After modifying a test stand to accommodate the boiling hydrofluoric acid electrolyte, the cell was operated for a total of 40 hours. A polarization curve taken after 32 hours of operation is shown in Fig. 155.

For comparison, in Fig. 156, cell performance is shown for hydrofluoric acid (azeotrope) and two concentrations of phosphoric acid. These cells were not composed of the same electrodes. The cell was shut down after 40 hours test time to evaluate the hexane and octane.

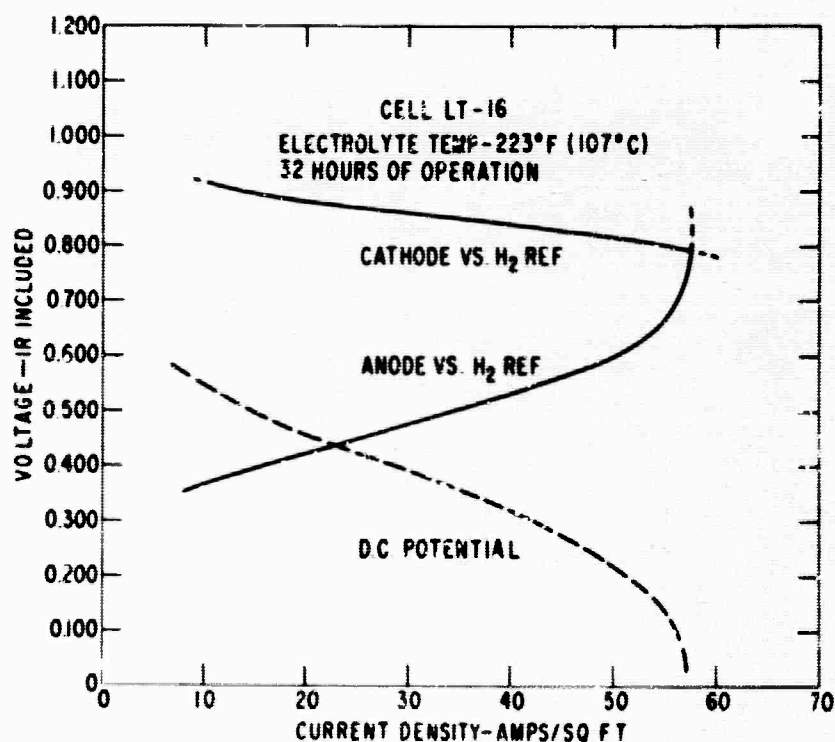


Fig. 155 Cell LT-16 C₃H₈/35% HF/Air

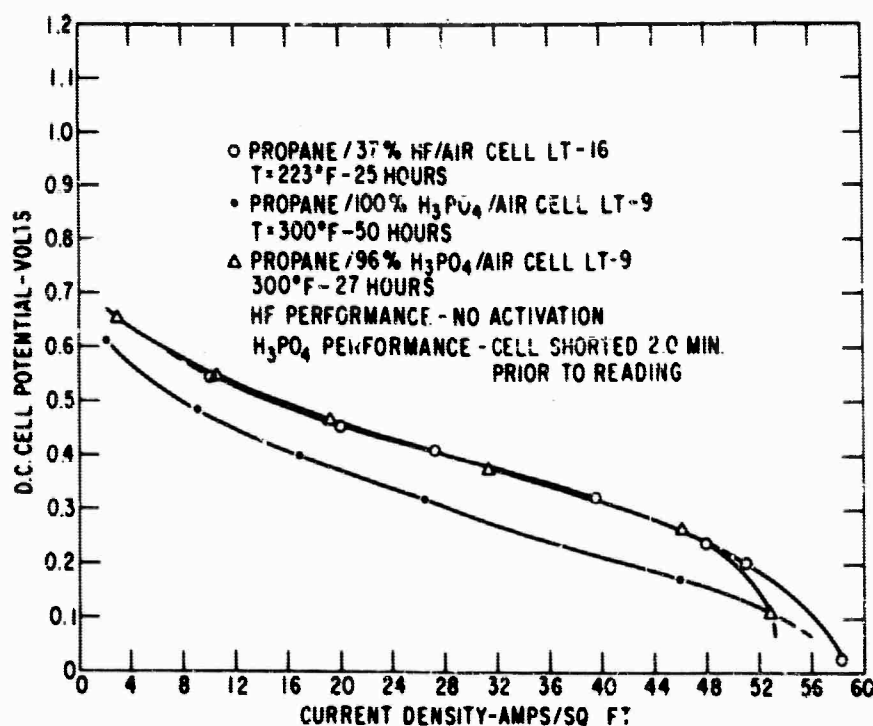


Fig. 156 Propane and Air Comparison of H_3PO_4 and HF Performance

4.5.2.2 Cell LT-16 Hexane/HF/Air

The same cell (LT-16) was operated with hexane and air as reactants for approximately 20 hours before self-shutdown. Average output was 16 A.S.F. at 210 mv at average cell temperature of 223° F (106° C). Electrolyte concentration was 37 wt % HF. After 26 hours total operating time, the cell was shut down by a testing problem due to erratic output caused by hexane vaporization in the pump solenoids and consequent unsteady fuel flow. Water-cooling has now been added to these valves.

4.5.2.3 Cell LT-20 Octane (Liquid)/HF/Air

The test stand was equipped with a liquid fuel anode chamber and FEP coated anode for evaluation of liquid octane with the constant boiling hydrofluoric acid electrolyte. Average concentration was 37 ± 0.5 wt % HF. The cell was continuously operated for a 100 hour period at 225° F (107° C).

A polarization curve taken at 50 hours with a cell temperature of 230° F (110° C) is shown in Fig. 157. A polarization curve for n-octane/ H_3PO_4 /Air is included in Fig. 157 for comparison.

During the 100 hours of testing with octane/HF/air on Cell LT-20, it was significant that no anode voltage cycling became evident. On the other hand, with H_3PO_4 , Cell LT-33 cycles 10-15 times per hour.

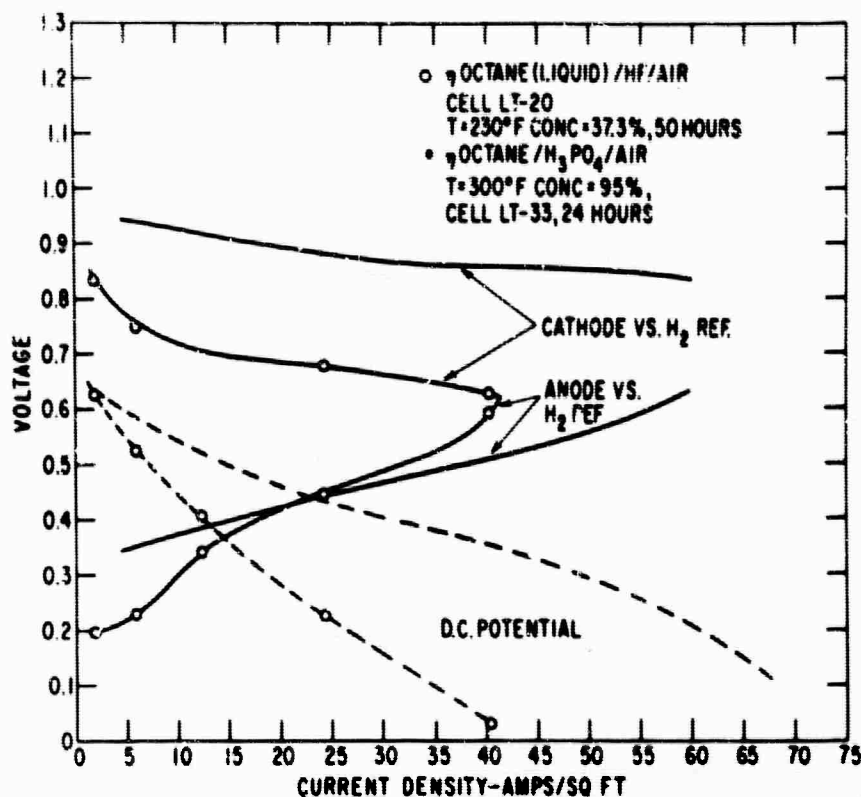


Fig. 157 Cells LT-20 and LT-33, Comparison of η Octane (Liquid)/HF/Air and η Octane/ H_3PO_4 /Air

4.5.2.4 Hydrofluoric Acid/Cesium Fluoride Electrolyte

After completion of boiling hydrofluoric acid testing, an evaluation of HF/CsF/ H_2O electrolyte was attempted. Hydrofluoric acid, cesium fluoride, and water were combined in a mole percentage of 60/30/10%, respectively, in an attempt to analyze performance at high temperature over the boiling point of aqueous hydrofluoric acid. The cells were operated at 300°F (149°C). Testing problems were encountered in this work and no conclusive life tests have been run yet.

4.5.2.5 Conclusions

Cells operated with Azeotropic aqueous hydrofluoric acid and n-octane at 223°F (106°C) exhibited none of the cycling characteristics of cells operated with phosphoric acid at 300°F (149°C).

As of this reporting period, performance with hydrofluoric acid/cesium fluoride electrolyte and 3-in. by 3-in. electrodes has not achieved the levels reported previously(2) for the 11.38 cm^2 electrodes. Closer control of electrolyte composition will be attempted with more rapid analytical procedures which are being developed. Four electrode pairs have been evaluated thus far with no marked improvement over the constant boiling HF electrolyte performance.

2. Ibid. p. 4-41 through 4-47.

Performance Summary

Performance on two different hydrocarbon fuels illustrative of typical hydrofluoric acid electrolyte fuel cell life are summarized below.

TABLE XXXIX
Typical Cell Performance

<u>TEST CELL</u>	<u>TIME (Hrs)</u>	<u>Temp. (°F)</u>	<u>ELECTROLYTE CONC. (Wgt. %)</u>	<u>POWER DENSITY (Watts/Ft²)</u>
LT-24 n-octane (liquid)/Air	50	230	36	5.6 @ 20 ASF.
LT-32 Propane/Air	32	223	36	12.5 @ 45 ASF.

4.6 STUDIES OF SELF-SUSTAINING OPERATION

Achieving self-sustaining operation of a hydrocarbon-air fuel cell requires an understanding of the power capability of the cell, heat and mass balance considerations, fuel and oxidant composition and utilization, and mass transport phenomena in liquid and gas streams as well as at interfaces. The effort during this period of the program was concerned with: a study of the behavior of binary fuel systems in specially designed laboratory fuel cell test vehicles; and the mass transport rates and overvoltage of an operating n-aliphatic/air fuel cell.

4.6.1 Reactivities and Fuel Utilization (P. J. Chludzinski/H. J. R. Maget)

The phosphoric acid electrolyte cell operating on pure single component hydrocarbon fuels and air has been extensively studied for various fuels, both from a performance and life viewpoint. In designing multi-cell stacks to run on mixtures of fuels, one could, of course, design for the least reactive species, and simply accept the performance bonus of the more reactive species. Indications are, however, that the cell output can range by a factor of four within this fuel cut, and by proper cell design, advantage can be taken of the relative reactivities. The staging of batteries of various sizes to progressively utilize the reactive and less reactive species and thus maintain an optimum weight and volume would be one design approach.

It was decided to attack the problem initially by studying binary systems such as propane/octane, octane/hexane, etc., to simplify the understanding of the phenomena. This could later be extended to more complex mixtures, some containing compounds known to exist in ordinary fuels and which are presently known to be extremely unreactive. Two test methods were primarily used, the first based on a system which recycled the fuels past the anode and removed product carbon dioxide chemically. This system had the advantage of allowing long term running and the accumulation of reaction by-products in the recycled stream. The system provided some data on pure propane, but would not function on propane/octane or propane/hexane mixes because of generation of excessive anode pressures, resulting in blowing fuel through the anode into the electrolyte.

The system presently being used is a once-through arrangement in which inlet fuel flow and composition are controlled, and exhaust composition is measured by a gas chromatograph.

4.6.1.1 Experimental Investigation

The recycle system is shown schematically in Fig. 158. An infusion pump was used to pump gaseous fuel to the anode and through a low pressure-drop KOH scrubber to remove the product carbon dioxide. An external line to the cycle fed propane through a flow measuring capillary to replenish the propane consumed. The liquid fuel was pumped by another infusion pump. Fuel utilization could be obtained by inference from the propane feed rate and total carbon

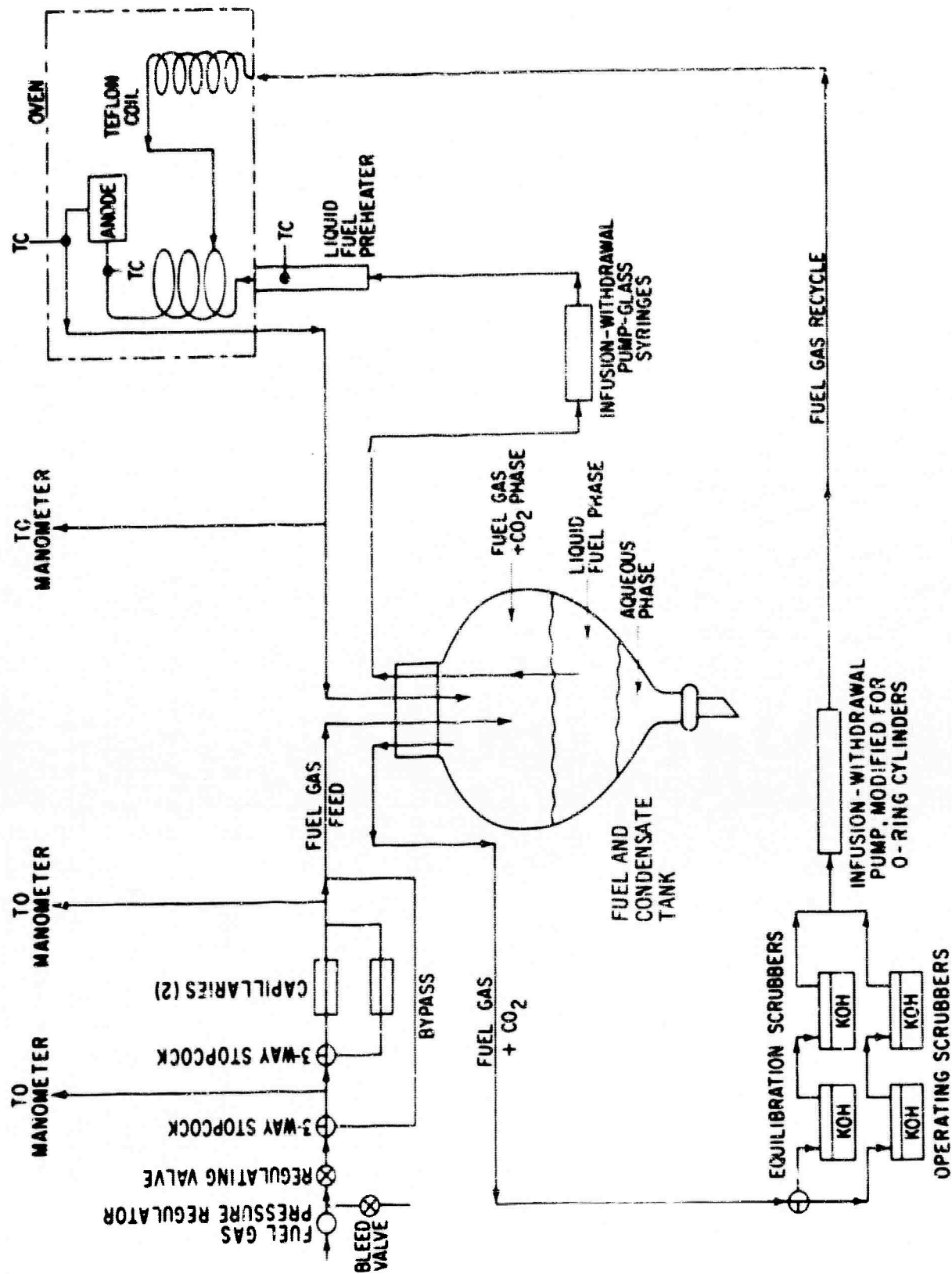


Fig. 158 Binary Fuel Recycle System

dioxide production. The amount of carbon dioxide was best determined by first absorbing and neutralizing it to carbonate in the scrubbers, and then washing out each scrubber into separate volumetric flasks. Two samples per flask were treated, one with excess BaCl_2 and then HCl titration to determine the caustic remaining in the scrubber, and the second by HCl titration with methyl orange to get the total carbonate plus caustic. Carbonate content was obtained by difference.

The system was workable but required excessive time to equilibrate, because the carbon dioxide concentration in the fuel and condensate tank had to reach steady state conditions before the propane demand system would respond. Before steady state efflux of carbon dioxide to the scrubbers was established, the anode pressure tended to increase because of transient accumulation of carbon dioxide. It would finally decrease to the point where a pressure drop across the propane flow capillary could be maintained constant, the whole process taking hours to accomplish. Once steady state was established, the equilibration scrubbers were bypassed and the operating scrubbers switched in, at which point the actual test was begun. At the end of the test, the scrubbers were again switched, and carbon dioxide analyses made. The efficiency of the first scrubber was usually sufficient to pick up all the product carbon dioxide.

The system proved to be unworkable on a feed of propane and octane (or hexane). Excess pressure was produced by the vaporization of the liquid fuel, even though the fuel was recondensed at the exhaust. This could not even be overcome by progressive bleeding down at the system pressure, and fuel was blown through the anode.

Work was then initiated on a one pass fuel system and a chromatograph provided with a gas sampling valve and thermal conductivity cell. It was calibrated with known amounts of carbon monoxide, carbon dioxide, propane, hexane, octane, methane, air and mixtures of these constituents for a six foot, 1/8 inch O.D. column packed with silica gel. Separation of air, carbon monoxide, and methane could be accomplished with the column at room temperature, carbon dioxide and propane at 150°C , and hexane and octane at 250°C . The carrier gas was helium, set at 30 cc/min at 150°C , and although the chromatograph had flow compensators to keep carrier flow constant through a temperature excursion (temperature programming), the flow decreased somewhat at 250°C . The decrease was reproducible and constant while the hexane and octane peaks were being measured. Error was minimized by calibrating the chromatograph and running a fuel cell sample under the same conditions of temperature programming.

It was necessary to heat the sample valve, the sampling tube, and all fuel exhaust lines that were exposed to room ambient in order to prevent condensation of the higher boiling constituents. The lines were kept constant at about 150°C and monitored by thermocouples in various locations.

The anode exhaust was directed to a heated teflon dehumidifier containing two chambers, one which trapped electrolyte leakage, and the other which contained phosphorous pentoxide

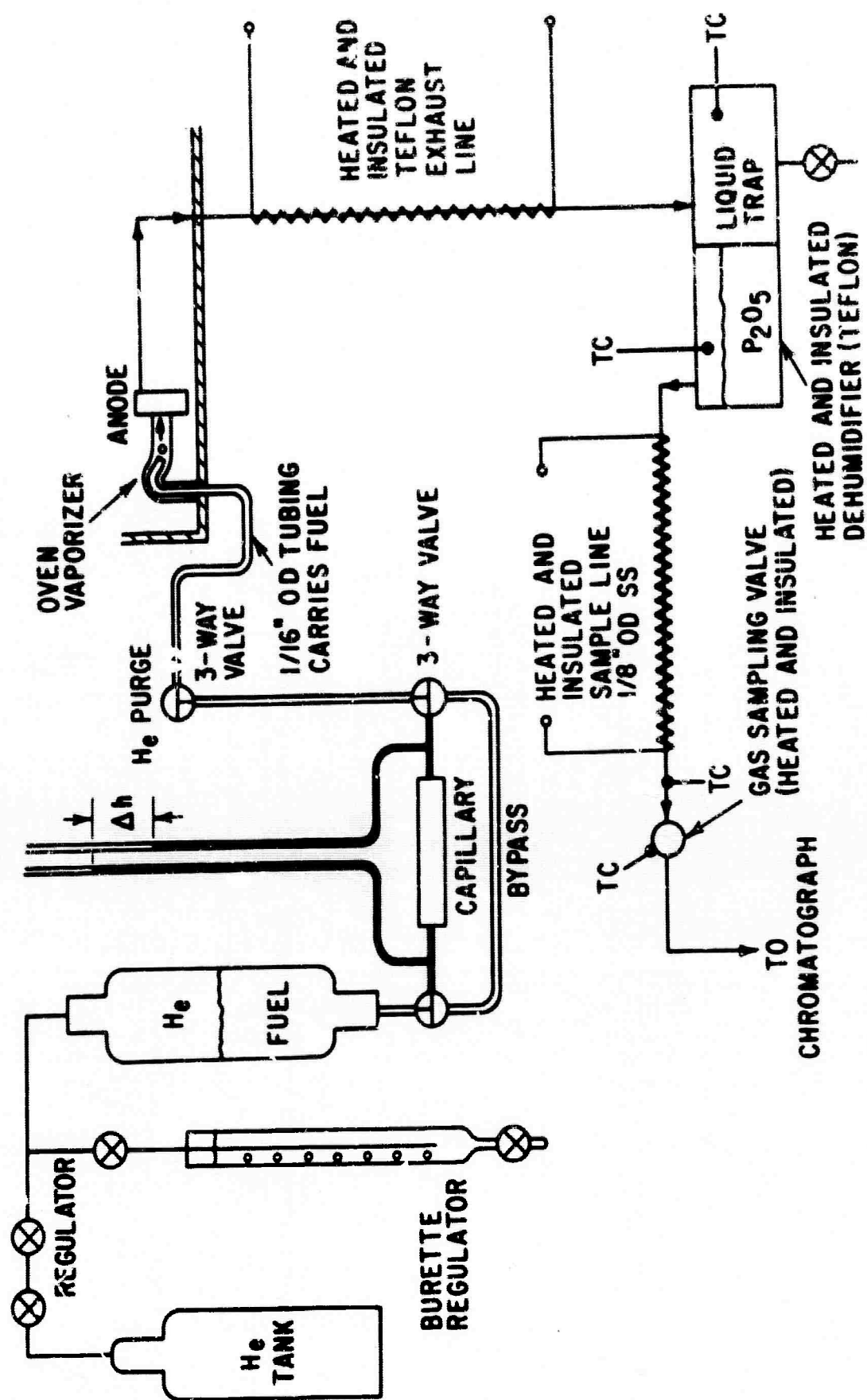


Fig. 159 Fuel Feed and Exhaust for Chromatograph System - Binary Fuels

to remove water vapor from the fuel and carbon dioxide vapor before introduction to the silica gel column. The liquid fuel mixture was pumped to the anode with an infusion-withdrawal pump. Flow rates of fuel were established in the range of .02 cc/minute to give a maximum of ten times the theoretical amount of fuel needed at 20 A.S.F. (10X stoichiometric). Very small flow rates were difficult to maintain at steady state because of the mechanical lag in the pump when the stroke of the syringes was reversed. A compromise was made by using large syringes at very low plunger speeds. This method provided 40 hours of running on one stroke. Further calibration checks showed that the glass syringes did not move smoothly, but with small pulses, probably caused by syringe friction. The method finally chosen discarded the infusion pump and used a flow capillary.

A schematic illustration of fuel feed and exhaust for the chromatograph system is shown in Fig. 159. Helium was used to pressurize the fuel tank because its presence in the fuel would not be detected by the chromatograph. The capillary inlet pressure was regulated, and a bleed to a column of water utilized to dampen small fluctuations in regulator pressure. The bypass allowed the fuel feed line to the cell to be quickly filled prior to testing. The usual one-quarter inch diameter tube was discarded in preference to an oven-heater vaporizer composed of coaxial 1/16 and 1/8 tubing. It was felt that preferential distillation of the more volatile constituent in the fuel mixture would be prevented. The system provided very satisfactory operation, with reproducible calibration and smooth, steady flow.

4.6.1.2 Results and Discussion

A. Recycle System

With the recycle system, data was obtained only on pure propane because of the difficulties previously described. Table XL lists the results of propane consumption and carbon dioxide production. The cell currents ranged from 1 to 3 amps. held constant by the Kordesch Marko Bridge. The actual fuel feed as demanded by the system was about 15 to 20% lower than the theoretical feed, except in the case of the longest run which was 9% lower. This is an indication of the problem of equilibrating the recycle system. The CO₂ production rates were low by about 10% on the early runs, and about 3% low on later repeats, with the longest run giving quite close to theoretical amounts of CO₂. These results indicate that the electrochemical oxidation of propane is essentially complete.

B. Chromatograph System

The Perkin-Elmer Model 801 Vapor Fractometer was calibrated with about 50 samples of chemical species and mixtures of species to determine separation time, peak heights, areas, and proper column temperatures for a silica gel column. This seemed to be the best column available for separation of all species from air, to paraffins as high as octane. The

calibration was based on the area of the "peak" as described by a mechanical integrator on the Leeds-Northrup recorder. The data was reduced to a characteristic constant for each constituent that described the micro gram mols of constituent in terms of thermal conductivity, cell attenuation, and area under the peak for a constant helium carrier gas flow and column temperature. These results are tabulated in Appendix 5.5.1.1.

TABLE XL
Propane Consumption and CO₂ Production — Recycle System —
Pure Propane / Air / H₂ PO₄

Recycle fuel feed = .0151 SCFH
Phosphoric acid concentration = 98 wt %
Cell temperature = 300°F

Date	Cell Current (amps)	Theo. Fuel Feed (SCFH x10 ³)	Actual Fuel Feed (SCFH x10 ³)	Ratio (Actual/Theo) Fuel Feed	Duration of Run (hr)	Theo. CO ₂ Produced (m-mol)	Actual CO ₂ Production (m-mol)	Ratio (Actual/Theo) CO ₂ Produced	Anode Potential (IR incl.) (volts)	Cathode Potential (IR incl.) (volts)
9/16/4	2.00	2.94	2.35	.80	7.25	81.1	73.2	.903	.506	.856
9/17/4	3.02	4.44	3.65	.82	6.74	113.9	109.7	.963	.571	.831
9/21/4	1.01	1.49	1.35	.91	16.92	95.7	95.8	1.001	.469	.902
9/22/4	2.00	2.94	2.55	.87	7.50	84.0	83.0	.988	Cycling	

SCFH = Standard cubic feet per hour

Theo. = Theoretical (assuming 3 mols CO₂ per mol C₃H₈)

m-mol = milli-gram mol

Air, carbon monoxide, and methane were not calibrated extensively at low column temperatures, but the separation times were determined. This was necessary because first anode exhaust samples showed a peak at 150°C that could have been either carbon monoxide, methane or air (which were not separable at 150°C). By running a few tests on the cell with the column at room temperature, it was found that the peak corresponded to air or nitrogen, not carbon monoxide or methane. Remaining tests were run at an initial column temperature of 150°C, then programmed to 250°C, rather than 20°C to 250°C. This procedure eliminated the lengthy time period necessary to cool the chromatograph to room temperature.

The amount of each species of fuel used by the cell was determined by considering a mass balance on the anode, dealing only with the fuels and product carbon dioxide. Fig. 100 shows a block diagram for the mass balance.

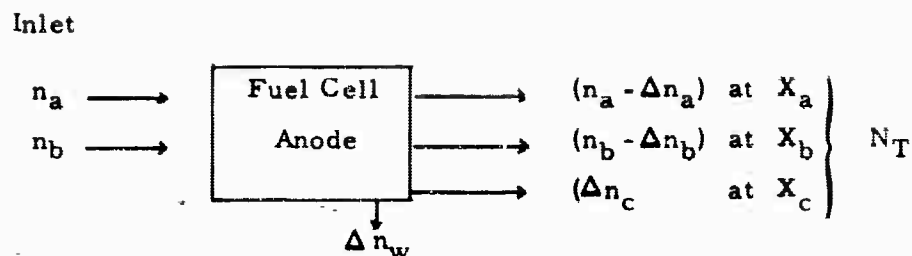


Fig. 160 Anode Mass Balance

where:

n 's are molal flow rates

Δn 's are molal, utilization rates, or production rates

subscripts a, b, c, and w, refer to fuel a, fuel b, carbon dioxide, and water, respectively

X 's refer to mol fraction

N_T is the total exit molal flow rate

The water which was transported through the anode was removed prior to entrance to the chromatograph, so it is not included in N_T . Removal of water was accomplished using a bed of phosphorous pentoxide which was kept hot to prevent fuel condensation.

$$\Delta n_a = \frac{n_a (M_b X_b + X_c) - M_b n_b X_a}{M_a X_a + M_b X_b + X_c} \quad (61)$$

$$\Delta n_b = \frac{n_b (M_a X_a + X_c) - M_a n_a X_b}{M_a X_a + M_b X_b + X_c} \quad (62)$$

$$N_T = \frac{M_a n_a + M_b n_b}{M_a X_a + M_b X_b + X_c} \quad (63)$$

where the symbols M_a and M_b refer to the number of molecules of carbon dioxide produced by a molecule of the respective fuel species. Since it has been proved that oxidation of propane and octane are essentially complete, then M may be assumed to equal the number of carbon atoms in a molecule of the respective fuel species. Appendix 5.5.1.2 contains the results of the single and binary fuel experiments. The main points are summarized in the following paragraphs.

1. Pure Octane

Octane on open circuit showed a carbon dioxide content in the anode exhaust of one per cent. If this is assumed to be chemical combustion from oxygen migrating to the anode from the cathode, it corresponds to a loss of about 0.3 A.S.F. Pure octane at 20 A.S.F. showed

utilization and carbon dioxide production within 2% of theoretical, and if the chemical combustion value from the open circuit tests was subtracted out, the agreement was within 1 percent.

2. Binary Fuel Mixtures of Octane and Hexane

On open circuit, the results from the utilization equations (61) and (62) gave positive and negative numbers of usage of individual species, since the equations are very sensitive to small errors in flow rate and exhaust composition. The arithmetic sum of chemical combustion currents were still of the order found for pure octane, indicating that chemical combustion is probably very low.

When mixtures of n-octane and n-hexane were run in the fuel cell on current drain, the following general observations were made. On a 50/50 by volume mixture, the hexane provided about 80 to 90 percent of the cell current when the fuel feed rate was high, corresponding to about four times excess octane and four times excess hexane to theoretically support the cell current. When the amount of hexane was less than needed for the total cell current, the octane provided the bulk of the current. On a fuel feed of 20% by volume of hexane, the octane provided the bulk of the current when there was 100% excess hexane over that needed to support the entire cell current.

One would believe that the rate of reaction of each species (and therefore the current supplied by the species) would be dependent on the concentration of the species in the anode chamber. Fig. 161 shows that, within the limits of experimental error, the hexane current is proportional to the hexane concentration and to the square root of the total cell current.

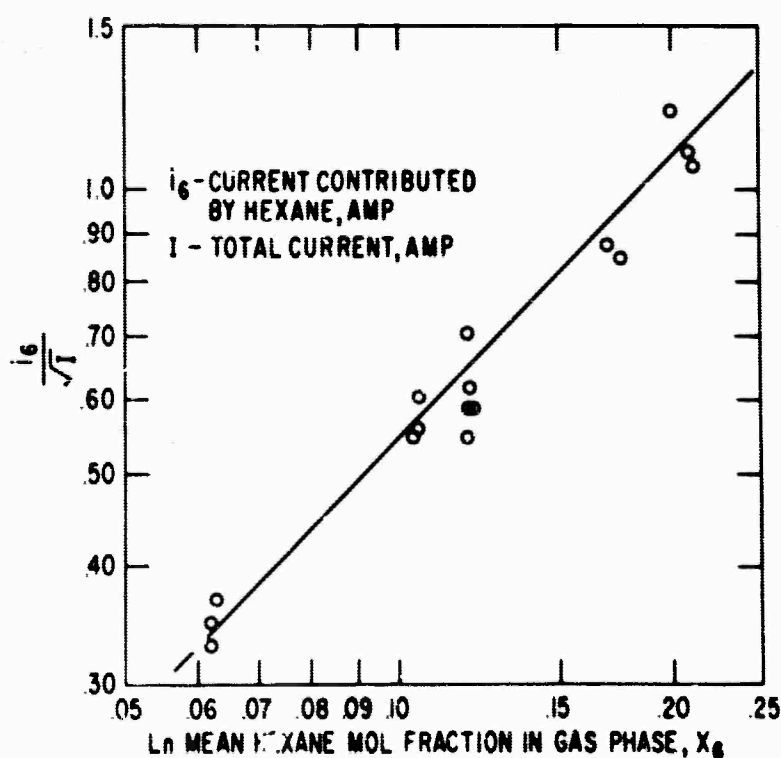


Fig. 161 Dependence of Hexane Current in Hexane/Octane Fuel Mixtures

The relationship is empirical, and the parameter containing the square root of the total current was needed to bring the data at different cell currents into agreement. The equation predicting hexane current is:

$$\frac{i_a}{\sqrt{I}} = (5.4 \pm 0.4) X_6$$

where the current is measured in amperes and X_6 is the log mean mol fraction of hexane in the anode, accounting for water partial pressure in equilibrium with the electrolyte.

The analogous relationship for the octane in the mixture is not true; there presently seems to be no relationship between the current which the octane supplies, and the concentration of octane in the anode chamber. No explanation is available for this behavior at the present time. The octane current can, as yet, only be calculated from the difference between the total cell current and the predicted hexane current.

3. Non-Vaporizing Liquid Fuels

A very desirable form of liquid electrolyte - direct hydrocarbon cell would use a stagnant non-vaporizing fuel which rejects carbon dioxide to the electrolyte. The electrolyte would be circulating to maintain heat and mass transfer equilibria and would reject the carbon dioxide to external process equipment with a minimum of fuel loss. Work is progressing to define the characteristics of such fuels and economical ways of rejecting carbon dioxide. Earlier work with decane, in the life test area, pointed out the electrode wetting problems of these fuels and led the way to changes in electrode structure to overcome the problem.

A new test vehicle has been designed and built to study the operation of fuels that are liquid at the cell operating temperature. This test vehicle will provide greater flexibility in experimentation and will extend the investigations over a larger range of process variables. The design of the anode chamber is shown in Fig. 162. It incorporates a movable rectangular quartz window. The window is sealed by a peripheral o-ring and can be positioned at heights varying from .040 to 0.50 inch above the anode. Liquid fuel enters and leaves through internal manifolds and under built-in dams which keep gas out of the liquid streams. Gases are ported through a separate internal manifold at controlled pressures. The anode chamber fits the standard electrolyte spacers and cathode chambers, so that standard electrodes can be used. The oven which provides cell temperature has a glass top for visibility. Fig. 163 shows a photograph of the test vehicle with the oven removed.

Schematics of the fuel and electrolyte streams are shown in Fig. 164. Fuel feed is by an infusion pump pressurized with nitrogen in accumulator type tanks. Electrolyte is pumped by a teflon diaphragm pump with pressurized accumulators at the pump inlet and outlet. The cathode is supplied with dead-headed oxygen. The system is designed for pressures up to 5 psig, and vents are provided to quickly reduce the pressure of any stream to study the

performance and carbon dioxide rejection effects. The electrodes are supported with Teflon ribs to reduce stresses.

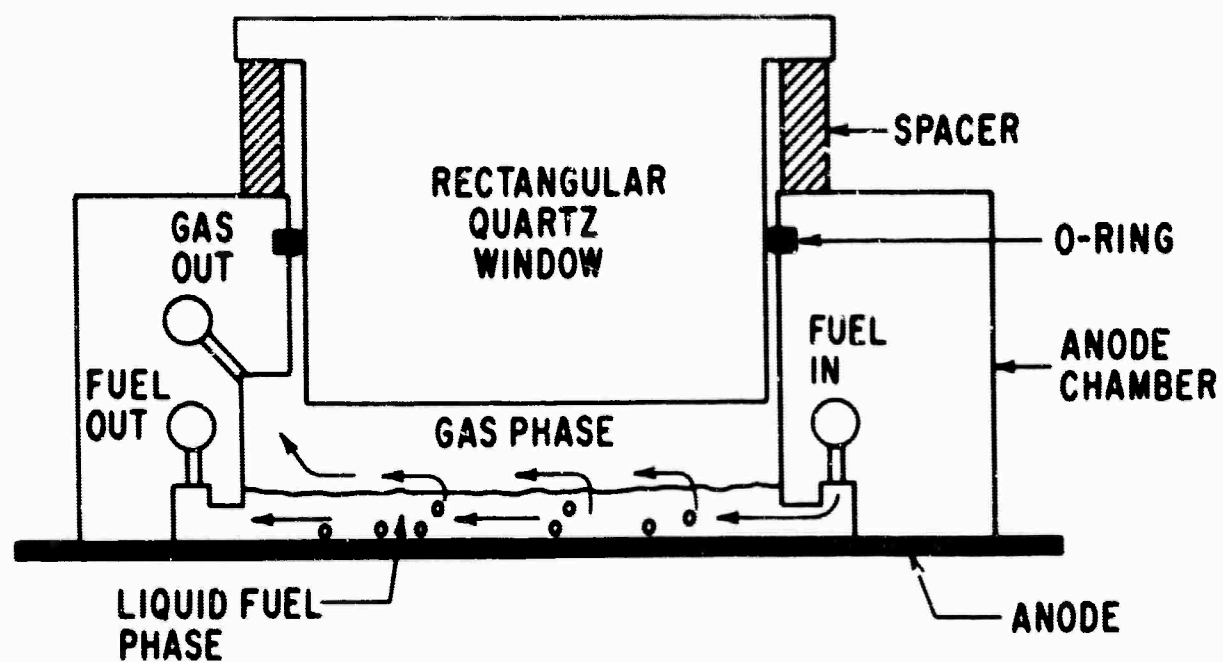


Fig. 162 "See-Through" Anode Chamber

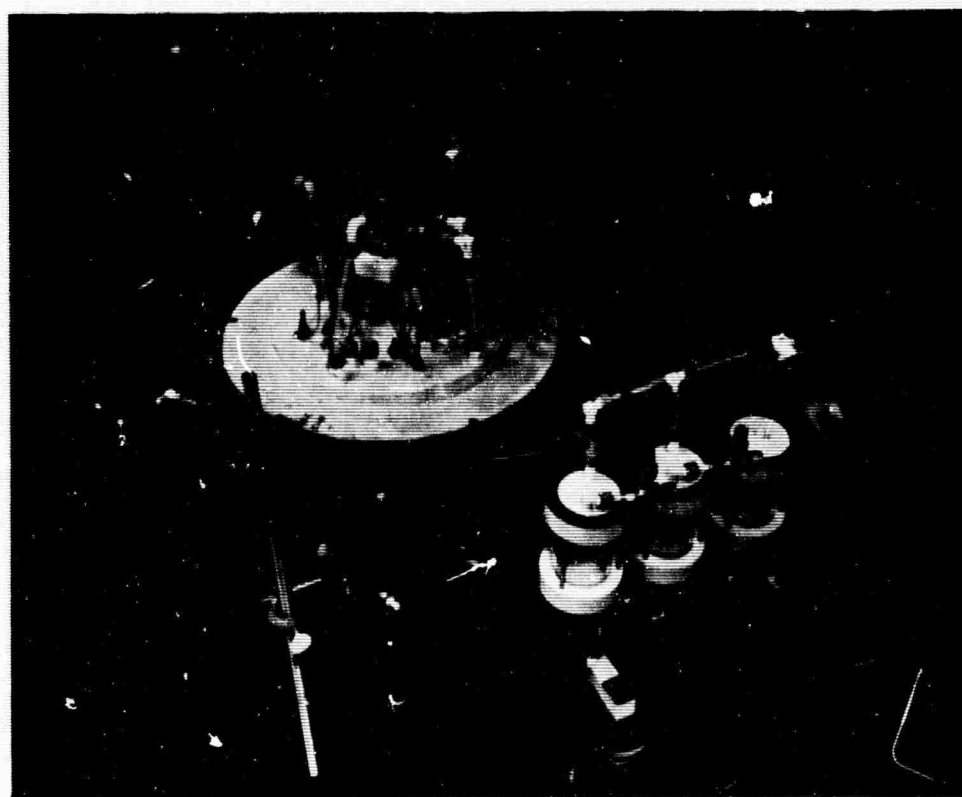


Fig. 163 Liquid Hydrocarbon Fuel Anode Test Apparatus

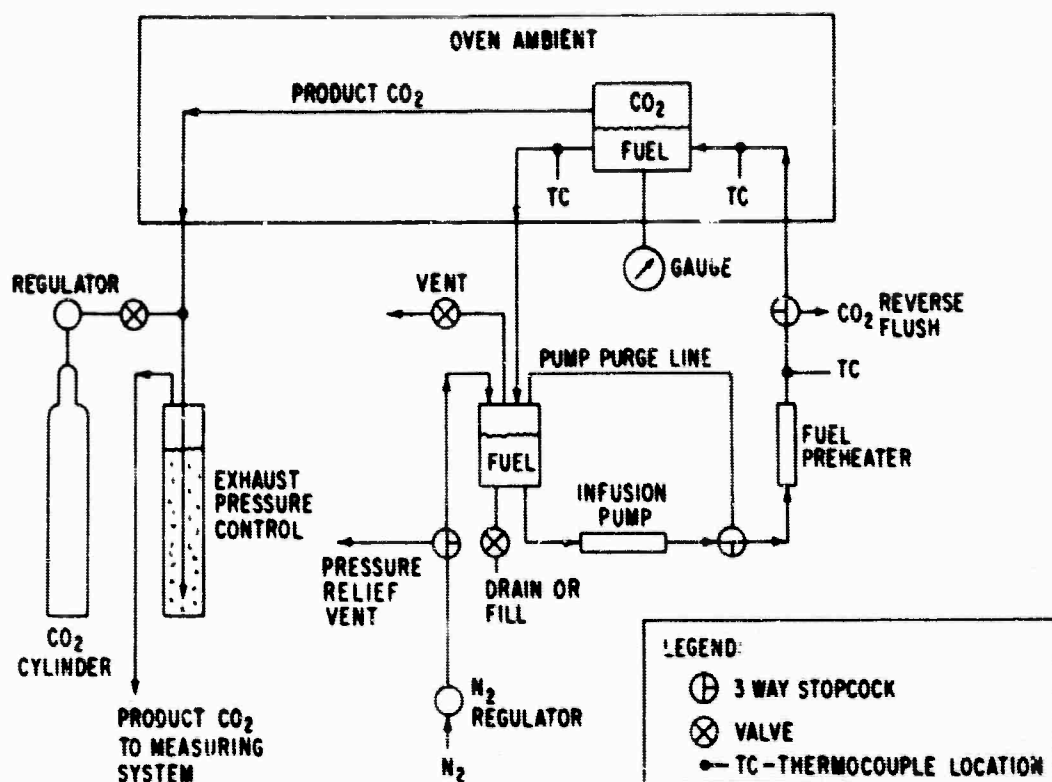


Fig. 164a Non-Vaporizing Fuel System.

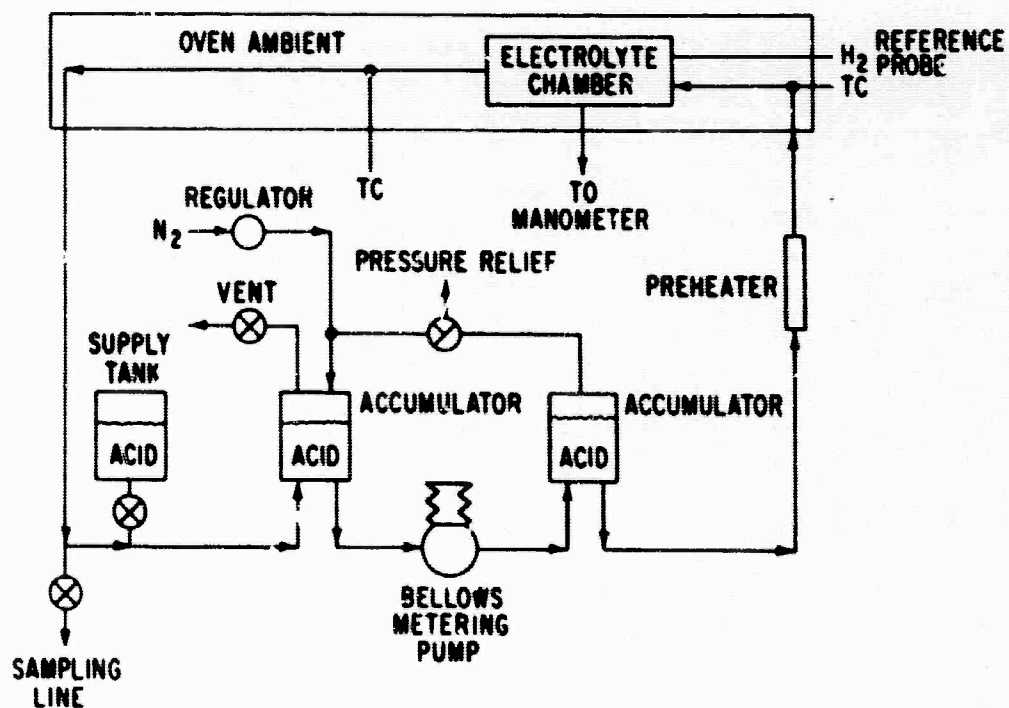


Fig. 164b Pressurized Electrolyte System.

4.6.1.3 Conclusions

1) Propane and n-octane have been shown to completely oxidize electrochemically in the phosphoric acid cell.

2) A preliminary correlation for the cell current contributions of n-hexane/n-octane fuel mixtures show that the hexane current is proportional to the hexane concentration in the anode. No correlation could be obtained to predict the octane current independently.

4.6.2 Transport Rates (R. E. Kegan)

The work reported in this section is concerned with the mass transport rates and overvoltage of an operating n-Aliphatic/air fuel cell and is a continuation of that reported in (1) and (2). The objectives were to provide data and analysis of fuel cell performance as affected by heat and mass transfer. Of primary concern is the anode (IR free) potential and its relation to operating conditions such as the type of fuel, acid concentration, temperature, fuel mixtures, etc.

The basis of evaluating anode performance (IR free overvoltage) for normal aliphatic fuels is the following equation, suggested in (3):

$$\eta = d + a \log_{10} I + c \log_{10} \frac{I_L}{I_L - I} \quad (64)$$

where: η = overvoltage, volts

I = current density, amps/ft²

I_L = limiting current density, amps/ft² when $d\eta/dI \rightarrow \infty$

d, a, c = parametric coefficients, volts

At low current densities, the first two terms to the right of equation (64) are important and are usually called the Taffel region. The last term on the right becomes important at high current densities and, because of finite transport rates, $d\eta/dI$ becomes infinite at some $I = I_L$. The true value of equation (64) comes from the excellent correlation it gives with the experimental data, as will be shown in Section 4.6.2.2.

The limiting current phenomenon was studied for propane in previous work (1), and the results indicated that limiting current was a function of the square root of the mol fraction of propane in the fuel gas stream. Water and CO₂ were used as diluents. The results also indicated that the limiting current was significantly affected by the presence of water vapor. Using water vapor, rather than CO₂, had a pronounced effect of increasing the limiting currents. Further, the data indicated that the fuel stream velocity had an effect on limiting current. In fact, I_L (limiting current) tends to correlate to the one-third power of this velocity. The variation of I_L with fuel partial pressure suggested (3) that the gas phase transport resistance was important. On the other hand, the effect of the water vapor suggested that the electrolyte film transport resistance was important. The latter was considered (1) and a preliminary correlation was attempted by introducing the effect of water vapor on electrolyte transport properties.

1. Technical Report #4, July-December 1963, Contract No. DA 44-009-ENG-4909, USAERDL., Ft. Belvoir, Virginia, p. 5-192.
2. Technical Report #5, 1 January 1964 - 30 June 1964, Contract No. DA 44-009-ENG-4909 and DA 44-009-AMC-479 (T), USAERDL, Ft. Belvoir, Virginia, p. 4-124.
3. H. A. Liebhafsky, et al., "Current Density in the Fuel Cell and Electrode Structure", Advances in Chemistry, American Chemical Society, to be published.

The experimental work which followed (2) for hexane and octane seemed to point out that the gas phase resistance was important. The data collected were correlated with gas phase parameters and the square root of the fuel partial pressure. The latter relation was difficult to reconcile in trying to justify that gas phase resistance is controlling, since a linear relation is expected. Consultation with Dr. E.N. Lightfoot (4) revealed that one might expect limiting currents one to two orders of magnitude higher, if the gas phase was controlling. His analysis was based upon mass transfer coefficients estimated from the analogous heat transfer coefficient for laminar flow. Subsequent analysis indicated that velocity dependence was probably no more than an integrated effect of the fuel concentration along its channel. Hence, the correlation between gas phase parameters (presented in (2)) is now considered to be fortuitous.

During this report, a total of eleven cells was used in obtaining approximately 140 IR-free, anode polarization curves for propane, hexane, and octane, and for binary mixtures of the three. Variations in fuel concentration, acid concentration, fuel water vapor concentration and temperature were made to cover the range of fuel cell operating conditions. An exception to this was the fuel flow which was purposely kept at high stoichiometric rate to avoid the complicating integrated effect along the fuel channel of fuel concentration. Generally, twenty or more polarization points were obtained for each set of conditions, from current densities less than 1 amp/ft² to limiting current. The points were applied to equation (64) for the determination of the d, a, and c overvoltage coefficients by a multiple regression analysis. This was accomplished by a digital program (5) with the results of the computation and the experimental conditions given in Table III of Appendix 5.5.

4.6.2.1 Experimental

The test fuel cells utilized in the investigations are 2.68" x 2.68" Alford-Niedrach electrodes mounted in a Teflon structure (electrode data are given in Table V of Appendix 5.5). The fuel and air spaces and circulating phosphoric acid electrolyte space are each 1/8" thick. The complete fuel cell and a hydrogen reference cell (through which the same electrolyte is circulated) are contained in a thermally regulated nitrogen atmosphere. Inlet and outlet fuel, air, and electrolyte temperatures are monitored to ensure isothermal conditions. The IR free anode potentials referenced to the hydrogen electrode are obtained by a Kordes-Marko bridge. All other experimental details such as the measurement of fuel flow rates, electrolyte flow, acid concentrations, etc. were reported previously (1, 2). An important note is that the anode was held at 1.0 volt for 1 minute (current varied) prior to each set of polarization points.

-
4. Private consultation R.E. Kegan, Direct Energy Conversion Operation (DECO), General Electric Co., and Dr. E.N. Lightfoot, University of Wisconsin, at DECO on September 2, 1964.
 5. "Least Square Multiple Regression Program - L0048B. Internal, for IBM 7044 Digital Computer." General Electric Company Report R58AGT348.

4.6.2.2 Overvoltage Coefficients at Constant Temperature

The detailed test data is given in Appendix 5.5.2. Its significance is discussed in the following paragraphs.

Cells 2-189 to 2-195 (6 cells) were operated at 300°F. Polarization curves were obtained for propane, hexane, and octane, and for binary mixtures of these for 100% fuel to several percent (diluted with water vapor). Phosphoric acid concentrations varied from 87-98%. Values of d , a and c for the iR free overvoltage, equation (64), were obtained by multiple linear regression at a significance level less than 0.05. In general, 80% or greater of the overvoltage variance can be attributed to the terms $(a \log_{10} I)$ and $(c \log_{10} I_L / I_L - I)$. These results indicate that equation (64) provides a very good relationship for correlating any particular set of polarization data.

The individual coefficients d , a and c were ranked, tabulated from highest to lowest values, with all other operating data given in Table III, Appendix 5.5. It appeared that the coefficients were practically unrelated to acid flow rate, were very weakly related to fuel concentration, and did not seem to be too dependent upon what cell was used. They appeared to vary with acid concentration, mol fraction of water in the fuel and, perhaps, most strongly with the type of fuel. Various graphical plots were made to ascertain how the coefficients varied with these three factors. The best correlation, although not significant in all cases, seemed to be the following:

$$\bar{Y} = \alpha \bar{X}^\beta \quad (65)$$

- where: \bar{Y} = values of d , a or c ; volts
 \bar{X} = $(1 - X_{H_2O})/X_A$
 X_{H_2O} = mol fraction of water in fuel stream
 X_A = water vapor pressure of the acid in mm Hg/760 mm Hg
 α = coefficient determined from linear regression analysis, volts
 β = exponent determined from linear regression analysis

Plots of the coefficients for the various fuels versus the variable \bar{X} are given on Figs. 1a through 1r of Appendix 5.5. The regression lines, evaluated by the digital program, are also given. The following tabulation gives the coefficient and exponents of equation (65) and the correlation coefficient of the regression analysis. Table XLI shows that correlation was obtained for practically all "d" coefficients except for fuel 3 and 8, that very little correlation was obtained for "a", and "c" correlated except for fuel 3 and 6.

The coefficient α and exponent β versus the number of carbon atoms in the hydrocarbon are plotted on Fig. 165. Averages are taken for the mixtures, i.e., 3 and 8 are represented by 5.5, 3 and 6 by 4.5, and 6 and 8 by 7. Only those values for which a significant correlation coefficient was obtained are plotted. In the case of the coefficient "a", only the α value is plotted

TABLE XLI
Coefficient and Exponents of Equation (65) and the Correlation Coefficient
of the Regression Analysis

Fuel	Overtage Coefficient	Coefficient α	Exponent β	Correlation Coefficient-R	R for 0.05 Significance Level
3-Propane	d	.210	.165	.773	$\pm .433$
	a	.110	.0662	.410	$\pm .433$
	c	.0865	-.231	-.900	$\pm .433$
6-Hexane	d	.263	.116	.947	$\pm .707$
	a	.079	.147	.912	$\pm .707$
	c	.120	-.159	-.902	$\pm .707$
8-Octane	d	.242	.0845	.731	$\pm .381$
	a	.095	.0308	.118	$\pm .381$
	c	.131	-.0937	-.588	$\pm .381$
6 and 8	d	.264	.0956	.922	$\pm .707$
	a	.074	.110	.622	$\pm .707$
	c	.129	-.102	-.845	$\pm .707$
3 and 8	d	.297	-.0224	-.12	$\pm .632$
	a	.073	.117	.490	$\pm .632$
	c	.117	-.213	-.793	$\pm .632$
3 and 6	d	.190	.339	.782	$\pm .878$
	a	.099	-.0305	-.108	$\pm .878$
	c	.064	-.260	-.154	$\pm .878$

as it approximates the average value for all the data. Comment on this figure is deferred until further analysis has been made to ascertain its significance. The values obtained for all the coefficients d, a and c are comparable in magnitude to those reported in reference (3).

4.6.2.3 Limiting Current at Constant Temperature

The approach to analyzing limiting current, I_L , in terms of operating conditions for the data in Table I of Appendix 5.5 has been essentially empirical. In view of the difficulties encountered in past interpretations, (1, 2) the empirical approach seemed advisable for now. The values of I_L for all IR free anode polarization curves for cells 2-189 through 2-195 at 300°F were ranked with their associated data. The values for binary mixtures were omitted. The ranking indicated that the particular electrode, the fuel, and the fuel partial pressure or water vapor partial pressure (one being the value one minus the other) were important.

A multiple regression was made for each cell for a product relation of the electrical equivalents, n, for the fuel and the fuel partial pressure, X_F . Surprisingly, the significant

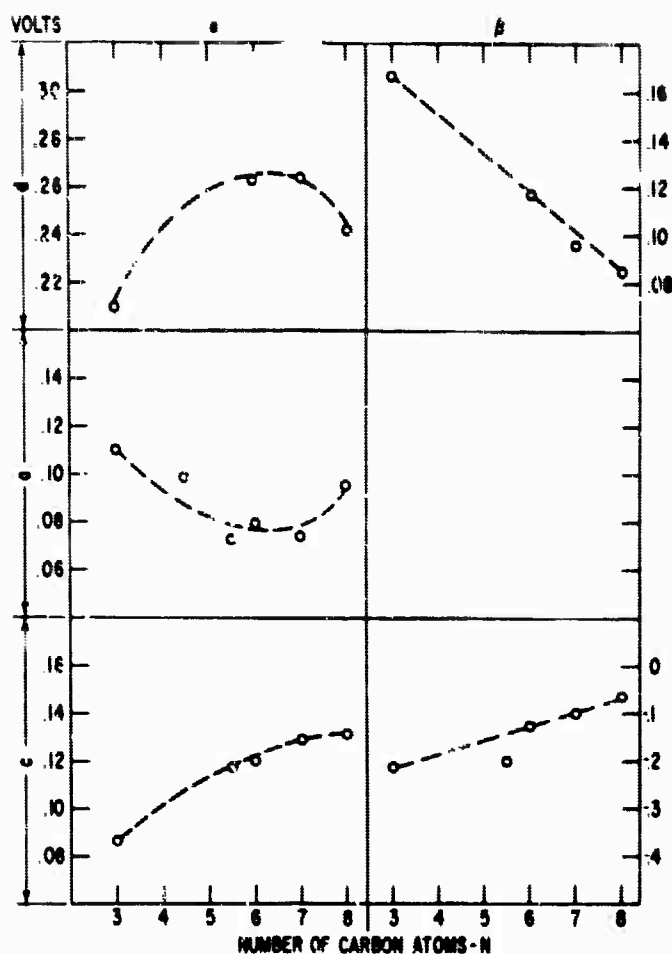


Fig. 165 Correlation of Regression Coefficients and Exponents of Equation (65)
With a Number of Carbon Atoms in the Fuel

correlation was with the fuel electrical equivalents, i.e., 20 equivalents for one mol of propane, 38 for hexane and 50 for octane; and it indicated an inverse relation. The fuel partial pressure did not give a significant correlation and the regression analysis produced a small exponent of the order of 0.1. In all cases it substantially deviated from 0.5 found for propane as previously reported (1). The regression relation for n produced a negative exponent which varied from -0.5 to -0.9.

At first thought, one might have expected a linear relation with n . Perhaps this result is a consequence of the dependence of limiting current on the magnitude of the solubility and diffusion properties. Furthermore, the deviation of the square root relation of I_L and X_F indicates that water vapor in the fuel introduces an important effect on the overall transport of the fuel in the electrolyte. The proportionality $I_L \sim X_F^{1/2}$ still appears to be justifiable as it was obtained with propane in an operating fuel cell(1), and, more recently, it has been found in the thin film mass transport study of Section 4.1.4. Perhaps, as the fuel partial pressure decreases by dilution with water vapor, the increased water vapor pressure produces condensation at the electrolyte film which enhances the transport of the fuel. Further conclusions will be deferred until the fundamental phenomenon is better understood.

In consideration of what was discussed above, the following "working" correlation was made:

$$\bar{Y} = \frac{I_L^n}{X_F^{1/2}} = \alpha' \bar{X}^b = \alpha' \left[\frac{(1 - X_{H_2O})}{X_A} \right]^b \quad (66)$$

- where: I_L = limiting current, amp/ft²
 n = electrical equivalents of hydrocarbon per mol
 X_F = mol fraction of fuel
 X_{H_2O} = mol fraction of water ($X_F = 1 - X_{H_2O}$ for no CO₂)
 X_A = water vapor pressure of acid in mm Hg/760 mm Hg
 α' = coefficient determined from linear regression analysis
 b = exponent determined from linear regression analysis

A correlation of this type is at first sight objectionable as \bar{Y} and \bar{X} have a common term, namely X_F . This is justified on the basis of:

(1) convenience, as \bar{X} is used in determining the overvoltage coefficients;

(2) anticipatory, for similar treatment of cases of fuel mixtures and water and for fuel, water and carbon dioxide mixtures. The data are plotted on Figs. 2a through 2e of Appendix 5.5. The figure for cell 2-192 is omitted as its electrodes were significantly different. Briefly, it has a similar correlation and its limiting currents were substantially less than the others. The coefficients and exponents for equation (66) are given in the following tabulation.

Cell	$\alpha' \times 10^3$	b	R
2-189	6.65	-.470	-.903
2-190	5.78	-.412	-.931
2-191	7.70	-.516	-.899
2-194	5.40	-.453	-.914
2-195	4.37	-.437	-.946
All Cells	5.40	-.420	-.846

The correlation coefficient, R, is high, as would be expected. The deviation of the data points from the regression line would probably be minimized by introducing an exponent to the factor n and by using a combination of n and the number of carbon atoms, N . The exponent, b , is of the order of -.5 which bears out the observation stated earlier that the original ranking correlation indicated I_L to be almost independent of X_F . At present, no assessment has been made to connect limiting current behavior and electrode properties (see Table V, Appendix 5.5).

The evaluation of limiting current performance with fuel binary mixtures has to be deferred until more experimental data has been obtained from the "Reactivities and Fuel Utilization" effort in this program. The data reported in Table III of Appendix 5.5 does not contain a mass balance as none was made experimentally.

4.6.2.4 Effect of Temperature

A. Overvoltage Coefficients

The investigation of the effect of temperature on overvoltage was done with cells 2-196 through 2-200. Again, the fuels were propane, hexane, octane and binary mixtures of same. The set of data for each polarization curve was fitted to equation (64) and the regression analyses were also conducted with the digital program. The data and results are given in Tables III and IV, respectively, of Appendix 5.5.

From electrochemical considerations, the coefficients d , a and c are partially comprised of the factor RT , the gas constant and absolute temperature. Cross-plotting the coefficient with T and \bar{X} indicated that the coefficients were inversely proportional to the temperature. These results have been very recently obtained and a statistical analysis has not been completed. Therefore, the product of the coefficients and absolute temperature have been plotted versus \bar{X} (Figs. 3a to 3o of the appendix) and the regression lines for the various fuels and mixtures at 300° F have been included from their respective Figs. 1a to 1r. In many cases, the regression line did not fall within the new points at different temperatures; however, there was a trend in the similarity of slopes. The deviation may be due, in part, to the fact that different electrodes are being compared.

B. Limiting Current

The results for the effect of temperature on limiting current are rather incomplete. Again, only single fuels have been considered. The results are given in Tables III and IV of Appendix 5.5. The data for octane from cell 2-196 are shown in Fig. 4a, for hexane from cells 2-197, 198 and 200 are shown in Fig. 4b, and for propane from cell 2-200 are shown in Fig. 4c. With the limited data available it is difficult to surmise what the effect of temperature is. The data points for \bar{Y} versus \bar{X} seem to follow a line with a -0.5 slope, again, showing very little dependence upon the mol fraction of fuel, X_F , with water as a diluent.

4.6.2.5 Conclusions

The electrochemical semi-empirical overvoltage equation, (64) provides a correlation of IR-free, anode, polarization data of high statistical significance.

The empirically determined coefficients of the overvoltage equation gave values comparable to those of other investigators for propane, hexane, and octane with the Alford-Niedrach electrodes in phosphoric acid. In addition, these coefficients appear to be dependent upon the water vapor in the fuel, the acid concentration and the temperature as well as the fuel. The temperature was inversely related to the coefficients, and there seemed to be a small variation for different electrodes.

The limiting current behavior remains unresolved. High water vapor concentrations in the fuel improve the limiting current over comparable fuel concentrations with carbon dioxide. The empirical relation $I_L \sim X_F^{1/2}$ is not obeyed under these conditions. Effects of temperature are inconclusive. Limiting currents for binary mixtures were not correlated, as relative fuel consumption rates were not available till near the end of this reporting period.

5.0 APPENDIX

5.1 ELECTROCHEMICAL OXIDATION OF HYDROCARBONS (W. T. Grubb)

Apparatus Used In Macro Anode Studies

The experimental system used in the macro anode work is schematically depicted in Figs. 1 and 2. The electrical system consists of a modified Anatrol Model 4100 controller operating either as a potentiostat or a galvanostat. Fig. 1 shows the potentiostatic connection in which the potential between the working electrode A and the hydrogen reference electrode R is controlled. For galvanostatic operation, the potential across a standard resistor, "Res.", was controlled in series with the working electrode of the cell. The potential between the working electrode and the reference electrode was measured by a Kiethley Model 200B electrometer which also acted as a power amplifier and fed the input voltage signal to the Y axis input of a Moseley Autograph X-Y recorder. This unit operated as voltage-time recorder by use of a time scale input on the X axis. Voltage-time plots were directly obtained on a standard graph paper.

Current through the cell was accurately measured by a precision ammeter (Sensitive Instrument Co. Polyranger) and recorded against time from the 0-100 mv current output jacks of the Anatrol using a Varian Model G-10 recorder.

The cell and gas flow system are schematically depicted in Fig. 2. The working electrode A consisted of a fuel cell electrode gasketed in a Teflon housing supplied with gas inlet and outlet lines, electrical leads, and a tube forming a Luggin capillary and communicating with the hydrogen reference electrode contained in a separate chamber. The entire working electrode, Luggin capillary, and reference electrode were immersed in electrolyte. Unwanted diffusion of hydrogen to the working electrode was prevented by the use of porous Teflon diffusion barriers. Both the counter electrode and the reference electrode were platinized platinum screens over which electrolytic grade hydrogen was continuously bubbled.

The gas flow system provided for the maintaining of helium sweep gas or fuel in the anode chamber, either flowing at a known flow rate or static. The double syringe system consisted of two syringes moved in opposition by a double rack and pinion gear so that the gas in the anode chamber could be changed without changing the volume of the system. In this way, it was possible to measure volume uptake of a fuel cell by the working electrode using the manometer system shown in Fig. 2. It was also possible to flood the anode chamber with degassed water using this system. Helium sweep gas was purified over copper turnings in a tube furnace maintained at 700°C.

The double syringe system could also be used to sample the gas composition of the anode chamber after a static run. Helium was swept from the left-hand syringe through the cell

to the right-hand syringe and the gas sample stirred with the magnetic stirring bar. It could then be forced into gas chromatograph system for analysis. The gas chromatograph system was conventional.

The working electrode was a porous Teflon-bonded, platinum black electrode of the Niedrach-Alford structure. Some of its characteristics were obtained by adsorbing hydrogen, filling the anode chamber with de-oxygenated and oxidizing off the hydrogen galvanostatically. A typical electrode had a capacity of 17 coulombs of hydrogen and a double layer capacity of 5.0 ± 0.2 farads. This was equal to about 50 microfarads per square cm of real platinum area.

For operation at elevated temperatures, the system was maintained in a silicone oil thermostat controlling to ± 0.1 degree.

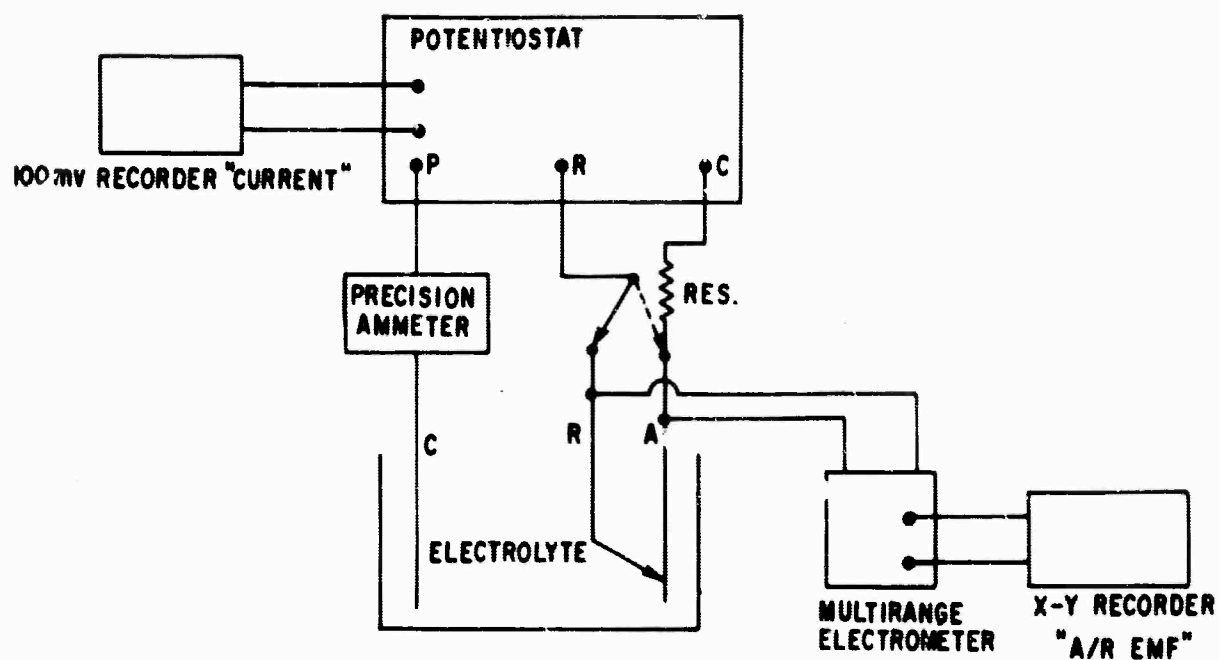


Fig. 1 Power Conductance Cell

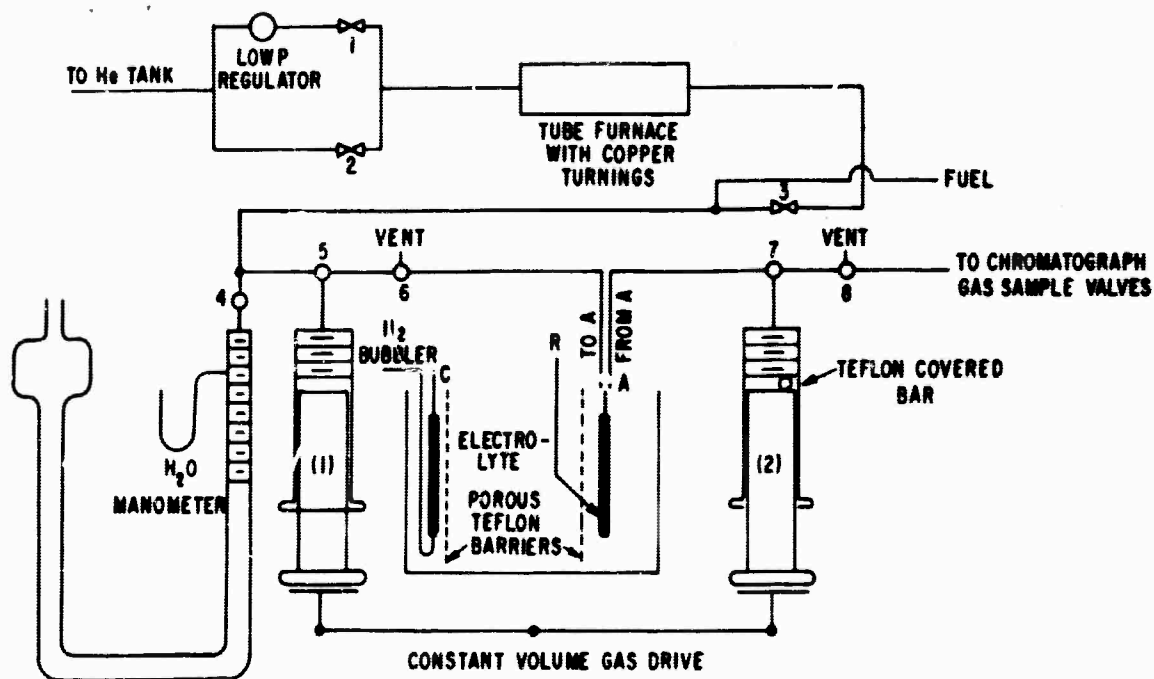


Fig. 2 Resistivities of Platinum Activated Boron Carbide Powders

5.2 ELECTROCATALYST RESEARCH

5.2.1 Platinum Activated Boron Carbides

5.2.1.1 Cell for Measuring Conductivity of Pressed Powder Samples (W.T. Grubb)

For making satisfactory fuel cell electrodes, a catalyst or catalyst support should have a resistivity (ρ) low enough to avoid excessive ohmic losses in the electrode. When a supporting screen is used, powders possessing ρ below about 500 ohm-cm would be satisfactory. A given material may show different values, for instance, boron carbides from different sources have shown values of resistivity ranging from 0.2 to 8,000 ohm-cm, and platinum activation and other treatments have some influence on this property. It was therefore desirable to have a method for routine measurement of the resistivities of powders. High accuracy was not required.

A cell satisfactorily used for this purpose is shown in Figure 1. The cell consists of a piece of precision bore glass tubing of 0.2519" I.D. and two brass electrodes machined to a close sliding fit in this tube. The cell holder of Fig. 1 is made also of brass and is provided with a hexagonal fitting such that a reproducible force can be imposed on the powder sample between the two brass electrodes by tightening the hex screw to a constant torque setting, typically 8 lb. inches, with a torque wrench. The screw pitch on the cell holder being 40 threads per inch, a pressure of up to 4000 psi is exerted on the powder.

The resistance of the sample is measured with a 1000 cycle or D.C. bridge and the cell constant determined by subtracting micrometer readings of the cell length with and without the sample, and combining this value with the area determined from the I.D. of the precision bore tube.

The resistivities of platinum activated boron carbide powders measured with this device varied with the amount of platinum present and with the method of activation, i.e., the type of platinum salt used. In Figure 2 are shown the resistivities of various catalyst preparations as a function of platinum content. Catalysts #14, 21, 19, and 20 were used in electrodes #57, 86, 87, and 89 (cf. Figs. 82-89, Section 4.2.2). Some increase in resistivity of the boron carbide powder with activation was noted. When chloride salts were used as in catalysts #4, 26, and 27, little increase was noted. Catalyst #4 was anomalous because of the use of a wet hydrogen treatment at 400°C in an attempt to remove residual chloride. All catalysts of Fig. 2 have resistivities well within the acceptable range for fuel cell electrodes.

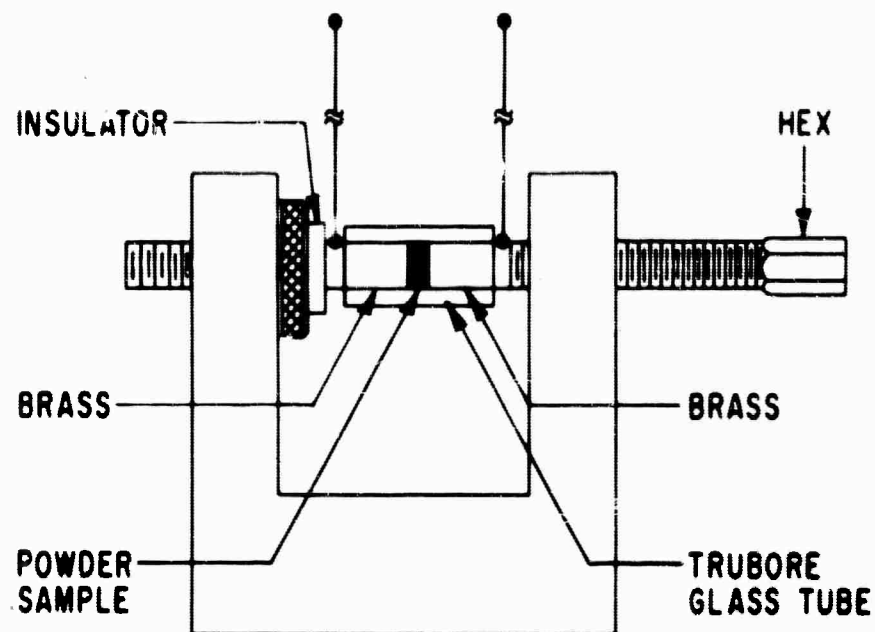


Fig. 1 Macro Anode Electrical System

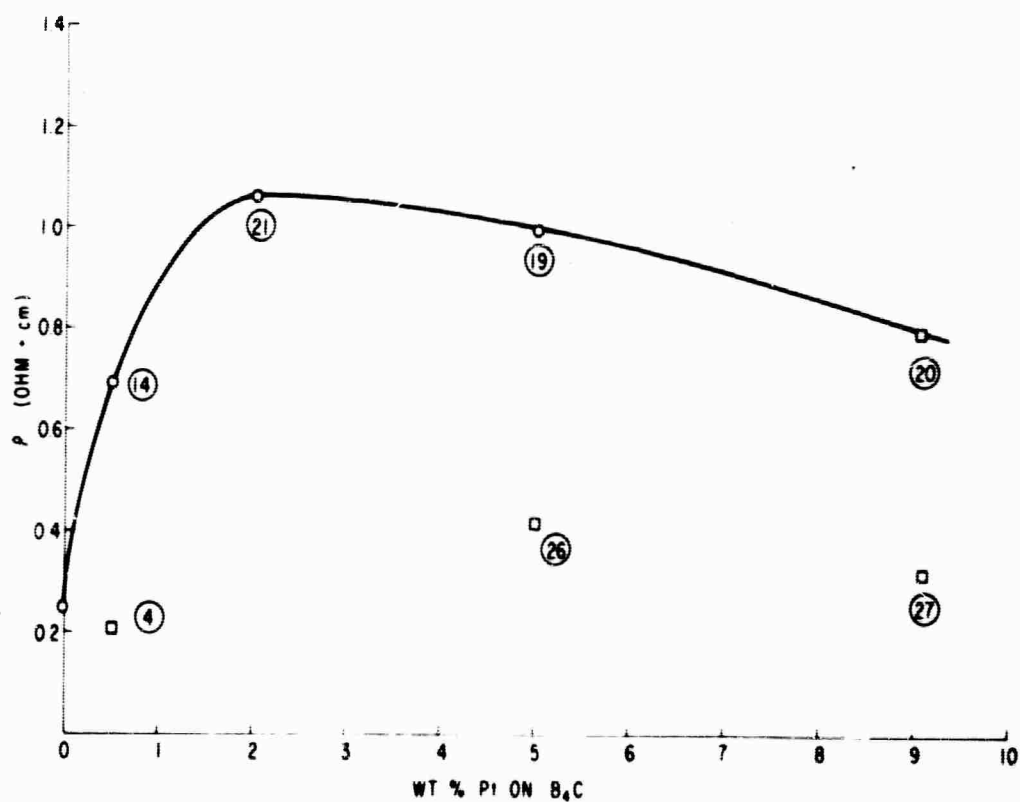


Fig. 2 Macro Anode Gas Flow System

5.2.1.2 Materials

Three different boron carbides were at least partially evaluated during this period. They were the following:

1. A high purity stoichiometric B_4C from Semi-Elements, Inc. This material was of relatively high resistivity, approximately 8,000 ohm. cm. Its particle size was larger than desirable for fuel cell electrode fabrication and no further investigation was carried out.
2. Norbide 1000^oF grit size boron carbide: This material had a specific surface area of about 14 m²/gram. Electrode fabrication was satisfactory, but the material was contaminated with a considerable amount of iron oxide impurity which had a detrimental effect on fuel cell performance. Pretreatment of the material with nitric acid to remove the iron produced a satisfactory material for the electrodes but was laborious.
3. Norbide 800 grit size boron carbide: This material had a specific surface area of about 12 m²/gram and could be made into satisfactory fuel cell electrodes without any pretreatment. Some pretreatments were tried, none of which produced a discernible improvement in fuel cell electrode performance (nitric acid and potassium hydroxide leaching at 110-140^oC for 10-24 hours in the presence and absence of oxygen).

As a result of such exploratory experiments, it was elected to employ 800 grit size Norbide without any pretreatment and all electrodes including Electrode No. 57 and subsequent electrodes employed this boron carbide as the starting material.

Norbide boron carbide was obtained from the Norton Abrasives Co., Worcester, Mass. It is described by the manufacturer as a technical grade of boron carbide with the following typical analysis:

B	70-72%
C	22-26%
B+C	94-97%
B ₂ O ₃	1-3%

Stoichiometric B_4C contains 78.3% boron by weight. The Norbide powder contains some free carbon, and this may contribute to the low resistivity of the materials which was 0.2 ohm-cm for the compacted powder as measured by the method described in this appendix.

5.2.1.3 Platinum Activation Procedures

Only a limited exploration of the variables in this area has been accomplished to date. General procedure for all activated boron carbide catalysts was the same. The powder was mixed with a solution of a platinum salt. The pasty mixture was dried thoroughly, ground in a boron carbide mortar to break up large lumps, and then reduced in a platinum boat in flowing hydrogen in a tube furnace for 20 hours at 400^oC. In a single case, the high temperature reduction step was eliminated and the resultant catalyst had a lower activity in fuel cell electrodes.

Two platinum salt solutions were tried, chloroplatinic acid in water, and diammino-dinitrito-platinum in aqueous nitric acid. The latter consistently gave materials of higher activity in fuel cell electrodes.

5.2.1.4 Electrode Fabrication

The delamination of Teflon-bonded electrodes prepared by pressing two spreads prepared from a paste of boron carbide with diluted, aqueous Teflon T-30 suspension on opposite sides of a supporting screen prevented their use at elevated temperatures due to blistering and the onset of massive electrolyte leakage when such blisters broke. This problem was eliminated by employing a version of the old pasted screen method¹ of preparing electrodes. A mixture of boron carbide powder (usually activated with platinum) with aqueous Teflon T-30 solution was pasted directly onto the supporting screen, dried and then press cured between aluminum foils at 350°C at 8,000 pounds total press force (on an area of about 3 square inches) for 2 minutes. Electrodes prepared in this way showed no blistering and better performance in fuel cells.

1. Grubb, W. T. and Michalske, C. J. J. Electrochem. Soc. 111 477 (1964).

5.2.2 Platinum Activated Tantalum

5.2.2.1 Ball-Milling Procedures

Various methods for the comminution of tantalum powders were discussed in the previous report (1). Because the ball milling method proved most promising, further extensions of this method were investigated. Tantalum powder from the National Research Corp. having an area of $0.37 \text{ m}^2/\text{g}$ was used as the starting material. It was ball milled using a solution of $\text{Al}(\text{NO}_3)_3 \cdot 9\text{H}_2\text{O}$ in 100% ethanol (70g salt/300 ml ethanol) as a grinding aid. The aluminum nitrate was used because it had previously been shown to be a very effective aid for milling nickel powders from 2.5μ down to 0.1μ (2). Prior to milling the tantalum powder was hydrided to embrittle it. (1)

The powder was milled in a Carboloy ball mill, 3" long and having an internal diameter of 1-7/8". A mixture of 1/8", 1/4" and 3/8" Carboloy balls was used. The mill was filled with its charge of powder under an argon atmosphere and then topped with the solution of aluminum nitrate. On the basis of previous experience a milling time of 144 hours was used.

5.2.2.2 Dialysis Procedure for Recovering Powder

Upon completion of the milling, the aluminum nitrate was removed from the high area powder by dialysis. The dialyzer tubing employed was 1-1/8" diameter seamless cellulose supplied by Fisher Scientific Co. A three-foot length was suspended within a section of Pyrex pipe having an internal diameter of 3". The volume of the cellulose tube which contained the tantalum suspension was about 500 cc. The volume of wash water contained in the Pyrex pipe was about 3 liters. Both the suspension and the wash water were stirred by a flow of nitrogen bubbling through the liquids. Dialysis was continued for several days during which time the wash water was changed every 8 hours. At least 30 changes of the wash water were used. Following this treatment the tantalum powder was dried and sieved.

5.2.2.3 Surface Areas

The ball milling with aluminum nitrate in ethanol as a grinding aid resulted in powders having surface areas of $7-8 \text{ m}^2/\text{g}$ as measured by nitrogen adsorption with a Perkin-Elmer-Shell Sorptometer. Table 1 following shows the relative effectiveness of all the comminution procedures that have been used.

-
1. Technical Summary Report No. 5 "Hydrocarbon-Air Fuel Cells", Jan. 1 - June 30, 1964, Contract Nos. DA-44-009-ENG-4909 and DA-44-009-ENG-479(T), p. 4-113.
 2. Quatinetz, M., et.al., in "Ultrafine Particles", ed. by W.E. Kuhn, H. Lamprey and C. Sheer, John Wiley and Sons, New York, 1963, p. 271 ff.

TABLE I
Surface Areas of Tantalum Powders After Various Treatments

McKay Ta Powder				National Research Corp. Ta Powder							
Mortar Ground		Mortar Ground		Dry Milled*		Wet Milled*		Wet Milled with			
Time (hrs)	Surface Area (m ² /g)	Time (hrs)	Surface Area (m ² /g)	Time (hrs)	Surface Area (m ² /g)	Time (hrs)	Surface Area (m ² /g)	Al(NO ₃) ₃ · 9H ₂ O in Ethanol	Time (hrs)	Surface Area (m ² /g)	
0	0.087	0	0.37	0	.37	0	.37		0	.37	
17	.62	30	.45	17	.31	50	1.11		144	7.04 **	
30	1.23	54	.80	42	.28	144	3.00		144	8.00 **	
72	1.60	123	1.68	96	.31	144	4.55 **				
100	1.23	132	1.53								

* Carboloy ball mill — 1-7/8" d. x 3"; 1/8", 1/4", 3/8" d. balls.

** Hydrated

5.3 ELECTRODE STRUCTURE RESEARCH

5.3.1 Low Cost Substrate Material

5.3.1.1 Preliminary Corrosion Data for Hydrofluoric Acid

The preliminary data for corrosion rates in 48% HF are given in Table I. Of the materials tested, all the noble metals as well as the alloys of palladium-nickel, gold-nickel, and palladium-silver-gold appear excellent for stability in HF electrolyte at 100°C. Molybdenum-tungsten alloy also appears promising. Among the materials tested and found unsatisfactory are nickel, molybdenum, stainless steels, titanium-palladium and tantalum.

5.3.1.2 Corrosion Data for Phosphoric Acid

A summary of the data for "chemical" corrosion of alloys in 88 wt % phosphoric acid (C.P.) at 150°C in either reducing (fuel gas bubbling) or oxidizing (oxygen gas bubbling) environment is provided in Table II. The corrosion rates reported must be regarded as only approximate, particularly in those cases where the weight loss is less than one or two milligrams, since in such cases the relative error in the calculated corrosion rates is likely to be large. The density data required to calculate the corrosion rates, in mils per year, for many experimental alloys were not readily available from the literature. In the cases of specimens with well defined geometric shapes, the density was experimentally determined from the weight and the volume. In the case of highly irregular shaped specimens the density values were calculated on the assumption that the density of each element in the alloy was approximately the same as in the elemental form. The error involved in the corrosion rates due to the error in the density values is negligible. In some cases of the tungsten base alloys, the composition was not readily available from the supplier, hence the rates in mils per year are calculated based on an approximate measured value.

TABLE No. I

"Chemical" Corrosion of Metals and Alloys in 48% Hydrofluoric Acid at Two Temperatures

Specimen	Serial No.	Test No.	Environment		Temp (°C)	Geometric Area, In ²	Initial Wt. (grams)	Final Wt. (grams)	Wt. Loss (grams)	Hours on Test	Density (gms/cm ³)	Corrosion Rate		Remarks
			Gas	No.								Milligrams Ft ² /Day	Mils Per Year	
Pd	1	28	O ₂		100	3.0	0.2906	0.2906	0.000	93	12	Nil	Nil	Prom- ising
Pd	2	8	None		100	3.0	0.2913	0.2906	0.0007	504	12	1.6	0.02	Prom- ising
Pt	3	9	None		100	3.0	0.5773	0.5769	0.0004	504	21.4	0.915	0.007	Prom- ising
Au	4	10	None		100	2.03	1.6550	1.6545	0.0005	505	19.3	1.7	0.014	Prom- ising
Ag	5	27	O ₂		100	3.03	1.2590	1.2580	0.0010	93	10.5	12.3	0.18	Prom- ising
Ag	6	11	None		100	3.03	1.2620	1.2590	0.0030	505	10.5	6.8	0.10	Prom- ising
80% Pd, 20% Ni	7	12	None		23	3.03	1.2893	1.2893	0.0000	17	11.4	Nil	Nil	Prom- ising
80% Pd, 20% Ni	8	17	None		100	3.03	1.3939	1.3939	0.0000	502	11.4	Nil	Nil	Prom- ising
40% Pd, 30% Au, 30% Ag	9	16	None		23	0.76	0.9306	0.9306	0.0000	17	14.7	Nil	Nil	Prom- ising
40% Pd, 30% Au, 30% Ag	10	18	None		100	3.05	3.1618	3.1618	0.0000	525	14.7	Nil	Nil	Prom- ising
82% Au, 18% Ni	11	21	None		23	0.5	0.1158	0.1158	0.0000	19	15.8	Nil	Nil	Prom- ising
82% Au, 18% Ni	12	22	None		100	0.5	0.1158	0.1158	0.0000	481	15.8	Nil	Nil	Prom- ising
70% Mo, 30% W	13	19	None		23	3.41	23.6385	23.6373	0.0012	21	12.94	58	0.70	Prom- ising

TABLE No. I (Cont.)

Specimen	Serial No.	Test No.	Environment	Temp (°C)	Geometric Area, In ²	Initial Wt. (grams)	Final Wt. (grams)	Wt. Loss (grams)	Hours on Test	Density (gms/cm ³)	Corrosion Rate		Remarks
											Milligrams Ft ² /Day	Mils Per Year	
70% Mo, 30% W	14	20	None	100	3.46	26.4149	26.3246	0.0903	70	12.34	129	1.6	Doubt- ful
W	15	15	None	23	1.03	1.5268	1.5240	0.0028	18	19.3	525	4.2	Doubt- ful
W	16	13	None	100	3.05	4.7270	4.6637	0.0633	143	19.3	500	4.0	Doubt- ful
Ni	17	24	None	23	3.03	0.2100	0.1955	0.0145	71	8.9	230	4.0	Doubt- ful
Ni	18	25	None	100	3.0	0.2224	--	--	68	8.9	Dissolved	--	Unsuit- able
Mo	19	5	None	100	3.03	1.2220	1.0148	0.2072	164	10.2	1450	22	Unsuit- able
C-20-3	20	6	None	100	3.35	11.7812	11.2135	0.5677	21	8.0	28,000	545	Unsuit- able
Ti-Pd	21	7	None	100	3.35	6.7372	4.3844	2.3528	1.5	5.55	1.6 x 10 ⁶	Exces- sive	Unsuit- able
Cr. Plated, S.S.	22	26	None	23	3.19	6.8970	3.5488	3.3482	16	8.0	228,000	Exces- sive	Unsuit- able
Ta	23	14	None	23	3.05	0.4864	--	--	17	16.6	Dissolved	--	Unsuit- able

TABLE No. II

"Chemical" Corrosion of Alloys in 88 Wt % Phosphoric Acid (C.P.) at 150°C

Specimen	Serial No.	Test No.	Gas Environment	Contact with Pt Electrode Yes or No	Geometric Area, In ² (grams)	Initial Wt. (grams)	Final Wt. (grams)	Wt. Loss (grams)	Hours on Test	Density (gms/cm ³)	Corrosion Rate		Remarks	
											Milligrams Ft ² /Day	Mils Per Year	Acid Color	Sample Appearance
W.Screen	1	36-A	H ₂	No	1.87	1.1630	1.1596	0.0034	115	19.3	55	0.44	Yellow- ish	Same
W.Screen	2	37-A	H ₂	Yes	1.87	1.2310	1.2285	0.0025	115	19.3	40	0.32	Color- less	Same
W.Screen	3	81-A	C ₃ H ₈	No	1.87	0.9088	0.9080	0.0008	43	19.3	34	0.27	Color- less	Same
W.Screen	4	81-A ¹	C ₃ H ₈	No	1.87	0.9080	0.9076	0.0004	65	19.3	11	0.09	Color- less	Same
W.Screen	5	82-A	C ₃ H ₈	Yes	1.87	0.8720	0.8701	0.0019	43	19.3	82	0.66	Color- less	Same
W.Screen	6	82-A ¹	C ₃ H ₈	Yes	1.87	0.8701	0.8698	0.0003	65	19.3	8.5	0.07	Color- less	Same
W.Screen	7	35-A	O ₂	No	1.87	1.2270	1.0938	0.1332	115	19.3	2300	18	Color- less	Black
W.Screen	8	45-A ¹	O ₂	No	1.87	1.1886	1.0935	0.0951	89.5	19.3	1970	16	Color- less	Black
W.Screen	9	38-A	O ₂	Yes	1.87	1.2968	0.8957	0.4011	115	19.3	6500	52	Color- less	Black
W.Screen	10	46-A ¹	O ₂	Yes	1.87	1.2660	0.9225	0.3435	89.5	19.3	7100	57	Color- less	Black
W.Screen	11	34-A	None	No	1.87	1.1847	1.1799	0.0048	115	19.3	78	0.62	Brown- ish	Same
W.Screen	12	39-A	None	Yes	1.87	1.2289	1.2254	0.0035	115	19.3	56	0.45	Brown- ish	Same
93%W, 7%Ni	13	56-A	H ₂	No	0.41	4.6785	4.6785	0.0000	45	18.0	Nil	Nil	Light Blue	Same

TABLE No. II (Cont.)

Specimen	Serial No.	Test No.	Environment	Contact with Pt Electrode	Geometric Area, In ²	Initial Wt. (grams)	Final Wt. (grams)	Wt. Loss (grams)	Hours on Test	Density (gms/cm ³)	Corrosion Rate		Remarks	
											Milligrams Ft ² /Day	Mils Per Year	Acid Color	Sample Appearance
93% W, 7% Ni	14	83-A	C ₃ H ₈	No	0.38	4.6561	4.6561	0.0000	43	18.0	Nil	Nil	Color-less	Same
93% W, 7% Ni	15	83-A ¹	C ₃ H ₈	No	0.38	4.6561	4.6560	0.0001	65	18.0	14	0.12	Color-less	Same
93% W, 7% Ni	16	84-A	C ₃ H ₈	Yes	0.38	4.6785	4.6768	0.0017	43	18.0	36	0.31	Color-less	Same
93% W, 7% Ni	17	84-A ¹	C ₃ H ₈	Yes	0.38	4.6768	4.6760	0.0008	65	18.0	112	0.96	--	--
93% W, 7% Ni	18	55-A	O ₂	No	0.38	4.6605	4.6561	0.0044	45	18.0	890	7.6	Yellow-ish	etched
93% W, 7% Ni	19	100-A	O ₂	No	0.38	4.6091	4.5948	0.0143	91	18.0	1430	12	Color-less	Brown
93% W, 7% Ni	20	94-A	O ₂	Yes	0.38	4.6560	4.6079	0.0481	66	18.0	6650	57	Color-less	--
93% W, 7% Ni	21	99-A ¹	O ₂	Yes	0.38	4.6762	4.6168	0.0594	91	18.0	5940	51	Yellow-ish	Charcoal Color
82% W, 18% Ni	22	54-A	H ₂	No	0.47	5.0875	5.0874	0.0001	45	15.9	16.4	0.15	Color-less	Same
82% W, 18% Ni	23	85-A	C ₃ H ₈	No	0.47	5.0874	5.0862	0.0012	43	15.9	205	1.9	Color-less	Same
82% W, 18% Ni	24	86-A	C ₃ H ₈	Yes	0.47	6.0820	6.0674	0.0146	43	15.9	2,500	23	Yellow-ish	--
82% W, 18% Ni	25	53-A	O ₂	No	0.47	6.1040	6.0820	0.0220	45	15.9	3,600	33	Yellow-ish	S; etched
67% W, 33% Ni	26	52-A	H ₂	No	0.44	3.8457	3.8449	0.0008	45	13.3	140	1.3	Color-less	Same
67% W, 33% Ni	27	87-A	C ₃ H ₈	No	0.43	3.8449	3.8421	0.0028	43	13.3	524	4.8	Yellow-ish	--

TABLE No. II (Cont.)

Specimen	Serial No.	Test No.	Gas Environment	Contact with Pt Electrode Yes or No	Geometric Area, In. ² (Grams)	Initial Wt. (Grams)	Final Wt. (Grams)	Wt. Loss (Grams)	Hours on Test	Density (Gms./cm ³)	Corrosion Rate		Remarks	
											Milligrams Ft ² /Day	Mil. Per Year	Acid Color	Sample Appearance
67% W, 33% Ni	28	88-A	C ₃ H ₈	Yes	0.45	4.5015	4.4660	0.0355	43	13.3	6,400	58	Greenish	--
67% W, 33% Ni	29	88-A ¹	C ₃ H ₈	Yes	0.45	3.8421	3.7888	0.0533	65	13.3	6,300	57	Green	--
67% W, 33% Ni	30	51-A	O ₂	No	0.45	4.5250	4.5015	0.0235	45	13.3	4,000	36	Yellowish	S; etched
W. Alloy No. 10	31	41-A	O ₂	No	0.56	4.0178	3.9941	0.0237	95	19	1,540	13	Colorless	Black
W. Alloy No. 10	32	29-A	None	No	0.56	4.0200	4.0178	0.0022	95	19	144	1.2	Brownish	--
W. Alloy No. 11	33	42-A	O ₂	No	0.29	2.0966	2.0913	0.0053	95	19	665	5.4	Brown	Black
W. Alloy No. 11	34	27-A	O ₂	Yes	0.29	2.0916	2.0584	0.0332	91	19	435	3.5	Colorless	Black
W. Alloy No. 11	35	30-A	None	No	0.29	2.0985	2.0966	0.0019	95	19	238	2.0	Brown	Same
W. Alloy No. 12	36	43-A	O ₂	No	0.39	5.1388	5.1190	0.0198	95	19	1,850	15	Colorless	Black
W. Alloy No. 12	37	98-A	O ₂	Yes	0.39	5.1194	5.0718	0.0476	91	19	4,650	38	Yellowish	Black
W. Alloy No. 12	38	31-A	None	No	0.39	5.1408	5.1388	0.0020	95	19	187	1.5	Brownish	Same
W. Alloy No. 13	39	44-A	O ₂	No	0.59	8.6728	8.6440	0.0288	95	19	1,750	14	Greenish	Same
W. Alloy No. 13	40	32-A	None	No	0.59	8.6742	8.6728	0.0014	95	19	86	0.66	Brownish	Same
89% Mo, 11% Ni	41	68-A	H ₂	No	0.43	2.8065	2.8065	0.0000	41	10.1	Nil	Nil	Colorless	Same

TABLE No. II (Cont.)

Specimen	Serial No.	Test No.	Gas Environment	Contact with Pt Electrode	Geometric Area, In ²	Initial Wt. (grams)	Final Wt. (grams)	Wt. Loss (grams)	Hours on Test	Density (gms/cm ³)	Corrosion Rate		Remarks	
											Milligrams Ft ² /Day	Mils Per Year	Acid Color	Sample Appearance (S ^x)
89% Mo, 11% Ni	42	89-A	C ₃ H ₈	No	0.43	2.7314	2.7302	0.0012	43	10.1	225	3.4	Yellowish	Same
89% Mo, 11% Ni	43	89-A ¹	C ₃ H ₈	No	0.43	2.7302	2.7273	0.0029	65	10.1	358	5.5	Yellowish	--
89% Mo, 11% Ni	44	90-A	C ₃ H ₈	Yes	0.44	2.8065	2.8058	0.0007	43	10.1	124	1.9	Yellowish	--
89% Mo, 11% Ni	45	90-A ¹	C ₃ H ₈	Yes	0.44	2.8058	2.8045	0.0013	65	10.1	153	2.3	Yellowish	--
89% Mo, 11% Ni	46	67-A	O ₂	No	0.43	2.7542	2.7314	0.0228	41	10.1	4,500	69	Greenish	Small Crack
89% Mo, 11% Ni	47	101-A	O ₂	No	0.44	2.7277	2.6568	0.0709	91	10.1	6,130	94	Acid Green	--
89% Mo, 11% Ni	48	102-A	O ₂	Yes	0.44	2.8050	2.3844	0.4206	91	10.1	36,400	560	Dark Blue	Pitted
71% Mo, 29% Ni	49	77-A	H ₂	No	0.53	3.4730	3.4830	[†] 0.0100	66	9.9	999 (gain)	gain	Colorless	
71% Mo, 29% Ni	50	80-A	H ₂	No	0.52	3.4830	3.4826	0.0004	23	9.9	115	1.8	Colorless	
71% Mo, 29% Ni	51	93-A	H ₂	Yes	0.55	3.8426	3.4775	0.3651	66	9.9	34,800	550	Yellowish	
29% Mo, 71% Ni	52	66-A	H ₂	No	0.49	2.8332	2.8255	0.0077	41	9.4	1,330	22	Amber	etched
29% Mo, 71% Ni	53	91-A	C ₃ H ₈	No	0.49	3.1439	3.1237	0.0202	43	9.4	3,340	56	Amber	
29% Mo, 71% Ni	54	92-A	C ₃ H ₈	Yes	0.49	2.8255	2.7650	0.0605	43	9.4	9,900	165	Amber	
29% Mo, 71% Ni	55	65-A	O ₂	No	0.49	3.1552	3.1439	0.0113	41	9.4	1,950	35	Greenish	S, etched

S^x — phase separation or segregation of the alloy constituents during test

TABLE No. II (Cont.)

Specimen	Serial No.	Test No.	Environment	Contact with Pt Electrode Yes or No	Geometric Area, In ²	Initial Wt. (grams)	Final Wt. (grams)	Wt. Loss (grams)	Hours on Test	Density (gms/cm ³)	Corrosion Rate		Acid Color	Remarks
											Milligrams Ft ² /Day	Mils Per Year		
81% Fe, 19% Cr	56	58-A	H ₂	No	0.56	3.3158	2.4465	0.8693	19	7.7	284,000	5,800	Green	Boundary cracks
81% Fe, 19% Cr	57	57-A	O ₂	No	0.59	3.5943	3.3150	0.2793	19	7.7	86,000	1,700	Green	Pitted, cracks
62% Fe, 38% Cr	58	60-A	H ₂	No	0.50	2.7029	2.5724	0.1305	19	7.6	46,300	950	Green	Pitted, cracks
62% Fe, 38% Cr	59	59-A	O ₂	No	0.52	2.9467	2.8605	0.0862	19	7.6	30,200	620	Green	Pitted, cracks
42% Fe, 58% Cr	60	62-A	H ₂	No	0.61	3.5800	3.4048	0.1752	19	7.4	52,000	1,500	Green	Pitted, cracks
42% Fe, 58% Cr	61	61-A	O ₂	No	0.58	3.4605	3.4380	0.0225	19	7.4	7,300	150	Green	etched
21% Fe, 79% Cr	62	64-A	H ₂	No	0.61	3.5626	3.4194	0.1432	21	7.35	38,600	820	Green	Pitted, cracks
21% Fe, 79% Cr	63	63-A	O ₂	No	0.62	3.7240	2.9227	0.8013	21	7.35	240,000	5,100	Green	Pitted, cracks
82% Co, 18% Cr	64	70-A	H ₂	No	0.49	2.9928	2.9602	0.0326	19	8.55	12,000	220	Violet	Etched
82% Co, 18% Cr	65	69-A	O ₂	No	0.50	3.0275	2.9633	0.0642	19	8.55	23,500	430	Violet	S; etched
60% Co, 40% Cr	66	72-A	H ₂	No	0.45	1.9442	1.9272	0.0172	19	8.1	7,000	130	Char-coal	S; etched
60% Co, 40% Cr	67	71-A	O ₂	No	0.45	2.4057	2.3620	0.0437	19	8.1	17,600	340	Char-coal	S; etched
22% Co, 78% Cr	68	74-A	H ₂	No	0.48	2.3695	2.0935	0.2760	19	7.5	100,000	2000	Dark Green	Pitted
22% Co, 78% Cr	69	73-A	O ₂	No	0.49	2.6485	2.3633	0.2852	19	7.5	106,000	2200	Dark Green	Pitted

TABLE No. II (Cont.)

Specimen	Serial No.	Test No.	Gas Environment	Contact with Pt Electrode Yes or No	Geometric Area, In ²	Initial Wt. (grams)	Final Wt. (grams)	Wt. Loss (grams)	Hours on Test	Density (gms/cm ³)	Corrosion Rate		Remarks	
											Milligrams Ft ² /Day	Mils Per Year	Acid Color	Sample Appearance
57% Cr, 43% Ni	70	76-A	H ₂	No	0.50	2.6475	0.8768	1.7707	19	7.85	Excessive	Excessive	Dark Green	Pitted
57% Cr, 43% Ni	71	75-A	O ₂	No	0.51	2.8380	2.7938	0.0442	19	7.85	16,000	320	Green	S, etched
Hafnium Carbide	72	79-A	O ₂	No	0.27	0.9096	0.9064	0.0032	23	11.4	1,780	24	Colorless	Same
Hafnium Carbide	73	96-A	O ₂	Yes	0.27	0.9067	0.8032	0.1035	91	11.4	15,000	200	Brown	Black
Hafnium Carbide	74	78-A	None	No	0.27	0.9171	0.9096	0.0075	65	11.4	1,480	20	Brown	Black
Ti-Carbide	75	95-A	O ₂	No	0.88	11.4958	11.4930	0.0028	91	4.93	121	3.8	Yellowish	Same
Pt-6% Rh	76	40-A	O ₂	No	0.38	0.4652	0.4659	⁺ 0.0007	113.5	20.6	Nil	Nil	Yellowish	Same
Nionel-825	77	27-A	H ₂	No	1.39	9.0902	9.0886	0.0016	141	7.86	28	0.6	Yellowish	Straw
Nionel-825	78	26-A	O ₂	No	1.39	9.0254	9.0135	0.0119	19	7.86	1,580	31	Green	etched
Bronze Screen	79	48-A	H ₂	No	1.05	0.3130	0.3107	0.0023	72	8.8	105	1.9	Colorless	Unchanged
Bronze Screen	80	49-A	H ₂	Yes	1.05	0.3075	0.2831	0.0244	65	8.8	1,240	22	Colorless	Same
Bronze Screen	81	50-A	O ₂	No	1.05	0.2966	--	--	65	8.8	Dissolved	--	--	--
Bronze Screen	82	47-A	O ₂	Yes	1.05	0.3076	--	--	4	8.8	Dissolved	--	--	--

5.3.2 Developmental Electrodes

Performance data obtained for developmental electrodes is presented in the following Tables III through XV.

TABLE III

Heavy and fluffy wetproofing films sprayed on standard Niedrach-Alford electrodes with 10% T-30. Performance on propane, oxygen and air. Electrode potentials in mv, 150° C, 85% H_3PO_4

CURRENT DENSITY (A.S.F.)												Limiting Current Density
Electrode Number	Film (mg/inch ²)	0	10	20	30	40	50	100	150	200		
ELECTRODE POTENTIALS (mv)												
PROPANE												
3207	4.9	280	430	460	490	505	520	600			140	
5111	5	Poor Performance										
3215	20	150	370	405	410	425	435	480	530	560		
3185	40	220	340	375	400	410	420	450	475	500		
3214	40	220	330	370	390	410	425	460	490	515		
3221	40	150	360	385	410	425	440	480	505	530		
3222	40	140	340	375	400	415	430	460	485	505		
3188	60	210	375	400	410	420	430	455	480	510		
3189	80	260	380	410	435	450	460	490	525	555		
5129	110	220	375	400	420	440	450	520	580	620		
5113	160	200	Poor Performance									
OXYGEN												
3207	4.9	1080	1000	980	960	950	935	910	885	860		
5111	5											
3215	20	1040	975	950	940	930	925	905	885	870		
3185	40	1080	965	940	925	915	910	895	870	855		
3214	40	1040	980	965	940	930	920	900	880	860		
3221	40	1040	945	930	920	910	900	870	850	835		
3222	40	1040	940	925	915	905	900	880	860	845		
3188	60	1040	1000	975	960	950	940	920	905	885		
3189	80	1040	995	965	945	930	920	905	890	870		
5129	110	1040	980	950	930	915	900	865	845	830		
5113	160	1033	824	746		658						
AIR												
3207	4.9	1020	940	915	890	875	860	820	790	755		
5111	5	911	178	42								
3215	20	1000	900	870	845	825	810	765	725	690		
3185	40	1060	940	910	880	870	860	825	805	785		
3214	40	1040	950	920	900	885	870	835	810	780		
3221	40											
3222	40											
3188	60	1000	965	940	920	905	895	870	840	810		
3189	80	1020	950	920	910	890	880	845	805	770		
5129	110	1020	930	905	885	870	850	810	780	760		
5113	160	1010	645	537		325						

TABLE IV

Heavy and fluffy wetproofing films sprayed on electrodes with various Teflon concentrations in catalyst layer. Performance on propane, oxygen and air.

			<u>CURRENT DENSITY A.S.F.</u>										Limiting Current Density
	<u>Electrode Number</u>	<u>Film (mg/sq in.)</u>	<u>0</u>	<u>10</u>	<u>20</u>	<u>30</u>	<u>40</u>	<u>50</u>	<u>100</u>	<u>150</u>	<u>200</u>		
<u>PROPANE</u>			<u>ELECTRODE POTENTIALS (mv)</u>										
With 20%	5116	10	200	540								15	
T-30	5116*	10	280	450	490	415	440	455				100	
	5110	40	246	500	550	620							
	5110*	40	180	405	440	465	480	495	550	600	650		
	5120	60	240	500	550	580	620	720					
	5120*	60	200	440	480	500	525	550					
With 20%	5123	10	280	440	480	520	560	670				50	
T-7	5123*	10	300	460	500	530	550	590	740				
	5122	40	230	440	460	485	510	530	645				
	5122*	40	260	380	415	435	450	470	560				
With 30%	5115	10	250	450	490	530	570	630					
T-7	5115*	10	300	470	510	535	565	595				70	
	5112	40	200	380	430	460	485	505	620			130	
	5112*	40	140	440	485	510	530	560					
<u>OXYGEN</u>													
With 20%	5116	10	950	830	760	710	670	635	540	460	385	15	
T-30	5116*	10	1010	940	900	880	865	855	820	810	800	100	
	5110	40											
	5110*	40	1020	970	950	935	930	920	900	885	780		
	5120	60	1030	960	925	900	880	865	830	815	800		
	5120*	60	1020	940	905	880	860	845	815	800	785		
With 20%	5123	10	1060	990	965	940	920	905	875	850	830	50	
T-7	5123*	10	1070	970	930	900	880	870	825	795	770		
	5122	40	1070	1020	990	970	960	945	915	885	855		
	5122*	40	1060	950	925	900	885	870	850	830	810		
With 30%	5115	10	1020	950	920	890	880	865	850	840	830		
T-7	5115*	10	990	940	910	880	860	840	810	795	785	70	
	5112	40	1020	970	940	910	900	890	850	830	820	130	
	5112*	40	1010	950	920	900	890	875	830	780	730		

*Electrodes and films pressed with 20-ton pressure after first test.

TABLE IV (Continued)

AIR

	Electrode Number	Film (mg/inch ²)	CURRENT DENSITY (A.S.F.)								
			0	10	20	30	40	50	100	150	200
ELECTRODE POTENTIALS (mv)											
On 20% T-30	5116	10	870	650	550	470	410	360	90		
	5116*	10	1000	880	850	820	800	780	740	720	700
	5110	40									
	5110*	60	990	950	930	910	850	880	835	805	780
	5120	60	1020	905	860	830	810	790	750	715	680
	5120*		1000	885	840	810	780	765	710	655	600
On 20% T-7	5123	10	1010	950	920	890	870	855	800	760	710
	5123*	10	1040	890	850	820	790	770	700	660	615
	5122	40	990	920	900	875	860	850	820	795	770
	5122*	40	1020	900	860	830	810	795	750	710	670
On 30% T-7	5115	10	980	840	810	775	750	740	710	710	710
	5115*	10	980	890	850	800	775	750	690	655	615
	5112	40	990	905	870	820	805	790	755	730	705
	5112*	40	940	840	740	680	600	460	-		

* Electrodes and films pressed with 20-ton pressure after first test.

TABLE V

Heavy and fluffy wetproofing films. Performance gain or loss after hot pressing with 20 tons.

Electrode Number	Film (mg/sq in.)	CURRENT DENSITY (A.S.F.)								
		0	10	20	30	40	50	100	150	200
<u>PROPANE</u>		PERFORMANCE GAIN OR LOSS (mv)								
5116	10	-80	+90	i_L increased from 15 to 100						
5110	40									
5120	60	+40	+60	+70	+80	+95	+170			
5123	10	-20	-20	-20	-10	+10	+ 80			
5122	40	-30	+60	+45	+50	+60	+ 80	+85		
5115	10	-50	-20	-20	- 5	+ 5	+ 35			
5112	40	+60	-60	-55	-50	-55	- 55			
<u>OXYGEN</u>										
5116	10	+60	+90	+140	+170	+195	+220	+280	+350	+415
5110	40									
5120	60	-10	-20	- 20	- 20	- 20	- 20	- 15	- 15	- 15
5123	10	+10	-20	- 35	- 40	- 40	- 35	- 50	- 55	- 60
5122	10	+10	-70	- 65	- 70	- 75	- 70	- 65	- 55	- 45
5115	10	-30	-10	- 10	- 10	- 20	- 22	- 40	- 45	- 45
5112	40	-10	-20	- 20	- 10	- 10	- 15	- 20	- 50	- 90
<u>AIR</u>										
5116	10	+130	+230	+300	+350	+390	+420			
5110	40									
5120	60	- 20	-20	- 20	- 20	- 30	- 25	- 40	- 60	- 80
5123	10	+ 30	-60	- 70	- 70	- 80	- 85	-100	-100	- 95
5122	40	+ 30	-20	- 40	- 45	- 50	- 55	- 70	- 85	-100
5115	10	-	+50	- 40	+ 25	+ 25	+ 10	- 20	- 55	- 95
5112	40	- 50	-60	-130	-140	-205	-330			

+ = Gain in performance (lower electrode potential for propane).

- = Loss in performance (higher electrode potential for propane).

TABLE VI

Asbestos-filled electrodes. Performance on propane, oxygen and air.

Electrode Number	CURRENT DENSITY (A.S.F.)									Limiting Current Density
	0	10	20	30	40	50	100	150	200	
<u>PROPANE</u>										
	ELECTRODE POTENTIALS (mv)									
3239	260	375	410	430	445	460	505	530	550	145
3240	Good performance									
3241	270	360	395	415	430	445	490	515	550	
3242	260	430	470	500	520	535	650			
3243	220	315	345	360	375	380	415	430	460	
3244	150	380	430	445	455	465	510	530	540	
3245	250	365	390	410	425	430	470	500	520	
(*)		350	380	400	415	430	460	490	515	
<u>OXYGEN</u>										
3239	1020	970	950	935	925	920	895	870	860	
3240	Good performance									
3241	1080	990	970	950	940	930	905	885	870	
3242	1040	935	915	900	885	875	835	825	820	
3243	1040	980	960	950	945	935	910	895	880	
3244	1020	970	950	935	920	915	890	875	860	
3245	1060	980	965	950	940	930	905	890	880	
<u>AIR</u>										
3239	1000	930	905	890	875	865	830	800	780	
3240	Good performance									
3241	1040	940	915	890	880	870	830	805	780	
3242	920	860	830	800	780	760	660	560	460	
3243	1020	940	920	900	885	875	840	815	795	
3244	1000	920	900	885	875	860	810	785	785	
3245	980	930	900	885	870	855	820	810	780	

(*) Average performance of standard electrodes with heavy wet-proofing films (40 mg/inch²) for comparison.

TABLE VII

Composition and catalyst loading of asbestos-filled electrodes.

Electrode Number	Concentrations			Catalyst Loading (gr/cm ²)
	% Pt	% Asbestos	% T-30	
3239	72	18	10	29.5
3240	72	18	10	29.5
3241	72	18	10	29.5
3242	53	27	20	22.0
3243	83	7	10	34.3
3244	57	25	18	23.6
3245	72	18	10	29.5

TABLE VIII

Composition of Double-Layer Electrodes

A. With two layers of different teflon content

Electrode Number	Composition of Layer	
	Gas Side	Electrolyte Side
5174	30% T-30 (1.2 gr)	10% T-30 (1.2 gr)
5106	10% T-30 "	30% T-30 "
824	30% T-7 "	10% T-7 "
3163	30% T-7 "	10% T-7 "
825	10% T-7 "	30% T-7 "

B. With a tantalum layer and a platinum layer

3198	Pt + 30% T-7 (1.2 gr)	Ta + 20% T-7 (2 gr)
3209	Pt + 30% T-7 "	*Ta + Ni + 20% T-7 (2 gr)

* 80% Ta + 20% Ni, Ni dissolved from electrode.

C. With sandwiched wetproofing films

Electrode Number	Film (mg/sq in.)	Composition of Layer	
		Gas Side	Electrolyte Side
3226	1.6	Ta + 20% T-7	Pt + 10% T-7
3228	6.0	Ta + 20% T-7	Pt + 10% T-7
3229	6.0	Ta + 20% T-7	Pt + 16% T-7
3230	24.0	Ta + 20% T-7	Pt + 10% T-7

TABLE IX

Performance of double layer electrodes with two layers of different teflon content.

Electrode Number	CURRENT DENSITY (A.S.F.)									Limiting Current Density
	<u>0</u>	<u>10</u>	<u>20</u>	<u>30</u>	<u>40</u>	<u>50</u>	<u>100</u>	<u>150</u>	<u>200</u>	
	ELECTRODE POTENTIALS (mv)									
5174*	250	400	450	465	480	490	560			140
5106	240	37 ⁺	410	440	460	470	540	590	640	
824	200	400	430	440	455	460	490	530	570	
3163	260	425	455	480	495	510	590			140
825	240	890	430	450	460	480	525	570	615	
		350	380	400	415	420	460	490	515**	

*Only cold-pressed electrode.

**Mean values of standard electrodes with heavy, fluffy wetproofing films of 40 mg/sq in.

TABLE X

Performance of double-layer electrodes with a tantalum and a platinum layer. Nickel used as spacing agent in electrode 3209.

Electrode Number	CURRENT DENSITY (A.S.F.)									Limiting Current Density
	<u>0</u>	<u>10</u>	<u>20</u>	<u>30</u>	<u>40</u>	<u>50</u>	<u>100</u>	<u>150</u>	<u>200</u>	
	ELECTRODE POTENTIALS (mv)									
<u>PROPANE</u>										
3198	130	490	560	630	700					45
3209	220	360	400	420	430	450	590			110
<u>OXYGEN</u>										
3198	1040	900	840	815	780	760	590	420		
3209	1000	910	895	880	870	860	795	735	680	

TABLE XI

Performance of double-layer electrodes with sandwiched wetproofing films.

Electrode Number	CURRENT DENSITY (A.S.F.)									Limiting Current Density
	0	10	20	30	40	50	100	150	200	
	ELECTRODE POTENTIALS (mv)									
<u>PROPANE</u>										
3226	220	450	520							23
3226*	280	380	410	430	450	465				80
3228	220	360	420	460	500					50
3228*	200	400	440	460	495	530				80
3229	140	320	380	410	440	470				80
3230	140	360	415	460	510					45
<u>OXYGEN</u>										
3226	1040	940	895	850	815	755	720	690		
3226*	1000	950	915	885	880	870	845	825	810	
3228	1020	960	930	915	910	885	865	840	820	
3228*	1050	940	920	905	890	885	850	825	800	
3229	1050	995	970	950	940	925	880	840	825	
3230	1030	960	925	910	905	890	850	820	795	
<u>AIR</u>										
3226	990	810	730	690	660	630	545	480	425	
3226*	1000	900	850	825	810	795	750	720	695	
3228	1000	890	860	840	825	805	750	715	685	
3228*	1010	880	850	820	800	780	720	680	630	
3229	1020	925	880	845	820	790	670	580	490	
3230	1000	900	845	805	780	755	655	520		190

*These electrodes were tested with the platinum layer on the gas side after spraying of a wetproofing film on that side.

TABLE XII

Performance of standard electrodes with wetproofing film. 5135 applied by spraying under vacuum; 5150 with filtered-on film

Electrode Number	<u>CURRENT DENSITY (A.S.F.)</u>									
	<u>0</u>	<u>10</u>	<u>20</u>	<u>30</u>	<u>40</u>	<u>50</u>	<u>100</u>	<u>150</u>	<u>200</u>	
	<u>ELECTRODE POTENTIALS (mv)</u>									
<u>PROPANE</u>										
5135	260	405	440	455	470	485	535	590	600	
5135*	220	365	400	420	430	440	475	495	510	
5150	230	360	395	420	440	455	495	525	550	
<u>OXYGEN</u>										
5153	1070	1000	970	955	940	925	890	870	855	
5135*	1020	960	935	920	910	900	870	845	825	
5150	1020	965	940	930	925	915	885	865	850	
<u>AIR</u>										
5135	1040	945	910	890	875	860	810	780	760	
5135*	980	900	880	860	840	875	795	775	755	
5150	1010	925	900	885	870	855	810	785	770	

*Hot pressed with 20 tons after first performance test.

TABLE XIII

Performance of Electrode 832. Tantalum substructure activated by filtered-on platinum black - T-30 slurry.

filtered-on platinum black - T-30 slurry.										Limiting Current Density
CURRENT DENSITY (A.S.F.)										
<u>0</u>	<u>10</u>	<u>20</u>	<u>30</u>	<u>40</u>	<u>50</u>	<u>100</u>	<u>150</u>	<u>200</u>		
ELECTRODE POTENTIALS (mv)										
<u>PROPANE</u>	310	410	420	435	450	460				80
<u>OXYGEN</u>	1060	910	880	860	845	835	820	805	795	
<u>AIR</u>	900	840	805	780	760	740	660	525	515	

TABLE XIV

Standard electrodes with various catalyst loadings. Performance on propane.

Electrode Number	Catalyst (gr. total)	CURRENT DENSITY (A.S.F.)										Limiting Current Density
		0	10	20	30	40	50	100	150	200		
		ELECTRODE POTENTIALS (mv)										
3204	3.6	220	370	400	425	445	460	530	610	730		
3197	1.5	250	390	410	430	440	450	485	500	510		
7115	1.2	280	350	380	400	410	415	(450)			80	

TABLE XV

Performance of standard electrode No. 5104, pressed at 100 tons.

	<u>CURRENT DENSITY (A.S.F.)</u>								
	<u>0</u>	<u>10</u>	<u>20</u>	<u>30</u>	<u>40</u>	<u>50</u>	<u>100</u>	<u>150</u>	<u>200</u>
	<u>ELECTRODE POTENTIALS (mv)</u>								
PROPANE	280	380	415	440	450	460	490	530	565
OXYGEN	1030	985	960	950	940	930	915	895	880
AIR	1020	955	925	905	885	870	840	810	780

TABLE I

Summary of Electrochemical Cell Life Testing Data

Cell	Electrodes	Composition	Reactants	Electrolyte	Life	Reason for Replacement
LT-7	A-3143 C-5078	30% T-7, 70% Pt, Ta screen, T-30 film 5 mg/in. ² 19% T-30, 90% Pt, Ta screen, T-30 film 5 mg/in. ²	Iso-octane Air	H ₃ PO ₄	1990 hrs	Could not sustain reaction. Cracked substrate both electrodes.
LT-8	A-825 C-392	Gas side - 10% T-7, 90% Pt, Ta screen Electrolyte side - 70% Pt, 30% T-7, Ta screen Both sides 40% Ta, 40% Pt, 20% T-7 (3.2 gms)	n-octane Air	H ₃ PO ₄	3940 hrs	Still operational.
LT-9	A-3185 C-7111B	10% T-30, 90% Pt, Ta screen, 40 mg/in. ² , T-30 film 20% T-30, 80% Pt., Ta screen 5 mg/in. ² , T-30 film	Propane Air	H ₃ PO ₄	3280 hrs	Still operational.
LT-10	A-3110 C-3126	10% T-30, 90% Pt, Ta screen, 5 mg/in. ² , T-30 film 10% T-30, 90% Pt, Ta screen	Decane (liquid) Air	H ₃ PO ₄	3 hrs	Anode wetted by decane. Leaks.
LT-11	A-3144 C-3126	50% T-7, 50% Pt, Ta screen 10% T-30, 90% Pt, Ta screen	Decane	H ₃ PO ₄	24 hrs	Replaced anode. Poor performance Decane leak.
LT-12	A-3206 C-3126	20% T-30, 80% Pt, Ta screen, .069 gms FEP film pressed with 40 tons at 700°F. 10% T-7, 90% Pt, Ta screen	Decant Air	H ₃ PO ₄	980 hrs 1007 hrs	Cathode leak.
LT-13	A-3110 C-3201B	Std. electrode, 10% T-30, 90% Pt Std. electrode-loplex on electrolyte side @ 100°C, press - 2 min./12 ton pressure.	Iso-octane Air	H ₃ PO ₄	100 hrs	Water vapor suppression test.
LT-14	A-3110 C-5131	Std. electrode Std. electrode, 10% T-30, 90% Pt, Ta screen	Iso-octane Air	H ₃ PO ₄	100 hrs	Water transport evaluation.

TABLE I (Cont.)

<u>Cell</u>	<u>Electrodes</u>	<u>Composition</u>	<u>Reactants</u>	<u>Electrolyte</u>	<u>Life</u>	<u>Reason for Replacement</u>
LT-15	A-3110	Std. electrode-Ioplex on electrolyte side	Iso-octane	H ₃ PO ₄	100 hrs	Water vapor suppression evaluation
	C-5131	Std. electrode-Ioplex on electrolyte side	Air			
LT-16	A-3173	Std. electrode - Pt screen	Propane	HF	50 hrs	HF electrolyte evaluation.
	A-5142	Std. electrode - Pt screen	Air	HF	26 hrs	
			Hexane			
			Air			
LT-17	A-3223	Std. electrode-FEP film, 20% T-30, 80% Pt, Ta screen	Iso-octane	H ₃ PO ₄	8 hrs	No performance with FEP film and gaseous reactants.
	C-3224	Std. electrode - FEP film	Air			
LT-18	A-5134	Std. electrode, Ta screen 10% T-30, 90% Pt	Iso-octane	H ₃ PO ₄	2 hrs	Film lifted from Ta screen, leaks.
	C-5133	Std. electrode, Ta screen, 10% T-30, 90% Pt.	Air			Poor performance.
LT-19	A-3206	Std. electrode - FEP film	Decane (liquid)	H ₃ PO ₄	1798 hrs	Reaction product buildup.
	C-5136	Std. electrode, Ta screen, 10% T-30	Air			Degraded performance.
LT-20	A-3227	Std. electrode, 10% T-30, 90% Pt, Pt screen, .078 gms FEP film, no press	Octane (liquid)	HF	100 hrs	Cathode leaking approximately 8 ml/hr.
	C-5142	Std. electrode, Pt screen	Air			
LT-21	A-5140	Std. electrode, Ta screen, 10% T-30	Iso-octane	H ₃ PO ₄	50 hrs	Film lifted from Ta screen. Anode leaks.
	C-5137	Std. electrode, Ta screen, 10% T-30	Air			
LT-22	A-5139	Std. electrode, Ta screen, 10% T-30	Iso-octane	H ₃ PO ₄	50 hrs	Anode leaks. Film again lifted from Ta screen.
	C-5137	Std. electrode	Air			
LT-23	A-5167	Std. electrode, Ta screen - 10% T-30 (Catalyst - 34 m ² /gm)	Iso-octane	H ₃ PO ₄	20 hrs	Anode leak. Blister developed on gas side.
	C-5137	Std. electrode	Air			

TABLE I (Cont.)

Cell	Electrodes	Composition	Reactants	Electrolyte	Life	Reason for Replacement
LT-24	A-5145	Std. electrode - Pt screen	Octane	HF/C ₅ F	15 hrs	Poor performance. Replaced electrodes. White crystalline deposit on gas side (probably C ₅ F).
	C-3237	Std. electrode - Pt screen	Air			
LT-25	A-5168	Std. electrode mix, Ta screen, 10% T-30 (catalyst - 33 m ² /gm Pt)	Iso-octane		2 hrs	Anode leak. Film lifted from Ta screen.
	C-5137	Std. electrode, Ta screen, 10% T-30	Air			
LT-26	A-3238	Std. electrode, Ta screen	Iso-octane	H ₃ PO ₄	1 hr	Anode leak. Film lifted from screen. De-lamination of mix.
	C-5137	Std. electrode, Ta screen	Air			Poor performance.
LT-27	A-3172	Std. electrode - Pt screen	Iso-octane	HF/C ₅ F		
	C-3237	Std. electrode, Pt screen	Air			
LT-28	A-3219	Std. electrode, Pt screen, 10% T-30	Iso-octane	H ₃ PO ₄	40 hrs	Still operational.
	C-3220	10% T-30, Pt. screen, fluffy T-30 film, 40 mg/in. ² , no press	Air			
LT-29	A-3172	Std. electrode - Pt screen	Iso-octane	H ₃ PO ₄	1 hr	Check HF performance against H ₃ PO ₄ performance. Poor performance.
	C-3237	Std. electrode - Pt screen	Air		250 hrs	Still operating.
LT-30	A-3223	Std. electrode - 80% Pt, 20% T-30, .065 gms FEP film, unpressed	Decane (liquid)	H ₃ PO ₄		
	C-3238	10% T-30, Ta screen	Air			
LT-31	A-3246	Std. electrode - Pt screen, 10% T-30, 90% Pt.	Iso-octane	H ₃ PO ₄	1 hr	Check performance.
	A-3247	Std. electrode - Pt screen - 10% T-30, 90% Pt.	Air			H ₃ PO ₄ before HF/C ₅ F evaluation.
LT-32	A-3241	70% Pt, 18% asbestos, 11% T-30 catalyst mix	Iso-octane	H ₃ PO ₄	1 hr	Leaking anode.
	C-3239	Same as anode	Air			

TABLE I (Cont.)

<u>Cell</u>	<u>Electrodes</u>	<u>Composition</u>	<u>Reactants</u>	<u>Electrolyte</u>	<u>Life</u>	<u>Reason for Replacement</u>	
Lt-33	A-5182	Std. electrode, 20% T-7, Pt screen (34 m ² /gm Pt catalyst)	n-octane	H ₃ PO ₄	50 hrs	Still operational.	
	C-5163	Std. electrode, 10% T-30, Ta screen	Air				
LT-34	A-3248	Std. electrode, Pt screen	Iso-octane	HF/C _s F	4 hrs	Poor performance; HF.	
	C-3249	Std. electrode. Pt screen	Air				
LT-35	A-3244	59% Pt, 27% asbestos, 14% T-30, 5 mg/in. ² T-30 film, Asbestos filled	n-octane	H ₃ PO ₄	2 hrs	Still operational.	
	C-3245	71% Pt, 18% Asbestos, 11% Ta, 5 mg/in. ² T-30 film, asbestos filled					Air

BLANK PAGE

5.5 SELF-SUSTAINING OPERATION

5.5.1 Reactivities and Fuel Utilization (P. J. Chludzinski.)

5.5.1.1 Calibration Results of Chromatograph

The calibration results for the chromatograph - Perkin Elmer Model 801 Vapor Fractionator are shown in Table I. Test set up and conditions were: column type - 6 foot long, 1/8 inch OD stainless tubing packed with silica gel, sample tube volume - 1 cc., helium carrier gas flow - 30 cc/min at 100°C, 23 cc/min at 250°C, and thermal conductivity cell temperature at 150°C.

Table I

Species	K ($\frac{\text{area} \times \text{atten.}}{\mu \text{ g mol}}$)	Separation Time (min, sec.)	Column Temp (°C)
Air	178	0' 45"	150
CO ₂	206	1' 50"	150
C ₃ H ₈	293	3' 12"	150
C ₆ H ₁₄	685	9' 45" *	250
C ₈ H ₁₈	809	17' 53" *	250
Air	-	1' 0"	20
CO	-	1' 16"	20
CH ₄	-	1' 48"	20

*After starting temperature program 4 min., 30 sec. from time of sample injection. Program rate = 48°C/min.

5.5.1.2 Results of n-octane/n-hexane Fuel Mixture Experiments

Test results are tabulated in Table II. The test conditions were: electrolyte (H₃PO₄) concentration 93 weight per cent, cell temperature 307°F, cell area = 2.68 inch x 2.68 inch = 0.05 ft², and anode chamber height of 0.125 inch.

Table II

Run No.	Total Fuel Feed NT_i ($\frac{\mu g \text{ mol}}{\text{min}}$)	Mol Fraction Hexane in Fuel Feed X'_e	Cell Current i (amp)	Hexane Current i_h (amp)	Octane Current i_o (amp)	Exhaust Composition (dry basis)		
						Hexane X_a	Octane X_b	Carbon Dioxide X_c
36	149.7	.555	1.02	.845	.116	.302	.285	.413
39	126.3	.555	2.00	1.71	.281	.145	.182	.672
41	128.6	.555	2.00	1.54	.400	.159	.181	.660
42	126.3	.555	1.90	1.44	.390	.167	.185	.648
43	74.2	.555	1.89	1.15	.674	.098	.109	.794
44	73.6	.555	1.89	1.18	.625	.097	.112	.790
47	52.9	.246	2.00	.46	1.47	.022	.101	.878
51	196	.246	2.02	.788	.902	.100	.409	.491
52	196	.246	2.01	.750	1.066	.098	.391	.511
55	181	.246	1.01	.566	.350	.130	.519	.351
56	181	.246	1.01	.675	.241	.130	.527	.343
57	181	.246	1.01	.551	.438	.132	.508	.360

Run 36 through 44 were 50% by volume hexane. Run 47 through 57 were 20% by volume hexane.

5.5.2 Transport Rates (R. E. Kegan)

The detailed operating data and results for the test fuel cells are provided in Tables III and IV. These data have been expressed graphically in Figs. 1 through 4. Table V contains the composition and process data for the electrodes used in these tests.

Table III

Cell Number and Plot Symbol	Run Number	Temperature °F	Acid Conc., %	Acid Flow, cc/min	Fuel	Fuel Flow x 10 ³ lb-mol/hr	Fuel Flow x 10 ⁵ lb-mol/hr	Water Flow x 10 ⁶ lb-mol/hr	Total Flow x 10 ⁶ lb-mol/hr	Limiting Current, amps/ft ²	d, volts	a, volts	c, volts	Fuel	Mol Fraction	Fuel	Mol Fraction	Water Mol Fraction
2 - 189 ○	5	300	90.4	4.0	3	557	0	2,496	3,053	215	.171	.130	.101	3	.182			.818
	6		91.1	4.0	3	557		19,970	20,527	125	.163	.0919	.156	3	.0271			.973
	7		91.2	4.0	3	557		9,985	10,542	157	.143	.116	.139	3	.0528			.947
	8		91.3	3.6	3	557		999	1,556	214	.203	.127	.0754	3	.358			.642
	9		91.4	3.2	3	557		0	557	149	.230	.114	.0712	3	1.00			0
	10		91.4	3.3	8	552		9,985	10,537	112	.203	.0980	.197	8	.0524			.948
	11	300	92.2	3.3	8	552		4,992	5,544	90.9	.192	.104	.133	8	.0996			.900
	1	300	88.0	5.1	8	552		9,985	10,537	54.0	.171	.151	.158	8	.0524			.948
	2		88.0	6.2	8	552		4,992	5,544	58.0	.200	.108	.168	8	.0996			.900
	3		87.8	3.6	8	552		2,496	3,048	68.0	.203	.122	.147	8	.181			.819
	4		87.8	2.7	8	552		998	1,550	57.2	.216	.135	.0984	8	.356			.644
2 - 190 □	5		89.1	3.2	8	552		492	1,051	46.8	.206	.139	.116	8	.525			.475
	6		89.1	3.6	8	552		250	802	50.3	.242	.109	.144	8	.689			.311
	7		89.1	4.4	3	557		0	557	168	.193	.123	.0789	3	1.00			0
	9		88.2	6.1	3	557		2,496	3,053	150	.126	.0940	.157	3	.182			.818
	10	300	88.2	11.1	3	557		9,980	10,542	86.0	.100	.0972	.169	3	.0528			.947
	2	300	89.7	14.3	3	557		2,496	3,053	235	.145	.125	.103	3	.182			.818
	3		90.3	5.9	3	557		9,985	10,542	169	.150	.0904	.138	3	.0528			.947
	4		88.7	10.0	3	557		19,970	20,527	103	.175	.0555	.173	3	.0271			.973
	5		88.7	15.4	3	557		4,993	5,550	191	.180	.0951	.121	3	.100			.900
	6		88.5	4.0	3	557		998	1,555	258	.204	.107	.0898	3	.358			.642
	7		89.3	6.7	3	557		250	807	278	.272	.0789	.0848	3	.691			.309
2 - 191 △	8		90.2	9.3	3	557		499	1,056	278	.232	.102	.0711	3	.527			.473
	9		90.6	6.7	8	552		998	1,555	102	.246	.0923	.137	8	.356			.644
	10		90.6	12.9	8	552		9,985	10,537	96.2	.207	.0922	.144	8	.0524			.948
	11		90.0	13.3	8	552		2,496	3,048	96.0	.229	.0907	.152	8	.181			.819
	12		90.0	13.8	8	552		19,970	20,522	78.0	.195	.0810	.163	8	.0269			.973
	13		89.8	8.0	8	552		499	1,051	114	.229	.124	.123	8	.525			.475
	14	300	89.8	8.3	8	552	0	4,992	5,544	110	.201	.0793	.165	8	.0996			.900
	2	300	89.7	14.3	3	557		2,496	3,053	235	.145	.125	.103	3	.182			.818
	3		90.3	5.9	3	557		9,985	10,542	169	.150	.0904	.138	3	.0528			.947
	4		88.7	10.0	3	557		19,970	20,527	103	.175	.0555	.173	3	.0271			.973
	5		88.7	15.4	3	557		4,993	5,550	191	.180	.0951	.121	3	.100			.900

Table III (cont.)

Cell Number and Plot Symbol	Run Number	Temperature °F	Acid Conc., %	Acid Flow, cc/min.	Fuel	Fuel Flow x 10 ⁶ lb-mol/hr	Fuel	Fuel Flow x 10 ⁶ lb-mol/hr	Fuel Flow x 10 ⁶ lb-mol/hr	Water Flow x 10 ⁶ lb-mol/hr	Total Flow x 10 ⁶ lb-mol/hr	Limiting Current, Amps/ft ²	d, volts	a, volts	c, volts	Fuel	Mol Fraction	Fuel	Mol Fraction	Water Mol Fraction
2 - 191 (Cont.) ▲	15	300	90.8	10.5	8	552	8	552	0	250	802	109	.277	.0867	.0965	8	.689	8	.311	0
	16	300	90.8	9.1	3	100	8	552	552	0	652	113	.273	.0991	.0789	3	.153	8	.847	0
	17	300	92.4	6.4	3	100	8	276	276	0	376	116	.283	.0778	.0912	3	.266	8	.734	0
	18	300	92.4	7.0	3	100	8	1,100	1,100	0	1,200	112	.285	.0899	.0937	3	.0833	8	.917	0
	19	300	93.9	6.9	3	100	8	110	110	0	210	156	.284	.0746	.0988	3	.476	8	.524	0
	20	300	93.9	6.1	3	100	8	2,200	2,200	0	2,300	96.6	.325	.0707	.0933	3	.0435	8	.956	0
	21	300	94.5	3.4	3	100	6	692	692	0	792	235	.317	.0925	.0548	3	.126	6	.874	0
	22	300	94.5	4.4	3	100	6	347	347	0	447	238	.311	.0900	.0486	3	.224	6	.776	0
	23	300	95.3	3.7	3	100	6	1,390	1,390	0	1,490	163	.350	.103	.0220	3	.0671	6	.993	0
	24	300	96.2	3.8	3	100	6	139	139	0	239	244	.326	.0884	.0413	3	.418	6	.582	0
	25	300	96.6	4.0	3	100	6	2,780	2,780	0	2,880	98.6	.389	.0932	.0420	3	.0347	6	.965	0
	26	300	97.5	3.8	3	100	8	552	552	0	652	113	.329	.0780	.0819	3	.153	8	.847	0
	27	300	97.5	4.0	3	100	8	1,100	1,100	0	1,200	103	.324	.0901	.0792	3	.0833	8	.917	0
	28	300	92.5	2.7	3	100	8	276	276	0	376	152	.234	.117	.0651	3	.266	8	.734	0
	29	300	96.0	2.5	3	100	8	2,200	2,200	0	2,300	75.0	.323	.0978	.0683	3	.0435	8	.956	0
	30	300	98.0	2.5	3	100	8	110	110	0	210	144	.297	.103	.0579	3	.476	8	.524	0
	31	300	87.0	5.0	8	552	8	0	0	0	552	119	.218	.0726	.166	8	1.00	0	0	0
	32	300	87.0	8.0	6	692	6	692	692	0	692	175	.182	.0682	.162	6	1.00	0	0	0
2 - 192 ◇	5	300	91.7	12.1	6	692	6	692	692	0	692	111	.318	.136	.0780	6	1.00	0	0	0
	6	300	92.1	8.0	6	692	6	692	692	2,496	3,188	54.7	.270	.104	.114	6	.217	0	.783	0
	7	300	92.1	8.0	6	692	6	692	692	9,985	10,677	0	.240	.106	.139	6	.0648	0	.935	0
	8	300	91.8	11.8	6	692	6	692	692	4,992	5,084	30.4	.322	.129	.0856	6	.122	0	.878	0
	9	300	91.8	9.5	6	692	6	692	692	19,970	20,602	31.6	.239	.0908	.145	6	.0335	0	.966	0
	10	300	91.1	8.0	6	692	6	692	692	250	942	35.6	.319	.129	.0729	6	.735	0	.265	0
	11	300	91.1	10.0	6	692	6	692	692	4,992	5,684	33.8	.252	.115	.143	6	.122	0	.878	0
	12	300	90.6	10.0	6	692	6	692	692	998	1,690	27.2	.324	.109	.101	6	.409	0	.591	0
	13	300	90.6	13.3	8	552	8	552	552	0	552	34.8	.303	.119	.120	8	1.00	0	0	0

Table III (cont.)

Cell Number and Plot Symbol	Run Number	Temperature °F	Acid Conc., %	Acid Flow, cc/min.	Fuel	Fuel Flow x 10 ⁶ lb-mol/hr	Fuel Flow x 10 ⁶ lb-mol/hr	Water Flow x 10 ⁶ lb-mol/hr	Total Flow x 10 ⁶ lb-mol/hr	Limiting Current, Amps/ft ²	d, volts	a, volts	c, volts	Fuel	Mol Fraction	Fuel	Mol Fraction	Water Mol Fraction
2 - 194 ○	1	300	88.3	19.1	3	557	0	0	557	232	.212	.118	.0543	3	1.00			0
	2	300	91.0	5.7	3	557	0	0	557	220	.267	.0877	.0785	3	1.00			0
	3		91.9	5.5	8	552	0	0	552	92.4	.254	.102	.108	8	1.00			0
	4		91.6	3.6	8	552	2,496	3,048	5,544	99.2	.207	.0880	.156	8	.181			.819
	5		89.5	6.5	8	552	9,985	10,537	20,522	65.8	.203	.0679	.154	8	.0524			.948
	6		90.5	3.6	8	552	4,992	5,544	10,537	81.6	.260	.0917	.127	8	.0996			.900
	7		90.3	5.0	8	552	19,970	20,522	40,492	65.4	.198	.0548	.175	8	.0269			.973
	8		91.0	4.4	8	552	2,496	3,048	5,544	68.0	.268	.0854	.139	8	.181			.819
	9		91.4	4.4	8	552	4,992	5,544	10,537	74.0	.213	.0688	.166	8	.0996			.900
	10		91.4	4.4	8	552	998	1,550	2,548	73.2	.256	.0769	.134	8	.356			.644
	11		91.3	5.7	3	1,392	0	0	1,392	116	.287	.104	.0825	8	1.00			0
	12		91.3	6.2	3	1,392	9,985	11,377	21,362	118	.157	.125	.123	3	.122			.818
	13		92.4	4.7	3	1,392	2,496	3,888	6,384	126	.193	.125	.0965	3	.358			.642
	14	300	92.1	6.0	3	1,392	4,992	6,384	11,376	130	.166	.126	.119	3	.218			.782
2 - 195 ○	1	300	91.4	31.0	6	495	495	0	991	68.4	.284	.0856	.110	6	.50	8	.50	0
	2	300	91.1	14.3	6	248	248	2,496	2,991	63.8	.237	.0770	.127	6	.0828	8	.0128	.834
	3		90.9	16.0	6	248	248	9,985	10,480	43.6	.221	.0592	.165	6	.0236	8	.0236	.953
	4		90.9	11.4	6	248	248	499	995	52.8	.277	.0708	.146	6	.249	8	.249	.502
	5		90.4	14.3	6	248	248	19,970	20,465	48.0	.206	.0634	.163	6	.0121	8	.0121	.976
	6		91.0	14.3	6	248	248	250	745	55.8	.296	.0810	.118	6	.332	8	.332	.335
	7		91.0	14.3	6	248	248	4,992	5,487	51.6	.209	.0404	.168	6	.0451	8	.0451	.910
	8		90.8	27.0	6	248	248	998	1,494	66.8	.241	.0759	.128	6	.166	8	.166	.668
	9		92.7	10.5	6	1,390	0	0	1,390	53.6	.305	.102	.0938	6	1.0	8	1.0	0
	10		92.7	11.8	6	692	692	2,496	3,188	82.4	.247	.0781	.117	6	.217	6	.217	.783
	11		91.8	11.1	6	692	692	9,985	10,677	52.4	.216	.0631	.180	6	.0648	6	.0648	.935
	12		91.6	20.0	6	692	692	499	1,191	65.4	.285	.0817	.113	6	.581	6	.581	.419
	13		91.6	21.1	6	692	692	19,970	20,662	46.8	.203	.0517	.171	6	.0335	6	.0335	.966
	14		91.5	8.0	6	692	692	250	942	64.2	.263	.0814	.129	6	.735	6	.735	.265
	15		91.7	10.0	6	692	692	4,992	5,684	68.0	.212	.0723	.137	6	.122	6	.122	.878
	16	300	91.7	8.7	6	692	692	998	1,691	62.8	.278	.0698	.115	6	.409	6	.409	.591

Table III (cont.)

Cell Number and Plot Symbol	Run Number	Temperature °F	Acid Conc., %	Acid Flow, cc/min.	Fuel	Fuel Flow x 10 ⁶ lb-mol/hr	Fuel Flow x 10 ⁶ lb-mol/hr	Water Flow x 10 ⁶ lb-mol/hr	Total Flow x 10 ⁶ lb-mol/hr	Limiting Current, Amps/ft ²	d, volts	a, volts	c, volts	Fuel	Mol Fraction	Fuel	Mol Fraction	Water Fraction
2 - 195 (Cont.)	17	300	92.8	8.0	8	1,100	0	0	1,100	61.0	.299	.0717	.310	8	1.00	0	0	0
	18	↓	92.8	13.3	8	552	2,496	2,496	3,048	63.0	.227	.0526	.168	8	.181	↓	.819	
	19	300	92.5	13.3	8	552	9,985	9,985	10,537	51.6	.204	.0575	.172	8	.0524	0	.948	
2 - 196	1	275	93.7	4.0	8	1,100	0	0	1,100	78.0	.333	.0829	.0927	8	1.00	0	0	0
	2	↑	93.0	7.3	8	1,100	250	250	1,350	69.4	.317	.0701	.134	8	.815	↑	.185	
	3	↓	94.1	5.7	8	1,100	2,496	2,496	3,596	100	.265	.0727	.113	8	.306	↓	.694	
	4	↑	94.2	2.65	8	1,100	0	0	2,492	101	.370	.0748	.0799	8	.441	↑	.559	0
	5	↓	93.4	8.0	8	1,100	250	250	2,742	87.6	.341	.0813	.0964	8	.401	↓	.508	.051
	6	275	93.1	5.3	8	1,100	2,496	2,496	4,988	94.4	.270	.0727	.148	8	.220	3	.279	.501
	7	325	95.0	4.0	8	1,100	0	0	1,100	134	.288	.0766	.105	8	1.0	0	0	0
	8	↑	95.4	4.2	8	1,100	250	250	1,350	135	.261	.0802	.116	8	.815	↑	.185	
	9	↓	94.6	4.0	8	1,100	2,496	2,496	3,596	137	.215	.0626	.154	8	.306	↓	.694	
	10	↑	94.7	2.75	8	1,100	0	0	2,492	140	.308	.0599	.111	8	.441	↑	.559	0
	11	↓	94.4	2.75	8	1,100	250	250	2,742	130	.296	.0509	.145	8	.401	↓	.508	.051
	12	325	95.2	2.2	8	1,100	2,496	2,496	4,988	139	.229	.0811	.131	8	.220	3	.279	.501
	13	350	95.3	5.2	8	1,100	0	0	1,100	128	.265	.0714	.103	8	1.0	0	0	0
	14	↑	95.2	13.3	8	1,100	250	250	1,350	136	.250	.0689	.127	8	.815	↑	.185	
	15	↓	95.6	13.3	8	1,100	2,496	2,496	3,596	141	.227	.0506	.158	8	.306	↓	.694	
	16	↑	95.8	7.3	8	1,100	0	0	2,492	146	.275	.0696	.110	8	.441	↑	.559	0
	17	↓	96.0	11.4	8	1,100	250	250	2,742	148	.244	.0598	.148	8	.401	↓	.508	.051
	18	350	97.1	11.4	8	1,100	2,496	2,496	4,988	160	.252	.0554	.176	8	.220	3	.279	.501
	19	300	96.3	6.7	8	1,100	0	0	1,100	75.4	.345	.0652	.0926	8	1.00	0	0	0
	20	↑	96.1	5.3	8	1,100	250	250	1,350	74.4	.368	.0533	.114	8	.815	↑	.185	
	21	300	95.9	6.3	8	1,100	2,496	2,496	3,596	106	.241	.0490	.183	8	.306	0	.694	
2 - 197	1	325	95.5	6.2	6	1,390	0	0	1,390	144	.258	.0588	.122	6	1.00	0	0	0
	2	↑	95.8	4.4	6	1,390	250	250	1,639	124	.267	.0595	.106	6	.848	↑	.152	
	3	↓	94.9	5.7	6	1,390	2,496	2,496	3,886	78.8	.231	.0391	.176	6	.357	↓	.643	
	4	↑	95.5	2.9	6	1,390	0	0	2,783	89.6	.258	.0351	.180	6	.499	↑	.501	0
	5	↓	95.7	2.9	6	1,390	250	250	3,033	73.0	.253	.0506	.140	6	.458	↓	.459	.093

Table III (cont.)

Cell Number and Plot Symbol	Run Number	Temperature °F	Acid Conc., %	Acid Flow, cc/min.	Fuel	Fuel Flow x 10 ⁵ lb-mol/hr	Fuel	Fuel Flow x 10 ⁵ lb-mol/hr	Water Flow x 10 ⁵ lb-mol/hr	Total Flow x 10 ⁵ lb-mol/hr	Limiting Current, Amp/ft ²	d, volts	a, volts	c, volts	Fuel	Mol Fraction	Fuel	Mol Fraction	Water Fraction
2 - 198 □	1	325	95.5	2.0	6	1,390	3	1,390	0	1,390	136	.322	.0707	.0727	9	1.00	9	1.00	0
	2	↕	94.7	5.7	6	1,390	6	1,390	250	1,690	144	.289	.0971	.0639	6	.848	6	.848	.152
	3	↕	95.6	4.0	6	1,390	6	1,390	2,496	3,886	143	.270	.0566	.119	6	.57	6	.57	.643
	4	↕	94.9	5.1	6	1,390	3	1,393	0	2,783	147	.303	.0819	.0732	6	.499	6	.499	0
	5	↕	95.8	5.7	6	1,390	3	1,393	250	3,033	149	.287	.0921	.0710	6	.458	6	.458	.093
	6	↕	94.8	4.3	6	1,390	3	1,393	2,496	3,279	147	.251	.0669	.114	6	.263	6	.263	.474
	7	↕	95.9	3.2	6	1,390	6	1,390	0	1,390	154	.265	.0838	.0970	6	1.00	6	1.00	0
	8	↕	95.4	3.9	6	1,390	6	1,390	250	1,639	154	.263	.0783	.109	6	.848	6	.848	.152
	9	↕	95.4	2.8	6	1,390	6	1,390	2,496	3,886	155	.241	.0718	.119	6	.357	6	.357	.643
	10	350	96.4	3.0	6	1,390	3	1,393	0	2,783	154	.301	.0841	.0626	6	.499	6	.499	0
2 - 200 ▽	1	350	96.0	3.2	6	1,390	3	1,393	0	2,783	156	.280	.0786	.105	6	.499	6	.499	0
	2	↕	95.2	10.0	6	1,390	3	1,393	250	3,033	149	.248	.0821	.112	6	.458	6	.458	.093
	3	350	95.2	2.9	6	1,390	3	1,393	2,496	5,279	153	.229	.0842	.135	6	.263	6	.263	.474
	4	300	95.6	3.2	6	1,390	6	1,390	0	1,390	156	.344	.0967	.0560	6	1.00	6	1.00	0
	5	↕	95.0	5.9	6	1,390	6	1,390	250	1,639	154	.284	.108	.0879	6	.848	6	.848	.152
	6	↕	95.5	6.5	6	1,390	6	1,390	2,496	3,886	157	.261	.0897	.0924	6	.357	6	.357	.643
	7	↕	95.2	3.1	6	1,390	3	1,393	0	2,783	151	.347	.0847	.0752	6	.499	6	.499	0
	8	↕	95.3	2.4	6	1,390	3	1,393	250	3,033	152	.308	.108	.0665	6	.458	6	.458	.043
	9	300	95.0	4.4	6	1,390	3	1,393	2,496	5,279	156	.251	.0763	.118	6	.263	6	.263	.474
	10	325	95.1	4.0	3	1,393	3	1,393	0	1,393	167	.309	.0767	.0984	3	1.00	3	1.00	0
	11	↕	95.2	3.2	3	1,393	3	1,393	250	1,643	166	.293	.0837	.0833	3	.847	3	.847	.153
	12	325	96.0	4.0	3	1,393	3	1,393	2,496	3,889	172	.211	.0722	.147	3	.358	3	.358	.642
	13	350	95.3	4.4	3	1,393	3	1,393	0	1,393	169	.308	.0572	.122	3	1.00	3	1.00	0
	14	↕	95.5	5.3	3	1,393	3	1,393	250	1,643	174	.286	.0662	.122	3	.847	3	.847	.153
	15	350	95.6	5.0	3	1,393	3	1,393	2,496	3,889	176	.240	.0534	.162	3	.358	3	.358	.642
	16	300	95.0	2.9	3	1,393	3	1,393	0	1,393	156	.363	.0763	.0915	3	1.00	3	1.00	0
	17	↕	94.5	2.0	3	1,393	3	1,393	250	1,643	162	.296	.0855	.0974	3	.847	3	.847	.153
	18	300	92.7	6.7	3	1,393	3	1,393	2,496	3,889	168	.319	.0752	.102	3	.358	3	.358	.642

Table IV

Cell Number and Plot Symbol	Run Number	Temperature, °F	3 - Propane Fuel 6 - Hexane 8 - Octane	d, volts	a, volts	c, volts	Acid V. P. (mm Hg) $X_A = \frac{760}{760 + \text{mm Hg}}$	X_{H_2O} - Mol Fraction Water in Fuel Stream	$\frac{(1 - X_{H_2O})}{X_A}$	I_L - Limiting Current, Amps/ft ²	n = equiv. of elect. Propane = 20 Hexane = 38 Octane = 50	$X_F^{1/2}$ X_F = Mol Fraction of Fuel	I_L^n $X_F^{1/2}$ $\times 10^{-5}$
2 - 189 ○	5	300	3/8	.171	.130	.101	.473	.818	.382	215	20	.427	10.0
	6	↕	3	.163	.0719	.156	.427	.973	.063	125	↕	.165	15.2
	7	↕	3	.143	.116	.139	.421	.947	.125	157	↕	.230	13.6
	8	↕	3	.203	.127	.0754	.414	.642	.864	214	↕	.600	7.13
	9	↕	3	.280	.114	.0712	.355	0	2.816	149	20	1.00	2.98
	10	↕	8	.203	.0980	.197	.355	.948	.147	112	50	.229	24.4
	11	300	8	.192	.104	.133	.361	.900	.275	90.9	↕	.316	12.8
2 - 190 □	1	300	8	.171	.151	.158	.638	.948	.082	54.0	↕	.229	11.8
	2	↕	8	.200	.108	.168	.638	.900	.156	58.0	↕	.316	9.18
	3	↕	8	.203	.122	.147	.657	.819	.275	68.0	↕	.426	8.01
	4	↕	8	.216	.135	.0984	.657	.644	.541	57.2	↕	.597	4.80
	5	↕	8	.206	.139	.116	.559	.475	.939	46.8	↕	.725	3.23
	6	↕	8	.242	.109	.144	.559	.311	1.232	50.3	50	.830	3.02
	7	↕	3	.193	.123	.0789	.559	0	1.788	168.8	20	1.00	3.36
	9	↕	3	.126	.0940	.157	.631	.818	.288	150.	↕	.427	7.02
	10	300	3	.100	.0972	.169	.631	.947	.0836	86.0	↕	.230	7.48
2 - 191 Δ	2	300	3	.145	.125	.103	.520	.818	.350	235	↕	.427	11.0
	3	↕	3	.150	.0904	.138	.493	.947	.107	169	↕	.230	14.7
	4	↕	3	.175	.0555	.173	.592	.973	.045	103	↕	.165	12.4
	5	↕	3	.180	.0951	.121	.592	.900	.168	191	↕	.316	12.1
	6	↕	3	.204	.107	.0895	.611	.642	.585	258	↕	.598	8.63
	7	↕	3	.272	.0789	.0848	.552	.309	1.251	278	↕	.832	6.68
	8	↕	3	.232	.102	.0711	.486	.473	1.084	278	20	.726	7.65
	9	↕	8	.246	.0823	.137	.460	.644	.773	102	50	.596	8.56
	10	↕	8	.207	.0922	.144	.460	.948	.133	96.2	↕	.229	21.0
	11	↕	8	.229	.0907	.152	.500	.819	.362	96.0	↕	.426	11.3
	12	↕	8	.195	.0810	.163	.500	.973	.0538	78.0	↕	.164	23.8
	13	↕	8	.229	.124	.123	.513	.475	1.023	114	↕	.724	7.90
	14	↕	8	.201	.0793	.165	.513	.900	.194	110	↕	.316	17.4
	15	↕	8	.277	.0867	.0965	.447	.311	1.541	109	50	.830	6.57
	16	↕	3/8	.273	.0991	.0789	.447	0	2.237	113			
	17	↕	3/8	.283	.0778	.0912	.352	0	2.840	116			
	18	↕	3/8	.285	.0899	.0937	.352	0	2.840	112			
	19	↕	3/8	.284	.0746	.0988	.263	0	3.802	156			
	20	↕	3/8	.325	.0707	.0933	.263	0	3.802	96.6			
	21	300	3/6	.317	.0925	.0548	.221	0	4.524	235			
	22	300	3/6	.311	.0900	.0486	.221	0	4.524	238			

Table IV (Cont.)

Cell Number and Plot Symbol	Run Number	Temperature, °F	Fuel 3 - Propane 6 - Hexane 8 - Octane	d, volts	a, volts	c, volts	$X_A =$ Acid V.P. (mm Hg) 760 (mm Hg)	X_{H_2O} - Mol Fraction Water in Fuel Stream	$(1 - X_{H_2O})$ X_A	I_L - Limiting Current, Amps/ft ²	n = equiv. of elect. Propane = 20 Hexane = 38 Octane = 50	$X_F^{1/2}$ X_F = Mol Fraction of Fuel	$\frac{I_L n}{X_F^{1/2}} \times 10^{-3}$
2 - 191 (Cont) Δ	23	300	3/6	.350	.103	.0220	.193	0	4.524	238			
	24		3/6	.326	.0884	.0413	.157	↑	6.369	244			
	25		3/6	.389	.0932	.0420	.138		7.246	98.6			
	26		3/8	.329	.0790	.0819	.105		9.523	113			
	27		3/8	.324	.0901	.0792	.105		9.53	103			
	28		3/8	.234	.117	.0651	.103		9.708	152			
	29		3/8	.323	.0978	.0683	.086		11.627	75.0			
	30		3/8	.297	.103	.0579	.086		11.627	144			
	31		8	.218	.0726	.166	.710		1.408	119	50	1.00	5.95
	32		6	.182	.0682	.162	.710		1.408	175	38	1.00	7.01
2 - 192 \diamond	5	300	6	.318	.136	.0780	.389	0	2.570	43.8	38	1.00	1.75
	6		6	.270	.104	.114	.368	.783	.589	55.0	↑	.466	4.73
	7		6	.240	.106	.139	.368	.935	.176	49.0		.255	7.68
	8		6	.322	.129	.0896	.381	.878	.320	30.4		.350	3.47
	9		6	.239	.0908	.145	.381	.966	.087	31.8		.183	6.96
	10		6	.319	.129	.0729	.427	.265	1.721	35.6		.858	1.66
	11		6	.252	.115	.14	.427	.878	.285	33.8		.350	3.86
	12		6	.324	.109	.101	.460	.591	.889	27.2		.640	1.70
	13		8	.303	.119	.120	.460	0	2.171	34.8		1.00	1.74
2 - 194 \circ	1	300	3	.212	.118	.0543	.585	0	1.709	232	20	1.00	4.64
	2		3	.267	.0877	.0785	.434	0	2.304	220	20	1.00	4.40
	3		8	.254	.102	.108	.381	0	2.624	92.4	50	1.00	4.62
	4		8	.207	.0880	.156	.394	.819	.459	99.2	↑	.426	11.6
	5		8	.203	.0679	.154	.532	.948	.098	65.8		.229	14.3
	6		8	.260	.0917	.127	.467	.900	.213	81.6		.316	12.9
	7		8	.198	.0548	.175	.480	.973	.056	65.4		.164	19.9
	8		8	.268	.0854	.139	.434	.819	.417	68.0		.426	7.98
	9		8	.213	.0688	.166	.407	.900	.244	74.0		.316	11.7
	10		8	.256	.0769	.134	.407	.644	.874	73.2		.597	6.13
	11		3	.287	.104	.0825	.414	0	2.415	116		1.00	2.32
	12		3	.157	.125	.123	.414	.878	.294	118		.350	6.74
	13		3	.193	.125	.0965	.355	.642	1.008	126		.599	4.20
	14		3	.166	.126	.119	.368	.782	.592	130		.467	5.58

Table IV (Cont.)

Cell Number and Plot Symbol	Run Number	Temperature, °F	3 - Propane Fuel 6 - Hexane 8 - Octane	d, volts	a, volts	c, volts	$X_A = \frac{\text{Acid V.P. (mm Hg)}}{760 \text{ (mm Hg)}}$	X_{H_2O} - Mol Fraction Water in Fuel Stream	$\frac{(1 - X_{H_2O})}{X_A}$	I_L - Limiting Current, Amps/ft ² n = equiv. of elect. Propane = 20 Hexane = 50 Octane = 50	$X_F^{1/2}$ X_F = Mol Fraction of Fuel	$\frac{I_L n}{X_F^{1/2}} \times 10^{-3}$	
2 - 195 ▽	1	300	3/8	.284	.0856	.110	.407	0	2.457	68.4			
	2	↑	6/8	.237	.0770	.127	.427	.834	.388	63.8			
	3		6/8	.221	.0592	.165	.440	.953	.106	43.6			
	4		6/8	.277	.0708	.146	.440	.502	1.131	52.8			
	5		6/8	.206	.0634	.163	.473	.975	.050	48.0			
	6		6/8	.296	.0810	.118	.434	.335	1.527	55.8			
	7		6/8	.209	.0404	.168	.434	.910	.207	51.6			
	8		6/8	.241	.0759	.128	.447	.668	.742	66.8			
	9		6	.305	.102	.098	.335	0	2.985	53.6	38	1.00	2.14
	10		6	.247	.0781	.111	.335	.783	.647	82.4	↑	.466	7.08
	11		6	.216	.0631	.180	.384	.935	.168	52.4		.254	8.25
	12		6	.285	.0817	.113	.394	.419	1.474	65.4		.763	3.43
	13		6	.203	.0517	.171	.394	.966	.085	46.8		.183	10.2
	14		6	.263	.0814	.129	.401	.265	1.832	64.2		.858	2.99
	15		6	.212	.0723	.137	.388	.878	.314	68.0	↓	.349	7.79
	16		6	.278	.0698	.115	.388	.591	1.054	62.8	38	.640	3.92
	17		8	.299	.0717	.130	.328	0	3.048	61.0	50	1.00	3.05
	18		8	.227	.0526	.168	.328	.819	.551	63.0	↑	.426	7.39
	19	300	8	.204	.0575	.172	.346	.948	.151	51.6		.229	11.2
2 - 196 ◻	1	275	8	.333	.0829	.0927	.171	0	5.847	78.0		1.00	3.90
	2	↑	8	.317	.0701	.134	.197	.185	4.137	69.4	↓	.903	3.84
	3		8	.265	.0727	.113	.155	.694	1.974	100	50	.553	9.08
	4		3/8	.370	.0748	.0799	.151	0	6.622	101	↑		
	5		3/8	.341	.0813	.0964	.181	.051	5.243	87.6			
	6	275	3/8	.270	.0727	.148	.188	.501	2.654	94.4	↓		
	7	325	8	.288	.0766	.105	.328	0	3.048	134	50	1.00	6.72
	8	↑	8	.261	.0802	.116	.185	.185	2.698	135	50	.903	7.50
	9		8	.215	.0626	.154	.355	.694	.861	137	50	.551	12.4
	10		3/8	.308	.0599	.111	.355	0	2.816	140	↑		
	11	↓	3/8	.296	.0509	.145	.368	.051	2.578	130			
	12	325	3/8	.229	.0811	.131	.322	.501	1.547	139	↓		
	13	350	8	.265	.0714	.103	.500	0	2.000	128	50	1.00	6.42
	14	↑	8	.250	.0689	.127	.493	.185	1.653	136	50	.903	7.54
	15		8	.227	.0506	.158	.460	.694	.665	141	50	.553	12.7
	16	↓	3/8	.275	.0696	.110	.414	0	2.415	146			
	17	350	3/8	.244	.0598	.148	.401	.051	2.366	149	↓		

Table IV (Cont.)

Cell Number and Plot Symbol	Run Number	Temperature, °F	3 - Propane 6 - Hexane 8 - Octane	d, volts	a, volts	c, volts	$X_A = \frac{\text{Acid V. P. (mm Hg)}}{760 \text{ (mm Hg)}}$	X_{H_2O} - Mol Fraction Water in Fuel Stream	$\frac{(1 - X_{H_2O})}{X_A}$	I_L - Limiting Current, Amps/ft ²	n = equiv. of elect. Propane = 20 Hexane = 38 Octane = 50	$X_F^{1/2}$ X_F = Mol Fraction of Fuel	$\frac{I_L^n}{X_F^{1/2}} \times 10^{-3}$
2 - 196 (Cont)	18	350	3/8	.252	.0553	.176	.328	.501	1.5	160			
	19	300	8	.345	.0652	.0926	.147	0	6.8	75.4	50	1.00	3.77
	20	300	8	.368	.0533	.114	.160	.185	5.0	74.4	50	.903	4.12
	21	300	8	.241	.0490	.183	.168	.695	1.821	106	50	.553	9.61
2 - 197 Δ	1	325	6	.258	.0588	.122	.301	0	3.322	144	38	1.00	5.76
	2	325	6	.267	.0595	.106	.282	.152	3.007	127	38	.920	5.39
	3	325	6	.231	.0391	.176	.394	.643	.906	78.8	38	.598	5.27
	4	325	3/6	.258	.0351	.180	.301	0	3.322	89.6	38		
	5	325	3/6	.253	.0506	.140	.289	.093	3.138	73.0	38		
2 - 198 \square	1	325	6	.322	.0707	.0727	.289	0	3.460	136	38	1.00	5.44
	2	325	6	.289	.0971	.0639	.348	.152	2.436	144	38	.920	6.26
	3	325	6	.270	.0566	.119	.276	.643	1.293	143	38	.598	9.56
	4	325	3/6	.303	.0819	.0732	.342	0	2.923	147	38		
	5	325	3/6	.287	.0921	.0710	.269	.093	3.371	149			
	6	325	3/6	.251	.0669	.114	.348	.474	1.511	147			
	7	350	6	.265	.0838	.0970	.401	0	2.493	154	38	1.00	6.16
	8	350	6	.263	.0783	.109	.434	.152	1.953	154	38	.920	6.69
	9	350	6	.241	.0718	.119	.440	.643	.811	155	38	.598	10.37
	10	350	3/6	.301	.0840	.0626	.355	0	2.816	154			
2 - 200 \triangle	1	350	3/6	.280	.0788	.105	.414	0	2.415	156			
	2	350	3/6	.248	.0821	.112	.486	.093	1.866	149			
	3	350	3/6	.229	.0842	.135	.500	.474	1.052	153			
	4	300	6	.344	.0967	.0560	.177	0	5.649	156	38	1.00	6.24
	5	300	6	.284	.108	.0879	.210	.152	4.038	154	38	.920	6.69
	6	300	6	.261	.0897	.0924	.184	.643	1.940	157	38	.598	10.50
	7	300	3/6	.347	.0847	.0752	.197	0	5.076	151			
	8	300	3/6	.308	.108	.0665	.190	.093	4.773	152			
	9	300	3/6	.251	.0763	.118	.210	.474	2.257	156			
	10	325	3	.309	.0767	.0984	.322	0	3.105	167	20	1.00	3.34
	11	325	3	.293	.0837	.0833	.315	.153	2.688	166	20	.92	3.61
	12	325	3	.211	.0722	.147	.250	.642	1.432	172	20	.598	5.75
	13	350	3	.308	.0572	.122	.500	0	2.000	169	20	1.00	3.38
	14	350	3	.286	.0662	.122	.468	.153	1.810	174	20	.92	3.78
	15	350	3	.240	.0534	.162	.461	.642	.778	176	20	.598	5.89
	16	300	3	.363	.0763	.0915	.211	0	4.740	156	20	1.00	3.12
	17	300	3	.296	.0855	.0974	.231	.153	3.660	162	20	.92	3.52
	18	300	3	.319	.0752	.102	.329	.642	1.090	168	20	.598	5.62

Table V.

Cell	Electrode No.	Mix First Side	Mix Second Side	Screen	Film (Teflon)	Notes
2-189	3180	Pt-10% T-30 (1.2g)	Pt-10% T-30 (1.2g)	New Ta	Std. sp. sin. (650°F for 3.5 min.)	Masked
2-190	5110	Pt-10% T-30 (1.2g)	Pt-10% T-30 (1.2g)	New Ta	Masking pressed, film only sintered Pilot Plant 40 mg/in ² (8X normal)	Fluffy
2-191	3199	Pt-10% T-30 (1.2g)	Pt-10% T-30 (1.2g)	New Ta	Pilot Plant 40 mg/in ² (8X normal)	Fluffy
2-192	824	Pt-30% T-30 (1.2g)	Pt-10% T-30 (1.2g)	New Ta	Std. sp. sin. (650°F for 3.5 min.)	Film Pressed
2-194	3221	Pt-10% T-30 (1.2g)	Pt-10% T-30 (1.2g)	New Pt	Pilot Plant 40 mg/in ² (8X normal)	Fluffy
2-195	3222	Pt-10% T-30 (1.2g)	Pt-10% T-30 (1.2g)	New Pt	Pilot Plant 40 mg/in ² (8X normal)	Fluffy
2-196	5146	Pt-10% T-30 (1.2g)	Pt-10% T-30 (1.2g)	New Pt	Four x std. load sp. sin. (650°F-15 min)	Fluffy
2-197	5147	Pt-10% T-30 (1.2g)	Pt-10% T-30 (1.2g)	New Pt	Double std. load sp. sin. (650°F-6 min)	Fluffy
2-198	5173	Pt-10% T-30 (1.2g)	Pt-10% T-30 (1.2g)	New Pt	Four x std. load sp. sin. (650°F-15 min)	Fluffy
2-200	5185	Pt-10% T-30 (1.2g)	Pt-10% T-30 (1.2g)	New Pt	Four x std. load sp. sin. (650°F-15 min)	Fluffy

Notes: (1) Teflon Film

The Pilot Plant films are sintered at 650°F for 50 minutes (not pressed).

Std. load = about 5 mg/inch²; sp = sprayed, std = standard; sin = sintered.

Only 824 has a pressed film.

(2) Pt. Loading

2.4 gr on 58 cm² total area for all except electrode #824.

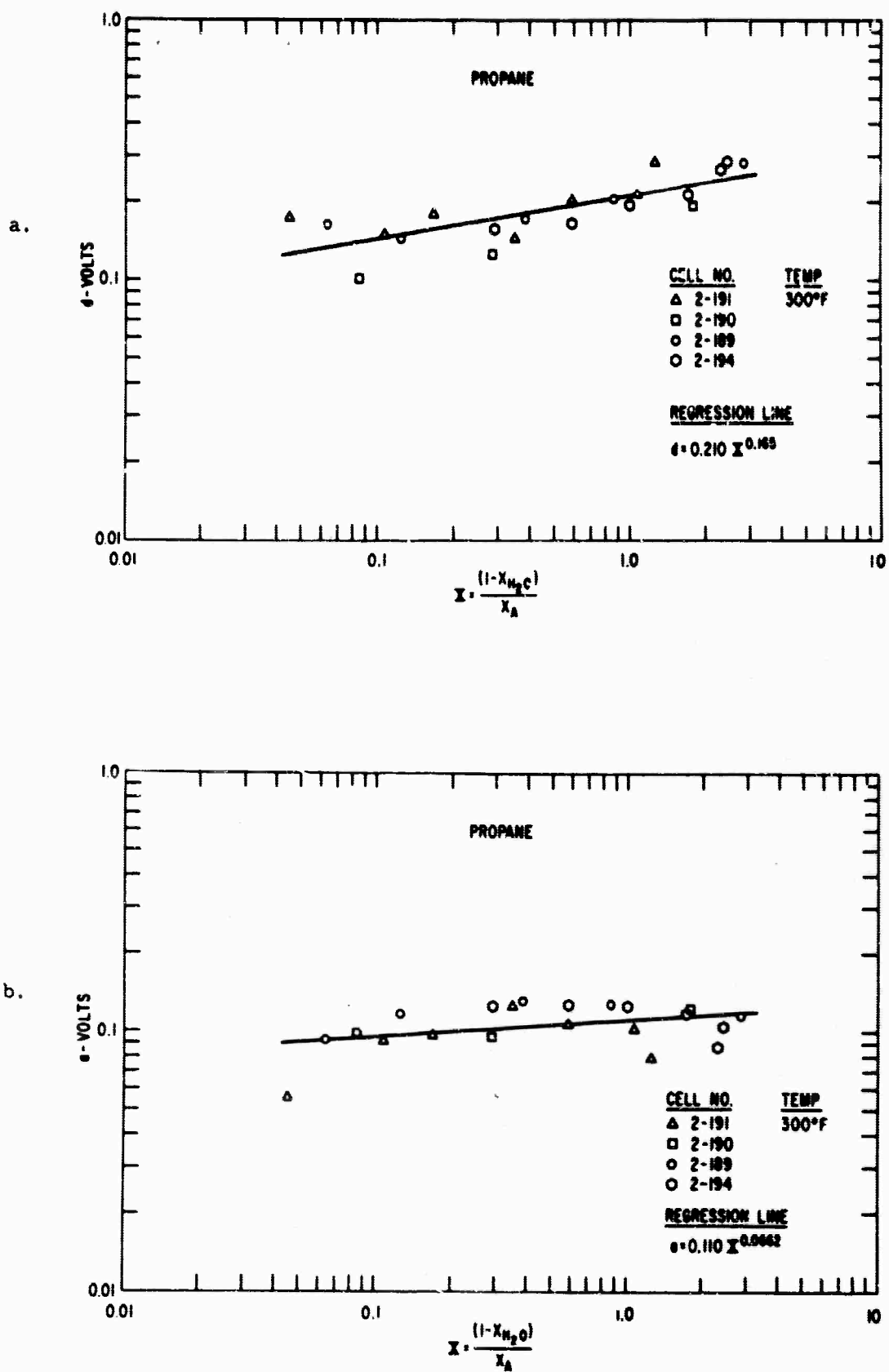
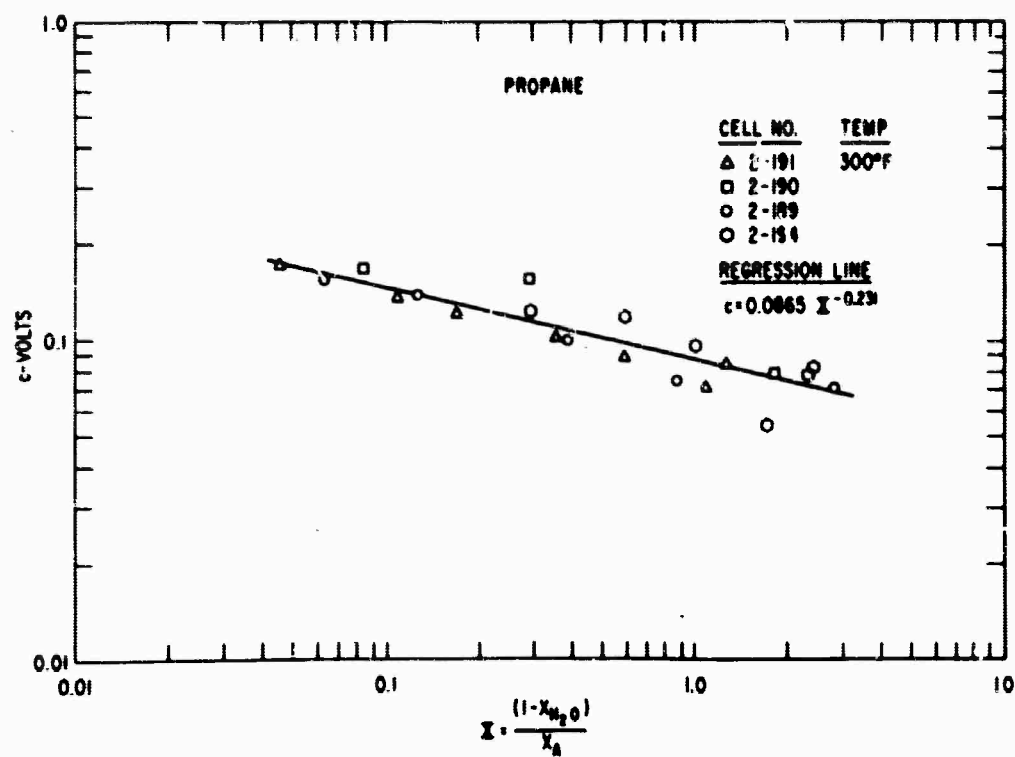


Fig. 1 Correlation of Coefficients of Over-Voltage Equation with Water Vapor

c.



d.

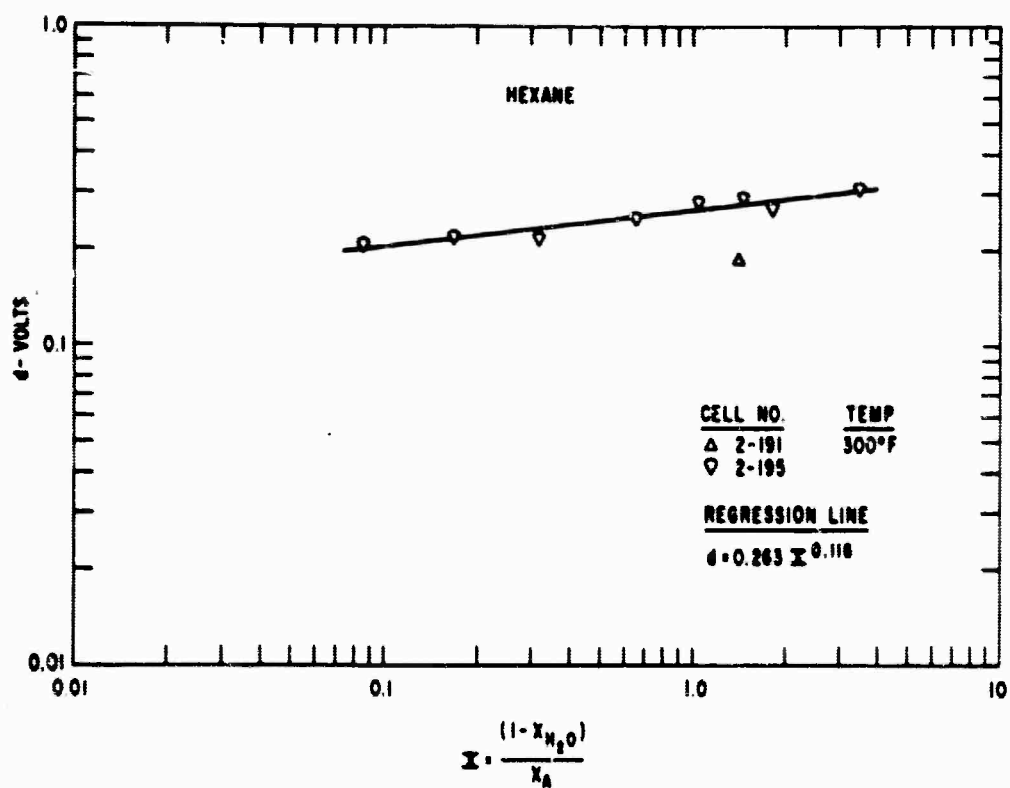


Fig. 1 (Cont.)

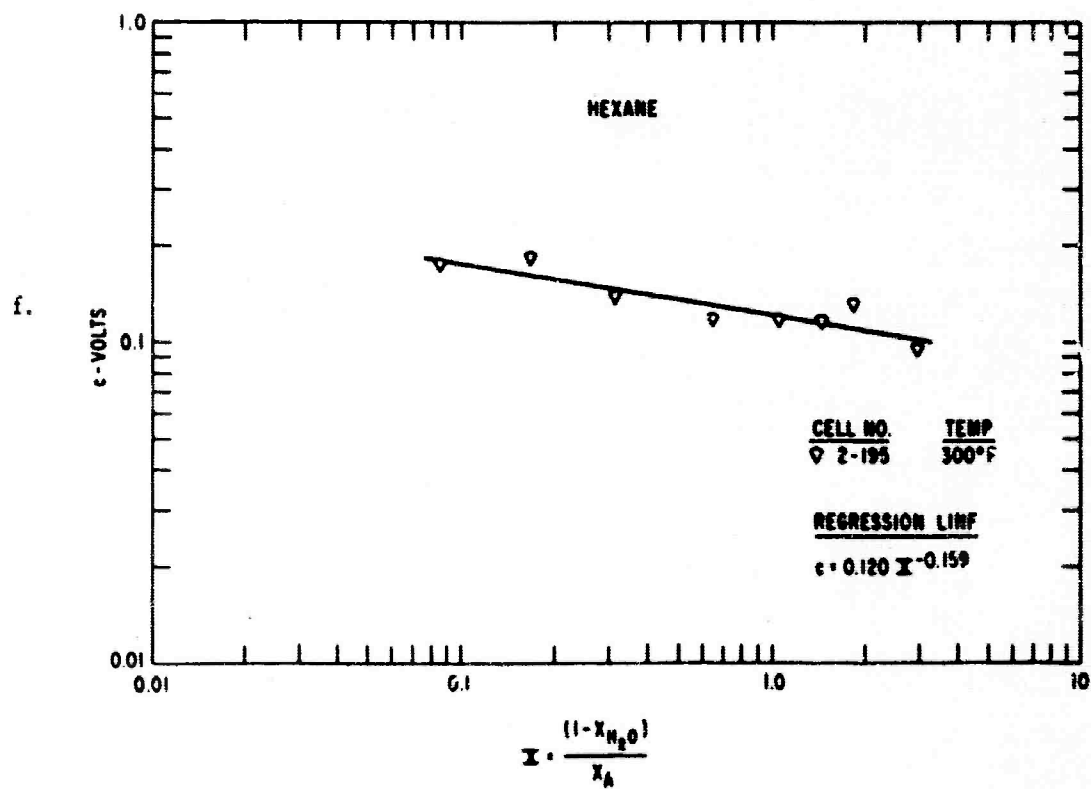
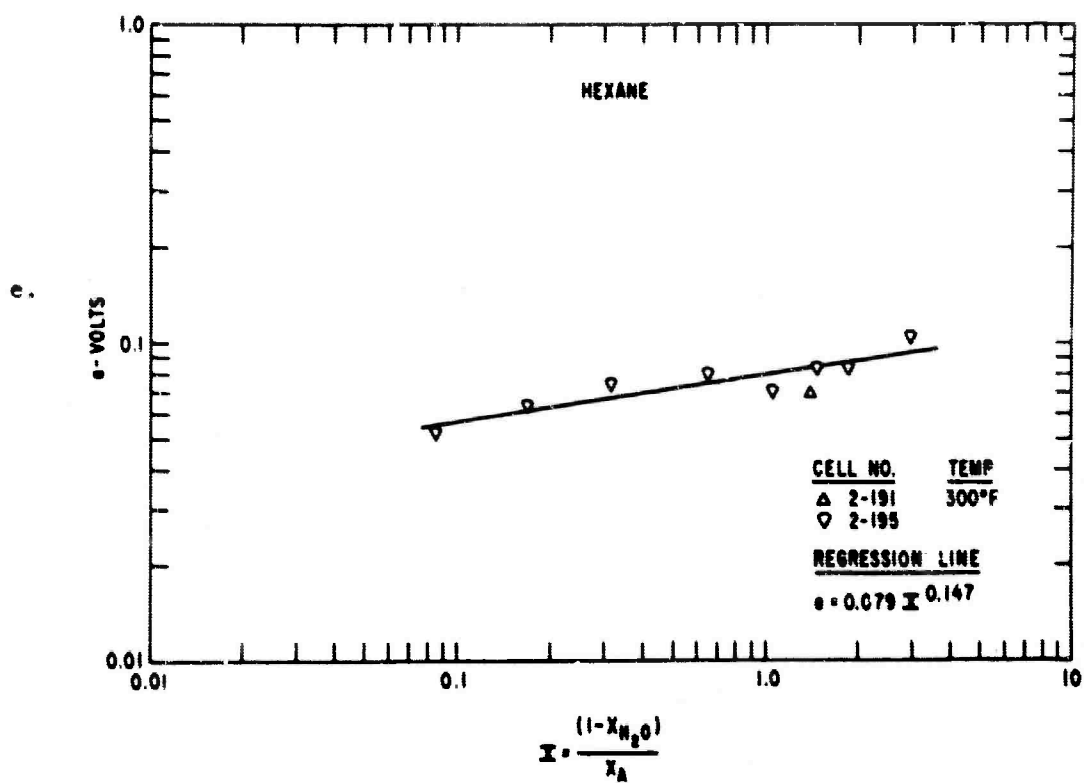
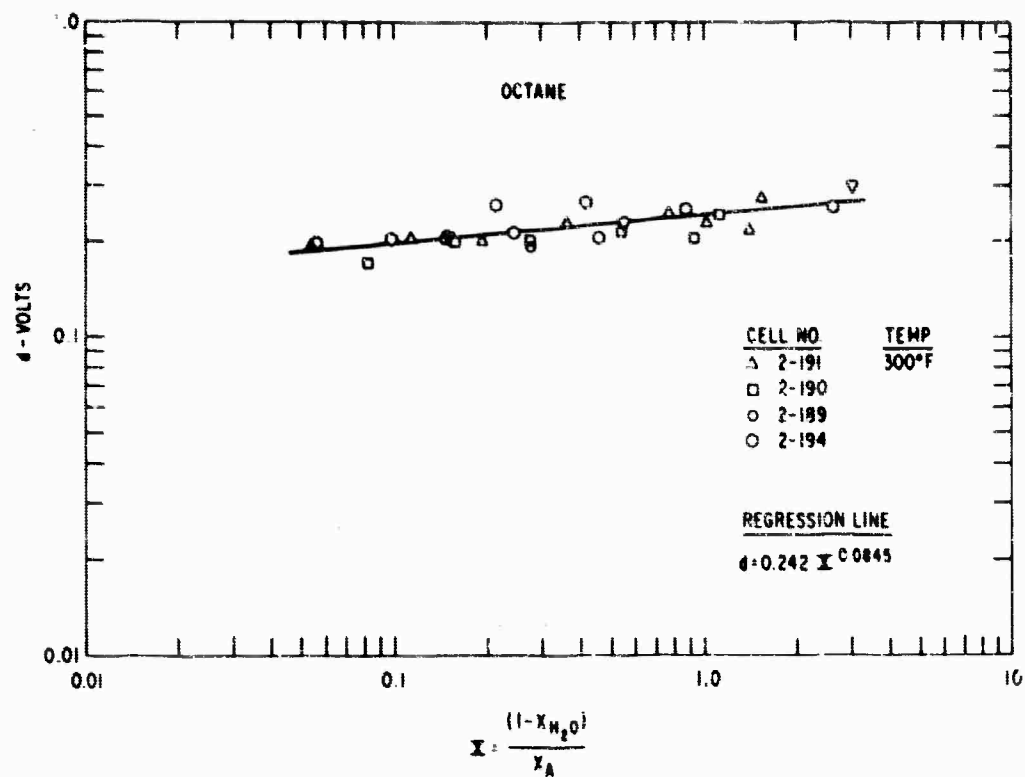


Fig. 1 (Cont.)

g.



h.

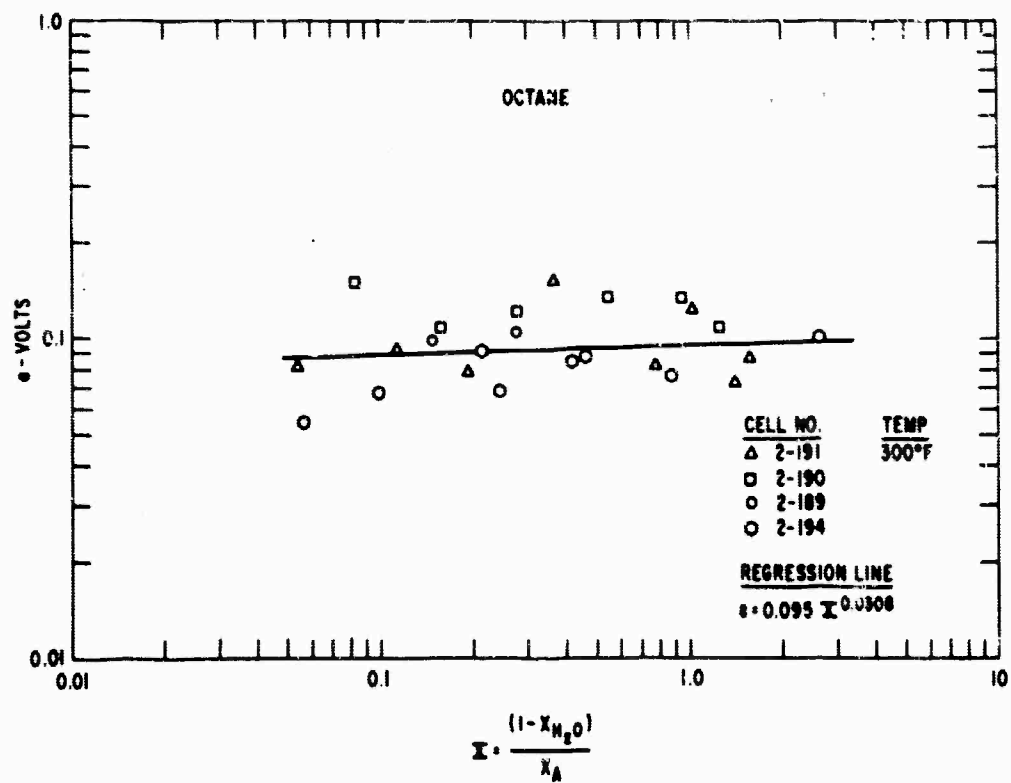


Fig. 1 (Cont.)

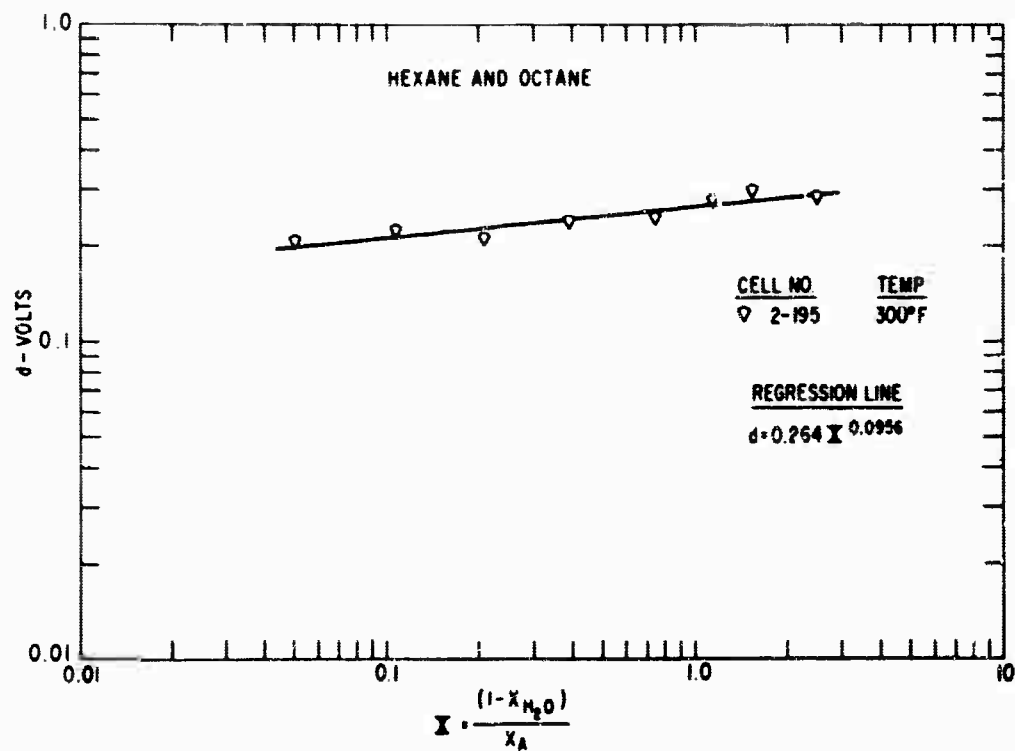
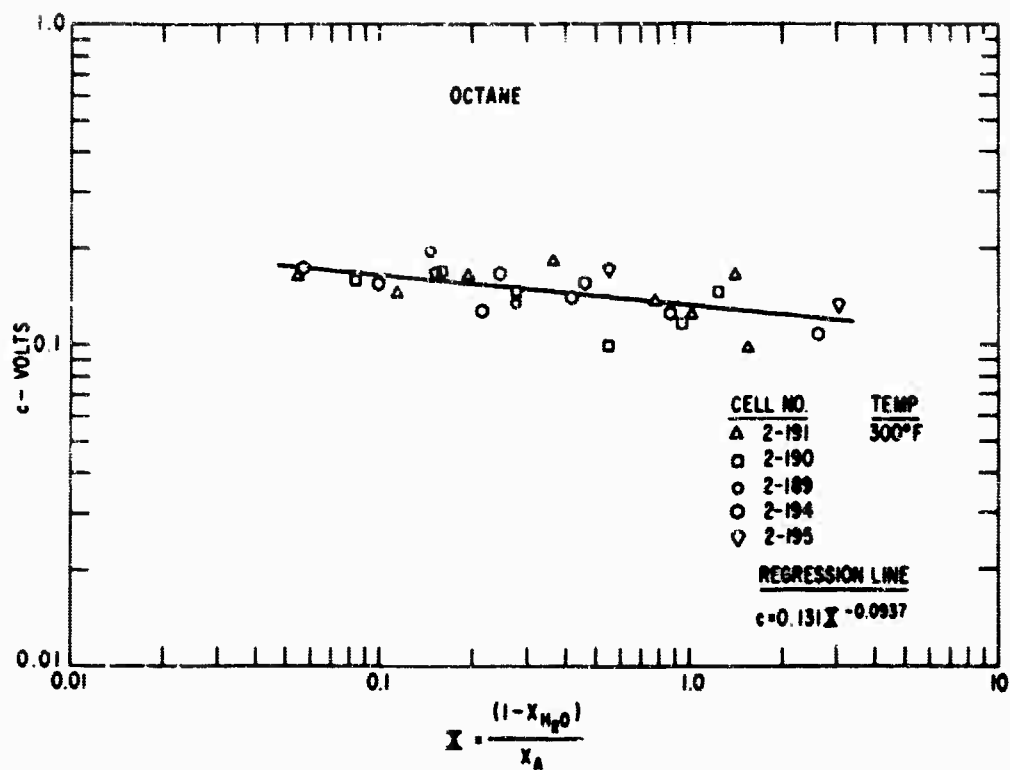


Fig. 1 (Cont.)

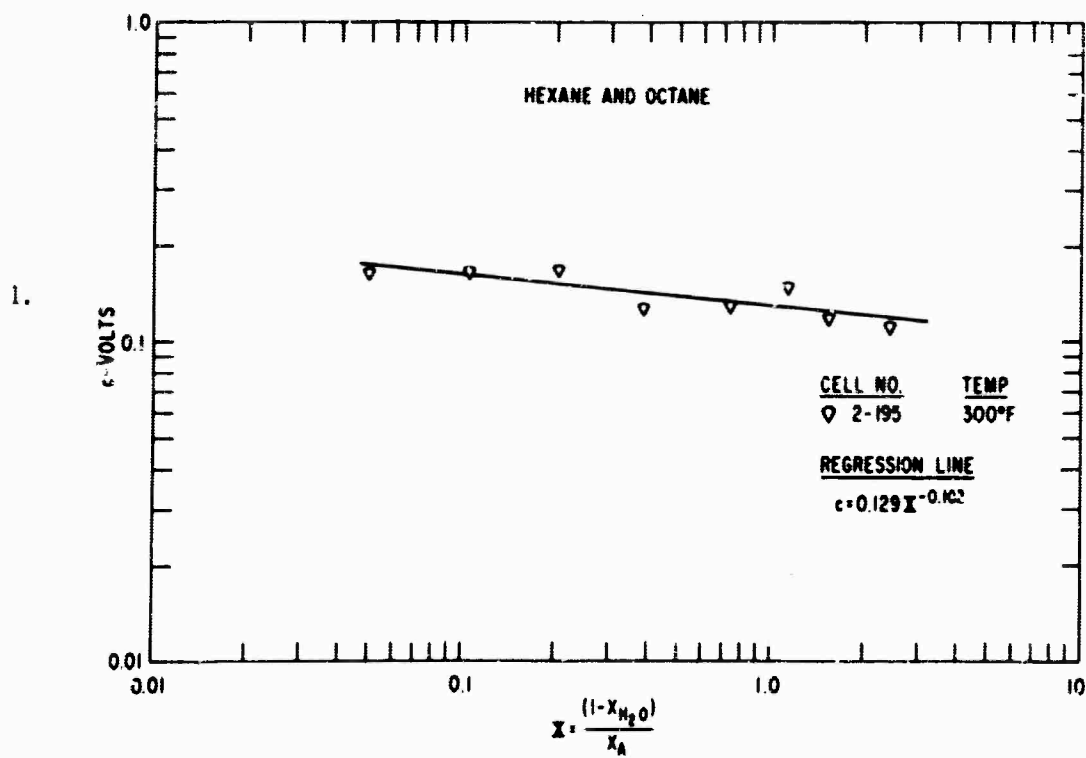
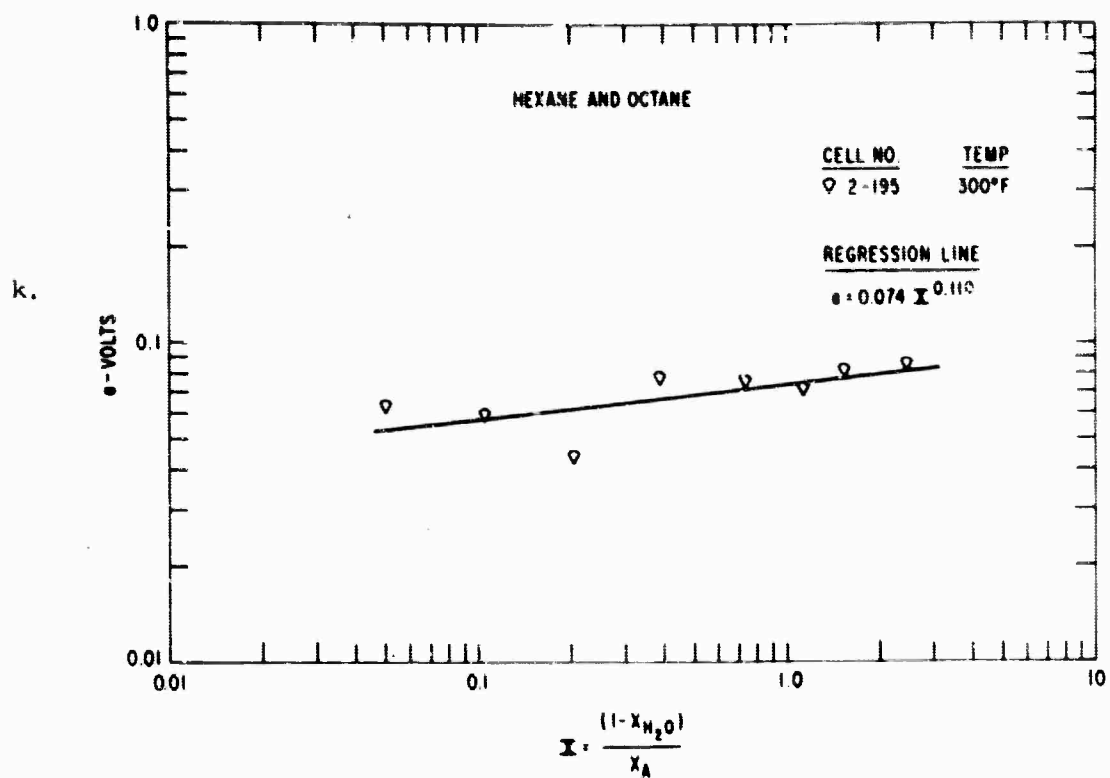
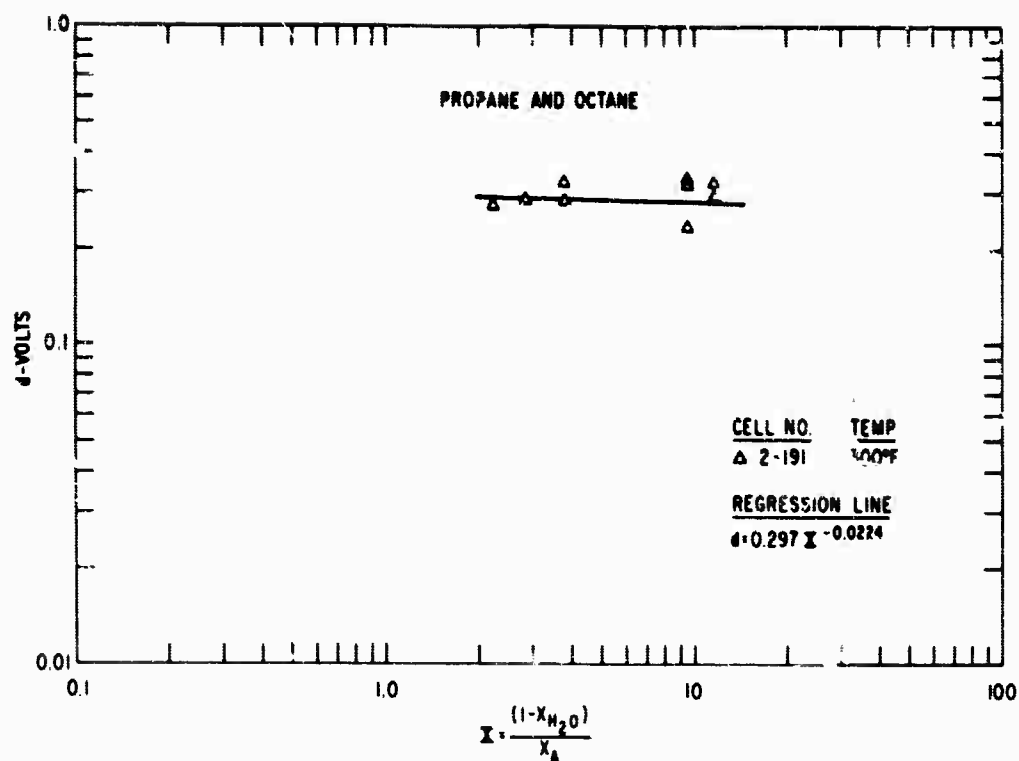


Fig. 1 (Cont.)

m.



n.

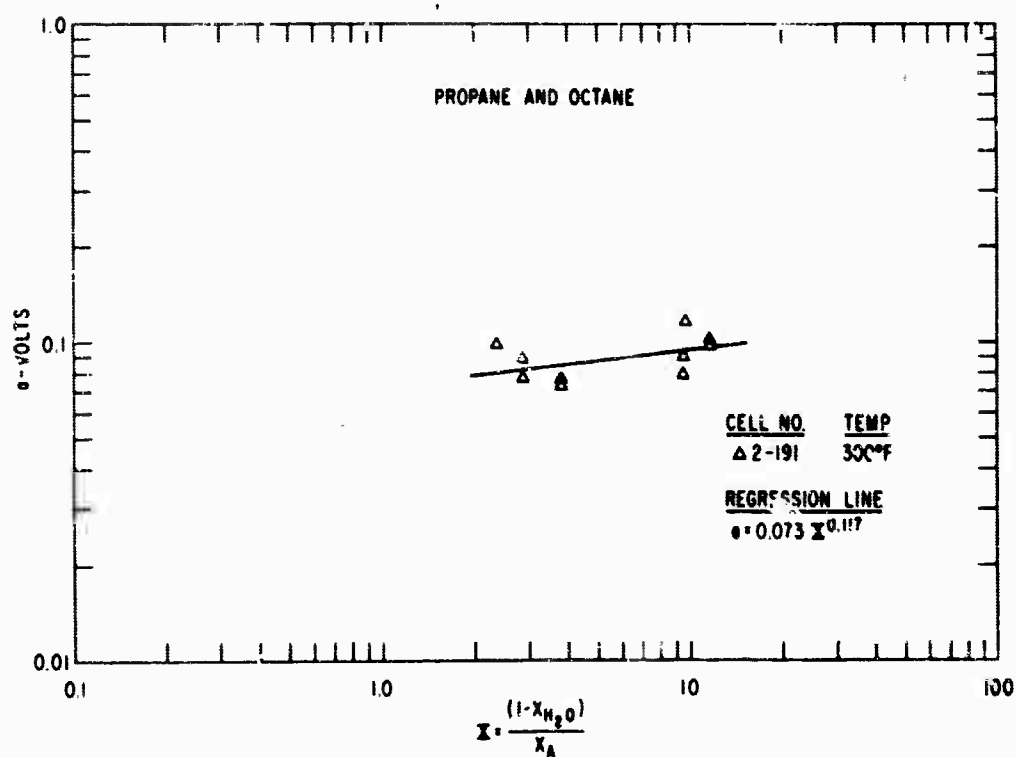


Fig. 1 (Cont.)

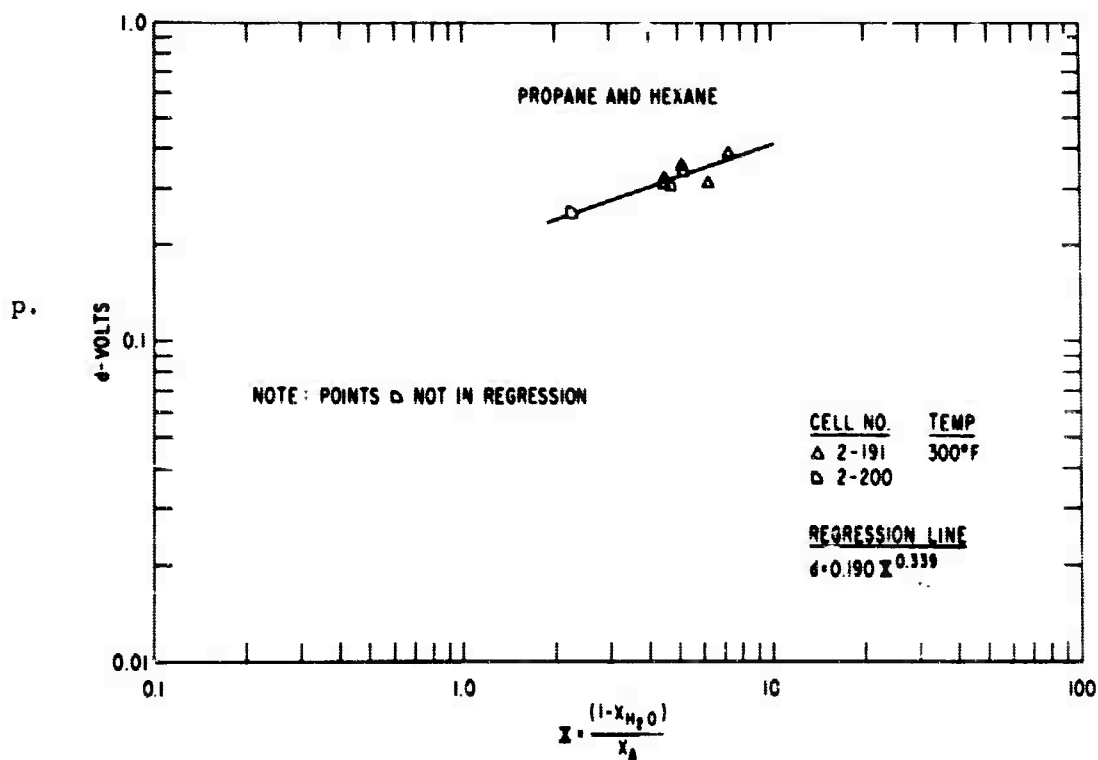
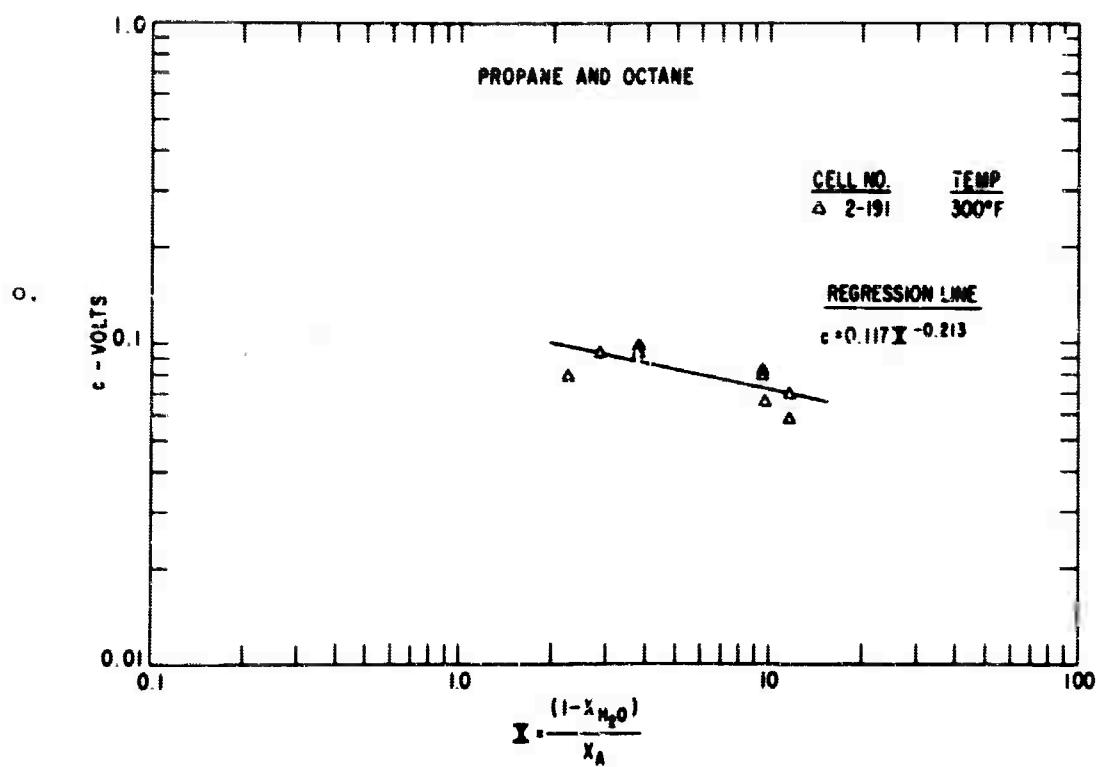


Fig. 1 (Cont.)

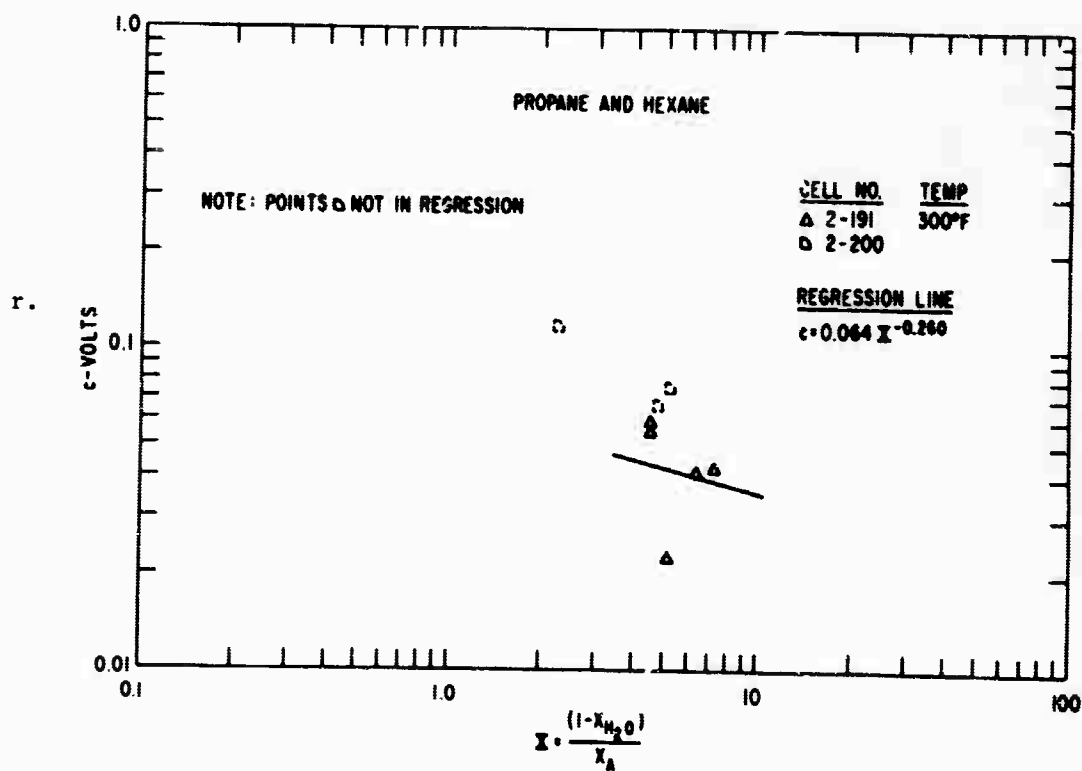
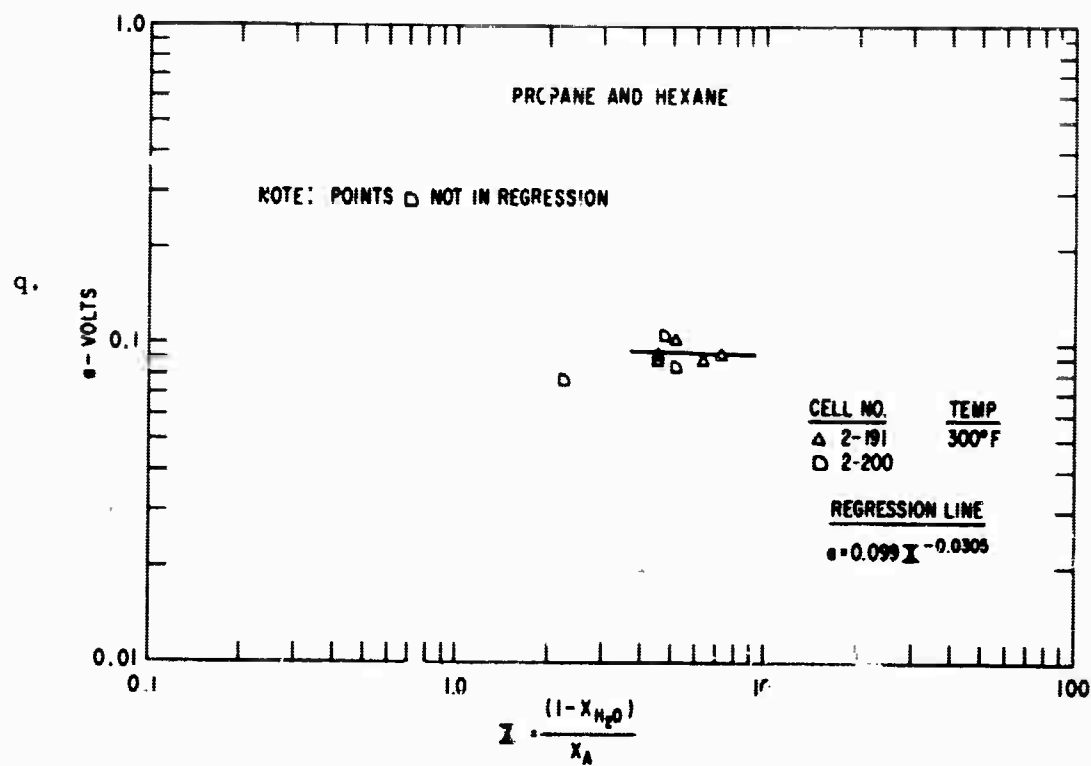


Fig. 1 (Cont.)

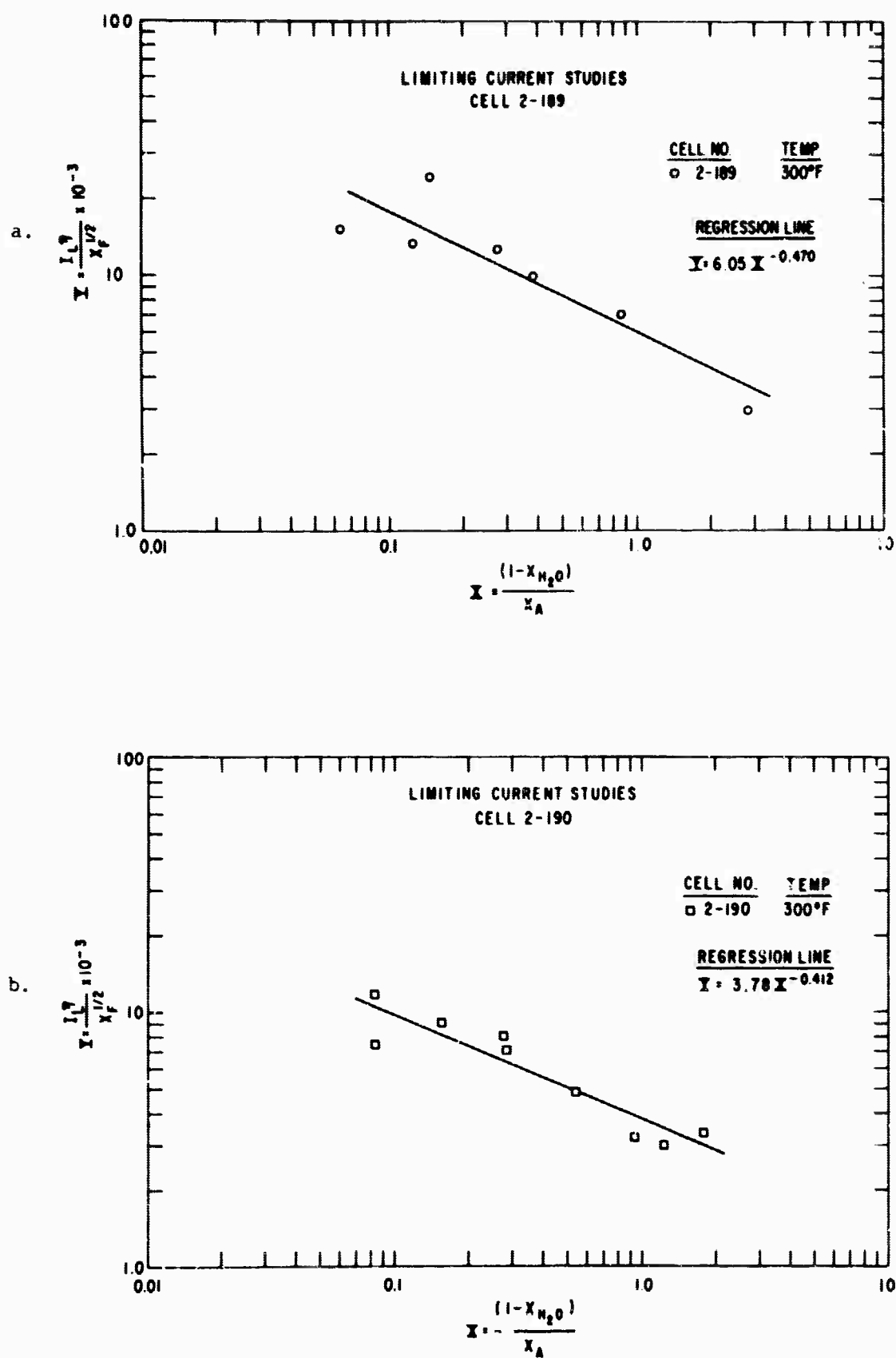
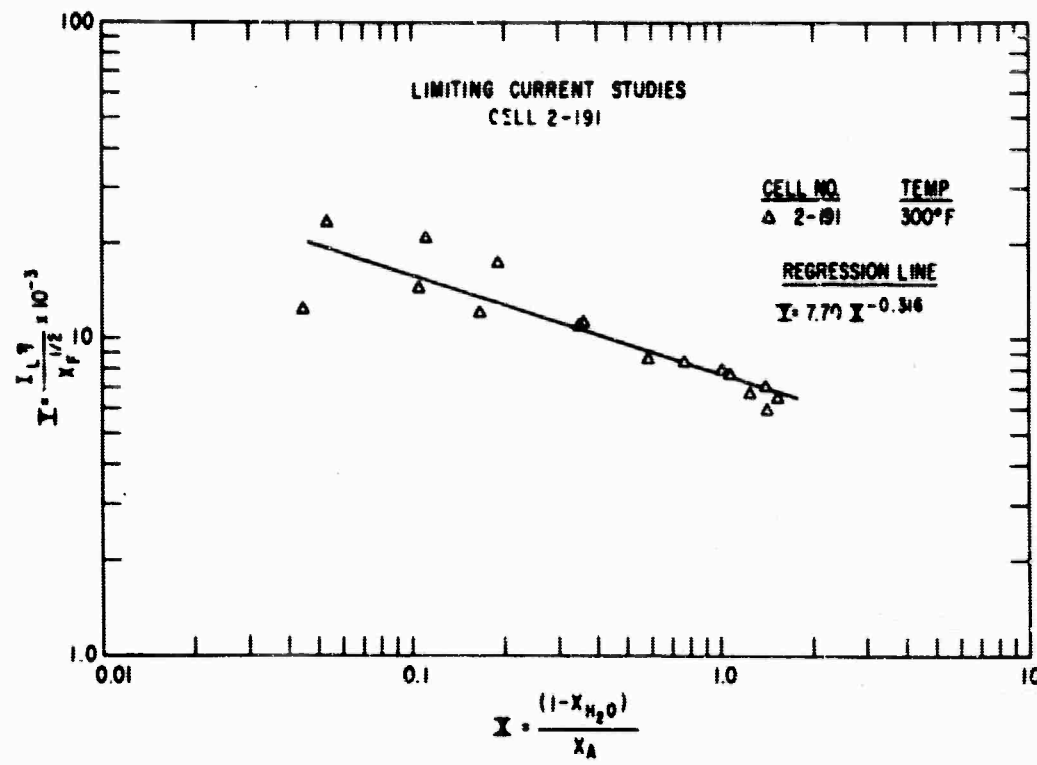


Fig. 2 Correlation of Limiting Current with Operating Parameters

c.



d.

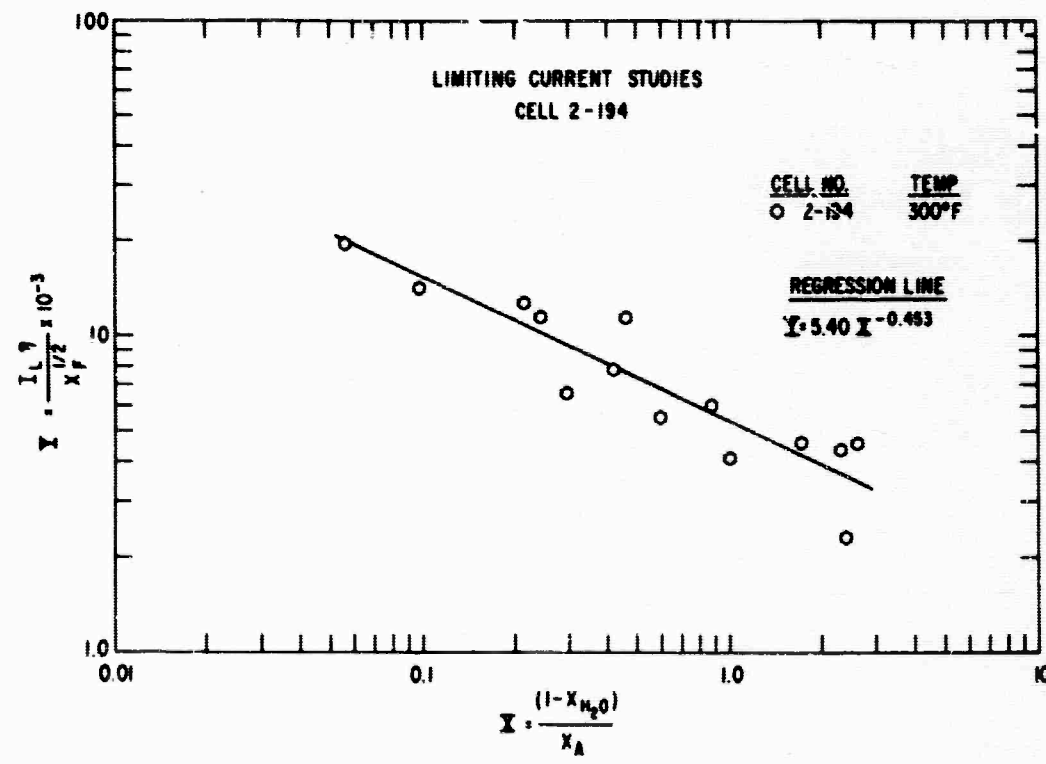


Fig. 2 (Cont.)

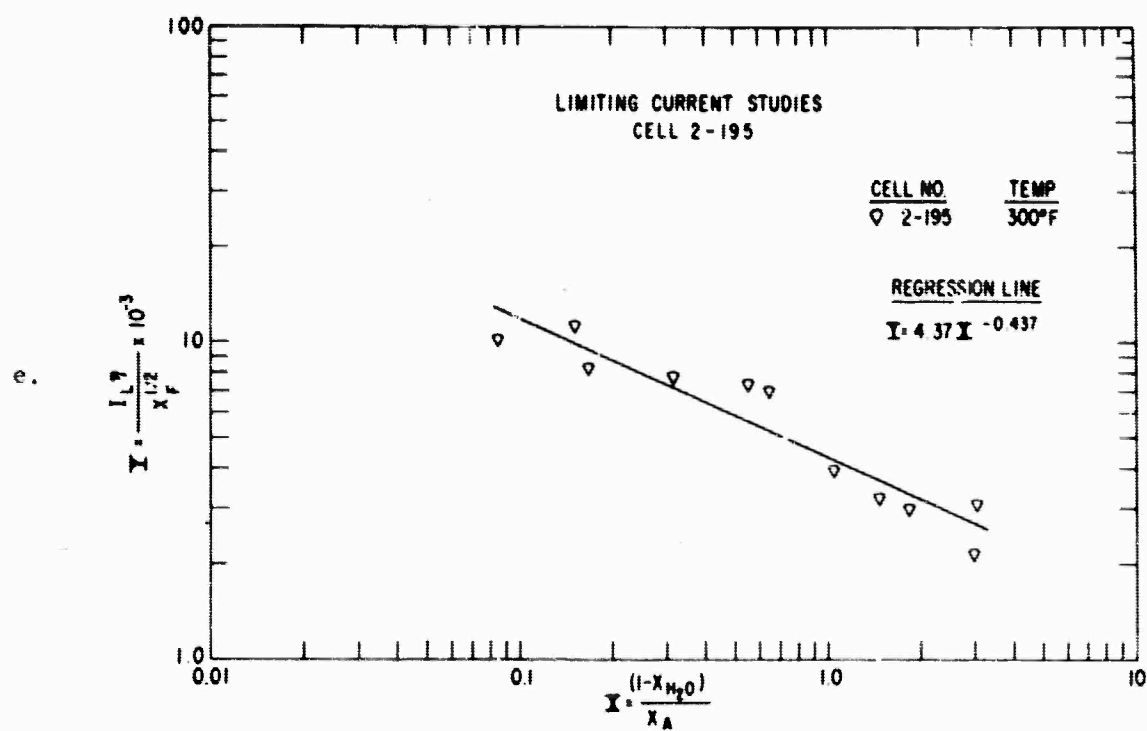
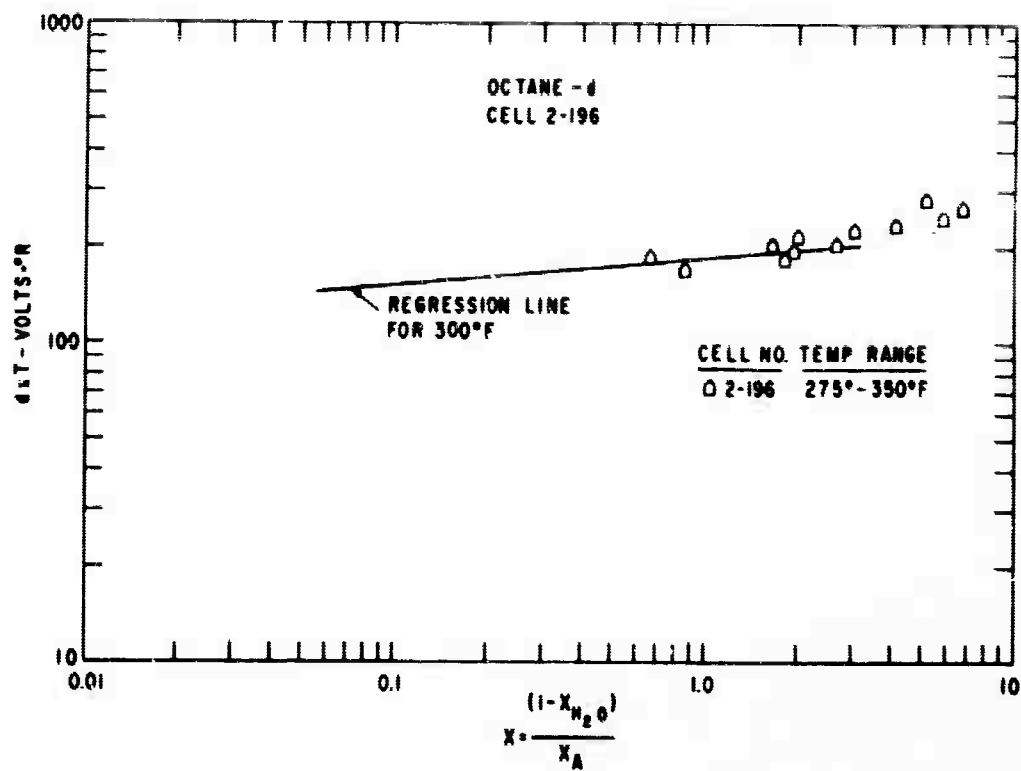


Fig. 2 (Cont)

a.



b.

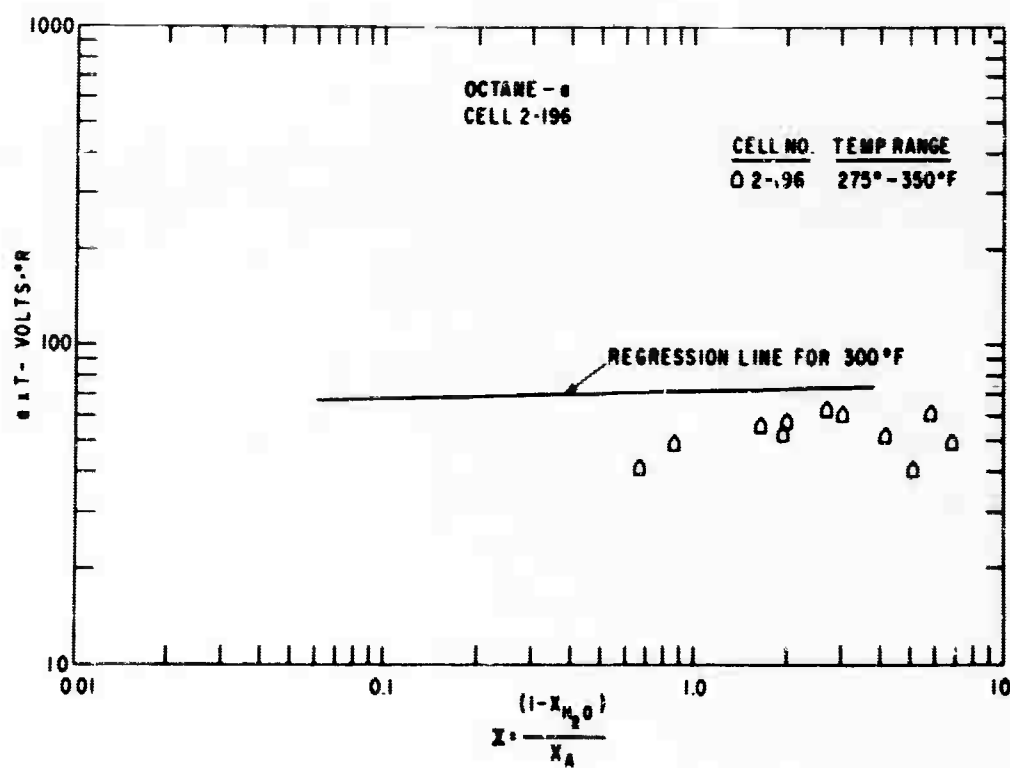


Fig. 3 Temperature Variation on the Over-Voltage

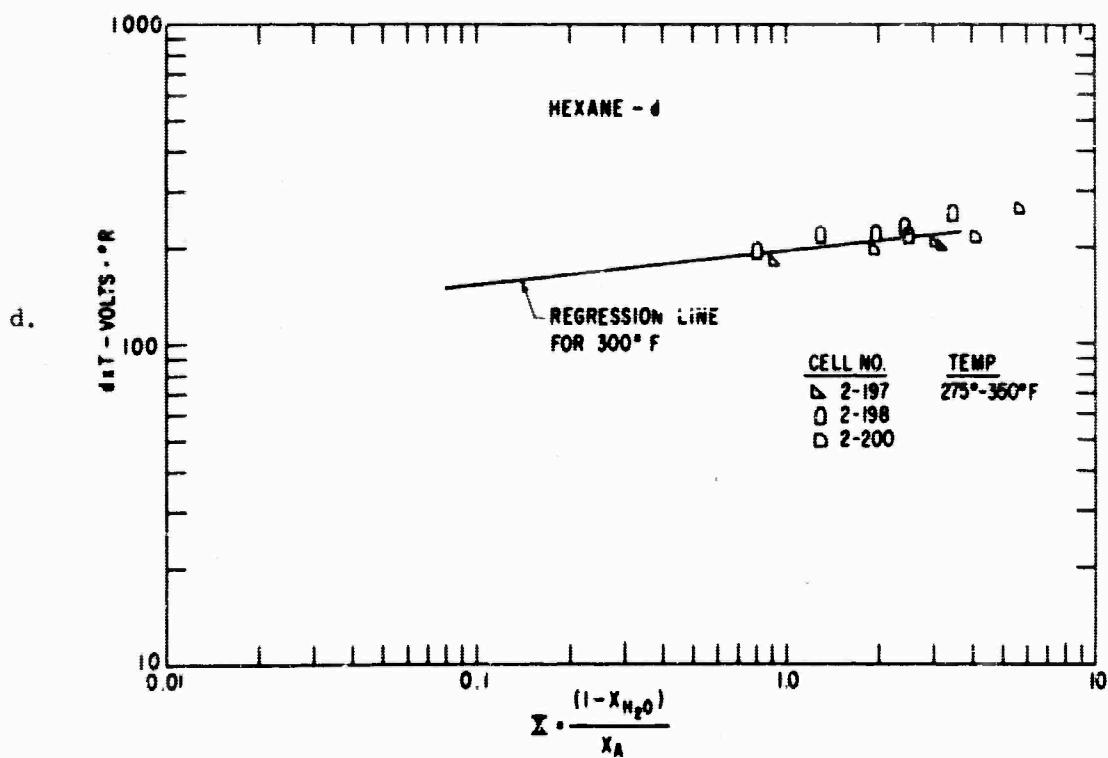
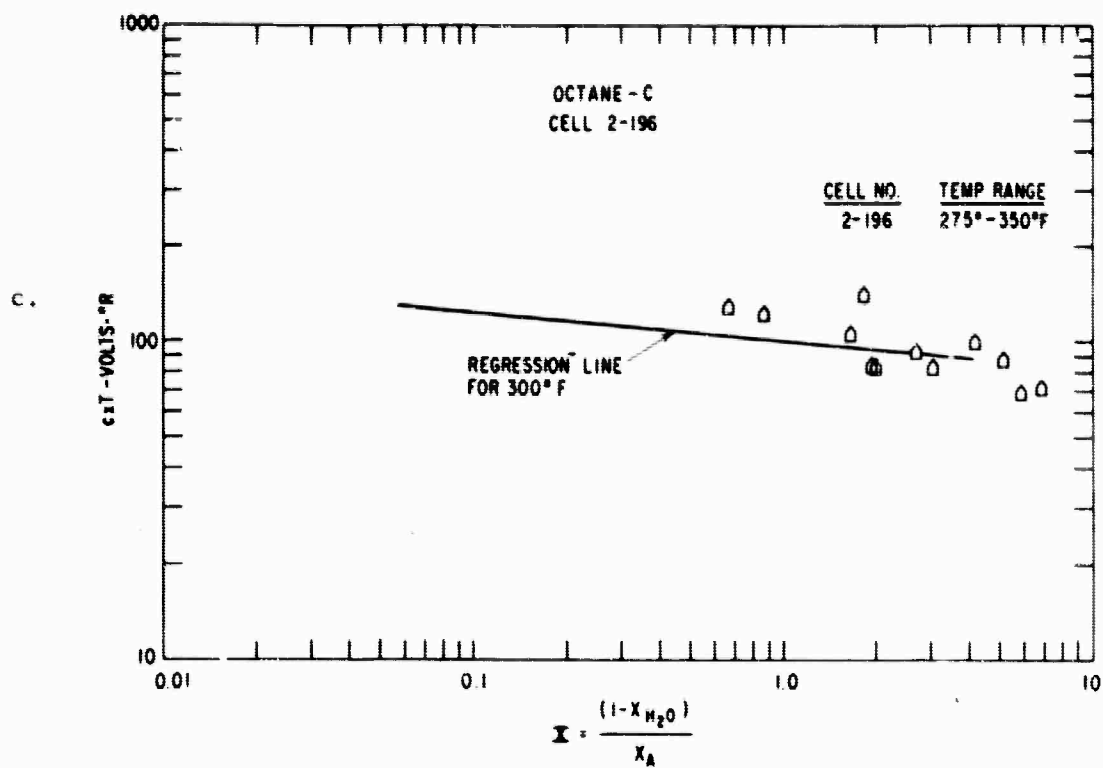


Fig. 3 (Cont.)

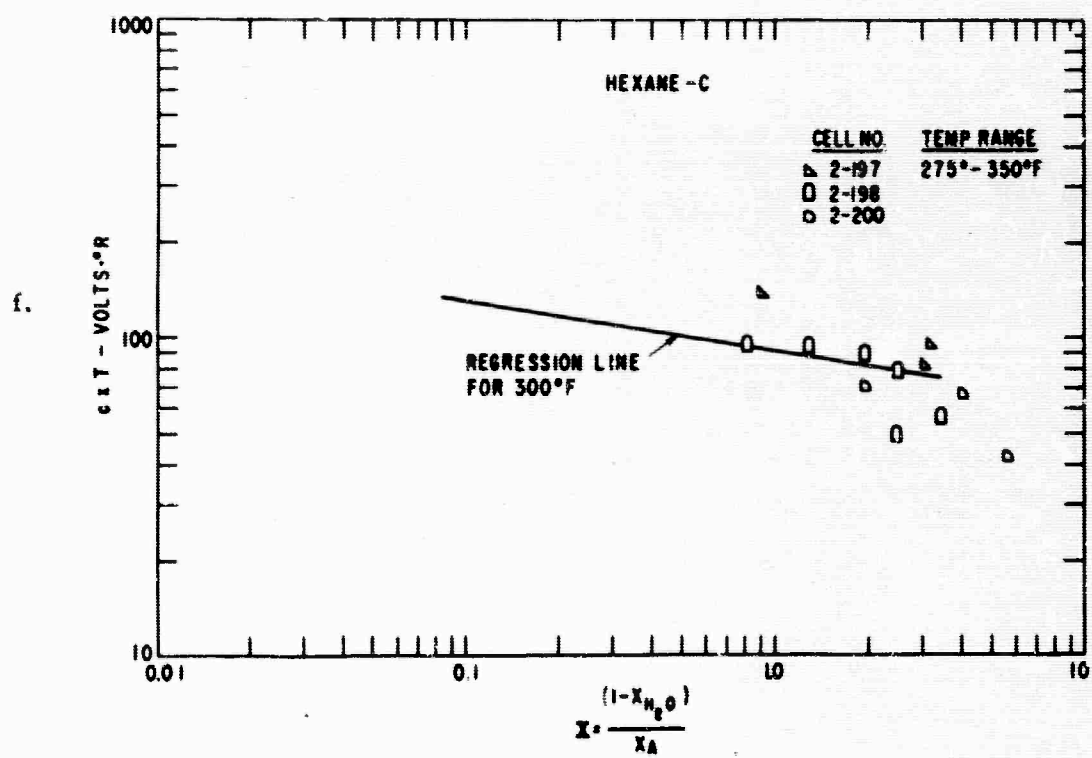
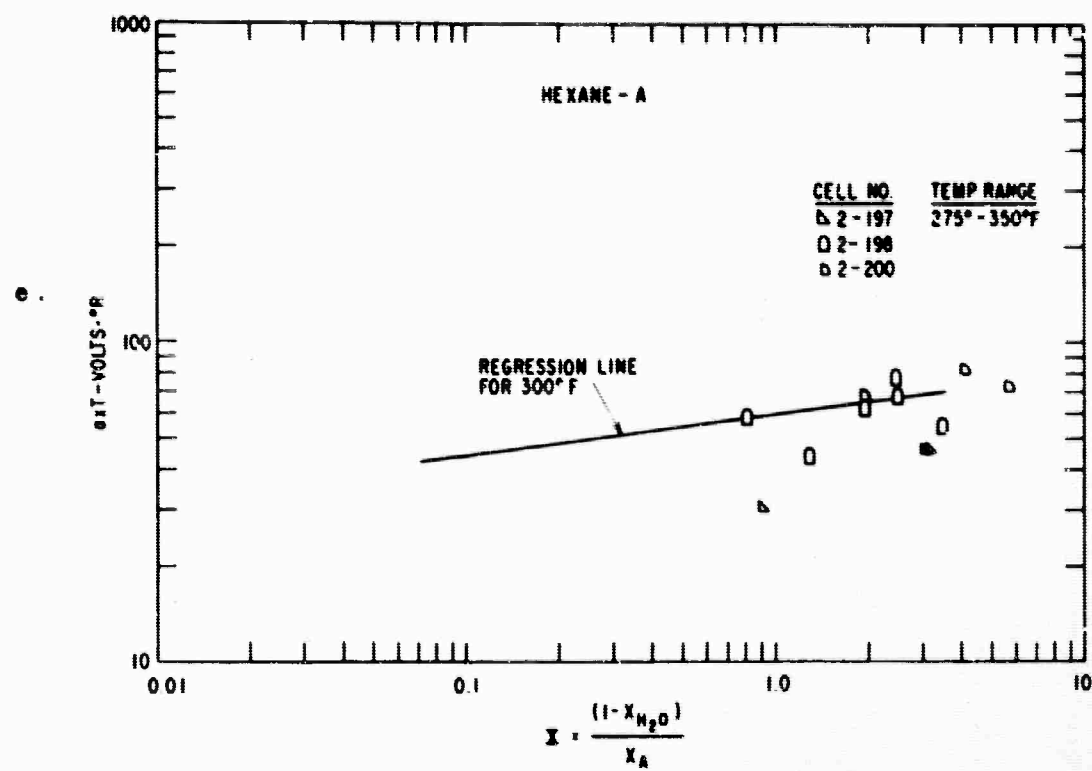


Fig. 3 (Cont.)

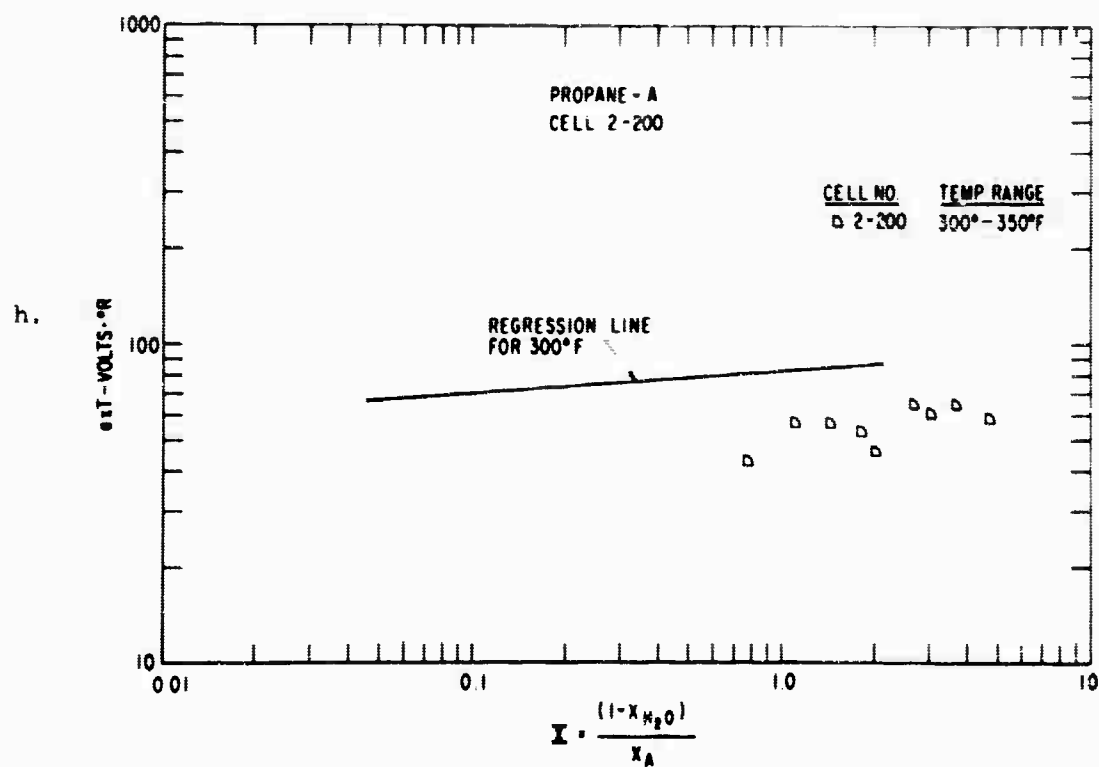
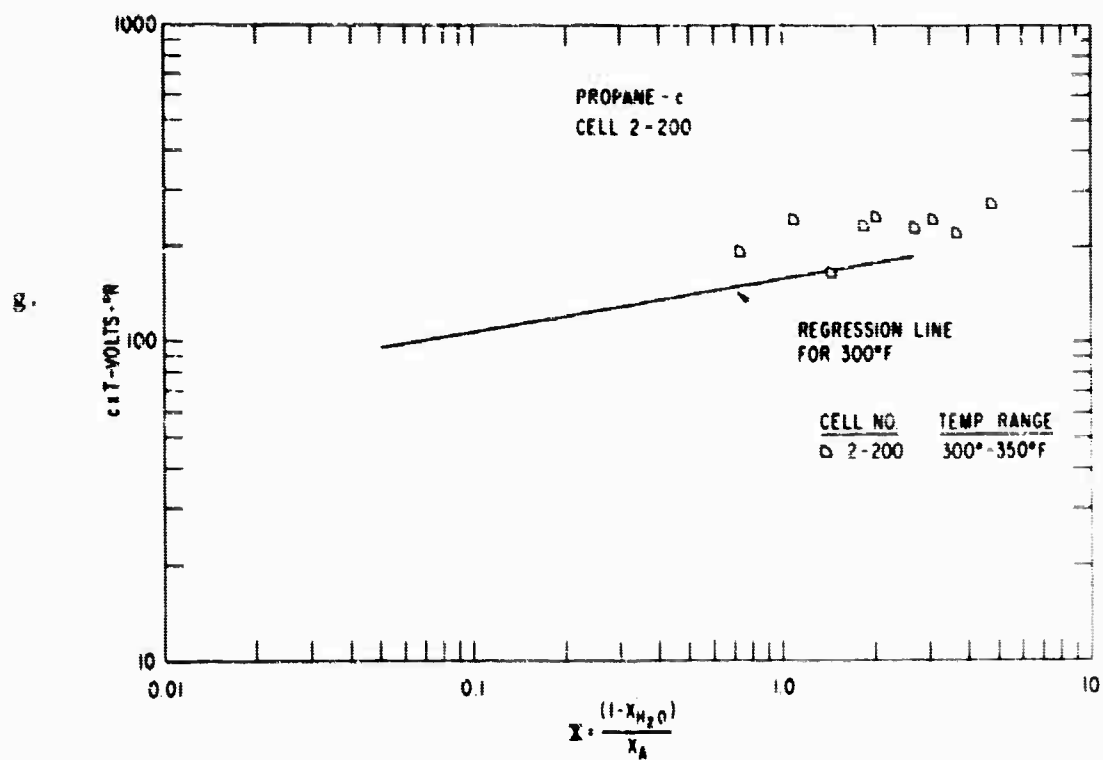
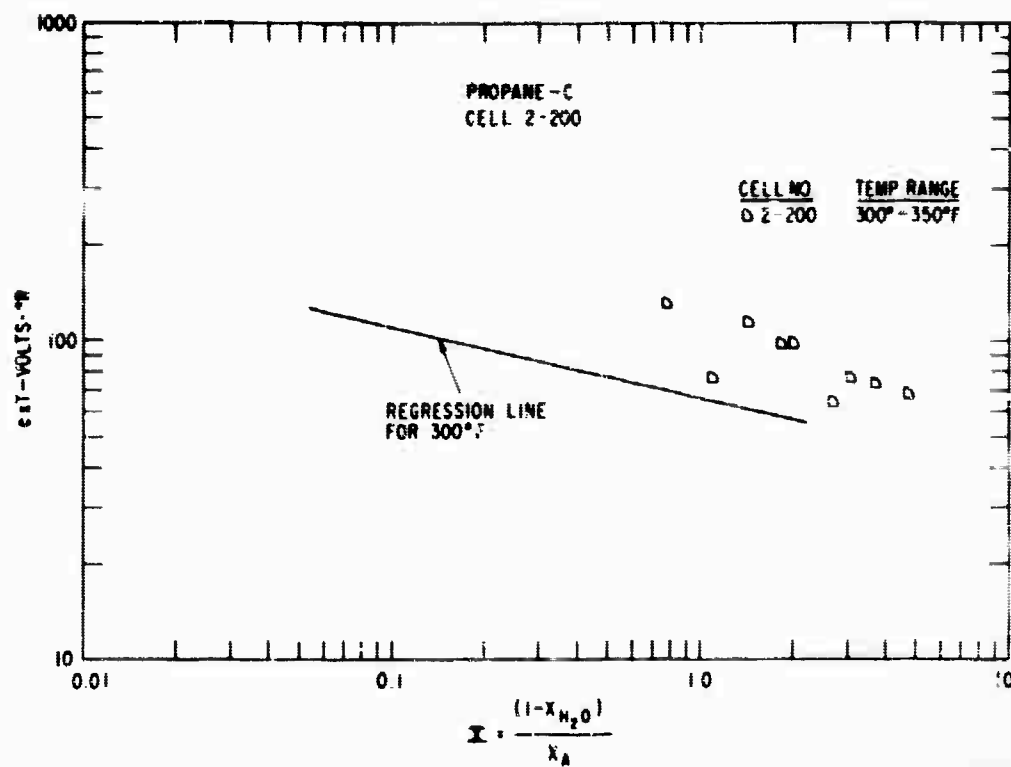


Fig. 3 (Cont.)

i.



j.

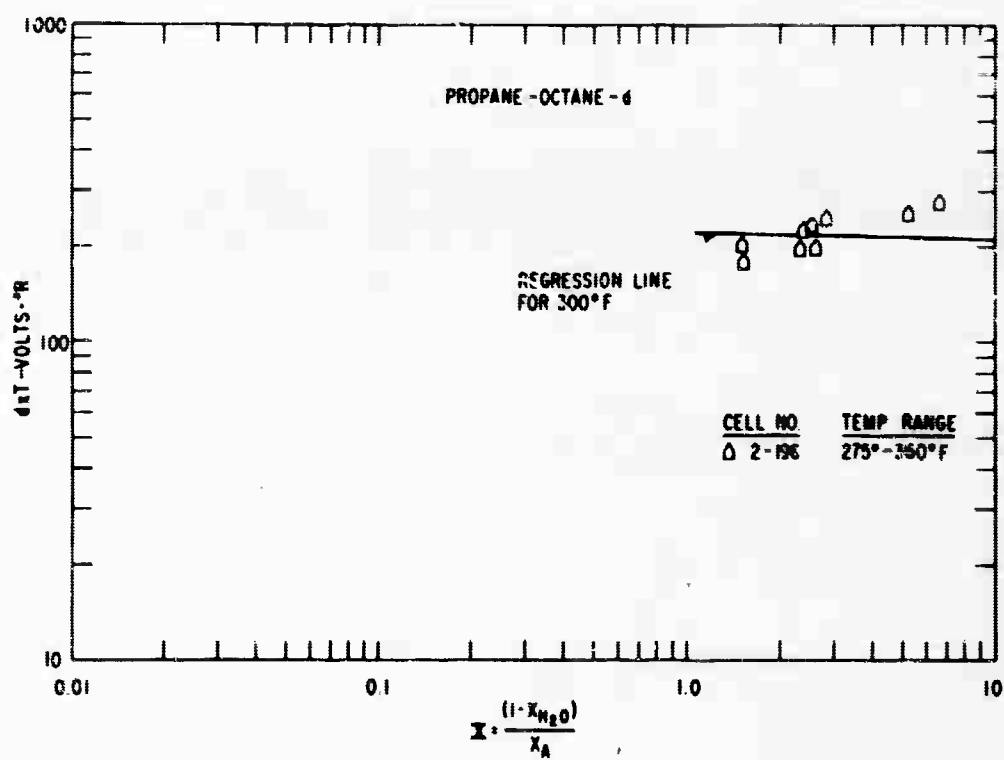


Fig. 3 (Cont.)

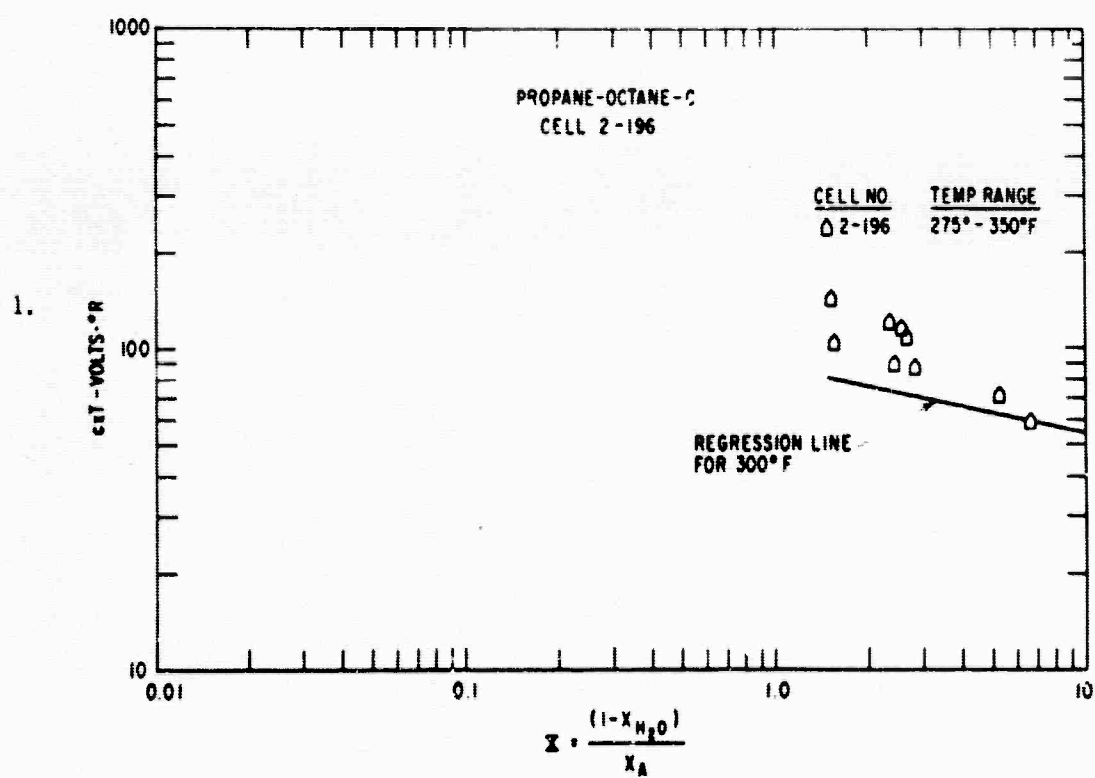
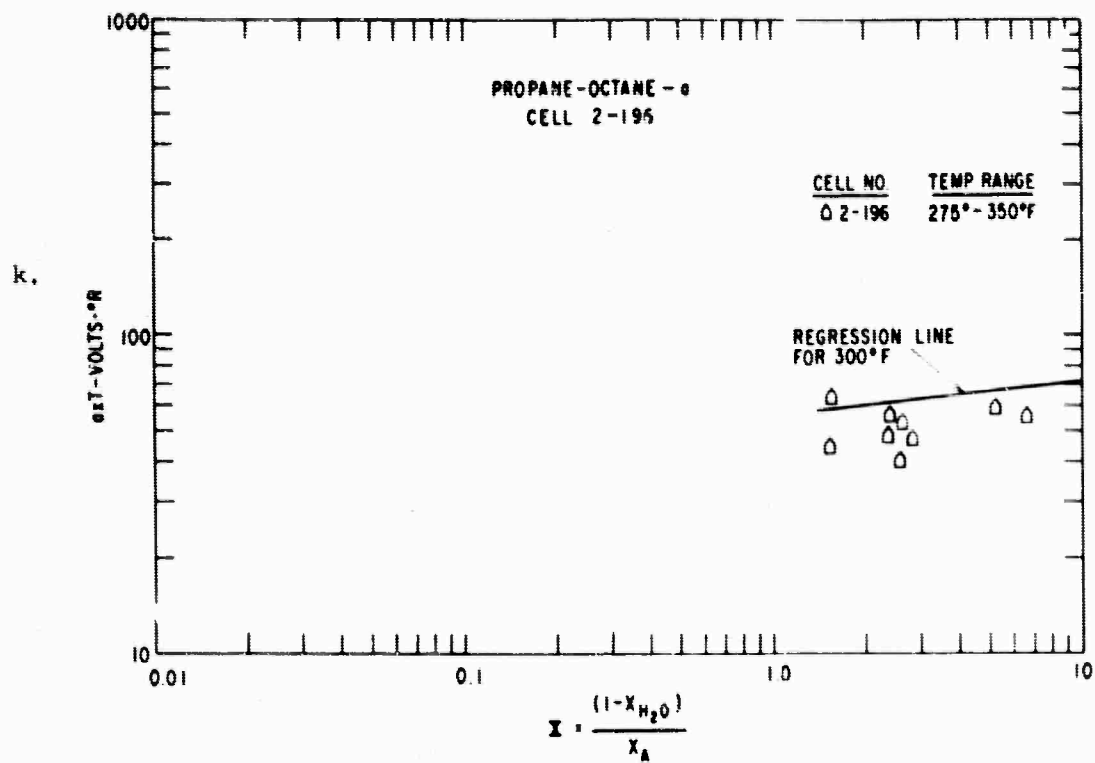


Fig. 3 (Cont.)

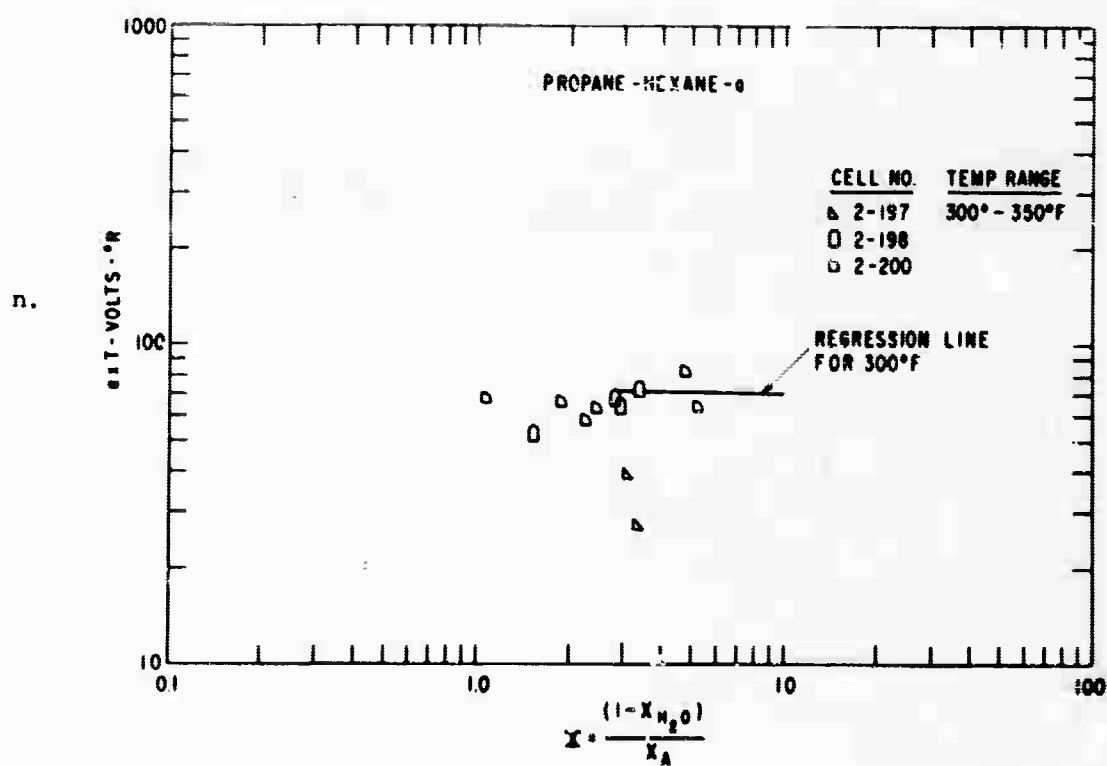
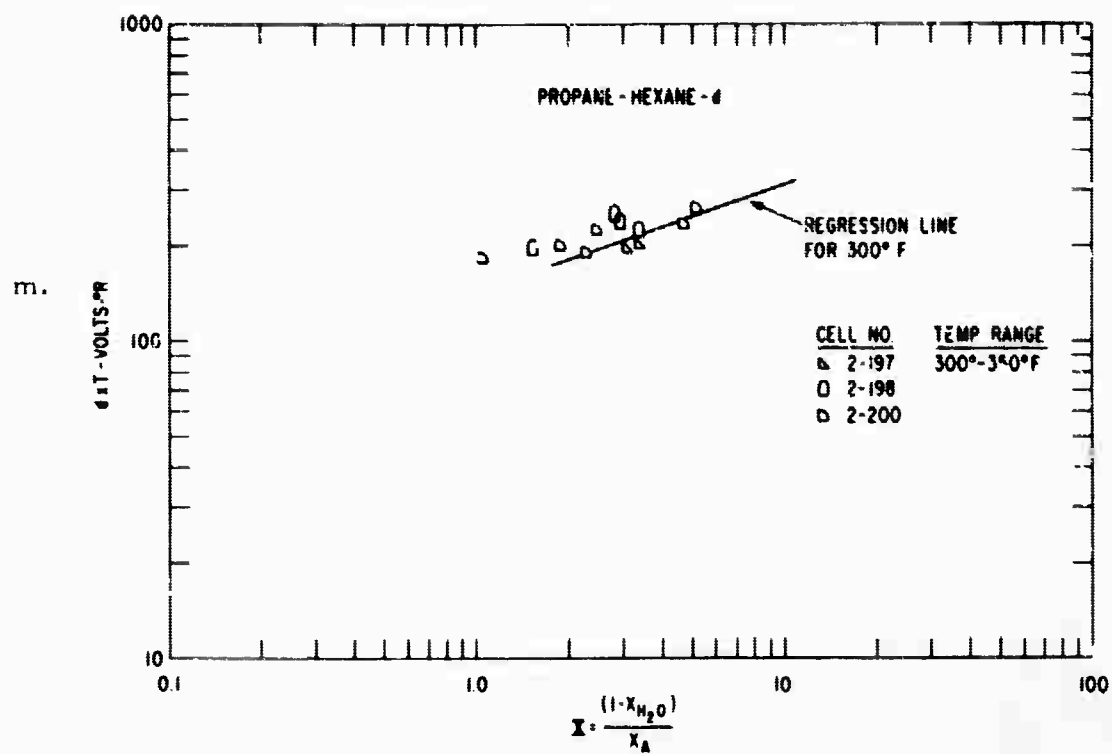


Fig. 3 (Cont.)

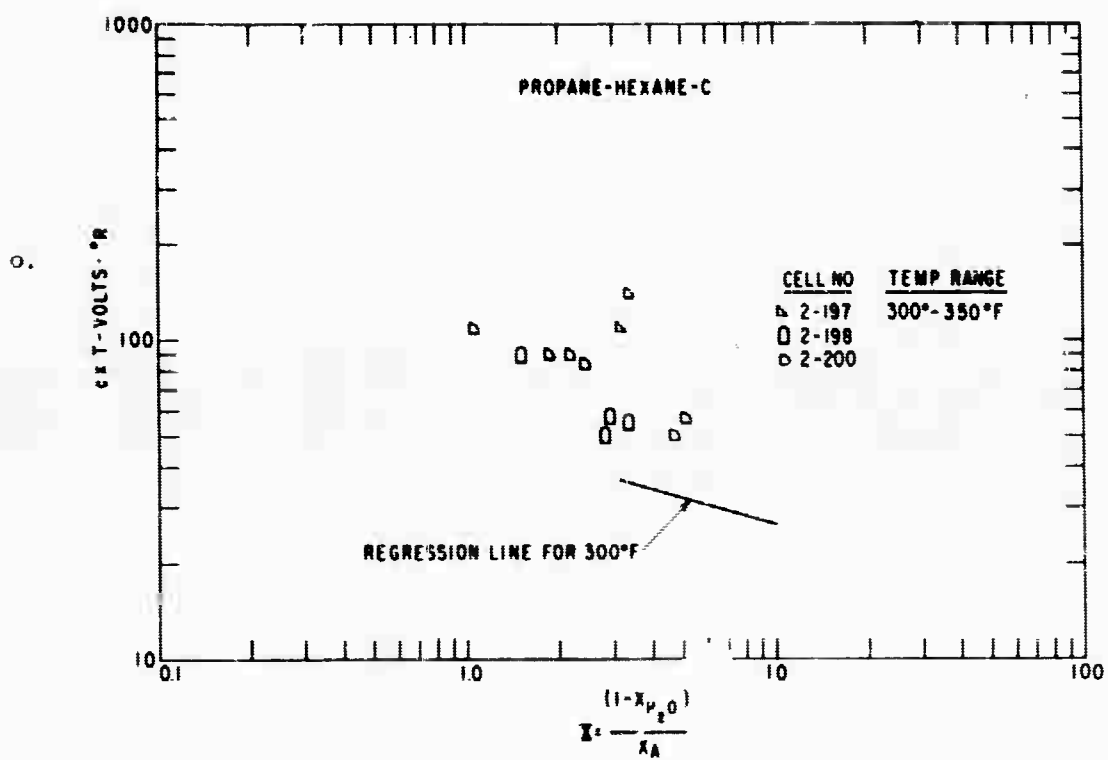


Fig. 3 (Cont.)

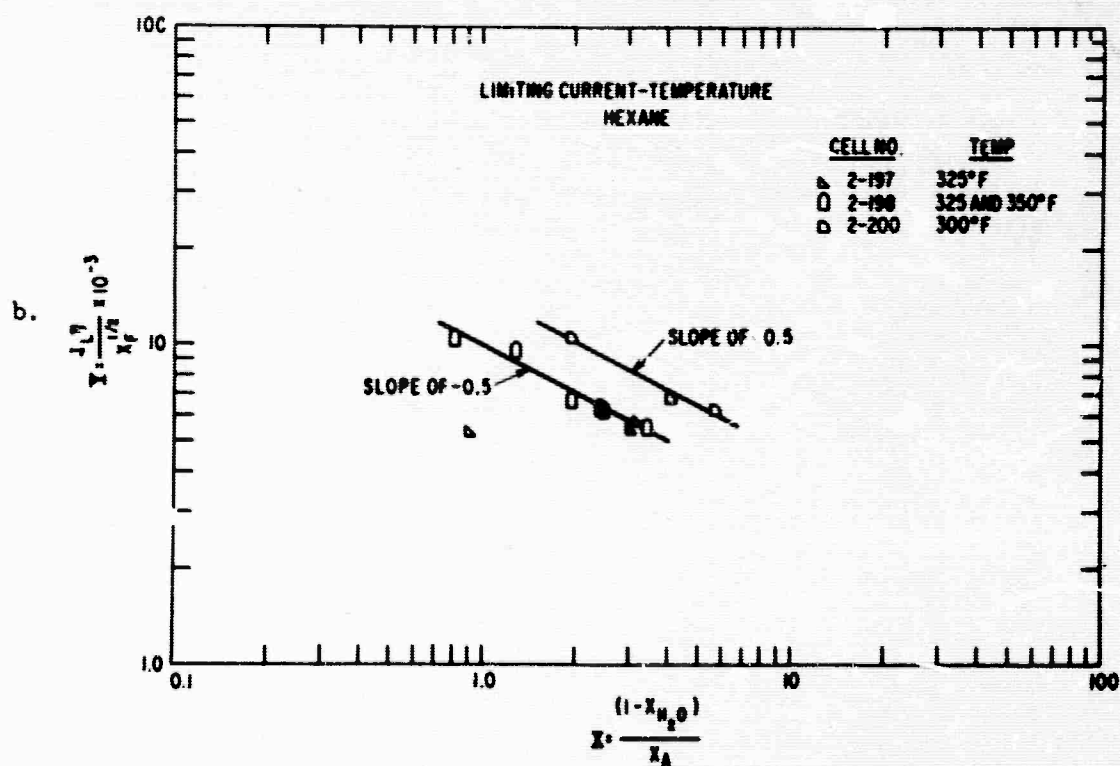
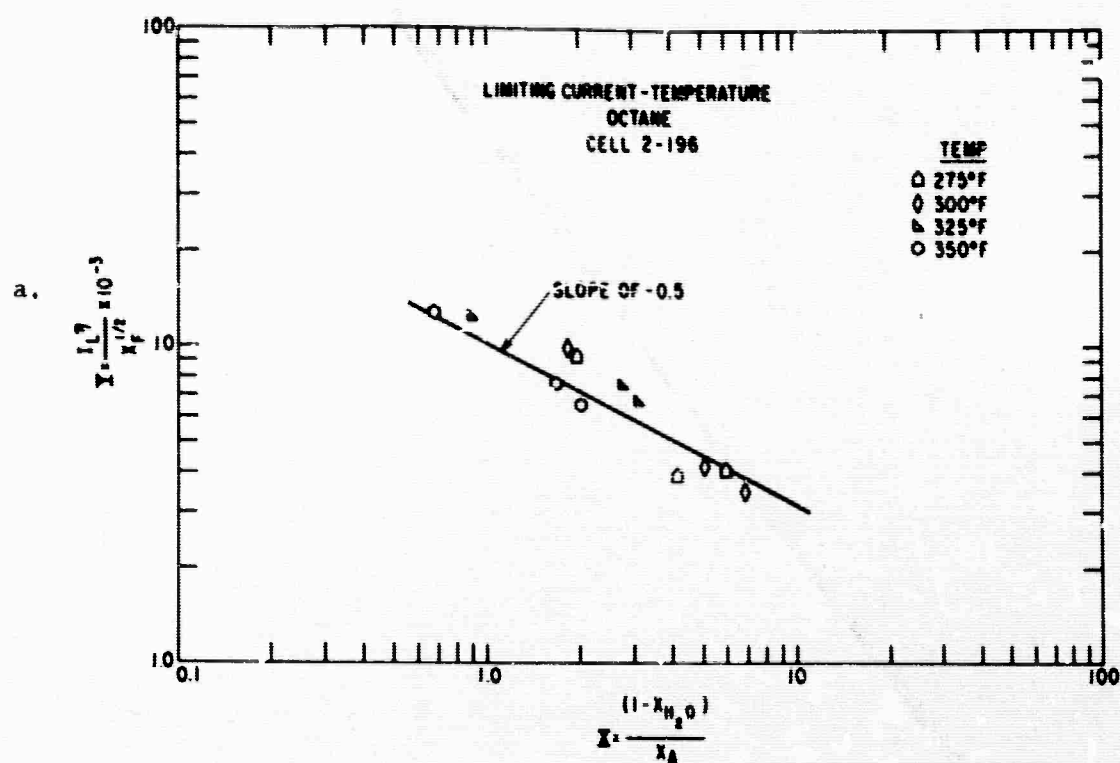


Fig. 4 Temperature Variation on the Limiting Current

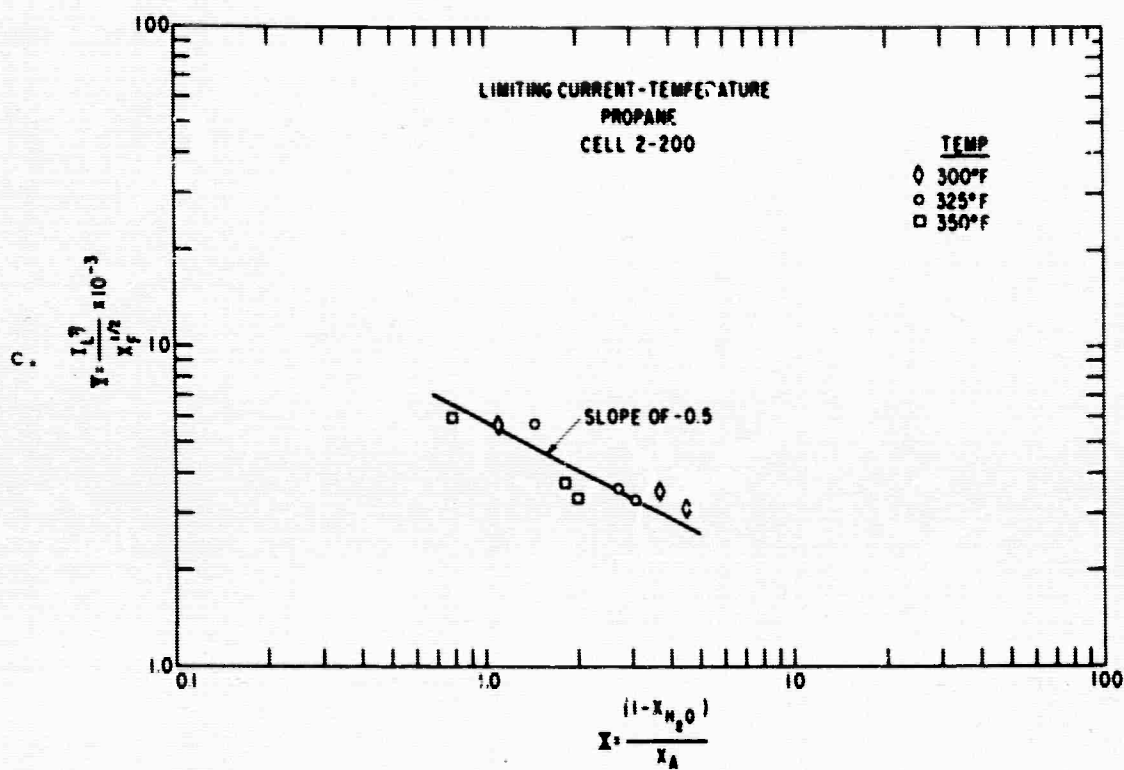


Fig. 4 (Cont.)

AD- _____ Accession No. _____	UNCLASSIFIED
<p>Direct Energy Conversion Operation, General Electric Company, Lynn, Massachusetts</p> <p>HYDROCARBON-AIR FUEL CELLS, TECHNICAL SUMMARY REPORT NO. 6, 1 July 1964-31 December, 1964, 355 p. incl. illus., tables. Contract Nos. DA 44-009-ENG-4909 and DA 44-009-AMC-479(T). ARPA Order No. 247. Unclassified Report.</p> <p>Detailed information is presented on a continuing re- search and development program to develop a direct hydrocarbon oxidation-air fuel cell technology. Current work included research on electrochemical oxidation processes, electrocatalysts, electrolytes, electrode structures, fuel cell life testing, and studies of self- sustaining operation. Multi-pulse potentiodynamic tech- niques have been further developed for analyzing hydro- carbon surface processes. Performance of fuel cell systems with hydrogen fluoride and cesium fluoride electrolytes have been studied for high performance</p>	<p>1. Fuel Cells 2. Liquid Electrolytes 3. Hydrocarbon Oxidation</p> <p>I. Contract Nos. DA 44-009-ENG-4909 DA 44-009-AMC-479(T) ARPA Order No. 247</p> <p>II. U.S. Army-E.R.D. L. III. General Electric Company, Direct Conversion Opera- tion, Lynn, Mass.</p>

AD- _____ Accession No. _____	UNCLASSIFIED
<p>Direct Energy Conversion Operation, General Electric Company, Lynn, Massachusetts</p> <p>HYDROCARBON-AIR FUEL CELLS, TECHNICAL SUMMARY REPORT NO. 6, 1 July 1964-31 December, 1964, 355 p. incl. illus., tables. Contract Nos. DA 44-009-ENG-4909 and DA 44-009-AMC-479(T). ARPA Order No. 247. Unclassified Report.</p> <p>Detailed information is presented on a continuing re- search and development program to develop a direct hydrocarbon oxidation-air fuel cell technology. Current work included research on electrochemical oxidation processes, electrocatalysts, electrolytes, electrode structures, fuel cell life testing, and studies of self- sustaining operation. Multi-pulse potentiodynamic tech- niques have been further developed for analyzing hydro- carbon surface processes. Performance of fuel cell systems with hydrogen fluoride and cesium fluoride electrolytes have been studied for high performance</p>	<p>1. Fuel Cells 2. Liquid Electrolytes 3. Hydrocarbon Oxidation</p> <p>I. Contract Nos. DA 44-009-ENG-4909 DA 44-009-AMC-479(T) ARPA Order No. 247</p> <p>II. U.S. Army-E.R.D. L. III. General Electric Company, Direct Conversion Opera- tion, Lynn, Mass.</p>

AD- _____ Accession No. _____	UNCLASSIFIED
<p>Direct Energy Conversion Operation, General Electric Company, Lynn, Massachusetts</p> <p>HYDROCARBON-AIR FUEL CELLS, TECHNICAL SUMMARY REPORT NO. 6, 1 July 1964-31 December, 1964, 355 p. incl. illus., tables. Contract Nos. DA 44-009-ENG-4909 and DA 44-009-AMC-479(T). ARPA Order No. 247. Unclassified Report.</p> <p>Detailed information is presented on a continuing re- search and development program to develop a direct hydrocarbon oxidation-air fuel cell technology. Current work included research on electrochemical oxidation processes, electrocatalysts, electrolytes, electrode structures, fuel cell life testing, and studies of self- sustaining operation. Multi-pulse potentiodynamic tech- niques have been further developed for analyzing hydro- carbon surface processes. Performance of fuel cell systems with hydrogen fluoride and cesium fluoride electrolytes have been studied for high performance</p>	<p>1. Fuel Cells 2. Liquid Electrolytes 3. Hydrocarbon Oxidation</p> <p>I. Contract Nos. DA 44-009-ENG-4909 DA 44-009-AMC-479(T) ARPA Order No. 247</p> <p>II. U.S. Army-E.R.D. L. III. General Electric Company, Direct Conversion Opera- tion, Lynn, Mass.</p>

AD- _____ Accession No. _____	UNCLASSIFIED
<p>Direct Energy Conversion Operation, General Electric Company, Lynn, Massachusetts</p> <p>HYDROCARBON-AIR FUEL CELLS, TECHNICAL SUMMARY REPORT NO. 6, 1 July 1964-31 December, 1964, 355 p. incl. illus., tables. Contract Nos. DA 44-009-ENG-4909 and DA 44-009-AMC-479(T). ARPA Order No. 247. Unclassified Report.</p> <p>Detailed information is presented on a continuing re- search and development program to develop a direct hydrocarbon oxidation-air fuel cell technology. Current work included research on electrochemical oxidation processes, electrocatalysts, electrolytes, electrode structures, fuel cell life testing, and studies of self- sustaining operation. Multi-pulse potentiodynamic tech- niques have been further developed for analyzing hydro- carbon surface processes. Performance of fuel cell systems with hydrogen fluoride and cesium fluoride electrolytes have been studied for high performance</p>	<p>1. Fuel Cells 2. Liquid Electrolytes 3. Hydrocarbon Oxidation</p> <p>I. Contract Nos. DA 44-009-ENG-4909 DA 44-009-AMC-479(T) ARPA Order No. 247</p> <p>II. U.S. Army-E.R.D. L. III. General Electric Company, Direct Conversion Opera- tion, Lynn, Mass.</p>

AD-

hydrocarbon oxidation. Boron carbide has been successfully employed as a substrate for high surface area platinum, and the results and application to Teflon bonded electrodes are reported. A variety of modified Teflon-bonded developmental electrodes were evaluated including the initial results of asbestos reinforced Teflon. Performance and electrode life in excess of 3000 hours on best electrodes are reported for a variety of hydrocarbon fuels. Studies to define the requirements for self-sustaining operation are also included.

UNCLASSIFIED

AD-

hydrocarbon oxidation. Boron carbide has been successfully employed as a substrate for high surface area platinum, and the results and application to Teflon bonded electrodes are reported. A variety of modified Teflon-bonded developmental electrodes were evaluated including the initial results of asbestos reinforced Teflon. Performance and electrode life in excess of 3000 hours on best electrodes are reported for a variety of hydrocarbon fuels. Studies to define the requirements for self-sustaining operation are also included.

UNCLASSIFIED

AD-

hydrocarbon oxidation. Boron carbide has been successfully employed as a substrate for high surface area platinum, and the results and application to Teflon bonded electrodes are reported. A variety of modified Teflon-bonded developmental electrodes were evaluated including the initial results of asbestos reinforced Teflon. Performance and electrode life in excess of 3000 hours on best electrodes are reported for a variety of hydrocarbon fuels. Studies to define the requirements for self-sustaining operation are also included.

UNCLASSIFIED

AD-

hydrocarbon oxidation. Boron carbide has been successfully employed as a substrate for high surface area platinum, and the results and application to Teflon bonded electrodes are reported. A variety of modified Teflon-bonded developmental electrodes were evaluated including the initial results of asbestos reinforced Teflon. Performance and electrode life in excess of 3000 hours on best electrodes are reported for a variety of hydrocarbon fuels. Studies to define the requirements for self-sustaining operation are also included.

UNCLASSIFIED

AD- _____ Accession No. _____	UNCLASSIFIED
<p>Direct Energy Conversion Operation, General Electric Company, Lynn, Massachusetts</p> <p>HYDROCARBON-AIR FUEL CELLS, TECHNICAL SUMMARY REPORT NO. 6, 1 July 1964-31 December, 1964. 355 p. incl. illus., tables. Contract Nos. DA 44-009-ENG-4909 and DA 44-009-AMC-479(T). ARPA Order No. 247. Unclassified Report.</p> <p>Detailed information is presented on a continuing re- search and development program to develop a direct hydrocarbon oxidation-air fuel cell technology. Current work included research on electrochemical oxidation processes, electrocatalysts, electrolytes, electrode structures, fuel cell life testing, and studies of self- sustaining operation. Multi-pulse potentiodynamic tech- niques have been further developed for analyzing hydro- carbon surface processes. Performance of fuel cell systems with hydrogen fluoride and cesium fluoride electrolytes have been studied for high performance</p>	<p>1. Fuel Cells</p> <p>2. Liquid Electrolytes</p> <p>3. Hydrocarbon Oxidation</p> <p>I. Contract Nos. DA 44-009-ENG-4909 DA 44-009-AMC-479(T) ARPA Order No. 247</p> <p>II. U.S. Army-E. R. D. L.</p> <p>III. General Electric Company, Direct Conversion Opera- tion, Lynn, Mass.</p>

AD- _____ Accession No. _____	UNCLASSIFIED
<p>Direct Energy Conversion Operation, General Electric Company, Lynn, Massachusetts</p> <p>HYDROCARBON-AIR FUEL CELLS, TECHNICAL SUMMARY REPORT NO. 6, 1 July 1964-31 December, 1964. 355 p. incl. illus., tables. Contract Nos. DA 44-009-ENG-4909 and DA 44-009-AMC-479(T). ARPA Order No. 247. Unclassified Report.</p> <p>Detailed information is presented on a continuing re- search and development program to develop a direct hydrocarbon oxidation-air fuel cell technology. Current work included research on electrochemical oxidation processes, electrocatalysts, electrolytes, electrode structures, fuel cell life testing, and studies of self- sustaining operation. Multi-pulse potentiodynamic tech- niques have been further developed for analyzing hydro- carbon surface processes. Performance of fuel cell systems with hydrogen fluoride and cesium fluoride electrolytes have been studied for high performance</p>	<p>1. Fuel Cells</p> <p>2. Liquid Electrolytes</p> <p>3. Hydrocarbon Oxidation</p> <p>I. Contract Nos. DA 44-009-ENG-4909 DA 44-009-AMC-479(T) ARPA Order No. 247</p> <p>II. U.S. Army-E. R. D. L.</p> <p>III. General Electric Company, Direct Conversion Opera- tion, Lynn, Mass.</p>

AD- _____ Accession No. _____	UNCLASSIFIED
<p>Direct Energy Conversion Operation, General Electric Company, Lynn, Massachusetts</p> <p>HYDROCARBON-AIR FUEL CELLS, TECHNICAL SUMMARY REPORT NO. 6, 1 July 1964-31 December, 1964. 355 p. incl. illus., tables. Contract Nos. DA 44-009-ENG-4909 and DA 44-009-AMC-479(T). ARPA Order No. 247. Unclassified Report.</p> <p>Detailed information is presented on a continuing re- search and development program to develop a direct hydrocarbon oxidation-air fuel cell technology. Current work included research on electrochemical oxidation processes, electrocatalysts, electrolytes, electrode structures, fuel cell life testing, and studies of self- sustaining operation. Multi-pulse potentiodynamic tech- niques have been further developed for analyzing hydro- carbon surface processes. Performance of fuel cell systems with hydrogen fluoride and cesium fluoride electrolytes have been studied for high performance</p>	<p>1. Fuel Cells</p> <p>2. Liquid Electrolytes</p> <p>3. Hydrocarbon Oxidation</p> <p>I. Contract Nos. DA 44-009-ENG-4909 DA 44-009-AMC-479(T) ARPA Order No. 247</p> <p>II. U.S. Army-E. R. D. L.</p> <p>III. General Electric Company, Direct Conversion Opera- tion, Lynn, Mass.</p>

AD- _____ Accession No. _____	UNCLASSIFIED
<p>Direct Energy Conversion Operation, General Electric Company, Lynn, Massachusetts</p> <p>HYDROCARBON-AIR FUEL CELLS, TECHNICAL SUMMARY REPORT NO. 6, 1 July 1964-31 December, 1964. 355 p. incl. illus., tables. Contract Nos. DA 44-009-ENG-4909 and DA 44-009-AMC-479(T). ARPA Order No. 247. Unclassified Report.</p> <p>Detailed information is presented on a continuing re- search and development program to develop a direct hydrocarbon oxidation-air fuel cell technology. Current work included research on electrochemical oxidation processes, electrocatalysts, electrolytes, electrode structures, fuel cell life testing, and studies of self- sustaining operation. Multi-pulse potentiodynamic tech- niques have been further developed for analyzing hydro- carbon surface processes. Performance of fuel cell systems with hydrogen fluoride and cesium fluoride electrolytes have been studied for high performance</p>	<p>1. Fuel Cells</p> <p>2. Liquid Electrolytes</p> <p>3. Hydrocarbon Oxidation</p> <p>I. Contract Nos. DA 44-009-ENG-4909 DA 44-009-AMC-479(T) ARPA Order No. 247</p> <p>II. U.S. Army-E. R. D. L.</p> <p>III. General Electric Company, Direct Conversion Opera- tion, Lynn, Mass.</p>